ASME
SETTING THE STANDARD

Transactions of the ASME, Journal of Applied Mechanics (ISSN 0021-8936) is published bimonthly (Jan., Mar., May, July, Sept., Nov.) by The American Society of Mechanical Engineers, Three Park Avenue, New York, NY 10016. Periodicals postage paid at New York, NY and additional mailing offices. POSTMASTER: Send address changes to Transactions of the ASME, Journal of Applied Mechanics, c/o THE AMERICAN SOCIETY OF MECHANICAL ENGINEERS, 22 Law Drive, Box 2300, Fairfield, NJ 07007-2300. **CHANGES OF ADDRESS** must be received at Society headquarters seven weeks before they are to be effective. Please send old label and new address.

Journal of Applied Mechanics

Published Bimonthly by ASME

VOLUME 77 • NUMBER 1 • JANUARY 2010

RESEARCH PAPERS

(Contents continued on inside back cover)

This journal is printed on acid-free paper, which exceeds the ANSI Z39.48-1992 specification for permanence of paper and library materials. ♾™
♻ 85% recycled content, including 10% post-consumer fibers.

Journal of Applied Mechanics Volume 77, Number 1 JANUARY 2010

TECHNICAL BRIEFS

The ASME Journal of Applied Mechanics is abstracted and indexed in the following:

Alloys Index, Aluminum Industry Abstracts, Applied Science & Technology Index, Ceramic Abstracts, Chemical Abstracts, Civil Engineering Abstracts, Compendex (The electronic equivalent of Engineering Index), Computer & Information Systems Abstracts, Corrosion Abstracts, Current Contents, EEA (Earthquake Engineering Abstracts Database), Electronics & Communications Abstracts Journal, Engineered Materials Abstracts, Engineering Index, Environmental Engineering Abstracts, Environmental Science and Pollution Management, Fluidex, Fuel & Energy Abstracts, GeoRef, Geotechnical Abstracts, INSPEC, International Aerospace Abstracts, Journal of Ferrocement, Materials Science Citation Index, Mechanical Engineering Abstracts, METADEX (The electronic equivalent of Metals Abstracts and Alloys Index), Metals Abstracts, Nonferrous Metals Alert, Polymers Ceramics Composites Alert, Referativnyi Zhurnal, Science Citation Index, SciSearch (Electronic equivalent of Science Citation Index), Shock and Vibration Digest, Solid State and Superconductivity Abstracts, Steels Alert, Zentralblatt MATH

The Flexural Instability of Spinning Flexible Cylinder Partially Filled With Viscous Liquid

R. D. Firouz-Abadi
e-mail: firouzabadi@sharif.edu

H. Haddadpour
e-mail: haddadpour@sharif.edu

Department of Aerospace Engineering,
Sharif University of Technology,
Tehran 11155-8639, Iran

This paper deals with the flexural instability of flexible spinning cylinders partially filled with viscous fluid. Using the linearized Navier–Stokes equations for the incompressible flow, a two-dimensional model is developed for fluid motion. The resultant force exerted on the flexible cylinder wall as the result of the fluid motion is calculated as a function of lateral acceleration of the cylinder axis in the Laplace domain. Applying the Hamilton principle, the governing equations of flexural motion of the rotary flexible cylinder mounted on general viscoelastic supports are derived. Then combining the equations describing the fluid force on the flexible cylinder with the structural dynamics equations, the coupled-field governing equations of the system are obtained. A numerical technique is devised with the obtained model for stability analysis of the flexible cylinder and some examples are presented. The effect of material viscoelasticity and structural damping on the stability margins of the flexible cylinder is examined, and some parameter studies on the governing parameters of the critical spinning speed are carried out.
[DOI: 10.1115/1.3172143]

1 Introduction

The problem of fluid motion in a spinning flexible cylinder is considered as an appealing research field in the fluid mechanics studies. The spinning cylinders conveying liquid have many industrial uses in space vehicles, liquid-cooled gas turbines, and marine and food industries such as milk centrifuges and juice concentration processes. As the consequence of extensive engineering applications, many research projects have been done on the fluid motion and stability in a spinning flexible cylinder conveying liquid. Some of the research works in this issue are brought together in the form of a book chapter by Ibrahim [1] in which he reviewed what had been published concerning rotary sloshing problems to date. The dynamics and stability conditions of undamped rotors partially filled with inviscid fluid were the main subject of many research papers [2–5]. Zhang et al. [6] determined the dynamic stability of a high-spinning liquid-filled rigid rotor with both internal and external damping. The effect of anisotropic elastically damping bearing supports on the stability of rigid rotors partially filled with ideal fluid was investigated by Daich and co-workers [7,8] and Hendricks and Morton [9]. They showed that if the fluid viscosity is not taken into account, the rotor will experience a weak instability in a range of spinning speeds as well as a strong instability for the remaining range. Considering the fluid viscosity, Daich and Bar [7] showed that the weak instability transforms into an asymptotic stability and the strong instability range of spinning speed diminishes. Zhu [10–13] documented some numerical and experimental results on the whirling dynamics and stability of rigid rotors. Zhu analyzed the stability of spinning cylinders partially filled with inviscid or viscous fluid and also studied the effect of anisotropic elastic supports on the instability boundaries. Derendyayev and Soldatov [14] and Derendyaev [15] proposed a discrete model of a rigid rotor system with a fluid and determined the stability condition together with the Hopf bifurcation of cylinders partially filled with liquid. They showed that when the parameters governing the rotor dynamics exceed the stability boundaries, the Andronov–Hopf bifurcation occurs. Tao and Zhang [16] used a perturbation approach to study the motion of a spinning rigid rotor mounted on the elastic supports and partially filled with a viscous liquid. They showed that the smaller the external damping the larger the stable region of spinning speed. Limarchenko [17] considered the nonsteady rotation of a cylindrical storage tank partially filled with a viscous fluid. Berman et al. [18] considered the nonlinear dynamics of the rotor partially filled with viscous fluid and determined the amplitude of the vibration in the main unstable region. Holm-Christenson and Träger [19] employed the Navier–Stokes equations and numerically solved the flow field. Yan and Farouk [20] represented a numerical solution of the time-dependent axisymmetric Navier–Stokes equations using a homogeneous multiphase model. They investigated the spin-up from rest and the steady flow field in a partially filled rotating circular cylinder with an over-rotating lid. Ribando [21] studied the incompressible flow in a rapidly rotating cylinder partially filled with liquid and having a source/sink distribution in the lateral wall. Ribando used a finite-difference method to solve the axisymmetric governing equations of the flow field. Yuichi et al. [22] carried out an experimental study on the stability characteristics of a rigid rotor partially filled with water and examined the effect of discharging liquid by centrifugal force. The vibrations of a liquid partially filling a rotating conical cavity were studied by Khoroshilov [23]. Derendyaev and Senyatkin [24] determined the stability conditions of the steady-state rotation of a cylinder filled with a stratified nonuniform viscous incompressible liquid. Preussner and Kollmann [25] analyzed the stability of a rigid rotor spinning at constant angular velocity and having a cylindrical sectored and fluid filled cavity. They partitioned the cavity into n equal sectors by radially extending walls and assumed that each sector is partially filled with the same amount of an inviscid incompressible fluid.

There are few reports dealing with the flexural instability of spinning flexible cylinder partially filled with liquid in the literature. Tao and Zhang [26] used the model of Zhang et al. [6] for ideal-fluid motion and employed the simply supported Euler–Bernoulli beam as the structural model of the flexible cylinder.

Contributed by the Applied Mechanics Division of ASME for publication in the JOURNAL OF APPLIED MECHANICS. Manuscript received August 30, 2008; final manuscript received June 6, 2009; published online September 23, 2009. Review conducted by Nadine Aubry.

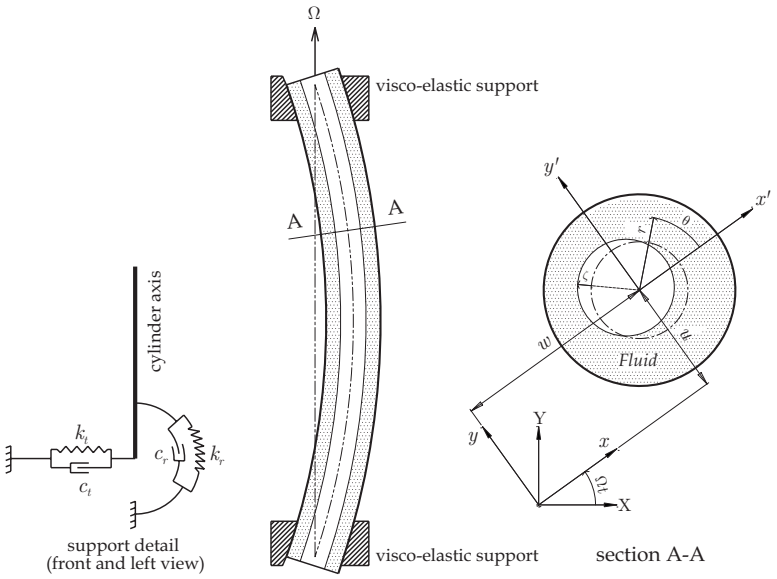

Fig. 1 Schematic of a spinning flexible cylinder partially with liquid

However, their structural model did not involve the Coriolis and inertial terms, which strongly affect the structural dynamics of the spinning flexible cylinder. Firouz-Abadi and Haddadpour [27] derived a general formulation for flexural motion of viscoelastic cylinders partially filled with inviscid fluid and investigated the stability regions of the flexible cylinder.

In the present paper, we propose an analytical model for the flexural vibrations of spinning cylinders partially filled with viscous fluid and mounted on general viscoelastic supports. The coupled-field equations of the structural motion and the fluid dynamics are derived in the Laplace domain. A numerical technique is devised along with the obtained model for stability analysis of the flexural motion of the flexible cylinder and some studies on the effect of governing parameters of the critical spinning speed are carried out.

2 Liquid Sloshing Dynamics

Consider a closed flexible cylinder partially filled with incompressible fluid. The flexible cylinder spins at a constant angular velocity Ω about its longitudinal axis. Assuming that the gravity force is very small as compared with the centrifugal force, the fluid will form an annular ring similar to that shown in Fig. 1. Figure 1 shows a flexible cylinder with general viscoelastic supports at both ends and the support detail in front and left views is shown. The flexural motion of the cylinder is described by u and w, which are measured in the rotating frame xy. From the basic principles of fluid mechanics, it is known that the motion is transmitted by shear stresses to the fluid and after a short time interval it will posses the same angular velocity throughout the cylinder.

Tao and Zhang [26] estimated the orders of magnitude of all terms in the governing equations and boundary conditions of three-dimensional flow in the slender flexible cylinder and showed that the flow can be modeled using a quasi-two-dimensional model. Accordingly, the small motions of the fluid in the rotating frame $x'y'$ can be described by the linearized Navier–Stokes equations as

$$\frac{\partial v_r}{\partial t} - r\Omega^2 - 2\Omega v_\theta + a_{x'}\cos\theta + a_{y'}\sin\theta = -\frac{1}{\rho}\frac{\partial P}{\partial r} + \nu\left(\nabla^2 v_r - \frac{v_r}{r^2} - \frac{2}{r^2}\frac{\partial v_\theta}{\partial \theta}\right) \tag{1}$$

$$\frac{\partial v_\theta}{\partial t} + 2\Omega v_r - a_{x'}\sin\theta + a_{y'}\cos\theta = -\frac{1}{\rho r}\frac{\partial P}{\partial \theta} + \nu\left(\nabla^2 v_\theta - \frac{v_\theta}{r^2} + \frac{2}{r^2}\frac{\partial v_r}{\partial \theta}\right) \tag{2}$$

where v_r and v_θ are the radial and tangential velocity components of fluid particles in the rotating $x'y'$ frame, ρ is the fluid density, P is the total pressure, ν is the kinematic viscosity, and $a_{x'}$ and $a_{y'}$ are the acceleration components of the origin of the $x'y'$ frame. Also, ∇^2 is the Laplacian operator as

$$\nabla^2 = \frac{\partial^2}{\partial^2 r} + \frac{1}{r}\frac{\partial}{\partial r} + \frac{1}{r^2}\frac{\partial^2}{\partial^2 \theta} \tag{3}$$

The continuity equation is

$$\frac{\partial (r v_r)}{\partial r} + \frac{\partial v_\theta}{\partial \theta} = 0 \tag{4}$$

The total pressure P in Eqs. (1) and (2) can be decomposed into a stationary part due to the centrifugal force, a small pressure caused by the translational acceleration of the $x'y'$ frame and a small pressure component p as the result of small motion of the fluid.

$$P = \frac{\rho\Omega^2 r^2}{2} - \rho r(a_{x'}\cos\theta + a_{y'}\sin\theta) + p(r,\theta,t) \tag{5}$$

where r_i is the cavity radius. Substituting Eq. (5) into the Navier–Stokes equations (1) and (2) and transforming the resulting equations into the Laplace domain, one obtains

$$s\bar{v}_r - 2\Omega\bar{v}_\theta = -\frac{1}{\rho}\frac{\partial \bar{p}}{\partial r} + \nu\left(\nabla^2\bar{v}_r - \frac{\bar{v}_r}{r^2} - \frac{2}{r^2}\frac{\partial \bar{v}_\theta}{\partial\,\theta}\right) \tag{6}$$

$$s\bar{v}_\theta + 2\Omega\bar{v}_r = -\frac{1}{\rho r}\frac{\partial \bar{p}}{\partial \theta} + \nu\left(\nabla^2\bar{v}_\theta - \frac{\bar{v}_\theta}{r^2} + \frac{2}{r^2}\frac{\partial \bar{v}_r}{\partial \theta}\right) \tag{7}$$

where the overbar symbol indicates the Laplace transformed variable and $s=\sigma+i\omega$ is the Laplace variable. The solution of $\bar{v}_r$, $\bar{v}_\theta$, and $\bar{p}$ can be assumed as

$$\bar{v}_r = r_o\Omega\sum_{-\infty}^{\infty}\hat{v}_{r(n)}(\xi)e^{in\theta}, \quad \bar{v}_\theta = r_o\Omega\sum_{-\infty}^{\infty}\hat{v}_{\theta(n)}(\xi)e^{in\theta}$$

$$\bar{p} = \rho r_o^2\Omega^2\sum_{-\infty}^{\infty}\hat{p}_{(n)}(\xi)e^{in\theta} \tag{8}$$

where $\xi = r/r_o$, $i = \sqrt{-1}$, and r_o is the cylinder inner radius. The Reynolds number Re and the cavity ratio κ are defined as

$$\mathrm{Re} = \frac{r_o^2\Omega}{\nu}, \quad \kappa = \frac{r_i}{r_o} \tag{9}$$

Substituting the solution given in Eq. (8) into Eqs. (4), (6), and (7) and by taking the coefficients of each $\exp(in\theta)$ equal on both sides of these equations one can obtain the governing equations of fluid motion in the following dimensionless form:

$$\hat{s}\hat{v}_{r(n)} - 2\hat{v}_{\theta(n)} = -\hat{p}'_{(n)} + \mathrm{Re}^{-1}\left(\hat{v}''_{r(n)} + \frac{1}{\xi}\hat{v}'_{r(n)} - \frac{(n^2+1)}{\xi^2}\hat{v}_{r(n)} - \frac{2in}{\xi^2}\hat{v}_{\theta(n)}\right) \tag{10}$$

$$\hat{s}\hat{v}_{\theta(n)} + 2\hat{v}_{r(n)} = -\frac{in}{\xi}\hat{p}_{(n)} + \mathrm{Re}^{-1}\left(\hat{v}''_{\theta(n)} + \frac{1}{\xi}\hat{v}'_{\theta(n)} - \frac{(n^2+1)}{\xi^2}\hat{v}_{\theta(n)} + \frac{2in}{\xi^2}\hat{v}_{r(n)}\right) \tag{11}$$

$$\hat{v}_{r(n)} + \xi\hat{v}'_{r(n)} + in\hat{v}_{\theta(n)} = 0 \tag{12}$$

where $\hat{s} = s/\Omega$ and the prime symbol is used for d/dr operator. Solving Eqs. (12) and (11) for $\hat{v}_{\theta(n)}$ and $\hat{p}_{(n)}$ gives

$$\hat{v}_{\theta(n)} = \frac{\hat{v}_{r(n)} + \xi\hat{v}'_{r(n)}}{n}i \tag{13}$$

$$\hat{p}_{(n)} = \frac{1}{n^2\xi\ \mathrm{Re}}[(s\ \mathrm{Re}\ \xi^2 i + 2\ \mathrm{Re}\ n\xi^2 - n^2 i + i)\hat{v}_{r(n)} + (s\ \mathrm{Re}\ \xi^3 - \xi + n^2\xi)i\hat{v}'_{r(n)} - 4\xi^2 i\hat{v}''_{r(n)} - \xi^3 i\hat{v}'''_{r(n)}] \tag{14}$$

Introducing Eqs. (13) and (14) into Eq. (10), we obtain the following ordinary differential equation for $\hat{v}_{r(n)}$:

$$\xi^4\hat{v}^{(4)}_{r(n)} + 6\xi^3\hat{v}'''_{r(n)} + (5 - 2n^2 - \mathrm{Re}\ \xi^2\hat{s})\xi^2\hat{v}''_{r(n)} - (2n^2 + 1 + 3\ \mathrm{Re}\ \xi^2\hat{s})\xi\hat{v}'_{r(n)} + (n^2 + \mathrm{Re}\ \xi^2\hat{s} - 1)(n^2 - 1)\hat{v}_{r(n)} = 0 \tag{15}$$

which has a solution of the form

$$\hat{v}_{r(n)} = \bar{c}_{1(n)}\xi^{-1-n} + \bar{c}_{2(n)}\xi^{1+n} + \bar{c}_{3(n)}\frac{J_n(\sqrt{-\mathrm{Re}\ \hat{s}}\xi)}{\xi} + \bar{c}_{4(n)}\frac{Y_n(\sqrt{-\mathrm{Re}\ \hat{s}}\xi)}{\xi} \tag{16}$$

where J_n and Y_n are the Bessel functions of the first and second kinds and order n. For the case of inviscid liquid, the Bessel function terms in Eq. (16) vanish as the Reynolds number goes to infinity and the solution of $\hat{v}_{r(n)}$ will be reduced to the form given in Ref. [26]. The nonpenetration boundary condition at the wetted surface of the cylinder gives

$$\hat{v}_{r(n)}|_{\xi=1} = 0 \tag{17}$$

Also the tangential component of fluid velocity $\hat{v}_{\theta(n)}$ at the wetted surface of the cylinder must be zero. Thus using Eq. (12) one can obtain

$$\hat{v}'_{r(n)}|_{\xi=1} = 0 \tag{18}$$

The free surface of the fluid must be free from shear stresses, namely,

$$\tau_{r\theta}|_{r=r_i} = \rho\nu\left.\left(\frac{1}{r}\frac{\partial v_r}{\partial\theta} + \frac{\partial v_\theta}{\partial r} - \frac{v_\theta}{r}\right)\right|_{r_i} = 0 \tag{19}$$

Using Eq. (13) in Eq. (19), the shear-stress-free boundary condition at the fluid free surface can be written in the following dimensionless form

$$\kappa\hat{v}''_{r(n)}|_{\xi=\kappa} + \hat{v}'_{r(n)}|_{\xi=\kappa} = 0 \tag{20}$$

The fluid free surface is defined by $r = r_i + \zeta(r,t)$, where $\zeta(r,t)$ is the free surface elevation. Thus, the following kinematic boundary condition is imposed on the free surface

$$v_r|_{r_i+\zeta} = \frac{\partial\zeta}{\partial t} \tag{21}$$

The cavity pressure remains constant; thus, evaluating Eq. (5) on the free surface and eliminating the nonlinear terms yields a dynamic boundary condition as

$$p + \rho r_i\Omega^2\zeta = \rho r_i(a_{x'}\cos\theta + a_{y'}\sin\theta) \tag{22}$$

Applying the Laplace transformation to the boundary condition equations (21) and (22) and combining them gives the following equation at the fluid free surface:

$$s\bar{p} + \rho r_i\Omega^2\bar{v}_r = s\rho r_i(\bar{a}_{x'}\cos\theta + \bar{a}_{y'}\sin\theta) \quad \text{at } r = r_i \tag{23}$$

Introducing the solution of $\bar{p}$ and $\bar{v}_r$ from Eq. (8) into Eq. (23) yields the following identity:

$$\sum_{n=-\infty}^{\infty}(\hat{sp}_{(n)} + \kappa\hat{v}_{r(n)})e^{in\theta} = \frac{\kappa}{2r_o\Omega^2}\hat{s}(\bar{a}_{x'} - i\bar{a}_{y'})e^{-i\theta} + \frac{\kappa}{2r_o\Omega^2}\hat{s}(\bar{a}_{x'} + i\bar{a}_{y'})e^{i\theta} \tag{24}$$

To satisfy the identity equation (24), the coefficient of $e^{in\theta}$ must be equal on the both sides of this equation for any mode number n and thus we have

$$\hat{sp}_{(-1)}|_{\xi=\kappa} + \kappa\hat{v}_{r(-1)}|_{\xi=\kappa} - \frac{\kappa}{2r_o\Omega^2}\hat{s}(\bar{a}_{x'} - i\bar{a}_{y'}) = 0 \tag{25}$$

$$\hat{sp}_{(1)}|_{\xi=\kappa} + \kappa\hat{v}_{r(1)}|_{\xi=\kappa} - \frac{\kappa}{2r_o\Omega^2}\hat{s}(\bar{a}_{x'} + i\bar{a}_{y'}) = 0 \tag{26}$$

$$\hat{sp}_{(n)}|_{\xi=\kappa} + \kappa\hat{v}_{r(n)}|_{\xi=\kappa} = 0, \quad n \neq -1, 1 \tag{27}$$

Substituting the solution of the radial component of fluid velocity from Eq. (16) into Eqs. (17), (18), (20), and (25)–(27), the boundary condition equations can be summarized in the following matrix form:

$$\mathbf{A}_{(-1)}\{\bar{c}_{(-1)}\} = \frac{\kappa}{2r_o\Omega^2}\hat{s}(\bar{a}_{x'} - i\bar{a}_{y'})[0\ \ 0\ \ 0\ \ 1]^T \tag{28}$$

$$\mathbf{A}_{(1)}\{\bar{c}_{(1)}\} = \frac{\kappa}{2r_o\Omega^2}\hat{s}(\bar{a}_{x'} + i\bar{a}_{y'})[0\ \ 0\ \ 0\ \ 1]^T \tag{29}$$

$$\mathbf{A}_{(n)}\{\bar{c}_{(n)}\} = \mathbf{0}, \quad n \neq -1, 1 \tag{30}$$

where $\{\bar{c}_n\} = [\bar{c}_{1(n)}\bar{c}_{2(n)}\bar{c}_{3(n)}\bar{c}_{4(n)}]^T$. Using Eqs. (28)–(30), the vectors $\{\bar{c}_{(1)}\}$ and $\{\bar{c}_{(-1)}\}$ are calculated as functions of $\bar{a}'_x$ and $\bar{a}'_y$. However to find a nontrivial solution for the case of $n \neq -1, 1$ the determinant of the coefficient matrix of $\{\bar{c}_n\}$ must be zero, namely,

$$|\mathbf{A}_{(n)}| = 0, \quad n \neq -1, 1 \tag{31}$$

The resultant forces exerted on the cylinder wall, as a result of fluid pressure and shear stress on the wetted cylinder surface, are evaluated as

$$\bar{F}_{x'} = \int_0^{2\pi} [\bar{P}|_{r=r_o} \cos\theta - \bar{\tau}_{r\theta}|_{r=r_o} \sin\theta] r_o d\theta$$
$$= \frac{\rho\pi r_o^3 \Omega^2}{\mathrm{Re}} [(\hat{v}'''_{r(1)}|_{\xi=1} + 5\hat{v}''_{r(1)}|_{\xi=1}) + (\hat{v}'''_{r(-1)}|_{\xi=1} + 5\hat{v}''_{r(-1)}|_{\xi=1})]$$
$$- \rho\pi r_o^2 \bar{a}_{x'} \tag{32}$$

$$\bar{F}_{y'} = \int_0^{2\pi} [\bar{P}|_{r=r_o} \sin\theta + \bar{\tau}_{r\theta}|_{r=r_o} \cos\theta] r_o d\theta$$
$$= \frac{\rho\pi r_o^3 \Omega^2}{\mathrm{Re}} [(\hat{v}'''_{r(1)}|_{\xi=1} + 5\hat{v}''_{r(1)}|_{\xi=1})i - (\hat{v}'''_{r(-1)}|_{\xi=1} + 5\hat{v}''_{r(-1)}|_{\xi=1})i]$$
$$- \rho\pi r_o^2 \bar{a}_{y'} \tag{33}$$

Using the solution of Eqs. (28) and (29) for $\{\bar{c}_{(1)}\}$ and $\{\bar{c}_{(-1)}\}$, the values of radial derivatives of $\hat{v}_{r(-1)}$ and $\hat{v}_{r(1)}$ at the wetted surface of the flexible cylinder are known as linear functions of $a_{x'}$ and $a_{y'}$. Consequently, we can show that Eqs. (32) and (33) can be expressed in the following form:

$$\begin{bmatrix} \bar{F}_{x'} \\ \bar{F}_{y'} \end{bmatrix} = \rho\pi r_o^2 (1-\kappa^2) \begin{bmatrix} \alpha & -\beta \\ \beta & \alpha \end{bmatrix} \begin{bmatrix} \bar{a}_{x'} \\ \bar{a}_{y'} \end{bmatrix} \tag{34}$$

3 Structural Dynamics

The flexural vibration of a viscoelastic slender flexible cylinder can be simulated using the Euler–Bernoulli beam model. Figure 1 shows the bending displacement components of the flexible cylinder axis u and w in the rotating xy frame. The elastic potential energy U due to the flexural deflection of the beam as well as the end spring deformations and the kinetic energy T of the beam can be calculated as [28]

$$U = \frac{1}{2}\int_0^L EI\left[\left(\frac{\partial^2 w}{\partial z^2}\right)^2 + \left(\frac{\partial^2 u}{\partial z^2}\right)^2\right] dz + \frac{1}{2}k_{t_0}(u^2|_{z=0} + w^2|_{z=0})$$
$$+ \frac{1}{2}k_{t_1}(u^2|_{z=L} + w^2|_{z=L}) + \frac{1}{2}k_{r_0}\left[\left(\frac{\partial u}{\partial z}\right)^2\Big|_{z=0} + \left(\frac{\partial w}{\partial z}\right)^2\Big|_{z=0}\right]$$
$$+ \frac{1}{2}k_{r_1}\left[\left(\frac{\partial u}{\partial z}\right)^2\Big|_{z=L} + \left(\frac{\partial w}{\partial z}\right)^2\Big|_{z=L}\right] \tag{35}$$

$$T = \frac{1}{2}\int_0^L m\left[\left(\frac{\partial w}{\partial t} - \Omega u\right)^2 + \left(\frac{\partial u}{\partial t} + \Omega w\right)^2\right] dz \tag{36}$$

where m is the mass per unit length density, I is the moment of inertia of the beam section, and E is Young's modulus of elasticity. The translational and rotational spring constants at the cylinder ends are indicated by k_t and k_r and the subindices 0 and 1 point to the cylinder supports at $z=0$ and $z=L$, respectively.

The viscoelastic damping is proportional to the time rate of strain and can be represented using the classical Kelvin–Voigt model. For the structural damping due to the internal friction, the energy loss per cycle of stress was found to be proportional to the amplitude squared and thus it can be modeled as a complex stiffness [28]. Thus, the Rayleigh dissipation function due to the material viscoelasticity and the structural hysteretic damping can be expressed in the form

$$R = \frac{1}{2}\int_0^L EI\left(\gamma\frac{\partial}{\partial t} + ig\right)\left[\left(\frac{\partial^2 w}{\partial z^2}\right)^2 + \left(\frac{\partial^2 u}{\partial z^2}\right)^2\right] dz \tag{37}$$

in which γ is the viscoelasticity loss factor and g is the structural damping factor. The dissipation function due to the external damping forces at the cylinder supports can be written as

$$R' = \frac{1}{2}c_{t_0}[(\dot{w}|_{z=0} - \Omega u|_{z=0})^2 + (\dot{u}|_{z=0} + \Omega w|_{z=0})^2]$$
$$+ \frac{1}{2}c_{t_1}[(\dot{w}|_{z=L} - \Omega u|_{z=L})^2 + (\dot{u}|_{z=L} + \Omega w|_{z=L})^2]$$
$$+ \frac{1}{2}c_{r_0}\left[\left(\frac{\partial \dot{w}}{\partial z}\Big|_{z=0} - \Omega\frac{\partial u}{\partial z}\Big|_{z=0}\right)^2 + \left(\frac{\partial \dot{u}}{\partial z}\Big|_{z=0} + \Omega\frac{\partial w}{\partial z}\Big|_{z=0}\right)^2\right]$$
$$+ \frac{1}{2}c_{r_1}\left[\left(\frac{\partial \dot{w}}{\partial z}\Big|_{z=L} - \Omega\frac{\partial u}{\partial z}\Big|_{z=L}\right)^2 + \left(\frac{\partial \dot{u}}{\partial z}\Big|_{z=L} + \Omega\frac{\partial w}{\partial z}\Big|_{z=L}\right)^2\right] \tag{38}$$

where c_t and c_r denote the translational and rotational viscous damping coefficients at the cylinder supports. The variation in work done by the fluid force on the flexible cylinder can be written as

$$\delta W = \int_0^L (F_{x'}\delta u + F_{y'}\delta w) dz \tag{39}$$

Using the Hamilton principle which states

$$\delta H = \int_0^t [\delta T - \delta U + \delta(R + R') + \delta W] dt = 0 \tag{40}$$

along with Eqs. (35)–(39), one can obtain the equations governing the flexural vibration of the flexible cylinder in the rotating xy frame. The Laplace transformed equations of motion can be written as

$$ms^2\bar{w} - 2m\Omega\bar{u}s + EI(1 + \gamma s + ig)\bar{w}^{(4)} - m\Omega^2\bar{w} = \bar{F}_{x'} \tag{41}$$

$$ms^2\bar{u} + 2m\Omega\bar{w}s + EI(1 + \gamma s + ig)\bar{u}^{(4)} - m\Omega^2\bar{u} = \bar{F}_{y'} \tag{42}$$

Using the following operator definitions

$$B_j^1 = (k_{t_j} + c_{t_j}s) + (-1)^j EI(1 + \gamma s + ig)\frac{\partial^3}{\partial z^3} \tag{43}$$

$$B_j^2 = (k_{r_j} + c_{r_j}s)\frac{\partial}{\partial z} - (-1)^j EI(1 + \gamma s + ig)\frac{\partial^2}{\partial z^2} \tag{44}$$

$$B_j^3 = \Omega c_{t_j} \tag{45}$$

$$B_j^4 = \Omega c_{r_j}\frac{\partial}{\partial z} \tag{46}$$

the boundary conditions for $\bar{w}$ are

$$B_0^1\bar{w} - B_0^3\bar{u} = 0, \quad B_0^2\bar{w} - B_0^4\bar{u} = 0 \quad \text{at } z = 0 \tag{47}$$

$$B_1^1\bar{w} - B_1^3\bar{u} = 0, \quad B_1^2\bar{w} - B_1^4\bar{u} = 0 \quad \text{at } z = L \tag{48}$$

and similarly for $\bar{u}$ we have

$$B_0^1\bar{u} + B_0^3\bar{w} = 0, \quad B_0^2\bar{u} + B_0^4\bar{w} = 0 \quad \text{at } z = 0 \tag{49}$$

$$B_1^1\bar{u} + B_1^3\bar{w} = 0, \quad B_1^2\bar{u} + B_1^4\bar{w} = 0 \quad \text{at } z = L \tag{50}$$

4 Coupled Fluid-Structure System and the Solution Method

The translational acceleration of the origin of the moving frame $x'y'$ at each section of the flexible cylinder is related to the flexural deflection of the cylinder as

$$\bar{a}_{x'} = \bar{w}s^2 - 2\Omega\bar{u}s - \bar{w}\Omega^2 \tag{51}$$

$$\bar{a}_{y'} = \bar{u}s^2 + 2\bar{w}\Omega s - \bar{u}\Omega^2 \tag{52}$$

Substituting $a_{x'}$ and $a_{y'}$ from Eqs. (51) and (52) into Eq. (34) and using the resulting expression for the fluid forces in Eqs. (41) and (42), the coupled fluid-structure equations of motion are derived. These equations involve highly transcendental expressions in terms of the dimensionless Laplace parameter $\hat{s}$, which makes it very complicated to find the root-locus and subsequently the stability margins of the coupled system of equations. In this section we propose a numerical method for stability analysis of the coupled equations of the fluid-structure system.

4.1 The Numerical Method for Stability Analysis. Using the following definition for the complex bending deformation

$$\bar{\Delta} = \bar{w} + i\bar{u} \tag{53}$$

the system of Eqs. (41) and (42) will be transformed into the following form

$$m(s^2 + 2\Omega is - \Omega^2)\bar{\Delta} + EI(1 + \gamma s + ig)\bar{\Delta}^{(4)} = \bar{F}_{x'} + i\bar{F}_{y'} \tag{54}$$

Using Eqs. (51) and (52) and substituting the fluid force expressions from Eq. (34) into Eq. (54), the governing equation of the coupled fluid-structure system can be written as

$$m(s^2 - \Omega^2 + 2i\Omega s)\bar{\Delta} + CIs\bar{\Delta}^{(4)} + EI(1 + \gamma s + ig)\bar{\Delta}^{(4)} - \rho\pi r_o^2(1 - \kappa^2)(\alpha + i\beta)(s^2 - \Omega^2 + 2i\Omega s)\bar{\Delta} = 0 \tag{55}$$

Furthermore, the combination of Eqs. (47)–(50) yields the following boundary conditions for the complex bending deflection $\bar{\Delta}$ as

$$(B_0^1 + iB_0^3)\bar{\Delta} = 0, \quad (B_0^2 + iB_0^4)\bar{\Delta} = 0 \quad \text{at } z = 0 \tag{56}$$

$$(B_1^1 + iB_1^3)\bar{\Delta} = 0, \quad (B_1^2 + iB_1^4)\bar{\Delta} = 0 \quad \text{at } z = L \tag{57}$$

The solution of the bending displacement of the flexible cylinder in the existence of the fluid can be expressed using the following modal expansion series:

$$\bar{\Delta} = \sum_{n=1}^{\infty} \bar{\eta}_n(\hat{s})\Psi_n \tag{58}$$

where Ψ_ns are the complex bending mode shapes of the nonrotating flexible cylinder, neglecting internal damping terms but with the same boundary conditions given in Eqs. (56) and (57). Thus, the mode shapes satisfy the following relation:

$$EI\Psi_n^{(4)} - m\omega_n^2\Psi_n = 0 \tag{59}$$

where ω_n is the complex natural frequency, which corresponds to Ψ_n. Many solution methods have been represented for determination of the mode shapes and complex natural frequencies of the beams on arbitrary supports, which can be used to solve the boundary value equation (59) subjected to the boundary condition equations (56) and (57) (see Refs. [29–33]).On the other hand, the numerical methods such as the finite-element method may be easily employed to solve such problem. Anyhow, substituting $\bar{\Delta}$ from Eq. (58) into Eq. (56) and using Eq. (59), one can obtain

$$\sum_{n=1}^{\infty} [(1 - \mu(\alpha + i\beta))(\hat{s} + i)^2 + (1 + \varepsilon\hat{s} + ig)\lambda_n^{-2}]m\Omega^2\Psi_n = 0 \tag{60}$$

where λ_n, ε, and μ are the dimensionless spinning frequency, the dimensionless viscoelastic loss factor, and the fluid mass ratio, respectively, and are defined as follows:

$$\lambda_n = \frac{\Omega}{\omega_n}, \quad \gamma = \varepsilon\Omega, \quad \mu = \frac{\rho\pi r_o^2(1 - \kappa^2)}{m} \tag{61}$$

To satisfy the identity equation (60), the expression in the brackets must be vanished, thus

$$\lambda_n = \underbrace{\frac{1}{\hat{s} + i}\sqrt{\frac{1 + \varepsilon\hat{s} + ig}{\mu(\alpha + i\beta) - 1}}}_{h} \tag{62}$$

At the instability boundary $\lambda_{n_{cr}}$, the flexible cylinder has a simple harmonic motion and thus we have $\hat{s} = i\omega/\Omega$. Furthermore, it is easy to show that for known values of stiffness and damping of the supports, for any mode number n, the left-hand-side of Eq. (62) is a function of Ω/ω^* where $\omega^* = \sqrt{EI/mL^4}$, and thus for the instability condition we have

$$\lambda_{n_{cr}}(\Omega/\omega^*) = h(i\omega/\Omega) \tag{63}$$

namely,

$$\Re(\lambda_{n_{cr}}) + i\Im(\lambda_{n_{cr}}) = \Re(h) + i\Im(h) \tag{64}$$

To solve for and map out the instability boundaries, the following procedure is outlined.

1. Specify the fluid mass ratio μ, the cavity ratio κ, the Reynolds number Re, the dimensionless viscoelastic loss factor ε, and the structural damping parameter g.
2. For a set of ω/Ω values, say, from 0.001 to 1.0, solve Eqs. (28) and (29) with $\hat{s} = i\omega/\Omega$ for $\{\bar{c}_{(-1)}\}$ and $\{\bar{c}_{(1)}\}$. Then using Eqs. (32) and (33) find the values of α and β and plot the imaginary part of h against its real part.
3. For a known mode number n and a set of Ω/ω^* values, plot the imaginary part of λ_n versus its real part in the same plane of h. The intersection of the h and λ_n graphs shows the critical condition in which Eq. (64) is satisfied.
4. Having the critical values of h and λ_n, determine the critical dimensionless spinning frequency Ω_{cr}/ω^* and the dimensionless instability frequency ω_{cr}/Ω.

The major advantage of Eq. (62) is that its right-hand-side h, which involves complicated expressions in terms of $\hat{s}$, is independent of the cylinder boundary conditions. It is of importance since the plot of h can be simply used for any arbitrary boundary conditions of the flexible cylinder. As another significant outline, it should be noted that if the cylinder supports do not have viscous damping, the values of ω_n are real for any mode number n and thus the intersection of the plot of h with the real axis illustrates the critical dimensionless spinning frequency Ω_{cr}/ω_n, which is unique for all of the mode numbers. This conclusion signifies that for the cylinders with purely elastic supports, the critical value of Ω_{cr}/ω_n is independent of the translational and rotational stiffness of the supports for any mode number n.

5 Numerical Results

This section is devoted to some numerical examples to demonstrate the method of solution for determination of the instability boundary of the spinning flexible cylinder partially filled with viscous fluid. Using the described method of solution some parameter studies are also carried out. Figure 2 depicts the procedure

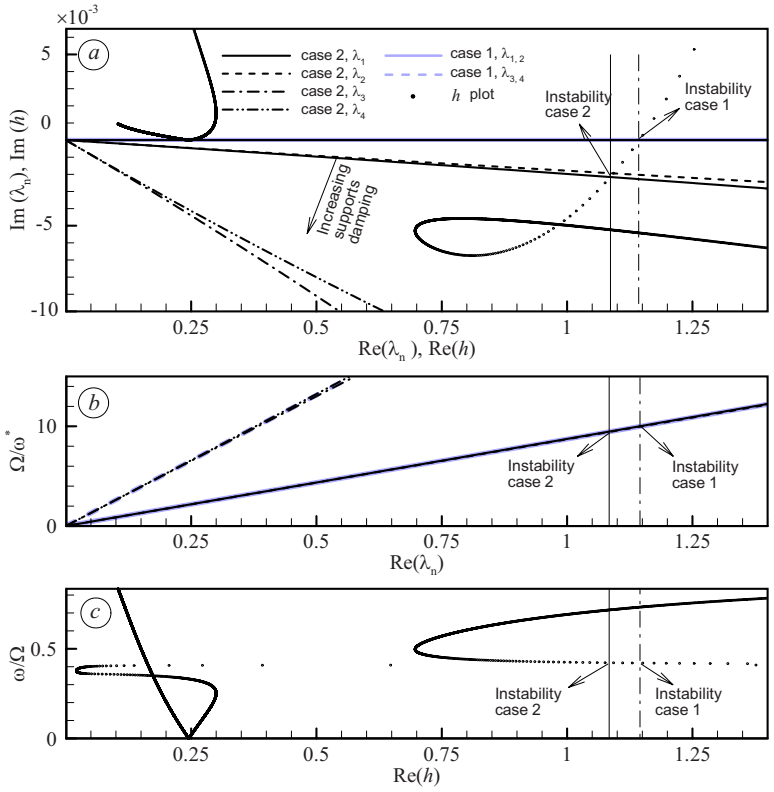

Fig. 2 Instability analysis graphs for cases 1 and 2: (*a*) plots of imaginary parts of h and λ_n versus their real parts, (*b*) plot of dimensionless spinning frequency Ω/ω^* against the real part of λ_n, and (*c*) plot of dimensionless frequency of the fluid-structure system ω/Ω against the real part of h

of determination of instability boundaries for two cylinders: a flexible cylinder on purely elastic supports with the following properties (case 1):

$$\frac{k_{t_0}}{mL\omega^{*2}} = \frac{k_{t_1}}{mL\omega^{*2}} = 80, \quad \frac{c_{t_0}}{mL\omega^*} = \frac{c_{t_1}}{mL\omega^*} = 0$$
$$\frac{k_{r_0}}{mL^2\omega^{*2}} = \frac{k_{r_1}}{mL^2\omega^{*2}} = 0, \quad \frac{c_{r_0}}{mL^2\omega^*} = \frac{c_{r_1}}{mL^2\omega^*} = 0 \tag{65}$$

and the same flexible cylinder with the same conditions but on viscoelastic supports as shown in the following (case 2):

$$\frac{k_{t_0}}{mL\omega^{*2}} = \frac{k_{t_1}}{mL\omega^{*2}} = 80, \quad \frac{c_{t_0}}{mL\omega^*} = \frac{c_{t_1}}{mL\omega^*} = 0.25$$
$$\frac{k_{r_0}}{mL^2\omega^{*2}} = \frac{k_{r_1}}{mL^2\omega^{*2}} = 0, \quad \frac{c_{r_0}}{mL^2\omega^*} = \frac{c_{r_1}}{mL^2\omega^*} = 0 \tag{66}$$

The fluid mass ratio is 10, the cavity ratio 0.6, the Reynolds number 10,000, and the viscoelastic loss factor and structural damping are zero. Figure 2(*a*) illustrates the plot of h and λ_n for the lowest four complex frequencies of the flexible cylinder for both test cases. For case 1, the real axis in Fig. 2(*a*) corresponds to all modes of motion. Figure 2(*b*) shows the values of Ω/ω^* against the real part of λ_n and specifies the critical value of spinning speed of the flexible cylinder. The instability frequency of the flexible cylinder can be found using Fig. 2(*c*). The results show that the viscous damping of supports decreases the critical spinning frequency of the flexible cylinder but Fig. 2(*c*) reveals that the instability frequency of the flexible cylinder is nearly constant.

The effect of viscoelasticity and structural damping of the cylinder material on the stability margins is represented in Figs. 3 and 4. Figure 3 shows the instability condition of cases 1 and 2 for various structural damping values when the viscoelastic loss factor is zero. The instability condition is shown by the letter "I" and the restabilization point is shown by the letter "R." It is seen from Fig. 3 that when the structural damping increases, first, the critical spinning speed of the cylinder decreases. Then, while enhancing

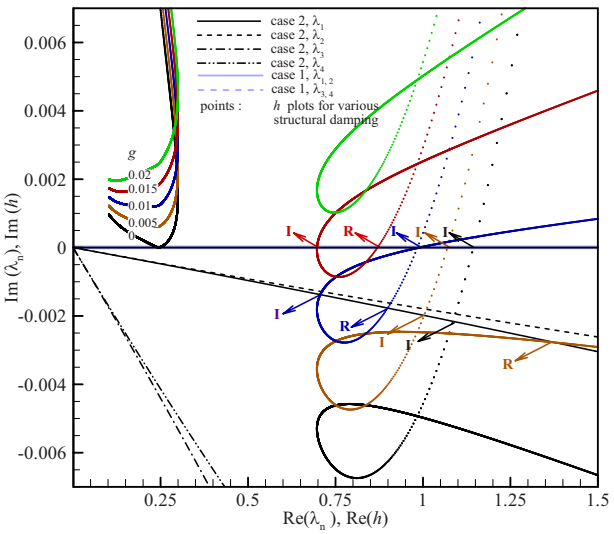

Fig. 3 The effect of structural damping on the stability margin of the cylinder partially filled with viscous fluid, cases 1 and 2

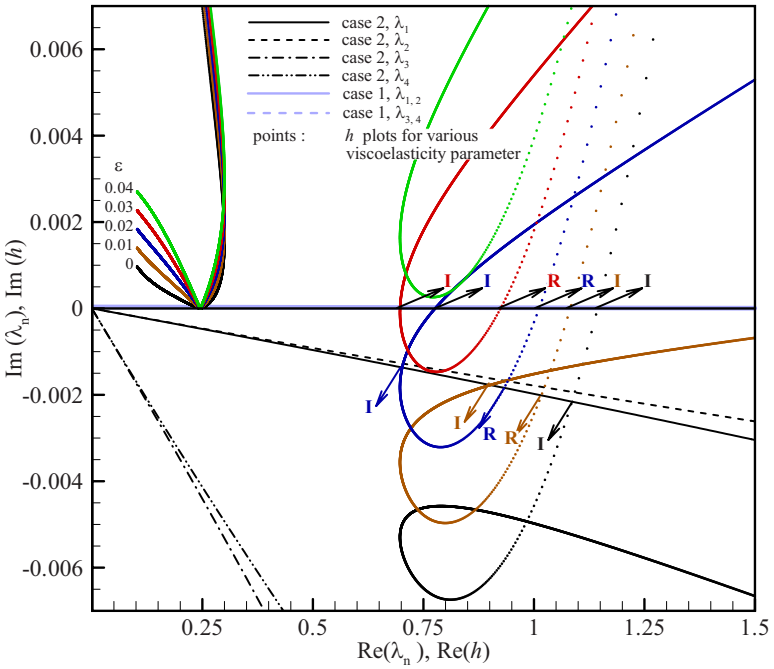

Fig. 4 The effect of material viscoelasticity on the stability margin of the cylinder partially filled with viscous fluid, cases 1 and 2

the structural damping decreases the critical spinning frequency, it causes the restabilization of the flexible cylinder after the critical condition. Furthermore, Fig. 3 shows that adding more structural damping makes the flexible cylinder stable at all spinning frequencies as seen for $g=0.02$.

Figure 4 depicts the stability boundaries of the viscoelastic cylinder without structural damping. Figure 4 represents an investigation on the effect of viscoelasticity on the cylinder material similar to that which was performed for the structural damping. The results show that the effect of viscoelastic damping on the stability margins is similar to the structural damping. Moreover, it should be noted that when the supports' damping increases, the imaginary part of λ_n will increase as shown in Fig. 2(*a*). Therefore, the effect of increasing the supports' damping can be explained similar to that of enhancing the material viscoelasticity or structural damping.

To investigate the effect of fluid mass ratio and the cavity ratio, a parameter study is done on the critical spinning speed of the flexible cylinder partially filled with liquid and mounted on purely elastic supports. Figure 5 shows the critical spinning frequency

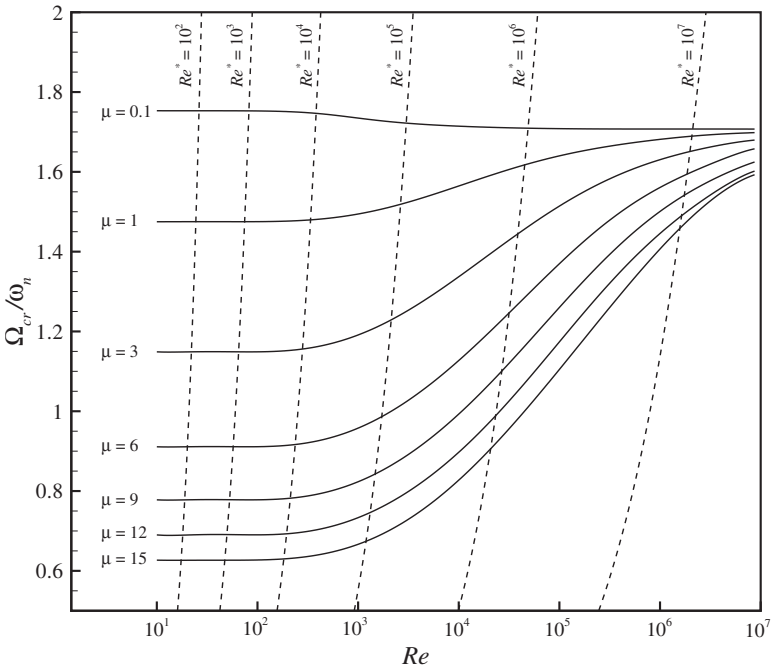

Fig. 5 Critical spinning speed of the cylinder on purely elastic supports for $\kappa=0.6$ and various μ

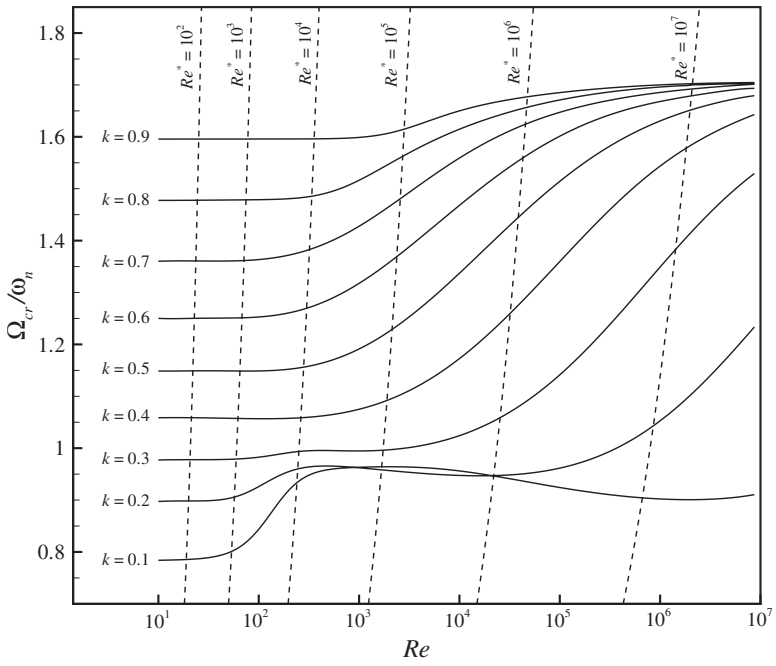

Fig. 6 Critical spinning speed of the cylinder on purely elastic supports for μ=3.0 and various κ

against the Reynolds number for various values of μ when κ =0.5 and Fig. 6 illustrates similar results for different values of κ and μ=3.0. The horizontal axis in Figs. 5 and 6 is logarithmic and $\mathrm{Re}^* = r_o^2 \omega_n / \nu$. Since the Reynolds number Re varies with spinning frequency Ω, it cannot be simply used to determine the instability condition and thus we define the new parameter Re^*. Having the structural parameters of the flexible cylinder, the values of ω_n are known for all the mode numbers and thus the known value of Re^* can be simply used in the graphs shown in Figs. 5 and 6 to find the critical spinning frequency for all the modes.

6 Conclusion

The stability of flexible spinning cylinders partially filled with viscous fluid was investigated in this research. Using an analytical solution to the linearized Navier–Stokes equations, the resultant forces exerted on the flexible cylinder due to fluid motion were determined in terms of flexural motion of the flexible cylinder in the Laplace domain. The Euler–Bernoulli beam model was employed to derive the structural dynamics equations of the flexible cylinder mounted on general viscoelastic supports and including the material viscoelasticity and structural damping. The coupled-field equations of the structural motion and the fluid dynamics were used to determine the critical spinning speed of the flexible cylinder. For this purpose, a numerical technique was introduced to find the instability conditions and then was used for some numerical examples. The performed investigations show that if the flexible cylinder is mounted on purely elastic supports, for known values of fluid mass ratio, cavity ratio, viscoelastic loss factor, and structural damping, all the flexural deflection modes become unstable at a unique dimensionless spinning speed. The numerical studies signify that when the supports' damping, material viscoelasticity, or the structural damping increase, first, the critical spinning speed of the flexible cylinder decreases. Then, while enhancing these damping quantities, decreases the critical spinning frequency, it causes the restabilization of the flexible cylinder after the critical condition and adding more damping may make the flexible cylinder stable at all spinning frequencies.

Acknowledgment

Sharif University of Technology is acknowledged for financial support of this research paper.

References

[1] Ibrahim, R. A., 2005, *Liquid Sloshing Dynamics*, Cambridge University Press, Cambridge, England.
[2] Kuipers, M., 1964, "On the Stability of a Flexibly Mounted Rotating Cylinder Partially Filled With Liquid," Appl. Sci. Res., Sect. A, **13**(1), pp. 121–137.
[3] Wolf, I. A., 1964, "Whirl Dynamics of a Rotor Partially Filled With Liquid," ASME J. Appl. Mech., **35**, pp. 676–682.
[4] Lichtenberg, G., 1982, "Vibration of an Elastically Mounted Spinning Rotor Partially Filled With Liquid," ASME J. Mech. Des., **104**(2), pp. 389–396.
[5] Wohlsbruck, R., 1985, "Stability of a Rotor Whose Cavity has an Arbitrary Meridian and Partially Filled With Fluid," ASME J. Vib., Acoust., Stress, Reliab. Des., **4**, pp. 440–445.
[6] Zhang, W., Tang, J., and Tao, M. D., 1996, "Dynamic Stability of a Rotor Filled or Partially Filled With Liquid," ASME J. Appl. Mech., **63**, pp. 101–105.
[7] Daich, I. M., and Bar, I. L., 1973, "Oscillations of a Rotating Rigid Body With a Cavity Partially Filled With a Viscous Liquid," ASME J. Appl. Mech., **9**(5), pp. 516–520.
[8] Daich, I. M., Bar, I. L., and Korzovskaya, I. D., 1976, "Nonlinear Oscillations of a Rotating Solid Body With Cavity Partially Filled With an Ideal Liquid," Int. Appl. Mech., **12**(6), pp. 616–620.
[9] Hendricks, S. L., and Morton, J. B., 1979, "Stability of a Rotor Partially Filled With a Viscous Incompressible Fluid," ASME J. Appl. Mech., **46**, pp. 913–918.
[10] Zhu, C. S., 2000, "Stability of a Rotor System on Support of Anisotropical Rigidity and Partially Filled With an Inviscid Fluid," Journal of Aerospace Power, **15**(4), pp. 431–434.
[11] Zhu, C. S., 2001, "Stability Behavior of an Isotropic Rotor System Anisotropically Mounted and Partially Filled With Inviscous Fluid," Proc. SPIE, **4359**(2), pp. 1278–1283.
[12] Zhu, C. S., 2001, "Stability Analysis of Symmetrical Rotors Partially Filled With a Viscous Incompressible Fluid," Int. J. Rotating Mach., **7**(5), pp. 301–310.
[13] Zhu, C. S., 2002, "Experimental Investigation Into the Instability of an Over-Hung Rigid Centrifuge Rotor Partially Filled With Fluid," ASME J. Vibr. Acoust., **124**(4), pp. 483–491.
[14] Derendyayev, N. V., and Soldatov, I. N., 2004, "The Stability of the Steady Motions of a Rotor System With a Fluid Using a Discrete Model," J. Appl. Math. Mech., **68**(6), pp. 883–892.
[15] Derendyaev, N. V., 2006, "Stability and Andronov-Hopf Bifurcation of Steady-State Motion of Rotor System Partly Filled With Liquid: Continuous and Discrete Models," ASME J. Appl. Mech., **73**(4), pp. 580–589.

[16] Tao, M., and Zhang, W., 2002, "Dynamic Stability of a Rotor Partially Filled With a Viscous Liquid," ASME J. Appl. Mech., **69**, pp. 705–707.
[17] Limarchenko, O. S., 1995, "Nonsteady Rotation of a Cylindrical Storage Tank Partially Filled With a Viscous Fluid," Int. Appl. Mech., **31**(5), pp. 406–411.
[18] Berman, S., Lundgren, T. S., and Cheng, A., 1985, "Asynchronous Whirl in a Rotating Cylinder Partially Filled With Liquid," J. Fluid Mech., **150**, pp. 311–427.
[19] Holm-Christensen, G., and Träger, K., 1991, "A Note on Rotor Instability Caused by Liquid Motion," ASME J. Appl. Mech., **58**, pp. 804–811.
[20] Yan, F., and Farouk, B., 2003, "Numerical Simulations of Flows Inside a Partially Filled Centrifuge," ASME J. Fluids Eng., **125**(6), pp. 1033–1042.
[21] Ribando, R. J., 2005, "Incompressible Flow in a Rapidly Rotating Cylinder With a Source/Sink Distribution in the Lateral Wall and a Free Inner Boundary," Int. J. Numer. Methods Fluids, **3**(6), pp. 529–542.
[22] Yuichi, S., Sheigeki, M., Takuo, N., and Yusuke, I., 2005, "Stability of a Rotating Hollow Rotor Partially Filled With Liquid (Effect of Discharging Liquid by Centrifugal Force)," JSME Int. J., Ser. C, **71**(702), pp. 359–365.
[23] Khoroshilov, V. S., 1971, "The Oscillations of a Liquid Partially Filling a Rotating Conical Cavity," Int. Appl. Mech., **7**(11), pp. 1285–1288.
[24] Derendyaev, N. V., and Senyatkin, V. A., 1984, "Stability Conditions for the Steady-State Rotation of a Cylinder Filled With a Stratified Nonuniform Viscous Incompressible Liquid," J. Appl. Mech. Tech. Phys., **25**(1), pp. 30–39.
[25] Preussner, C., and Kollmann, F. G., 1988, "On the Stability of a Spinning, Fluid Filled and Sectored Rotor," Comput. Struct., **30**(1–2), pp. 131–141.
[26] Tao, M., and Zhang, W., 2002, "Dynamic Stability of a Flexible Spinning Cylinder Partially Filled With a Liquid," ASME J. Appl. Mech., **69**, pp. 708–710.
[27] Firouz-Abadi, R. D., and Haddadpour, H., 2009, "Flexural Instability of Viscoelastic Cylinders Partially Filed With Liquid," Int. J. Struct. Stab. Dyn., **9**(1), pp. 45–60.
[28] Meirovitch, L., 1997, *Principles and Techniques of Vibrations*, Prentice-Hall, Englewood Cliffs, NJ.
[29] Fan, Z. J., Lee, J. H., Kang, K. H., and Kim, K. J., 1998, "The Forced Vibration of a Beam With Viscoelastic Boundary Supports," J. Sound Vib., **219**(5), pp. 562–571.
[30] Kang, K. H., and Kim, K. J., 1996, "Modal Properties of Beams and Plates on Resilient Supports With Rotational and Translational Complex Stiffness," J. Sound Vib., **190**(2), pp. 207–220.
[31] Saito, H., and Yaguchi, H., 1988, "Natural Vibrations of a Cantilever Beam With Support Damping," J. Sound Vib., **120**(3), pp. 511–515.
[32] Saito, H., and Otomi, K., 1979, "Parametric Response of Viscoelastically Supported Beams," J. Sound Vib., **63**(2), pp. 169–178.
[33] Li, W. L., 2001, "Dynamic Analysis of Beams With Arbitrary Elastic Supports at Both Ends," J. Sound Vib., **246**(4), pp. 751–756.

Poromechanics Solutions to Plane Strain and Axisymmetric Mandel-Type Problems in Dual-Porosity and Dual-Permeability Medium

Vinh X. Nguyen
Mewbourne School of Petroleum and Geological Engineering, PoroMechanics Institute, University of Oklahoma, Sarkeys Energy Center, Suite P119, 100 East Boyd Street, Norman, OK 73019
e-mail: nxvinh@ou.edu

Younane N. Abousleiman[1]
Mewbourne School of Petroleum and Geological Engineering, ConocoPhillips School of Geology and Geophysics, School of Civil Engineering and Environmental Science, PoroMechanics Institute, University of Oklahoma, Sarkeys Energy Center, Suite P119, 100 East Boyd Street, Norman, Oklahoma 73019
e-mail: yabousle@ou.edu

The two-dimensional Mandel-type problem geometry is well-known to biogeomechanicians for testing rocks, cartilages, and bones with solutions in Cartesian coordinates for rectangular specimens or polar coordinates for cylindrical and disk samples. To date, all existing solutions are only applicable to single-porosity and single-permeability models, which could fall short when the porous material exhibits multiporosity and/or multipermeability characteristics, such as secondary porosity or fracture. This paper extends the plane strain and axisymmetric Mandel-type solutions from single-to dual-porosity and dual-permeability poromechanics. The solutions are presented in explicit analytical forms and account for arbitrary time-dependent external loading conditions, e.g., cyclic and ramping. The derived analytical solutions and results exhibit general behaviors characterized by two time scales. Stresses, pore pressures, and displacements are plotted for various time scale ratios to illustrate the interplaying effects of permeability and stiffness contrast of both porous regions, in addition to the interporosity exchange, on the overall responses of the system. Also, examples with realistic loading conditions for laboratory testing or field simulation such as cyclic and ramping are provided to demonstrate the engineering applications of the presented dual-poroelastic formulation and solutions. [DOI: 10.1115/1.3172146]

Keywords: analytical solution, cylinder, dual-porosity, dual-permeability, fracture, poroelastic, unconfined compression

1 Introduction

The isotropic poromechanics solutions for laboratory setups with initial and boundary conditions on prepared samples easily traverse the boundaries of various fields such as biomechanics and geomechanics. The two-dimensional Mandel-type problem geometry assumes a rectangular strip shape in Cartesian coordinate or cylindrical disk samples in polar coordinate. In geomechanics, such configurations are used in common uniaxial and triaxial testings of porous rock specimens [1,2] or in simulating sudden stress relief of a long core removed from subsurface wellbore [3]. Meanwhile, this problem geometry is equivalent to the popular unconfined compression test in the biomechanics society, in particular, for testing cartilages and bones [4,5]. Hence, distributions and evolutions of stress, displacements, and pore pressure in the samples under these setups and conditions are of important values and have been investigated by many researchers.

In 1953, Mandel [6] presented the first solutions for the isotropic consolidation of an unconfined soil layer using Biot's theory of poroelasticity [7], demonstrating the nonmonotonic pore water pressure response, known as the "Mandel–Cryer effect," which is a distinctive feature of the coupled consolidation theory. Kenyon [8] provided solutions for transversely isotropic material but using Terzaghi's uncoupled consolidation theory [9], which is a limiting case of Biot's poroelasticity. Later, Abousleiman et al. [10] extended Mandel's original solution to the full transversely isotropic case and provided the explicit expressions for stress, pore pressure, displacements, and fluid flux. Recently, Hoang and Abousleiman [11] provided the poroviscoelastic solution accounting for the intrinsic nature of the orthotropic viscoelastic matrix structures of many porous materials such as articular cartilage. These poromechanical solutions to the original Mandel's problem have been used as a benchmark for testing the validity of numerical codes of poroelasticity [12–15]. In addition, the rectangular strip geometry also matches one of the testing configurations of stiff clay samples in geomechanics [1] or articular cartilages in biomechanics [16,17].

On the other hand, testing of solid cylindrical samples subjected to load perturbation can be considered an axisymmetric Mandel-type problem due to its radial symmetry and plane strain/generalized plane strain nature [18]. Armstrong et al., [19] following Mandel's approach, derived the isotropic poroelastic solution simulating the unconfined compression of articular cartilage disk and showed results for step and ramp loadings. Independently in the field of geomechanics, Abousleiman and Cui [2] published a more general cylinder solution accounting for the transversely isotropic nature of rock samples and arbitrary time-dependent loading condition. The solution was later extended to incorporate the effect of lateral confining stress and results for uniaxial and triaxial testing under ramp loading condition were demonstrated [20]. Subsequently, Cowin and Mehrabadi [21] also gave the same unconfined anisotropic poroelastic solution with results for bone testing.

All existing analytical solutions for the generalized Mandel-type problem model fluid-saturated porous medium as single-porosity and single-permeability medium and thus fall short in

[1]Corresponding author.

Contributed by the Applied Mechanics Division of ASME for publication in the JOURNAL OF APPLIED MECHANICS. Manuscript received September 5, 2008; final manuscript received May 24, 2009; published online September 23, 2009. Review conducted by Robert M. McMeeking.

describing the proper response of the well-known dual-porosity bone structures [22] or the behaviors of fractured rocks modeled as dual-porosity and dual-permeability porous media [23–25]. A differentiating characteristic of dual-poroelastic medium is that there are contrasting magnitudes in one or all material properties such as porosity, permeability, stiffness, etc., in portions of the medium compared with the rest. Therefore, a dual-porosity continuum approach, which has two distinct forms of porosity, permeability, and/or stiffness, one corresponding to the primary porosity porous phase and the other corresponding to the secondary porous phase, could be more appropriate for laboratory and field application modelings.

This paper shows the derivations of the analytical solutions for Mandel-type problems in isotropic dual-poroelastic media. By noting the parallelism between plane strain and radial symmetry, the solutions for strip and cylindrical samples are analogously derived and expressed in closed form in the Laplace transform domain. Corresponding analytical solutions in the time domain are also derived and presented to complement the Laplace transform domain solutions. The developed solutions describe the consolidation of a strip or circular disk sample under confined or unconfined compression test setups. The cylinder or strip is sandwiched between two impermeable rigid frictionless plates subjected to arbitrary time-dependent vertical loading and/or lateral confining pressure. The results for stresses, pore pressures, and displacements are plotted and compared with the corresponding single-poroelastic counterparts to highlight the characteristic two-time-scale behavior of the system manifested through the effects of dual-porosity, dual-permeability, dual-stiffness, and interporosity flow on the overall responses.

2 Dual-Porosity and Dual-Permeability Poroelastic Modeling

At the macroscopic level, the dual-porous medium system is considered to consist of two separate and distinct fluid-saturated porous continua: One represents the primary porosity of the porous medium occupying volume fraction v^{I} of the total bulk volume and the other represents the secondary porosity of the porous system occupying the remaining bulk volume fraction $\mathrm{v}^{\mathrm{II}}=1-\mathrm{v}^{\mathrm{I}}$. In other words, each medium is generally assumed to be a porous continuum possessing its own skeletal framework and material properties. As a result, dual-porosity and dual-permeability approaches will exhibit dual pore-pressure evolutions when subjected to stress and pressure perturbations. The two porous primary and secondary continua can communicate and may exchange fluid mass.

In the dual-poroelastic constitutive approach, since there are two distinct effective pore-pressure fields, the linear isotropic constitutive equations accounting for the effect of fractures follow naturally from the single-porosity poroelastic formulation as (compression is positive) [26]

$$\sigma_{ij}=\frac{3\bar{K}}{1+\bar{\upsilon}}[(1-2\bar{\upsilon})\varepsilon_{ij}+\bar{\upsilon}\varepsilon_{kk}\delta_{ij}]+(\bar{\alpha}^{\mathrm{I}}p^{\mathrm{I}}+\bar{\alpha}^{\mathrm{II}}p^{\mathrm{II}})\delta_{ij} \tag{1}$$

$$\zeta^{\mathrm{I}}=-\bar{\alpha}^{\mathrm{I}}\varepsilon_{kk}+\frac{p^{\mathrm{I}}}{\bar{M}^{\mathrm{I}}}+\frac{p^{\mathrm{II}}}{\bar{M}^{\mathrm{I,II}}} \tag{2}$$

$$\zeta^{\mathrm{II}}=-\bar{\alpha}^{\mathrm{II}}\varepsilon_{kk}+\frac{p^{\mathrm{I}}}{\bar{M}^{\mathrm{I,II}}}+\frac{p^{\mathrm{II}}}{\bar{M}^{\mathrm{II}}} \tag{3}$$

where the superscript $(N)=\mathrm{I},\mathrm{II}$ refers to the primary and secondary porosity continua, respectively; σ_{ij} is the total stress tensor and ε_{ij} is total strain tensor; $\varepsilon_{kk}=\Delta V/V$ denotes the overall bulk volumetric strain; $p^{(N)}$ represents the pore-fluid pressure in the primary or secondary porosity network; $\zeta^{(N)}$ indicates the corresponding change in local pore-fluid volume in a representative unit volume of the combined dual-porosity system; δ_{ij} is the Kronecker delta; and the overbar denotes the overall dual-porosity poroelastic material coefficients.

Equations (1)–(3) are direct extensions of single-porosity poroelastic to dual-porosity poroelastic in which fluid pressures and deformations in each porous medium are coupled through their constitutive relations. The formulation are characterized by effective material constants such as the overall drained elastic bulk modulus and Poisson's ratio $(\bar{K},\bar{\upsilon})$, the effective pore-pressure coefficients $(\bar{\alpha}^{\mathrm{I}},\bar{\alpha}^{\mathrm{II}})$, and the effective coupled Biot's moduli $(\bar{M}^{\mathrm{I}},\bar{M}^{\mathrm{II}},\bar{M}^{\mathrm{I,II}})$. These overall coefficients represent the combined responses of the whole system and are related to the intrinsic material constants and volume fractions of the constituting porous phases (primary and secondary porosities) as presented in Appendix A.

Other governing equations include the following:

- equilibrium equation (quasistatic)

$$\frac{\partial\sigma_{ij}}{\partial x_j}=0 \tag{4}$$

- strain-displacement relation

$$\varepsilon_{ij}=\frac{1}{2}\left(\frac{u_i}{\partial x_j}+\frac{u_j}{\partial x_i}\right) \tag{5}$$

- continuity equations of the fluid phases

$$\frac{\partial\zeta^{\mathrm{I}}}{\partial t}+\frac{\partial q_i^{\mathrm{I}}}{\partial x_i}=\Gamma(p^{\mathrm{II}}-p^{\mathrm{I}}) \tag{6}$$

$$\frac{\partial\zeta^{\mathrm{II}}}{\partial t}+\frac{\partial q_i^{\mathrm{II}}}{\partial x_i}=-\Gamma(p^{\mathrm{II}}-p^{\mathrm{I}}) \tag{7}$$

- Darcy's law

$$q_i^{(N)}=-\bar{\kappa}^{(N)}\frac{\partial p^{(N)}}{\partial x_i} \tag{8}$$

in which x_i represents the spatial coordinates; u_i is the displacement vector, $q_i^{(N)}$ denotes the specific fluid discharge vector; $\bar{\kappa}^{(N)}=\mathrm{v}^{(N)}\kappa^{(N)}=\mathrm{v}^{(N)}k^{(N)}/\mu^{(N)}$ is the effective macroscopic mobility coefficient where $k^{(N)}$ is the intrinsic permeability of the individual matrix or fracture porous region and $\mu^{(N)}$ is the fluid dynamic viscosity. The right hand side of Eqs. (6) and (7) signifies the interporosity fluid transfer, which is assumed to be proportional to the pressure differential between the primary and secondary porosities [24]. Γ is a transport coefficient depending on the characteristics of the dual-permeability material such as the primary and secondary porosities' geometry, distribution, and connectivity [24,25]. It should be noted that by mass conservation law, the interporosity exchange does not affect the change in total fluid content $\zeta=\zeta^{\mathrm{I}}+\zeta^{\mathrm{II}}$ in a saturated dual-porosity and dual-permeability medium.

The above governing equations are combined to yield a number of useful relations and field equations for obtaining analytical solutions of quantities such as the dual pore-pressure fields and stress/strain distributions. First, the equilibrium equation (4) combined with the stress-strain-pressure equation (1) and the strain-displacement relation (Eq. (5)) leads to the compatibility relation of the system as

$$\nabla^2\left(\varepsilon_{kk}+\frac{\bar{\eta}^{\mathrm{I}}}{\bar{G}}p^{\mathrm{I}}+\frac{\bar{\eta}^{\mathrm{II}}}{\bar{G}}p^{\mathrm{II}}\right)=0 \tag{9}$$

where ∇^2 is the Laplacian differential operator and $\bar{\eta}^{(N)}=\bar{\alpha}^{(N)}(1-2\bar{\upsilon})/2(1-\bar{\upsilon})$ and $\bar{G}=3\bar{K}(1-2\bar{\upsilon})/2(1+\bar{\upsilon})$. Next, the diffusion equations are obtained by substituting the fluid content constitu-

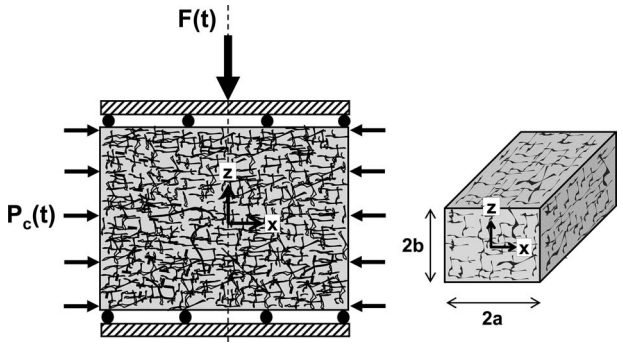

Fig. 1 The Mandel's problem geometry and setup for rectangular strip specimens

tive equations ((2) and (3)) and Darcy's law (Eq. (8)) into the fluid continuity equations ((6) and (7)) as follows:

$$-\bar{\alpha}^{\mathrm{I}}\frac{\partial \varepsilon_{kk}}{\partial t}+\frac{1}{\bar{M}^{\mathrm{I}}}\frac{\partial p^{\mathrm{I}}}{\partial t}+\frac{1}{\bar{M}^{\mathrm{I,II}}}\frac{\partial p^{\mathrm{II}}}{\partial t}=\bar{\kappa}^{\mathrm{I}}\nabla^2 p^{\mathrm{I}}+\Gamma(p^{\mathrm{II}}-p^{\mathrm{I}}) \quad (10)$$

$$-\bar{\alpha}^{\mathrm{II}}\frac{\partial \varepsilon_{kk}}{\partial t}+\frac{1}{\bar{M}^{\mathrm{I,II}}}\frac{\partial p^{\mathrm{I}}}{\partial t}+\frac{1}{\bar{M}^{\mathrm{II}}}\frac{\partial p^{\mathrm{II}}}{\partial t}=\bar{\kappa}^{\mathrm{II}}\nabla^2 p^{\mathrm{II}}-\Gamma(p^{\mathrm{II}}-p^{\mathrm{I}}) \quad (11)$$

In Secs. 3 and 4, these governing constitutive and field equations are applied to derive the analytical solutions for the response of dual-porosity and dual-permeability porous media under plane strain strip and generalized plane strain cylindrical geometries and loading conditions.

3 Mandel's Problem (Rectangular Strip)

3.1 Problem Descriptions. The original Mandel's problem involves an infinitely long rectangular specimen sandwiched between the top and bottom by two frictionless plates as illustrated in Fig. 1. It is assumed that the y-axis is infinitely long and the response along that direction is invariant. This geometry can be represented by a perpendicular cross section (x-z) in a state of plane strain, i.e., the displacement and fluxes vanish in the y direction (perpendicular to the paper). At time $t=0^+$, a constant compressive force $2F$ (per unit length) is applied to the rigid plates at the top and bottom, respectively. The left and right edges of the plates are stress-free and drained. The geometry and boundary conditions imply that every horizontal plane is a plane of folding symmetry. That is, horizontal planes remain horizontal ($\varepsilon_{zz}=\varepsilon_{zz}(t)$), fluid flow is parallel to the impermeable plates ($q_z^{\mathrm{I}}=q_z^{\mathrm{II}}=0$), and there are no shear stresses on the plane ($\sigma_{xz}=0$). In addition, the responses of all quantities are symmetric about the centerline z-axis ($f(x)=f(-x)$) [6,10].

Further in this work, the solutions account for external loading conditions that are generalized to time-dependent loading applications, i.e., $F=F(t)$, $P_c=P_c(t)$, and $p_o=p_o(t)$, where P_c and p_o are the confining stress and fluid pressure on the outer boundary ($x=\pm a$). Mathematically, the generalized boundary conditions are expressed as

$$x=\pm a: \quad \sigma_{xx}=P_c(t),\ p^{\mathrm{I}}=p^{\mathrm{II}}=p_o(t),\ \sigma_{xz}=0 \quad (12)$$

$$z=\pm b: \quad \sigma_{xz}=q_z^{\mathrm{I}}=q_z^{\mathrm{II}}=0,\ u_z=u_z(t) \quad (13)$$

$$z=\pm b: \quad \int_{-a}^{a}\sigma_{zz}dx=2F(t) \quad (14)$$

With the above boundary conditions, the governing equations can be reduced to one-dimensional and all variables are, at most, functions of x and t only. Specifically, the compatibility relation (Eq. (9)) is simplified to

$$\frac{\partial^2}{\partial x^2}\left(\varepsilon_{kk}+\frac{\bar{\eta}^{\mathrm{I}}}{\bar{G}}p^{\mathrm{I}}+\frac{\bar{\eta}^{\mathrm{II}}}{\bar{G}}p^{\mathrm{II}}\right)=0 \quad (15)$$

where $\varepsilon_{kk}=\varepsilon_{xx}+\varepsilon_{zz}$. Integrating twice and accounting for the symmetry about the centerline yields

$$\varepsilon_{kk}+\frac{\bar{\eta}^{\mathrm{I}}}{\bar{G}}p^{\mathrm{I}}+\frac{\bar{\eta}^{\mathrm{II}}}{\bar{G}}p^{\mathrm{II}}=C_o(t) \quad (16)$$

in which $C_o(t)$ is an integration constant depending only on time. Eliminating the volumetric strain ε_{kk} in Eqs. (10) and (11) leads to the reduced diffusion equations in terms of the dual fluid pressures. In compact matrix form, they are expressed as

$$\left([\mathbf{A}]\frac{\partial}{\partial t}-[\mathbf{D}]\frac{\partial^2}{\partial x^2}+[\mathbf{\Gamma}]\right)\begin{Bmatrix}p^{\mathrm{I}}\\ p^{\mathrm{II}}\end{Bmatrix}=\begin{Bmatrix}\bar{\alpha}^{\mathrm{I}}\\ \bar{\alpha}^{\mathrm{II}}\end{Bmatrix}\frac{\partial C_o(t)}{\partial t}, \quad (17)$$

where the coefficient matrices $[\mathbf{A}]$, $[\mathbf{D}]$, and $[\mathbf{\Gamma}]$ are defined as

$$[\mathbf{A}]=\begin{bmatrix}\dfrac{1}{\bar{M}^{\mathrm{I}}}+\dfrac{\bar{\alpha}^{\mathrm{I}}\bar{\eta}^{\mathrm{I}}}{\bar{G}} & \dfrac{1}{\bar{M}^{\mathrm{I,II}}}+\dfrac{\bar{\alpha}^{\mathrm{I}}\bar{\eta}^{\mathrm{II}}}{\bar{G}}\\ \dfrac{1}{\bar{M}^{\mathrm{I,II}}}+\dfrac{\bar{\alpha}^{\mathrm{II}}\bar{\eta}^{\mathrm{I}}}{\bar{G}} & \dfrac{1}{\bar{M}^{\mathrm{II}}}+\dfrac{\bar{\alpha}^{\mathrm{II}}\bar{\eta}^{\mathrm{II}}}{\bar{G}}\end{bmatrix} \quad (18)$$

$$[\mathbf{D}]=\begin{bmatrix}\bar{\kappa}^{\mathrm{I}} & 0\\ 0 & \bar{\kappa}^{\mathrm{II}}\end{bmatrix},\quad [\mathbf{\Gamma}]=\Gamma\begin{bmatrix}1 & -1\\ -1 & 1\end{bmatrix} \quad (19)$$

The system composed of Eqs. (16) and (17) is sufficient for the general solution of the three variables $\{\varepsilon_{kk},p^{\mathrm{I}},p^{\mathrm{II}}\}$ and the subsequent stresses and displacements as derived in the following.

3.2 Analytical Solutions. The diffusion equation (17) is uncoupled from the stress/strain fields and can be readily solved to obtain the general expressions for pore pressures. Applying the Laplace transform to the diffusion equation with the initial condition $\zeta^{\mathrm{I}}(x,0^+)=\zeta^{\mathrm{II}}(x,0^+)=0$ (fluid requires finite time to flow) yields

$$\left(s[\mathbf{A}]+[\mathbf{\Gamma}]-[\mathbf{D}]\frac{d^2}{dx^2}\right)\begin{Bmatrix}\tilde{p}^{\mathrm{I}}\\ \tilde{p}^{\mathrm{II}}\end{Bmatrix}=\begin{Bmatrix}\bar{\alpha}^{\mathrm{I}}\\ \bar{\alpha}^{\mathrm{II}}\end{Bmatrix}s\tilde{C}_o \quad (20)$$

where the tilde sign $\tilde{(\ )}$ denotes the corresponding quantity in Laplace transform domain, s is the Laplace transform parameter, and $\tilde{C}_o=\tilde{C}_o(s)$. The general solution of the above ordinary differential equation system is straightforward and admits the following form:

$$\tilde{p}^{\mathrm{I}}(x,s)=\tilde{C}_o f^{\mathrm{I}}+C_1^{\mathrm{I}}\cosh(\sqrt{\xi^{\mathrm{I}}}x)+C_1^{\mathrm{II}}\cosh(\sqrt{\xi^{\mathrm{II}}}x) \quad (21)$$

$$\tilde{p}^{\mathrm{II}}(x,s)=\tilde{C}_o f^{\mathrm{II}}+m^{\mathrm{I}}C_1^{\mathrm{I}}\cosh(\sqrt{\xi^{\mathrm{I}}}x)+m^{\mathrm{II}}C_1^{\mathrm{II}}\cosh(\sqrt{\xi^{\mathrm{II}}}x) \quad (22)$$

in which parts of the general solution involving $\sinh(\sqrt{\xi^{(N)}}x)$ have been omitted due to symmetry requirement. In the above, $C_1^{\mathrm{I}}(s)$ and $C_1^{\mathrm{II}}(s)$ are constants to be determined from boundary conditions, ξ^{I} and ξ^{II} are eigenvalues of the coefficient matrix $[\mathbf{Y}]=[\mathbf{D}]^{-1}(s[\mathbf{A}]+[\mathbf{\Gamma}])$, and $f^{\mathrm{I}}(s)$, $f^{\mathrm{II}}(s)$, $m^{\mathrm{I}}(s)$, and $m^{\mathrm{II}}(s)$ are coefficients defined as

$$\xi^{\mathrm{I}},\xi^{\mathrm{II}}=(Y_{11}+Y_{22}\pm\sqrt{(Y_{11}-Y_{22})^2+4Y_{12}Y_{21}})/2 \quad (23)$$

$$m^{\mathrm{I}}=\frac{\xi^{\mathrm{I}}-Y_{11}}{Y_{12}},\quad m^{\mathrm{II}}=\frac{\xi^{\mathrm{II}}-Y_{11}}{Y_{12}} \quad (24)$$

$$\begin{Bmatrix} f^{\mathrm{I}} \\ f^{\mathrm{II}} \end{Bmatrix} = s(s[\mathbf{A}] + [\mathbf{\Gamma}])^{-1} \begin{Bmatrix} \bar{\alpha}^{\mathrm{I}} \\ \bar{\alpha}^{\mathrm{II}} \end{Bmatrix} \tag{25}$$

Next, using the equilibrium, constitutive, and strain-displacement equations, it is easy to solve for the stresses and displacements in terms of the fluid pressures as

$$\tilde{\sigma}_{xx}(s) = \tilde{P}_c \tag{26}$$

$$\tilde{\sigma}_{zz}(x,s) = 2h^{\mathrm{I}}C_1^{\mathrm{I}} \cosh(\sqrt{\xi^{\mathrm{I}}}x) + 2h^{\mathrm{II}}C_1^{\mathrm{II}} \cosh(\sqrt{\xi^{\mathrm{II}}}x) + 2f\tilde{C}_o - \tilde{P}_c \tag{27}$$

$$2\bar{G}\tilde{u}_x(x,s) = -2h^{\mathrm{I}}C_1^{\mathrm{I}} \frac{\sinh(\sqrt{\xi^{\mathrm{I}}}x)}{\sqrt{\xi^{\mathrm{I}}}} - 2h^{\mathrm{II}}C_1^{\mathrm{II}} \frac{\sinh(\sqrt{\xi^{\mathrm{II}}}x)}{\sqrt{\xi^{\mathrm{II}}}} + [\tilde{P}_c - (2f - \bar{K}_v)\tilde{C}_o]x \tag{28}$$

$$2\bar{G}\tilde{u}_z(z,s) = (\bar{K}_v\tilde{C}_o - \tilde{P}_c)z \tag{29}$$

where $\bar{K}_v = \bar{K} + 4\bar{G}/3$, and the lumped coefficients $f(s)$, $h^{\mathrm{I}}(s)$, and $h^{\mathrm{II}}(s)$ are given as

$$f = \bar{\eta}^{\mathrm{I}}f^{\mathrm{I}} + \bar{\eta}^{\mathrm{II}}f^{\mathrm{II}} + \bar{K} + \bar{G}/3 \tag{30}$$

$$h^{\mathrm{I}} = \bar{\eta}^{\mathrm{I}} + m^{\mathrm{I}}\bar{\eta}^{\mathrm{II}}, \quad h^{\mathrm{II}} = \bar{\eta}^{\mathrm{I}} + m^{\mathrm{II}}\bar{\eta}^{\mathrm{II}} \tag{31}$$

The remaining three unknowns $\tilde{C}_o(s)$, $C_1^{\mathrm{I}}(s)$, and $C_1^{\mathrm{II}}(s)$ are determined from the fluid-pressure boundary conditions for p^{I} and p^{II} at the edges $x = \pm a$ and the vertical stress loading condition on top and bottom at $z = \pm b$. Detailed derivations of this solution are presented in Appendix B.

Hence, the complete solution in the Laplace transform domain is obtained. It is obvious that the solutions developed in here have the same functional forms as their single-poroelastic counterparts. The differences arise in the additional set of similar terms accounting for the secondary porosity coupled contributions. Requiring the secondary porosity porous medium to shrink to zero, all of the material parameters associated with the secondary porosity porous medium vanish, and the current solution naturally simplifies to a single-porosity solution as shown in Appendix C.

The newly developed dual-poroelastic solution in Laplace transform domain is too complicated to be inverted analytically back into the time domain. However, the time-domain solution can be efficiently computed using numerical inversion methods such as Stehfest's algorithm [27]. Though robust, the numerical inversion schemes may diverge and fall short in modeling certain loading conditions such as cyclic or piecewise loading function [28]. As a result, it is of benefit to obtain a true time-domain analytical solution for using where the numerical inversion method fails. Derivation of the general time-domain solution in terms of an infinite series is presented in Appendix D. Explicit expressions for three unconfined uniaxial loading cases such as step loading, cyclic loading, and linear ramp loading are also summarized in Appendix D. So far, the analysis applies only to strip problem in Cartesian coordinate. It will be shown in Sec. 4 that the extension to cylindrically axisymmetric problem is analogously straightforward.

4 The Axisymmetric Mandel-Type Problem (Circular Disk/Solid Cylinder)

4.1 Problem Descriptions. In this section, the compaction of a saturated cylinder sandwiched between top and bottom impermeable, rigid, and frictionless plates (Fig. 2) is investigated. The cross section of the cylinder is circular. A compressive force $F(t)$ is applied to the rigid plates at the top and bottom, respectively. Additionally, a confining stress $P_c(t)$ as well as a fluid pressure $p_o(t)$ can be applied on the lateral surface. In a common laboratory setting, the confining stress and fluid pressure at the outer boundary ($r=R$) are often the same, i.e., $P_c(t)=p_o(t)$.

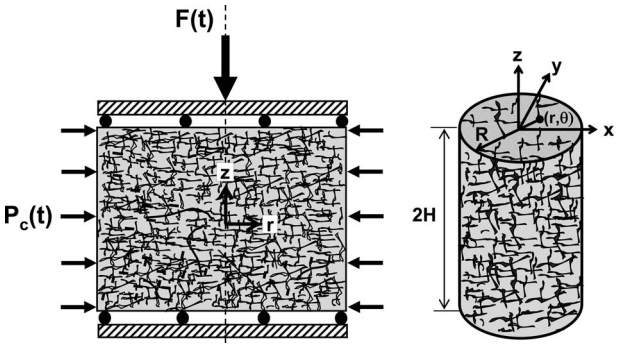

Fig. 2 The axisymmetric Mandel-type problem geometry and setup for cylindrical or circular disk samples

Mathematically, the boundary conditions are expressed in cylindrical coordinate as

$$r = R: \quad \sigma_{rr} = P_c(t), \quad p^{\mathrm{I}} = p^{\mathrm{II}} = p_o(t), \quad \sigma_{r\theta} = \sigma_{rz} = 0 \tag{32}$$

$$z = \pm H: \quad \sigma_{rz} = \sigma_{\theta z} = q_z^{\mathrm{I}} = q_z^{\mathrm{II}} = 0, \quad u_z = u_z(t) \tag{33}$$

$$z = \pm H: \quad \int_0^R r\sigma_{zz}dr = \frac{F(t)}{2\pi} \tag{34}$$

With the aforementioned setup, the problem is obviously axisymmetric providing that at any time the shear stresses and strains $\sigma_{r\theta}=\sigma_{\theta z}=0$, $\varepsilon_{r\theta}=\varepsilon_{\theta z}=0$, and all other variables are independent of θ. The geometry and boundary conditions imply that every horizontal cross section is a plane of folding symmetry. That is, horizontal planes remain horizontal ($\varepsilon_{zz}=\varepsilon_{zz}(t)$), fluid flow is in the radial direction only ($q_z^{\mathrm{I}}=q_z^{\mathrm{II}}=0$), and there are no shear stress on the plane ($\sigma_{rz}=0$).

Under such conditions, a generalized plane strain condition naturally manifests in any cross-sectional plane [18]. Consequently, the governing equations can be reduced to one-dimensional and all variables are, at most, functions of r and t only. Specifically, the compatibility relation (Eq. (9)) becomes

$$\left(\frac{\partial^2}{\partial r^2} + \frac{1}{r}\frac{\partial}{\partial r}\right)\left(\varepsilon_{kk} + \frac{\bar{\eta}^{\mathrm{I}}}{\bar{G}}p^{\mathrm{I}} + \frac{\bar{\eta}^{\mathrm{II}}}{\bar{G}}p^{\mathrm{II}}\right) = 0 \tag{35}$$

where $\varepsilon_{kk}=\varepsilon_{rr}+\varepsilon_{\theta\theta}+\varepsilon_{zz}$, $\varepsilon_{rr}=\partial u_r/\partial r$, $\varepsilon_{\theta\theta}=u_r/r$, and $\varepsilon_{zz}=\varepsilon_{zz}(t)$ remain to be determined. Integrating twice and seeking for bounded solution yields

$$\varepsilon_{kk} + \frac{\bar{\eta}^{\mathrm{I}}}{\bar{G}}p^{\mathrm{I}} + \frac{\bar{\eta}^{\mathrm{II}}}{\bar{G}}p^{\mathrm{II}} = C_o(t) \tag{36}$$

in which $C_o(t)$ is an integration constant depending only on time. The diffusion equation then becomes

$$\left[[\mathbf{A}]\frac{\partial}{\partial t} + [\mathbf{\Gamma}] - [\mathbf{D}]\left(\frac{\partial^2}{\partial r^2} + \frac{1}{r}\frac{\partial}{\partial r}\right)\right]\begin{Bmatrix} p^{\mathrm{I}} \\ p^{\mathrm{II}} \end{Bmatrix} = \begin{Bmatrix} \bar{\alpha}^{\mathrm{I}} \\ \bar{\alpha}^{\mathrm{II}} \end{Bmatrix}\frac{\partial C_o(t)}{\partial t} \tag{37}$$

Therefore, the diffusion equations are the same for strip and circular loadings in which the spatial Laplacian operator is changed from $\nabla^2 = \partial^2/\partial x^2$ to $\nabla^2 = \partial^2/\partial r^2 + (\partial/\partial r)/r$. The formal solution to the axisymmetric problem can be derived in a similar manner to the strip loading problem as shown in Sec. 4.2.

4.2 Analytical Solutions. Analogous to the strip loading problem, the Laplace transform general solutions for the fluid pressures are first derived as

$$\tilde{p}^{\mathrm{I}}(r,s) = \tilde{C}_o f^{\mathrm{I}} + C_1^{\mathrm{I}} I_0(\sqrt{\xi^{\mathrm{I}}} r) + C_1^{\mathrm{II}} I_0(\sqrt{\xi^{\mathrm{II}}} r) \tag{38}$$

$$\tilde{p}^{\mathrm{II}}(r,s) = \tilde{C}_o f^{\mathrm{II}} + m^{\mathrm{I}} C_1^{\mathrm{I}} I_0(\sqrt{\xi^{\mathrm{I}}} r) + m^{\mathrm{II}} C_1^{\mathrm{II}} I_0(\sqrt{\xi^{\mathrm{II}}} r) \tag{39}$$

in which I_0 is the modified Bessel function of the first kind of order zero, and all other parameters are the same as defined previously in the strip loading solution. Equations (38) and (39) also imply that all variables must be finite at $r=0$. Making use of the pressure expressions, other solutions for displacements, strains, and stresses follow naturally from the constitutive equation (1) as

$$2\bar{G}\tilde{u}_r(r,s) = -2h^{\mathrm{I}} C_1^{\mathrm{I}} \frac{I_1(\sqrt{\xi^{\mathrm{I}}} r)}{\sqrt{\xi^{\mathrm{I}}}} - 2h^{\mathrm{II}} C_1^{\mathrm{II}} \frac{I_1(\sqrt{\xi^{\mathrm{II}}} r)}{\sqrt{\xi^{\mathrm{II}}}} - [\bar{G}\tilde{\varepsilon}_{zz} + (f - \bar{K}_v)\tilde{C}_o] r \tag{40}$$

$$2\bar{G}\tilde{\varepsilon}_{rr}(r,s) = -2h^{\mathrm{I}} C_1^{\mathrm{I}} \left[I_0(\sqrt{\xi^{\mathrm{I}}} r) - \frac{I_1(\sqrt{\xi^{\mathrm{I}}} r)}{\sqrt{\xi^{\mathrm{I}}} r} \right] - 2h^{\mathrm{II}} C_1^{\mathrm{II}} \left[I_0(\sqrt{\xi^{\mathrm{II}}} r) - \frac{I_1(\sqrt{\xi^{\mathrm{II}}} r)}{\sqrt{\xi^{\mathrm{II}}} r} \right] - \bar{G}\tilde{\varepsilon}_{zz} - (f - \bar{K}_v)\tilde{C}_o \tag{41}$$

$$2\bar{G}\tilde{\varepsilon}_{\theta\theta}(r,s) = -2h^{\mathrm{I}} C_1^{\mathrm{I}} \frac{I_1(\sqrt{\xi^{\mathrm{I}}} r)}{\sqrt{\xi^{\mathrm{I}}} r} - 2h^{\mathrm{II}} C_1^{\mathrm{II}} \frac{I_1(\sqrt{\xi^{\mathrm{II}}} r)}{\sqrt{\xi^{\mathrm{II}}} r} - \bar{G}\tilde{\varepsilon}_{zz} - (f - \bar{K}_v)\tilde{C}_o \tag{42}$$

$$\tilde{\sigma}_{rr}(r,s) = 2h^{\mathrm{I}} C_1^{\mathrm{I}} \frac{I_1(\sqrt{\xi^{\mathrm{I}}} r)}{\sqrt{\xi^{\mathrm{I}}} r} + 2h^{\mathrm{II}} C_1^{\mathrm{II}} \frac{I_1(\sqrt{\xi^{\mathrm{II}}} r)}{\sqrt{\xi^{\mathrm{II}}} r} + f\tilde{C}_o - \bar{G}\tilde{\varepsilon}_{zz} \tag{43}$$

$$\tilde{\sigma}_{\theta\theta}(r,s) = 2h^{\mathrm{I}} C_1^{\mathrm{I}} \left[I_0(\sqrt{\xi^{\mathrm{I}}} r) - \frac{I_1(\sqrt{\xi^{\mathrm{I}}} r)}{\sqrt{\xi^{\mathrm{I}}} r} \right] + 2h^{\mathrm{II}} C_1^{\mathrm{II}} \left[I_0(\sqrt{\xi^{\mathrm{II}}} r) - \frac{I_1(\sqrt{\xi^{\mathrm{II}}} r)}{\sqrt{\xi^{\mathrm{II}}} r} \right] + f\tilde{C}_o - \bar{G}\tilde{\varepsilon}_{zz} \tag{44}$$

$$\tilde{\sigma}_{zz}(r,s) = 2h^{\mathrm{I}} C_1^{\mathrm{I}} I_0(\sqrt{\xi^{\mathrm{I}}} r) + 2h^{\mathrm{II}} C_1^{\mathrm{II}} I_0(\sqrt{\xi^{\mathrm{II}}} r) + (2f - \bar{K}_v)\tilde{C}_o + 2\bar{G}\tilde{\varepsilon}_{zz} \tag{45}$$

where f, h^{I}, and h^{II} are as defined in Eqs. (30) and (31). In addition to $\tilde{C}_o(s)$, $C_1^{\mathrm{I}}(s)$, and $C_1^{\mathrm{II}}(s)$, the fourth undetermined quantity in the solution is the axial strain $\tilde{\varepsilon}_{zz}(s)$. All of these coefficients and variables are determined using boundary conditions of vertical stress and dual pressure fields. Again, detailed derivations are presented in Appendix E.

It is easy to verify that the above solution reduces to the single-poroelastic solid cylinder solution as presented by Cui and Abousleiman [20] by allowing the secondary porosity porous medium to vanish. It should be noted that Cui and Abousleiman [20] expressed the solution using a different set of material coefficients such as undrained and drained Poisson ratios $\{v_u, v\}$ and storativity coefficient S. The reduction to single-poroelastic solution in the Laplace transform domain is illustrated in Appendix F. For completeness, the corresponding time-domain solution in terms of infinite series is also derived and presented in Appendix G.

5 Results and Discussions

In this section, results of the above derived dual-porosity and dual-permeability poroelastic solutions for strip and cylindrical geometries are presented and compared with the single-poroelastic solutions. Let $P_c(t)=p_o(t)=0$, resulting in an unconfined uniaxial testing condition. The original Mandel's problem (strip geometry) exhibits symmetry about the Cartesian coordinate plane and plane strain whereas the cylinder problem displays axisymmetry and generalized plane strain condition. Thus, it is of interest to investigate the dual-poroelastic behaviors of the two problems in a parallel manner to highlight the different responses in the two configurations.

5.1 Data for Numerical Analyses. The dual-poroelastic solutions are used herein to simulate the response of naturally fractured rock formations such as fractured shales in which the high permeability fractures are regarded as the secondary porosity porous phase (II). To demonstrate the solutions, the same set of data for a Gulf of Mexico shale [20] are adopted in this analysis as

$$K = 1100 \text{ MPa}, \quad G = 760 \text{ MPa}, \quad \alpha = 0.96, \quad M = 9100 \text{ MPa}$$

$$\phi = 0.14, \quad k = 5 \times 10^{-8} \text{ darcy}, \quad K_s = 27.6 \text{ GPa}$$

$$K_f = 1744 \text{ MPa}$$

The above data are assumed to be the properties of the nonfractured porous matrix phase (I) in the dual-porosity and dual-permeability model. The porous fracture region is expected to be much more compliant than the matrix one; thus, the bulk modulus of the porous fracture is assumed to be smaller than those of the porous rock matrix. In this example, to highlight the contrast in stiffness, the same Poisson's ratio is assumed for both matrix and fracture systems while the fracture's bulk modulus is specified to be 50 times smaller without loss of generality: $v^{\mathrm{I}}=v^{\mathrm{II}}=0.22$ and $K^{\mathrm{II}}=K^{\mathrm{I}}/50=22$ MPa. The local fracture porosity ϕ^{II} is the fracture pore volume divided by the fracture total bulk volume. Since the majority of the fracture are porous flow channels, the fracture porosity are usually close to 1. On the other hand, the fracture volume fraction v^{II} is the fracture bulk volume divided by the total bulk volume of the combined matrix-fracture formation. As such the fracture volume fractions depend on the fracture's spacing and geometry and usually is a small number less than 5% bulk volume, as reported in the literatures [29]. Here, fracture porosity and volume fraction are chosen as $\phi^{\mathrm{II}}=0.95$ and $\mathrm{v}^{\mathrm{II}}=5\%$. Subsequently, the fracture poroelastic parameters α^{II} and M^{II} can be determined using Eqs. (A7) and (A8), assuming that the same fluid is permeating the pore spaces $K_f^{\mathrm{I}}=K_f^{\mathrm{II}}=K_f$, $\mu^{\mathrm{I}}=\mu^{\mathrm{II}}=0.01$ Pa s (viscosity), and the porous matrix and porous fracture skeletons are comprised of the same mineral materials $K_s^{\mathrm{I}}=K_s^{\mathrm{II}}=K_s$.

The local or intrinsic fracture permeability is the macroscopic permeability that is assigned to the fracture system in a given volume of rock, and thus dependent on the fracture width and spacing. For isotropic modeling, the bulk fracture permeability can be estimated based on a simple sugar cube model (three orthogonal sets of fractures) as [29]

$$k^{\mathrm{II}} = (2/3) \times 8.35 \times 10^6 \times w^4/d$$

where w and d are the average fracture width and spacing in centimeters, respectively. Hence, assuming $w=0.004$ cm and $d=0.3$ cm leads to a fracture permeability of approximately 0.005 darcy (5×10^{-15} m^2). Correspondingly, the interporosity flow coefficient can be estimated to be proportional to the matrix mobility k^{I} adjusted by a geometric factor depending on fracture spacing d and volume fraction [24], e.g., $\Gamma = 60 \times \mathrm{v}^{\mathrm{II}} \kappa^{\mathrm{I}}/d^2 \approx 1.67 \times 10^{-7}$ (MPa s)$^{-1}$.

For the dual-porosity and dual-permeability approaches to apply, the nominal length scale of the testing sample must be at least an order of magnitude larger than the average fracture spacing to ensure continuum requirement of a representative elementary volume [30]. Therefore, the strip specimen is taken to have cross section of $2(a\times b)=6\times10$ cm while the cylinder's diameter and height are also $2(R\times H)=6\times10$ cm. A vertical/axial force of $F_{\mathrm{strip}}=3\times10^4$ N/m or $F_{\mathrm{cylinder}}=2.83\times10^3$ N/m is applied, which gives the same average vertical stress of $\sigma_o=1$ MPa for both testing configurations.

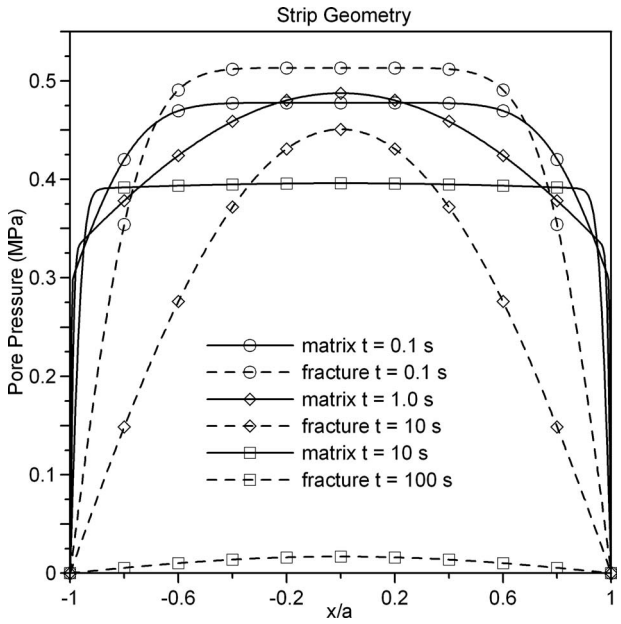

Fig. 3 Pore-pressure profile for strip geometry at various times

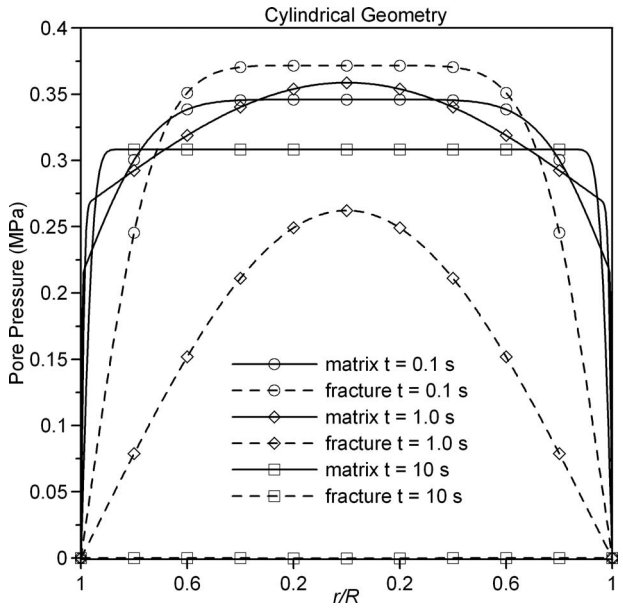

Fig. 4 Pore-pressure profile for cylindrical geometry at various times

5.2 Dual-Porosity and Dual-Permeability Poroelastic Responses. In this section, the dual-porosity and dual-permeability poroelastic predictions are analyzed in conjunction with the single-porosity and single-permeability responses. For ease of physical interpretation, the analysis is carried out for step loading condition. The results for other loading applications are discussed later.

The dual-poroelastic formulation reduces to two diffusion equations (Eqs. (10) and (11)) each of which is associated with an apparent diffusion coefficient. The analytical solution shows that there are two eigenvalues ξ_1^{I} and ξ^{II}, which physically correspond to the dual pressure-diffusion coefficients in the porous matrix and fracture continua, respectively. These eigenvalues indicate the characteristic time scales equal to the characteristic length (lateral width a for strip or radius R for cylinder) squared divided by the diffusion coefficients. Due to the contribution of interporosity flow, these apparent diffusion coefficients are not constant but time-dependent. Nevertheless, the eigenvalues—calculated by neglecting interporosity term—can be used to estimate the relative time scale among the two diffusion processes. From the above data, the reduced apparent diffusion coefficients $c^{(N)}=s/\xi^{(N)}$ and their associated characteristic times $t_c^{(N)}=a^2/c^{(N)}$ or $t_c^{(N)}=R^2/c^{(N)}$ are as follows:

$$c^{\mathrm{I}} = 9.20 \times 10^{-4}\ \mathrm{cm^2/s}, \quad c^{\mathrm{II}} = 2.10\ \mathrm{cm^2/s}$$

$$t_c^{\mathrm{I}} = 9800\ \mathrm{s} \cong 2.7\ \mathrm{hours}, \quad t_c^{\mathrm{II}} = 4.3\ \mathrm{s}$$

Hence, fluid diffusion process that takes only seconds in the fracture will require hours in the matrix. Figures 3 and 4 show results of pore-pressure profile for both geometries under step loading condition at various times. The fast pressure diffusion in the fracture is prominently displayed, e.g., the fracture's fluid pressure almost dissipates completely after 10 s while the matrix fluid pressure is still substantial. Figures 5 and 6 show the corresponding vertical and axial stress distributions in the samples. The results for stress and pore pressures display typical nonmonotonic poroelastic behaviors in terms of the Mandel–Cryer effect. As time progresses, the pore pressure near the edges must dissipate due to access to drainage, effectively making the specimen more compliant near the sides and stiffer in the center region. Therefore, there is a load transfer to the middle region such that the pressure continues to rise after its initial jump. At long time, the initial pore-pressure buildup decreases due to subsequent fluid diffusion.

Figures 7 and 8 illustrate the histories of pressures in the center of the specimens. Similar to the single-poroelastic response, the dual-poroelastic matrix and fracture pressures show typical nonmonotonic poroelastic behaviors as the pore pressures continue to rise after initial jumps due to Skempton's effect. From the solutions of pore pressures, the initial pore-pressure rises per unit volumetric stress applied are computed as $p_{0^+}^{(N)}=\gamma^{(N)}/2h$ for rectangular strip and $p_{0^+}^{(N)}=\gamma^{(N)}/(4h-\bar{K}_v)$ for cylinder ($\gamma^{(N)}$ and h are defined in Eqs. (D4) and (D14), respectively). For single-poroelastic, these values simplify to $p_{0^+}=B(1+v_u)/3$ for strip and $p_{0^+}=B/3$ for cylinder where B is Skempton's pore-pressure coef-

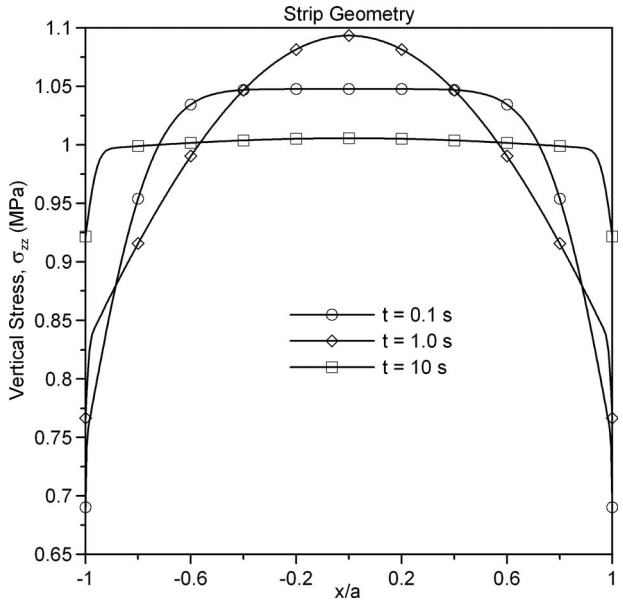

Fig. 5 Vertical stress profile for strip geometry at various times

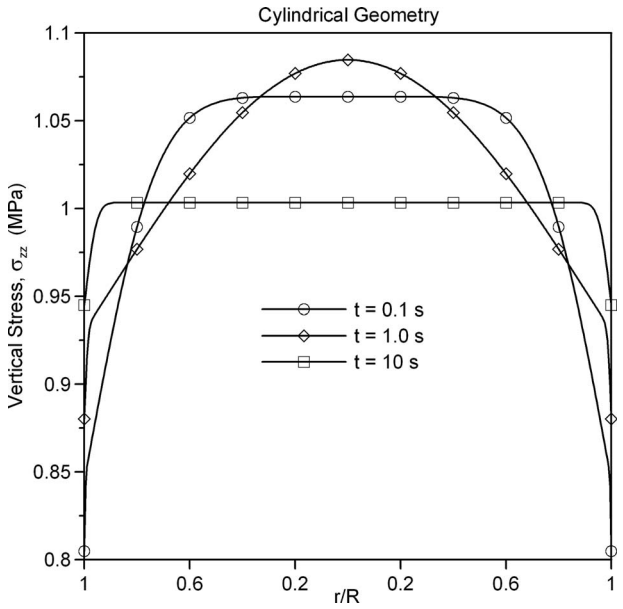

Fig. 6 Vertical stress profile for cylindrical geometry at various times

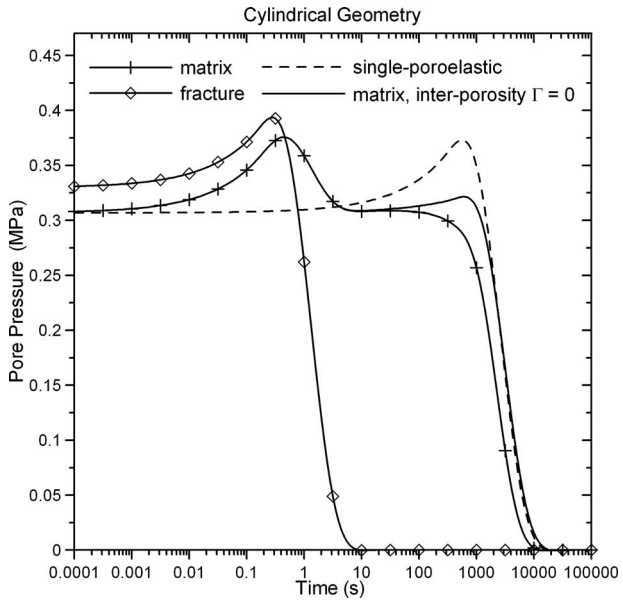

Fig. 8 Pore-pressure histories in the center of the cylinder

ficient and v_u is the undrained Poisson's ratio. Therefore, the load application on cylinder geometry is expected to generate less initial pore-pressure elevation than strip configuration. For this data set, the values of these pore pressure rises are calculated as $\{p^{\mathrm{I}}_{0^+}=0.458, p^{\mathrm{II}}_{0^+}=0.495, p_{0^+}=0.448\}$ for strip and $\{p^{\mathrm{I}}_{0^+}=0.31, p^{\mathrm{II}}_{0^+}=0.33, p_{0^+}=0.31\}$ for cylinder. Hence, the matrix and fracture continua exhibit higher initial pore-pressure elevations. This is reasonable since the combined matrix-fracture system is more compliant than the single-porosity (intact) rock. Clearly, there are two distinct responses, especially in the matrix pressure, signifying the dual time scales as estimated above. The first pressure buildup after about 1 s corresponds to the characteristic time of the fracture region. Being more fluid permeable, the porous fracture quickly dissipates this buildup and falls below the matrix pressure. As time progresses, the matrix pressure seeks to build up nonmonotonically again with characteristic time $t^{\mathrm{I}}_c=9800$ s–2.7 h while supplying flow into the fracture via interporosity fluid exchange. In fact, fluid loss due to interporosity exchange with the fracture negates the second pressure buildup in the matrix. To visualize the contribution of the interporosity process, the corresponding matrix pressure without interporosity is also plotted in Figs. 7 and 8. The separation between the matrix pressure with and without interporosity flow denotes the magnitude of interporosity exchange.

Figures 9 and 10 show the time evolution of the vertical and lateral displacements for both geometries. First, the dual-poroelastic predictions display similar consolidation features as single-poroelastic counterpart, i.e., lateral contraction after initial expansion as displayed in Fig. 10. However, the dual-poroelastic clearly exhibits dual responses in the consolidation process. For example, the samples consolidate vertically to an initial constant

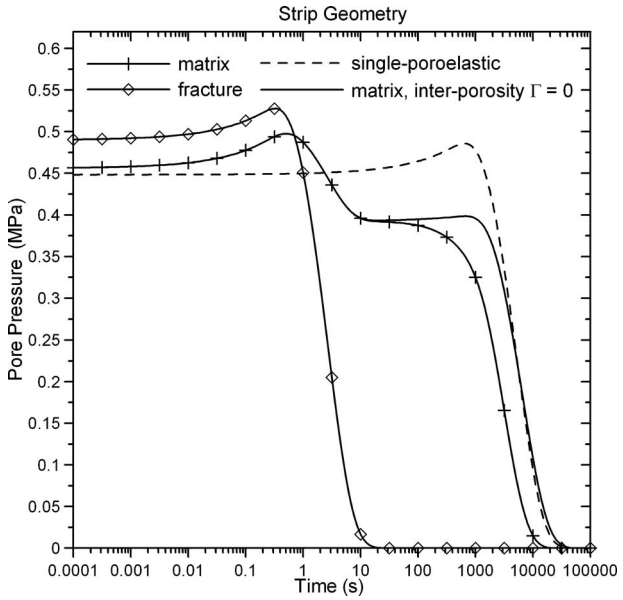

Fig. 7 Pore-pressure histories in the center of the rectangular strip

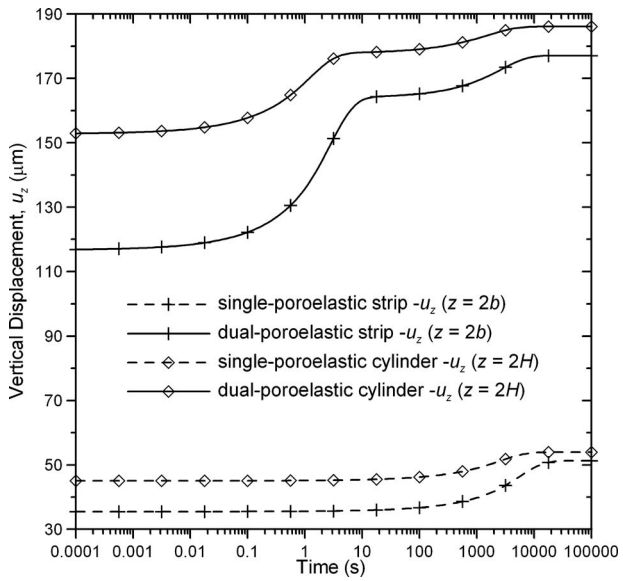

Fig. 9 Vertical displacement histories at the top of the sample for both strip and cylindrical geometries

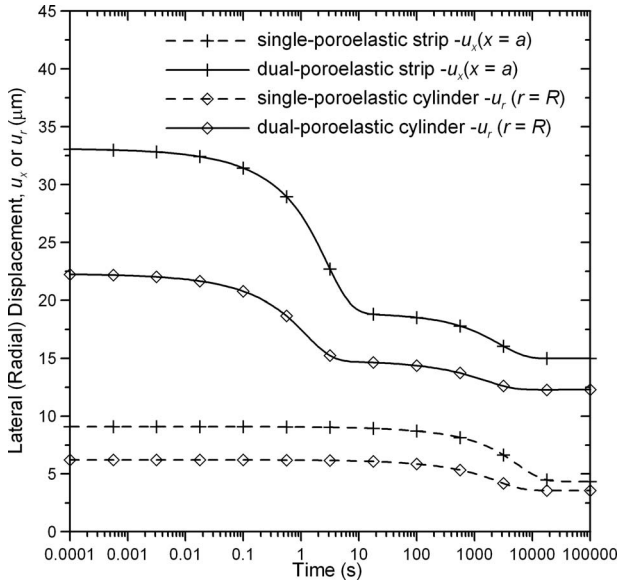

Fig. 10 Lateral displacement histories on the outside of the sample for both strip and cylindrical geometries

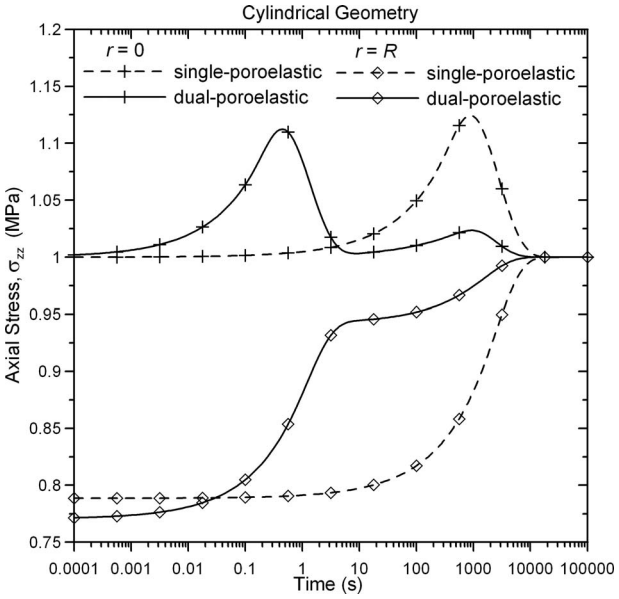

Fig. 12 Axial stress histories at $r=0$ and $r=R$ for cylinder

value after all the fluid has been drained out in the fracture (10 s) then compact to a final value when pressure buildup in the matrix diffuse completely (1200 s) as shown in Fig. 9. Additionally, the dual-poroelastic results naturally predict larger displacement than single-poroelastic ones since the presence of fractures typically renders the rock more compressible.

Similarly, Figs. 11 and 12 show the histories of vertical stress developed at the center ($x=0$ or $r=0$) and at the edges of a strip ($x=\pm a$) or the outer boundary of the cylinder ($r=R$). Again, a transient dual response is observed. At the center, there are dual buildups of vertical stress with initial magnitude of 10% and later 1.5% above the average applied stress. At the edges, the stress level at small time is less than single-permeability solution due to faster draining of the supporting fluid pressure. As time elapses, the stress everywhere in the sample evolves through two stages before converging to the equilibrium applied stress value.

Obviously, the general behavior of the dual-poroelastic system is characterized by two time scales. These two time scales are functions of the dual permeabilities, dual porosities and stiffness, and interporosity exchange. In the following, the effects of interporosity flow, permeability, and stiffness contrast on the overall response are investigated based on cylindrical sample calculations.

5.3 Effects of Interporosity Exchange. Figure 13 shows the matrix and fracture pressure at the cylinder center ($r=0$) for various values of interporosity exchange coefficient Γ at constant ratios of permeability $k^{II}/k^{I}=10^5$ and stiffness $K^{I}/K^{II}=50$. For no interflow, the matrix pressure has the widest separation with the fracture and mimicking the single-poroelastic counterpart after the

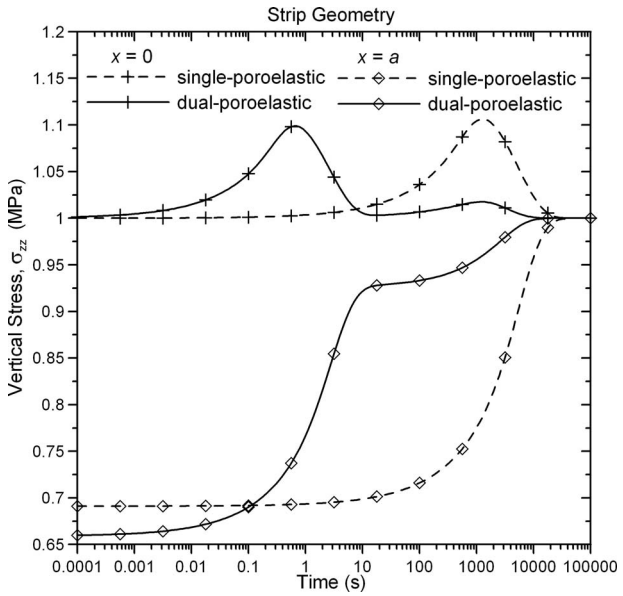

Fig. 11 Vertical stress histories at $x=0$ and $x=a$ for rectangular strip

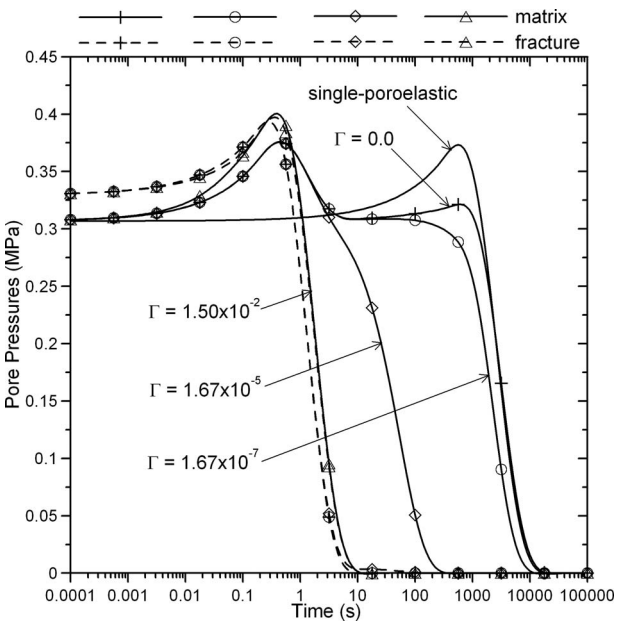

Fig. 13 Pore-pressure histories at the cylinder's center $r=0$ for different interporosity flow coefficients while keeping constant permeability contrast $k^{II}/k^{I}=10^5$ and stiffness ratio $K^{I}/K^{II}=50$

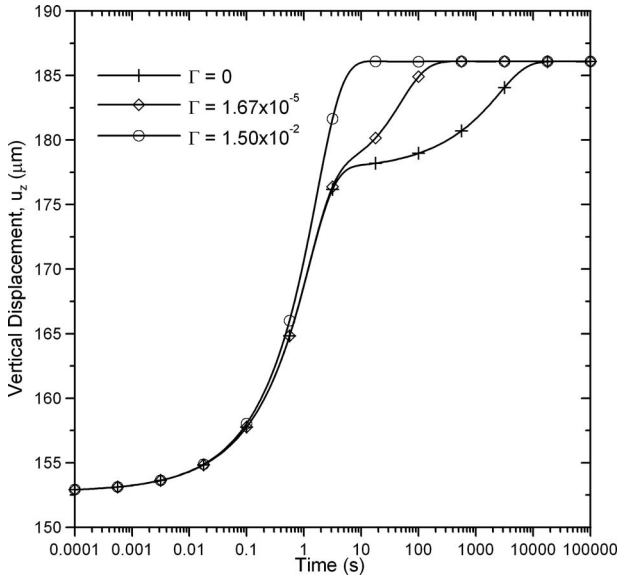

Fig. 14 Vertical displacement histories at the top of the cylinder for different interporosity flow coefficients while keeping constant permeability contrast $k^{II}/k^{I}=10^5$ and stiffness ratio $K^{I}/K^{II}=50$

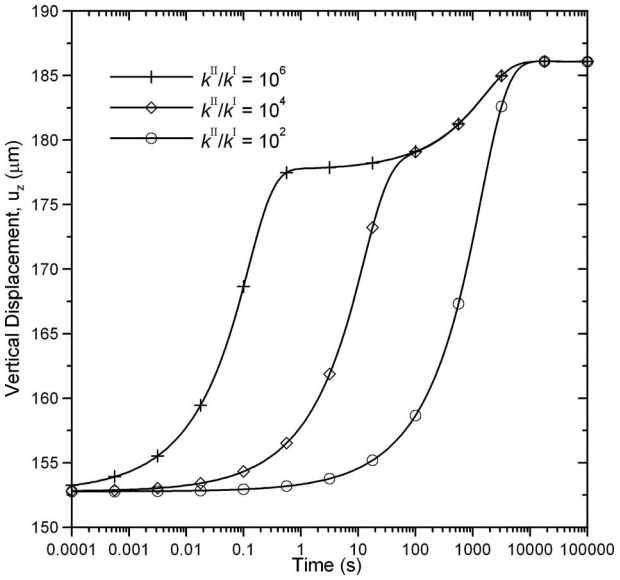

Fig. 16 Vertical displacement histories at the top of the cylinder for different permeability ratios while keeping constant stiffness contrast $K^{I}/K^{II}=50$ and interporosity flow $\Gamma=1.67\times10^{-7}$

initial buildup with the fracture pressure. The higher the interflow, the closer the matrix and fracture pressure converge to each other and the less significant the dual responses become. At large enough interflow magnitude ($\Gamma=1.50\times10^{-2}$ MPa^{-1} s^{-1}), the matrix and fracture pressure are the same, which renders the system single response in terms of the fracture time scale. Figure 14 plots the corresponding vertical displacement history. $\Gamma=0$ reveals two stages of consolidation whereas $\Gamma=1.50\times10^{-2}$ MPa^{-1} s^{-1} only exhibits a fast and single approach to final consolidation. In other words, interporosity exchange equilibrates the dual responses or reduces the effect of time scale contrast.

5.4 Effects of Permeability Contrast. While interporosity flow shrinks the difference between dual responses, the permeability contrast directly affect the time scale ratio. Figure 15 and 16 show the dual pressures and vertical displacement, respectively, for various values of permeability ratios k^{II}/k^{I} (keeping constant permeability in matrix and varying fracture's) at constant interflow $\Gamma=1.67\times10^{-7}$ MPa^{-1} s^{-1} and stiffness contrast $K^{I}/K^{II}=50$. It is seen that the higher the permeability ratio, the more pronounced the characteristic dual-response exhibits.

5.5 Effects of Stiffness Contrast. Analogously, Figs. 17 and 18 depict the dual pressures and consolidation for different values of stiffness ratios K^{I}/K^{II} at constant interflow $\Gamma=1.67\times10^{-7}$ MPa^{-1} s^{-1} and permeability contrast $k^{II}/k^{I}=10^5$. The stiffness ratio defined in this way counters the effect of permeability contrast. Thus, it can be observed in Fig. 17 that the higher the

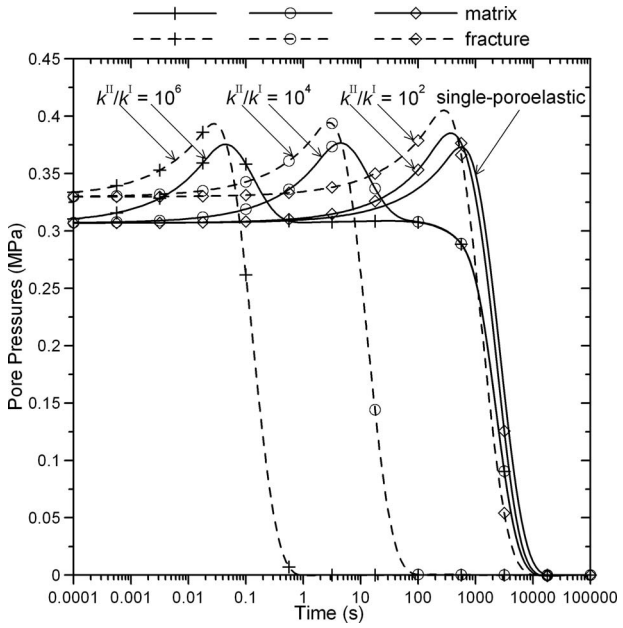

Fig. 15 Pore-pressure histories at the cylinder's center $r=0$ for different permeability ratios while keeping constant stiffness contrast $K^{I}/K^{II}=50$ and interporosity flow $\Gamma=1.67\times10^{-7}$

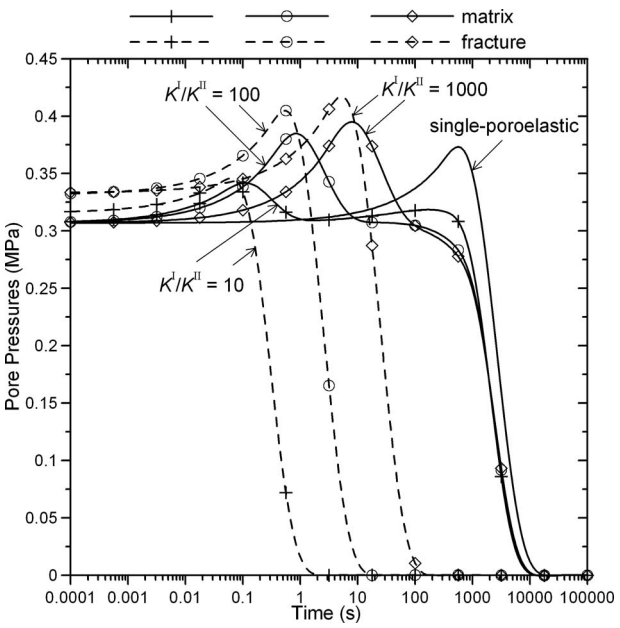

Fig. 17 Pore-pressure histories at the cylinder's center $r=0$ for different bulk modulus ratios while keeping constant permeability contrast $k^{II}/k^{I}=10^5$ and interporosity flow $\Gamma=1.67\times10^{-7}$

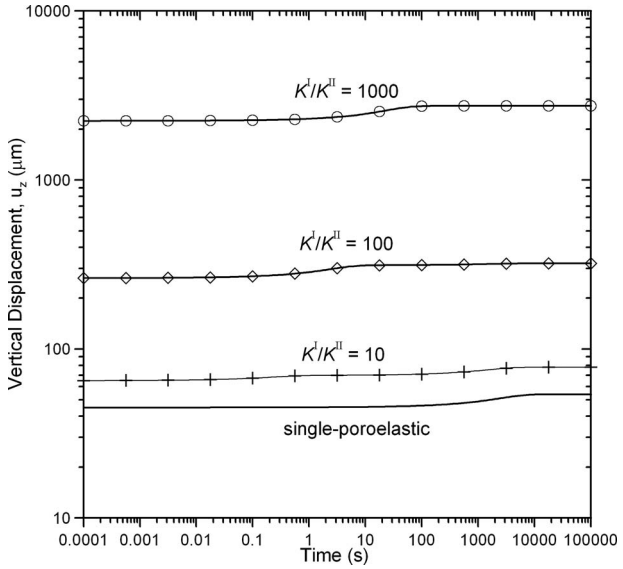

Fig. 18 Vertical displacement histories at the top of the cylinder for different bulk modulus ratios while keeping constant permeability contrast $k^{II}/k^I=10^5$ and interporosity flow $\Gamma=1.67\times10^{-7}$

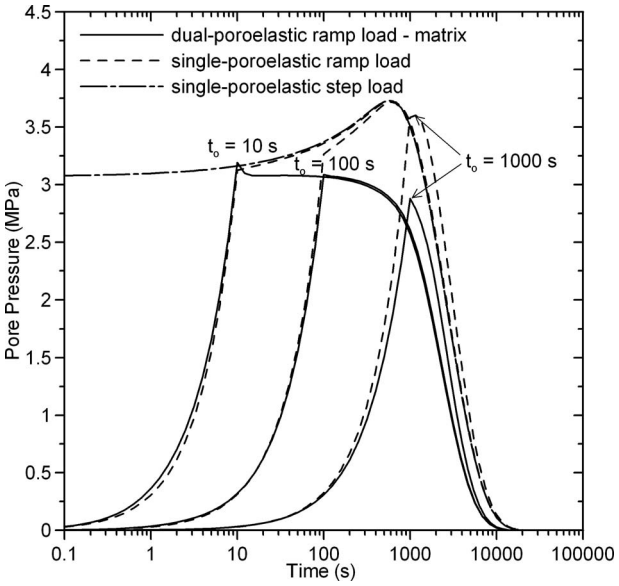

Fig. 20 Pore-pressures histories at the cylinder's center $r=0$ under different linear ramp loading rates

stiffness ratio, the less distinct the dual response becomes. The pressure responses also converge to the single-poroelastic one. However, the magnitude of vertical consolidation is different between dual- and single-poroelastic as shown in Fig. 18. In brief, the stiffness contrast modifies not only the relative time scale but also the magnitude of the final consolidation whereas permeability contrast and interporosity exchange only modified the time scales but does not affect final consolidation magnitude.

5.6 Time-Dependent Loading. So far, the results are shown only for step loading condition. In this section, the responses due to time-dependent loading situations such as cyclic loading, linear ramp loading, and/or combination are briefly demonstrated. For brevity, only the results for cylinder geometry are illustrated hereafter. The responses for rectangular strip sample should be interpreted analogously.

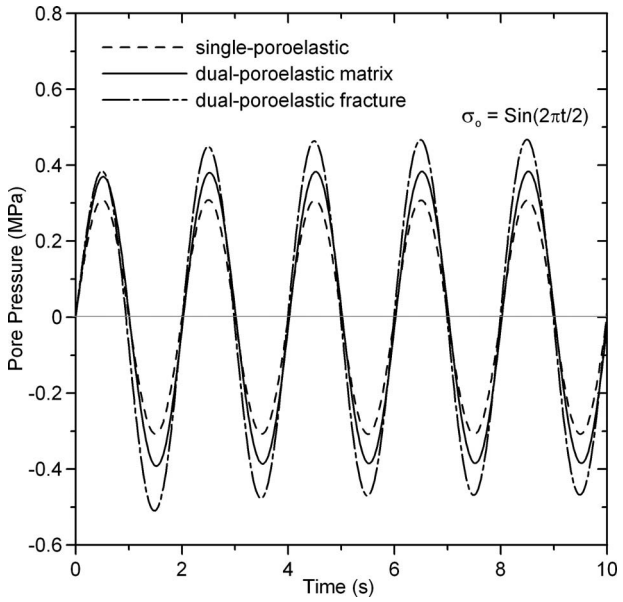

Fig. 19 Pore-pressures histories at the cylinder's center $r=0$ under cyclic loading

Figure 19 shows the pressure evolution at the center of the specimens under a cyclic axial stress with magnitude of 1 MPa and a period of 2 s (0.5 Hz): $\sigma_o(t)=F(t)/\pi R^2=\sin(\pi t)$ for the first five cycles. As expected, the pore pressures also show cyclic behaviors in which the pressure in the fracture is the highest because the loading period is smaller than the characteristic time scale of fracture ($t_c^I\sim4$ s). On the other hand, Fig. 20 demonstrates the pore-pressure response due to a linear ramp loading for three different buildup rates with characteristic times t_o of 10 s, 100 s, and 1000 s. The pressurization process is such that the average axial stress reaches 10 MPa at t_o time and remains constant at this level afterward. Evidently, the fast diffusion speed in fractured medium together with interporosity flow allow significantly less pore-pressure buildup in the sample. Finally, superposition of the basic loading solutions allows modeling of more complex loading processes. For example, combination of the above cyclic and linear ramp results yields the pore-pressure fluctuation during the first 28 s for the loading functions depicted in the inset of Fig. 21.

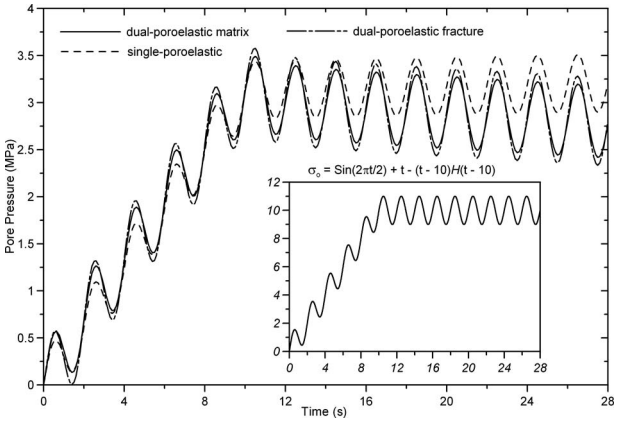

Fig. 21 Pore-pressure fluctuations at the cylinder's center ($r=0$) through times under combined cyclic and linear ramp loadings (the cyclic loading period is $T=2$ s and ramping characteristic time is $t_o=10$ s)

6 Conclusions

The generalized analytical poromechanical solutions have been derived for the two-dimensional Mandel-type problem geometries in both rectangular strip and cylindrical disk setups. The solutions are presented in explicit analytical forms and account for arbitrary time-dependent external loading conditions, e.g., cyclic and ramping. Analyses show that pore-pressure generations are higher during early loading intervals but dissipate faster through the course of time. The dual-porous system exhibits typical dual time scale responses. However, due to the different characteristic time scales among primary porosity, secondary porosity, interporosity flow, and external loading functions, the behaviors of the dual-porous system can vary significantly. As such, the corresponding poromechanical analytical solutions presented herein are general and find their applications spanning both geomechanic and biomechanic fields. Particularly in the petroleum industry, this solution allows geomechanicians the ability to study the effect of fractures on the overall behaviors of naturally fractured rocks and reservoirs. In biomechanics, the same solutions can also be applied to study the response of bones well-known for their multiporosity makeup.

Acknowledgment

The financial support of the PoroMechanics Institute Rock Mechanics Consortium at the University of Oklahoma is gratefully acknowledged.

Nomenclature

Capital Letters

- $\mathbf{A}$ = poroelastic coefficient matrix (Eq. (18))
- B = Skempton pore-pressure coefficient
- C_o = constant of integration (Eqs. (16) and (36))
- $C_1^{\mathrm{I}}, C_1^{\mathrm{II}}$ = general solution constants to be determined from boundary conditions
- $\mathbf{D}$ = transport coefficient matrix (Eq. (19))
- F = vertically applied load
- G = shear modulus
- H = half height of cylinder sample
- I_0, I_1 = modified Bessel function of the first kind of order zero and one
- J_0, J_1 = Bessel function of the first kind of order zero and one
- K = bulk modulus
- K_f = fluid modulus
- K_s = solid grain bulk modulus
- K_v = elastic modulus $(K+4G/3)$
- M = Biot modulus
- P_c = confining stress
- Q = function of Laplace parameter s as defined in Eq. (D20) or Eq. (G10)
- R = radius of cylinder sample
- $\bar{X}$ = overall dual-poroelastic coefficient $(X=K, G, M, \alpha, \eta)$
- $\mathbf{Y}$ = lumped coefficient matrix

Lowercase Letters

- a = half width of rectangular strip sample
- b = half height of rectangular strip sample
- d = fracture spacing
- d_{cylinder} = coefficient for cylinder solution in Laplace transform domain
- d_{strip} = coefficient for strip solution in Laplace transform domain
- f = coefficient as defined in Eq. (30)
- $f^{\mathrm{I}}, f^{\mathrm{II}}$ = solution coefficients in Laplace transform domain (Eq. (25))
- h = coefficient as defined in Eq. (D14)
- $h^{\mathrm{I}}, h^{\mathrm{II}}$ = solution coefficients in Laplace transform domain (Eq. (31))
- m = $(2n\text{-}1)\pi/2a$, Fourier transform parameters
- $m^{\mathrm{I}}, m^{\mathrm{II}}$ = solution coefficients in the Laplace transform domain (Eq. (24))
- n = 1,2,3,…, terms in Fourier or Hankel series summation
- q_i = specific fluid discharge vector
- r = radial coordinate of cylinder sample
- s = Laplace transform parameter
- $s_n^{\mathrm{I}}, s_n^{\mathrm{II}}$ = coefficients as defined in Eq. (D8)
- t = time
- t_o = characteristic time of linear ramp loading
- u_x = horizontal displacement
- u_z = vertical or axial displacement
- u_r = radial displacement
- $\mathrm{v}^{\mathrm{I}}, \mathrm{v}^{\mathrm{II}}$ = volume fraction of primary or secondary porosity porous phase
- w = fracture width
- $w_n^{\mathrm{I}}, w_n^{\mathrm{II}}$ = coefficients as defined in Eq. (D6)
- $z_n^{\mathrm{I}}, z_n^{\mathrm{II}}$ = coefficients as defined in Eq. (D7)

Greek Symbols

- Δ = coefficient as defined in Eq. (D11)
- Φ = coefficient as defined in Eq. (D15)
- Γ = interporosity flow coefficients
- Θ = time function as defined in Eq. (D19) or Eq. (G9)
- Ω = coefficient as defined in Eq. (D16)
- α = effective pore-pressure coefficient
- β_n = nth positive roots of $J_0(\beta R)=0$
- δ_{ij} = Kronecker delta
- ε_{ij} = strain tensor
- ε_{kk} = volumetric strain
- ε_{rr} = radial strain
- $\varepsilon_{\theta\theta}$ = tangential strain
- ε_{xx} = horizontal strain
- ε_{zz} = vertical or axial strain
- $\phi^{\mathrm{I}}, \phi^{\mathrm{II}}$ = porosity
- $\gamma^{\mathrm{I}}, \gamma^{\mathrm{II}}$ = coefficients as defined in Eq. (D4)
- η = poroelastic constant $(3\alpha G/(3K+4G))$
- $\varphi^{\mathrm{I}}, \varphi^{\mathrm{II}}$ = coefficients as defined in Eq. (D5)
- $\kappa^{\mathrm{I}}, \kappa^{\mathrm{II}}$ = mobility coefficient
- λ_i = roots of $Q(s)=1$
- μ = fluid viscosity
- υ = Poisson ratio
- υ_u = undrained Poisson ratio
- θ = angular coordinate
- σ_{ij} = stress tensor
- σ_o = average applied vertical or axial stress
- σ_{rr} = radial stress
- $\sigma_{\theta\theta}$ = tangential stress
- σ_{xx} = horizontal stress
- σ_{zz} = vertical or axial stress
- τ = dummy integration variable
- ω = angular frequency of cyclic loading
- $\xi^{\mathrm{I}}, \xi^{\mathrm{II}}$ = eigenvalues of matrix $\mathbf{Y}$ (Eq. (23))
- $\zeta^{\mathrm{I}}, \zeta^{\mathrm{II}}$ = fluid content

Superscripts

- I = primary porosity porous medium (matrix)
- II = secondary porosity porous medium (fracture)
- N = I or II
- I, II = cross coupling dual-poroelastic coefficient

Appendix A: Dual-Porosity Material Coefficients

Following Berryman and Pride [31], the effective constitutive coefficients for the dual-porosity composite material can be identified in terms of the individual constituent's properties as

$$\bar{\alpha}^{\mathrm{I}} = \alpha^{\mathrm{I}} \frac{\bar{K} - K^{\mathrm{II}}}{K^{\mathrm{I}} - K^{\mathrm{II}}} \tag{A1}$$

$$\bar{\alpha}^{\mathrm{II}} = \alpha^{\mathrm{II}} \frac{K^{\mathrm{I}} - \bar{K}}{K^{\mathrm{I}} - K^{\mathrm{II}}} \tag{A2}$$

$$\frac{1}{\bar{M}^{\mathrm{I}}} = \mathrm{v}^{\mathrm{I}} \bar{\bar{C}}^{\mathrm{I}} - \left(\frac{\alpha^{\mathrm{I}} K^{\mathrm{II}}}{K^{\mathrm{I}} - K^{\mathrm{II}}} \right)^2 \left(\frac{\mathrm{v}^{\mathrm{I}}}{K^{\mathrm{I}}} + \frac{\mathrm{v}^{\mathrm{II}}}{K^{\mathrm{II}}} - \frac{1}{\bar{K}} \right) - \frac{(\bar{\alpha}^{\mathrm{I}})^2}{\bar{K}} \tag{A3}$$

$$\frac{1}{\bar{M}^{\mathrm{I,II}}} = \frac{\alpha^{\mathrm{I}} \alpha^{\mathrm{II}} K^{\mathrm{I}} K^{\mathrm{II}}}{(K^{\mathrm{I}} - K^{\mathrm{II}})^2} \left(\frac{\mathrm{v}^{\mathrm{I}}}{K^{\mathrm{I}}} + \frac{\mathrm{v}^{\mathrm{II}}}{K^{\mathrm{II}}} - \frac{1}{\bar{K}} \right) - \frac{\bar{\alpha}^{\mathrm{I}} \bar{\alpha}^{\mathrm{II}}}{\bar{K}} \tag{A4}$$

$$\frac{1}{\bar{M}^{\mathrm{II}}} = \mathrm{v}^{\mathrm{II}} \bar{\bar{C}}^{\mathrm{II}} - \left(\frac{\alpha^{\mathrm{II}} K^{\mathrm{I}}}{K^{\mathrm{I}} - K^{\mathrm{II}}} \right)^2 \left(\frac{\mathrm{v}^{\mathrm{I}}}{K^{\mathrm{I}}} + \frac{\mathrm{v}^{\mathrm{II}}}{K^{\mathrm{II}}} - \frac{1}{\bar{K}} \right) - \frac{(\bar{\alpha}^{\mathrm{II}})^2}{\bar{K}} \tag{A5}$$

where v^{I} and $\mathrm{v}^{\mathrm{II}} = 1\text{-}\mathrm{v}^{\mathrm{I}}$ are the bulk volume fractions of the primary and secondary porosity media. The individual material coefficients are given as

$$\bar{\bar{C}}^{(N)} = \frac{(\alpha^{(N)})^2}{K^{(N)}} + \frac{1}{M^{(N)}} \tag{A6}$$

$$\alpha^{(N)} = 1 - \frac{K^{(N)}}{K_s^{(N)}} \tag{A7}$$

$$M^{(N)} = \frac{(K_s^{(N)})^2}{K_s^{(N)}[1 + \phi^{(N)}(K_s^{(N)}/K_f^{(N)} - 1)] - K^{(N)}} \tag{A8}$$

in which $K_s^{(N)}$ is grain modulus, $\phi^{(N)} = V_{\mathrm{pore}}^{(N)}/V^{(N)}$ is the local porosity; and $K_f^{(N)}$ is the pore-fluid modulus (inverse of fluid compressibility). The overall bulk modulus $\bar{K}$ can be estimated based on the individual bulk module $K^{(N)}$ by some averaging scheme, e.g., the harmonic average where $\bar{K} = (K^{\mathrm{I}} K^{\mathrm{II}})/(\mathrm{v}^{\mathrm{II}} K^{\mathrm{I}} + \mathrm{v}^{\mathrm{I}} K^{\mathrm{II}})$. It can be seen that when the secondary porosity medium vanishes, i.e., $\mathrm{v}^{\mathrm{II}} \to 0$, the material coefficients reduce naturally to the single-porosity counterparts.

Appendix B: Rectangular Strip Dual-Poroelastic Laplace Transform Domain Solution

The general solution has been listed in Sec. 3.2. Details of the derivations for stresses, displacements, and constants of integration are presented in here. First, integrating the equilibrium Eq. (4) in the x direction and making use of the confining stress boundary conditions at the two edges $x = \pm a$ leads to

$$\sigma_{xx} = P_c(t) \tag{B1}$$

As such, the following stress-strain-pressures relations can be obtained from the constitutive equation (1):

$$P_c(t) = 2\bar{G}\varepsilon_{xx} + (\bar{K} - 2\bar{G}/3)\varepsilon_{kk} + \bar{\alpha}^{\mathrm{I}} p^{\mathrm{I}} + \bar{\alpha}^{\mathrm{II}} p^{\mathrm{II}} \tag{B2}$$

$$\sigma_{zz} = 2\bar{G}\varepsilon_{zz} + (\bar{K} - 2\bar{G}/3)\varepsilon_{kk} + \bar{\alpha}^{\mathrm{I}} p^{\mathrm{I}} + \bar{\alpha}^{\mathrm{II}} p^{\mathrm{II}} \tag{B3}$$

Eliminating the strain using Eq. (16) gives the expression for vertical stress and subsequent displacements in terms of pore pressures as

$$\sigma_{zz} = 2\bar{\eta}^{\mathrm{I}} p^{\mathrm{I}} + 2\bar{\eta}^{\mathrm{II}} p^{\mathrm{II}} + 2(\bar{K} + \bar{G}/3) C_o(t) - P_c(t) \tag{B4}$$

$$2\bar{G}u_x = -2 \int (\bar{\eta}^{\mathrm{I}} p^{\mathrm{I}} + \bar{\eta}^{\mathrm{I}} p^{\mathrm{I}}) dx + [P_c(t) - (\bar{K} - 2\bar{G}/3) C_o(t)] x \tag{B5}$$

$$2\bar{G}u_z = [\bar{K}_v C_o(t) - P_c(t)] z \tag{B6}$$

Substitution of the pressure Eqs. (21) and (22) leads to the explicit general solutions Eqs. (26)–(29). The boundary conditions for fluid pressures at the two edges $x = \pm a$ and vertical stress at the top $z = b$ are

$$\tilde{p}^{\mathrm{I}}|_{x=a} = \tilde{C}_o f^{\mathrm{I}} + C_1^{\mathrm{I}} \cosh(\sqrt{\xi^{\mathrm{I}}} a) + C_1^{\mathrm{II}} \cosh(\sqrt{\xi^{\mathrm{II}}} a) = \tilde{p}_o \tag{B7}$$

$$\tilde{p}^{\mathrm{II}}|_{x=a} = \tilde{C}_o f^{\mathrm{II}} + m^{\mathrm{I}} C_1^{\mathrm{I}} \cosh(\sqrt{\xi^{\mathrm{I}}} a) + m^{\mathrm{II}} C_1^{\mathrm{II}} \cosh(\sqrt{\xi^{\mathrm{II}}} a) = \tilde{p}_o \tag{B8}$$

$$\int_{-a}^{a} \tilde{\sigma}_{zz} dx = 2 \left[2h^{\mathrm{I}} C_1^{\mathrm{I}} \frac{\sinh(\sqrt{\xi^{\mathrm{I}}} a)}{\sqrt{\xi^{\mathrm{I}}}} + 2h^{\mathrm{II}} C_1^{\mathrm{II}} \frac{\sinh(\sqrt{\xi^{\mathrm{II}}} a)}{\sqrt{\xi^{\mathrm{I}}}} + (2f\tilde{C}_o - \tilde{P}_c) a \right] = 2\tilde{F} \tag{B9}$$

Equations (B7)–(B9) are solved simultaneously for $\tilde{C}_o(s)$, $C_1^{\mathrm{I}}(s)$, and $C_1^{\mathrm{II}}(s)$ as

$$\tilde{C}_o(s) = \left\{ \begin{matrix} -2h^{\mathrm{I}}(1 - m^{\mathrm{II}}) \sqrt{\xi^{\mathrm{II}}} \sinh(\sqrt{\xi^{\mathrm{I}}} a) \cosh(\sqrt{\xi^{\mathrm{II}}} a) \\ +2h^{\mathrm{II}}(1 - m^{\mathrm{I}}) \sqrt{\xi^{\mathrm{I}}} \cosh(\sqrt{\xi^{\mathrm{I}}} a) \sinh(\sqrt{\xi^{\mathrm{II}}} a) \end{matrix} \right\} \frac{\tilde{p}_o}{d_{\mathrm{strip}}} + (m^{\mathrm{I}} - m^{\mathrm{II}}) \sqrt{\xi^{\mathrm{I}}} \sqrt{\xi^{\mathrm{II}}} \cosh(\sqrt{\xi^{\mathrm{I}}} a) \cosh(\sqrt{\xi^{\mathrm{II}}} a)^* (\tilde{F} + a\tilde{P}_c)/d_{\mathrm{strip}} \tag{B10}$$

$$C_1^{\mathrm{I}}(s) = \left\{ \begin{matrix} +2af(1 - m^{\mathrm{II}}) \sqrt{\xi^{\mathrm{I}}} \sqrt{\xi^{\mathrm{II}}} \cosh(\sqrt{\xi^{\mathrm{II}}} a) \\ +2h^{\mathrm{II}}(f^{\mathrm{I}} - f^{\mathrm{II}}) \sqrt{\xi^{\mathrm{I}}} \sinh(\sqrt{\xi^{\mathrm{II}}} a) \end{matrix} \right\} \frac{\tilde{p}_o}{d_{\mathrm{strip}}} - (f^{\mathrm{II}} - f^{\mathrm{I}} m^{\mathrm{II}}) \sqrt{\xi^{\mathrm{I}}} \sqrt{\xi^{\mathrm{II}}} \cosh(\sqrt{\xi^{\mathrm{II}}} a)^* (\tilde{F} + a\tilde{P}_c)/d_{\mathrm{strip}} \tag{B11}$$

$$C_1^{\mathrm{II}}(s) = \left\{ \begin{matrix} -2af(1 - m^{\mathrm{I}}) \sqrt{\xi^{\mathrm{I}}} \sqrt{\xi^{\mathrm{II}}} \cosh(\sqrt{\xi^{\mathrm{I}}} a) \\ -2h^{\mathrm{I}}(f^{\mathrm{I}} - f^{\mathrm{II}}) \sqrt{\xi^{\mathrm{II}}} \sinh(\sqrt{\xi^{\mathrm{I}}} a) \end{matrix} \right\} \frac{\tilde{p}_o}{d_{\mathrm{strip}}} + (f^{\mathrm{II}} - f^{\mathrm{I}} m^{\mathrm{I}}) \sqrt{\xi^{\mathrm{I}}} \sqrt{\xi^{\mathrm{II}}} \cosh(\sqrt{\xi^{\mathrm{I}}} a)^* (\tilde{F} + a\tilde{P}_c)/d_{\mathrm{strip}} \tag{B12}$$

$$d_{\mathrm{strip}}(s) = -2h^{\mathrm{I}}(f^{\mathrm{II}} - f^{\mathrm{I}} m^{\mathrm{II}}) \sqrt{\xi^{\mathrm{II}}} \sinh(\sqrt{\xi^{\mathrm{I}}} a) \cosh(\sqrt{\xi^{\mathrm{II}}} a) + 2h^{\mathrm{II}}(f^{\mathrm{II}} - f^{\mathrm{I}} m^{\mathrm{I}}) \sqrt{\xi^{\mathrm{I}}} \cosh(\sqrt{\xi^{\mathrm{I}}} a) \sinh(\sqrt{\xi^{\mathrm{II}}} a) + 2af(m^{\mathrm{I}} - m^{\mathrm{II}}) \sqrt{\xi^{\mathrm{I}}} \sqrt{\xi^{\mathrm{II}}} \cosh(\sqrt{\xi^{\mathrm{I}}} a) \cosh(\sqrt{\xi^{\mathrm{II}}} a) \tag{B13}$$

Appendix C: Rectangular Strip Reduced Single-Poroelastic Laplace Transform Domain Solution

Requiring the secondary porosity porous medium to shrink to zero, all of the material parameters associated with the secondary porosity porous medium vanish and the remaining parameters reduce to those of the primary porosity porous medium as follows:

$$\mathrm{v}^{\mathrm{II}} \to 0 \quad \Rightarrow \quad \bar{\alpha}^{\mathrm{II}}, \bar{M}^{\mathrm{I,II}}, \bar{M}^{\mathrm{II}}, \bar{\eta}^{\mathrm{II}}, \quad \Gamma \to 0$$

$$\bar{K} \to K^{\mathrm{I}}, \quad \bar{G} \to G^{\mathrm{I}}, \quad \bar{\alpha}^{\mathrm{I}} \to \alpha^{\mathrm{I}}, \quad \bar{M}^{\mathrm{I}} \to M^{\mathrm{I}}, \quad \bar{\eta}^{\mathrm{I}} \to \eta^{\mathrm{I}}$$

As a result, the diffusion equation for the secondary porosity porous medium becomes identically zero and the solution becomes

$$\tilde{p} = \tilde{C}_o f^{\mathrm{I}} + C_1^{\mathrm{I}} \cosh(\sqrt{\xi^{\mathrm{I}}} x) \tag{C1}$$

$$\tilde{\sigma}_{zz} = 2\eta^{\mathrm{I}} C_1^{\mathrm{I}} \cosh(\sqrt{\xi^{\mathrm{I}}}x) + 2f\tilde{C}_o - \tilde{P}_c \tag{C2}$$

$$2\bar{G}\tilde{u}_x = -2\eta^{\mathrm{I}} C_1^{\mathrm{I}} \frac{\sinh(\sqrt{\xi^{\mathrm{I}}}x)}{\sqrt{\xi^{\mathrm{I}}}} + [\tilde{P}_c - (2f - K_v^{\mathrm{I}})\tilde{C}_o]x \tag{C3}$$

$$\xi^{\mathrm{I}} = s/c^{\mathrm{I}}, \quad c^{\mathrm{I}} = \kappa^{\mathrm{I}}/\left(\frac{1}{M^{\mathrm{I}}} + \frac{\alpha^{\mathrm{I}}\eta^{\mathrm{I}}}{G^{\mathrm{I}}}\right) \tag{C4}$$

$$f^{\mathrm{I}} = \alpha^{\mathrm{I}}/\left(\frac{1}{M^{\mathrm{I}}} + \frac{\alpha^{\mathrm{I}}\eta^{\mathrm{I}}}{G^{\mathrm{I}}}\right), \quad f = \eta^{\mathrm{I}} f^{\mathrm{I}} + K^{\mathrm{I}} + G^{\mathrm{I}}/3 \tag{C5}$$

$$\tilde{C}_o(s) = [-2\eta^{\mathrm{I}} \sinh(\sqrt{\xi^{\mathrm{I}}}a)\tilde{p}_o + \sqrt{\xi^{\mathrm{I}}} \cosh(\sqrt{\xi^{\mathrm{I}}}a)^*(\tilde{F} + a\tilde{P}_c)]/d_{\mathrm{strip}} \tag{C6}$$

$$C_1^{\mathrm{I}}(s) = [2af\sqrt{\xi^{\mathrm{I}}}\tilde{p}_o + f^{\mathrm{I}}\sqrt{\xi^{\mathrm{I}}}^*(\tilde{F} + a\tilde{P}_c)]/d_{\mathrm{strip}} \tag{C7}$$

$$d_{\mathrm{strip}}(s) = -2\eta^{\mathrm{I}} f^{\mathrm{I}} \sinh(\sqrt{\xi^{\mathrm{I}}}a) + 2af\sqrt{\xi^{\mathrm{I}}} \cosh(\sqrt{\xi^{\mathrm{I}}}a) \tag{C8}$$

which is the corresponding generalized single-poroelastic solution. For the special case of unconfined step loading, i.e., $F(t) = F^* H(t)$; $P_c(t) = p_o(t) = 0$, Wang [3] showed that application of Laplace transform inversion theorem reproduce the exact single-poroelastic solution presented by Mandel [6] and Abousleiman et al. [10].

Appendix D: Rectangular Strip Dual-Poroelastic Time Domain Solution

The analytical solution can be derived in terms of infinite series using the combined Laplace and Fourier transform techniques. Introducing the finite cosine Fourier transform pair defined as [32]

$$P_n^{(N)}(n,t) = \int_0^a p^{(N)}(x,t)^* \cos(mx)dx$$
$$p^{(N)}(x,t) = \frac{2}{a}\sum_{n=1}^{\infty} P_n^{(N)}(n,t)^* \cos(mx) \tag{D1}$$

where $n = 1, 2, \ldots$ and $m = (2n\text{-}1)\pi/(2a)$ are the Fourier transform parameters, the solution for the Laplace–Fourier transformed pressures are

$$\begin{Bmatrix} \tilde{P}_n^{\mathrm{I}} \\ \tilde{P}_n^{\mathrm{II}} \end{Bmatrix} = \frac{(-1)^{n+1}}{m}[\mathbf{Z}_{n,s}]^{-1}\begin{Bmatrix} \bar{\alpha}^{\mathrm{I}} \\ \bar{\alpha}^{\mathrm{II}} \end{Bmatrix} s\tilde{C}_o + [\mathbf{Z}_{n,s}]^{-1}[\mathbf{D}]\begin{Bmatrix} m^*\tilde{p}_o \\ m^*\tilde{p}_o \end{Bmatrix} \tag{D2}$$

in which $[\mathbf{Z}_{n,s}]^{-1}$ is the inverse matrix of $[\mathbf{Z}_{n,s}] = s[\mathbf{A}] + [\mathbf{\Gamma}] + m^2[\mathbf{D}]$ and the fluid-pressure boundary condition at the two edges $x = \pm a$ has been used. To facilitate the inverse Laplace transform, the above expression is rearranged as

$$\tilde{P}_n^{(N)}(n,s) = \frac{(-1)^{n+1}}{m}\frac{\gamma^{(N)}(s + w_n^{(N)})}{(s + s_n^{\mathrm{I}})(s + s_n^{\mathrm{II}})}\{[s\tilde{C}_o - C_o(0)] + C_o(0)\} + m\frac{\varphi^{(N)}(s + z_n^{(N)})}{(s + s_n^{\mathrm{I}})(s + s_n^{\mathrm{II}})}\tilde{p}_o \tag{D3}$$

where the new coefficients are defined as

$$\gamma^{\mathrm{I}} = (A_{22}\bar{\alpha}^{\mathrm{I}} - A_{12}\bar{\alpha}^{\mathrm{II}})/\det[\mathbf{A}], \quad \gamma^{\mathrm{II}} = (A_{11}\bar{\alpha}^{\mathrm{II}} - A_{21}\bar{\alpha}^{\mathrm{I}})/\det[\mathbf{A}] \tag{D4}$$

$$\varphi^{\mathrm{I}} = (A_{22}D_{11} - A_{12}D_{22})/\det[\mathbf{A}], \quad \varphi^{\mathrm{II}} = (A_{11}D_{22} - A_{21}D_{11})/\det[\mathbf{A}] \tag{D5}$$

$$w_n^{\mathrm{I}} = [\bar{\alpha}^{\mathrm{I}}(m^2 D_{22} + \Gamma) + \bar{\alpha}^{\mathrm{II}}\Gamma]/(\gamma^{\mathrm{I}} \det[\mathbf{A}])$$
$$w_n^{\mathrm{II}} = [\bar{\alpha}^{\mathrm{II}}(m^2 D_{11} + \Gamma) + \bar{\alpha}^{\mathrm{I}}\Gamma]/(\gamma^{\mathrm{II}} \det[\mathbf{A}]) \tag{D6}$$

$$z_n^{\mathrm{I}} = [D_{11}(m^2 D_{22} + \Gamma) + D_{22}\Gamma]/(\varphi^{\mathrm{I}} \det[\mathbf{A}])$$
$$z_n^{\mathrm{II}} = [D_{22}(m^2 D_{11} + \Gamma) + D_{11}\Gamma]/(\varphi^{\mathrm{II}} \det[\mathbf{A}]) \tag{D7}$$

$$s_n^{(N)} = -(-B \pm \sqrt{\Delta})/(2 \det[\mathbf{A}]) \tag{D8}$$

$$\det[\mathbf{A}] = A_{11}A_{22} - A_{12}A_{21} \tag{D9}$$

$$B = (A_{11} + A_{22} + A_{12} + A_{21})\Gamma + m^2(D_{11} + D_{22}) \tag{D10}$$

$$\Delta = B^2 - 4 \det[\mathbf{A}]^*[(m^2 D_{11} + \Gamma)(m^2 D_{22} + \Gamma) - \Gamma^2] \tag{D11}$$

The Laplace inversion is carried out using the convolution theorem, i.e., $(f \circ g)(t) = \int_0^t f(\tau)g(t-\tau)d\tau$. In this case, we choose $\tilde{f}(s) = s\tilde{C}_o - C_o(0) \rightarrow f(t) = dC/dt$. Then the pressure general expression in time and space domain is

$$\begin{aligned} p^{(N)}(x,t) = \gamma^{(N)}\frac{2}{a}\sum_{n=1}^{\infty}\frac{(-1)^{n+1}}{m}\Bigg\{ & \int_0^t \frac{1}{s_n^{\mathrm{I}} - s_n^{\mathrm{II}}}[(s_n^{\mathrm{I}} - w_n^{(N)})e^{-s_n^{\mathrm{I}}(t-\tau)} \\ & - (s_n^{\mathrm{II}} - w_n^{(N)})e^{-s_n^{\mathrm{II}}(t-\tau)}]\frac{dC_o(\tau)}{d\tau}d\tau \\ & + C_o(0)\frac{(s_n^{\mathrm{I}} - w_n^{(N)})e^{-s_n^{\mathrm{I}}t} - (s_n^{\mathrm{II}} - w_n^{(N)})e^{-s_n^{\mathrm{II}}t}}{s_n^{\mathrm{I}} - s_n^{\mathrm{II}}}\Bigg\}\cos(mx) \\ & + \varphi^{(N)}\frac{2}{a}\sum_{n=1}^{\infty} m\Bigg\{\int_0^t \frac{(s_n^{\mathrm{I}} - z_n^{(N)})e^{-s_n^{\mathrm{I}}(t-\tau)} - (s_n^{\mathrm{II}} - z_n^{(N)})e^{-s_n^{\mathrm{II}}(t-\tau)}}{s_n^{\mathrm{I}} - s_n^{\mathrm{II}}} \\ & \times p_o(\tau)d\tau\Bigg\}\cos(mx) \end{aligned} \tag{D12}$$

Substitution of the above into Eq. (B4), the general expression for vertical stress is given as

$$\begin{aligned} \sigma_{zz}(x,t) = {} & 2hC(t) - P_c(t) \\ & - \frac{4}{a}\sum_{n=1}^{\infty}\Bigg\{\frac{(-1)^{n+1}}{m}\int_0^t [\Phi_n^{\mathrm{I}} s_n^{\mathrm{I}} e^{-s_n^{\mathrm{I}}(t-\tau)} \\ & - \Phi_n^{\mathrm{II}} s_n^{\mathrm{II}} e^{-s_n^{\mathrm{II}}(t-\tau)}]C(\tau)d\tau\Bigg\}\cos(mx) \\ & + \frac{4}{a}\sum_{n=1}^{\infty}\Bigg\{m\int_0^t [\Omega_n^{\mathrm{I}} e^{-s_n^{\mathrm{I}}(t-\tau)} \\ & - \Omega_n^{\mathrm{II}} e^{-s_n^{\mathrm{II}}(t-\tau)}]p_o(\tau)d\tau\Bigg\}\cos(mx) \end{aligned} \tag{D13}$$

where the new coefficients are defined as follows:

$$h = \bar{\eta}^{\mathrm{I}}\gamma^{\mathrm{I}} + \bar{\eta}^{\mathrm{II}}\gamma^{\mathrm{II}} + \bar{K} + \bar{G}/3 \tag{D14}$$

$$\Phi_n^{(N)} = \frac{\bar{\eta}^{\mathrm{I}}\gamma^{\mathrm{I}}(s_n^{(N)} - w_n^{\mathrm{I}}) + \bar{\eta}^{\mathrm{II}}\gamma^{\mathrm{II}}(s_n^{(N)} - w_n^{\mathrm{II}})}{(s_n^{\mathrm{I}} - s_n^{\mathrm{II}})} \tag{D15}$$

$$\Omega_n^{(N)} = \frac{\bar{\eta}^{\mathrm{I}}\varphi^{\mathrm{I}}(s_n^{(N)} - z_n^{\mathrm{I}}) + \bar{\eta}^{\mathrm{II}}\varphi^{\mathrm{II}}(s_n^{(N)} - z_n^{\mathrm{II}})}{(s_n^{\mathrm{I}} - s_n^{\mathrm{II}})} \tag{D16}$$

The arbitrary function of time $C_o(t)$ remains to be determined. Applying the vertical stress boundary condition along the top of the sample, $z=\pm b$ (Eq. (14)) gives

$$C_o(t)=\frac{F(t)+aP_c(t)}{2ah}-\frac{2}{a^2h}\sum_{n=1}^{\infty}\left\{(-1)^{n+1}\int_0^t[\Omega_n^{\mathrm{I}}e^{-s_n^{\mathrm{I}}(t-\tau)}-\Omega_n^{\mathrm{II}}e^{-s_n^{\mathrm{II}}(t-\tau)}]p_o(\tau)d\tau\right\}+\frac{2}{a^2h}\sum_{n=1}^{\infty}\left\{\frac{1}{m^2}\int_0^t[\Phi_n^{\mathrm{I}}s_n^{\mathrm{I}}e^{-s_n^{\mathrm{I}}(t-\tau)}-\Phi_n^{\mathrm{II}}s_n^{\mathrm{II}}e^{-s_n^{\mathrm{II}}(t-\tau)}]C(\tau)d\tau\right\} \tag{D17}$$

This is an integral equation with separable kernels having general solution (formula No. 19 of Sec. 2.2.1 in Ref. [33]).

$$C_o(t)=\Theta(t)-\int_0^t\sum_{i=1}^{\infty}\left[\frac{e^{\lambda_i(t-\tau)}}{Q'(s=\lambda_i)}\right]\Theta(\tau)d\tau \tag{D18}$$

in which the functions $\Theta(t)$ and $Q(s)$ are defined as

$$\Theta(t)=\frac{F(t)+aP_c(t)}{2ah}-\frac{2}{a^2h}\sum_{n=1}^{\infty}\left\{(-1)^{n+1}\int_0^t[\Omega_n^{\mathrm{I}}e^{-s_n^{\mathrm{I}}(t-\tau)}-\Omega_n^{\mathrm{II}}e^{-s_n^{\mathrm{II}}(t-\tau)}]p_o(\tau)d\tau\right\} \tag{D19}$$

$$Q(s)=\frac{2}{a^2h}\sum_{n=1}^{\infty}\frac{1}{m^2}\left(\frac{\Phi_n^{\mathrm{I}}s_n^{\mathrm{I}}}{s+s_n^{\mathrm{I}}}-\frac{\Phi_n^{\mathrm{II}}s_n^{\mathrm{II}}}{s+s_n^{\mathrm{II}}}\right) \tag{D20}$$

where $Q'(s)$ denotes $dQ(s)/ds$, and λ_i are roots of the equation $1-Q(s)=0$.

As a result, $C_o(t)$ can assume various forms depending on the type of external loading functions $F(t)$, $p_o(t)$, and $P_c(t)$. Here, the explicit solutions of $C_o(t)$ and pore pressures for some special unconfined uniaxial loading conditions such as step loading, cyclic loading, and linear ramp loading are summarized as follows:

- step loading (original Mandel's problem): $p_o(t)=P_c(t)=0$; $F(t)=F^*H(t)$

$$C_o(t)=\frac{F}{2ah}\left\{1+\sum_{i=1}^{\infty}\left[\frac{(1-e^{\lambda_i t})}{\lambda_i Q'(s=\lambda_i)}\right]\right\} \tag{D21}$$

$$p^{(N)}(x,t)=\frac{\gamma^{(N)}}{2h}\frac{F}{a}\frac{2}{a}\sum_{n=1}^{\infty}\frac{(-1)^{n+1}}{m(s_n^{\mathrm{I}}-s_n^{\mathrm{II}})}\left\{(s_n^{\mathrm{I}}-w_n^{(N)})e^{-s_n^{\mathrm{I}}t}-(s_n^{\mathrm{II}}-w_n^{(N)})e^{-s_n^{\mathrm{II}}t}+\sum_{i=1}^{\infty}\left[\frac{(s_n^{\mathrm{I}}-w_n^{(N)})(e^{\lambda_i t}-e^{-s_n^{\mathrm{I}}t})}{(s_n^{\mathrm{I}}+\lambda_i)Q'(\lambda_i)}-\frac{(s_n^{\mathrm{II}}-w_n^{(N)})(e^{\lambda_i t}-e^{-s_n^{\mathrm{II}}t})}{(s_n^{\mathrm{II}}+\lambda_i)Q'(\lambda_i)}\right]\right\}\cos(mx) \tag{D22}$$

- cyclic loading: $p_o(t)=P_c(t)=0$; $F(t)=F^*\sin(\omega t)$

$$C_o(t)=\frac{F}{2ah}\left\{\sin(\omega t)-\sum_{i=1}^{\infty}\left[\frac{\omega e^{\lambda_i t}-\omega\cos(\omega t)-\lambda_i\sin(\omega t)}{(\lambda_i^2+\omega^2)Q'(s=\lambda_i)}\right]\right\} \tag{D23}$$

$$p^{(N)}(x,t)=-\frac{\gamma^{(N)}}{2h}\frac{F\omega}{a}\frac{2}{a}\sum_{n=1}^{\infty}\frac{(-1)^{n+1}}{m(s_n^{\mathrm{I}}-s_n^{\mathrm{II}})}\cos(mx)\left\{(s_n^{\mathrm{I}}-w_n^{(N)})\frac{s_n^{\mathrm{I}}e^{-s_n^{\mathrm{I}}t}-s_n^{\mathrm{I}}\cos(\omega t)-\omega\sin(\omega t)}{(s_n^{\mathrm{I}})^2+\omega^2}\right.$$
$$-(s_n^{\mathrm{II}}-w_n^{(N)})\frac{s_n^{\mathrm{II}}e^{-s_n^{\mathrm{II}}t}-s_n^{\mathrm{II}}\cos(\omega t)-\omega\sin(\omega t)}{(s_n^{\mathrm{II}})^2+\omega^2}+\sum_{i=1}^{\infty}\left[\frac{(s_n^{\mathrm{I}}-w_n^{(N)})\lambda_i(e^{\lambda_i t}-e^{-s_n^{\mathrm{I}}t})}{(s_n^{\mathrm{I}}+\lambda_i)(\lambda_i^2+\omega^2)Q'(\lambda_i)}-\frac{(s_n^{\mathrm{II}}-w_n^{(N)})\lambda_i(e^{\lambda_i t}-e^{-s_n^{\mathrm{II}}t})}{(s_n^{\mathrm{II}}+\lambda_i)(\lambda_i^2+\omega^2)Q'(\lambda_i)}\right]$$
$$+\sum_{i=1}^{\infty}\left[\frac{(s_n^{\mathrm{I}}-w_n^{(N)})\{(\lambda_i s_n^{\mathrm{I}}+\omega^2)[e^{-s_n^{\mathrm{I}}t}-\cos(\omega t)]+\omega(s_n^{\mathrm{I}}-\lambda_i)\sin(\omega t)\}}{[(s_n^{\mathrm{I}})^2+\omega^2](\lambda_i^2+\omega^2)Q'(\lambda_i)}\right]$$
$$\left.-\sum_{i=1}^{\infty}\left[\frac{(s_n^{\mathrm{II}}-w_n^{(N)})\{(\lambda_i s_n^{\mathrm{II}}+\omega^2)[e^{-s_n^{\mathrm{II}}t}-\cos(\omega t)]+\omega(s_n^{\mathrm{II}}-\lambda_i)\sin(\omega t)\}}{[(s_n^{\mathrm{II}})^2+\omega^2](\lambda_i^2+\omega^2)Q'(\lambda_i)}\right]\right\} \tag{D24}$$

- linear ramp loading: $p_o(t)=P_c(t)=0$; $F(t)=F^*[tH(t)-(t-t_o)H(t-t_o)]/t_o$

$$C_o(t)=\frac{F(t)}{2ah}-\frac{F}{2ah}\sum_{i=1}^{\infty}\frac{1}{t_o\lambda_i^2Q'(s=\lambda_i)}[\{e^{\lambda_i t}-1-\lambda_i t)\}H(t)+\{e^{\lambda_i(t-t_o)}-1-\lambda_i(t-t_o)\}H(t-t_o)] \tag{D25}$$

$$p^{(N)}(x,t)=\frac{\gamma^{(N)}}{2h}\frac{F}{at_o}\frac{2}{a}\sum_{n=1}^{\infty}\frac{(-1)^{n+1}}{m(s_n^{\mathrm{I}}-s_n^{\mathrm{II}})}\cos(mx)\Bigg\{(s_n^{\mathrm{I}}-w_n^{(N)})\frac{1-e^{-s_n^{\mathrm{I}}t}-[1-e^{-s_n^{\mathrm{I}}(t-t_o)}]H(t-t_o)}{s_n^{\mathrm{I}}}$$
$$-(s_n^{\mathrm{II}}-w_n^{(N)})\frac{1-e^{-s_n^{\mathrm{II}}t}-[1-e^{-s_n^{\mathrm{II}}(t-t_o)}]H(t-t_o)}{s_n^{\mathrm{II}}}+\sum_{i=1}^{\infty}\left[\frac{(s_n^{\mathrm{I}}-w_n^{(N)})(s_n^{\mathrm{I}}e^{\lambda_i t}+\lambda_i e^{-s_n^{\mathrm{I}}t}-s_n^{\mathrm{I}}-\lambda_i)}{s_n^{\mathrm{I}}(s_n^{\mathrm{I}}+\lambda_i)\lambda_i Q'(\lambda_i)}\right]$$
$$-\sum_{i=1}^{\infty}\left[\frac{(s_n^{\mathrm{II}}-w_n^{(N)})(s_n^{\mathrm{II}}e^{\lambda_i t}+\lambda_i e^{-s_n^{\mathrm{II}}t}-s_n^{\mathrm{II}}-\lambda_i)}{s_n^{\mathrm{II}}(s_n^{\mathrm{II}}+\lambda_i)\lambda_i Q'(\lambda_i)}\right]+\sum_{i=1}^{\infty}\left[\frac{(s_n^{\mathrm{I}}-w_n^{(N)})(s_n^{\mathrm{I}}e^{\lambda_i(t-t_o)}+\lambda_i e^{-s_n^{\mathrm{I}}(t-t_o)}-s_n^{\mathrm{I}}-\lambda_i)H(t-t_o)}{s_n^{\mathrm{I}}(s_n^{\mathrm{I}}+\lambda_i)\lambda_i Q'(\lambda_i)}\right]$$
$$-\sum_{i=1}^{\infty}\left[\frac{(s_n^{\mathrm{II}}-w_n^{(\mathrm{N})})(s_n^{\mathrm{II}}e^{\lambda_i(t-t_o)}+\lambda_i e^{-s_n^{\mathrm{II}}(t-t_o)}-s_n^{\mathrm{II}}-\lambda_i)H(t-t_o)}{s_n^{\mathrm{II}}(s_n^{\mathrm{II}}+\lambda_i)\lambda_i Q'(\lambda_i)}\right]\Bigg\} \tag{D26}$$

Thus, the final time-domain solutions for all quantities are completed by substituting the suitable expressions of $C_o(t)$ and fluid pressures into the general equations ((B4)–(B6)).

Appendix E: Solid Cylinder Dual-Poroelastic Laplace Transform Domain Solution

The general solution for fluid pressures has been derived in Eqs. (38) and (39). Here, the detailed derivations for other quantities are illustrated.

First, the radial displacement is obtained by integration noting that $\varepsilon_{kk}=(1/r)\,\partial(ru_r)/\partial r+\varepsilon_{zz}$.

$$2\bar{G}u_r=-\frac{2}{r}\int(\bar{\eta}^{\mathrm{I}}p^{\mathrm{I}}+\bar{\eta}^{\mathrm{II}}p^{\mathrm{II}})rdr+\bar{G}[C_o(t)-\varepsilon_{zz}(t)]r \tag{E1}$$

Other expressions for strains and stresses follow naturally from the constitutive equation (1) as

$$2\bar{G}\varepsilon_{rr}=\frac{2}{r^2}\int(\bar{\eta}^{\mathrm{I}}p^{\mathrm{I}}+\bar{\eta}^{\mathrm{II}}p^{\mathrm{II}})rdr-2(\bar{\eta}^{\mathrm{I}}p^{\mathrm{I}}+\bar{\eta}^{\mathrm{II}}p^{\mathrm{II}})+\bar{G}[C_o(t)-\varepsilon_{zz}(t)] \tag{E2}$$

$$2\bar{G}\varepsilon_{\theta\theta}=-\frac{2}{r^2}\int(\bar{\eta}^{\mathrm{I}}p^{\mathrm{I}}+\bar{\eta}^{\mathrm{II}}p^{\mathrm{II}})rdr+\bar{G}[C_o(t)-\varepsilon_{zz}(t)] \tag{E3}$$

$$\sigma_{rr}=\frac{2}{r^2}\int(\bar{\eta}^{\mathrm{I}}p^{\mathrm{I}}+\bar{\eta}^{\mathrm{II}}p^{\mathrm{II}})rdr+(\bar{K}+\bar{G}/3)C_o(t)-\bar{G}\varepsilon_{zz}(t) \tag{E4}$$

$$\sigma_{\theta\theta}=-\frac{2}{r^2}\int(\bar{\eta}^{\mathrm{I}}p^{\mathrm{I}}+\bar{\eta}^{\mathrm{II}}p^{\mathrm{II}})rdr+2(\bar{\eta}^{\mathrm{I}}p^{\mathrm{I}}+\bar{\eta}^{\mathrm{II}}p^{\mathrm{II}})+(\bar{K}+\bar{G}/3)C_o(t)-\bar{G}\varepsilon_{zz}(t) \tag{E5}$$

$$\sigma_{zz}=2(\bar{\eta}^{\mathrm{I}}p^{\mathrm{I}}+\bar{\eta}^{\mathrm{II}}p^{\mathrm{II}})+(\bar{K}-2\bar{G}/3)C_o(t)+2\bar{G}\varepsilon_{zz}(t) \tag{E6}$$

Substitution of the pressure equations ((38) and (39)) into the above leads to the explicit general solutions as expressed in Eqs. (40)–(45). The applicable boundary conditions for this geometry and setting are the fluid-pressure and confining stress boundary conditions at the cylinder's outer surface $r=R$, and the axial stress loading condition on the top and bottom.

$$\tilde{p}^{\mathrm{I}}|_{r=R}=\tilde{C}_o f^{\mathrm{I}}+C_1^{\mathrm{I}}I_0(\sqrt{\xi^{\mathrm{I}}}R)+C_1^{\mathrm{II}}I_0(\sqrt{\xi^{\mathrm{II}}}R)=\tilde{p}_o \tag{E7}$$

$$\tilde{p}^{\mathrm{II}}|_{r=R}=\tilde{C}_o f^{\mathrm{II}}+m^{\mathrm{I}}C_1^{\mathrm{I}}I_0(\sqrt{\xi^{\mathrm{I}}}R)+m^{\mathrm{II}}C_1^{\mathrm{II}}I_0(\sqrt{\xi^{\mathrm{II}}}R)=\tilde{p}_o \tag{E8}$$

$$\tilde{\sigma}_{rr}|_{r=R}=2h^{\mathrm{I}}C_1^{\mathrm{I}}\frac{I_1(\sqrt{\xi^{\mathrm{I}}}R)}{\sqrt{\xi^{\mathrm{I}}}R}+2h^{\mathrm{II}}C_1^{\mathrm{II}}\frac{I_1(\sqrt{\xi^{\mathrm{II}}}R)}{\sqrt{\xi^{\mathrm{II}}}R}+f\tilde{C}_o-\bar{G}\tilde{\varepsilon}_{zz}=\tilde{P}_c \tag{E9}$$

$$\int_0^R\tilde{\sigma}_{zz}rdr=2h^{\mathrm{I}}C_1^{\mathrm{I}}\frac{RI_0(\sqrt{\xi^{\mathrm{I}}}R)}{\sqrt{\xi^{\mathrm{I}}}}+2h^{\mathrm{II}}C_1^{\mathrm{II}}\frac{RI_0(\sqrt{\xi^{\mathrm{II}}}R)}{\sqrt{\xi^{\mathrm{II}}}}+[(2f-\bar{K}_v)\tilde{C}_o+2\bar{G}\tilde{\varepsilon}_{zz}]\frac{R^2}{2}=\frac{\tilde{F}}{2\pi} \tag{E10}$$

Equations (E7)–(E10) are solved simultaneously for $\tilde{C}_o(s)$, $C_1^{\mathrm{I}}(s)$, $C_1^{\mathrm{II}}(s)$, and $\tilde{\varepsilon}_{zz}$ as

$$\tilde{C}_o(s)=\left\{\begin{matrix}-4h^{\mathrm{I}}(1-m^{\mathrm{II}})\sqrt{\xi^{\mathrm{II}}}I_1(\sqrt{\xi^{\mathrm{I}}}R)I_0(\sqrt{\xi^{\mathrm{II}}}R)\\+4h^{\mathrm{II}}(1-m^{\mathrm{I}})\sqrt{\xi^{\mathrm{I}}}I_0(\sqrt{\xi^{\mathrm{I}}}R)I_1(\sqrt{\xi^{\mathrm{II}}}R)\end{matrix}\right\}\frac{\tilde{p}_o}{d_{\mathrm{cylinder}}}+(m^{\mathrm{I}}-m^{\mathrm{II}})R\sqrt{\xi^{\mathrm{I}}}\sqrt{\xi^{\mathrm{II}}}I_0(\sqrt{\xi^{\mathrm{I}}}R)I_0(\sqrt{\xi^{\mathrm{II}}}R)^*(\tilde{F}/2\pi R^2+\tilde{P}_c)/d_{\mathrm{cylinder}} \tag{E11}$$

$$C_1^{\mathrm{I}}(s)=\{+(2f-\bar{K}_v/2)(1-m^{\mathrm{II}})R\sqrt{\xi^{\mathrm{I}}}\sqrt{\xi^{\mathrm{II}}}I_0(\sqrt{\xi^{\mathrm{II}}}R)+4h^{\mathrm{II}}(f^{\mathrm{I}}-f^{\mathrm{II}})\sqrt{\xi^{\mathrm{I}}}I_1(\sqrt{\xi^{\mathrm{II}}}R)\}\frac{\tilde{p}_o}{d_{\mathrm{cylinder}}}-(f^{\mathrm{II}}-f^{\mathrm{I}}m^{\mathrm{II}})R\sqrt{\xi^{\mathrm{I}}}\sqrt{\xi^{\mathrm{II}}}I_0(\sqrt{\xi^{\mathrm{II}}}R)^*(\tilde{F}/2\pi R^2+\tilde{P}_c)/d_{\mathrm{cylinder}} \tag{E12}$$

$$C_1^{\mathrm{II}}(s)=\{-(2f-\bar{K}_v/2)(1-m^{\mathrm{I}})R\sqrt{\xi^{\mathrm{I}}}\sqrt{\xi^{\mathrm{II}}}I_0(\sqrt{\xi^{\mathrm{I}}}R)-4h^{\mathrm{I}}(f^{\mathrm{I}}-f^{\mathrm{II}})\sqrt{\xi^{\mathrm{II}}}I_1(\sqrt{\xi^{\mathrm{I}}}R)\}\frac{\tilde{p}_o}{d_{\mathrm{cylinder}}}+(f^{\mathrm{II}}-f^{\mathrm{I}}m^{\mathrm{I}})R\sqrt{\xi^{\mathrm{I}}}\sqrt{\xi^{\mathrm{II}}}I_0(\sqrt{\xi^{\mathrm{I}}}R)^*(\tilde{F}/2\pi R^2-\tilde{P}_c)/d_{\mathrm{cylinder}} \tag{E13}$$

$$d_{\mathrm{cylinder}}(s)=-4h^{\mathrm{I}}(f^{\mathrm{II}}-f^{\mathrm{I}}m^{\mathrm{II}})\sqrt{\xi^{\mathrm{II}}}I_1(\sqrt{\xi^{\mathrm{I}}}R)I_0(\sqrt{\xi^{\mathrm{II}}}R)+4h^{\mathrm{II}}(f^{\mathrm{II}}-f^{\mathrm{I}}m^{\mathrm{I}})\sqrt{\xi^{\mathrm{I}}}I_0(\sqrt{\xi^{\mathrm{I}}}R)I_1(\sqrt{\xi^{\mathrm{II}}}R)+(2f-\bar{K}_v/2)(m^{\mathrm{I}}-m^{\mathrm{II}})R\sqrt{\xi^{\mathrm{I}}}\sqrt{\xi^{\mathrm{II}}}I_0(\sqrt{\xi^{\mathrm{I}}}R)I_0(\sqrt{\xi^{\mathrm{II}}}R) \tag{E14}$$

$$\bar{G}\tilde{\varepsilon}_{zz}(s)=-2h^{\mathrm{I}}C_1^{\mathrm{I}}\frac{I_1(\sqrt{\xi^{\mathrm{I}}}R)}{\sqrt{\xi^{\mathrm{I}}}R}-2h^{\mathrm{II}}C_1^{\mathrm{II}}\frac{I_1(\sqrt{\xi^{\mathrm{II}}}R)}{\sqrt{\xi^{\mathrm{II}}}R}+\tilde{F}/2\pi R^2-(f-\bar{K}_v/2)\tilde{C}_o \tag{E15}$$

Therefore, the general Laplace transform solution for cylinder is complete.

Appendix F: Solid Cylinder Reduced Single-Poroelastic Laplace Transform Domain Solution

Requiring the secondary porosity porous medium to shrink to zero, the diffusion equation for the secondary porosity porous medium becomes identically zero and the solution becomes

$$\tilde{p} = \tilde{C}_o f^{\mathrm{I}} + C_1^{\mathrm{I}} I_0(\sqrt{\xi^{\mathrm{I}}} r) \tag{F1}$$

$$2G^{\mathrm{I}}\tilde{u}_r = -2\eta^{\mathrm{I}} C_1^{\mathrm{I}} \frac{I_1(\sqrt{\xi^{\mathrm{I}}} r)}{\sqrt{\xi^{\mathrm{I}}}} - [G^{\mathrm{I}}\tilde{\varepsilon}_{zz} + (f - K_v^{\mathrm{I}})\tilde{C}_o]r \tag{F2}$$

$$2G^{\mathrm{I}}\tilde{\varepsilon}_{rr} = -2\eta^{\mathrm{I}} C_1^{\mathrm{I}} \left[I_0(\sqrt{\xi^{\mathrm{I}}} r) - \frac{I_1(\sqrt{\xi^{\mathrm{I}}} r)}{\sqrt{\xi^{\mathrm{I}}} r} \right] - G^{\mathrm{I}}\tilde{\varepsilon}_{zz} - (f - K_v^{\mathrm{I}})\tilde{C}_o \tag{F3}$$

$$2G^{\mathrm{I}}\tilde{\varepsilon}_{\theta\theta} = -2\eta^{\mathrm{I}} C_1^{\mathrm{I}} \frac{I_1(\sqrt{\xi^{\mathrm{I}}} r)}{\sqrt{\xi^{\mathrm{I}}} r} - G^{\mathrm{I}}\tilde{\varepsilon}_{zz} - (f - K_v^{\mathrm{I}})\tilde{C}_o \tag{F4}$$

$$\tilde{\sigma}_{rr} = 2\eta^{\mathrm{I}} C_1^{\mathrm{I}} \frac{I_1(\sqrt{\xi^{\mathrm{I}}} r)}{\sqrt{\xi^{\mathrm{I}}} r} + f\tilde{C}_o - G^{\mathrm{I}}\tilde{\varepsilon}_{zz} \tag{F5}$$

$$\tilde{\sigma}_{\theta\theta} = 2\eta^{\mathrm{I}} C_1^{\mathrm{I}} \left[I_0(\sqrt{\xi^{\mathrm{I}}} r) - \frac{I_1(\sqrt{\xi^{\mathrm{I}}} r)}{\sqrt{\xi^{\mathrm{I}}} r} \right] + f\tilde{C}_o - G^{\mathrm{I}}\tilde{\varepsilon}_{zz} \tag{F6}$$

$$\tilde{\sigma}_{zz} = 2\eta^{\mathrm{I}} C_1^{\mathrm{I}} I_0(\sqrt{\xi^{\mathrm{I}}} r) + (2f - K_v^{\mathrm{I}})\tilde{C}_o + 2G^{\mathrm{I}}\tilde{\varepsilon}_{zz} \tag{F7}$$

where the reduced coefficients ξ^{I}, f^{I}, and f are the same as defined in Eqs. (C4) and (C5). The constants determined from boundary conditions simplify to

$$\tilde{C}_o(s) = [-4\eta^{\mathrm{I}} I_1(\sqrt{\xi^{\mathrm{I}}} R)\tilde{p}_o - R\sqrt{\xi^{\mathrm{I}}} I_0(\sqrt{\xi^{\mathrm{I}}} R)^*(\tilde{F}/2\pi R^2 + \tilde{P}_c)]/d_{\mathrm{cylinder}} \tag{F8}$$

$$C_1^{\mathrm{I}}(s) = [(2f - K_v^{\mathrm{I}}/2)R\sqrt{\xi^{\mathrm{I}}}\tilde{p}_o + f^{\mathrm{I}} R\sqrt{\xi^{\mathrm{I}}}^*(\tilde{F}/2\pi R^2 + \tilde{P}_c)]/d_{\mathrm{cylinder}} \tag{F9}$$

$$d_{\mathrm{cylinder}}(s) = 4\eta^{\mathrm{I}} f^{\mathrm{I}} I_1(\sqrt{\xi^{\mathrm{I}}} R) - (2f - K_v^{\mathrm{I}}/2)R\sqrt{\xi^{\mathrm{I}}} I_0(\sqrt{\xi^{\mathrm{I}}} R) \tag{F10}$$

$$G^{\mathrm{I}}\tilde{\varepsilon}_{zz}(s) = -2\eta^{\mathrm{I}} C_1^{\mathrm{I}} \frac{I_1(\sqrt{\xi^{\mathrm{I}}} R)}{\sqrt{\xi^{\mathrm{I}}} R} + \tilde{F}/2\pi R^2 - (f - K_v^{\mathrm{I}}/2)\tilde{C}_o \tag{F11}$$

which is the corresponding generalized single-poroelastic solution that matches the solution as published by Cui and Abousleiman [20].

Appendix G: Solid Cylinder Dual-Poroelastic Time Solution

Due to the cylindrical geometry of the problem, the finite Hankel transform is used instead of the Fourier transform as in the strip loading problem. Introducing the finite Hankel transform pair defined as [32]

$$P_n^{(N)}(\beta_n, t) = \int_0^R r p^{(N)}(r,t)^* J_0(\beta_n r) dr$$

$$p^{(N)}(r,t) = \frac{2}{R^2}\sum_{n=1}^{\infty} P_n^{(\mathrm{N})}(\beta_n, t)^* \frac{J_0(\beta_n r)}{J_1(\beta_n R)^2} \tag{G1}$$

where β_n are positive roots of $J_0(\beta R) = 0$. The solution for the Laplace–Hankel transform pressures are

$$\begin{Bmatrix} \tilde{P}_n^{\mathrm{I}} \\ \tilde{P}_n^{\mathrm{II}} \end{Bmatrix} = [\mathbf{Z}_{n,s}]^{-1} \begin{Bmatrix} \bar{\alpha}^{\mathrm{I}} \\ \bar{\alpha}^{\mathrm{II}} \end{Bmatrix} \frac{RJ_1(\beta_n R)}{\beta_n}(s\tilde{C}_o) + [\mathbf{Z}_{n,s}]^{-1}[\mathbf{D}]\beta_n R J_1(\beta_n R) \begin{Bmatrix} \tilde{p}_o \\ \tilde{p}_o \end{Bmatrix} \tag{G2}$$

in which $[\mathbf{Z}_{n,s}]^{-1}$ is now the inverse matrix of $[\mathbf{Z}_{n,s}] = s[\mathbf{A}] + [\mathbf{\Gamma}] + \beta_n^2[\mathbf{D}]$ and the fluid-pressure boundary conditions at $r = R$ has been used. Similarly, to facilitate the inverse Laplace transform the above equation is rearranged as

$$\tilde{P}_n^{(N)}(\beta_n, s) = \frac{\gamma^{(N)}(s + w_n^{(N)})}{(s + s_n^{\mathrm{I}})(s + s_n^{\mathrm{II}})}\{[s\tilde{C}_o - C_o(0)] + C_o(0)\}\frac{RJ_1(\beta_n R)}{\beta_n} + \frac{\varphi^{(N)}(s + z_n^{(N)})}{(s + s_n^{\mathrm{I}})(s + s_n^{\mathrm{II}})}\beta_n R J_1(\beta_n R) * \tilde{p}_o \tag{G3}$$

where all of the parameters $\gamma^{(N)}$, $\varphi^{(N)}$, $s_n^{(N)}$, $w_n^{(N)}$, and $z_n^{(N)}$ are the same as defined previously in Eqs. (D4)–(D11) in which the coefficient m is replaced by β_n. Applying convolution theorem, the pressure general expression in time and space domain is

$$\begin{aligned} p^{(N)}(r,t) = \gamma^{(N)}\frac{2}{R^2}\sum_{n=1}^{\infty} \Bigg\{ & \int_0^t \frac{1}{s_n^{\mathrm{I}} - s_n^{\mathrm{II}}}[(s_n^{\mathrm{I}} - w_n^{(N)})e^{-s_n^{\mathrm{I}}(t-\tau)} \\ & - (s_n^{\mathrm{II}} - w_n^{(N)})e^{-s_n^{\mathrm{II}}(t-\tau)}]\frac{dC_o(\tau)}{d\tau}d\tau \\ & + C_o(0)\frac{(s_n^{\mathrm{I}} - w_n^{(N)})e^{-s_n^{\mathrm{I}}t} - (s_n^{\mathrm{II}} - w_n^{(N)})e^{-s_n^{\mathrm{II}}t}}{s_n^{\mathrm{I}} - s_n^{\mathrm{II}}} \Bigg\} \frac{RJ_0(\beta_n r)}{\beta_n J_1(\beta_n R)} \\ & + \varphi^{(N)}\frac{2}{R^2}\sum_{n=1}^{\infty} \Bigg\{ \int_0^t \frac{(s_n^{\mathrm{I}} - z_n^{(N)})e^{-s_n^{\mathrm{I}}(t-\tau)} - (s_n^{\mathrm{II}} - z_n^{(N)})e^{-s_n^{\mathrm{II}}(t-\tau)}}{s_n^{\mathrm{I}} - s_n^{\mathrm{II}}} \\ & \times p_o(\tau)d\tau \Bigg\} \frac{\beta_n RJ_0(\beta_n r)}{J_1(\beta_n R)} \end{aligned} \tag{G4}$$

Substituting the above pressure expression into Eqs. (E4) and (E6), the general solutions for radial and vertical stresses are given as

$$\begin{aligned} \sigma_{rr}(r,t) = & -[\bar{G}\varepsilon_{zz}(t) - hC_o(t)] \\ & - \frac{4}{R^2}\sum_{n=1}^{\infty} \Bigg\{ \int_0^t [\Phi_n^{\mathrm{I}} s_n^{\mathrm{I}} e^{-s_n^{\mathrm{I}}(t-\tau)} - \Phi_n^{\mathrm{II}} s_n^{\mathrm{II}} e^{-s_n^{\mathrm{II}}(t-\tau)}]C_o(\tau)d\tau \Bigg\} \\ & \times \frac{RJ_1(\beta_n r)}{\beta_n^2 r J_1(\beta_n R)} + \frac{4}{R^2}\sum_{n=1}^{\infty} \Bigg\{ \int_0^t [\Omega_n^{\mathrm{I}} e^{-s_n^{\mathrm{I}}(t-\tau)} \\ & - \Omega_n^{\mathrm{II}} e^{-s_n^{\mathrm{II}}(t-\tau)}]p_o(\tau)d\tau \Bigg\} \frac{RJ_1(\beta_n r)}{rJ_1(\beta_n R)} \end{aligned} \tag{G5}$$

$$\begin{aligned} \sigma_{zz}(r,t) = & [2\bar{G}\varepsilon_{zz}(t) + (2h - \bar{K}_v)C_o(t)] - \frac{4}{R^2}\sum_{n=1}^{\infty} \Bigg\{ \int_0^t [\Phi_n^{\mathrm{I}} s_n^{\mathrm{I}} e^{-s_n^{\mathrm{I}}(t-\tau)} \\ & - \Phi_n^{\mathrm{II}} s_n^{\mathrm{II}} e^{-s_n^{\mathrm{II}}(t-\tau)}]C_o(\tau)d\tau \Bigg\} \frac{RJ_0(\beta_n r)}{\beta_n J_1(\beta_n R)} \\ & + \frac{4}{R^2}\sum_{n=1}^{\infty} \Bigg\{ \int_0^t [\Omega_n^{\mathrm{I}} e^{-s_n^{\mathrm{I}}(t-\tau)} \\ & - \Omega_n^{\mathrm{II}} e^{-s_n^{\mathrm{II}}(t-\tau)}]p_o(\tau)d\tau \Bigg\} \frac{\beta_n RJ_0(\beta_n r)}{J_1(\beta_n R)} \end{aligned} \tag{G6}$$

where h, $\Phi_n^{(N)}$, and $\Omega_n^{(N)}$ are defined in Eqs. (D14)–(D16). The

remaining undetermined items are $C_o(t)$ and $\varepsilon_{zz}(t)$. Applying the lateral confining stress and vertical loading boundary conditions gives

$$\bar{G}\varepsilon_{zz}(t) = hC_o(t) - P_c(t) + \frac{4}{R^2}\sum_{n=1}^{\infty}\left\{\int_0^t [\Omega_n^{\mathrm{I}} e^{-s_n^{\mathrm{I}}(t-\tau)} - \Omega_n^{\mathrm{II}} e^{-s_n^{\mathrm{II}}(t-\tau)}]p_o(\tau)d\tau\right\} - \frac{4}{R^2}\sum_{n=1}^{\infty}\left\{\int_0^t [\Phi_n^{\mathrm{I}} s_n^{\mathrm{I}} e^{-s_n^{\mathrm{I}}(t-\tau)} - \Phi_n^{\mathrm{II}} s_n^{\mathrm{II}} e^{-s_n^{\mathrm{II}}(t-\tau)}]C_o(\tau)d\tau\right\}\frac{1}{\beta_n^2} \tag{G7}$$

$$(2h - \bar{K}_v/2)C_o(t) = [F(t)/2\pi R^2 + P_c(t)] - \frac{8}{R^2}\times\sum_{n=1}^{\infty}\left\{\int_0^t [\Omega_n^{\mathrm{I}} e^{-s_n^{\mathrm{I}}(t-\tau)} - \Omega_n^{\mathrm{II}} e^{-s_n^{\mathrm{II}}(t-\tau)}]p_o(\tau)d\tau\right\} + \frac{8}{R^2}\sum_{n=1}^{\infty}\left\{\int_0^t [\Phi_n^{\mathrm{I}} s_n^{\mathrm{I}} e^{-s_n^{\mathrm{I}}(t-\tau)} - \Phi_n^{\mathrm{II}} s_n^{\mathrm{II}} e^{-s_n^{\mathrm{II}}(t-\tau)}]C_o(\tau)d\tau\right\}\frac{1}{\beta_n^2} \tag{G8}$$

Again, the integral equation (G8) has the same form and general solution as shown in the strip geometry (Eq. (D18)) as follows:

$$C_o(t) = \Theta(t) - \int_0^t \sum_{i=1}^{\infty}\left[\frac{e^{\lambda_i(t-\tau)}}{Q'(s=\lambda_i)}\right]\Theta(\tau)d\tau$$

in which the functions $\Theta(t)$ and $Q(s)$ are redefined as

$$(2h - \bar{K}_v/2)\Theta(t) = [F(t)/2\pi R^2 + P_c(t)] - \frac{8}{R^2}\times\sum_{n=1}^{\infty}\left\{\int_0^t [\Omega_n^{\mathrm{I}} e^{-s_n^{\mathrm{I}}(t-\tau)} - \Omega_n^{\mathrm{II}} e^{-s_n^{\mathrm{II}}(t-\tau)}]p_o(\tau)d\tau\right\} \tag{G9}$$

$$(2h - \bar{K}_v/2)Q(s) = \frac{8}{R^2}\sum_{n=1}^{\infty}\frac{1}{\beta_n^2}\left(\frac{\Phi_n^{\mathrm{I}} s_n^{\mathrm{I}}}{s + s_n^{\mathrm{I}}} - \frac{\Phi_n^{\mathrm{II}} s_n^{\mathrm{II}}}{s + s_n^{\mathrm{II}}}\right) \tag{G10}$$

where $Q'(s)$ denotes $dQ(s)/ds$ and λ_i are roots of the equation $1-Q(s)=0$.

Once $C_o(t)$ is determined, it can be substituted into Eq. (G7) to obtain $\varepsilon_{zz}(t)$. Similar to the strip loading case, the explicit solutions of $C_o(t)$ and pore pressures for some special unconfined uniaxial loading conditions such as step loading, cyclic loading, and linear ramp loading are given as follows:

- step loading (original Mandel's problem): $p_o(t)=P_c(t)=0$; $F(t)=F^*H(t)$

$$C_o(t) = \frac{1}{(4h - \bar{K}_v)}\frac{F}{\pi R^2}\left\{1 + \sum_{i=1}^{\infty}\left[\frac{(1 - e^{\lambda_i t})}{\lambda_i Q'(s=\lambda_i)}\right]\right\} \tag{G11}$$

$$p^{(N)}(r,t) = \frac{\gamma^{(N)}}{4h - \bar{K}_v}\frac{F}{\pi R^2} * \frac{2}{R^2}\sum_{n=1}^{\infty}\frac{1}{s_n^{\mathrm{I}} - s_n^{\mathrm{II}}}\left\{(s_n^{\mathrm{I}} - w_n^{(N)})e^{-s_n^{\mathrm{I}} t} - (s_n^{\mathrm{II}} - w_n^{(N)})e^{-s_n^{\mathrm{II}} t} + \sum_{i=1}^{\infty}\left[\frac{(s_n^{\mathrm{I}} - w_n^{(N)})(e^{\lambda_i t} - e^{-s_n^{\mathrm{I}} t})}{(s_n^{\mathrm{I}} + \lambda_i)Q'(\lambda_i)} - \frac{(s_n^{\mathrm{II}} - w_n^{(N)})(e^{\lambda_i t} - e^{-s_n^{\mathrm{II}} t})}{(s_n^{\mathrm{II}} + \lambda_i)Q'(\lambda_i)}\right]\right\}\frac{RJ_0(\beta_n r)}{\beta_n J_1(\beta_n R)} \tag{G12}$$

- cyclic loading: $p_o(t)=P_c(t)=0$; $F(t)=F^*\sin(\omega t)$

$$C_o(t) = \frac{1}{4h - \bar{K}_v}\frac{F}{\pi R^2}\left\{\sin(\omega t) - \sum_{i=1}^{\infty}\left[\frac{\omega e^{\lambda_i t} - \omega\cos(\omega t) - \lambda_i \sin(\omega t)}{(\lambda_i^2 + \omega^2)Q'(s=\lambda_i)}\right]\right\} \tag{G13}$$

$$p^{(N)}(r,t) = -\frac{\gamma^{(N)\mathrm{I}}}{4h - \bar{K}_v}\frac{F\omega}{\pi R^2}\frac{2}{R^2}\sum_{n=1}^{\infty}\frac{1}{(s_n^{\mathrm{I}} - s_n^{\mathrm{II}})}\frac{RJ_0(\beta_n r)}{\beta_n J_1(\beta_n R)} * \left\{(s_n^{\mathrm{I}} - w_n^{(N)})\frac{s_n^{\mathrm{I}} e^{-s_n^{\mathrm{I}} t} - s_n^{\mathrm{I}}\cos(\omega t) - \omega\sin(\omega t)}{(s_n^{\mathrm{I}})^2 + \omega^2} - (s_n^{\mathrm{II}} - w_n^{(N)})\frac{s_n^{\mathrm{II}} e^{-s_n^{\mathrm{II}} t} - s_n^{\mathrm{II}}\cos(\omega t) - \omega\sin(\omega t)}{(s_n^{\mathrm{II}})^2 + \omega^2} + \sum_{i=1}^{\infty}\left[\frac{(s_n^{\mathrm{I}} - w_n^{(N)})\lambda_i(e^{\lambda_i t} - e^{-s_n^{\mathrm{I}} t})}{(s_n^{\mathrm{I}} + \lambda_i)(\lambda_i^2 + \omega^2)Q'(\lambda_i)} - \frac{(s_n^{\mathrm{II}} - w_n^{(N)})\lambda_i(e^{\lambda_i t} - e^{-s_n^{\mathrm{II}} t})}{(s_n^{\mathrm{II}} + \lambda_i)(\lambda_i^2 + \omega^2)Q'(\lambda_i)}\right] + \sum_{i=1}^{\infty}\left[\frac{(s_n^{\mathrm{I}} - w_n^{(N)})\{(\lambda_i s_n^{\mathrm{I}} + \omega^2)[e^{-s_n^{\mathrm{I}} t} - \cos(\omega t)] + \omega(s_n^{\mathrm{I}} - \lambda_i)\sin(\omega t)\}}{[(s_n^{\mathrm{I}})^2 + \omega^2](\lambda_i^2 + \omega^2)Q'(\lambda_i)}\right] - \sum_{i=1}^{\infty}\left[\frac{(s_n^{\mathrm{II}} - w_n^{(N)})\{(\lambda_i s_n^{\mathrm{II}} + \omega^2)[e^{-s_n^{\mathrm{II}} t} - \cos(\omega t)] + \omega(s_n^{\mathrm{II}} - \lambda_i)\sin(\omega t)\}}{[(s_n^{\mathrm{II}})^2 + \omega^2](\lambda_i^2 + \omega^2)Q'(\lambda_i)}\right]\right\} \tag{G14}$$

- linear ramp loading: $p_o(t)=P_c(t)=0$; $F(t)=F^*[tH(t)-(t-t_o)H(t-t_o)]/t_o$

$$C_o(t) = \frac{1}{4h - \bar{K}_v}\frac{F(t)}{\pi R^2} - \frac{1}{4h - \bar{K}_v}\frac{F}{\pi R^2}\frac{1}{t_o}\sum_{i=1}^{\infty}\frac{1}{\lambda_i^2 Q'(\lambda_i)}\{[e^{\lambda_i t} - 1 - \lambda_i t)]H(t) + [e^{\lambda_i(t-t_o)} - 1 - \lambda_i(t-t_o)]H(t-t_o)\} \tag{G15}$$

$$p^{(N)}(r,t)=\frac{\gamma^{(N)}}{4h-\bar{K}_v}\frac{F}{\pi R^2 t_o}\frac{2}{R^2}\sum_{n=1}^{\infty}\frac{1}{(s_n^{\mathrm{I}}-s_n^{\mathrm{II}})}\frac{RJ_0(\beta_n r)}{\beta_n J_1(\beta_n R)}\Bigg\{(s_n^{\mathrm{I}}-w_n^{(N)})\frac{1-e^{-s_n^{\mathrm{I}}t}-[1-e^{-s_n^{\mathrm{I}}(t-t_o)}]H(t-t_o)}{s_n^{\mathrm{I}}}$$
$$-(s_n^{\mathrm{II}}-w_n^{(N)})\frac{1-e^{-s_n^{\mathrm{II}}t}-[1-e^{-s_n^{\mathrm{II}}(t-t_o)}]H(t-t_o)}{s_n^{\mathrm{II}}}+\sum_{i=1}^{\infty}\left[\frac{(s_n^{\mathrm{I}}-w_n^{(N)})(s_n^{\mathrm{I}}e^{\lambda_i t}+\lambda_i e^{-s_n^{\mathrm{I}}t}-s_n^{\mathrm{I}}-\lambda_i)}{s_n^{\mathrm{I}}(s_n^{\mathrm{I}}+\lambda_i)\lambda_i Q'(\lambda_i)}\right]$$
$$-\sum_{i=1}^{\infty}\left[\frac{(s_n^{\mathrm{II}}-w_n^{(N)})(s_n^{\mathrm{II}}e^{\lambda_i t}+\lambda_i e^{-s_n^{\mathrm{II}}t}-s_n^{\mathrm{II}}-\lambda_i)}{s_n^{\mathrm{II}}(s_n^{\mathrm{II}}+\lambda_i)\lambda_i Q'(\lambda_i)}\right]+\sum_{i=1}^{\infty}\left[\frac{(s_n^{\mathrm{I}}-w_n^{(N)})(s_n^{\mathrm{I}}e^{\lambda_i (t-t_o)}+\lambda_i e^{-s_n^{\mathrm{I}}(t-t_o)}-s_n^{\mathrm{I}}-\lambda_i)H(t-t_o)}{s_n^{\mathrm{I}}(s_n^{\mathrm{I}}+\lambda_i)\lambda_i Q'(\lambda_i)}\right]$$
$$-\sum_{i=1}^{\infty}\left[\frac{(s_n^{\mathrm{II}}-w_n^{(N)})(s_n^{\mathrm{II}}e^{\lambda_i (t-t_o)}+\lambda_i e^{-s_n^{\mathrm{II}}(t-t_o)}-s_n^{\mathrm{II}}-\lambda_i)H(t-t_o)}{s_n^{\mathrm{II}}(s_n^{\mathrm{II}}+\lambda_i)\lambda_i Q'(\lambda_i)}\right]\Bigg\} \tag{G16}$$

The complete time-domain results are computed by substituting the suitable expressions for $C_o(t)$ and fluid pressures into the general solution equations ((E1)–(E6)).

References

[1] Dickey, J. W., Ladd, C. C., and Ringer, J. J., 1968, "A Plane Strain Device for Testing Clays," Civil Engineering Research Report No. R68-3.

[2] Abousleiman, Y., and Cui, L., 1998, "Poroelastic Solutions in Transversely Isotropic Media for Wellbore and Cylinder," Int. J. Solids Struct., **35**(34–35), pp. 4905–4929.

[3] Wang, H., 2000, *Theory of Poroelasticity With Applications to Geomechanics and Hydrology*, Princeton University Press, Princeton, NJ, Chap. 7 and 8.

[4] Woo, S. L.-Y., Simon, B. R., Kuei, S. C., and Akeson, W. S., 1980, "Quasi-Linear Viscoelastic Properties of Normal Articular Cartilage," ASME J. Biomech. Eng., **102**(2), pp. 85–90.

[5] Buschmann, M. D., Soulhat, J., Shirazi-Ald, A., Jurvelin, J. S., and Hunziker, E. B., 1998, "Confined Compression of Articular Cartilage: Linearity in Ramp and Sinusoidal Tests and the Importance of Interdigitation and Incomplete Confinement," J. Biomech., **31**(2), pp. 171–178.

[6] Mandel, J., 1953, "Consolidation des sols (étude mathématique)," Geotechnique, **3**(7), pp. 287–299.

[7] Biot, M. A., 1941, "General Theory of Three-Dimensional Consolidation," J. Appl. Phys., **12**(2), pp. 155–164.

[8] Kenyon, D. E., 1979, "Consolidation in Transversely Isotropic Solids," ASME J. Appl. Mech., **46**(1), pp. 65–70.

[9] Terzaghi, K., 1943, *Theoretical Soil Mechanics*, Wiley, New York.

[10] Abousleiman, Y., Cheng, A. H.-D., Cui, L., Detournay, E., and Roegiers, J.-C., 1996, "Mandel's Problem Revisited," Geotechnique, **46**(2), pp. 187–195.

[11] Hoang, S. K., and Abousleiman, Y., 2009, "Poroviscoelastic Two-Dimensional Anisotropic Solution With Application to Articular Cartilage Testing," J. Eng. Mech., **135**(5), pp. 367–374.

[12] Christian, J. T., and Boehmer, J. W., 1970, "Plane Strain Consolidation by Finite Elements," J. Soil Mech. Found. Div., **96**(4), pp. 1435–1457.

[13] Cui, L., Abousleiman, Y., Cheng, A. H.-D., and Kaliakin, V., 1996, "Finite Element Analyses of Anisotropic Poroelasticity: A Generalized Mandel's Problem and an Inclined Borehole Problem," Int. J. Numer. Analyt. Meth. Geomech., **20**(6), pp. 381–401.

[14] Yin, S., Rothenburg, L., and Dusseault, M. B., 2006, "3D Coupled Displacement Discontinuity and Finite Element Analysis of Reservoir Behavior During Production in Semi-Infinite Domain," Transp. Porous Media, **65**(3), pp. 425–441.

[15] Phillips, P. J., and Wheeler, M. F., 2007, "A Coupling of Mixed and Continuous Galerkin Finite Element Methods For Poroelasticity I: The Continuous Time Case," Comput. Geosci., **11**(2), pp. 131–144.

[16] Odgaard, A., and Linde, F., 1991, "The Underestimation of Young's Modulus in Compressive Testing of Cancellous Bone Specimens," J. Biomech., **24**(8), pp. 691–698.

[17] Wang, C., Chahine, N., Hung, C., and Ateshian, G., 2003, "Optical Determination of Anisotropic Material Properties of Bovine Articular Cartilage in Compression," J. Biomech., **36**, pp. 339–353.

[18] Saada, A., 1974, *Elasticity: Theory and Applications*, Pergamon Press, New York.

[19] Armstrong, C. G., Lai, W. M., and Mow, V. C., 1984, "An Analysis of the Unconfined Compression of Articular Cartilage," ASME J. Biomech. Eng., **106**(5), pp. 165–173.

[20] Cui, L., and Abousleiman, Y., 2001, "Time-Dependent Poromechanical Responses of Saturated Cylinders," J. Eng. Mech., **127**(4), pp. 391–398.

[21] Cowin, S. C., and Mehrabadi, M. M., 2007, "Compressible and Incompressible Constituents in Anisotropic Poroelasticity: The Problem of Unconfined Compression of a Disk," J. Mech. Phys. Solids, **55**, pp. 161–193.

[22] Cowin, S. C., 1999, "Bone Poroelasticity," J. Biomech., **32**, pp. 217–238.

[23] Barenblatt, G. I., Zheltov, I. P., and Kochina, I. N., 1960, "Basic Concept in the Theory of Seepage of Homogeneous Liquid in Fissured Rocks," J. Appl. Math. Mech., **24**(5), pp. 1286–1303.

[24] Warren, J. E., and Root, P. J., 1963, "The Behavior of Naturally Fractured Reservoirs," SPEJ, **228**, pp. 245–255.

[25] Wilson, R. K., and Aifantis, E. C., 1982, "On the Theory of Consolidation With Double Porosity," Int. J. Eng. Sci., **20**, pp. 1009–1035.

[26] Berryman, J. G., 2002, "Extension of Poroelastic Analysis to Double-Porosity Materials: New Technique in Microgeomechanics," J. Eng. Mech., **128**(8), pp. 840–847.

[27] Stehfest, H., 1970, "Numerical Inversion of Laplace Transforms," Commun. ACM, **13**, pp. 47–49.

[28] Cheng, A. H.-D., Sidauruk, P., and Abousleiman, Y., 1994, "Approximate Inversion of Laplace Transform," Math. J., **4**(2), pp. 76–82.

[29] Aguilera, D., 1995, *Naturally Fractured Reservoirs*, 2nd ed., PennWell Books, Tulsa, OK, Chap. 1.

[30] Bear, J., 1972, *Dynamics of Fluids in Porous Media*, 3rd ed., American Elsevier, New York, Chap. 1.

[31] Berryman, J. G., and Pride, S. R., 2002, "Models for Computing Geomechanical Constants of Double-Porosity Materials from the Constituents' Properties," J. Geophys. Res., **107**(B3), pp. ECV2-1–ECV2-14.

[32] Churchill, R. V., 1972, *Operational Mathematics*, McGraw-Hill, New York.

[33] Polyanin, A. D., and Manzhirov, A. V., 1998, *Handbook of Integral Equations*, 1st ed., CRC, Florida, Chap. 2.

J. Xiao
Department of Mechanical Engineering,
Northwestern University,
Evanston, IL 60208

A. Carlson
Department of Materials Science and Engineering,
University of Illinois at Urbana-Champaign,
Urbana-Champaign, IL 61801

Z. J. Liu
Institute of High Performance Computing,
1 Fusionopolis Way,
No. 16-16 Connexis,
Singapore 138632, Singapore

Y. Huang
Department of Mechanical Engineering,
and Department of Civil and Environmental Engineering,
Northwestern University,
Evanston, IL 60208

J. A. Rogers
Department of Materials Science and Engineering
and Beckman Institute,
and Seitz Materials Research Laboratory,
University of Illinois at Urbana-Champaign,
Urbana-Champaign, IL 61801

Analytical and Experimental Studies of the Mechanics of Deformation in a Solid With a Wavy Surface Profile

The analytical solution is obtained for a semi-infinite linear elastic solid with a sinusoidal, "wavy" surface profile subject to applied strain. The amplitude A of a deformed wavy surface is related to the initial amplitude A_0 and the applied strain ε_a through the simple expression $A=A_0(1-\varepsilon_a)$. This relation is confirmed independently by finite element analyses and experimental measurements of strained wavy poly(dimethylsiloxane) surfaces. Analytical solutions are also obtained for a wavy solid subject to stretch and lateral displacement. [DOI: 10.1115/1.3132184]

1 Introduction

Controlled buckling of thin films on prestrained elastomeric substrates has the potential to be a critical fabrication route for technologies in many areas of study, such as stretchable electronics [1–11], micro- and nanometrology methods [12,13], tunable phase optics [14,15], and pattern formation at the micro-/nanoscale [16–19]. The mechanics of such systems have been investigated extensively [20–26]. Although these systems have many attractive features, one disadvantage is that compressive strains in the buckled films, established during fabrication, provide film stretchability at the expense of reduced compressibility. Recently, an alternative approach was presented in which the thin stiff films were deposited directly onto a compliant substrate with prefabricated sinusoidal, "wavy" surface relief features [27]. Use of such wavy systems would avoid any initial film strain, therefore achieving both high stretchability and compressibility.

The objective of this paper is to develop an analytical method for studying the wavy substrate under applied strains or "stretch." Such a framework would provide a foundation for future studies of stretchability and compressibility of stiff thin films on compliant substrates. Analytical methods are described in Sec. 2, leading to the solution for surface profile deformation of a bare, wavy substrate subject to uniaxial tension. In Sec. 3 this solution is compared with experimental and numerical results. Finally, Sec. 4 presents another analytical solution for a wavy substrate subject to lateral displacements; an analysis directly related to the system of a stiff thin film on a compliant substrate.

Contributed by the Applied Mechanics Division of ASME for publication in the JOURNAL OF APPLIED MECHANICS. Manuscript received May 27, 2008; final manuscript received December 1, 2008; published online September 23, 2009. Review conducted by Robert M. McMeeking.

2 Theory

Figure 1 shows a semi-infinite solid with a wavy surface profile $y=A_0\cos kx$ subject to an applied strain ε_a in the x direction, where A_0 is the amplitude, $k=2\pi/\lambda$, and λ is the wavelength. The solid is linear elastic with Young's modulus E and Poisson's ratio ν. A new coordinate system

$$\xi = x, \quad \eta = y - A_0 \cos kx \tag{1}$$

is introduced such that the wavy boundary $y=A_0\cos kx$ of the solid becomes a straight line $\eta=0$ in the (ξ,η) plane. The solid in Fig. 1 is thus transformed to a semi-infinite solid $(-\infty<\xi<\infty, -\infty<\eta<0)$ in the new coordinate system. The partial derivatives with respect to the physical coordinates (x,y) can be written in terms of (ξ,η) as

$$\frac{\partial}{\partial x} = \frac{\partial}{\partial \xi} + A_0 k \sin k\xi \frac{\partial}{\partial \eta}, \quad \frac{\partial}{\partial y} = \frac{\partial}{\partial \eta} \tag{2}$$

To determine the change in profile amplitude under applied strains, we first consider displacements in the x and y directions, u_x and u_y, respectively. In terms of these displacements, the strains are given by

$$\varepsilon_{xx} = \frac{\partial u_x}{\partial x} = \frac{\partial u_x}{\partial \xi} + A_0 k \sin k\xi \frac{\partial u_x}{\partial \eta}$$

$$\varepsilon_{yy} = \frac{\partial u_y}{\partial y} = \frac{\partial u_y}{\partial \eta}$$

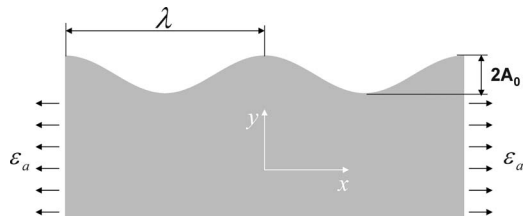

Fig. 1 A solid with wavy surface subject to the applied strain ε_a. The wavelength is λ and initial amplitude is A_0.

$$2\varepsilon_{xy} = \frac{\partial u_x}{\partial y} + \frac{\partial u_y}{\partial x} = \frac{\partial u_x}{\partial \eta} + \frac{\partial u_y}{\partial \xi} + A_0 k \sin k\xi \frac{\partial u_y}{\partial \eta} \tag{3}$$

Substrate stresses can be obtained via the linear elastic relation for plain-strain deformation

$$\sigma_{xx} = \frac{E}{(1+\nu)(1-2\nu)}[(1-\nu)\varepsilon_{xx} + \nu\varepsilon_{yy}]$$

$$\sigma_{yy} = \frac{E}{(1+\nu)(1-2\nu)}[(1-\nu)\varepsilon_{yy} + \nu\varepsilon_{xx}]$$

$$\sigma_{xy} = \frac{E}{1+\nu}\varepsilon_{xy} \tag{4}$$

For plane-stress deformation, E and ν are replaced by $E(1+2\nu)/(1+\nu)^2$ and $\nu/(1+\nu)$, respectively.

Substitution of Eqs. (3) and (4) into the equilibrium equation (5), given as

$$\frac{\partial \sigma_{xx}}{\partial \xi} + A_0 k \sin k\xi \frac{\partial \sigma_{xx}}{\partial \eta} + \frac{\partial \sigma_{xy}}{\partial \eta} = 0$$

$$\frac{\partial \sigma_{xy}}{\partial \xi} + A_0 k \sin k\xi \frac{\partial \sigma_{xy}}{\partial \eta} + \frac{\partial \sigma_{yy}}{\partial \eta} = 0 \tag{5}$$

yields the following two partial differential equations for u_x and u_y:

$$(1-2\nu)\left(\frac{\partial^2 u_x}{\partial \xi^2} + \frac{\partial^2 u_x}{\partial \eta^2}\right) + \frac{\partial}{\partial \xi}\left(\frac{\partial u_x}{\partial \xi} + \frac{\partial u_y}{\partial \eta}\right) + A_0 k \sin k\xi \left[4(1-\nu)\frac{\partial^2 u_x}{\partial \xi \partial \eta} + \frac{\partial^2 u_y}{\partial \eta^2}\right] + 2(1-\nu)A_0 k^2 \cos k\xi \frac{\partial u_x}{\partial \eta} + 2(1-\nu)A_0^2 k^2 \sin^2 k\xi \frac{\partial^2 u_x}{\partial \eta^2} = 0$$

$$(1-2\nu)\left(\frac{\partial^2 u_y}{\partial \xi^2} + \frac{\partial^2 u_y}{\partial \eta^2}\right) + \frac{\partial}{\partial \eta}\left(\frac{\partial u_x}{\partial \xi} + \frac{\partial u_y}{\partial \eta}\right) + A_0 k \sin k\xi \left[2(1-2\nu)\frac{\partial^2 u_y}{\partial \xi \partial \eta} + \frac{\partial^2 u_x}{\partial \eta^2}\right] + (1-2\nu)A_0 k^2 \cos k\xi \frac{\partial u_y}{\partial \eta} + (1-2\nu)A_0^2 k^2 \sin^2 k\xi \frac{\partial^2 u_y}{\partial \eta^2} = 0 \tag{6}$$

Boundary conditions for the system include a traction-free top surface of the solid such that

$$\boldsymbol{n} \cdot \begin{pmatrix} \sigma_{xx} & \sigma_{xy} \\ \sigma_{xy} & \sigma_{yy} \end{pmatrix} = 0 \quad \text{at} \quad \eta = 0 \tag{7}$$

where $\boldsymbol{n}$ represents the unit normal on the surface and is in the direction $(A_0 k \sin kx, 1)$. This direction is equivalent to $(A_0 k \sin k\xi, 1)$. Simplifying these boundary conditions yield the expressions

$$A_0 k \sin k\xi \sigma_{xx} + \sigma_{xy} = 0, \quad A_0 k \sin k\xi \sigma_{xy} + \sigma_{yy} = 0 \quad \text{at} \quad \eta = 0 \tag{8}$$

Remote boundary conditions require $\varepsilon_{xx}|_{\eta \to -\infty} = \varepsilon_a$ due to the applied strain and vanishing tractions, i.e., $\sigma_{xy} = 0$ and $\sigma_{yy} = 0$.

For small amplitude ($A_0 \ll \lambda$, or equivalently $A_0 k \ll 1$), the perturbation method is used to write the displacements as

$$u_x = u_x^{(0)} + (A_0 k) u_x^{(1)} + (A_0 k)^2 u_x^{(2)} + \cdots$$

$$u_y = u_y^{(0)} + (A_0 k) u_y^{(1)} + (A_0 k)^2 u_y^{(2)} + \cdots \tag{9}$$

By sorting terms according to the power of $A_0 k$, substitution of Eq. (9) into the equilibrium equation (6) and boundary condition (8) leads to the following partial differential equations and boundary conditions for $u_x^{(i)}$ and $u_y^{(i)}$ $(i = 0, 1, 2, \ldots)$ under plane-strain deformation.

For zeroth (leading) order,

$$(1-2\nu)\left(\frac{\partial^2 u_x^{(0)}}{\partial \xi^2} + \frac{\partial^2 u_x^{(0)}}{\partial \eta^2}\right) + \frac{\partial}{\partial \xi}\left(\frac{\partial u_x^{(0)}}{\partial \xi} + \frac{\partial u_y^{(0)}}{\partial \eta}\right) = 0$$

$$(1-2\nu)\left(\frac{\partial^2 u_y^{(0)}}{\partial \xi^2} + \frac{\partial^2 u_y^{(0)}}{\partial \eta^2}\right) + \frac{\partial}{\partial \eta}\left(\frac{\partial u_x^{(0)}}{\partial \xi} + \frac{\partial u_y^{(0)}}{\partial \eta}\right) = 0 \tag{10a}$$

$$\frac{\partial u_x^{(0)}}{\partial \eta} + \frac{\partial u_y^{(0)}}{\partial \xi} = 0, \quad \nu \frac{\partial u_x^{(0)}}{\partial \xi} + (1-\nu)\frac{\partial u_y^{(0)}}{\partial \eta} = 0, \quad \text{at} \quad \eta = 0 \tag{10b}$$

$$\frac{\partial u_x^{(0)}}{\partial \eta} + \frac{\partial u_y^{(0)}}{\partial \xi} = 0, \quad \nu \frac{\partial u_x^{(0)}}{\partial \xi} + (1-\nu)\frac{\partial u_y^{(0)}}{\partial \eta} = 0, \quad \text{at} \quad \eta \to -\infty \tag{10c}$$

$$\frac{\partial u_x^{(0)}}{\partial \xi} = \varepsilon_a, \quad \text{at} \quad \eta \to -\infty \tag{10d}$$

For first order,

$$(1-2\nu)\left(\frac{\partial^2 u_x^{(1)}}{\partial \xi^2} + \frac{\partial^2 u_x^{(1)}}{\partial \eta^2}\right) + \frac{\partial}{\partial \xi}\left(\frac{\partial u_x^{(1)}}{\partial \xi} + \frac{\partial u_y^{(1)}}{\partial \eta}\right) = -\sin k\xi \left[4(1-\nu)\frac{\partial^2 u_x^{(0)}}{\partial \xi \partial \eta} + \frac{\partial^2 u_y^{(0)}}{\partial \eta^2}\right] - 2(1-\nu)k \cos k\xi \frac{\partial u_x^{(0)}}{\partial \eta}$$

$$(1-2\nu)\left(\frac{\partial^2 u_y^{(1)}}{\partial \xi^2} + \frac{\partial^2 u_y^{(1)}}{\partial \eta^2}\right) + \frac{\partial}{\partial \eta}\left(\frac{\partial u_x^{(1)}}{\partial \xi} + \frac{\partial u_y^{(1)}}{\partial \eta}\right) = -\sin k\xi \left[2(1-2\nu)\frac{\partial^2 u_y^{(0)}}{\partial \xi \partial \eta} + \frac{\partial^2 u_x^{(0)}}{\partial \eta^2}\right] - (1-2\nu)k \cos k\xi \frac{\partial u_y^{(0)}}{\partial \eta} \tag{11a}$$

$$\frac{\partial u_x^{(1)}}{\partial \eta} + \frac{\partial u_y^{(1)}}{\partial \xi} = -\frac{\sin k\xi}{(1-2\nu)}\left[2(1-\nu)\frac{\partial u_x^{(0)}}{\partial \xi} + \frac{\partial u_y^{(0)}}{\partial \eta}\right] \text{ and}$$

$$(1-\nu)\frac{\partial u_y^{(1)}}{\partial \eta} + \nu \frac{\partial u_x^{(1)}}{\partial \xi} = -\frac{\sin k\xi}{2}\left[\frac{\partial u_x^{(0)}}{\partial \eta} + (1-2\nu)\frac{\partial u_y^{(0)}}{\partial \xi}\right] \quad \text{at} \quad \eta = 0 \tag{11b}$$

$$\frac{\partial u_x^{(1)}}{\partial \eta} + \frac{\partial u_y^{(1)}}{\partial \xi} = -\sin k\xi \frac{\partial u_y^{(0)}}{\partial \eta} \text{ and}$$

$$(1-\nu)\frac{\partial u_y^{(1)}}{\partial \eta} + \nu \frac{\partial u_x^{(1)}}{\partial \xi} = -\nu \sin k\xi \frac{\partial u_x^{(0)}}{\partial \eta} \quad \text{at} \quad \eta \to -\infty \tag{11c}$$

For second order,

$$(1-2\nu)\left(\frac{\partial^2 u_x^{(2)}}{\partial \xi^2}+\frac{\partial^2 u_x^{(2)}}{\partial \eta^2}\right)+\frac{\partial}{\partial \xi}\left(\frac{\partial u_x^{(2)}}{\partial \xi}+\frac{\partial u_y^{(2)}}{\partial \eta}\right)$$
$$=-2(1-\nu)k\cos k\xi\frac{\partial u_x^{(1)}}{\partial \eta}-\sin k\xi\left[4(1-\nu)\frac{\partial^2 u_x^{(1)}}{\partial \xi\,\partial \eta}+\frac{\partial^2 u_y^{(1)}}{\partial \eta^2}\right]$$
$$-2(1-\nu)\sin^2 k\xi\frac{\partial^2 u_x^{(0)}}{\partial \eta^2}$$

$$(1-2\nu)\left(\frac{\partial^2 u_y^{(2)}}{\partial \xi^2}+\frac{\partial^2 u_y^{(2)}}{\partial \eta^2}\right)+\frac{\partial}{\partial \eta}\left(\frac{\partial u_x^{(2)}}{\partial \xi}+\frac{\partial u_y^{(2)}}{\partial \eta}\right)$$
$$=-(1-2\nu)k\cos k\xi\frac{\partial u_y^{(1)}}{\partial \eta}-\sin k\xi\left[2(1-2\nu)\frac{\partial^2 u_y^{(1)}}{\partial \xi\,\partial \eta}+\frac{\partial^2 u_x^{(1)}}{\partial \eta^2}\right]$$
$$-(1-2\nu)\sin^2 k\xi\frac{\partial^2 u_y^{(0)}}{\partial \eta^2} \tag{12a}$$

$$\frac{\partial u_x^{(2)}}{\partial \eta}+\frac{\partial u_y^{(2)}}{\partial \xi}=-\frac{\sin k\xi}{(1-2\nu)}\left[\frac{\partial u_y^{(1)}}{\partial \eta}+2(1-\nu)\frac{\partial u_x^{(1)}}{\partial \xi}\right.$$
$$\left.+2(1-\nu)\sin k\xi\frac{\partial u_x^{(0)}}{\partial \eta}\right]$$

$$(1-\nu)\frac{\partial u_y^{(2)}}{\partial \eta}+\nu\frac{\partial u_x^{(2)}}{\partial \xi}=-\frac{\sin k\xi}{2}\left[\frac{\partial u_x^{(1)}}{\partial \eta}+(1-2\nu)\frac{\partial u_y^{(1)}}{\partial \xi}\right.$$
$$\left.+(1-2\nu)\sin k\xi\frac{\partial u_y^{(0)}}{\partial \eta}\right] \quad \text{at} \quad \eta=0 \tag{12b}$$

$$\frac{\partial u_x^{(2)}}{\partial \eta}+\frac{\partial u_y^{(2)}}{\partial \xi}=-\sin k\xi\frac{\partial u_y^{(1)}}{\partial \eta}$$

$$(1-\nu)\frac{\partial u_y^{(2)}}{\partial \eta}+\nu\frac{\partial u_x^{(2)}}{\partial \xi}=-\nu\sin k\xi\frac{\partial u_x^{(1)}}{\partial \eta} \quad \text{at} \quad \eta\to-\infty \tag{12c}$$

The solution of the zeroth-(leading) order of Eq. (10) is

$$u_x^{(0)}=\varepsilon_a\xi, \quad u_y^{(0)}=-\frac{\nu}{1-\nu}\varepsilon_a\eta \tag{13}$$

The corresponding stress field is the plane-strain tension in the x direction, $\sigma_{xx}^{(0)}=E/(1-\nu^2)\varepsilon_a$, $\sigma_{yy}^{(0)}=0$, and $\sigma_{xy}^{(0)}=0$.

First-order solutions of Eq. (11) are

$$u_x^{(1)}=\frac{-2+2\nu-k\eta}{1-\nu}\frac{\varepsilon_a}{k}e^{k\eta}\sin k\xi$$

$$u_y^{(1)}=\left(\frac{-1+2\nu+k\eta}{1-\nu}\frac{\varepsilon_a}{k}e^{k\eta}-\frac{\nu}{1-\nu}\frac{\varepsilon_a}{k}\right)\cos k\xi+\frac{\varepsilon_a}{k} \tag{14}$$

The corresponding stress fields are $\sigma_{xx}^{(1)}=-E\varepsilon_a e^{k\eta}/(1-\nu^2)(2+k\eta)\cos k\xi$, $\sigma_{yy}^{(1)}=E\varepsilon_a e^{k\eta}/(1-\nu^2)k\eta\cos k\xi$, and $\sigma_{xy}^{(1)}=-E\varepsilon_a e^{k\eta}/(1-\nu^2)(1+k\eta)\sin k\xi$, which decrease exponentially away from the top surface $\eta=0$.

The solution to the second-order equation (12) is

$$u_x^{(2)}=\frac{\varepsilon_a\sin 2k\xi}{2k(1-\nu)}[(3-2\nu+2k\eta)e^{2k\eta}-(3-2\nu+k\eta)e^{k\eta}]$$

$$u_y^{(2)}=\frac{\varepsilon_a\cos 2k\xi}{2k(1-\nu)}[-2(\nu+k\eta)e^{2k\eta}+(2\nu+k\eta)e^{k\eta}]$$
$$+\frac{2\nu+k\eta}{2k(1-\nu)}\varepsilon_a e^{k\eta}-\frac{\nu}{k(1-\nu)}\varepsilon_a \tag{15}$$

with a corresponding stress field of

$$\sigma_{xx}^{(2)}=\frac{E\varepsilon_a}{2(1-\nu^2)}[2e^{2k\eta}\cos 2k\xi(3+2k\eta)-e^{k\eta}(3+k\eta)(1+\cos 2k\xi)]$$

$$\sigma_{yy}^{(2)}=\frac{E\varepsilon_a}{2(1-\nu^2)}[-2e^{2k\eta}(1+2k\eta)\cos 2k\xi+e^{k\eta}(1+k\eta)(1+\cos 2k\xi)]$$

and

$$\sigma_{xy}^{(2)}=\frac{E\varepsilon_a\sin 2k\xi}{2(1-\nu^2)}[4e^{2k\eta}(1+k\eta)-e^{k\eta}(2+k\eta)]$$

These fields decrease exponentially away from the top surface $\eta=0$.

Conditions $u_x=u_y=0$ at $\xi=\eta=0$ are imposed to eliminate the rigid body motion. Displacement along the x and y directions on the solid's top surface can be obtained by substituting Eqs. (13)–(15) into Eq. (9)

$$u_x(\eta=0)=\varepsilon_a x-2A_0\varepsilon_a\sin kx$$
$$u_y(\eta=0)=A_0\varepsilon_a(1-\cos kx) \tag{16}$$

This gives the amplitude of deformed wavy profile as

$$A=A_0(1-\varepsilon_a) \tag{17}$$

The error is of order $O(\varepsilon_a A_0^2/\lambda^2)$ as compared with unity, i.e., the amplitude can be written as $A=A_0[1-\varepsilon_a+\varepsilon_a\cdot O(A_0^2/\lambda^2)]$.

3 Results and Experimental Procedures

Samples having a wavy surface profile were fabricated in a sequential process in which features designed on a rigid silicon template were imprinted into an elastomeric polymer such as poly(dimethylsiloxane) (PDMS). The critical steps of this fabrication process are illustrated in Fig. 2(*a*). To generate the silicon master, plasma-enhanced chemical vapor deposition (PECVD) formed a thin (200 nm) silicon nitride layer on a Si (100) wafer (SQI, Inc.). Conventional photolithography and plasma etching formed patterns of alternating lines and spaces, creating an etch mask in the nitride layer. After stripping the remaining photoresist, the Si (100) was anisotropically etched in a hot (90 °C) isopropyl alcohol buffered 25% potassium hydroxide (KOH) solution for 35 min. Removing the nitride mask with concentrated hydrofluoric acid (49% HF) then exposed the underlying silicon surface which had saw-tooth relief features similar to the first panel of Fig. 2(*a*). A thin layer of photoresist (MicroChem S1805) was spin cast at 3500 rpm for 90 s onto the silicon, converting the saw-tooth relief into an approximately sinusoidal shape able to be replicated in a compliant material like PDMS.

Two consecutive molding steps were used to reproduce the smoothed surface profile of the silicon/photoresist structure in a thin (300 μm) layer of PDMS supported by a glass substrate. The inverse of the saw-tooth profile was generated in a layer (75 μm) of negative tone photoresist (SU-8 50; MicroChem Corp.) by pressing the glass/PDMS element into liquid SU-8 on a thin (100 μm) plastic substrate (PET), flood exposing the system with ultraviolet light (λ=365 nm) for 30–40 s from both the top and bottom, followed by a 5 min hotplate bake at 65 °C. After separating the PDMS and cured SU-8, spin-casting a layer of SU-8 2 (MicroChem Corp.) diluted to $\frac{1}{2}$ volume fraction with SU-8 thin-

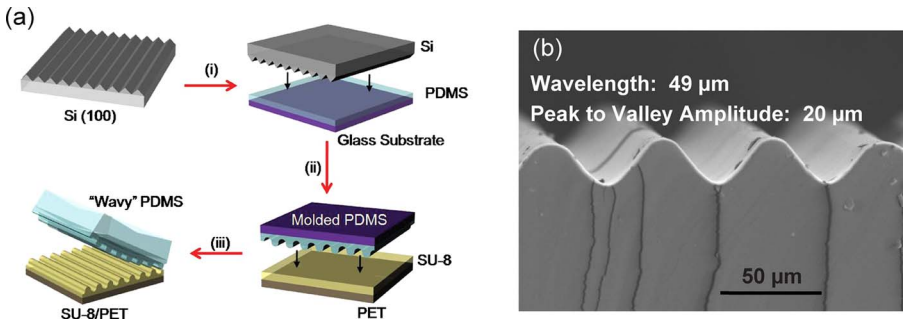

Fig. 2 Critical fabrication steps for generating wavy surface profiles in PDMS, (*a*). Anisotropic etching of a Si (100) wafer yields a saw-tooth surface relief, which after partial smoothing can be replicated through sequential imprinting into layers of PDMS prepolymer (i). The approximately sinusoidal relief can be molded into a layer of SU-8 supported on a plastic substrate (ii), cured, and undergone a final smoothing step. The molded SU-8 is then used as a template for a final PDMS imprinting step, (iii). The resulting PDMS substrate has a sinusoidal profile like that in (*b*), with a wavelength of 49 μm and tunable peak to valley amplitude.

ner onto the molded SU-8 smoothed the relief valleys. A final molding step was used to replicate the fully smoothed, sinusoidal surface in a PDMS substrate of specified thickness ($\sim$2 mm), as in Fig. 2(*b*).

The mechanics of these structures were examined through surface profilometry at various levels of strain. Rectangular samples ($20\times5\times2$ mm^3) having wavy surface profiles were clamped at each end in a custom designed tensioning stage, which was used to uniaxially strain the samples. At small strains ($<6\%$), changes in the profile amplitude and wavelength were measured using a profilometer (Dektak 3030). Figure 3 compares experimentally measured amplitudes A (denoted by squares) versus the applied strain ε_a for a wavy PDMS substrate ($E=2$ MPa, $\nu=0.48$) [28] with a wavelength $\lambda=49$ μm and initial amplitudes of $A_0=6.7$, 8.4, and 9.7 μm. The analytical solution of Eq. (17), also shown in Fig. 3 and denoted by the solid lines, agrees well with the experiments for $A_0=6.7$ and 8.4 μm, but is slightly lower than the experimental data for $A_0=9.7$ μm.

Finite element methods were also used to study a wavy PDMS profile subject to stretching. For simulations, we used the plane-strain element CPE4 in the ABAQUS finite element program [29], and linear geometry was used since the strain level is very small in the current study. Figure 4 shows the basic finite element mesh with a much finer mesh at the wavy surface; the smallest element size is 0.5 μm. Numerical results from the finite element analysis are shown by circles in Fig. 3, and agree well with the experimental measurements.

The analytical solution (17) exhibits better agreement with experiments and finite element analysis for $A_0=6.7$ and 8.4 μm than with $A_0=9.7$ μm. This is due largely to the small amplitude assumptions, $A_0/\lambda \ll 1$, of the perturbation method. Figure 5 illustrates the distribution of tangential strain ε_{tt} of the wavy surface. The analytical solution, up to the second order, is

$$\varepsilon_{tt} = \varepsilon_a[1 - 2A_0k\cos kx - (A_0k)^2(1 - \cos 2kx)] \qquad (18)$$

and is indicated by the dotted lines in Fig. 5 for a wavelength $\lambda=49$ μm, and small amplitude $A_0=3$ μm and large amplitude $A_0=9.7$ μm. The zeroth-order solution is the uniform strain, $\varepsilon_{tt}=\varepsilon_a$, shown by the horizontal solid line in Fig. 5, while the solution up to the first order is $\varepsilon_{tt}=\varepsilon_a(1-2A_0k\cos kx)$ shown as dashed curves. For $A_0=3$ μm, the difference between the first- and second-order solutions (dashed versus dotted lines) is small, and the wavy surface is in tension ($\varepsilon_{tt}>0$). For $A_0=9.7$ μm, the difference between the first- and second-order solutions (dashed versus dotted lines) becomes quite large, and part of the wavy surface is in compression ($\varepsilon_{tt}<0$). Results from the finite element analysis are also shown in Fig. 5 for comparison. For $A_0=3$ μm, the second-order solution has better agreement with finite element

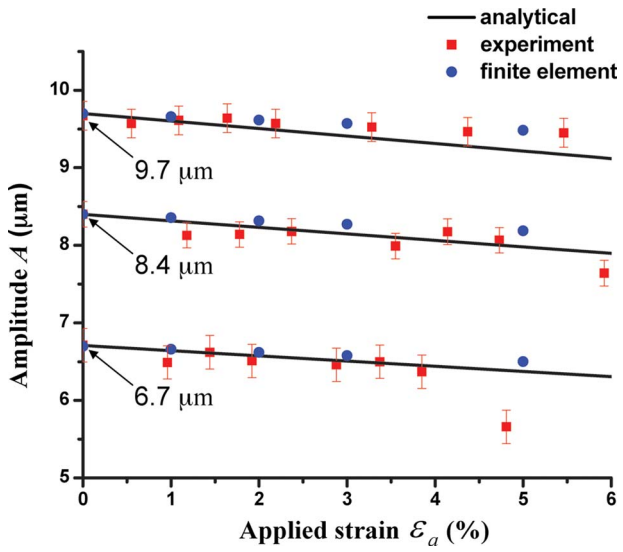

Fig. 3 The analytical, experimental, and numerical results of amplitude *A* versus the applied strain ε_a for a wavy PDMS ($E=2$ MPa, $\nu=0.48$), with wavelength $\lambda=49$ μm and initial amplitudes $A_0=6.7$, 8.4, and 9.7 μm.

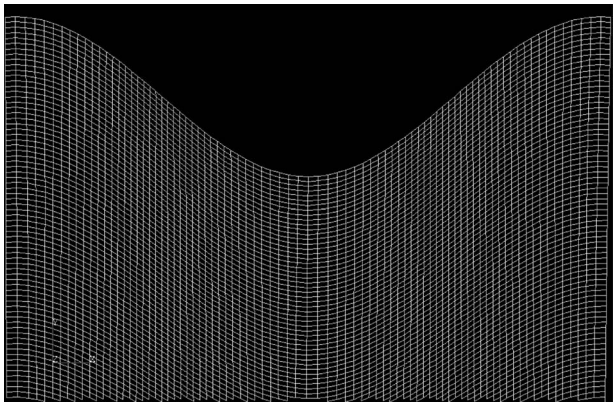

Fig. 4 Finite element mesh for the solid with the wavy surface

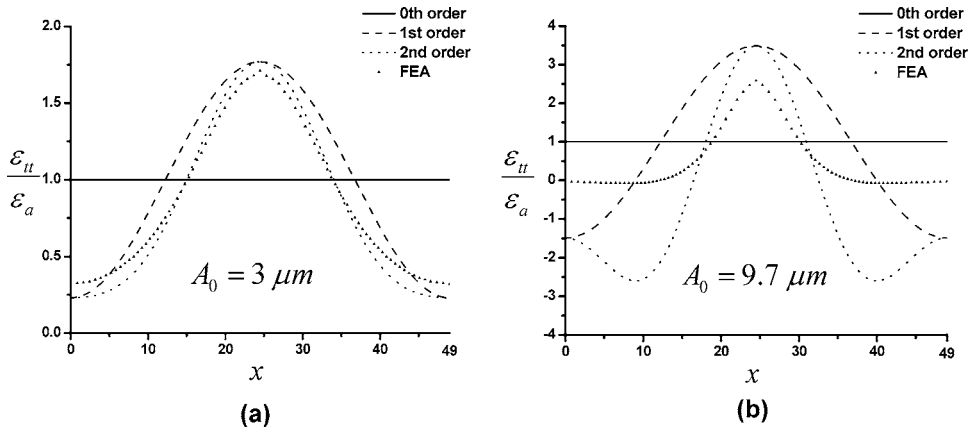

Fig. 5 Distribution of tangential strain ε_{tt} of the wavy surface up to the zeroth-, first-, and second-order normalized by the applied strain ε_a. The wavelength is λ=49 μm, and initial amplitudes are (*a*) A_0=3 μm and (*b*) A_0=9.7 μm. The results from the finite element analysis are also shown.

analysis than the first-order solution. However, for A_0=9.7 μm, the difference between the analytical solution and the finite element analysis is still large. This is because the error of the ratio $\varepsilon_{tt}/\varepsilon_a$ given by Eq. (18) is of order $O[(A_0k)^3]$, which is very small for A_0=3 μm, but for A_0=9.7, $A_0k \sim 1$.

4 An Analytical Solution for the Wavy Thin Film/Substrate System

Compliant wavy substrate with conformally integrated stiff thin film provides an alternative approach to fabricate stretchable electronics [27]. This avoids introducing any initial strain into the thin film, and thus achieves both high stretchability and compressibility. Fabrication of this wavy thin film/substrate system is the same to the process described in Sec. 3, except that thin Au films are deposited onto the SU-8 surface before the final molding step. Detailed information for fabricating such a system can be found in Ref. [27].

The profile of the wavy thin film/substrate system before deformation is described as $y=A_0 \cos kx$. It changes to $y=(A_0-B)\cos kx$ after a small applied strain ε_a in the x direction. The wavy substrate in this system could be modeled as a semi-infinite solid with a wavy surface profile $y=A_0 \cos kx$ that is subject to a normal displacement, $u_y=B \cos kx$. It has been established [21,27] that the effect of interface shear traction is negligible, since the elastic modulus of the PDMS substrate ($\sim$2 MPa) is several orders of magnitude smaller than that of Au film ($\sim$70 GPa). Equations (1)–(6) in Sec. 3 remain valid, however the traction-free boundary conditions (7) must be modified to yield

$$\begin{aligned} &u_y = B\cos kx \\ &\boldsymbol{n}\cdot\begin{pmatrix}\sigma_{xx} & \sigma_{xy}\\ \sigma_{xy} & \sigma_{yy}\end{pmatrix}\cdot\boldsymbol{t}=0 \quad \text{at} \quad \eta=0 \end{aligned} \tag{19}$$

where the second equation represents the vanishing shear traction, and $\boldsymbol{t}$ is the unit vector along the tangential direction $(1, -A_0k \sin k\xi)$.

The zeroth-(leading), first-, and second-order solutions then become

$$u_x^{(0)} = \varepsilon_a \xi, \quad u_y^{(0)} = -\frac{\nu}{1-\nu}\varepsilon_a \eta \tag{20}$$

$$u_x^{(1)} = \frac{e^{k\eta}\sin k\xi}{2k(1-\nu)}\left[(1-2\nu+k\eta)\frac{B}{A_0} - (3-2\nu+k\eta)\varepsilon_a\right]$$

$$u_y^{(1)} = \frac{\cos k\xi}{2k(1-\nu)}\left\{-2\nu\varepsilon_a + e^{k\eta}\left[(2-2\nu-k\eta)\frac{B}{A_0} + (2\nu+k\eta)\varepsilon_a\right]\right\} \tag{21}$$

$$\begin{aligned} u_x^{(2)} = \frac{\sin 2k\xi}{16k(1-\nu)^2}\Bigg\langle & 4(1-\nu)e^{k\eta}\left[\frac{B}{A_0}(2-2\nu+k\eta) - \varepsilon_a(4-2\nu+k\eta)\right] - e^{2k\eta}\left\{\frac{B}{A_0}[5-12\nu+8\nu^2+2(3-4\nu)k\eta] - \varepsilon_a[19-28\nu+8\nu^2+2(5-4\nu)k\eta]\right\}\Bigg\rangle \end{aligned}$$

$$\begin{aligned} u_y^{(2)} = \frac{\cos 2k\xi}{16k(1-\nu)^2}\Bigg\langle & 4(1-\nu)e^{k\eta}\left[\frac{B}{A_0}(1-2\nu-k\eta) + \varepsilon_a(1+2\nu+k\eta)\right] - 2e^{2k\eta}\left\{\frac{B}{A_0}[2(1-3\nu+2\nu^2) - (3-4\nu)k\eta] + \varepsilon_a[2(1+\nu-2\nu^2) + (5-4\nu)k\eta]\right\}\Bigg\rangle + \frac{1}{4k(1-\nu)}\left\{e^{k\eta}\left[\frac{B}{A_0}(1-2\nu-k\eta) + \varepsilon_a(1+2\nu+k\eta)\right] - \left[\frac{B}{A_0}(1-2\nu) + \varepsilon_a(1+2\nu)\right]\right\} \end{aligned} \tag{22}$$

The strain energy U per wavelength can be obtained analytically. For applied strain ε_a=0, it is given by

$$U(\varepsilon_a = 0) = \frac{\pi}{4}\frac{E}{1-\nu^2}B^2 \tag{23}$$

It shows excellent agreement with the finite element analysis in Fig. 6 versus the ratio B/A_0 for the wavelength λ=49 μm and amplitude A_0=3 μm.

The derivative of strain energy U per wavelength with respect to B, which is necessary in the study of thin film/substrate system, is given by

$$\frac{dU}{dB} = \frac{\pi}{2}\frac{E}{1-\nu^2}(B + \varepsilon_a A_0) \tag{24}$$

It is important to account for the second-order term in the above expression since U is a quadratic function of the displacement, $\boldsymbol{u}=\boldsymbol{u}^{(0)}+(A_0k)\boldsymbol{u}^{(1)}+(A_0k)^2\boldsymbol{u}^{(2)}+\cdots$. The strain energy U per wavelength can be similarly written as $U=U^{(0)}+(A_0k)U^{(1)}$

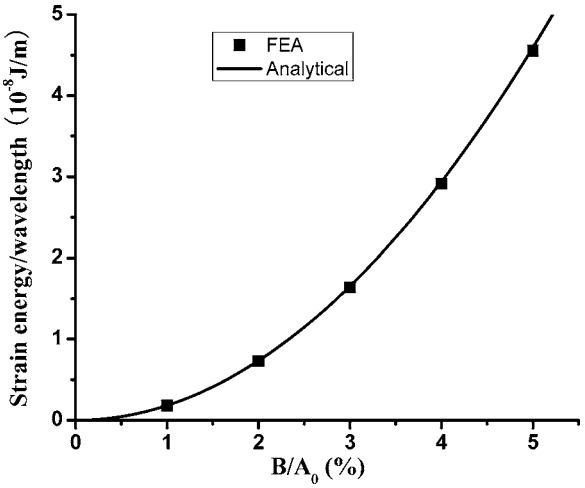

Fig. 6 Strain energy/wavelength versus the ratio B/A_0 with applied strain $\varepsilon_a=0$, for the wavelength $\lambda=49$ μm and amplitude $A_0=3$ μm

$+(A_0k)^2U^{(2)}+\cdots$, where $U^{(0)}$ is a constant such that $dU^{(0)}/dB=0$. Likewise, $U^{(1)}$ involves a cross term between $\boldsymbol{u}^{(0)}$ and $\boldsymbol{u}^{(1)}$ whose integration over the wavelength provides a vanishing contribution, $U^{(1)}=0$, leaving only $U^{(2)}$ to make a nonzero contribution to dU/dB since $U^{(2)}$ involves the quadratic terms of $\boldsymbol{u}^{(1)}$ and the cross term between $\boldsymbol{u}^{(0)}$ and $\boldsymbol{u}^{(2)}$.

5 Concluding Remarks

The analytical solution for a semi-infinite linear elastic solid with a wavy surface subject to uniaxial strain or "stretch" is obtained via the perturbation method. The amplitude A of the deformed wavy surface is related to the initial amplitude A_0 by $A=A_0(1-\varepsilon_a)$, where ε_a is the applied strain. This simple expression agrees well with both experimental measurements and finite element analyses for small amplitude wavy profiles. The analytical solution is also obtained for a wavy solid subject to stretching and lateral displacement, an important addition for the study of thin films on a wavy substrate.

Acknowledgment

This material is based on work supported by the National Science Foundation under Grant No. DMI-0328162 and the U.S. Department of Energy, Division of Materials Sciences under Award No. DEFG02-91ER45439, through the Frederick Seitz MRL and Center for Microanalysis of Materials at the University of Illinois at Urbana-Champaign. Y.H. acknowledges financial support from the National Natural Science Foundation of China (NSFC). A.C. acknowledges support from the Department of Defense (DoD) through the National Defense Science and Engineering Graduate (NDSEG) Fellowship Program.

References

[1] Rogers, J. A., Bao, Z., Baldwin, K., Dodabalapur, A., Crone, B., Raju, V. R., Kuck, V., Katz, H., Amundson, K., Ewing, J., and Drzaic, P., 2001, "Paper-Like Electronic Displays: Large-Area Rubber-Stamped Plastic Sheets of Electronics and Microencapsulated Electrophoretic Inks," Proc. Natl. Acad. Sci. U.S.A., **98**, pp. 4835–4840.

[2] Jacobs, H. O., Tao, A. R., Schwartz, A., Gracias, D. H., and Whitesides, G. M., 2002, "Fabrication of a Cylindrical Display by Patterned Assembly," Science, **296**, pp. 323–325.

[3] Ko, H. C., Stoykovich, M. P., Song, J., Malyarchuk, V., Choi, W. M., Yu, C.-J., Geddes, J. B., Xiao, J., Wang, S., Huang, Y., and Rogers, J. A., 2008, "A Hemispherical Electronic Eye Camera Based on Compressible Silicon Optoelectronics," Nature (London), **454**, pp. 748–753.

[4] Someya, T., Sekitani, T., Iba, S., Kato, Y., Kawaguchi, H., and Sakurai, T., 2004, "A Large-Area, Flexible Pressure Sensor Matrix With Organic Field-Effect Transistors for Artificial Skin Applications," Proc. Natl. Acad. Sci. U.S.A., **101**, pp. 9966–9970.

[5] Lacour, S. P., Wagner, S., Huang, Z. Y., and Suo, Z., 2003, "Stretchable Gold Conductors on Elastomeric Substrates," Appl. Phys. Lett., **82**, pp. 2404–2406.

[6] Lacour, S. P., Jones, J., Suo, Z., and Wagner, S., 2004, "Design and Performance of Thin Metal Film Interconnects for Skin-Like Electronic Circuits," IEEE Electron Device Lett., **25**, pp. 179–181.

[7] Lacour, S. P., Jones, J., Wagner, S., Li, T., and Suo, Z. G., 2005, "Stretchable Interconnects for Elastic Electronic Surfaces," Proc. IEEE, **93**, pp. 1459–1467.

[8] Khang, D. Y., Jiang, H., Huang, Y., and Rogers, J. A., 2006, "A Stretchable Form of Single-Crystal Silicon for High-Performance Electronics on Rubber Substrates," Science, **311**, pp. 208–212.

[9] Kim, D.-H., Ahn, J.-H., Choi, W. M., Kim, H.-S., Kim, T.-H., Song, J., Huang, Y. Y., Liu, Z. J., Lu, C., and Rogers, J. A., 2008, "Stretchable and Foldable Silicon Integrated Circuits," Science, **320**, pp. 507–511.

[10] Choi, W. M., Song, J., Khang, D.-Y., Jiang, H., Huang, Y. Y., and Rogers, J. A., 2007, "Biaxially Stretchable "Wavy" Silicon Nanomembranes," Nano Lett., **7**, pp. 1655–1663.

[11] Sun, Y., Choi, W.-M., Jiang, H., Huang, Y., and Rogers, J. A., 2006, "Controlled Buckling of Semiconductor Nanoribbons for Stretchable Electronics," Nat. Nanotechnol., **1**, pp. 201–207.

[12] Stafford, C. M., Harrison, C., Beers, K. L., Karim, A., Amis, E. J., Vanlandingham, M. R., Kim, H. C., Volksen, W., Miller, R. D., and Simonyi, E. E., 2004, "A Buckling-Based Metrology for Measuring the Elastic Moduli of Polymeric Thin Films," Nature Mater., **3**, pp. 545–550.

[13] Stafford, C. M., Vogt, B. D., Harrison, C., Julthongpiput, D., and Huang, R., 2006, "Elastic Moduli of Ultrathin Amorphous Polymer Films," Macromolecules, **39**, pp. 5095–5099.

[14] Harrison, C., Stafford, C. M., Zhang, W. H., and Karim, A., 2004, "Sinusoidal Phase Grating Created by a Tunably Buckled Surface," Appl. Phys. Lett., **85**, pp. 4016–4018.

[15] Efimenko, K., Rackaitis, M., Manias, E., Vaziri, A., Mahadevan, L., and Genzer, J., 2005, "Nested Self-Similar Wrinkling Patterns in Skins," Nature Mater., **4**, pp. 293–297.

[16] Bowden, N., Brittain, S., Evans, A. G., Hutchinson, J. W., and Whitesides, G. M., 1998, "Spontaneous Formation of Ordered Structures in Thin Films of Metals Supported on an Elastomeric Polymer," Nature (London), **393**, pp. 146–149.

[17] Huck, W. T. S., Bowden, N., Onck, P., Pardoen, T., Hutchinson, J. W., and Whitesides, G. M., 2000, "Ordering of Spontaneously Formed Buckles on Planar Surfaces," Langmuir, **16**, pp. 3497–3501.

[18] Sharp, J. S., and Jones, R. A. L., 2002, "Micro-Buckling as a Route Towards Surface Patterning," Adv. Mater., **14**, pp. 799–802.

[19] Yoo, P. J., Suh, K. Y., Park, S. Y., and Lee, H. H., 2002, "Physical Self-Assembly of Microstructures by Anisotropic Buckling," Adv. Mater., **14**, pp. 1383–1387.

[20] Chen, X., and Hutchinson, J. W., 2004, "Herringbone Buckling Patterns of Compressed Thin Films on Compliant Substrates," ASME J. Appl. Mech., **71**, pp. 597–603.

[21] Huang, Z. Y., Hong, W., and Suo, Z., 2005, "Nonlinear Analyses of Wrinkles in a Film Bonded to a Compliant Substrate," J. Mech. Phys. Solids, **53**, pp. 2101–2118.

[22] Jiang, H., Khang, D.-Y., Song, J., Sun, Y., Huang, Y., and Rogers, J. A., 2007, "Finite Deformation Mechanics in Buckled Thin Films on Compliant Supports," Proc. Natl. Acad. Sci. U.S.A., **104**, pp. 15607–15612.

[23] Jiang, H., Sun, Y., Rogers, J. A., and Huang, Y., 2007, "Mechanics of Precisely Controlled Thin Film Buckling on Elastomeric Substrate," Appl. Phys. Lett., **90**, pp. 133119.

[24] Koh, C. T., Liu, Z. J., Khang, D.-Y., Song, J., Lu, C., Huang, Y., Rogers, J. A., and Koh, C. G., 2007, "Edge Effects in Buckled Thin Films on Elastomeric Substrates," Appl. Phys. Lett., **91**, pp. 133113.

[25] Huang, R., 2005, "Kinetic Wrinkling of an Elastic Film on a Viscoelastic Substrate," J. Mech. Phys. Solids, **53**, pp. 63–89.

[26] Huang, R., and Suo, Z., 2002, "Instability of a Compressed Elastic Film on a Viscous Layer," Int. J. Solids Struct., **39**, pp. 1791–1802.

[27] Xiao, J., Carlson, A., Liu, Z. J., Huang, Y., Jiang, H., and Rogers, J. A., 2008, "Stretchable and Compressible Thin Films of Stiff Materials on Compliant Wavy Substrates," Appl. Phys. Lett., **93**, p. 013109.

[28] Schneider, F., Fellner, T., Wilde, J., and Wallrabe, U., 2008, "Mechanical Properties of Silicones for MEMS," J. Micromech. Microeng., **18**, pp. 065008.

[29] ABAQUS Inc., 2004, ABAQUS Analysis User's Manual V6.5.

Particular Solutions of a Two-Dimensional Infinite Wedge for Various Boundary Conditions With Weak Singularity

Z. L. Li[1]

Ch. Wang

Digital Engineering and Simulation Research Center,
School of Hydropower and Digitalization Engineering,
Huazhong University of Science & Technology,
Wuhan, Hubei 430074, China

The particular solutions of a two-dimensional infinite wedge for various boundary conditions with lnr weak singularity have been investigated in this paper. The relations of the weak singularities and the discontinuities of the first kind of the boundary variables at a corner of a two-dimensional elastic body have been established. By using the relations, the singular behaviors of the unknown boundary variables at a corner of an elastic body can be obtained before solving the boundary value problem by using the boundary element method (BEM). Especially, if the boundary conditions at a corner are displacements prescribed, the values of the unknown tractions at the corner can be determined in advance. Thus, the difficulty related to the multivalued tractions at a corner in BEM analysis for problems with boundary displacements prescribed has been overcome completely. In addition, more appropriate shape functions for the unknown boundary field variables of a corner element can be constructed, and the accuracy of the BEM may be greatly increased. [DOI: 10.1115/1.3168599]

Keywords: corner problem, boundary displacement and traction, discontinuity of the first kind, weak singularity, boundary element method

1 Introduction

The 2D solutions for the displacements and stresses in an infinite elastic wedge are of major interest in elasticity problems. Since the boundary conditions at infinity are unspecified, there are infinite solutions for the problem. The boundary conditions at infinity can be divided into two sets: The first set balances the boundary conditions on the wedge sides, and the second set is self-balanced. The solution of the self-balanced boundary conditions at infinity is called a homogeneous solution, which satisfies zero boundary conditions on the two sides of the wedge. The solution of the prescribed nonzero boundary conditions on the wedge sides and their corresponding balancing boundary conditions at infinity is called a particular solution.

The homogeneous solutions of an infinite wedge with angle 2α have been resolved analytically for more than 50 years ago in the pioneering theoretical work of Williams [1] by using complex variable analysis and eigenfunction expansion. Three cases of homogeneous boundary conditions were considered by Williams [1]: free-free, clamped-clamped, and clamped-free. Let r denote the distance from the wedge-tip. The main conclusion about the homogeneous solutions is that the stresses at the wedge-tip for all three cases considered may have singularity of $r^{-\lambda}$ $(0<\lambda<1)$, where λ is a function of α. The detailed information of the behavior of λ for the free-free case can be found in Refs. [2–7]. The singular behaviors of a multiwedge system can be found in Refs. [8,9].

Particular solutions are less studied than homogeneous solutions. By using a generalized Airy stress function, Dempsey [6] and Ting [7] obtained a particular solution of an infinite wedge subjected to a uniform loading on each side of the wedge; Wang [10] obtained a particular solution of an infinite wedge subjected to tractions in proportion to $r^n(n\geq 0)$. The stresses of the particular solutions provided in Refs. [6,7,10]. are bounded for all angles except for $2\alpha=\pi$, 2π, and $2\alpha^*$, where α^* is the root of the equation $\tan(2\alpha)=2\alpha$. The stresses for $2\alpha=\pi$, 2π and $2\alpha^*$ may include ln r weak singularity. Since the superposition of a homogeneous solution to a particular solution is also a particular solution, particular solution may also have $r^{-\lambda}$ singularity. However, it is always possible to find a particular solution, which does not have $r^{-\lambda}$ singularity; in the following, this kind of particular solution will be considered. For simplicity, the derivative of a boundary displacement component in the boundary tangent direction is called "boundary displacement derivative" in the following. We point out that, in Refs. [6,7,10], the prescribed tractions at the wedge-tip only have the discontinuity of the first kind. It is found that the boundary tangent displacement derivative at the wedge-tip only has discontinuity of the first kind like the prescribed tractions; however, in addition to the discontinuity of the first kind, the boundary normal displacement derivative at the wedge-tip also has weak singularity.

Although there are many practical corner problems with prescribed displacement boundary conditions, we have not found any reports, so far, about particular solutions of an infinite wedge with some kind of prescribed displacements on its sides. To investigate this type of problems, a general form of the boundary displacement field should be assumed first. From the above discussions for traction prescribed wedge problems, the simplest form of the boundary displacement derivatives at the wedge-tip should include the discontinuity of the first kind and weak singularity. It will be shown in this paper that the stresses of the particular solution for prescribed boundary displacements on the sides of the wedge may also have weak singularity at the wedge-tip. General discussions about weak singularities of stresses at a wedge-tip were reported by Sinclair [11]. Although the type of weak singularity of tractions is unlikely to occur in practice, it will play an important role in establishing the relations between boundary displacement derivatives and tractions at a corner.

[1]Permanent address: Solid Mechanics Research Center, Beijing University of Aeronautics and Astronautics, Beijing China.

Contributed by the Applied Mechanics Division of ASME for publication in the JOURNAL OF APPLIED MECHANICS. Manuscript received July 16, 2008; final manuscript received April 15, 2009; published online September 24, 2009. Review conducted by Professor Subrata Mukherjee.

The boundary integral equation (BIE) for an elasticity problem is a statement of the exact solution to the problem. Errors of the solution of a BIE obtained by using the boundary element method (BEM) are due to discretization and numerical approximation in BEM [12]. If the discretization and the numerical integration procedure are made sufficiently sophisticated, the errors introduced can be very small. BEM is more accurate than other numerical methods and it is more suitable for problems with sharp gradients, e.g., corner problems, crack problems, problems with discontinuous, or singular boundary conditions.

The treatment of corners has been a subject of considerable interest in solving an elastic boundary value problem by BEM. The displacement and stress fields near a corner can be approximated by the solution of an infinite wedge comprised by the two tangent lines at the corner. In BEM analysis, there are two difficulties that one needs to pay attention to. One is the $r^{-\lambda}$ singular behavior of the boundary field variables at the corner, which is related to the homogeneous solution of the infinite wedge; the other is the discontinuity of the first kind and weak singularity of the boundary field variables at the corner, which is related to the particular solution of the infinite wedge. The strategies to deal with these two difficulties are quite different.

First consider the possible $r^{-\lambda}$ singular behavior of the unknown boundary variables at a corner. Similar to crack problems, the strength of the singular behavior of the field variables can be represented by the stress intensity factor (SIF) at the corner-tip that is the coefficient of the singular term $r^{-\lambda}$. Note that the SIF of an infinite wedge-tip depends on the self-balanced boundary conditions at infinity, hence, the SIF of the corner of a finite elastic body will depend on the circumferential boundary conditions of the elastic body. Therefore, the strategy used in BEM when boundary fields have $r^{-\lambda}$ singularity at a corner is similar to that for crack problems: In order to improve the efficiency and precision of the numerical calculation, the interpolation function must include terms, which can account for the analytical form of the singularity with SIF as a unknown parameter. From many investigations in this problem, for example, refer to Portela et al. [13] who developed the boundary element singularity subtraction technique to provide an efficient and accurate method to deal with the singular behavior of boundary field variables when investigating V-shape notch problems. The problem of $r^{-\lambda}$ singular behavior of the field variables, which is related to the homogeneous solution of the infinite wedge problem, will be excluded in this paper.

Now consider the discontinuous and weakly singular behavior of the unknown boundary variables at a corner, which is related to the particular solution of the corresponding infinite wedge. If the boundary conditions at and near a corner are displacements alone being prescribed, since the unknown tractions are multivalued, the number of degrees of freedom will exceed the number of equations. Many techniques have been proposed to overcome this difficulty in literatures, for example: (1) to round off the corner [14]. An obvious disadvantage of this procedure is that the accuracy of the results at and near the corner will be lost. (2) To use multiple boundary nodes [15–17] or to add source points that are not on the boundary [18,19] avoiding direct collocation at the corner. The major drawback of this technique is that the positions of the added off-corner nodes should not be too close to the corner otherwise computation instability would occur. (3) To add a set of auxiliary relations of boundary field variables [20]. Theoretically, the last technique is the right way, but some of the auxiliary relations used may not be strictly correct, for example, the equivalent law of shearing stresses and Hooke's law, which are not always valid at a corner, were used as the auxiliary relations. In contrast to the $r^{-\lambda}$ singular behavior, we will show that the intensities of the discontinuity, and the weak singularity at the corner of the unknown field variables only depend on the corresponding intensities of the known field variables at the corner. Therefore, the values of the unknown field variables at the corner can be obtained in advance. Thus, the difficulty of the multivalued unknown tractions does not exist anymore.

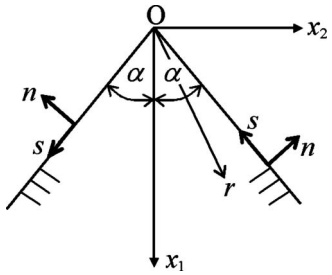

Fig. 1 An infinite wedge with angle 2α

The main work of this paper is to establish the analytical relations between the boundary field variables at a corner. Instead of using a generalized Airy stress function, as in Refs [6,7,10], to obtain the particular solution of a wedge problem for traction prescribed problem, a general form of displacement field is used to obtain the particular solutions of a wedge problem for any type of boundary conditions in this paper. The stresses and the displacement derivatives deduced from the general form include three terms: a weakly singular term, a discontinuous term, and a continuous term. This form actually includes most situations in practical as well as theoretical problems. Although boundary displacement and traction are independent field variables in the boundary conditions of an elasticity problem, the values of the discontinuity and the possible weak singularity of the unknown tractions or boundary displacement derivatives at a corner can be obtained from the prescribed boundary conditions by using the particular solutions of the wedge problem. Therefore, the problem of multivalued corner tractions, if the boundary conditions at a corner are displacements alone being prescribed, is solved completely. Furthermore, since the possible weak singularities of the field variables are also obtained, more appropriate shape functions of the unknown boundary field variables in the corner element can be constructed, and the accuracy of the BEM may be greatly increased.

2 Weakly Singular Tractions

Let O be a boundary smooth or corner point of an elastic body, and s be the boundary length with origin at point O. In elastic theory, mechanical models of traction with various singularities are introduced, such as discontinuity of the first kind, $\ln|s|$ weak singularity, $|s|^{-\lambda}$ singularity, concentrated force, etc. Since it is quite difficult to handle concentrated force when using BEM to solve the BIE of an elasticity problem, the concentrated force model will be excluded in the following discussion. The stress field near point O may be approximated by the solution of an infinite wedge comprised by the two tangent lines at point O. Consider an infinite elastic wedge with angle 2α as shown in Fig. 1, where (r,θ) and (x_1,x_2) are the polar and Cartesian coordinate systems with the origin located at the wedge-tip O, respectively; n and s denote the boundary normal and tangent directions, respectively. As mentioned in the introduction, the stresses with $|s|^{-\lambda}$ singularity are related to the homogenous solutions of the wedge, it will also be excluded in the following discussion.

Let $t_i(s)$, $i=n$ or s, be a traction component, which is related to the particular solutions of the wedge. Here, t_i may be discontinuous and weakly singular at $s=0$. It is supposed that the discontinuity of a traction component is bounded. If O is a smooth boundary point, the weakly singular part of the traction component at $s=0$ may be expressed as the form $p_i \ln|s|$, where p_i is called the weak singularity intensity of the traction component. In this mean-

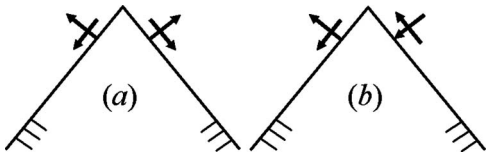

Fig. 2 Tractions of a symmetric (*a*) and an antisymmetric (*b*) wedge

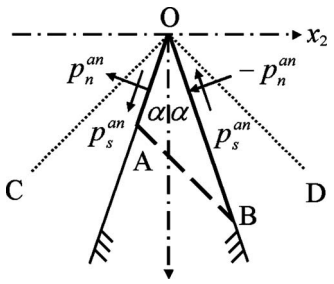

Fig. 3 Weak singularity intensities of tractions at an antisymmetric wedge-tip

ing, the weakly singular part of a traction component at $s=0$ is formally said to be continuous. We indicate that p_n and p_s are independent parameters.

If O is a boundary corner point, the weakly singular part of a traction component at $s=0$ should be expressed in the form $p_{i\pm}\ln|s|$, where the plus and minus signs are for $s>0$ and $s<0$, respectively. Next, we will demonstrate that $p_{n\pm}$ and $p_{s\pm}$ are not independent parameters.

Let $\sigma_{ij}(r,\theta)$ denote the stress field near a corner. Assume that $\sigma_{ij}(r,\theta)$ is single-valued if $r\neq 0$, it may be weakly singular but $\sigma_{ij}(r,\theta_1)-\sigma_{ij}(r,\theta_2)$ is bounded for any θ_1 and θ_2 as $r\to 0$. $\sigma_{ij}(r,\theta)$ may be expressed as

$$\sigma_{ij}(r,\theta)=\sigma_{ij}^{c}(r,\theta)\ln r+\sigma_{ij}^{d}(r,\theta)$$

where $\sigma_{ij}^{d}(r,\theta)$ is single-valued if $r\neq 0$, it is bounded but it may be multivalued at $r=0$; $\sigma_{ij}^{c}(r,\theta)$ is single-valued and bounded for all r. Therefore, $\sigma_{ij}^{c}(r,\theta)$ is independent of θ as $r\to 0$.

$$\sigma_{ij}^{c}(0,\theta)=k_{ij}$$

where k_{ij} is called the weak singularity intensity of the stress component σ_{ij} at the corner. Let $t_n^c(s)\ln|s|$ and $t_s^c(s)\ln|s|$ denote the weakly singular terms of the normal and tangent tractions related to $\sigma_{ij}^{c}(r,\theta)\ln r$, we have

$$p_{n\pm}=\lim_{s\to\pm 0}t_n^c(s)=k_{ij}n_{j\pm}n_{i\pm}$$

$$p_{s\pm}=\lim_{s\to\pm 0}t_s^c(s)=k_{ij}n_{j\pm}s_{i\pm}$$

The stresses near the wedge-tip can always be considered as the superposition of a symmetric problem and an antisymmetric problem, as shown in Fig. 2. The symmetric and antisymmetric stress fields have the following properties:

$$\sigma_{\theta\theta}^{sy}(r,-\theta)=\sigma_{\theta\theta}^{sy}(r,\theta),\quad \sigma_{r\theta}^{sy}(r,-\theta)=-\sigma_{r\theta}^{sy}(r,\theta),$$

$$\sigma_{rr}^{sy}(r,-\theta)=\sigma_{rr}^{sy}(r,\theta)$$

$$\sigma_{\theta\theta}^{an}(r,-\theta)=-\sigma_{\theta\theta}^{an}(r,\theta),\quad \sigma_{r\theta}^{an}(r,-\theta)=\sigma_{r\theta}^{an}(r,\theta),$$

$$\sigma_{rr}^{an}(r,-\theta)=-\sigma_{rr}^{an}(r,\theta)$$

Letting

$$p_n^{sy}=p_{n+}^{sy},\quad p_s^{sy}=p_{s+}^{sy},\quad p_n^{an}=p_{n+}^{an},\quad p_s^{an}=p_{s+}^{an}$$

we have

$$p_{n-}^{sy}=p_n^{sy},\quad p_{s-}^{sy}=-p_s^{sy},\quad p_{n-}^{an}=-p_n^{an},\quad p_{s-}^{an}=p_s^{an}$$

2.1 Symmetric Tractions. If $2\alpha\neq\pi$, the symmetric stresses σ_{ij}^{sy} are single-valued, so the weak singularity intensity of the stress component k_{ij}^{sy} may be of any finite value. Therefore the weak singularity intensities of the tractions p_n^{sy} and p_s^{sy} may take any finite values. If $2\alpha=\pi$, the shear stress component σ_{12}^{sy} is discontinuous at $r=0$. Since the weakly singular part of σ_{12}^{sy} is continuous by definition, the tangent weak singularity intensity p_s^{sy} must be zero.

2.2 Antisymmetric Tractions. The weak singularity intensities of normal and tangent tractions at an antisymmetric wedge-tip are shown in Fig. 3. First consider the case of $2\alpha\neq\pi$. Note that the equivalent law of shearing stresses is generally not valid at an antisymmetric wedge-tip. However, if the ratio of the normal and tangent tractions at an antisymmetric wedge-tip equals to a certain value, the equivalent law of shearing stresses may be valid there. In Fig. 3, OC is perpendicular to OD, and the included angle between OD and x_1 axis is $\pi/4$. Denote the shear stress components of the surface OC and OD by t_s^{OC} and t_s^{OD}, respectively. Note that $t_s^{OC}=t_s^{OD}$ for this antisymmetric problem. The force equilibrium conditions of the triangle OAB in the direction of AB, where AB is parallel to OD, can be written as

$$l_{AB}t_s^{OD}=l_{OA}(p_n^{an}\cos\beta-p_s^{an}\sin\beta)+l_{OB}(p_n^{an}\sin\beta+p_s^{an}\cos\beta) \tag{2.1}$$

where

$$l_{OB}=l_{OA}\cot\beta,\quad \beta=\frac{\pi}{4}-\alpha$$

The equivalent law of shearing stresses for this antisymmetric configuration requires that $t_s^{OD}=t_s^{OC}=0$. In this case, the stresses at the antisymmetric wedge-tip are single-valued. By letting the right side of Eq. (2.1) be zero, we obtain

$$\frac{p_n^{an}}{p_s^{an}}=-\tan 2\alpha \tag{2.2}$$

It is easy to see that if the condition (2.2) is satisfied, the antisymmetric stress field is pure shear. If $2\alpha=\pi$, the normal stress component σ_{22}^{an} is discontinuous at $r=0$; since the weakly singular part of σ_{22}^{an} is continuous by definition, the normal weak singularity intensity p_n^{an} must be zero. In fact, this result has already been included in Eq. (2.2).

2.3 General Problem. Let $p_{n\pm}$ and $p_{s\pm}$ denote the weak singularity intensity of the normal and tangent tractions at the wedge-tip of a general problem, respectively. The symmetric and antisymmetric weak singularity intensities of the tractions at the wedge-tip of the general problem are as follows:

$$p_n^{sy}=\frac{p_{n+}+p_{n-}}{2},\quad p_s^{sy}=\frac{p_{s+}-p_{s-}}{2} \tag{2.3}$$

$$p_n^{an}=\frac{p_{n+}-p_{n-}}{2},\quad p_s^{an}=\frac{p_{s+}+p_{s-}}{2} \tag{2.4}$$

Substitution of Eq. (2.4) into Eq. (2.2) yields

$$\frac{p_{n+}-p_{n-}}{p_{s+}+p_{s-}}=-\tan 2\alpha \tag{2.5}$$

Equation (2.5) shows that the four weak singularity intensities at the wedge-tip $p_{n\pm}$ and $p_{s\pm}$ are dependent on each other. If the boundary conditions of an infinite wedge are tractions prescribed,

but Eq. (2.5) is not satisfied, then the stresses at the wedge-tip must have infinite discontinuities at the wedge-tip. This case will be excluded in this paper.

3 Particular Solutions of an Infinite Symmetric Wedge

3.1 Expressions of Displacement and Stress Fields. The displacement field of the particular solutions of a symmetric wedge is assumed to be the following general form:

$$u_r^{sy} = r[(a + b\cos 2\theta)\ln r + c\cos 2\theta + d\theta\sin 2\theta + e] + \bar{u}_r^{sy}(r,\theta) \tag{3.1a}$$

$$u_\theta^{sy} = r(f\sin 2\theta\ln r + g\sin 2\theta + h\theta\cos 2\theta + i\theta) + \bar{u}_\theta^{sy}(r,\theta) \tag{3.1b}$$

where the gradients of displacements $\bar{u}_r^{sy}$, $\bar{u}_\theta^{sy}$ are continuous and their values are zero at $r=0$. The corresponding stresses $\bar{\sigma}_{rr}^{sy}$, $\bar{\sigma}_{\theta\theta}^{sy}$, and $\bar{\sigma}_{r\theta}^{sy}$ satisfy the stress equilibrium equations and their values are zero at $r=0$. It is easy to show that the gradients of the total displacement field (3.1*a*) and (3.1*b*) are continuous for $r\neq 0$. But, as $r\to 0$, the gradients of the displacement field (3.1*a*) and (3.1*b*) may have discontinuity of the first kind and ln r weak singularity.

The stress field corresponding to the displacement field Eqs. (3.1*a*) and (3.1*b*) can be obtained through Hooke's law as follows:

$$\begin{aligned}\sigma_{rr}^{sy} = {} & 2\mu\{[s_1(a + b\cos 2\theta) + 2s_2 f\cos 2\theta]\ln r + [s_1 c + s_2(2g + h) \\ & + s_3 b]\cos 2\theta + (s_1 d - 2s_2 h)\theta\sin 2\theta + s_3 a + s_1 e + s_2 i\} \\ & + \bar{\sigma}_{rr}^{sy}(r,\theta)\end{aligned} \tag{3.2a}$$

$$\begin{aligned}\sigma_{\theta\theta}^{sy} = {} & 2\mu\{[s_1(a + b\cos 2\theta) + 2s_3 f\cos 2\theta]\ln r + [s_1 c + s_3(2g + h) \\ & + s_2 b]\cos 2\theta + (s_1 d - 2s_3 h)\theta\sin 2\theta + s_2 a + s_1 e + s_3 i\} \\ & + \bar{\sigma}_{\theta\theta}^{sy}(r,\theta)\end{aligned} \tag{3.2b}$$

$$\begin{aligned}\sigma_{r\theta}^{sy} = {} & 2\mu\left(-b\sin 2\theta\ln r - \frac{2c - d - f}{2}\sin 2\theta + d\theta\cos 2\theta\right) \\ & + \bar{\sigma}_{r\theta}^{sy}(r,\theta)\end{aligned} \tag{3.2c}$$

where μ is the shear modulus, and

$$s_1 = \frac{2}{\kappa - 1}, \quad s_2 = \frac{3 - \kappa}{2(\kappa - 1)}, \quad s_3 = \frac{\kappa + 1}{2(\kappa - 1)} \tag{3.3}$$

where κ is related to Poisson's ratio ν.

$$\kappa = \begin{cases} 3 - 4\nu & \text{(plane strain)} \\ (3 - \nu)/(1 + \nu) & \text{(plane stress)} \end{cases}$$

Substitution of the stress field (3.2*a*), (3.2*b*), and (3.2*c*) into the stress equilibrium equations yields

$$d = f = h = -b, \quad g = -c, \quad i = 2s_3 a \tag{3.4}$$

Therefore, the coefficients in the displacement expression (3.1*a*) and (3.1*b*) are dependent.

Using relations (3.4), Eqs. (3.1*a*), (3.1*b*), (3.2*a*), (3.2*b*), and (3.2*c*) are simplified as

$$u_r^{sy} = r[(a + b\cos 2\theta)\ln r + c\cos 2\theta - b\theta\sin 2\theta + e] + \bar{u}_r^{sy}(r,\theta) \tag{3.5a}$$

$$u_\theta^{sy} = r(-b\sin 2\theta\ln r - c\sin 2\theta - b\theta\cos 2\theta + 2s_3 a\theta) + \bar{u}_\theta^{sy}(r,\theta) \tag{3.5b}$$

and

$$\begin{aligned}\sigma_{rr}^{sy} = {} & 2\mu[(s_1 a + b\cos 2\theta)\ln r + (b + c)\cos 2\theta - b\theta\sin 2\theta + s_1 s_3 a \\ & + s_1 e] + \bar{\sigma}_{rr}^{sy}(r,\theta)\end{aligned} \tag{3.6a}$$

$$\begin{aligned}\sigma_{\theta\theta}^{sy} = {} & 2\mu[(s_1 a - b\cos 2\theta)\ln r - (b + c)\cos 2\theta + b\theta\sin 2\theta + (s_2 \\ & + 2s_3^2)a + s_1 e] + \bar{\sigma}_{\theta\theta}^{sy}(r,\theta)\end{aligned} \tag{3.6b}$$

$$\sigma_{r\theta}^{sy} = 2\mu[-b\sin 2\theta\ln r - (b + c)\sin 2\theta - b\theta\cos 2\theta] + \bar{\sigma}_{r\theta}^{sy}(r,\theta) \tag{3.6c}$$

respectively. Letting $\theta = \mp\alpha$ in Eqs. (3.6*b*) and (3.6*c*), we obtain the following:

$$\sigma_{\theta\theta}^{sy}(r, \mp\alpha) = p_n^{sy}\ln r + p_{n0}^{sy} + P_n^{sy}(r) \tag{3.7a}$$

$$\sigma_{r\theta}^{sy}(r, \mp\alpha) = \mp p_s^{sy}\ln r \mp p_{s0}^{sy} \mp P_s^{sy}(r) \tag{3.7b}$$

where

$$p_n^{sy} = 2\mu(s_1 a - b\cos 2\alpha) \tag{3.8a}$$

$$p_s^{sy} = -2\mu b\sin 2\alpha \tag{3.8b}$$

$$p_{n0}^{sy} = 2\mu[-(b + c)\cos 2\alpha + b\alpha\sin 2\alpha + (s_2 + 2s_3^2)a + s_1 e] \tag{3.8c}$$

$$p_{s0}^{sy} = -2\mu[(b + c)\sin 2\alpha + b\alpha\cos 2\alpha] \tag{3.8d}$$

and

$$P_n^{sy}(r) = \bar{\sigma}_{\theta\theta}^{sy}(r,\alpha), \quad (P_n^{sy}(0) = 0)$$

$$P_s^{sy}(r) = -\bar{\sigma}_{r\theta}^{sy}(r,\alpha), \quad (P_s^{sy}(0) = 0)$$

The tractions as the functions of the boundary length s can be obtained from Eqs. (3.7*a*) and (3.7*b*) as follows:

$$t_n^{sy}(s) = p_n^{sy}\ln|s| + p_{n0}^{sy} + P_n^{sy}(|s|) \tag{3.9a}$$

$$t_s^{sy}(s) = \pm p_s^{sy}\ln|s| \pm p_{s0}^{sy} \pm P_s^{sy}(|s|), \quad s > 0 \text{ for plus sign}, \quad s < 0 \text{ for minus sign} \tag{3.9b}$$

where p_n^{sy} and p_s^{sy} are the weak singularity intensities of the normal and tangent tractions at the wedge-tip, respectively; p_{n0}^{sy} and p_{s0}^{sy} are the values of the finite parts of the normal and tangent tractions at the wedge-tip, respectively.

The displacement derivatives with respect to r can be obtained from Eqs. (3.5*a*) and (3.5*b*) as follows:

$$\frac{\partial u_\theta^{sy}(r,\theta)}{\partial r} = -b\sin 2\theta\ln r - (b + c)\sin 2\theta - b\theta\cos 2\theta + 2s_3 a\theta + \frac{\partial\bar{u}_\theta^{sy}(r,\theta)}{\partial r} \tag{3.10a}$$

$$\frac{\partial u_r^{sy}(r,\theta)}{\partial r} = (a + b\cos 2\theta)\ln r + (b + c)\cos 2\theta - b\theta\sin 2\theta + a + e + \frac{\partial\bar{u}_r^{sy}(r,\theta)}{\partial r} \tag{3.10b}$$

Substituting of $\theta = \mp\alpha$ into Eqs. (3.10*a*) and (3.10*b*) yields

$$\frac{\partial u_\theta^{sy}(r, \mp\alpha)}{\partial r} = \mp w_n^{sy}\ln r \mp w_{n0}^{sy} \mp W_n^{sy}(r) \tag{3.11a}$$

$$\frac{\partial u_r^{sy}(r, \mp\alpha)}{\partial r} = w_s^{sy}\ln r + w_{s0}^{sy} + W_s^{sy}(r) \tag{3.11b}$$

where

$$w_n^{sy} = -b\sin 2\alpha \tag{3.12a}$$

$$w_s^{sy} = a + b\cos 2\alpha \tag{3.12b}$$

$$w_{n0}^{sy} = -(b + c)\sin 2\alpha - b\alpha\cos 2\alpha + 2s_3 a\alpha \tag{3.12c}$$

$$w_{s0}^{sy} = (b+c)\cos 2\alpha - b\alpha \sin 2\alpha + a + e \tag{3.12d}$$

and

$$W_n^{sy}(r) = \frac{\partial \bar{u}_\theta^{sy}(r,\alpha)}{\partial r}, \quad (W_n^{sy}(0) = 0)$$

$$W_s^{sy}(r) = \frac{\partial \bar{u}_r^{sy}(r,\alpha)}{\partial r}, \quad (W_s^{sy}(0) = 0)$$

The boundary displacement derivatives as functions of s can be obtained from Eqs. (3.11a) and (3.11b), the results are

$$u_n'^{sy}(s) = \pm w_n^{sy} \ln|s| \pm w_{n0}^{sy} \pm W_n^{sy}(|s|),$$

$$s > 0 \text{ for plus sign}, \quad s < 0 \text{ for minus sign} \tag{3.13a}$$

$$u_s'^{sy}(s) = w_s^{sy} \ln|s| + w_{s0}^{sy} + W_s^{sy}(|s|) \tag{3.13b}$$

where w_n^{sy} and w_s^{sy} are the weak singularity intensities of the normal and tangent displacement derivatives at the wedge-tip, respectively; w_{n0}^{sy} and w_{s0}^{sy} are the values of the finite parts of the normal and tangent displacement derivatives at the wedge-tip, respectively. Equations (3.9a), (3.9b), (3.13a), and (3.13b) indicate that the tractions and the boundary displacement derivatives at the wedge-tip are composed of a finite part and a weakly singular part. Moreover, the discontinuity value of the finite part at the wedge-tip has been separated from the other part. In the following, the relations between tractions and boundary displacement derivates at the wedge-tip will be determined.

3.2 Tractions Prescribed Problem. If the boundary conditions are tractions prescribed, p_n^{sy}, p_s^{sy}, p_{n0}^{sy}, and p_{s0}^{sy} in the right sides of Eqs. (3.9a) and (3.9b) are known. From the linear algebraic Eqs. (3.8a), (3.8b), (3.8c), and (3.8d), we obtain

$$a = \frac{\kappa - 1}{4\mu}(p_n^{sy} - p_s^{sy} \cot 2\alpha) \tag{3.14a}$$

$$b = -\frac{1}{2\mu \sin 2\alpha} p_s^{sy} \tag{3.14b}$$

$$c = \frac{1}{2\mu \sin 2\alpha}[(1 + \alpha \cot 2\alpha)p_s^{sy} - p_{s0}^{sy}] \tag{3.14c}$$

$$e = \frac{\kappa - 1}{4\mu}\left\{ -\frac{3\kappa - 1}{2(\kappa - 1)} p_n^{sy} + \left[\frac{3\kappa - 1}{2(\kappa - 1)} \cot 2\alpha + \alpha(\cot^2 2\alpha + 1) \right] p_s^{sy} + p_{n0}^{sy} - p_{s0}^{sy} \cot 2\alpha \right\} \tag{3.14d}$$

Substituting Eqs. (3.14a), (3.14b), (3.14c), and (3.14d) into Eqs. (3.12a), (3.12b), (3.12c), and (3.12d) yields

$$w_n^{sy} = \frac{1}{2\mu} p_s^{sy} \tag{3.15a}$$

$$w_s^{sy} = \frac{1}{4\mu}[(\kappa - 1)p_n^{sy} - (\kappa + 1)p_s^{sy} \cot 2\alpha] \tag{3.15b}$$

$$w_{n0}^{sy} = \frac{1}{4\mu}[(\kappa + 1)\alpha(p_n^{sy} - p_s^{sy} \cot 2\alpha) + 2p_{s0}^{sy}] \tag{3.15c}$$

$$w_{s0}^{sy} = \frac{\kappa + 1}{4\mu}\left[-\frac{1}{2} p_n^{sy} + \left(\alpha \cot^2 2\alpha + \frac{1}{2} \cot 2\alpha + \alpha \right) p_s^{sy} + \frac{\kappa - 1}{\kappa + 1} p_{n0}^{sy} - p_{s0}^{sy} \cot 2\alpha \right] \tag{3.15d}$$

Now consider the case when the infinite wedge subjected to a uniform loading. It is easy to find that $\bar{\sigma}_{\theta\theta}^{sy}$ and $\bar{\sigma}_{r\theta}^{sy}$ are zero. Since the tractions at the wedge-tip do not have weak singularity, we have $p_n^{sy} = p_s^{sy} = 0$. Thus Eqs. (3.14a), (3.14b), (3.14c), and (3.14d) becomes

$$a = b = 0$$

$$c = -\frac{1}{2\mu \sin 2\alpha} p_{s0}^{sy}$$

$$e = \frac{\kappa - 1}{4\mu}(p_{n0}^{sy} - p_{s0}^{sy} \cot 2\alpha)$$

Substitution of the above results into Eqs. (3.5a), (3.5b), (3.6a), and (3.6b) yields

$$u_r^{sy} = \frac{r}{2\mu}\left[\frac{\kappa - 1}{2} p_{n0}^{sy} - \left(\frac{\cos 2\theta}{\sin 2\alpha} + \frac{\kappa - 1}{2} \cot 2\alpha \right) p_{s0}^{sy} \right] \tag{3.16a}$$

$$u_\theta^{sy} = \frac{r}{2\mu}\left(\frac{\sin 2\theta}{\sin 2\alpha} p_{s0}^{sy} \right) \tag{3.16b}$$

and

$$\sigma_{rr}^{sy} = p_{n0}^{sy} - \frac{\cos 2\theta + \cos 2\alpha}{\sin 2\alpha} p_{s0}^{sy} \tag{3.17a}$$

$$\sigma_{\theta\theta}^{sy} = p_{n0}^{sy} + \frac{\cos 2\theta - \cos 2\alpha}{\sin 2\alpha} p_{s0}^{sy} \tag{3.17b}$$

$$\sigma_{r\theta}^{sy} = \frac{\sin 2\theta}{\sin 2\alpha} p_{s0}^{sy} \tag{3.17c}$$

respectively. Equations (3.16a), (3.16b), (3.17a), and (3.17b) are the same with Ting's results [7].

The stress field (3.17a) and (3.17b) in the Cartesian coordinate system becomes

$$\sigma_{xx}^{sy} = \sigma_{rr}^{sy} \cos^2\theta + \sigma_{\theta\theta}^{sy} \sin^2\theta - \sigma_{r\theta}^{sy} \sin 2\theta = p_{n0}^{sy} - \frac{\cos 2\alpha + 1}{\sin 2\alpha} p_{s0}^{sy}$$

$$\sigma_{yy}^{sy} = \sigma_{rr}^{sy} \cos^2\theta + \sigma_{\theta\theta}^{sy} \sin^2\theta + \sigma_{r\theta}^{sy} \sin 2\theta = p_{n0}^{sy} - \frac{\cos 2\alpha - 1}{\sin 2\alpha} p_{s0}^{sy}$$

$$\sigma_{xy}^{sy} = \tfrac{1}{2}(\sigma_{rr}^{sy} - \sigma_{\theta\theta}^{sy}) \sin 2\theta + \sigma_{r\theta}^{sy} \cos 2\theta = 0$$

Thus, the stress field of the wedge is constant. From Eqs. (3.15a), (3.15b), (3.15c), and (3.15d) we obtain

$$w_n^{sy} = w_s^{sy} = 0 \tag{3.18a}$$

$$w_{n0}^{sy} = \frac{p_{s0}^{sy}}{2\mu} \tag{3.18b}$$

$$w_{s0}^{sy} = \frac{1}{4\mu}[(\kappa - 1)p_{n0}^{sy} - (\kappa + 1)p_{s0}^{sy} \cot 2\alpha] \tag{3.18c}$$

Substituting Eqs. (3.18a), (3.18b), and (3.18c) into Eqs. (3.13a) and (3.13b) and letting $s = 0$, we obtain

$$u_n'^{sy}(0_\pm) = \pm \frac{1}{2\mu} p_{s0}^{sy} \tag{3.19a}$$

$$u_s'^{sy}(0_\pm) = \frac{1}{2\mu}\left[\frac{\kappa - 1}{2} p_{n0}^{sy} - \left(\frac{\kappa + 1}{2} \cot 2\alpha \right) p_{s0}^{sy} \right] \tag{3.19b}$$

The discontinuous values of the displacement derivatives can be obtained from Eqs. (3.19a) and (3.19b).

$$\Delta u_n'^{sy} = u_n'^{sy}(0_+) - u_n'^{sy}(0_-) = \frac{p_{s0}^{sy}}{\mu} \tag{3.20a}$$

$$\Delta u_s'^{sy} = u_s'^{sy}(0_+) - u_s'^{sy}(0_-) = 0 \tag{3.20b}$$

3.3 Displacement Prescribed Problem. If the boundary conditions is displacement prescribed, w_n^{sy}, w_s^{sy}, w_{n0}^{sy}, and w_{s0}^{sy} in the right sides of Eqs. (3.13*a*) and (3.13*b*) are known. From the linear algebraic Eqs. (3.12*a*), (3.12*b*), (3.12*c*), and (3.12*d*), we obtain the following

$$a = w_n^{sy} \cot 2\alpha + w_s^{sy} \tag{3.21a}$$

$$b = -\frac{w_n^{sy}}{\sin 2\alpha} \tag{3.21b}$$

$$c = \frac{1}{\sin 2\alpha}\left[\left(1 + \frac{2\kappa}{\kappa - 1}\alpha \cot 2\alpha\right)w_n^{sy} + \frac{\kappa + 1}{\kappa - 1}\alpha w_s^{sy} - w_{n0}^{sy}\right] \tag{3.21c}$$

$$e = -\left(\frac{2\kappa}{\kappa - 1}\alpha \cot^2 2\alpha + \cot 2\alpha + \alpha\right)w_n^{sy} - \left(\frac{\kappa + 1}{\kappa - 1}\alpha \cot 2\alpha + 1\right)w_s^{sy} + w_{n0}^{sy} \cot 2\alpha + w_{s0}^{sy} \tag{3.21d}$$

Substituting Eqs. (3.21*a*), (3.21*b*), (3.21*c*), and (3.21*d*) into Eqs. (3.8*a*), (3.8*b*), (3.8*c*), and (3.8*d*) yields

$$p_n^{sy} = 2\mu\left(\frac{\kappa + 1}{\kappa - 1}w_n^{sy} \cot 2\alpha + \frac{2}{\kappa - 1}w_s^{sy}\right) \tag{3.22a}$$

$$p_s^{sy} = 2\mu w_n^{sy} \tag{3.22b}$$

$$p_{n0}^{sy} = 2\mu\frac{\kappa + 1}{\kappa - 1}\left\{\left[-\frac{2\kappa}{\kappa - 1}\alpha \cot^2 2\alpha + \frac{1}{\kappa - 1}\cot 2\alpha - \alpha\right] w_n^{sy} - \left[\frac{\kappa + 1}{\kappa - 1}\alpha \cot 2\alpha - \frac{1}{\kappa - 1}\right]w_s^{sy} + w_{n0}^{sy} \cot 2\alpha + \frac{2}{\kappa + 1}w_{s0}^{sy}\right\} \tag{3.22c}$$

$$p_{s0}^{sy} = -2\mu\left[\frac{\kappa + 1}{\kappa - 1}\alpha(w_n^{sy} \cot 2\alpha + w_s^{sy}) - w_{n0}^{sy}\right] \tag{3.22d}$$

Now consider the case when the boundary displacement derivatives do not have weak singularity, $w_n^{sy} = w_s^{sy} = 0$. Equations (3.22*a*), (3.22*b*), (3.22*c*), and (3.22*d*) becomes

$$p_n^{sy} = p_s^{sy} = 0 \tag{3.23a}$$

$$p_{n0}^{sy} = \frac{2\mu}{\kappa - 1}[(\kappa + 1)w_{n0}^{sy} \cot 2\alpha + 2w_{s0}^{sy}] \tag{3.23b}$$

$$p_{s0}^{sy} = 2\mu w_{n0}^{sy} \tag{3.23c}$$

Equations (3.23*a*), (3.23*b*), and (3.23*c*) is in consistence with Eqs. (3.18*a*), (3.18*b*), and (3.18*c*)

4 Four Particular Solutions of an Infinite Antisymmetric Wedge

4.1 Expressions of Displacement and Stress Fields. The displacement field of particular solutions of an antisymmetric wedge is assumed to be the of the following general form:

$$u_r^{an} = r(a \sin 2\theta \ln r + b \sin 2\theta + c\theta \cos 2\theta + d\theta) + \bar{u}_r^{an}(r, \theta) \tag{4.1a}$$

$$u_\theta^{an} = r[(e + f \cos 2\theta)\ln r + g \cos 2\theta + h\theta \sin 2\theta + i] + \bar{u}_\theta^{an}(r, \theta) \tag{4.1b}$$

where the gradients of displacements $\bar{u}_r^{an}$ and $\bar{u}_\theta^{an}$ are continuous and their values are zero at $r=0$. The corresponding stresses $\bar{\sigma}_{rr}^{an}$, $\bar{\sigma}_{\theta\theta}^{an}$, and $\bar{\sigma}_{r\theta}^{an}$ satisfy the stress equilibrium equations and their values are zero at $r=0$. It is easy to show that the gradients of the total displacement field (4.1) are continuous for $r \neq 0$. But, as $r \to 0$, the gradients of the displacement field (4.1) may have discontinuity of the first kind and $\ln r$ weak singularity.

The stress field corresponding to the displacement field Eq. (4.1) can be obtained through Hooke's law as follows:

$$\sigma_{rr}^{an} = 2\mu\{(s_1 a - 2s_2 f)\sin 2\theta \ln r + [s_3 a + s_1 b + s_2(h - 2g)]\sin 2\theta + (s_1 c + 2s_2 h)\theta \cos 2\theta + s_1 d\theta\} + \bar{\sigma}_{rr}^{an}(r, \theta) \tag{4.2a}$$

$$\sigma_{\theta\theta}^{an} = 2\mu\{(s_1 a - 2s_3 f)\sin 2\theta \ln r + [s_2 a + s_1 b + s_3(h - 2g)]\sin 2\theta + (s_1 c + 2s_3 h)\theta \cos 2\theta + s_1 d\theta\} + \bar{\sigma}_{\theta\theta}^{an}(r, \theta) \tag{4.2b}$$

$$\sigma_{r\theta}^{an} = 2\mu\left(a \cos 2\theta \ln r + \frac{2b + c + f}{2}\cos 2\theta - c\theta \sin 2\theta + \frac{d + e}{2}\right) + \bar{\sigma}_{r\theta}^{an}(r, \theta) \tag{4.2c}$$

where s_1, s_2, and s_3 are defined by Eq. (3.3).

Substitution of the stress field (4.2) into the stress equilibrium equations yields

$$c = f = -h = a, \quad g = b, \quad e = -2s_3 d \tag{4.3}$$

Therefore, the coefficients in the displacement expression (4.1) are dependent.

Using relations (4.3), Eqs. (4.1) and (4.2) are simplified as

$$u_r^{an} = r(a \sin 2\theta \ln r + b \sin 2\theta + a\theta \cos 2\theta + d\theta) + \bar{u}_r^{an}(r, \theta) \tag{4.4a}$$

$$u_\theta^{an} = r[(-2s_3 d + a \cos 2\theta)\ln r + b \cos 2\theta - a\theta \sin 2\theta + i] + \bar{u}_\theta^{an}(r, \theta) \tag{4.4b}$$

and

$$\sigma_{rr}^{an} = 2\mu[a \sin 2\theta \ln r + (a + b)\sin 2\theta + a\theta \cos 2\theta + s_1 d\theta] + \bar{\sigma}_{rr}^{an}(r, \theta) \tag{4.5a}$$

$$\sigma_{\theta\theta}^{an} = 2\mu(a \sin 2\theta \ln r - (a + b)\sin 2\theta - a\theta \cos 2\theta + s_1 d\theta) + \bar{\sigma}_{\theta\theta}^{an}(r, \theta) \tag{4.5b}$$

$$\sigma_{r\theta}^{an} = 2\mu\left(a \cos 2\theta \ln r + (a + b)\cos 2\theta - a\theta \sin 2\theta - \tfrac{1}{2}s_1 d\right) + \bar{\sigma}_{r\theta}^{an}(r, \theta) \tag{4.5c}$$

respectively. Letting $\theta = \mp\alpha$ in Eqs. (4.5*b*) and (4.5*c*), we obtain the following:

$$\sigma_{\theta\theta}^{an}(r, \mp\alpha) = \pm p_n^{an} \ln r \pm p_{n0}^{an} \pm P_n^{an}(r) \tag{4.6a}$$

$$\sigma_{r\theta}^{an}(r, \mp\alpha) = -p_s^{an} \ln r - p_{s0}^{an} - P_s^{an}(r) \tag{4.6b}$$

where

$$p_n^{an} = 2\mu a \sin 2\alpha \tag{4.7a}$$

$$p_s^{an} = -2\mu a \cos 2\alpha \tag{4.7b}$$

$$p_{n0}^{an} = 2\mu[(a + b)\sin 2\alpha + a\alpha \cos 2\alpha - s_1 d\alpha] \tag{4.7c}$$

$$p_{s0}^{an} = 2\mu\left[-(a + b)\cos 2\alpha + a\alpha \sin 2\alpha + \tfrac{1}{2}s_1 d\right] \tag{4.7d}$$

and

$$P_n^{an}(r) = \bar{\sigma}_{\theta\theta}^{an}(r, -\alpha), \quad (P_n^{an}(0) = 0)$$

$$P_s^{an}(r) = -\bar{\sigma}_{r\theta}^{an}(r,-\alpha), \quad (P_s^{an}(0)=0)$$

The tractions as the functions of the boundary length s can be obtained from Eq. (4.6):

$$t_n^{an}(s) = \pm p_n^{an}\ln|s| \pm p_{n0}^{an} \pm P_n^{an}(|s|), \quad s>0 \text{ for plus sign}, \quad s<0 \text{ for minus sign} \tag{4.8a}$$

$$t_s^{an}(s) = p_s^{an}\ln r + p_{s0}^{an} + P_s^{an}(|s|) \tag{4.8b}$$

where p_n^{an} and p_s^{an} are the weak singularity intensities of the normal and tangent tractions at the wedge-tip, respectively; p_{n0}^{an} and p_{s0}^{an} are the values of the finite parts of the normal and tangent tractions at the wedge-tip, respectively. Equations (4.8*a*) and (4.8*b*) show that the tractions at the wedge-tip consist of two parts, one being weakly singular, and the other being bounded. From Eqs. (4.7*a*) and (4.7*b*) we obtain the following:

$$\frac{p_n^{an}}{p_s^{an}} = -\tan 2\alpha \tag{4.9}$$

Equation (4.9), which is in consistence with Eq. (2.2), shows that the weak singularity intensities of the normal and tangent tractions are dependent. The meaning of Eq. (4.9) has been discussed in the Sec. 2.

The displacement derivatives with respect to r can be obtained from Eqs. (4.4*a*) and (4.4*b*):

$$\frac{\partial u_\theta^{an}(r,\theta)}{\partial r} = (-2s_3 d + a\cos 2\theta)\ln r + (a+b)\cos 2\theta - a\theta\sin 2\theta - 2s_3 d + i + \frac{\partial \bar{u}_\theta^{an}(r,\theta)}{\partial r} \tag{4.10a}$$

$$\frac{\partial u_r^{an}(r,\theta)}{\partial r} = a\sin 2\theta\ln r + (a+b)\sin 2\theta + a\theta\cos 2\theta + d\theta + \frac{\partial \bar{u}_r^{an}(r,\theta)}{\partial r} \tag{4.10b}$$

Substituting $\theta = \mp\alpha$ into Eqs. (4.10*a*) and (4.10*b*) yields

$$\frac{\partial u_\theta^{an}(r,\mp\alpha)}{\partial r} = -w_n^{an}\ln r - w_{n0}^{an} - W_n^{an}(r) \tag{4.11a}$$

$$\frac{\partial u_r^{an}(r,\mp\alpha)}{\partial r} = \pm w_s^{an}\ln r \pm w_{s0}^{an} \pm W_s^{an}(r) \tag{4.11b}$$

where

$$w_n^{an} = 2s_3 d - a\cos 2\alpha \tag{4.12a}$$

$$w_s^{an} = -a\sin 2\alpha \tag{4.12b}$$

$$w_{n0}^{an} = -(a+b)\cos 2\alpha + a\alpha\sin 2\alpha + 2s_3 d - i \tag{4.12c}$$

$$w_{s0}^{an} = -(a+b)\sin 2\alpha - a\alpha\cos 2\alpha - d\alpha \tag{4.12d}$$

and

$$W_n^{an}(r) = -\frac{\partial \bar{u}_\theta^{an}(r,-\alpha)}{\partial r}, \quad (W_n^{an}(0)=0)$$

$$W_s^{an}(r) = \frac{\partial \bar{u}_r^{an}(r,-\alpha)}{\partial r}, \quad (W_s^{an}(0)=0)$$

The boundary displacement derivatives with respect to s can be obtained from Eqs. (4.11*a*) and (4.11*b*); the results are

$$u_n'^{an}(s) = w_n^{an}\ln|s| + w_{n0}^{an} + W_n^{an}(|s|) \tag{4.13a}$$

$$u_s'^{an}(s) = \pm w_s^{an}\ln|s| \pm w_{s0}^{an} \pm W_s^{an}(|s|), \quad s>0 \text{ for plus sign}, \quad s<0 \text{ for minus sign} \tag{4.13b}$$

where w_n^{an} and w_s^{an} are the weak singularity intensities of the normal and tangent displacement derivatives at the wedge-tip, respectively; w_{n0}^{an} and w_{s0}^{an} are the values of the finite parts of the normal and tangent displacement derivatives at the wedge-tip, respectively. Equations (4.8*a*) and (4.8*b*) and (4.13*a*) and (4.13*b*) indicate that the tractions and the boundary displacement derivates of the wedge consist of a finite part and a weakly singular part. Moreover, the discontinuity value of the finite part at the wedge-tip has been separated from the other part. In the following, the relations between tractions and boundary displacement derivates at the wedge-tip will be determined.

4.2 Tractions Prescribed Problem. If the boundary conditions are tractions prescribed, p_n^{an}, p_s^{an}, p_{n0}^{an}, and p_{s0}^{an} in the right sides of Eqs. (4.8*a*) and (4.8*b*) are known. Note that the four linear algebraic Eqs. (4.7*a*), (4.7*b*), (4.7*c*), and (4.7*d*) are not independent. The unknown constant a, b, and d can be obtained from Eqs. (4.7*a*), (4.7*c*), (4.7*d*), and (4.7*b*), as follows:

$$a = \frac{p_n^{an}}{2\mu\sin 2\alpha} \tag{4.14a}$$

$$b = \frac{1}{2\mu Q}\left[-\left(\alpha\cot 2\alpha + 2\alpha^2 + \frac{Q}{\sin 2\alpha}\right)p_n^{an} + p_{n0}^{an} + 2\alpha p_{s0}^{an}\right] \tag{4.14b}$$

$$d = \frac{\kappa-1}{2\mu Q}\left(-\frac{\alpha}{\sin 2\alpha}p_n^{an} + p_{n0}^{an}\cos 2\alpha + p_{s0}^{an}\sin 2\alpha\right) \tag{4.14c}$$

where $Q = \sin 2\alpha - 2\alpha\cos 2\alpha$.

Substituting Eqs. (4.14*a*), (4.14*b*), and (4.14*c*) into Eqs. (4.12*a*), (4.12*b*), (4.12*c*), and (4.12*d*) yields

$$w_n^{an} = \frac{\kappa+1}{2\mu Q}\left[-\left(\frac{Q}{\kappa+1}\cot 2\alpha + \frac{\alpha}{\sin 2\alpha}\right)p_n^{an} + p_{n0}^{an}\cos 2\alpha + p_{s0}^{an}\sin 2\alpha\right] \tag{4.15a}$$

$$w_s^{an} = -\frac{p_n^{an}}{2\mu} \tag{4.15b}$$

$$w_{n0}^{an} = \frac{1}{2\mu Q}[\kappa\alpha p_n^{an} + \kappa p_{n0}^{an}\cos 2\alpha + (Q+\kappa\sin 2\alpha)p_{s0}^{an}] - i \tag{4.15c}$$

$$w_{s0}^{an} = \frac{\kappa+1}{2\mu Q}\left[\frac{\alpha^2}{\sin 2\alpha}p_n^{an} - \left(\frac{Q}{\kappa+1} + \alpha\cos 2\alpha\right)p_{n0}^{an} - \alpha p_{s0}^{an}\sin 2\alpha\right] \tag{4.15d}$$

The expression of the finite part of the boundary normal displacement derivative Eq. (4.12*c*) includes a constant i that is irrelevant to the stress field as shown in Eqs. (4.5*a*), (4.5*b*), and (4.5*c*). In fact, i is related to a rigid body rotation. The antisymmetric stresses at the wedge-tip are generally multivalued, hence the boundary displacement derivatives cannot be calculated from the stresses through Hooke's law.

Now consider the case when the infinite wedge subjected to a uniform loading. It is easy to find that $\bar{\sigma}_{\theta\theta}^{an}$ and $\bar{\sigma}_{r\theta}^{an}$ are zero. Since the tractions at the wedge-tip do not have any weak singularity, we have $p_n^{an} = p_s^{an} = 0$. Thus Eqs. (4.14*a*), (4.14*b*), and (4.14*c*) become

$$a = 0$$

$$b = \frac{p_{n0}^{an} + 2\alpha p_{s0}^{an}}{2\mu Q}$$

$$d = \frac{\kappa - 1}{2\mu Q}(p_{n0}^{an} \cos 2\alpha + p_{s0}^{an} \sin 2\alpha)$$

Substitution of the above results into Eqs. (4.4*a*), (4.4*b*), (4.5*a*), (4.5*b*), and (4.5*c*) yields

$$u_r^{an} = \frac{r}{2\mu Q}\{[\sin 2\theta + (\kappa - 1)\theta \cos 2\alpha]p_{n0}^{an} + [2\alpha \sin 2\theta + (\kappa - 1)\theta \sin 2\alpha]p_{s0}^{an}\} \quad (4.16a)$$

$$u_\theta^{an} = \frac{r}{2\mu Q}[-(\kappa + 1)(p_{n0}^{an} \cos 2\alpha + p_{s0}^{an} \sin 2\alpha)\ln r + (p_{n0}^{an} + 2\alpha p_{s0}^{an})\cos 2\theta] + ri \quad (4.16b)$$

and

$$\sigma_{rr}^{an} = \frac{1}{Q}[(\sin 2\theta + 2\theta \cos 2\alpha)p_{n0}^{an} + (2\alpha \sin 2\theta + 2\theta \sin 2\alpha)p_{s0}^{an}] \quad (4.17a)$$

$$\sigma_{\theta\theta}^{an} = \frac{1}{Q}[(-\sin 2\theta + 2\theta \cos 2\alpha)p_{n0}^{an} + (-2\alpha \sin 2\theta + 2\theta \sin 2\alpha)p_{s0}^{an}] \quad (4.17b)$$

$$\sigma_{r\theta}^{an} = \frac{1}{Q}[(\cos 2\theta - \cos 2\alpha)p_{n0}^{an} + (2\alpha \cos 2\theta - \sin 2\alpha)\ p_{s0}^{an})] \quad (4.17c)$$

respectively. Equations (4.16*a*), (4.16*b*), (4.17*a*), (4.17*b*), and (4.17*c*) are the same with Ting's results [7].

For $p_n^{an} = p_s^{an} = 0$, Eqs. (4.15*a*), (4.15*b*), (4.15*c*), and (4.15*d*) are simplified to

$$w_n^{an} = \frac{\kappa + 1}{2\mu Q}(p_{n0}^{an} \cos 2\alpha + p_{s0}^{an} \sin 2\alpha) \quad (4.18a)$$

$$w_s^{an} = 0 \quad (4.18b)$$

$$w_{n0}^{an} = \frac{1}{2\mu Q}[\kappa p_{n0}^{an} \cos 2\alpha + (Q + \kappa \sin 2\alpha)p_{s0}^{an}] - i \quad (4.18c)$$

$$w_{s0}^{an} = -\frac{\kappa + 1}{2\mu Q}\left[\left(\frac{Q}{\kappa + 1} + \alpha \cos 2\alpha\right)p_{n0}^{an} + \alpha p_{s0}^{an} \sin 2\alpha\right] \quad (4.18d)$$

Equation (4.18*a*) shows that the boundary normal displacement derivative is generally weakly singular, while Eq. (4.18*b*) shows that the boundary tangent displacement derivative has no weak singularity. The discontinuous values of the displacement derivatives at the wedge-tip can be obtained from Eqs. (4.18*c*) and (4.18*d*); the results are as follows:

$$\Delta u_n'^{an} = 0 \quad (4.19a)$$

$$\Delta u_s'^{an} = -\frac{\kappa + 1}{\mu Q}\left[\left(\frac{Q}{\kappa + 1} + \alpha \cos 2\alpha\right)p_{n0}^{an} + \alpha p_{s0}^{an} \sin 2\alpha\right] \quad (4.19b)$$

Let α^* be the root of the equation

$$Q = \sin 2\alpha - 2\alpha \cos 2\alpha = 0$$

If $\alpha = \alpha^*$, the displacement expression (4.16*a*) and (4.16*b*) tends to be infinite; this is a paradox. The paradox was solved by Ting [7] if the tractions at the corner do not have weak singularities.

4.3 Displacement Prescribed Problem. If the boundary conditions are displacement prescribed, w_n^{an}, w_s^{an}, w_{n0}^{an}, and w_{s0}^{an} in the right sides of Eqs. (4.13*a*) and (4.13*b*) are known. From the linear algebraic equations (4.12*a*), (4.12*b*), and (4.12*d*), we obtain

$$a = -\frac{w_s^{an}}{\sin 2\alpha} \quad (4.20a)$$

$$b = \frac{1}{\sin 2\alpha}\left[-\frac{\kappa - 1}{\kappa + 1}\alpha w_n^{an} + \left(1 + \frac{2\kappa}{\kappa + 1}\alpha \cot 2\alpha\right)w_s^{an} - w_{s0}^{an}\right] \quad (4.20b)$$

$$d = \frac{\kappa - 1}{\kappa + 1}(w_n^{an} - w_s^{an} \cot 2\alpha) \quad (4.20c)$$

Substituting Eqs. (4.20*a*), (4.20*b*), and (4.20*c*) into Eqs. (4.7*a*), (4.7*b*), (4.7*c*), and (4.7*d*) yields

$$p_n^{an} = -2\mu w_s^{an} \quad (4.21a)$$

$$p_s^{an} = 2\mu w_s^{an} \cot 2\alpha \quad (4.21b)$$

$$p_{n0}^{an} = -2\mu(\alpha w_n^{an} - \alpha w_s^{an} \cot 2\alpha + w_{s0}^{an}) \quad (4.21c)$$

$$p_{s0}^{an} = 2\mu\left[\left(\frac{\kappa - 1}{\kappa + 1}\alpha \cot 2\alpha + \frac{1}{\kappa + 1}\right)\ w_n^{an} - \left(\frac{2\kappa}{\kappa + 1}\alpha \cot^2 2\alpha + \frac{1}{\kappa + 1}\cot 2\alpha + \alpha\right)w_s^{an} + w_{s0}^{an} \cot 2\alpha\right] \quad (4.21d)$$

If $w_s^{an} = 0$, Eqs. (4.21*a*) and (4.21*b*) shows that the tractions have no weak singularity, and Eqs. (4.21*c*) and (4.21*d*) are simplified as

$$p_{n0}^{an} = -2\mu(\alpha w_n^{an} + w_{s0}^{an}) \quad (4.22a)$$

$$p_{s0}^{an} = 2\mu\left[\left(\frac{\kappa - 1}{\kappa + 1}\alpha \cot 2\alpha + \frac{1}{\kappa + 1}\right)w_n^{an} + w_{s0}^{an} \cot 2\alpha\right] \quad (4.22b)$$

Equations (4.22*a*) and (4.22*b*) can also be obtained through Eqs. (4.18*a*) and (4.18*c*). Note that the boundary normal displacement derivative intensity w_n^{an} will not produce any traction weak singularity.

5 Relations of Displacement Derivatives and Tractions at Corners

Suppose that the tractions at a corner of an elastic body may have discontinuity of the first kind and weak singularity. Let s be the boundary length with origin located at the corner, and 2α be the angle comprised by the two boundary tangent lines at the corner. In the following, the subscript i may take n or s. The tractions near the corner are written in the following form:

$$t_i(s) = p_{i\pm} \ln|s| + p_{i0\pm} + P_i(s), \quad s > 0 \text{ for plus sign}, \quad s < 0 \text{ for minus sign} \quad (5.1)$$

where $p_{i\pm}$ are the traction weak singularity intensities as $s \to 0\pm$, $p_{i0\pm}$ are constants, $P_i(s)$ are bounded and continuous functions of s, and $P_i(0) = 0$. Note that $p_{n\pm}$ and p_{s+} are not independent, they are constrained to Eq. (2.5). Now expressing tractions near the corner as the superposition of a symmetric part t_i^{sy} and an antisymmetric part t_i^{an}, and letting

$$p_{i+}^{sy} = p_i^{sy}, \quad p_{i0+}^{sy} = p_{i0}^{sy}, \quad p_{i+}^{an} = p_i^{an}, \quad p_{i0+}^{an} = p_{i0}^{an}$$

we obtain

$$p_{n+} = p_{n\pm}^{sy} + p_{n\pm}^{an} = p_n^{sy} \pm p_n^{an}, \quad p_{n0\pm} = p_{n0\pm}^{sy} + p_{n0\pm}^{an} = p_{n0}^{sy} \pm p_{n0}^{an} \quad (5.2a)$$

$$p_{s\pm} = p_{s\pm}^{sy} + p_{s\pm}^{an} = \pm p_s^{sy} + p_s^{an}, \quad p_{s0\pm} = p_{s0\pm}^{sy} + p_{s0\pm}^{an} = \pm p_{s0}^{sy} + p_{s0}^{an} \tag{5.2b}$$

where

$$p_n^{sy} = \frac{p_{n+} + p_{n-}}{2}, \quad p_{n0}^{sy} = \frac{p_{n0+} + p_{n0-}}{2} \tag{5.3a}$$

$$p_n^{an} = \frac{p_{n+} - p_{n-}}{2}, \quad p_{n0}^{an} = \frac{p_{n0+} - p_{n0-}}{2} \tag{5.3b}$$

$$p_s^{sy} = \frac{p_{s+} - p_{s-}}{2}, \quad p_{s0}^{sy} = \frac{p_{s0+} - p_{s0-}}{2} \tag{5.3c}$$

$$p_s^{an} = \frac{p_{s+} + p_{s-}}{2}, \quad p_{s0}^{an} = \frac{p_{s0+} + p_{s0-}}{2} \tag{5.3d}$$

Suppose that the boundary displacement derivatives may have discontinuity of the first kind and weak singularity. The boundary displacement derivatives near the corner are written in the following form:

$$u_i'(s) = w_{i\pm} \ln|s| + w_{i0\pm} + W_i(s), \quad s > 0 \text{ for plus sign}, \quad s < 0 \text{ for minus sign} \tag{5.4}$$

where $w_{i\pm}$ are the weak singularity intensities of the boundary displacement derivatives as $s \to 0\pm$, $w_{i0\pm}$ are constants; $W_i(s)$ are bounded and continuous functions of s, and $W_i(0)=0$.

Expressing the boundary displacement derivatives near the corner as the superposition of a symmetric part $u_i'^{sy}$ and an antisymmetric part $u_i'^{an}$, and letting

$$w_{i+}^{sy} = w_i^{sy}, \quad w_{i0+}^{sy} = w_{i0}^{sy}, \quad w_{i+}^{an} = w_i^{an}, \quad w_{i0+}^{an} = w_{i0}^{an}$$

we obtain the following:

$$w_{n\pm} = w_{n\pm}^{sy} + w_{n\pm}^{an} = \pm w_n^{sy} + w_n^{an}, \quad w_{n0\pm} = w_{n0\pm}^{sy} + w_{n0\pm}^{an} = \pm w_{n0}^{sy} + w_{n0}^{an} \tag{5.5a}$$

$$w_{s\pm} = w_{s\pm}^{sy} + w_{s\pm}^{an} = w_s^{sy} \pm w_s^{an}, \quad w_{s0\pm} = w_{s0\pm}^{sy} + w_{s0\pm}^{an} = w_{s0}^{sy} \pm w_{s0}^{an} \tag{5.5b}$$

where

$$w_n^{sy} = \frac{w_{n+} - w_{n-}}{2}, \quad w_{n0}^{sy} = \frac{w_{n0+} - w_{n0-}}{2} \tag{5.6a}$$

$$w_n^{an} = \frac{w_{n+} + w_{n-}}{2}, \quad w_{n0}^{an} = \frac{w_{n0+} + w_{n0-}}{2} \tag{5.6b}$$

$$w_s^{sy} = \frac{w_{s+} + w_{s-}}{2}, \quad w_{s0}^{sy} = \frac{w_{s0+} + w_{s0-}}{2} \tag{5.6c}$$

$$w_s^{an} = \frac{w_{s+} - w_{s-}}{2}, \quad w_{s0}^{an} = \frac{w_{s0+} - w_{s0-}}{2} \tag{5.6d}$$

Let

$$\Delta p_i = p_{i+} - p_{i-}, \quad \Delta p_{i0} = p_{i0+} - p_{i0-}$$

$$\Sigma p_i = p_{i+} + p_{i-}, \quad \Sigma p_{i0} = p_{i0+} + p_{i0-}$$

$$\Delta w_i = w_{i+} - w_{i-}, \quad \Delta w_{i0} = w_{i0+} - w_{i0-}$$

$$\Sigma w_i = w_{i+} + w_{i-}, \quad \Sigma w_{i0} = w_{i0+} + w_{i0-}$$

Next we will consider two kinds of simple boundary valued problems.

5.1 Tractions Prescribed Problem. Assume that all the traction components near a corner of an elastic body are known and Eq. (2.5) is satisfied. Thus, $p_{i\pm}$ and $p_{i0\pm}$ are known values. First, p_i^{sy}, p_{i0}^{sy}, p_i^{an}, and p_{i0}^{an} are calculated from Eqs. (5.3*a*), (5.3*b*), (5.3*c*), and (5.3*d*). Then, w_i^{sy} and w_{i0}^{sy} are calculated from Eqs. (3.15*a*), (3.15*b*), (3.15*c*), and (3.15*d*), w_n^{an}, w_s^{an}, and w_{s0}^{an} are calculated from Eqs. (4.15*a*), (4.15*b*), (4.15*c*), and (4.15*d*). Finally, the weak singularity intensities and the values of the finite parts of the boundary displacement derivatives at $s=0$ are obtained by using Eqs. (5.5*a*) and (5.5*b*) as follows:

$$w_{n\pm} = \frac{1}{4\mu}\left\{\frac{\kappa+1}{Q}\left[-\left(\frac{Q\cot 2\alpha}{\kappa+1} + \frac{1}{\sin 2\alpha}\alpha\right)\Delta p_n + (\Delta p_{n0}\cos 2\alpha + \Sigma p_{s0}\sin 2\alpha)\right] \pm \Delta p_s\right\} \tag{5.7a}$$

$$w_{s\pm} = \frac{1}{8\mu}[(\kappa-1)\Sigma p_n - (\kappa+1)\Delta p_s \cot 2\alpha \mp 2\Delta p_n] \tag{5.7b}$$

$$w_{n0\pm} = \frac{1}{8\mu Q}\{2[\kappa\alpha\Delta p_n + \kappa\Delta p_{n0}\cos 2\alpha + (\kappa\sin 2\alpha + Q)\Sigma p_{s0}] \pm Q[(\kappa+1)\alpha(\Sigma p_n - \Delta p_s\cot 2\alpha) + 2\Delta p_{s0}]\} - i \tag{5.7c}$$

$$w_{s0\pm} = \frac{\kappa+1}{4\mu}\left\{-\frac{1}{2}\left[\frac{\Sigma p_n}{2} - \left(\alpha\cot^2 2\alpha + \frac{\cos 2\alpha}{2} + \alpha\right)\Delta p_s - \frac{\kappa-1}{\kappa+1}\Sigma p_{n0} + \Delta p_{s0}\cot 2\alpha\right] \pm \frac{1}{Q}\left[\frac{\alpha^2}{\sin 2\alpha}\Delta p_n - \left(\frac{Q}{\kappa+1} + \alpha\cos 2\alpha\right)\Delta p_{n0} - \alpha\Sigma p_{s0}\sin 2\alpha\right]\right\} \tag{5.7d}$$

If the tractions at the corner have no weak singularity, i.e., $p_{n\pm} = p_{s\pm} = 0$, we have

$$t_{n\pm} = t_n(0_\pm) = p_{n0\pm}, \quad t_{s\pm} = t_s(0_\pm) = p_{s0\pm}$$

$$\Delta t_n = \Delta p_{n0}, \quad \Delta t_s = \Delta p_{s0}$$

$$\Sigma t_n = \Sigma p_{n0}, \quad \Sigma t_s = \Sigma p_{s0}$$

By using the above expressions, Eqs. (5.7*a*), (5.7*b*), (5.7*c*), and (5.7*d*) are simplified to

$$w_{n\pm} = \frac{\kappa+1}{4\mu Q}(\Delta t_n\cos 2\alpha + \Sigma t_s\sin 2\alpha) \tag{5.8a}$$

$$w_{s\pm} = 0 \tag{5.8b}$$

$$w_{n0\pm} = \frac{1}{4\mu}\left[\frac{\kappa}{Q}\Delta t_n\cos 2\alpha + \left(1 + \frac{\kappa}{Q}\sin 2\alpha\right)\Sigma t_s \pm \Delta t_s\right] - i \tag{5.8c}$$

$$w_{s0\pm} = \frac{1}{8\mu}\left\{[(\kappa-1)\Sigma t_n - (\kappa+1)\Delta t_s\cot 2\alpha] \pm \frac{2(\kappa+1)}{Q}\left[\left(\frac{Q}{\kappa+1} + \alpha\cos 2\alpha\right)\Delta t_n + \alpha\Sigma t_s\sin 2\alpha\right]\right\} \tag{5.8d}$$

Equation (5.8*a*) shows that the weak singularities of boundary normal displacement derivatives are the same when $s \to 0_\pm$, i.e., $w_{n+}=w_{n-}$. Therefore, $\Delta u_n'$, the discontinuity value of the boundary normal displacement derivative is only related to the finite part $w_{n0\pm}$. The discontinuous values of the boundary displacement derivatives can be obtained by using Eqs. (5.8*a*), (5.8*b*), (5.8*c*), and (5.8*d*) as follows:

$$\Delta u_n' = \frac{1}{2\mu}\Delta t_s \tag{5.9a}$$

$$\Delta u_s' = \frac{1}{2\mu Q}\{[Q + (\kappa+1)\alpha\cos 2\alpha]\Delta t_n + [(\kappa+1)\alpha\sin 2\alpha]\Sigma t_s\} \tag{5.9b}$$

Equations (5.8*a*), (5.8*b*), (5.8*c*), and (5.8*d*) also show that if the tractions have no weak singularity, the boundary displacement tangent derivative has no weak singularity either, but the boundary normal displacement derivative may have weak singularity. Equation (5.9*a*) shows that the discontinuity value of the boundary normal displacement derivative at the corner is proportional to the discontinuity value of the tangent traction at the corner. Equation (5.9*b*) shows that the discontinuity value of the boundary tangent displacement derivative at the corner is proportional not only to the discontinuity value of the normal traction, but also to the sum of the two tangent tractions at the corner. These results should be taken care of when BEM is used to solve corner problems.

5.2 Displacement Prescribed Problem. Assume that all the displacement components near the corner are known. Thus $w_{i\pm}$ and $w_{i0\pm}$ are known values. First, w_i^{sy}, w_{i0}^{sy}, w_i^{an}, and w_{i0}^{an} are calculated from Eqs. (5.6*a*), (5.6*b*), (5.6*c*), and (5.6*d*). Then, p_i^{sy} and p_{i0}^{sy} are calculated from Eqs. (3.22*a*), (3.22*b*), (3.22*c*), and (3.22*d*); p_i^{an} and p_{i0}^{an} are calculated from Eqs. (4.21*a*), (4.21*b*), (4.21*c*), and (4.21*d*). Finally, the weak singularity intensities and the values of the finite parts of the tractions at $s=0$ are obtained by using Eqs. (5.2*a*) and (5.2*b*) as follows:

$$p_{n\pm} = \mu\left[\frac{\kappa+1}{\kappa-1}\Delta w_n\cot 2\alpha + \frac{2}{\kappa-1}\Sigma w_s \mp \Delta w_s\right] \tag{5.10a}$$

$$p_{s\pm} = \mu(\pm\Delta w_n - \Delta w_s\cot 2\alpha) \tag{5.10b}$$

$$p_{n0\pm} = \mu\left\{\left(\frac{\kappa+1}{\kappa-1}\right)^2\left(\frac{1}{\kappa+1} - \alpha\cot 2\alpha\right)(\Delta w_n\cot 2\alpha + \Sigma w_s) + \frac{\kappa+1}{\kappa-1}\Delta w_{n0}\cot 2\alpha + \frac{2}{\kappa-1}\Sigma w_{s0} \pm (\alpha\Sigma w_n - \alpha\Delta w_s\cot 2\alpha + \Delta w_{s0})\right\} \tag{5.11a}$$

$$p_{s0\pm} = \mu\left\{\left[\frac{\kappa-1}{\kappa+1}\alpha\cot 2\alpha + \frac{1}{\kappa+1}\right]\Sigma w_n - \left[\alpha + \frac{\cot 2\alpha}{\kappa+1}(2\kappa\alpha\cot 2\alpha + 1)\right]\Delta w_s + \Delta w_{s0}\cot 2\alpha \pm \left[-\frac{\kappa+1}{\kappa-1}\alpha(\Delta w_n\cot 2\alpha + \Sigma w_s) + \Delta w_{n0}\right]\right\} \tag{5.11b}$$

If the boundary normal displacement derivative at the corner is continuous, i.e., $w_{n+}=w_{n-}=w_n$, and the boundary tangent displacement derivative at the corner is zero, i.e., $w_{s\pm}=0$, Eqs. (5.10*a*) and (5.10*b*) yield $p_{n\pm}=p_{s\pm}=0$. Hence, Eq. (5.4) is simplified to

$$u_n'(s) = w_n\ln|s| + w_{n0\pm} + W_n(s), \quad s>0 \text{ for plus sign}, \quad s<0 \text{ for minus sign} \tag{5.12a}$$

$$u_s'(s) = w_{s0\pm} + W_s(s), \quad s>0 \text{ for plus sign}, \quad s<0 \text{ for minus sign} \tag{5.12b}$$

Equations (5.11*a*) and (5.11*b*) are simplified to

$$t_{n\pm} = \mu\left[\frac{\kappa+1}{\kappa-1}\left(\Delta u_n'\cot 2\alpha + \frac{2}{\kappa+1}\Sigma u_s'\right) \pm (-2\alpha w_n - \Delta u_s')\right] \tag{5.13a}$$

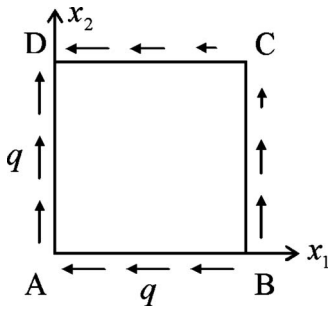

Fig. 4 Square ABCD under antisymmetric shear loading at corner A

$$t_{s\pm} = \mu\left[2\left(\frac{\kappa-1}{\kappa+1}\alpha\cot 2\alpha + \frac{1}{\kappa+1}\right)w_n + \cot 2\alpha\Delta u_s' \pm \Delta u_n'\right] \tag{5.13b}$$

where

$$\Delta u_n' = w_{n0+} - w_{n0-}, \quad \Delta u_s' = w_{s0+} - w_{s0-}, \quad \Sigma u_s' = w_{s0+} + w_{s0-}$$

Therefore, the discontinuous values of the tractions at the corner are as follows:

$$\Delta t_n = -2\mu(2\alpha w_n + \Delta u_s') \tag{5.14a}$$

$$\Delta t_s = 2\mu\Delta u_n' \tag{5.14b}$$

6 Numerical Example

6.1 A Square Under Antisymmetric Shear Loading at a Corner. In order to illustrate the application of the theory developed in this paper, a singular corner problem with analytical solution needs to be proposed. First consider an infinite antisymmetric wedge of angle $\pi/2$ subjected to an antisymmetric shear loading q as shown in Fig. 4, where A is the wedge-tip. The analytical displacements and stresses of the antisymmetric wedge can be obtained by using the results in Sec. 4. Now consider the unit square ABCD, which is a part of the infinite wedge as shown in Fig. 4. The tractions on the boundary of ABCD are as follows:

$$t_1 = -q, \quad t_2 = 0, \quad 0\le x_1\le 1, \quad x_2 = 0 \tag{6.1a}$$

$$t_1 = q\left[-\frac{2x_2}{1+x_2^2} + 2\tan^{-1}\left(\frac{1-x_2}{1+x_2}\right) + \frac{\pi}{2}\right], \quad t_2 = q\frac{1-x_2^2}{1+x_2^2}, \quad x_1 = 1, \quad 0\le x_2\le 1 \tag{6.1b}$$

$$t_1 = -q\frac{1-x_1^2}{1+x_1^2}, \quad t_2 = q\left[\frac{2x_1}{1+x_1^2} - 2\tan^{-1}\left(\frac{1-x_1}{1+x_1}\right) - \frac{\pi}{2}\right], \quad 0\le x_1\le 1, \quad x_2 = 1 \tag{6.1c}$$

$$t_1 = 0, \quad t_2 = q, \quad x_1 = 0, \quad 0\le x_2\le 1 \tag{6.1d}$$

The distribution of the shear tractions on ABCD are also shown in Fig. 4 (the nonzero normal tractions on BC and CD are not shown in Fig. 4). The displacements on the boundary of ABCD are as follows:

$$u_1 = \frac{\pi b}{4}x_1, \quad u_2 = bx_1\ln x_1, \quad 0\le x_1\le 1, \quad x_2 = 0$$

$$u_1 = -\frac{b}{2}x_2\ln r_2^2 + a\tan^{-1}\left(\frac{1-x_2}{1+x_2}\right) + \frac{\pi c}{4}, \quad u_2 = \frac{b}{2}\ln r_2^2 + ax_2\tan^{-1}\left(\frac{1-x_2}{1+x_2}\right) - \frac{\pi c}{4}x_2 \tag{6.2a}$$

$$x_1 = 1, \quad 0 \le x_2 \le 1,$$

$$u_1 = -\frac{b}{2}\ln r_1^2 - a x_1 \tan^{-1}\left(\frac{1-x_1}{1+x_1}\right) + \frac{\pi c}{4}x_1, \quad u_2 = \frac{b}{2}x_1 \ln r_1^2 - a \tan^{-1}\left(\frac{1-x_1}{1+x_1}\right) - \frac{\pi c}{4} \tag{6.2b}$$

$$x_2 = 1, \quad 0 \le x_1 \le 1 \tag{6.2c}$$

$$u_1 = -bx_2 \ln x_2, \quad u_2 = -\frac{\pi b}{4}x_2, \quad x_1 = 0, \quad 0 \le x_2 \le 1 \tag{6.2d}$$

where

$$a = q(\kappa - 1)/2\mu, \quad b = q(\kappa + 1)/2\mu, \quad c = q/\mu, \quad r_1^2 = 1 + x_1^2, \quad r_2^2 = 1 + x_2^2$$

6.2 Boundary Integration Equations and Numerical Methods. The displacement and traction boundary integral equations of an elastic body are [12] as follows:

$$\frac{1}{2}u_k(\mathbf{y}) + \int_S T_{ki}(\mathbf{x};\mathbf{y})u_i(\mathbf{x})dS(\mathbf{x}) = \int_S U_{ki}(\mathbf{x};\mathbf{y})t_i(\mathbf{x})dS(\mathbf{x}) \tag{6.3a}$$

and

$$\frac{1}{2}t_k(\mathbf{y}) = \int_S E_{ki}(\mathbf{x};\mathbf{y})t_i(\mathbf{x})dS(\mathbf{x}) - \int_S F_{ki}(\mathbf{x};\mathbf{y})\frac{du_i(\mathbf{x})}{dS}dS(\mathbf{x}) \tag{6.3b}$$

where the integration kernel U_{ki} has weak singularity, while the integration kernels T_{ki}, E_{ki}, and F_{ki} have Cauchy singularities when the field point $\mathbf{x}$ coincides with the source point $\mathbf{y}$. Note that a sufficient condition for the existence of Cauchy principal value integral is that density function in the integrand is continuous. Therefore, the traction BIE (6.3*b*) requires that tractions and displacement derivatives are continuous at the source points.

In traditional 2D BEMs, boundary displacements and tractions in an element are often represented by three-node quadratic element (BEM3n) shape functions, and the source and field points share the same nodes, namely, isoparametric element. A singular boundary point is usually located at an element intersection. Thus the field variables are always continuous inside an element. An element with a singular point located at its end is called singular element. Note that in order to satisfy the sufficient condition for the existence of Cauchy principal value integral, source point should not be located at the end point of a singular element. To overcome this problem, discontinuous element is used for singular elements, since all nodes in a discontinuous element are internal points of the element. The price of using discontinuous element is that the displacement continuity is lost at element intersection points. Details on discontinuous element can be found in Refs. [21,22,18]. Single-node quadratic element (SNQE) proposed by Li et al. [23] and Ke et al. [24] can solve this problem completely. SNQE has only one internal node, and the boundary displacement at all element intersection points are automatically continuous. Furthermore, if an element intersection point is not a singular point, the boundary displacement derivatives are discontinuous for BEM3n, but they are also automatically continuous for SNQE. This fact is very important to get highly accurate numerical results. SNQE not only can simplify the work of programming but also improve the computation precision greatly.

6.3 Numerical Results. In this section, BEM will be used to solve the square problem with displacement boundary conditions (6.2*a*), (6.2*b*), (6.2*c*), and (6.2*d*). In order to obtain accurate numerical results, it is important to determine the singularities of the boundary displacement derivatives first. The boundary displacement derivatives can be calculated from the prescribed boundary displacement (6.2*a*), (6.2*b*), (6.2*c*), and (6.2*d*) as follows:

$$\text{AB:} \quad \frac{du_1}{dx_1} = \frac{\pi b}{4}, \quad \frac{du_2}{dx_1} = b \ln x_1 + b \tag{6.4a}$$

$$\text{BC:} \quad \frac{du_1}{dx_2} = -\frac{b}{2}\ln r_2^2 - \frac{bx_2^2 + a}{r_2^2}, \quad \frac{du_2}{dx_2} = \frac{cx_2}{r_2^2} + a \tan^{-1}\left(\frac{1-x_2}{1+x_2}\right) - \frac{\pi c}{4} \tag{6.4b}$$

$$\text{CD:} \quad \frac{du_1}{dx_1} = -\frac{cx_1}{r_1^2} + a \tan^{-1}\left(\frac{1-x_1}{1+x_1}\right) + \frac{\pi c}{4}, \quad \frac{du_2}{dx_1} = \frac{b}{2}\ln r_1^2 + \frac{bx_1^2 + a}{r_1^2} \tag{6.4c}$$

$$\text{DA:} \quad \frac{du_1}{dx_2} = -b \ln x_2 - b, \quad \frac{du_2}{dx_2} = -\frac{\pi b}{4} \tag{6.4d}$$

Let A^+ denote $x_2 = 0$, $x_1 \to 0$, and A^- denote $x_1 = 0$, $x_2 \to 0$. At A^+ and A^-, we have

$$u'_{n+}(s) = -\frac{du_2}{dx_1}, \quad u'_{s+}(s) = \frac{du_1}{dx_1}; \quad u'_{n-}(s) = \frac{du_1}{dx_2}, \quad u'_{s-}(s) = \frac{du_2}{dx_2}$$

By using the above relations, it can be shown from Eqs. (6.4*a*), (6.4*b*), (6.4*c*), and (6.4*d*) that the intensities of the weak singularity of boundary normal displacement derivative at A^+ and A^- are of equal value $-b$, while the tangent displacement derivative at corner A has no weak singularity. The boundary displacement derivatives at corner A is of the same form as Eqs. (5.12*a*) and (5.12*b*). Hence, it can be concluded that the tractions at corner A have no weak singularity. The boundary displacement derivatives at the other three corners of the square are bounded, thus all tractions are bounded there. The tractions at the four corners of the square can be obtained by substituting the values of weak singularities and finite parts of the boundary displacement derivatives calculated from Eqs. (6.4*a*), (6.4*b*), (6.4*c*), and (6.4*d*) into Eqs. (5.11*a*) and (5.11*b*) ($\alpha = \pi/4$) as

$$\text{Corner A:} \quad t_1^{A+} = -q, \quad t_2^{A+} = 0; \quad t_1^{A-} = 0, \quad t_2^{A-} = q \tag{6.5a}$$

$$\text{Corner B:} \quad t_1^{B+} = \pi q, \quad t_2^{B+} = q; \quad t_1^{B-} = -q, \quad t_2^{B-} = 0 \tag{6.5b}$$

$$\text{Corner C:} \quad t_1^{C+} = 0, \quad t_2^{C+} = (1 - \pi/2)q; \quad t_1^{C-} = (\pi/2 - 1)q, \quad t_2^{C-} = 0 \tag{6.5c}$$

$$\text{Corner D:} \quad t_1^{D+} = 0, \quad t_2^{D+} = q; \quad t_1^{D-} = -q, \quad t_2^{D-} = -\pi q \tag{6.5d}$$

In traditional BEM, at a corner with displacements prescribed there are four unknown traction components, so, two auxiliary equations are needed. Since the four traction components are obtained before BEM analysis here, this difficulty does not exist anymore.

In the following, the square problem with boundary displacement boundary conditions (6.2*a*) and (6.2*b*) will be solved by BEM. For simplicity, let BEM3n and SNQE designate traditional three-node Lagrangian quadric isoparametric element and single node quadratic continuous element, respectively, and let TU and FE designate the displacement boundary integration (Eq. (6.3*a*)) and traction boundary integration (Eq. (6.3*b*)), respectively. Four

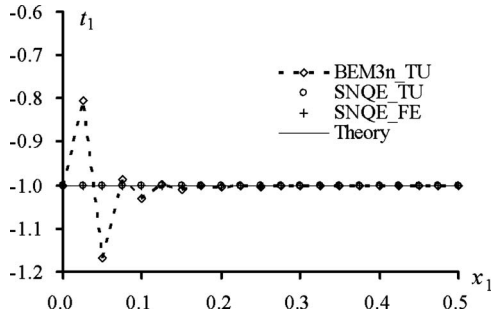

Fig. 5 Numerical and theoretical results of traction component t_1 on side AB for $0 \le x_1 \le 0.5$

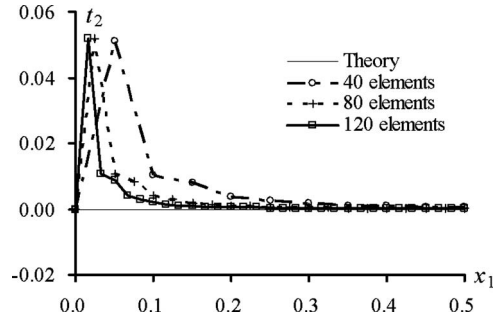

Fig. 8 Numerical results of traction component t_2 on side AB by using BEM3n_TU

possible methods with different combinations of BEM and boundary integration equation are BEM3n_TU, BEM3n_FE, SNQE_TU, and SNQE_FE, respectively, where, for example, BEM3n_TU means that displacement boundary integration (Eq. (6.3*a*)) with traditional three-node Lagrangian quadric isoparametric element is used to solve an elastic boundary value problem. It is important to indicate that BEM3n_FE cannot be used, since the tractions and displacement derivatives represented by the shape functions of BEM3n in BEM analysis at interelement nodes are discontinuous. The numerical results of tractions obtained from various methods will be compared with the theoretical results (6.1*a*), (6.1*b*), (6.1*c*), and (6.1*d*). In all cases, $q=1$ and 80 equal size elements are used. The numerical results of tractions on the side AB for $0 \le x_1 \le 0.5$ are shown in Figs. 5 and 6.

Figures 5 and 6 show that the numerical results by using SNQE are in good agreement with the theoretical results, and the result of SNQE_FE is a little better than that of SNQE_TU. However, large errors of the numerical results of BEM3n_TU appear near the corner A. Furthermore, the large errors for BEM3n_TU do not disappear with increasing numbers of elements that can be shown in Figs. 7 and 8.

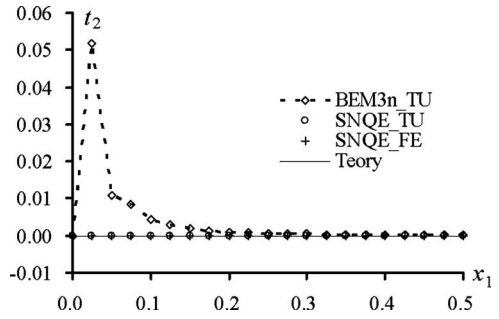

Fig. 6 Numerical and theoretical results of traction component t_2 on side AB for $0 \le x_1 \le 0.5$

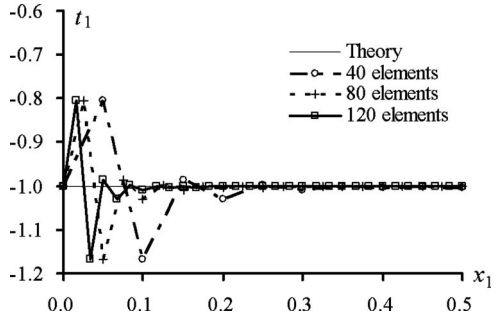

Fig. 7 Numerical results of traction component t_1 on side AB by using BEM3n_TU

The reason behind the large errors for BEM3n_TU near corner A comes from the fact that the boundary normal displacement derivative is weakly singular and the equivalent law of shearing stresses is not valid at corner A. Since BEM3n_TU is only C^0 continuous, it cannot reflect the singular behavior at corner A. However SNQE is C^1 continuous, it can correctly reflect the relations between the singularities of tractions and boundary displacement derivatives at corner A.

7 Discussions and Conclusions

The theoretical relations between the tractions and the boundary displacement derivatives at a corner of an elastic body have been studied in this paper. The prescribed boundary field variables (the tractions or the boundary displacement derivatives) at the corner are supposed to have discontinuity of the first kind and weak singularity but without any higher singularity. The singularity intensities of the unknown boundary variables can be obtained from the information of prescribed boundary field variables. Especially, if the boundary conditions at the corner are displacements prescribed, the values of the unknown tractions can be obtained at the very beginning of the BEM analysis, thus the difficulty of multivalued tractions at a corner is solved completely. By using this information, more appropriate shape functions for the unknown boundary field variables of a corner element can be constructed, and the accuracy of the BEM may be greatly increased.

Acknowledgment

The authors would like to acknowledge the funding support of the National Natural Science Foundation of China, Major Program No. 30490230 and First-Phase Preparations of 973 Program No. 2004ccA02500.

References

[1] Williams, M. L., 1952, "Stress Singularities Resulting From Various Boundary Conditions in Angular Comers of Plates in Extension," J. Appl. Mech., **19**, pp. 526–528.
[2] England, A. H., 1971, "On Stress Singularities in Linear Elasticity," Int. J. Eng. Sci., **9**, pp. 571–585.
[3] Rösel, R., 1987, "On the Wedge Notch Eigenvalues," Int. J. Fract., **33**, pp. 61–71.
[4] Vasilopoulos, D., 1988, "On the Determination of Higher Order Terms of Singular Elastic Stress Fields Near Corners," Numer. Math., **53**, pp. 51–95.
[5] Dempsey, J. P., and Sinclair, G. B., 1979, "On the Stress Singularities in the Plane Elasticity of the Composite Wedge," J. Elast., **9**, pp. 373–391.
[6] Dempsey, J. P., 1981, "The Wedge Subjected to Tractions: A Paradox Resolved," J. Elast., **11**, pp. 1–10.
[7] Ting, T. C. T., 1984, "The Wedge Subjected to Tractions: A Paradox Re-Examined," J. Elast., **14**, pp. 235–247.
[8] Blinova, V. G., and Linkov, A. M., 1995, "A Method to Find Asymptotic Forms at the Common Apex of Elastic Wedges," J. Appl. Math. Mech., **59**(2), pp. 187–195.
[9] Linkov, A. M., and Rybarska-Rusinek, L., 2008, "Numerical Method and Models for Anti-Plane Strain of a System With a Thin Elastic Wedge," Arch. Appl. Mech., **78**, pp. 821–831.
[10] Wang, M. Z., 1986, "The Wedge Subjected to General Tractions: A Paradox Resolved," Acta Mech. Sin., **18**, pp. 243–252 (in Chinese).
[11] Sinclair, G. B., 1999, "Logarithmic Stress Singularities Resulting From Vari-

ous Boundary Conditions in Angular Corners of Plates in Extension," ASME J. Appl. Mech., **66**, pp. 556–560.
[12] Brebbia, C. A., Telles, J. C. F., and Wrobel, L. C., 1984, *Boundary Element Techniques*, Spring-Verlag, New York.
[13] Portela, A., Aliabadi, M. H., and Rooke, D. P., 1991, "Efficient Boundary Element Analysis of Sharp Notched Plates," Int. J. Numer. Methods Eng., **32**, pp. 445–470.
[14] Jaswon, M. A., and Symm, G. T., 1977, *Integral Equation Methods in Potential Theory and Elasto-Statics*, Academic, London.
[15] Riccardella, P., 1973, "An Implementation of the Boundary Integral Techniques for Plane Problems in Elasticity and Elasto-Plasticity," Ph.D. thesis, Carnegie Mellon University, Pittsburgh, PA.
[16] Patterson, C., and Sheik, M. A., 1984, "Interelement Continuity in the Boundary Element Method," *Topics in Boundary Element Research*, C. A. Brebbia, ed., Springer-Verlag, Berlin, Vol. 1, pp. 123–141.
[17] Ma, J., and Le, M., 1992, "A New Method for Coupling of Boundary Element Method and Finite Element Method," Appl. Math. Model., **16**, pp. 43–46.
[18] Mitra, A. K., and Ingber, M. S., 1987, "Resolving Difficulties in The BIEM Caused by Geometric Comers and Discontinuous Boundary Conditions," *Boundary Elements IX*, C. A. Brebbia, ed., Computational Mechanics Publications, San Diego, CA/Academic, New York, Vol. 1, pp. 519–532.
[19] Rudolphi, T., Agarwal, R., and Mitra, A., 1991, "Coupling Boundary Integral Equations With Nonsingular Functional Equations by Exterior Collocation," Eng. Anal. Boundary Elem., **8**(5), pp. 245–251.
[20] Gray, L. J., and Lutz, E., 1990, "On the Treatment of Comers in the Boundary Element Method," J. Comput. Appl. Math., **32**, pp. 369–86.
[21] Krishnasamy, G., Rizzo, F. J., and Rudolphi, T. J., 1992, "Continuity Requirements for Density Functions in the Boundary Integral Equation Method," Comput. Mech., **9**, pp. 267–284.
[22] Martin, P. A., and Rizzo, F. J., 1996, "Hypersingular Integrals: How Smooth Must the Density Be," Int. J. Numer. Methods Eng., **39**, pp. 687–704.
[23] Li, Z. L., Zhan, F. L., and Du, S. H., 2000, "A Highly Accurate BEM in Fracture Mechanics," Key Eng. Mater., **183-187**, pp. 91–96.
[24] Ke, L., Wang, Ch., and Zhan, F. L., 2002, "BEM With Single-Node Quadratic Element in Crack Analysis," Acta Mech. Solida Sinica, **23**, pp. 54–64 (in Chinese).

Modeling and Nonlinear Vibration Analysis of a Rigid Rotor System Supported by the Magnetic Bearing (Effects of Delays of Both Electric Current and Magnetic Flux)

Tsuyoshi Inoue
Department of Mechanical Science and Engineering,
School of Engineering,
Nagoya University,
Nagoya 464-8603, Japan
e-mail: inoue@nuem.nagoya-u.ac.jp

Yasuhiko Sugawara
Daihatsu Motor Co., Ltd.,
1-1 Daihatsu-cho,
Ikeda,
Osaka 563-8651, Japan

Motoki Sugiyama
Tokai Rika Co., Ltd.,
3-260 Toyota,
Oguchi-cho, Niwa-gun,
Aichi 480-0195, Japan

Active magnetic bearing (AMB) becomes widely used in various kinds of rotating machinery. However, as the magnetic force is nonlinear, nonlinear phenomena may occur when the rotating speed becomes high and delays of electric current or magnetic flux in the AMB relatively increase. In this paper, the magnetic force in the AMB is modeled by considering both the second-order delay of the electric current and the first-order delay of the magnetic flux. The magnetic flux in the AMB is represented by a power series function of the electric current and shaft displacement, and its appropriate representation for AMB is discussed. Furthermore, by using them, the nonlinear theoretical analysis of the rigid rotor system supported by the AMB is demonstrated. The effects of the delays and other AMB parameters on the nonlinear phenomena are clarified theoretically, and they are confirmed experimentally. [DOI: 10.1115/1.3172139]

1 Introduction

Active magnetic bearing (AMB) [1,2] is practically used in various industries because it has the superior features such as no friction, no wear, and extremely small mechanical loss, compared with a rolling bearing or a journal bearing. Moreover, the application of AMB for the vibration control has been researched [3].

Because the magnetic force is nonlinear, various nonlinear phenomena, which cannot be clarified by conventional linear analysis, may occur in the rotor systems supported by magnetic bearing [4–15]. The jump phenomena [7] and superharmonic resonances [10] can be given as examples. So far, most of these studies on such nonlinear phenomena have been based on numerical simulations, and considered special cases such as the case with small damping effects. These researches may fail to give the solutions for the nonlinear phenomena in practical systems up to now.

The dynamics of the control system are generated by the factors such as slight delays of electric current and magnetic flux. When a high-speed rotor system is supported by the magnetic bearing, these dynamics of control system become relatively large and not negligible. Then, they couple with the nonlinearity of the AMB, and may cause nonlinear phenomena. Thus, the occurrence mechanism of such nonlinear phenomena and clarification of these characteristics are important in the vibration suppression of the high-speed rotor supported by the magnetic bearing. However, no other research has been reported on the above topic.

Recently, Inoue et al. [16] investigated the nonlinear vibration of rotor supported by the magnetic bearing considering the effect of the delay of control force. In that paper, the delay of control force is simply modeled by the first-order delay of electric current, and the synergistic effects of both the delay and the nonlinearity of magnetic force are reported. However, the detailed influence of the delay of the actual control circuit, which consists of both electric and magnetic circuits, is not clarified. In order to avoid vibration problems, the difference of the delay in the electric part and magnetic part on the vibration characteristic should be clarified.

This study considers the rigid rotor system supported vertically by the magnetic bearing, and investigates the influences of the delays of both the electric part and the magnetic part of the AMB on the dynamical characteristics. Such delays may occur in various parts in AMB such as sensors, analog-to-digital (A/D) and digital-to-analog (D/A) converters, the electric current in the power amplifier, and the magnetic flux in the electromagnet. This study performs the nonlinear analysis in order to clarify the effects of parameters of magnetic bearing on the vibration characteristics, and confirms the theoretical results by experiments.

2 Theoretical Model

2.1 Equations of Motion for the Rotor System. This study considers the vertical rigid rotor that is supported by the AMB at the lower end as shown in Fig. 1. The upper end of the shaft is simply supported by a ball bearing. Two disks, disk 1 and disk 2, are mounted on the shaft. The displacement of disk 2 is represented by the coordinates (x, y).

The bias electric current of the AMB is I_0, and the electric currents applied for electromagnets $x1$, $x2$, $y1$, and $y2$, shown in Fig. 1(*b*), are $I_{x1}=I_0-i_x$, $I_{x2}=I_0+i_x$, $I_{y1}=I_0-i_y$, and $I_{y2}=I_0+i_y$, respectively. Electromagnetic forces of these electromagnets are expressed by F_{x1}, F_{x2}, F_{y1}, and F_{y2}, respectively. Forces F_{x1} and F_{x2} show the magnetic forces in the x direction, and forces F_{y1} and F_{y2} show the magnetic forces in the y direction, respectively.

By using the notation of shaft length l and the relationships $x=l\theta_x$ and $y=l\theta_y$, the equations of motion in terms of the shaft displacements x and y are obtained as

$$I_d\ddot{x} + I_p\omega\dot{y} = l^2(F_{x1} - F_{x2}) + l^2me\omega^2 \cos \omega t$$

Contributed by the Applied Mechanics Division of ASME for publication in the JOURNAL OF APPLIED MECHANICS. Manuscript received September 8, 2008; final manuscript received April 28, 2009; published online September 24, 2009. Review conducted by N. Sri Namachchivaya.

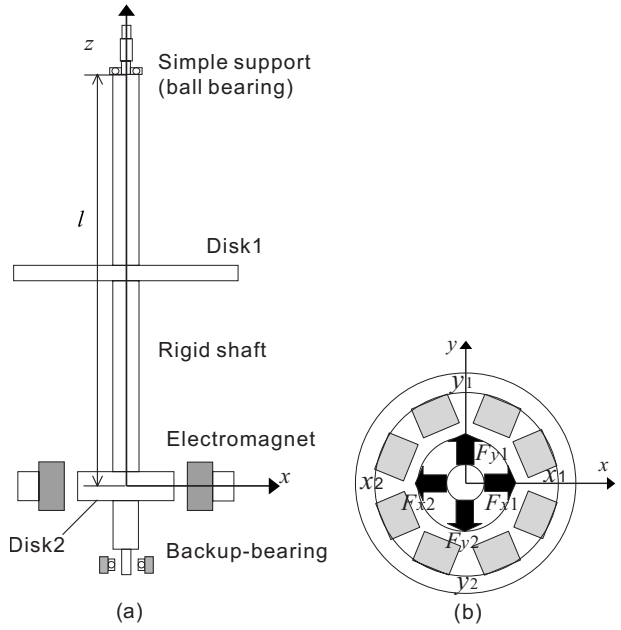

Fig. 1 Model of the AMB and the rotor system

$$I_d\ddot{\psi} - I_p\omega\dot{x} = l^2(F_{y1} - F_{y2}) + l^2me\omega^2 \sin \omega t \tag{1}$$

where I_d is the diametral moment of inertia of the rotor about the upper support point, I_p is the polar moment of inertia, m is the equivalent mass at disk 2 position, e is the equivalent static unbalance at disk 2, ω is the rotational speed, and t is time. The second term in the left side represents gyroscopic effect.

It is assumed that magnetic flux saturation does not occur in the electromagnet core. In this case, in general, the magnetic flux density B[T] and the magnetic force f_m[N] of the electromagnet can be represented as follows [1,2]:

$$B = \frac{\mu_0 NI}{\left(2R + \dfrac{l_m}{\mu_s}\right)} = \frac{\mu_0 NI}{2(R+\delta)}$$

$$f_m = \frac{B^2}{2\mu_0}2S = k_m\frac{I^2}{(R+\delta)^2} \tag{2}$$

Here, N is the turn number of the coil, I is the electric current, μ_0 is the magnetic permeability in the vacuum, μ_s is the relative permeability of the electromagnet iron core, l_m is the magnetic path length of the electromagnet, S is the area of the electromagnet pole, and R is the gap between the rotor and the electromagnet. The notations $k_m = \mu_0 SN^2/4$ and $\delta = l_m/2\mu_s$ are the characteristic constants of magnetic force.

In this paper, in order to consider the delay of magnetic flux, the magnetic force is represented in terms of magnetic flux density. The four magnetic forces of the AMB, F_{x1}, F_{x2}, F_{y1}, and F_{y2} shown in Fig. 1(*b*), are represented from Eq. (2) as follows:

$$F_{x1} = \frac{S}{\mu_0}(B_0 + B_{x1})^2, \quad F_{x2} = \frac{S}{\mu_0}(B_0 + B_{x2})^2$$

$$F_{y1} = \frac{S}{\mu_0}(B_0 + B_{y1})^2, \quad F_{y2} = \frac{S}{\mu_0}(B_0 + B_{y2})^2 \tag{3}$$

Here, B_0 is the bias magnetic flux density due to the bias electric current I_0. The notations B_{x1}, B_{x2}, B_{y1}, and B_{y2} are the variations of magnetic flux density in electromagnet poles $x1$, $x2$, $y1$, and $y2$, respectively. The bias magnetic flux density B_0 is obtained from Eq. (2) as

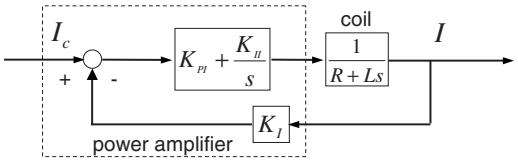

Fig. 2 Block diagram of the amplifier

$$B_0 = \frac{\mu_0 N}{2}\frac{I_0}{(R_0+\delta)} \tag{4}$$

Here, R_0 is the equilibrium gap.

Thus, the equations of motion, Eq. (1), are re-arranged in terms of the magnetic flux density as

$$I_d\ddot{x} + I_p\omega\dot{y} = l^2\frac{S}{\mu_0}\{(B_0 + B_{x1})^2 - (B_0 + B_{x2})^2\} + l^2me\omega^2 \cos \omega t$$

$$I_d\ddot{y} - I_p\omega\dot{x} = l^2\frac{S}{\mu_0}\{(B_0 + B_{y1})^2 - (B_0 + B_{y2})^2\} + l^2me\omega^2 \sin \omega t \tag{5}$$

2.2 Dynamical Equations of the Electric Circuit and the Magnetic Circuit. It is known that the magnetic flux density of the electromagnet shows the characteristic that is similar to the first-order dynamical characteristic [2]. In this paper, it is assumed that the variations of magnetic flux densities $B_{x1}, \ldots, B_{y2}$ around the bias magnetic flux density B_0 have the first-order dynamical characteristics, and they are represented as follows [2]:

$$B_0 + B_{x1} + \beta\dot{B}_{x1} = \frac{\mu_0 N}{2}\frac{(I_0 - i_x)}{(R_0 + \delta - x)}$$

$$B_0 + B_{x2} + \beta\dot{B}_{x2} = \frac{\mu_0 N}{2}\frac{(I_0 + i_x)}{(R_0 + \delta + x)}$$

$$B_0 + B_{y1} + \beta\dot{B}_{y1} = \frac{\mu_0 N}{2}\frac{(I_0 - i_y)}{(R_0 + \delta - y)}$$

$$B_0 + B_{y2} + \beta\dot{B}_{y2} = \frac{\mu_0 N}{2}\frac{(I_0 + i_y)}{(R_0 + \delta + y)} \tag{6}$$

Here, i_x and i_y are the electric current variations of the electromagnets.

There are many types of power operational amplifiers, which supply only positive electric current. Furthermore, in order to avoid the destabilization, the electromagnet current is usually not supplied when the reference (ordered) value becomes negative. When such an amplifier is used or such a control method is applied, the right sides of Eq. (6) show piecewise characteristics. For example, the right side of the first equation of Eq. (6) becomes

$$B_0 + B_{x1} + \beta\dot{B}_{x1} = \begin{cases} \dfrac{\mu_0 N}{2}\dfrac{(I_0 - i_x)}{(R_0 + \delta - x)} & (i_x < I_0) \\ 0 & (i_x > I_0) \end{cases} \tag{7}$$

Next, the dynamical equations of the electric current variations i_x and i_y are represented. In this modeling, the characteristics of a current-control-type power amplifier, which is used in the experiment, are taken into consideration. Figure 2 shows the block diagram of such a current-control-type power amplifier, and it shows the dynamics of electric current variation i_x. Symbols K_{PI}, K_{II}, and K_I are the parameters in the power amplifier, and symbols R and L are the parameters, which denote the resistance and the inductance of the coil. The input signal I_c and the output current I of the power amplifier are $I_c = K_I(I_0 + k_p x + k_d\dot{x})$ and $I = I_0 + i_x$, respectively. The parameters k_p and k_d are the feedback coefficients for displacement and velocity of the rotor. The used power amplifier

has the PI control characteristic. From the block diagram, the governing equation of the electric current variation i_x can be derived as

$$i_x + \alpha_1 \dot{i}_x + \alpha_2 \ddot{i}_x = k_p x + k_v \dot{x} + k_a \ddot{x} \tag{8}$$

where α_1 and α_2 are the coefficients of the first- and second-order derivatives of the electric current variation. These coefficients are determined in terms of the parameters of power amplifier and coil as follows:

$$\alpha_1 = \frac{R + K_I K_{PI}}{K_I K_{II}}, \quad \alpha_2 = \frac{L}{K_I K_{II}}, \quad k_v = k_d + \frac{K_{PI}}{K_{II}} k_p, \quad k_a = \frac{K_{PI}}{K_{II}} k_d \tag{9}$$

The governing equation of the electric current variation i_y is also derived in the same manner.

2.3 Dimensionless Form. By using the coefficient of the electromagnet $k_m = \mu_0 S N^2/4$, by eliminating the time derivative terms in Eqs. (6) and (8), and by performing the system linearization of Eqs. (5) and (6) for the equilibrium position, the stiffness coefficient k of the linearized system, $I_d \ddot{x} + I_p \omega \dot{y} + kx = l^2 m e \omega^2 \cos \omega t$, is obtained as $k = 4l^2 k_m I_0 \{k_p - I_0/(R_0 + \delta)\}/(R_0 + \delta)^2$. Then, by using the natural frequency $p = \sqrt{k/I_d}$ for the nonrotating condition, the dimensionless values are obtained as

$$\acute{i}_p = I_p/I_d, \quad \acute{\omega} = \omega/p, \quad \acute{t} = tp, \quad \acute{e} = l^2 m e/(I_d R_0)$$

$$\acute{x} = x/R_0, \quad \acute{y} = y/R_0, \quad \acute{i}_x = i_x/I_0, \quad \acute{i}_y = i_y/I_0$$

$$\acute{B}_{x1} = B_{x1}/B_0, \quad \acute{B}_{x2} = B_{x2}/B_0, \quad \acute{B}_{y1} = B_{y1}/B_0, \quad \acute{B}_{y2} = B_{y2}/B_0$$

$$\acute{k}_p = k_p R_0/I_0, \quad \acute{k}_d = k_d R_0 p/I_0, \quad \acute{k}_v = k_v R_0 p/I_0 \tag{10}$$

$$\acute{k}_a = k_a R_0 p^2/I_0, \quad \acute{k}_m = \frac{l^2 I_0^2 k_m}{k R_0 (R_0 + \delta)^2}$$

$$\acute{\alpha}_1 = \alpha_1 p, \quad \acute{\alpha}_2 = \alpha_2 p^2, \quad \acute{\beta} = \beta p, \quad \acute{\delta} = \delta/R_0$$

Thus, the dimensionless forms of the equations of motion, Eqs. (5), (6), and (8), are represented as

$$\ddot{x}' + i_p \omega' \dot{y}' = k_m' \{(1 + B_{x1}')^2 - (1 + B_{x2}')^2\} + e' \omega'^2 \cos \omega' t'$$
$$\ddot{y}' - i_p \omega' \dot{x}' = k_m' \{(1 + B_{y1}')^2 - (1 + B_{y2}')^2\} + e' \omega'^2 \sin \omega' t' \tag{11}$$

$$1 + B_{x1}' + \beta' \dot{B}_{x1}' = \begin{cases} (1 + \delta') \left(\dfrac{1 - i_x'}{1 + \delta' - x'} \right) & (i_x' < 1) \\ 0 & (i_x' > 1) \end{cases}$$

$$1 + B_{x2}' + \beta' \dot{B}_{x2}' = \begin{cases} (1 + \delta') \left(\dfrac{1 + i_x'}{1 + \delta' + x'} \right) & (i_x' > -1) \\ 0 & (i_x' < -1) \end{cases} \tag{12}$$

$$1 + B_{y1}' + \beta' \dot{B}_{y1}' = \begin{cases} (1 + \delta') \left(\dfrac{1 - i_y'}{1 + \delta' - y'} \right) & (i_y' < 1) \\ 0 & (i_y' > 1) \end{cases}$$

$$1 + B_{y2'} + \beta' \dot{B}_{y2'} = \begin{cases} (1 + \delta') \left(\dfrac{1 + i_y'}{1 + \delta' + y'} \right) & (i_y' > -1) \\ 0 & (i_y' < -1) \end{cases}$$

Table 1 Parameter values

K_{PI}	15.0 V/V
K_I	1.0 V/A
R_0	0.8 mm
I_0	0.5 A
I_d	5.43×10^5 kg mm^2
m	2.043 kg
α_1	3.795×10^{-2} s
β	3.66×10^{-3} s
K_{II}	606 V/V s
k_m	1.56×10^4 kg mm^3/A^2 s^2
δ	0.141 mm
l	5.00×10^2 mm
I_p	1.33×10^4 kg mm^2
e	2.928×10^{-2} mm
α_2	2.29×10^{-5} s^2
N	300 turns

$$\alpha_2' \dddot{i}_x' + \alpha_1' \ddot{i}_x' + \dot{i}_x' = k_p' x' + k_v' \dot{x}' + k_a' \ddot{x}'$$
$$\alpha_2' \dddot{i}_y' + \alpha_1' \ddot{i}_y' + \dot{i}_y' = k_p' y' + k_v' \dot{y}' + k_a' \ddot{y}' \tag{13}$$

In the following analysis, these equations in the dimensionless form are used. The symbol ($'$), which denotes dimensionless value, is omitted.

Table 1 shows the system parameters used in this paper. The feedback coefficients k_p and k_d are designed by the optimal regulator theory. The obtained values of the feedback coefficients k_p and k_d for the parameters in Table 1 are $k_{p\text{opt}} = 1.062$ A/mm and $k_{d\text{opt}} = 0.01149$ A s/mm in dimensional form. In this paper, the standard values of k_p and k_d are set to $k_p = 1.1$ A/mm and $k_d = 0.007$ A s/mm. The natural frequency $p = \sqrt{k/I_d}$ in the nonrotating condition is calculated for these standard values of k_p and k_d and the values of Table 1, and is obtained as $p = 83.856$ rad/s ($\simeq 800$ rpm) as shown in Table 2.

2.4 Power Series Approximate Model for Magnetic Flux Density. Figure 3 shows the magnetic flux density $(1 + B_{x1})$ in the static case ($\dot{B}_{x1} = 0$) of Eq. (12). In the usage of conventional nonlinear analysis techniques, such an expression with piecewise characteristic is not suitable. Thus, this paper introduces the expression of the magnetic flux density, which is represented in terms of power series function of both the electric current and shaft displacement.

First, the power series approximation for Eq. (12) is performed, and then, the accuracy of approximation is investigated by comparing the numerical simulation results obtained from the case of piecewise model and the case of power series approximation model. As the result, it is clarified that at least the seventh-order power series function is required for the accurate approximation. In the case of seventh-order power series function, 35 terms ap-

Table 2 Values used in nondimensionalization (feedback parameter values and natural frequency) and delay coefficient in dimensionless value

	Dimensional value	Dimensionless value
k_{p0}	1.100 A/mm	1.76
k_{d0}	0.007 A s/mm	0.587
p	800 rpm	1.0
R_0	0.8 mm	1.0
I_0	0.5 A	1.0
α_{10}	3.795×10^{-2} s	3.180
α_{20}	2.29×10^{-5} s^2	0.161
β_0	3.66×10^{-3} s	0.307

pear in the approximation of each electromagnet, and the total number of the terms for the AMB attains 140, which is a large number for the nonlinear theoretical analysis.

Then, the more appropriate transformation of the expression of magnetic flux density is considered in order to reduce the number of power series terms. To this end, the first term of the right side of the Eq. (11) is noted, and is arranged as

$$k_m\{(1+B_{x1})^2-(1+B_{x2})^2\}=k_m(2+B_{x1}+B_{x2})(B_{x1}-B_{x2})$$

$$\equiv k_m(2+B_{xp})B_{xm} \tag{14}$$

where the new variables of magnetic flux density $B_{xp}=B_{x1}+B_{x2}$ and $B_{xm}=B_{x1}-B_{x2}$ are introduced. The governing equations of B_{xp} and B_{xm} are obtained by the calculations of addition and subtraction of the first and second equations in Eq. (12) as

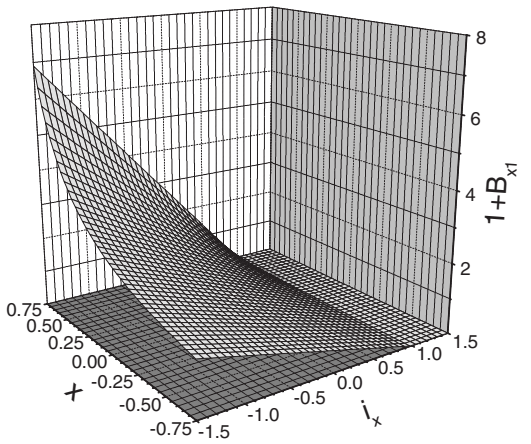

Fig. 3 Magnetic flux density B_{x1} (piecewise function expression)

$$2+B_{xp}+\beta\dot{B}_{xp}=\begin{cases}(1+\delta)\left(\dfrac{1-i_x}{1+\delta-x}\right) & (i_x<-1)\\ (1+\delta)\left\{\left(\dfrac{1-i_x}{1+\delta-x}\right)+\left(\dfrac{1+i_x}{1+\delta+x}\right)\right\} & (-1<i_x<1)\\ (1+\delta)\left(\dfrac{1+i_x}{1+\delta+x}\right) & (1<i_x)\end{cases}$$

$$B_{xm}+\beta\dot{B}_{xm}=\begin{cases}(1+\delta)\left(\dfrac{1-i_x}{1+\delta-x}\right) & (i_x<-1)\\ (1+\delta)\left\{\left(\dfrac{1-i_x}{1+\delta-x}\right)-\left(\dfrac{1+i_x}{1+\delta+x}\right)\right\} & (-1<i_x<1)\\ -(1+\delta)\left(\dfrac{1+i_x}{1+\delta+x}\right) & (1<i_x)\end{cases} \tag{15}$$

The governing equations of B_{yp} and B_{ym} in the y direction are also derived in the same manner.

Figures 4(a) and 5(a) show the values of the terms in the right sides of Eq. (15). From the observations of Figs. 4(a) and 5(a), it seems that the proposed expressions of B_{xp} and B_{xm} can be represented by even and odd order power series functions of x and i_x, respectively. In this paper, they are represented up to the seventh-order terms as

$$\begin{aligned}2+B_{xp}+\beta\dot{B}_{xp}=&\,2+a_{20}x^2+a_{11}xi_x+a_{02}i_x^2+a_{40}x^4+a_{31}x^3i_x\\&+a_{22}x^2i_x^2+a_{13}xi_x^3+a_{04}i_x^4+a_{60}x^6+a_{51}x^5i_x\\&+a_{42}x^4i_x^2+a_{33}x^3i_x^3+a_{24}x^2i_x^4+a_{15}xi_x^5+a_{06}i_x^6\end{aligned}$$

$$\begin{aligned}B_{xm}+\beta\dot{B}_{xm}=&\,a_{10}x+a_{01}i_x+a_{30}x^3+a_{21}x^2i_x+a_{12}xi_x^2+a_{03}i_x^3\\&+a_{50}x^5+a_{41}x^4i_x+a_{32}x^3i_x^2+a_{23}x^2i_x^3+a_{14}xi_x^4\\&+a_{05}i_x^5+a_{70}x^7+a_{61}x^6i_x+a_{52}x^5i_x^2+a_{43}x^4i_x^3\\&+a_{34}x^3i_x^4+a_{25}x^2i_x^5+a_{16}xi_x^6+a_{07}i_x^7\end{aligned} \tag{16}$$

In this modeling, the total number of terms in the AMB is reduced from 140 to 70, which is a half of the case of power series approximation for Eq. (12).

In the coefficients $a_{10},\ldots,a_{07}$ in Eq. (16), the linear coefficients a_{10} and a_{01} are obtained analytically from Eq. (15), and the other nonlinear coefficients are obtained by using the least square method. These dimensionless values a_{ij} depend only on the value of δ because the expressions in the right sides of Eq. (15) have only the parameter δ. When the dimensionless value $\delta=0.141$ for the experimental setup is substituted in Eq. (15), the coefficients $a_{10},\ldots,a_{07}$ are obtained as

$$a_{10}=\frac{2}{1+\delta},\ a_{01}=-2,\ a_{20}=1.667,\ a_{11}=-1.709,\ a_{02}=-0.158$$

$$a_{30}=1.430,\ a_{21}=-1.120,\ a_{12}=-0.151,\ a_{03}=-0.267$$

$$a_{40}=0.109,\ a_{31}=-1.114,\ a_{22}=-0.303,\ a_{13}=-0.046$$

$$a_{04}=0.245,\ a_{50}=0.052,\ a_{41}=-1.394,\ a_{32}=-0.257$$

$$a_{23}=-0.382,\ a_{14}=0.232,\ a_{05}=0.406$$

$$a_{60}=2.310,\ a_{51}=-1.837,\ a_{42}=0.276,\ a_{33}=0.215$$

$$a_{24}=0.192,\quad a_{15}=0.080,\quad a_{06}=-0.032$$

$$a_{70}=2.016,\quad a_{61}=-1.424,\quad a_{52}=0.211,\quad a_{43}=0.396$$

$$a_{34}=0.170,\quad a_{25}=0.152,\quad a_{16}=-0.036,\quad a_{07}=-0.099 \tag{17}$$

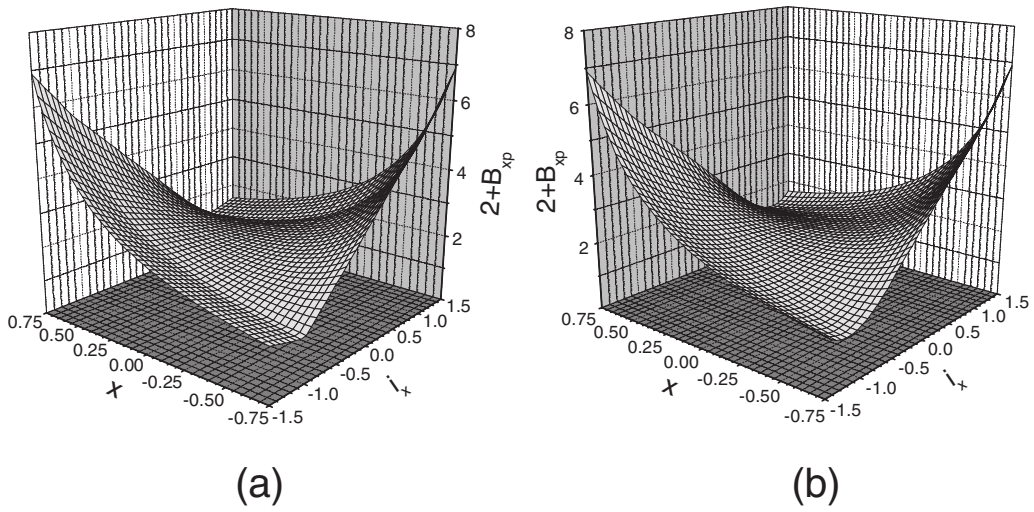

Fig. 4 Comparison between two expressions (B_{xp}): (*a*) piecewise model and (*b*) seventh-order power series model

In this calculation of the least square method, the data of the ranges $-1.5 < i < 1.5$ and $-0.75 < x < 0.75$ are used.

Figures 4(*b*) and 5(*b*) show the values of the right sides in Eq. (16). It is shown that they are satisfactory approximations of Figs. 4(*a*) and 5(*a*).

3 Nonlinear Theoretical Analysis

Figure 6 shows the time histories of the rotor displacement, control current, and the magnetic flux density at the rotational speed $\omega = 1.18$, which is close to the resonance peak. The orbits of rotor displacement, control current, and magnetic flux density B_{xm}, B_{ym} show the circle shape, and their spectrum diagram shows only ω component. The orbit of magnetic flux density B_{xp}, B_{yp} shows a line shape, and its spectrum diagram shows both constant component and $\pm 2\omega$ components.

In this paper, the method of Van der Pol [18] is used for the nonlinear theoretical analysis. In this method, the solution is assumed first based on the observation and insight, and it is substituted into the equation of motion. Then, a set of the fundamental equations with unknown variables is derived in a harmonic balance manner, but it includes the terms of the time derivative of the unknown variables. Hence, by this method, the stability of the steady state solution is also able to analyze [18].

In this case, from the observation of Fig. 6, the solution is assumed as

$$x = P_c \cos \omega t - P_s \sin \omega t, \quad y = P_s \cos \omega t + P_c \sin \omega t$$

$$i_x = C_{ic} \cos \omega t - C_{is} \sin \omega t, \quad i_y = C_{is} \cos \omega t + C_{ic} \sin \omega t$$

$$B_{xm} = B_{mc} \cos \omega t - B_{ms} \sin \omega t, \quad B_{ym} = B_{ms} \cos \omega t + B_{mc} \sin \omega t$$

$$B_{xp} = B_{xa} + B_{pc} \cos 2\omega t - B_{ps} \sin 2\omega t$$

$$B_{yp} = B_{ya} - B_{pc} \cos 2\omega t + B_{ps} \sin 2\omega t \tag{18}$$

The number of the variables is ten in this case. For the comparison, if the solution was assumed for the equations in terms of B_{x1}, B_{x2}, B_{y1}, and B_{y2}, the number of the variables would be at least 14. Therefore, the proposed expression of Eq. (16) can reduce the number of the variables in the assumed solution. It makes the nonlinear theoretical analysis much simpler.

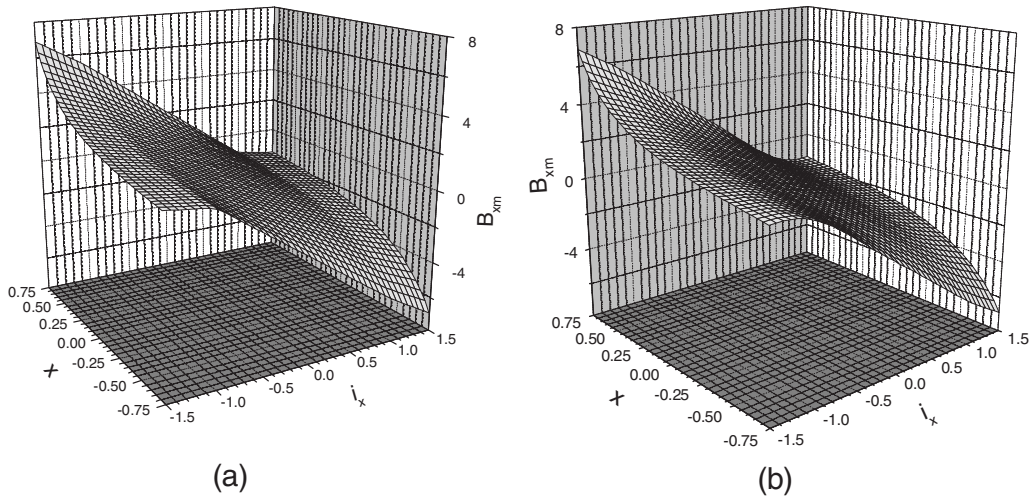

Fig. 5 Comparison between two expressions (B_{xm}): (*a*) piecewise model and (*b*) seventh-order power series model

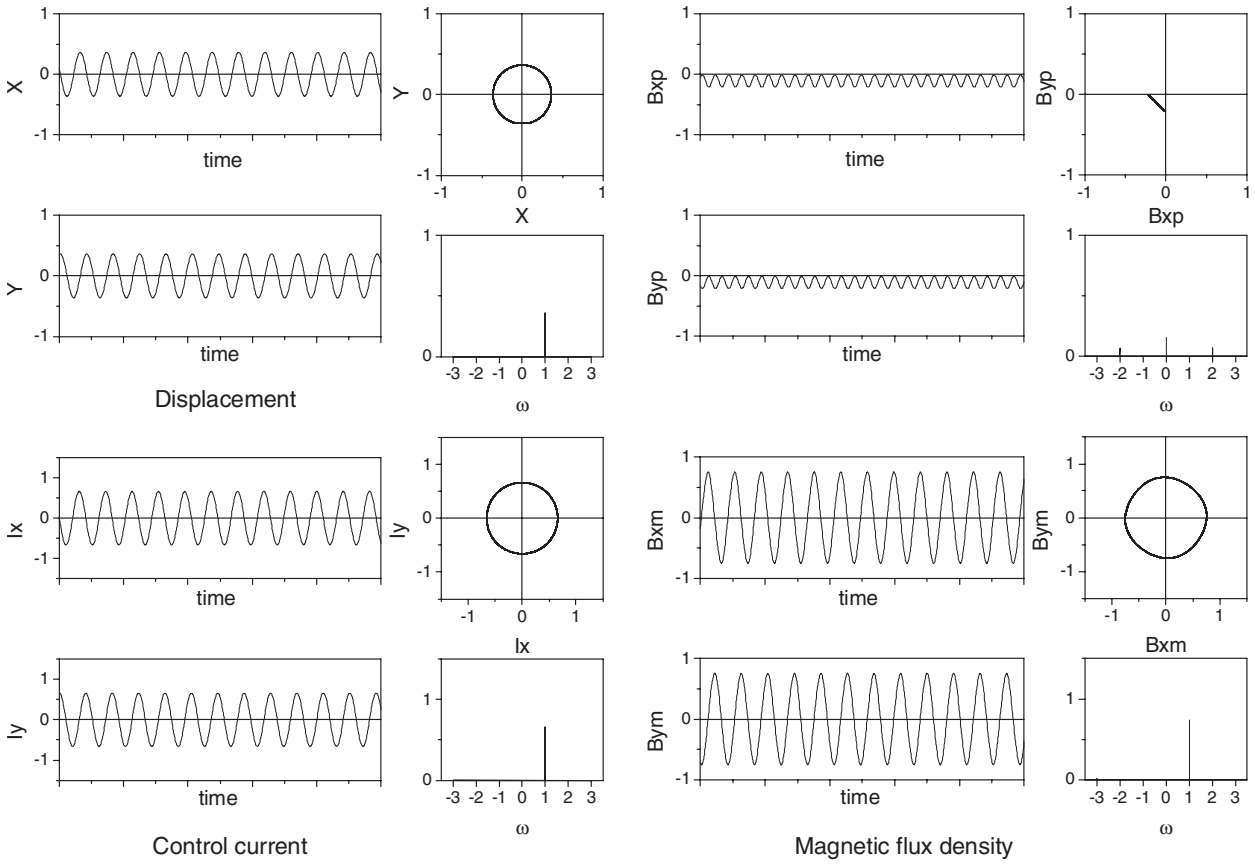

Fig. 6 Time histories at ω=1.18 (close to the critical speed). The parameters correspond to those of Fig. 7.

Equation (18) is substituted into equations of motion, Eqs. (11), (13), and (16). Here, variables P_c, P_s, C_{ic}, C_{is}, B_{mc}, B_{ms}, B_{pc}, B_{ps}, B_{xa}, and B_{ya} are assumed to be "functions, which vary slowly with the time" [17,18]. Thus, for example, the magnitudes of $\dot{P}_c$ and $\ddot{P}_c$ are considered as $O(\varepsilon)$ and $O(\varepsilon^2)$, respectively. Here, the symbol $O(\varepsilon)$ expresses the magnitudes of the same order as the small parameter ε. The coefficients of $\sin\omega t$ and $\cos\omega t$ on both sides of the six equations, which are Eqs. (11) and (13) and the second equation of Eq. (16), are equated in the accuracy of $O(\varepsilon)$. Furthermore, the constant components and the coefficients of $\sin 2\omega t$ and $\cos 2\omega t$ on both sides of the first equation of Eq. (16) are equated in the accuracy of $O(\varepsilon)$. Then, the following fundamental equations are obtained as follows. The seventh-order power series expression of Eq. (16) is used in this calculation. The concrete forms of these equations are not shown for the sake of brevity.

$$\dot{P}_c = f_1(P_c, P_s, C_{ic}, C_{is}, B_{mc}, B_{ms}, B_{pc}, B_{ps}, B_{xa}, B_{ya})$$

$$\dot{P}_s = f_2(P_c, \ldots, B_{ya})$$

$$\dot{C}_{ic} = f_3(P_c, \ldots, B_{ya}), \quad \dot{C}_{is} = f_4(P_c, \ldots, B_{ya})$$

$$\dot{B}_{mc} = f_5(P_c, \ldots, B_{ya}), \quad \dot{B}_{ms} = f_6(P_c, \ldots, B_{ya})$$

$$\dot{B}_{xa} = f_7(P_c, \ldots, B_{ya}), \quad \dot{B}_{ya} = f_8(P_c, \ldots, B_{ya})$$

$$\dot{B}_{pc} = f_9(P_c, \ldots, B_{ya}), \quad \dot{B}_{ps} = f_{10}(P_c, \ldots, B_{ya}) \tag{19}$$

The steady state solutions, P_{c0}, P_{s0}, C_{ic0}, C_{is0}, B_{mc0}, B_{ms0}, B_{pc0}, B_{ps0}, B_{xa0}, and B_{ya0}, are obtained by setting the derivative terms on the left sides of Eq. (19) equal to 0 and by solving these nonlinear algebraic equations. The stability of these obtained steady state solutions is investigated by the eigenvalue analysis.

Figure 7 shows the resonance curves of the amplitude P of the harmonic component $+\omega$. The abscissa shows the rotational speed ω, which is the dimensionless value to the natural frequency p. The ordinate r shows the shaft amplitude, which is the dimensionless value to the equilibrium gap R_0. Both values p and R_0 are shown in Table 2. The values of parameters k_p, k_d, and I_0 are the dimensionless value denoting the ratio from the dimensional values in Table 2. The line represents the solution obtained from Eq. (19), and the solid line denotes the stable solution. The circle

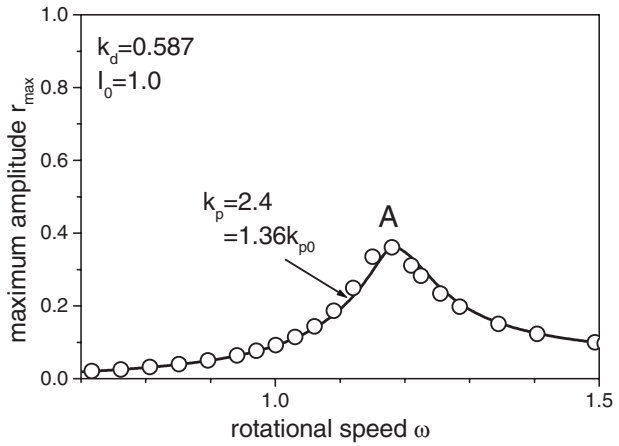

Fig. 7 Resonance curve: solid line: stable solution and open circle: steady state oscillation. The dimensional values of parameters k_p, k_d, and I_0 are shown in Table 2.

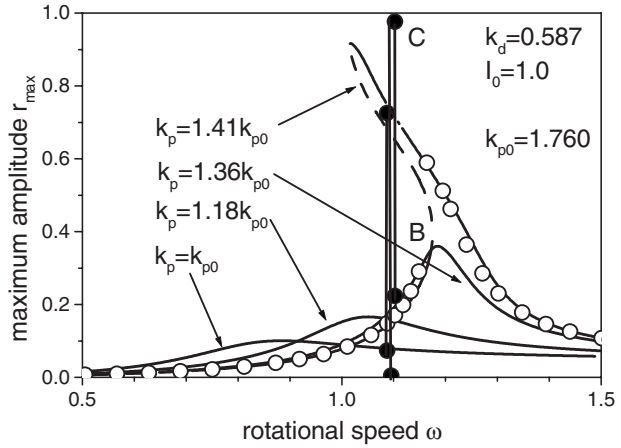

Fig. 8 Influence of feedback coefficient k_p: solid line: stable solution, dashed line: unstable solution for the case with a positive real eigenvalue, dashed-dotted line: unstable solution for the case with a pair of conjugate complex eigenvalues with a positive real part (due to Hopf Bifurcation), solid circle: maximum and minimum amplitudes of almost periodic motion, and open circle: steady state oscillation. The dimensional values of parameters k_p, k_d, and I_0 are shown in Table 2.

symbol represents the result of numerical simulation, and the open circle denotes the amplitude of steady state solution.

4 Influences of Parameters

In this section, the values of k_p, k_d, and bias current I_0 shown in Table 2 are set as the standard values. The influences of these parameters are investigated by changing the dimensionless parameter values from these standard values.

4.1 Influences of Feedback Coefficients. Figure 8 shows the influence of the position-feedback coefficient k_p on the resonance curve. Both the dashed line and the dashed-dotted line represent the unstable solutions. The dashed line denotes the instability for the case with a positive real eigenvalue, and the dashed-dotted line denotes the instability for the case with a pair of conjugate complex eigenvalues with a positive real part, which indicates the occurrence of the Hopf bifurcation [19,20]. The solid circles connected with a vertical line denote the maximum and minimum amplitudes of almost periodic motion [20].

The agreement of the resonance curve and the numerical result indicates the validity of the theoretical analysis. As the value of k_p increases from the standard value $k_{p0}=1.76$, the peak amplitude of the major critical speed increases, and the resonance curve shows a soft spring type shape. The saddle-node bifurcation occurs at point B when $k_p=1.41k_{p0}$. The solid circles with a vertical line indicating the occurrence of Hopf bifurcation occurs along the dashed-dotted curve from the higher speed side [19,20]. It shows that the almost periodic vibration occurs in the numerical simulation around this dashed-dotted curve. The time histories, orbit, and spectra of the almost periodic motion at point C are shown in Fig. 9.

Figure 10 shows the influence of the velocity-feedback coefficient k_d on the resonance curve. As the value of k_d increases from the standard value $k_{d0}=0.587$, the damping effect generated by electromagnet increases. As the result, the maximum amplitude of the major critical speed decreases.

4.2 Influence of the Bias Electric Current. Figure 11 shows the influence of the bias electric current I_0. The feedback coefficients k_p and k_d are calculated for each value of I_0 by optimal regulator theory. The value $I_0=1.0$ shown in Table 2 is set as the standard value in this parameter study. As the value of bias current I_0 decreases from 1.0, the linear spring coefficient of the magnetic

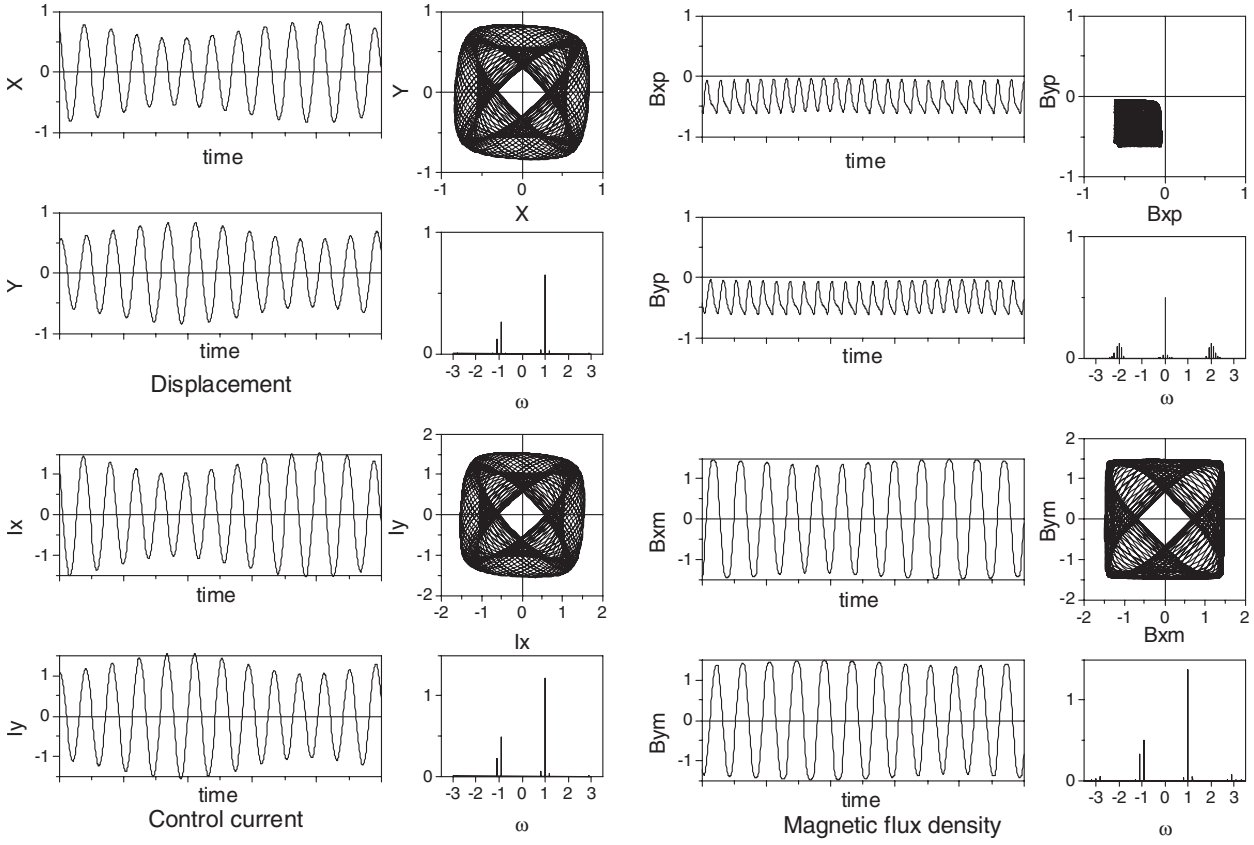

Fig. 9 Time histories at point *C*

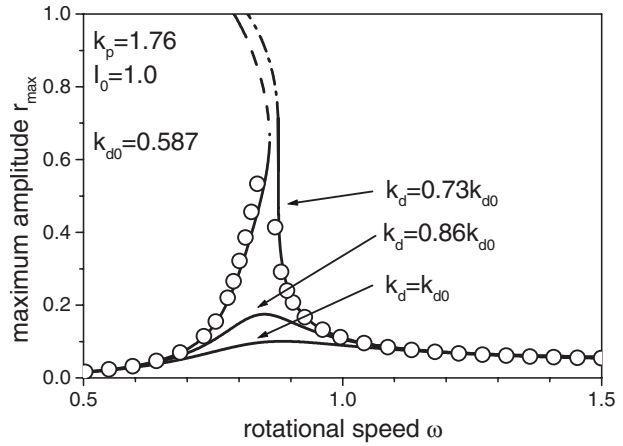

Fig. 10 Influence of feedback coefficient k_d: solid line: stable solution, dashed line: unstable solution for the case with a positive real eigenvalue, dashed-dotted line: unstable solution for the case with a pair of conjugate complex eigenvalues with a positive real part (due to Hopf Bifurcation), solid circle: maximum and minimum amplitudes almost periodic motion, and open circle: amplitude of steady state oscillation. The dimensional values of parameters k_p, k_d, and l_0 are shown in Table 2.

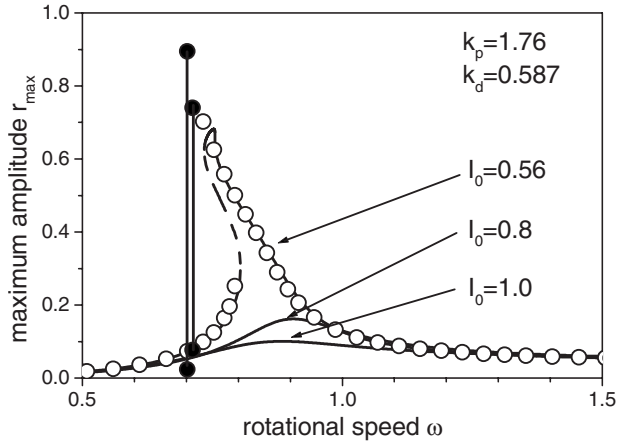

Fig. 11 Influence of bias current l_0: solid line: stable solution, dashed line: unstable solution, solid circle: maximum and minimum amplitudes almost periodic motion, and open circle: steady state oscillation. The dimensional values of parameters k_p, k_d, and l_0 are shown in Table 2.

bearing decreases, and the critical speed moves to the lower speed side. In this case, the vibration amplitude becomes large, and the resonance curve becomes the soft spring type shape due to the effect of magnetic force nonlinearity. The saddle-node bifurcation occurs, and the almost periodic vibration occurs at around $\omega = 0.742$ in the numerical simulation for the case $I_0 = 0.56$ (=0.28 A).

4.3 Influence of the Electric Current Delay. The dynamical characteristic of the magnetic force is influenced by the delays of electric current that depends on the electric circuit of power amplifier. Figures 12(*a*) and 12(*b*) show the influence of the electric current delays α_1 and α_2. The values $\alpha_1 = 3.180$ and $\alpha_2 = 0.161$ are the dimensionless values of the dimensional value shown in Table 1, and are set as the standard values in this parameter study.

As the value of α_1 increases as shown in Fig. 12(*a*), the amplitude of the vibration increases, and the resonance point decreases. However, neither softening nor hardening effect appears.

While, as the value of α_2 increases as shown in Fig. 12(*b*), the amplitude of the vibration increases, and the resonance point slightly increases. Furthermore, softening effect appears in the larger amplitude area. In such area, the curve becomes unstable due to Hopf bifurcation, and almost periodic motion occurs in the numerical simulation.

4.4 Influence of the Magnetic Flux Delay. The dynamical characteristic of the magnetic force is also influenced by the delays of magnetic flux that depends on the material of electromagnet core. Figure 13 shows the influence of the magnetic flux delay β. The value $\beta_0 = 0.307$ is the dimensionless value of the dimensional value $\beta_0 = 3.66 \times 10^{-3}$ s shown in Table 1, and it is set as the standard value in this parameter study. As the value of β increases, the amplitude of the vibration increases, and the resonance curve shows the soft spring type. The curve becomes unstable at the large amplitude area due to Hopf bifurcation.

5 Experiment

5.1 Experimental Setup. The experimental setup is shown in Fig. 14. A rigid shaft with a circular cross section is simply supported at the upper side by a self-aligning double-row ball bearing and supported at the lower side by a magnetic bearing. This shaft is driven by the motor, which is connected to the upper end of the shaft via a flexible coupling. The material of the shaft is stainless steel, and the length of the shaft is $l_s = 600$ mm and its diameter is $\phi_s = 20$ mm. The positions of disks 1–3 from the upper end of the

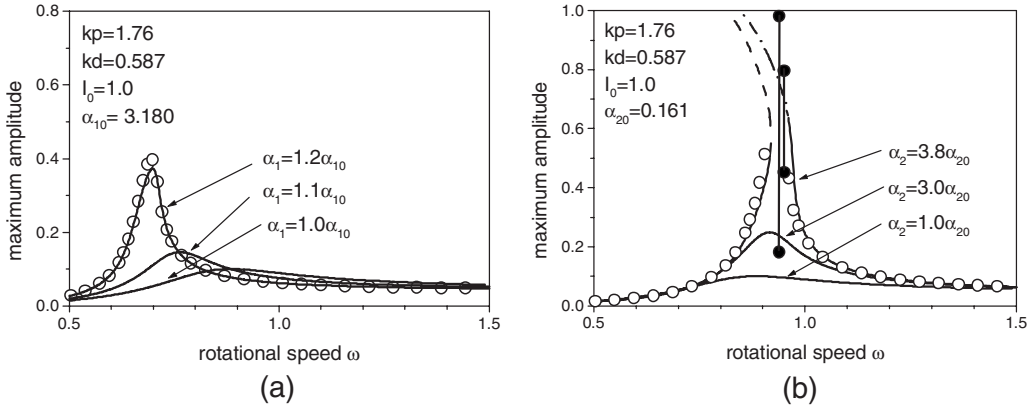

Fig. 12 Influence of the electric current delay: (*a*) influence of α_1 and (*b*) influence of α_2: solid line: stable solution, dashed line: unstable solution for the case with a positive real eigenvalue, dashed-dotted line: unstable solution for the case with a pair of conjugate complex eigenvalues with a positive real part (due to Hopf Bifurcation), solid circle: maximum and minimum amplitudes almost periodic motion, and open circle: steady state oscillation. The values $\alpha_1 = 3.180$ and $\alpha_2 = 0.161$ are the dimensionless value of the dimensional value shown in Table 1. The dimensional values of parameters k_p, k_d, and l_0 are shown in Table 2.

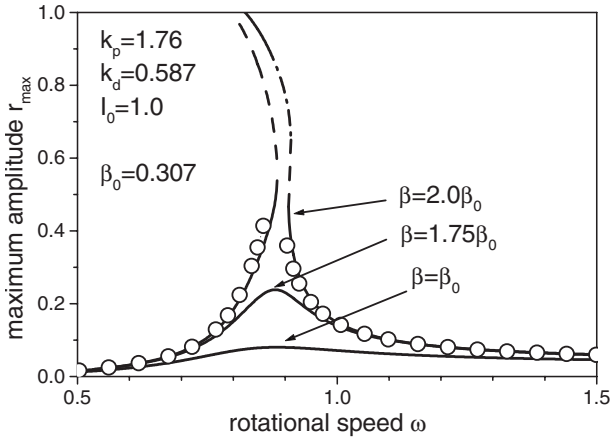

Fig. 13 Influence of the Magnetic Flux Delay β: solid line: stable solution, dashed line: unstable solution for the case with a positive real eigenvalue, dashed-dotted line: unstable solution for the case with a pair of conjugate complex eigenvalues with a positive real part (due to Hopf Bifurcation), solid circle: maximum and minimum amplitudes almost periodic motion, and open circle: steady state oscillation. The value $\beta_0=0.307$ is the dimensionless value of the dimensional value $\beta_0=3.66\times10^{-3}$ s shown in Table 1. The dimensional values of parameters k_p, k_d, and I_0 are shown in Table 2.

shaft are 276 mm, 487 mm, and 342.5 mm, respectively. The diameter and the thickness of disk 1 are 200 mm and 10 mm. The diameter and the thickness of disk 2, which is the rotor of the magnetic bearing, are 80 mm and 30 mm. The shaft displacements in the x and y directions are measured at the position of disk 3 by eddy-current sensors. The diameter and the thickness of disk 3 are 44 mm and 24 mm. The radius gap of the magnetic bearing is $R_0=0.8$ mm, and the radius gap of the backup bearing is 0.6 mm. The turn number of each electromagnet coil of AMB is 300 turns.

The electric currents and gaps of four electromagnets are measured, and the coefficients k_m and δ corresponding to Eq. (2) are calculated for all electromagnets. Table 3 shows the obtained results. When the coefficients k_m and δ are measured, some differences among four magnets are inevitable due to the causes such as irregularity of the turn number of coil, differences among the power amplifiers, and so on. In this study, the influence of these differences among magnets is eliminated by tuning the bias current I_0 for each magnet.

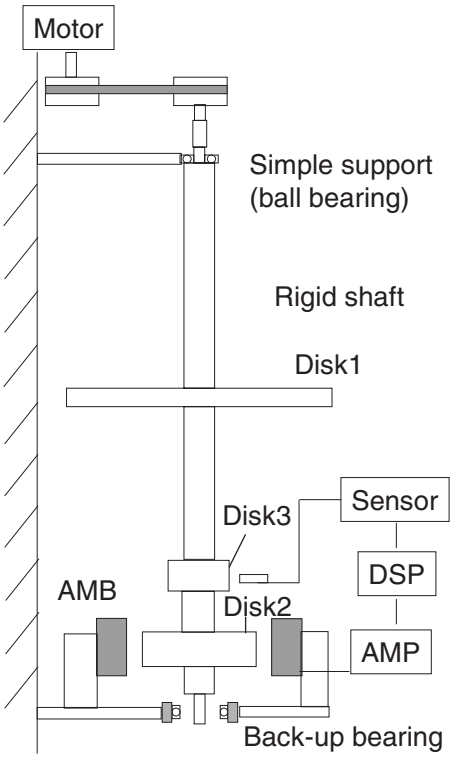

Fig. 14 Experimental model

Table 3 Coefficients of electromagnets

	k_m (kg m^3/A^2 s^2)	δ (m)
Electromagnet A	1.19×10^{-5}	0.015×10^{-3}
Electromagnet B	1.88×10^{-5}	0.229×10^{-3}
Electromagnet C	1.47×10^{-5}	0.133×10^{-3}
Electromagnet D	1.69×10^{-5}	0.187×10^{-3}

5.2 Experimental Results. Experiments were performed by changing the feedback coefficients, k_p and k_d, and bias current I_0. The fundamental values of these parameters were set as $k_p=1.5$ A/mm, $k_d=0.007$ A s/mm, and $I_{0x}=0.5$ A. The current I_{0y} was tuned for each case.

Figure 15 shows the influence of the displacement feedback coefficient k_p. As the value of k_p increased, the resonance point increased and the resonance curve began to show soft spring type nonlinear characteristics. The case of $k_p=1.5$ A/mm in Fig. 15 indicated the occurrence of the jump phenomena, and showed the existence of the rotational speed range with multiple stable solutions by a shaded area. By comparing Fig. 15 with the theoretical result shown in Fig. 8, the theoretical results are validated qualitatively by the experiments in the following points such as the values of critical speeds, the shapes of resonance curves, and the occurrences of the saddle-node bifurcations.

Figure 16 shows the influence of the velocity-feedback coefficient k_d. As the value of k_d decreased, the resonance point did not move so much and only the amplitude of the resonance curve increases. These experimental results shown in Fig. 16 validated qualitatively the theoretical result shown in Fig. 10.

Figure 17 shows the influence of the bias current I_0. As the value of I_0 decreased, the resonance point decreased and the resonance curve began to show soft spring type nonlinear characteristics. Figure 17 validated qualitatively the theoretical result shown in Fig. 11.

6 Conclusions

This paper considers the dynamical characteristics of the rigid rotor system supported vertically by the magnetic bearing. Both the effects of magnetic force nonlinearity and the dynamics of

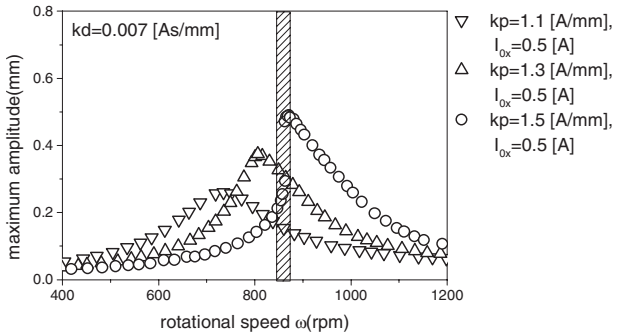

Fig. 15 Experimental results (influence of feedback coefficient k_p)

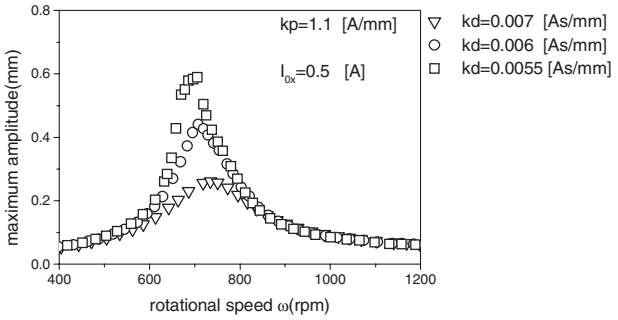

Fig. 16 Experimental results (influence of feedback coefficient k_d)

control system are clarified. Especially, the influences of the delays of both the electric current and the magnetic flux are explained. The following results are obtained.

This study proposes the nonlinear power series approximation model for the magnetic flux of magnetic bearing. This model can substitute the piecewise characteristics of the magnetic flux, which is caused by the general control procedure of the AMB or by the directional characteristic of the power amplifier. Especially, the expression of the set of magnetic flux in magnetic bearing is considered and new representation is proposed. By using this expression, the number of the terms, which are required for the power series approximation, is reduced to be a half. Furthermore, the number of the variables, which are required in the nonlinear theoretical analysis, is also reduced. Therefore, this expression of the set of magnetic flux makes the nonlinear theoretical analysis much simpler. By using this model, the nonlinear vibration analysis is performed on the rotor system supported by the magnetic bearing including the delay of magnetic force.

The analytical procedure of the nonlinear vibration analysis of the rotor system supported by the magnetic bearing including the delay in both the electric and magnetic circuits is developed. By using this procedure, the fundamental analytical equations are obtained, and the nonlinear dynamical characteristics of the rigid rotor system supported by the magnetic bearing are clarified theoretically. Especially, the effects of parameters of the magnetic bearing are explained.

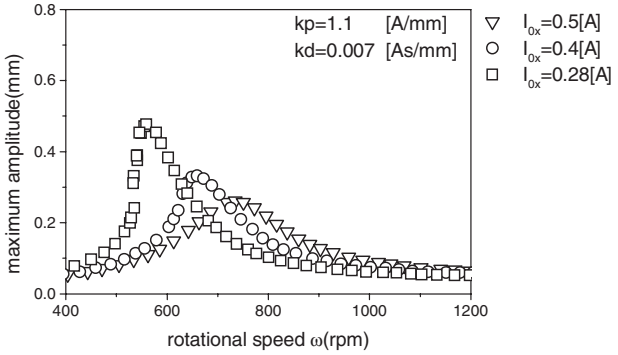

Fig. 17 Experimental results (influence of bias current I_0)

When the coefficient of position feedback increases or the bias electric current decreases, the resonance curve shows soft spring characteristic and saddle-node bifurcation, which leads the rotational speed range with multiple stable solutions to occur. Concerning on the delay coefficients, the second order of electric current delay and the first order of magnetic flux delay have effects on the nonlinear phenomena. Therefore, the nonlinear phenomena in the rotor system supported by the AMB are due to the nonlinearity of the magnetic bearing, and it appears strongly as the delays of the electric current or the magnetic flux increase. The obtained theoretical results, such as the jump phenomena and the existence of the rotational speed range with multiple stable solutions, are confirmed by the experiments.

The outcomes of this study enable us to analyze the nonlinear vibration characteristics of the rigid rotor system supported by the active magnetic bearing.

References

[1] Schweitzer, G., Bleuler, H., and Traxler, A., 1994, *Active Magnetic Bearings*, Hochschulverlag AG an der ETH, Zürich.

[2] JSME, ed., 1995, *The Basis and Application of the Magnetic Bearings*, Yokendo Co., Ltd., Tokyo, in Japanese.

[3] Ishida, S., 1991, "Vibration Control by Active Magnetic Bearings," Trans. Jpn. Soc. Mech. Eng., Ser. C, **57**(534), pp. 576–581.

[4] Knight, J. D., and Ecker, H., 1996, "Simulation of Nonlinear Dynamics in Magnetic Bearing," *Proceedings of the Computer Simulation Conference*, Portland, OR.

[5] Chinta, M., and Palazzolo, A. B., 1998, "Stability and Bifurcation of Rotor Motion in a Magnetic Bearing," J. Sound Vib., **214**(5), pp. 793–803.

[6] Steinschaden, N., and Springer, H., 1999, "Some Nonlinear Effects of Magnetic Bearings," *Proceedings of the DETC ASME Conference*, Las Vegas, NV, Paper No. VIB-8063.

[7] Chang, S. C., and Tung, P. C., 1999, "Nonlinear Identification of a Magnetic Bearing System With Closed Loop Control," JSME Int. J., Ser. C, **42**(4), pp. 982–990.

[8] Ji, J. C., Yu, L., and Leung, A. Y. T., 2000, "Bifurcation Behavior of a Rotor Supported by Active Magnetic Bearing," J. Sound Vib., **235**(1), pp. 133–151.

[9] Ji, J. C., and Hansen, C. H., 2001, "Non-Linear Oscillations of a Rotor in Active Magnetic Bearing," J. Sound Vib., **240**(4), pp. 599–612.

[10] Ji, J. C., and Leung, A. Y. T., 2003, "Non-Linear Oscillation of a Rotor-Magnetic Bearing System Under Superharmonic Resonance Conditions," Int. J. Non-Linear Mech., **38**(6), pp. 829–835.

[11] Ji, J. C., 2003, "Dynamics of a Jeffcott Rotor-Magnetic Bearing System With Time Delay," Int. J. Non-Linear Mech., **38**(9), pp. 1387–1401.

[12] Ji, J. C., 2003, "Stability and Hopf Bifurcation of a Magnetic Bearing System With Time Delays," J. Sound Vib., **259**(4), pp. 845–856.

[13] Ho, Y. S., Liu, H., and Yu, L., 2003, "Effect of Thrust Magnetic Bearing on Stability and Bifurcation of a Flexible Rotor Active Magnetic Bearing System," Trans. ASME, J. Vib. Acoust., **125**(3), pp. 307–316.

[14] Murakami, S., Ikeda, T., and Kanada, S., 2005, "Nonlinear Characteristics of Restoring Force Due to a Magnetic Bearing," Journal of the Japan Society of Applied Electromagnetics and Mechanics, **13**(1), pp. 71–76, in Japanese.

[15] Polajzer, B., Stumberger, G., Ritonja, J., Tezak, O., Dolinar, D., and Hameyer, K., 2004, "Impact of Magnetic Nonlinearities and Cross-Coupling Effects on Properties of Radial Active Magnetic Bearings," IEEE Trans. Magn., **40**(2), pp. 798–801.

[16] Inoue, T., Ishida, Y., and Murakami, S., 2007, "Theoretical Analysis and Experiments of the Nonlinear Vibration in a Vertical Rigid Rotor Supported by the Magnetic Bearing System (Case Considering the Delay of Control Force)," Journal of System Design and Dynamics, **1**(2), pp. 295–306.

[17] Yamamoto, T., and Ishida, Y., 2001, *Linear and Nonlinear Rotordynamics*, Wiley, New York.

[18] Stoker, J. J., 1950, *Nonlinear Vibrations in Mechanical and Electrical Systems*, Wiley, New York.

[19] Ishida, Y., and Inoue, T., 2005, "International Resonance Phenomena of an Asymmetrical Rotating Shaft," J. Vib. Control, **11**(9), pp. 1173–1193.

[20] Ishida, Y., and Inoue, T., 2004, "Internal Resonance Phenomena of the Jeffcott Rotor With Nonlinear Spring Characteristics," ASME J. Vibr. Acoust., **126**(4), pp. 476–484.

The Bounds on the Coefficients of Restitution for the Frictional Impact of Rigid Pendulum Against a Fixed Surface

V. A. Lubarda
Department of Mechanical and Aerospace Engineering, University of California, San Diego, La Jolla, CA 92093-0411
e-mail: vlubarda@ucsd.edu

Upper bounds on Newton's, Poisson's, and energetic coefficients of normal restitution for the frictional impact of rigid pendulum against a fixed surface are derived, demonstrating that the upper bound on Newton's coefficient is smaller than 1, while the upper bound on Poisson's coefficient is greater than 1. The upper bound on the energetic coefficient of restitution, which is a geometric mean of Newton's and Poisson's coefficients of normal restitution, is equal to 1. Lower bound on all three coefficients is equal to zero. The bounds on the tangential impact coefficient, defined by the ratio of the frictional and normal impulses, are also derived. Its lower bound is negative, while its upper bound is equal to the kinetic coefficient of friction. Simplified bounds in the case of a nearly vertical impact are also derived. [DOI: 10.1115/1.3172198]

Keywords: bounds, coefficient of restitution, energy loss, frictional impact, impulse, pendulum, slip

1 Introduction

The determination of the rebounding velocity components of colliding bodies is an old mechanics problem, with its origin in early work by Newton and Poisson. Newton defined the coefficient of normal restitution as the ratio of the relative normal velocities after and before the impact. In contrast to Newton's kinematic definition, Poisson's kinetic definition is based on the ratio of the magnitudes of the normal impulses corresponding to the periods of restitution and compression. In the absence of friction (frictionless impact), the Poisson definition of the coefficient of normal restitution yields the same expression, in terms of the relative velocities, as does the Newton definition, which is demonstrated in standard dynamics textbooks, e.g., Ref. [1]. In the presence of friction, however, the two definitions are, in general, not equivalent. The simplest theory of the frictional impact is that of Whittaker [2], in which it is assumed that the frictional impulse is in the slip direction and is equal to the product of the coefficient of friction and the magnitude of the normal impulse. Kane [3] observed that this theory leads to an increase in kinetic energy upon the impact of a double pendulum with a rough horizontal surface, for some values of the coefficients of friction and normal restitution, and for some kinematic parameters of motion. Keller [4] explained this by noting that Whittaker's theory [2] applies only when the direction of sliding is constant throughout the collision. If there is a reversal of the slip direction during the impact process, the coefficient of the proportionality between the tangential and normal impulses is different from the coefficient of kinetic friction. Keller's [4] analysis also demonstrated the advantage of using the normal impulse as an independent variable, instead of physical time, to cast and analyze the governing differential equations of motion during the impact process. Stronge [5] introduced an energetic coefficient of normal restitution, whose square is equal to the negative ratio of the elastic strain energy released during restitution and the internal energy of deformation absorbed during compression phase of the impact. Numerous papers, proposing different models of frictional impact, were published since. A comprehensive treatment of the subject, with a historical outline, can be found in the monographs or review articles [6–9].

In this paper we revisit a classical problem of frictional impact of rigid pendulum against a fixed surface. By employing Keller's [4] method of analysis, we derive the expressions for the angular velocity in terms of the monotonically increasing normal impulse during the impact process. Three different definitions of the coefficient of normal restitution are used to specify the rebounding angular velocity and the total normal impulse: Newton's kinematic, Poisson's kinetic, and Stronge's energetic definitions. It is shown that the energetic coefficient of normal restitution is a geometric mean of the Newton and Poisson coefficients of normal restitution. The upper bounds on all three coefficients are established, demonstrating that the upper bound on the Newton coefficient is smaller than 1, while the upper bound on the Poisson coefficient is greater than 1. For the pendulum striking a rough surface elastically, without dissipation due to deformation, the Newton and Poisson coefficients are the reciprocals of each other. If, upon the impact, the pendulum sticks to the ground, there is no restitution phase of the impact, and all three coefficients of normal restitution are equal to zero, which represents their lower bound. The bounds on the tangential impact coefficient, defined by the ratio of the frictional and normal impulses, are also derived. Its lower bound is negative, while its upper bound is equal to the kinetic coefficient of friction. Simplified bounds in the case of a nearly vertical impact are also derived.

2 Rigid Pendulum Striking a Fixed Surface

Figure 1 shows a rigid pendulum, rotating around a frictionless pin at O and striking a fixed horizontal surface at the point with coordinates $(a,-b)$, relative to the origin at O. The (incidence) angular velocity of the pendulum just before the impact is $\omega^- < 0$ (negative value indicating its clockwise direction). If $\omega^+ > 0$ is the (rebounding) angular velocity immediately after the impact of duration t_1, then, by the impulse principle,

Contributed by the Applied Mechanics Division of ASME for publication in the JOURNAL OF APPLIED MECHANICS. Manuscript received October 2, 2008; final manuscript received April 12, 2009; published online September 24, 2009. Review conducted by Vikram Deshpande.

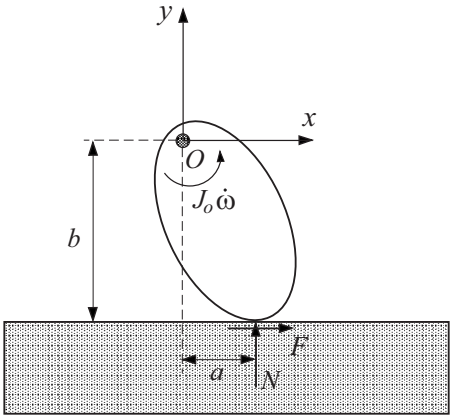

Fig. 1 A rigid pendulum, suspended from a frictionless pin *O*, strikes a fixed horizontal surface with the incidence angular velocity ω^-. The componential reactions at the contact point with the coordinates $(a,-b)$ are *N* and *F*.

$$J_0\omega^- + \int_0^{t_1} (Na + Fb)\mathrm{d}t = J_0\omega^+ \tag{1}$$

where J_0 is the pendulum's moment of inertia about the point O, and N and F are the normal and friction forces acting on the pendulum at the contact point with the rough horizontal surface. The coordinates of the contact points a and b change only infinitesimally during the time of the impact $t \in [0, t_1]$, so that the equation of motion during the impact is

$$J_0 \frac{\mathrm{d}\omega}{\mathrm{d}t} = Na + Fb \tag{2}$$

The weight of the pendulum mg, as a nonimpulsive force, does not contribute to Eqs. (1) and (2). Following Ref. [4] and introducing a monotonically increasing impulse parameter (Fig. 2)

$$\tau = \int_0^t N\mathrm{d}t, \quad \mathrm{d}\tau = N\mathrm{d}t \tag{3}$$

Eq. (2) can be recast as

$$J_0\mathrm{d}\omega = \left(a + b\frac{F}{N}\right)\mathrm{d}\tau, \quad \tau \in [0, \tau_1], \quad \tau_1 = \int_0^{t_1} N\mathrm{d}t \tag{4}$$

Since a and b are nearly constant during the impact process, Eq. (4) can be integrated to give

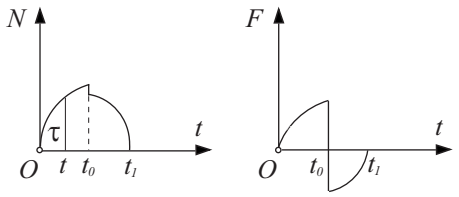

Fig. 2 Schematic time variation of the normal and friction components of the reactive force during the impact of duration t_1. The normal impulse up to an arbitrary time t is $\tau = \int_0^t N\mathrm{d}t$. The friction component of the reactive force is related to the normal component by the Amontons–Coulomb law of sliding friction $F = -\mu N\ \mathrm{sgn}(t - t_0)$, where t_0 is the time at which sliding changes its direction, and μ is the coefficient of kinetic friction.

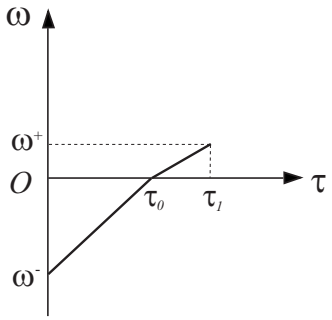

Fig. 3 Bilinear variation of the angular velocity $\omega = \omega(\tau)$, according to Eq. (9). The slopes in the compression and restitution phases of the impact are $(a + \mu b)/J_0$ and $(a - \mu b)/J_0$, respectively.

$$J_0(\omega - \omega^-) = a\tau + b\int_0^\tau \frac{F}{N}\mathrm{d}\tau \tag{5}$$

Let $0 < \tau_0 < \tau_1$ correspond to the instant t_0 when the angular velocity momentarily vanishes, $\omega(\tau_0) = 0$, and the slip reversal takes place at the transition between the compression and restitution phases of the impact. Assuming that during the impact the tangential component of the reactive force is related to the normal component by the Amontons–Coulomb law of sliding (dry) friction, and ignoring the tangential compliance of the colliding bodies, we can write

$$\frac{F}{N} = -\mu\ \mathrm{sgn}(\omega) = -\mu\ \mathrm{sgn}(\tau - \tau_0) \tag{6}$$

where μ is the coefficient of kinetic friction. The substitution into Eq. (5), upon integration, gives

$$\omega = \omega^- + \frac{a + \mu b}{J_0}\tau, \quad 0 \le \tau \le \tau_0$$

$$\omega = \frac{a - \mu b}{J_0}(\tau - \tau_0), \quad \tau_0 \le \tau \le \tau_1 \tag{7}$$

The normal impulse τ_0, determined from the condition $\omega(\tau_0) = 0$, is obtained from the first equation in Eq. (7), as

$$\tau_0 = -\frac{J_0\omega^-}{a + \mu b} \tag{8}$$

In order that $\omega > 0$ in the interval $(\tau_0, \tau_1]$, the coefficient of kinetic friction must be bounded by $\mu < a/b$. If $\mu \ge a/b$, the pendulum sticks to the ground after the impact, with no rebounding velocity.[1] By incorporating Eq. (8), the angular velocity expression (7) can be rewritten in a bilinear form (Fig. 3)

$$\omega = \left(1 - \frac{\tau}{\tau_0}\right)\omega^-, \quad 0 \le \tau \le \tau_0$$

$$\omega = \frac{a - \mu b}{a + \mu b}\left(1 - \frac{\tau}{\tau_0}\right)\omega^-, \quad \tau_0 \le \tau \le \tau_1 \tag{9}$$

The corresponding slopes $\mathrm{d}\omega/\mathrm{d}\tau$ in the compression and restitution phases of the impact are $(a + \mu b)/J_0$ and $(a - \mu b)/J_0$, respectively. The two slopes are equal only in the absence of friction.

3 Coefficient of Normal Restitution

The total normal impulse τ_1 is still an unknown quantity in the analysis, and cannot be determined without further assumptions.

[1] For small angle $\varphi = \arctan(a/b)$ there is no rebound if friction is sufficiently large ($\mu \ge \tan\varphi$); see Ref. [8], p. 180.

To proceed, we introduce the coefficient of normal restitution by the Poisson definition as the ratio of the normal impulses corresponding to restitution and compression phases of the impact, i.e.,

$$\kappa = \frac{\tau_1 - \tau_0}{\tau_0} > 0, \quad \tau_1 = (1+\kappa)\tau_0 \tag{10}$$

Since the duration of the impact and the variation of the normal force during the impact depend on friction, the ratio τ_1/τ_0 and thus the coefficient κ also depend on friction.[2] Assuming κ to be given, by using Eq. (10) it follows from Eq. (9) that the rebounding angular velocity $\omega^+ = \omega(\tau_1)$ is related to the incidence angular velocity by

$$\omega^+ = -\kappa \frac{a - \mu b}{a + \mu b}\omega^- \tag{11}$$

With this, the angular velocity during the restitution phase of the impact can be written, from the second equation in Eq. (9), as

$$\omega = \frac{1}{\kappa}\left(1 - \frac{\tau}{\tau_0}\right)\omega^+, \quad \tau_0 \le \tau \le \tau_1 \tag{12}$$

Introducing the horizontal and vertical velocity components of the contact point during the impact, $u = b\omega$ and $v = a\omega$, Eq. (11) can be rewritten as

$$v^+ + \mu u^+ = -\kappa(v^- - \mu u^-) \tag{13}$$

which demonstrates that in the case of rigid pendulum striking a fixed surface, the Poisson definition of the coefficient of normal restitution differs from the Newton definition[3]

$$\hat{\kappa} = -\frac{v^+}{v^-} = -\frac{\omega^+}{\omega^-} \tag{14}$$

Evidently, by using Eq. (11),

$$\hat{\kappa} = \frac{a - \mu b}{a + \mu b}\kappa = \frac{1 - \mu b/a}{1 + \mu b/a}\kappa \tag{15}$$

The two coefficients of normal restitution are therefore related to the coefficient that depends on the impact configuration, as represented by the ratio b/a, and the coefficient of friction μ. A physical interpretation of the parameter $\mu b/a$ will be further discussed in Sec. 6.1.

In order that there is a rebound, ω^- and ω^+ have to be of the opposite sign, so that $\hat{\kappa} > 0$. Thus, the coefficient of friction and the geometric parameters of the impact configuration (a,b) have to be such that $a - \mu b > 0$. If $\mu \ge a/b$, the pendulum sticks to the ground after the impact $(\omega^+ = 0)$, which establishes the lower bound on Newton's coefficient of normal restitution, $\hat{\kappa} = 0$.

The kinetic energy dissipated by the frictional impact is

$$\Delta E = E^- - E^+ = \tfrac{1}{2}J_0[(\omega^-)^2 - (\omega^+)^2] = \tfrac{1}{2}(1 - \hat{\kappa}^2)J_0(\omega^-)^2 \tag{16}$$

i.e., in view of Eq. (15),

$$\Delta E = \frac{1}{2}J_0(\omega^-)^2\left[1 - \kappa^2\frac{(a - \mu b)^2}{(a + \mu b)^2}\right] \tag{17}$$

Since ΔE must be non-negative $(\Delta E \ge 0$, the equality holding if and only if $\kappa = 1$ and $\mu = 0)$, and since $\kappa > 0$, Eq. (17) imposes an upper bound on Poisson's coefficient of normal restitution

$$\kappa \le \kappa_{\max}, \quad \kappa_{\max} = \frac{a + \mu b}{a - \mu b} \tag{18}$$

for all cases in which there is a rebound of the pendulum after the impact $(a - \mu b > 0)$. Since $\kappa_{\max} > 1$, the coefficient of normal restitution based on the Poisson definition can be greater than 1. This is also clear from relationship (15) between Poisson's and Newton's definitions of the coefficient of normal restitution, because $\hat{\kappa} \le 1$ in order that $\Delta E = (1 - \hat{\kappa}^2)E^- \ge 0$, and thus $\kappa_{\max} > 1$. Lower values of the upper bounds on κ and $\hat{\kappa}$ will be derived in Sec. 5 of this paper.

4 Energetic Coefficient of Restitution

Stronge [5] introduced an energetic coefficient of normal restitution, whose square is equal to the negative ratio of the elastic strain energy released during restitution and the internal energy of deformation absorbed during compression phase of the impact. If tangential compliance of colliding bodies is negligible, this coefficient equals the negative ratio of the work done by the normal component of the impulsive reaction during restitution and compression phases of the impact,

$$\eta^2 = -\frac{W_r^n}{W_c^n} \tag{19}$$

where

$$W_c^n = \int_0^{t_0} N v \, dt = \int_0^{\tau_0} v \, d\tau, \quad W_r^n = \int_{t_0}^{t_1} N v \, dt = \int_{\tau_0}^{\tau_1} v \, d\tau \tag{20}$$

The ratio $-W_r^n/W_c^n$ accounts for irreversible deformation in the contact region, it is presumingly independent of friction, and thus represents an appealing coefficient to account for the normal restitution during a frictional impact.[4] For the pendulum striking a fixed surface, the vertical velocity component of the contact point is $v = a\omega$, so that Eq. (20) becomes

$$W_c^n = a\int_0^{\tau_0} \omega \, d\tau, \quad W_r^n = a\int_{\tau_0}^{\tau_1} \omega \, d\tau \tag{21}$$

By using angular velocity expression (7), this gives

$$W_c^n = \tfrac{1}{2}a\tau_0\omega^-, \quad W_r^n = \tfrac{1}{2}\kappa a\tau_0\omega^+ \tag{22}$$

When Eq. (22) is incorporated into Eq. (19), there follows

$$\eta^2 = -\kappa\frac{\omega^+}{\omega^-} = \kappa\hat{\kappa} = \frac{a - \mu b}{a + \mu b}\kappa^2 = \frac{a + \mu b}{a - \mu b}\hat{\kappa}^2 \tag{23}$$

The expression $\eta^2 = \kappa\hat{\kappa}$, derived by a different route, was first reported in Ref. [7]. Thus, for the rigid pendulum striking a fixed surface, the energetic coefficient of normal restitution is a geometric mean of the Newton and Poisson coefficients of normal restitution, i.e.,

$$\eta = \sqrt{\kappa\hat{\kappa}} \tag{24}$$

In the case of frictionless impact $(\mu = 0)$, the three coefficients of normal restitution are equal to each other $(\kappa = \hat{\kappa} = \eta)$. For frictional impact, the energetic coefficient is smaller than Poisson's and greater than Newton's coefficient of normal restitution $(\hat{\kappa} < \eta < \kappa)$. Indeed, from Eq. (23),

$$\kappa = \left(\frac{a + \mu b}{a - \mu b}\right)^{1/2}\eta = \left(1 + \frac{2\mu b}{a - \mu b}\right)^{1/2}\eta$$

[2]The coefficient κ also depends on the material properties and the incidence angular velocity ω^-, affecting the nature of the deformation, but such dependence cannot be determined within a rigid body mechanics [10].

[3]The two definitions yield different expressions in many (but not all) frictional impact problems in which there is a change in the slip direction during the impact process. For example, Newton's and Poisson's definitions of the coefficient of normal restitution, as well as the energetic definition, to be discussed in Sec. 4, for a spinning disk striking a rough horizontal surface are all equivalent $(\kappa = \hat{\kappa} = \eta)$.

[4]From experimental or numerical finite element method evaluations, it may be anticipated that η depends on the material properties, the radius of pendulum's local curvature in the contact region, and the incidence angular velocity affecting the extent of inelastic deformation in the region of contact.

$$\hat{\kappa}=\left(\frac{a-\mu b}{a+\mu b}\right)^{1/2}\eta=\left(1-\frac{2\mu b}{a-\mu b}\right)^{1/2}\eta \tag{25}$$

For example, if $\mu=0.1$ and $a/b=0.3$, one has $\kappa=\sqrt{2}\eta$ and $\hat{\kappa}=\eta/\sqrt{2}$.

Since $\tau_1/\tau_0=1+\kappa$, and in view of Eq. (23), the relationship between the impulse ratio τ_1/τ_0 and the coefficient η is

$$\frac{\tau_1}{\tau_0}=1+\sqrt{\frac{a+\mu b}{a-\mu b}}\eta,\quad a-\mu b>0 \tag{26}$$

In an advanced treatise on impact mechanics [8], there is a mistake in the derivation presented in pages 178–180, where the impulse ratio and the energy coefficient of restitution are listed as[5]

$$\frac{p_f}{p_c}=1+e_*\sqrt{\frac{r_1+\mu r_3}{r_1-\mu r_3}},\quad e_*^2=\frac{r_1-\mu r_3}{r_1+\mu r_3}\frac{p_f^2-p_c^2}{p_c^2}$$

For example, if $\mu=0$, the first of these expressions yields $1+e_*=p_f/p_c$ and the second $1+e_*^2=p_f^2/p_c^2$, contradicting each other. The expression for e_*^2 in Ref. [8] is incorrect because of the mistake in the expression for the vertical velocity component used therein to evaluate the restitution work.

5 Bounds on the Coefficients of Restitution

An obvious upper bound on Newton's coefficient of normal restitution, appearing in the relationship $\omega^+=-\hat{\kappa}\omega^-$, is

$$\hat{\kappa}\le 1 \tag{27}$$

because the magnitude of ω^+ cannot be greater than the magnitude of ω^- (otherwise there would be an energy gain by the impact process $E^+-E^-<0$). In view of relationship (15), the corresponding upper bound on the Poisson coefficient of normal restitution is

$$\kappa\le\frac{a+\mu b}{a-\mu b} \tag{28}$$

Lower upper bounds on κ and $\hat{\kappa}$ can be deduced by first imposing the upper bound on the energetic coefficient of normal restitution,

$$\eta\le 1 \tag{29}$$

which must hold because the restitution phase of the impact cannot deliver more energy than what was stored during the compression phase, $\eta^2=-W_r^n/W_c^n\le 1$. The limiting case $\eta=1$ corresponds to purely elastic compression (dissipation of energy being associated with the frictional sliding only). Consequently, by recalling from Eq. (25) the relationships between the three coefficients of normal restitution,[6] inequality (29) yields the stronger (lower) upper bounds on the Poisson and Newton coefficients of normal restitution. For $a-\mu b>0$, these are

$$\kappa\le\left(\frac{a+\mu b}{a-\mu b}\right)^{1/2}=\left(1+\frac{2\mu b}{a-\mu b}\right)^{1/2}$$

$$\hat{\kappa}\le\left(\frac{a-\mu b}{a+\mu b}\right)^{1/2}=\left(1-\frac{2\mu b}{a+\mu b}\right)^{1/2} \tag{30}$$

In the presence of friction, the above upper bound on κ is greater than 1, and the upper bound on $\hat{\kappa}$ is smaller than 1, the two being the reciprocals of each other.

The corresponding upper bound on the normal impulse $\tau_1=(1+\kappa)\tau_0$ is

$$\tau_1\le\left[1+\left(1+\frac{2\mu b}{a-\mu b}\right)^{1/2}\right]\tau_0,\quad a-\mu b>0 \tag{31}$$

which shows that, for frictional impact, the upper bound on τ_1 is greater than $2\tau_0$. For frictionless impact, the upper bound on τ_1 is equal to $2\tau_0$, and is reached in the limit of perfectly elastic impact.

6 Energy Dissipated by Friction

The works done by the tangential component of impulse during the restitution and compression phases are

$$W_c^t=\int_0^{t_0}Fu\,\mathrm{d}t=\int_0^{\tau_0}\frac{F}{N}u\,\mathrm{d}\tau$$

$$W_r^t=\int_{t_0}^{t_1}Fu\,\mathrm{d}t=\int_{\tau_0}^{\tau_1}\frac{F}{N}u\,\mathrm{d}\tau \tag{32}$$

Since $F/N=-\mu\ \mathrm{sgn}(\tau-\tau_0)$, and by using the expression for the horizontal velocity component of the contact point $u=b\omega$, Eq. (32) becomes

$$W_c^t=\mu b\int_0^{\tau_0}\omega\,\mathrm{d}\tau,\quad W_r^t=-\mu b\int_{\tau_0}^{\tau_1}\omega\,\mathrm{d}\tau \tag{33}$$

i.e.,

$$W_c^t=\tfrac{1}{2}\mu b\tau_0\omega^-,\quad W_r^t=-\tfrac{1}{2}\mu b\kappa\tau_0\omega^+ \tag{34}$$

The total work dissipated by friction during the impact is

$$W^t=W_c^t+W_r^t=\tfrac{1}{2}\mu b\tau_0(\omega^--\kappa\omega^+) \tag{35}$$

This can be compared with the total work done by the normal component of impulse, which is, from Eq. (22),

$$W^n=W_c^n+W_r^n=\tfrac{1}{2}a\tau_0(\omega^-+\kappa\omega^+) \tag{36}$$

The dissipated energy by irreversible deformation due to normal force is

$$-W^n=-\tfrac{1}{2}a\tau_0\omega^-(1-\kappa\hat{\kappa})=\tfrac{1}{2}J_0(\omega^-)^2\frac{a}{a+\mu b}(1-\eta^2) \tag{37}$$

which is positive if $\eta<1$. See also a related discussion in Ref. [11].

6.1 Work Ratios. The total works done during the compression and restitution phases of the impact are

$$W_c=W_c^n+W_c^t=\tfrac{1}{2}(a+\mu b)\tau_0\omega^-=-\tfrac{1}{2}J_0(\omega^-)^2 \tag{38}$$

$$W_r=W_r^n+W_r^t=\tfrac{1}{2}(a-\mu b)\kappa\tau_0\omega^+=\tfrac{1}{2}J_0(\omega^+)^2 \tag{39}$$

These expressions can also be obtained directly by applying the energy-work principle to the compression and restitution phases of the impact separately ($E^-+W_c=0$ and $0+W_r=E^+$). The total work done by both the normal and tangential impulsive reactions is $W=W_c+W_r=W^n+W^t=E^+-E^-$.

From the derived work expressions, the following work ratios are observed:

$$-\frac{W_r^n}{W_c^n}=\frac{W_r^t}{W_c^t}=-\kappa\frac{\omega^+}{\omega^-}=\kappa\hat{\kappa}=\eta^2,\quad -\frac{W_r}{W_c}=\left(\frac{\omega^+}{\omega^-}\right)^2=\hat{\kappa}^2 \tag{40}$$

Thus, for the pendulum striking a fixed surface, the Newton coefficient of normal restitution, defined by the kinematic relation $\hat{\kappa}=-\omega^+/\omega^-$, can also be given an energy interpretation, via $\hat{\kappa}^2=-W_r/W_c=E^+/E^-$. Furthermore, the energetic coefficient of normal restitution is equal to either the normal work ratio $(-W_r^n/W_c^n)$, or the frictional work ratio (W_r^t/W_c^t), so that in the considered problem the frictional dissipation during the restitution phase is always

[5]The notations used in Ref. [8] are $p_c=\tau_0$, $p_f=\tau_1$, $e_*=\eta$, $r_1=a$, and $r_3=b$.

[6]If η is assumed to be given, then the kinematic and kinetic coefficients of normal restitution depend on η and the geometric parameter $\mu b/a$, accounting for friction and the pendulum impact configuration, represented by the ratio b/a. Clearly, the higher the value of η (less dissipation by the deformation), the higher the coefficients κ and $\hat{\kappa}$, and thus the higher the rebound (ω^+).

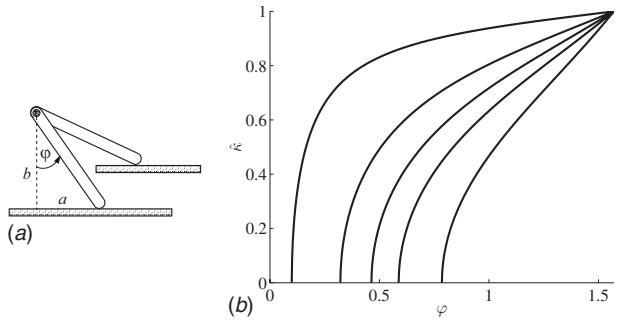

Fig. 4 (*a*) Two impact configurations of the rigid pendulum against a fixed surface, corresponding to two different values of the angle φ. (*b*) The variation of the Newton coefficient of normal restitution $\hat{\kappa}$ with φ (in radians), in the case of an elastic impact ($\eta=1$), with different coefficients of friction μ. The far left curve is for $\mu=0.1$, and the subsequent curves toward the right are for $\mu=1/3, 0.5, 2/3, 1$. As $\varphi\to\pi/2$, the coefficient $\hat{\kappa}=-\omega^+/\omega^-\to 1$ for all μ (passive friction for vertical impact).

smaller than during the compression phase ($W_r^t < W_c^t$ for $\eta<1$).

The ratio of the works associated with the tangential and normal impulses is

$$\frac{W^t}{W^n}=\frac{\mu b}{a}\frac{1+\eta^2}{1-\eta^2} \tag{41}$$

while

$$\frac{W_c^t}{W_c^n}=-\frac{W_r^t}{W_r^n}=\frac{\mu b}{a} \tag{42}$$

Thus, the parameter $\mu b/a$, appearing in the relationships between κ, $\hat{\kappa}$, and η, can be given a physical interpretation as energy ratio (42), in addition to being equal to the product of the force ratio $|F|/N$ and the velocity ratio u/v.

If, upon the impact, the pendulum sticks to the ground, there is no restitution ($W_r^t=W_r^n=0$), and $W_c^n=W_c^t=\tau_0 a\omega^-/2=-E^-/2$. In this case, all three coefficients of normal restitution are equal to zero, which represents their lower bound, and $\tau_1=\tau_0=-J_0\omega^-/(2a)$.

7 Impact With Elastic Compression

If $\eta=1$ in Eq. (40), then $W^n=0$ and $W_r^n=-W_c^n$, which corresponds to elastic deformation during the impact: The elastic energy stored during the compression phase is fully recovered and used for the liftoff of the pendulum during the restitution phase.[7] In this case, from Eq. (25), the Newton and Poisson coefficients of restitution are the reciprocals of each other ($\hat{\kappa}=1/\kappa$), and equal to

$$\kappa=\left(\frac{a+\mu b}{a-\mu b}\right)^{1/2}=\left(1+\frac{2\mu b}{a-\mu b}\right)^{1/2}>1$$

$$\hat{\kappa}=\left(\frac{a-\mu b}{a+\mu b}\right)^{1/2}=\left(1-\frac{2\mu b}{a+\mu b}\right)^{1/2}<1 \tag{43}$$

Thus, for the pendulum striking a rough surface elastically, Newton's coefficient of normal restitution is smaller than 1, and Poisson's coefficient is greater than 1. The plots of $\hat{\kappa}$ versus the angle $\varphi=\arctan(a/b)$, for various values of μ, are shown in Fig. 4. The plots are for the elastic impact. For each μ, there is no rebound if the angle φ is smaller than the angle corresponding to $\hat{\kappa}=0$. If the frictional impact is inelastic, the plots should be scaled by the corresponding value of $\eta<1$.

[7]The tangential stiffnesses of the pendulum and the surface are assumed to be infinite, so that the elastic energy is entirely due to deformation in the normal direction.

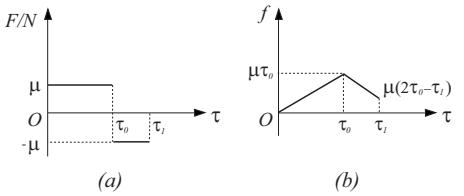

Fig. 5 (*a*) The force ratio F/N versus the normal impulse τ. (*b*) Routh's impact diagram showing the variation of the tangential impulse f versus the normal impulse τ.

The total normal impulse of the elastic impact is

$$\tau_1=\left[1+\left(1+\frac{2\mu b}{a-\mu b}\right)^{1/2}\right]\tau_0,\quad a-\mu b>0 \tag{44}$$

which is greater than $2\tau_0$ (unless $\mu=0$, in which case $\tau_1=2\tau_0$).

The average angular velocity during the elastic impact is zero, and

$$\omega^+=-\hat{\kappa}\omega^-=-\frac{\omega^-}{\kappa}=-\left(\frac{a-\mu b}{a+\mu b}\right)^{1/2}\omega^- \tag{45}$$

The total work done by the impulsive reactions is equal to the dissipated work by friction, which is, from Eq. (35),

$$W=W^t=\tfrac{1}{2}\mu b\tau_0(1+\kappa^2)(\omega^-)^2=-J_0\frac{\mu b}{a+\mu b}(\omega^-)^2 \tag{46}$$

8 Tangential Impact Coefficient

The tangential impulse at an arbitrary stage of the impact process is

$$f(\tau)=\int_0^t F\mathrm{d}t=\int_0^\tau \frac{F}{N}\mathrm{d}\tau \tag{47}$$

Since $F=-\mu N\ \mathrm{sgn}(\tau-\tau_0)$, one readily finds that

$$f(\tau)=\begin{cases}\mu\tau, & \tau\le\tau_0\\ \mu(2\tau_0-\tau), & \tau\ge\tau_0\end{cases} \tag{48}$$

Corresponding Routh's impact diagram is shown in Fig. 5.

Brach [6] defined the tangential impact coefficient as the ratio of the tangential and normal components of the impulse,

$$\hat{\mu}=\frac{\int_0^{t_1}F\mathrm{d}t}{\int_0^{t_1}N\mathrm{d}t}=\frac{f_1}{\tau_1} \tag{49}$$

For the rigid pendulum striking a fixed surface, this gives

$$\hat{\mu}=\frac{\mu(2\tau_0-\tau_1)}{\tau_1} \tag{50}$$

Since $\tau_1=(1+\kappa)\tau_0$, and thus $f_1=\mu(1-\kappa)\tau_0$, the substitution into Eq. (50) yields

$$\hat{\mu}=\frac{\mu(1-\kappa)}{1+\kappa} \tag{51}$$

as in Ref. [4]. The ratio of the tangential and normal components of the impulse is thus not equal to μ (as in Whittaker's theory of frictional impact [2]), but to $\hat{\mu}<\mu$, because there was a change in the slip direction at the transition between the compression and restitution phases of the impact [4,7,8]. If there is no rebound ($\omega^+=0$), then $\kappa=0$ and $\hat{\mu}=\mu$ (as expected, because, without re-

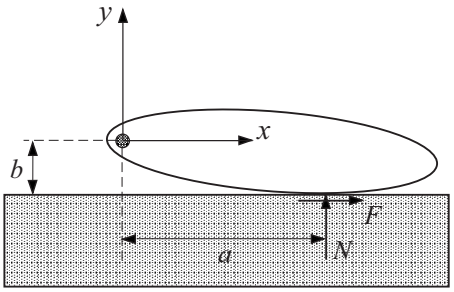

Fig. 6 A nearly vertical impact ($b \ll a$) of a rigid pendulum against a rough horizontal surface. The componential reactions at the contact point are *N* and *F*.

bound, there is no change in the slip direction). Note also that in Eq. (51), $\hat{\mu}<0$ if $\kappa>1$. If $\mu=0$, then $\hat{\mu}=0$, as well.

The energy dissipated by the impact $\Delta E=J_0[(\omega^-)^2-(\omega^+)^2]/2$ can be cast in the form of the generalized Thomson–Tait formula (e.g., Refs. (7) and (8))

$$\Delta E = -\tfrac{1}{2}f_1(u^- + u^+) - \tfrac{1}{2}\tau_1(v^- + v^+) \tag{52}$$

Indeed, from Eq. (1), one can write $a\tau_1+bf_1=-J_0(\omega^--\omega^+)$, so that

$$\Delta E = \tfrac{1}{2}J_0(\omega^- - \omega^+)(\omega^- + \omega^+) = -\tfrac{1}{2}(a\tau_1 + bf_1)(\omega^- + \omega^+) \tag{53}$$

Since $u=b\omega$ and $v=a\omega$, Eq. (53) takes Thomson–Tait form (52).

8.1 Bounds on the Tangential Impact Coefficient. Since Poisson's coefficient of normal restitution is bounded by

$$0 \le \kappa \le \left(\frac{a+\mu b}{a-\mu b}\right)^{1/2} \tag{54}$$

it readily follows from Eq. (51) that the bounds on $\hat{\mu}$ are

$$-\frac{a}{b}[1-\sqrt{1-(\mu b/a)^2}] \le \hat{\mu} \le \mu \tag{55}$$

The upper bound $\hat{\mu}=\mu$ is reached if the pendulum sticks to the ground upon the impact ($\kappa=0$), while the lower bound is reached in the case of elastic frictional impact ($\eta=1$), since then κ is equal to its upper bound. Note that the lower bound on $\hat{\mu}$ in Eq. (55) is negative, but greater than $-a/b$ (which itself must be greater than $-\mu$, for the rebound to take place). For small ratio $\mu b/a$, the lower bound on $\hat{\mu}$ is approximately equal to $-\mu/2$. The negative values of $\hat{\mu}$ mean that in these cases there is a longer lasting backward than forward slip during the impact, i.e., the duration of the restitution phase is longer (on the τ-scale) than that of the compression phase ($\tau_1-\tau_0>\tau_0$, and thus $\kappa>1$). For example, in the case of an elastic impact ($\eta=1$) with $\mu=0.1$ and $a/b=0.3$, so that $\kappa=\sqrt{2}$, one finds that $\tau_1-\tau_0=\sqrt{2}\tau_0$ and $\hat{\mu}\approx-0.017$.

9 Nearly Vertical Impact

The effect of friction on the impact response diminishes with the decrease in the ratio b/a. For a given coefficient of friction μ, and sufficiently small ratio b/a (nearly vertical impact, Fig. 6), from Eq. (23) there follows[8]

$$\kappa = (1+\mu b/a)\eta, \quad \hat{\kappa} = (1-\mu b/a)\eta$$

$$\kappa = (1+2\mu b/a)\hat{\kappa}, \quad \hat{\kappa} = (1-2\mu b/a)\kappa \tag{56}$$

to first order terms in $\mu b/a$ (neglecting the quadratic term $(\mu b/a)^2 \ll 1$). In this case, and to this order of accuracy, the bounds on the kinematic and kinetic coefficients of normal restitution are

$$0 \le \hat{\kappa} \le 1-\mu b/a, \quad 0 \le \kappa \le 1+\mu b/a \tag{57}$$

The corresponding bounds on the total normal impulse are

$$\tau_0 \le \tau_1 \le (2+\mu b/a)\tau_0 \tag{58}$$

The tangential impact coefficient can be expressed in terms of η as

$$\hat{\mu} = \mu\left[\frac{1-\eta}{1+\eta} - 2\mu\frac{b}{a}\frac{\eta}{(1+\eta)^2}\right] \tag{59}$$

to first order terms in $\mu b/a$, and is bounded by

$$-\frac{1}{2}\mu^2\frac{b}{a} \le \hat{\mu} \le \mu \tag{60}$$

For example, if $\mu=0.4$ and $a=4b$, so that $\mu b/a=0.1$, the bounds on the impact coefficients are $0\le\kappa\le1.1$, $0\le\hat{\kappa}\le0.9$, and $-0.02 \le \hat{\mu} \le 0.4$.

10 Conclusion

The frictional impact of rigid pendulum against a fixed surface was studied by using kinematic, kinetic, and energetic definitions of the coefficient of normal restitution, which specify the rebounding angular velocity and the total normal impulse during the impact. The tangential stiffnesses of the pendulum and the surface are assumed to be infinite, so that the elastic energy is entirely due to deformation in the normal direction. It is shown that the energetic coefficient of normal restitution is a geometric mean of the kinematic (Newton's) and kinetic (Poisson's) coefficients of normal restitution. In the case of frictionless impact, the three coefficients are equal to each other. For frictional impact, the energetic coefficient is smaller than Poisson's and greater than Newton's coefficient of normal restitution. The upper bounds on all three coefficients are established, demonstrating that, for the frictional impact, the upper bound on the Newton coefficient is smaller than 1, while the upper bound on the Poisson coefficient is greater than 1. The upper bound on the energetic coefficient of normal restitution is equal to 1, because the restitution phase of the impact cannot deliver more energy than what is stored during the compression phase. The frictional dissipation during the restitution phase is always smaller than during the compression phase. For the pendulum striking a rough surface elastically, without dissipation due to deformation (dissipation of energy being associated with the frictional sliding only), the Newton and Poisson coefficients are the reciprocals of each other. If, upon the impact, the pendulum sticks to the ground, there is no restitution phase of the impact, and all three coefficients of normal restitution are equal to zero, which represents their lower bound. The bounds on the tangential impact coefficient, defined by the ratio of the frictional and normal impulses (which is not equal to μ, because of the slip reversal at the transition from the compression to restitution phases of the impact), are also derived. Its lower bound is negative, while its upper bound is equal to the kinetic coefficient of friction. The simplified bounds on the impact coefficients are deduced in the case of a nearly vertical impact, for which friction exerts the least effect on the impact response. The obtained results may be of interest for the analysis of planar impacts of linkages and related problems in the mechanics of frictional impact [12–14].

Acknowledgment

Research support from the Montenegrin Academy of Sciences and Arts is kindly acknowledged.

[8]Thus, η is here the arithmetic mean of κ and $\hat{\kappa}$, i.e., $\eta=(\kappa+\hat{\kappa})/2$, which is in agreement with the exact geometric mean relationship $\eta=(\kappa\hat{\kappa})^{1/2}$, to first order terms in $\mu b/a$.

References

[1] Beer, F. P., Johnston, E. R., Jr., and Clausen, W. E., 2007, *Vector Mechanics for Engineers-Dynamics*, 8th ed., McGrawHill, New York.

[2] Whittaker, E. T., 1961, *A Treatise on the Analytical Dynamics of Particles and Rigid Bodies*, 4th ed., Cambridge University Press, Cambridge.

[3] Kane, T. R., 1984, "A Dynamics Puzzle," Stanford Mechanics Alumni Club Newsletter, p. 6.

[4] Keller, J. B., 1986, "Impact With Friction," ASME J. Appl. Mech., **53**, pp. 1–4.

[5] Stronge, W. J., 1990, "Rigid Body Collisions With Friction," Proc. R. Soc. London, Ser. A, **431**, pp. 169–181.

[6] Brach, R. M., 1991, *Mechanical Impact Dynamics-Rigid Body Collisions*, Wiley, New York.

[7] Brogliato, B., 1999, *Nonsmooth Mechanics*, Springer-Verlag, London, UK.

[8] Stronge, W. J., 2000, *Impact Mechanics*, Cambridge University Press, Cambridge.

[9] Stewart, D. E., 2000, "Rigid-Body Dynamics With Friction and Impact," SIAM Rev., **42**(1), pp. 3–39.

[10] Johnson, K. L., 1985, *Contact Mechanics*, Cambridge University Press, Cambridge.

[11] Stronge, W. J., 1991, "Friction in Collisions: Resolution of a Paradox," J. Appl. Phys., **69**(2), pp. 610–612.

[12] Guran, A., Pfeiffer, F., and Popp, K., 1996, *Dynamics With Friction: Modeling, Analysis and Experiment, Parts I and II*, World Scientific, Singapore.

[13] Chatterjee, A., and Ruina, A., 1998, "A New Algebraic Rigid-Body Collision Law Based on Impulse Space Considerations," ASME J. Appl. Mech., **65**, pp. 939–951.

[14] Lankarani, H. M., 2000, "A Poisson-Based Formulation for Frictional Impact Analysis of Multibody Mechanical Systems With Open or Closed Kinematic Chains," ASME J. Mech. Des., **122**, pp. 489–497.

The Nonlinear Output Frequency Response Functions of One-Dimensional Chain Type Structures

Z. K. Peng
Department of Automatic Control and Systems Engineering,
University of Sheffield,
Mappin Street,
Sheffield S1 3JD, UK;
State Key Laboratory of Mechanical System and Vibration,
Shanghai Jiao Tong University,
Shanghai 200240, P.R.C.
e-mail: pengzhike@tsinghua.org.cn

Z. Q. Lang
Department of Automatic Control and Systems Engineering,
University of Sheffield,
Mappin Street,
Sheffield S1 3JD, UK
e-mail: z.lang@sheffield.ac.uk

It is well-known that if one or a few components in a structure are of nonlinear properties, the whole structure will behave nonlinearly, and the nonlinear component is often the component where a fault or an abnormal condition occurs. Therefore it is of great significance to detect the position of nonlinear components in structures. Nonlinear output frequency response functions (NOFRFs) are a new concept proposed by the authors for the analysis of nonlinear systems in the frequency domain. The present study is concerned with investigating the NOFRFs of nonlinear one-dimensional chain type systems, which have been widely used to model many real life structures. A series of important properties of the NOFRFs of locally nonlinear one-dimensional chain type structures are revealed. These properties clearly describe the relationships between the NOFRFs of different masses in a one-dimensional chain type system, and allow effective methods to be developed for detecting the position of a nonlinear component in the system. The results are an extension of the authors' previous research studies to a more general and practical case, and have considerable significance in fault diagnosis and location in engineering systems and structures. [DOI: 10.1115/1.3173604]

Keywords: nonlinear vibration, frequency response functions, Volterra series, structure vibration

1 Introduction

There are many real life systems, which can be modeled as either finite or infinite, one-dimensional chain or multidimensional grid type structures. These systems range from simple structures, such as periodically supported beams [1–6] and plates [5,6], to building blocks [7]. The analysis of free and forced vibrations and the mode analysis for linear chain and grid structures are of particular interests [1–6]. Mead [8] provided an excellent review about the research studies on periodic structures, which are a specific class of one-dimensional chain type structures.

In engineering practice, there are considerable one-dimensional chain type structures that would behave nonlinearly due to various factors, and therefore extensive efforts have been made to the study of nonlinear one-dimensional type chain type structures [9–13]. Moreover, it has been revealed that some mechanical structures can behave nonlinearly just because one or a few components of the structures have nonlinear properties, and the nonlinear component is often the component where a fault or an abnormal condition occurs. One well-known example is the beam structures [14] with breathing cracks where the global nonlinear behaviors are caused by a few cracked elements. Therefore it is of great practical significance to effectively detect the position of nonlinear components in mechanical structures, such as beams, for the purpose of fault diagnosis. The detection of damage in large periodic structures has been studied by Zhu and Wu [15]. In their studies, a periodic structure with damage is considered to be linear, and the location and magnitude of damage in large mono-coupled periodic systems have been estimated using the measured changes in natural frequencies. Based on a one-dimensional chain type structure model, Fassois and Sakellariou [7,16] used a stochastic output error vibration-based methodology to detect the damage in structures where the damage elements were modeled as a component of cubic stiffness. In addition, many methods were also proposed for damage detections by observing the appearance of superharmonics and the subresonances [17,18] or using bispectrum analysis [19,20]. However, there are few references, which are especially devoted to the damage detections by detecting and locating nonlinear components in structures.

Motivated by the practical need of detecting and locating nonlinear components in locally nonlinear one-dimensional chain type structures, in a previous study [21] the authors have applied a novel concept known as nonlinear output frequency response functions (NOFRFs) [22,23], which is derived from the Volterra series theory [20] of nonlinear systems, to analyze the one-dimensional chain type structures with one nonlinear component. The study revealed a series of important properties of the NOFRFs for this class of structural systems. The results allow effective methods to be developed for the detection and location of nonlinearity in the structural systems and, therefore, have practical significance in fault diagnosis and location for engineering systems and structures. The present study is concerned with extending the analysis in Ref. [21] to a more general and practical case where the considered one-dimensional chain type structures are subjected to a force excitation added at any point of interest rather than only at the free end, as considered in the initial study in Ref. [21]. The new result is not only of theoretical importance but also has significant engineering implication, since it allows the inspecting signal needed for detection of the system nonlinearity to be applied at any point of an inspected structural system for the purpose of its fault diagnosis.

The paper is organized as follows. Section 2 describes the theoretical background of the Volterra series and the NOFRF concept. The NOFRF based analysis of locally nonlinear one-dimensional chain type structures, where the excitation force applied to the considered system is allowed to be at any point of

Contributed by the Applied Mechanics Division of ASME for publication in the JOURNAL OF APPLIED MECHANICS. Manuscript received August 1, 2007; final manuscript received April 22, 2009; published online September 30, 2009. Review conducted by Wei-Chau Xie.

interest is presented in Sec. 3. The analysis results reveal the properties of the NOFRFs of one-dimensional chain type structures in a more general and practical situation. In Sec. 4, these properties are verified by numerical studies, and the implications of the new results to structural system fault diagnosis are discussed. Finally conclusions are given in Sec. 5.

2 Nonlinear Output Frequency Response Functions

The definition of the NOFRFs is based on the Volterra series theory of nonlinear systems. The Volterra series extends the well-known convolution integral description for linear systems to a series of multidimensional convolution integrals, which can be used to represent a wide class of nonlinear systems [24,25].

Consider the class of nonlinear systems, which are stable at zero equilibrium and which can be described in the neighborhood of the equilibrium by the Volterra series

$$x(t) = \sum_{z=1}^{N} \int_{-\infty}^{\infty} \cdots \int_{-\infty}^{\infty} h_z(\tau_1, \ldots, \tau_z) \prod_{i=1}^{z} u(t-\tau_i) d\tau_i \tag{1}$$

where $x(t)$ and $u(t)$ are the output and input of the system, $h_z(\tau_1, \ldots, \tau_z)$ is the nth order Volterra kernel, and N denotes the maximum order of the system nonlinearity. Lang and Billings [26] derived an expression for the output frequency response of this class of nonlinear systems to a general input. The result is

$$X(j\omega) = \sum_{z=1}^{N} X_z(j\omega) \quad \text{for} \quad \forall\, \omega$$

$$X_z(j\omega) = \frac{1/\sqrt{z}}{(2\pi)^{z-1}} \int_{\omega_1+,\ldots,+\omega_z=\omega} H_z(j\omega_1, \ldots, j\omega_z) \prod_{i=1}^{z} U(j\omega_i) d\sigma_{z\omega} \tag{2}$$

In Eq. (2), $X(j\omega)$ is the spectrum of the system output, $X_z(j\omega)$ represents the zth order output frequency response of the system

$$H_z(j\omega_1, \ldots, j\omega_z) = \int_{-\infty}^{\infty} \cdots \int_{-\infty}^{\infty} h_z(\tau_1, \ldots, \tau_z) e^{-j(\omega_1\tau_1+,\ldots,+\omega_z\tau_z)} d\tau_1 \ldots d\tau_z \tag{3}$$

is called the generalized frequency response function (GFRF) of the system [27] and

$$\int_{\omega_1+,\ldots,+\omega_z=\omega} H_z(j\omega_1, \ldots, j\omega_z) \prod_{i=1}^{z} U(j\omega_i) d\sigma_{z\omega}$$

denotes the integration of $H_z(j\omega_1, \ldots, j\omega_z)\Pi_{i=1}^{z} U(j\omega_i)$ over the z-dimensional hyperplane $\omega_1+\cdots+\omega_z=\omega$, with $\sigma_{z\omega}$ representing the whole integral field satisfying the constraint $\omega_1+\cdots+\omega_z=\omega$ and $d\sigma_{z\omega}$ denoting an infinitely small element within this integral field.

When $z=1$, the GFRF, as defined in Eq. (3), becomes

$$H_1(j\omega_1) = \int_{-\infty}^{\infty} h_1(\tau_1) e^{-\omega_1\tau_1 j} d\tau_1$$

which is the well-known frequency response function (FRF) concept for linear systems. Therefore, the GFRFs extend the linear FRF concept to the nonlinear case, and Eq. (2) is an extension of the well-known linear relationship between the system input and output spectra $X(j\omega)=H(j\omega)U(j\omega)$, where $H(j\omega)=H_1(j\omega)$, to the nonlinear situation.

To demonstrate how the output spectrum of a nonlinear system can be expressed by Eq. (2), consider, as an example, a nonlinear oscillator described by the differential equation

$$m\ddot{x} + c\dot{x} + kx + r_2x^2 + r_3x^3 = u(t) \tag{4}$$

where m, c, and k are the linear characteristic parameters, and r_2 and r_3 are the nonlinear characteristic parameters.

Using the algorithm in Refs. [28–30], the GFRFs of system (4) can be determined as follows:

$$H_1(j\omega) = \frac{1}{-m\omega^2 + jc\omega + k} \tag{5}$$

$$H_2(j\omega_1, j\omega_2) = -r_2 H_1(j\omega_1) H_1(j\omega_2) H_1(j\omega_1 + j\omega_2) \tag{6}$$

$$\begin{aligned} H_3(j\omega_1, j\omega_2, j\omega_3) = &-\{(2/3) r_2 [H_1(j\omega_1) H_2(j\omega_2, j\omega_3) \\ &+ H_1(j\omega_2) H_2(j\omega_1, j\omega_3) + H_1(j\omega_3) H_2(j\omega_1, j\omega_2)] \\ &+ r_3 H_1(j\omega_1) H_1(j\omega_2) H_1(j\omega_3)\} \\ &\times H_1(j\omega_1 + j\omega_2 + j\omega_3) \end{aligned} \tag{7}$$

If the maximum order of the system nonlinearity can be taken as $N=3$, then, given the spectrum of the system input $U(j\omega)$, the output spectrum of system (4) can theoretically be determined as

$$X(j\omega) = \begin{bmatrix} H_1(j\omega)U(j\omega) + \dfrac{1/\sqrt{2}}{(2\pi)} \displaystyle\int_{\omega_1+\omega_2=\omega} H_2(j\omega_1, j\omega_2) U(j\omega_1) U(j\omega_2) d\sigma_{2\omega} \\ + \dfrac{1/\sqrt{3}}{(2\pi)^2} \displaystyle\int_{\omega_1+\omega_2+\omega_3=\omega} H_3(j\omega_1, j\omega_2, j\omega_3) U(j\omega_1) U(j\omega_2) U(j\omega_3) d\sigma_{3\omega} \end{bmatrix} \tag{8}$$

with $H_1(j\omega)$, $H_2(j\omega_1, j\omega_2)$, and $H_3(j\omega_1, j\omega_2, j\omega_3)$ being determined from Eqs. (5)–(7).

The NOFRFs are a new concept recently introduced by Lang and Billings [22]. The concept is defined as

$$G_z(j\omega) = \frac{\displaystyle\int_{\omega_1+,\ldots,+\omega_z=\omega} H_z(j\omega_1, \ldots, j\omega_z) \prod_{i=1}^{z} U(j\omega_i) d\sigma_{z\omega}}{\displaystyle\int_{\omega_1+,\ldots,+\omega_z=\omega} \prod_{i=1}^{z} U(j\omega_i) d\sigma_{z\omega}} \tag{9}$$

under the condition

$$U_z(j\omega) = \frac{1/\sqrt{z}}{(2\pi)^{z-1}} \int_{\omega_1+,\ldots,+\omega_z=\omega} \prod_{i=1}^{z} U(j\omega_i) d\sigma_{z\omega} \neq 0 \tag{10}$$

and can be considered to be an alternative extension of the FRF concept for linear systems to the nonlinear case. The most important advantage of the NOFRF concept over the GRFRs is the one-dimensional nature. This allows the analysis of the output frequency response of nonlinear systems to be conducted in a way similar to the analysis of the output frequency response of linear systems. This is because by introducing the NOFRF concept, Eq. (2) can be written as

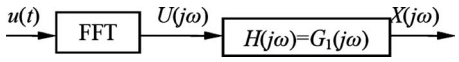

Fig. 1 The NOFRF based representation for the output frequency response of linear systems

$$X(j\omega) = \sum_{z=1}^{N} X_z(j\omega) = \sum_{z=1}^{N} G_z(j\omega)U_z(j\omega) \tag{11}$$

where $U_z(j\omega)$ is defined as Eq. (10). Equation (11) is similar to the description of the output frequency response for linear systems. Figures 1 and 2 illustrate how the NOFRF concept can be used to describe the output spectra of linear and nonlinear systems, respectively, which clearly shows the advantage of the NOFRFs' one-dimensional nature in describing the system output frequency responses.

To demonstrate the NOFRF based description for the output spectrum of nonlinear systems, consider system (4) again as an example and assume that the excitation force is a sinusoidal signal, e.g., $u(t)=A\cos(\omega_F t)$. In this case, it can be shown that condition (10) implies that the system zth order NOFRF $G_z(j\omega)$ is valid over the system zth order output frequency range given by

$$\Omega_z = \{(-z+2k)\omega_F, k = 0, 1, \cdots, z\} \tag{12}$$

and when $\omega \in \Omega_z$, $U_z(j\omega)$ can be given by

$$U_z(j(-z+2k)\omega_F) = \frac{1}{2^z}\frac{z!}{k!\,(z-k)!}|A|^z \tag{13}$$

Therefore, $G_1(j\omega)$, $G_2(j\omega)$, and $G_3(j\omega)$ are valid over the frequency ranges $\{-\omega_F, \omega_F\}$, $\{-2\omega_F, 0, 2\omega_F\}$, and $\{-3\omega_F, \omega_F, \omega_F, 3\omega_F\}$, respectively, and the NOFRFs of system (4) up to the third order at their corresponding valid frequency ranges can be determined from Eqs. (9), (5)–(7), and (13) as

$$G_1(j\omega_F) = \frac{1}{-m\omega_F^2 + jc\omega_F + k} \tag{14}$$

$$G_2(j0) = H_2(-j\omega_F, j\omega_F) = -\frac{r_2}{k}H_1(-j\omega_F)H_1(j\omega_F) \tag{15}$$

$$G_2(j2\omega_F) = H_2(j\omega_F, j\omega_F) = -r_2 H_1^2(j\omega_F)H_1(j2\omega_F) \tag{16}$$

$$G_3(j\omega_F) = H_3(-j\omega_F, j\omega_F, j\omega_F) = |H_1(j\omega_F)|^2 H_1^2(j\omega_F)\left[\frac{2r_2^2}{3}\left(H_1(j2\omega_F) + \frac{2}{k}\right) - r_3\right] \tag{17}$$

$$G_3(j3\omega_F) = H_3(j\omega_F, j\omega_F, j\omega_F) = H_1^3(j\omega_F)H_1(j3\omega_F)(2r_2^2 H_1(j2\omega_F) - r_3) \tag{18}$$

Consequently, when $N=3$, the output frequency response of system (4) over the total output frequency range $\Omega = \Omega_1 \cup \Omega_2 \cup \Omega_3 = \{\pm 3\omega_F, \pm 2\omega_F, \pm \omega_F, 0\}$ can be described using Eq. (11) as

$$X(j\omega_F) = U_1(j\omega_F)G_1(j\omega_F) + U_3(j\omega_F)G_3(j\omega_F) \tag{19}$$

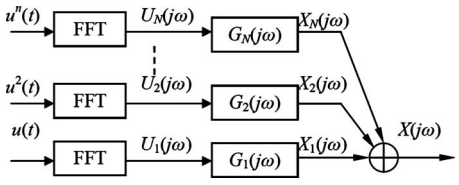

Fig. 2 The NOFRF based representation for the output frequency response of nonlinear systems

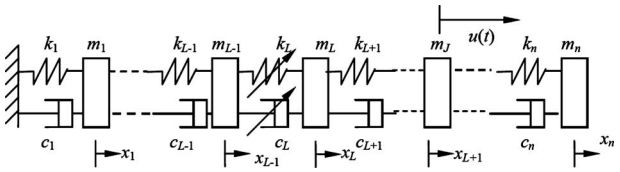

Fig. 3 A locally nonlinear multidegree freedom oscillator

$$X(j0) = U_2(j0)G_2(j0) \tag{20}$$

$$X(j2\omega_F) = U_2(j2\omega_F)G_2(j2\omega_F) \tag{21}$$

$$X(j3\omega_F) = U_3(j3\omega_F)G_3(j3\omega_F) \tag{22}$$

where $U_1(j\omega_F)$, $U_2(j0)$, $U_2(j2\omega_F)$, $U_3(j3\omega_F)$, and $U_3(j\omega_F)$ are obtained from Eq. (13).

For nonlinear systems, the dynamical properties are determined in the frequency domain by the GFRFs $H_z(j\omega_1, \ldots, j\omega_z)$ $(z=1, \ldots, N)$. It can be observed from Eq. (9) that the NOFRF $G_z(j\omega)$ is a weighted sum of the GFRF $H_z(j\omega_1, \ldots, j\omega_z)$ over the z-dimensional hyperplane $\omega_1 + \cdots + \omega_z = \omega$ with the weights depending on the system input. Therefore, when the system input is fixed, the NOFRF $G_z(j\omega)$ can be regarded as a one-dimensional description of the system properties represented by the GFRF $H_z(j\omega_1, \ldots, j\omega_z)$ and can be used to simplify the complicated GFRF based analysis of nonlinear systems in the frequency domain. The objective of the present study is to apply the NOFRF concept to analyze nonlinear one-dimensional chain type structures, in order to reveal the important properties of the systems. This will facilitate the detection of the nonlinear component in the system, which has significant implications for the fault diagnosis of practical engineering structural systems.

3 Analysis of Nonlinear One-Dimensional Chain Type Structures Using the NOFRFs

3.1 The GFRFs of Locally Nonlinear One-Dimensional Chain Type Structures. Consider the one-dimensional nonlinear chain type structures, as shown in Fig. 3, where the Lth component is nonlinear and a force excitation is applied on the Jth mass. This model has been used in Refs. [7,12–15] for nonlinear structural analysis and structural damage detection and assessment.

Assume that the restoring forces $S_{LS}(\Delta)$ and $S_{LD}(\dot{\Delta})$ of the Lth spring and damper are the polynomial functions of the deformation $\Delta = x_{L-1} - x_L$ and $\dot{\Delta} = \dot{x}_{L-1} - \dot{x}_L$ respectively, e.g.,

$$S_{LS}(\Delta) = \sum_{i=1}^{P} r_i \Delta^i, \quad S_{LD}(\dot{\Delta}) = \sum_{i=1}^{P} w_i \dot{\Delta}^i \tag{23}$$

where P is the degree of the polynomials and $k_L = r_1$ and $c_L = w_1$. Without loss of generality, further assume $L \neq 1, n$. Denote

$$F_{\text{non}} = \sum_{i=2}^{P} w_i(\dot{x}_{L-1} - \dot{x}_L)^i + \sum_{i=2}^{P} r_i(x_{L-1} - x_L)^i \tag{24}$$

$$F_N = (\overbrace{0 \cdots 0}^{L-2} \quad F_{\text{non}} \quad -F_{\text{non}} \quad \overbrace{0 \cdots 0}^{n-L})^T \tag{25}$$

Then the motion of the nonlinear oscillator in Fig. 3 can be described in a matrix form as

$$M\ddot{x} + C\dot{x} + Kx = -F_N + F(t) \tag{26}$$

where

$$M = \begin{bmatrix} m_1 & 0 & \cdots & 0 \\ 0 & m_2 & \cdots & 0 \\ \vdots & \vdots & \ddots & \vdots \\ 0 & 0 & \cdots & m_n \end{bmatrix}$$

$$C = \begin{bmatrix} c_1 + c_2 & -c_2 & 0 & \cdots & 0 \\ -c_2 & c_2 + c_3 & -c_3 & \ddots & \vdots \\ 0 & \ddots & \ddots & \ddots & 0 \\ \vdots & \ddots & -c_{n-1} & c_{n-1} + c_n & -c_n \\ 0 & \cdots & 0 & -c_n & c_n \end{bmatrix}$$

$$K = \begin{bmatrix} k_1 + k_2 & -k_2 & 0 & \cdots & 0 \\ -k_2 & k_2 + k_3 & -k_3 & \ddots & \vdots \\ 0 & \ddots & \ddots & \ddots & 0 \\ \vdots & \ddots & -k_{n-1} & k_{n-1} + k_n & -k_n \\ 0 & \cdots & 0 & -k_n & k_n \end{bmatrix}$$

are the system mass, damping, and stiffness matrices, respectively. $x=(x_1,\cdots,x_n)'$ is the displacement vector, and

$$F(t) = (\overbrace{0,\cdots,0}^{J-1},u(t),\overbrace{0,\cdots,0}^{n-J})^T \tag{27}$$

is the external force vector.

The system described by Eq. (26) is a typical locally nonlinear one-dimensional chain type structure. The Lth nonlinear component can make the whole system behave nonlinearly. The Volterra series can be used to describe the relationships between the displacements $x_i(t)$ $(i=1,\ldots,n)$ and the input force $u(t)$ of system (26) as

$$x_i(t) = \sum_{j=1}^{N} \int_{-\infty}^{\infty} \cdots \int_{-\infty}^{\infty} h_{(i,j)}(\tau_1,\ldots,\tau_j) \prod_{Z=1}^{j} u(t-\tau_Z) d\tau_Z \tag{28}$$

where $h_{(i,j)}(\tau_1,\ldots,\tau_j)$, $(i=1,\ldots,n,\ j=1,\ldots,N)$, represents the jth order Volterra kernel for the relationship between $u(t)$ and the displacement of mass m_i.

The Fourier transform of $h_{(i,j)}(\tau_1,\ldots,\tau_j)$ is its corresponding GFRF, which will be denoted by $H_{(i,j)}(j\omega_1,\ldots,j\omega_j)$ $(i=1,\cdots,n,\ j=1,\cdots,N)$ as follows.

It can be deduced (see Appendix A) that the n sets of GFRFs of system (26)

$$H_{(i,1)}(j\omega_1),\cdots,H_{(i,N)}(j\omega_1,\cdots,j\omega_N) \quad (i=1,2,\ldots,n)$$

satisfy the following relationships:

$$\frac{H_{(i,1)}(j\omega)}{H_{(i+1,1)}(j\omega)} = \frac{Q_{(i,J)}(j\omega)}{Q_{(i+1,J)}(j\omega)} = \lambda_1^{i,i+1}(\omega) \quad (i=1,\ldots,n-1) \tag{29}$$

and

$$\frac{H_{(i,\bar{N})}(j\omega_1,\ldots,j\omega_{\bar{N}})}{H_{(i+1,\bar{N})}(j\omega_1,\ldots,j\omega_{\bar{N}})} = \frac{Q_{i,L-1}(j(\omega_1+\cdots+\omega_{\bar{N}})) - Q_{i,L}(j(\omega_1+\cdots+\omega_{\bar{N}}))}{Q_{i+1,L-1}(j(\omega_1+\cdots+\omega_{\bar{N}})) - Q_{i+1,L}(j(\omega_1+\cdots+\omega_{\bar{N}}))} = \lambda_{\bar{N}}^{i,i+1}(\omega_1+\cdots+\omega_{\bar{N}}) \quad (\bar{N}>1; i=1,\ldots,n-1) \tag{30}$$

where

$$\begin{bmatrix} Q_{(1,1)}(j\omega) & \cdots & Q_{(1,n)}(j\omega) \\ \vdots & \ddots & \vdots \\ Q_{(n,1)}(j\omega) & \cdots & Q_{(n,n)}(j\omega) \end{bmatrix} = (-M\omega^2 + jC\omega + K)^{-1} \tag{31}$$

Equations (29) and (30) give a comprehensive description for the relationships between the GFRFs of any two consecutive masses for the nonlinear one-dimensional chain type system (25).

3.2 The NOFRFs of Locally Nonlinear One-Dimensional Chain Type Structures. According to the definition of the NOFRFs in Eq. (9), the $\bar{N}$th order NOFRF of the ith mass of system (26) can be expressed as

$$G_{(i,\bar{N})}(j\omega) = \frac{\int_{\omega_1+,\ldots,+\omega_{\bar{N}}=\omega} H_{(i,\bar{N})}(j\omega_1,\ldots,j\omega_{\bar{N}}) \prod_{q=1}^{\bar{N}} U(j\omega_q) d\sigma_{\bar{N}\omega}}{\int_{\omega_1+,\ldots,+\omega_{\bar{N}}=\omega} \prod_{q=1}^{\bar{N}} U(j\omega_q) d\sigma_{\bar{N}\omega}} \quad (1 \le \bar{N} \le N, 1 \le i \le n) \tag{32}$$

where $U(j\omega)$ is the Fourier transform of the input force $u(t)$.

Denote

$$G_{\bar{N}}(j\omega) = (G_{(1,\bar{N})}(j\omega)\cdots G_{(n,\bar{N})}(j\omega))^T \quad (1 \le \bar{N} \le N) \tag{33}$$

From Eqs. (A20) and (32) it can be deduced that

$$\boldsymbol{\Theta}(j\omega) G_{\bar{N}}(j\omega) = \boldsymbol{\Lambda}_{\bar{N}}(j\omega) \quad (2 \le \bar{N} \le N) \tag{34}$$

where

$$\boldsymbol{\Lambda}_{\bar{N}}(j\omega) = (\overbrace{0\cdots 0}^{L-2} \quad \boldsymbol{\Lambda}_{\bar{N}}^{L-1,L}(j\omega) \quad -\boldsymbol{\Lambda}_{\bar{N}}^{L-1,L}(j\omega) \quad \overbrace{0\cdots 0}^{n-L})^T \tag{35}$$

and

$$\boldsymbol{\Lambda}_{\bar{N}}^{L-1,L}(j\omega) = \frac{\int_{\omega_1+,\ldots,+\omega_{\bar{N}}=\omega} \boldsymbol{\Lambda}_{\bar{N}}^{L-1,L}(j\omega_1,\ldots,j\omega_{\bar{N}}) \prod_{q=1}^{\bar{N}} U(j\omega_q) d\sigma_{\bar{N}\omega}}{\int_{\omega_1+,\ldots,+\omega_{\bar{N}}=\omega} \prod_{q=1}^{\bar{N}} U(j\omega_q) d\sigma_{\bar{N}\omega}} \tag{36}$$

Moreover, according to Eq. (30), for any $\bar{N} \ge 2$, Eq. (32) can be rewritten as

$$G_{(i,\bar{N})}(j\omega) = \frac{\int_{\omega_1+,\ldots,+\omega_{\bar{N}}=\omega} \lambda_{\bar{N}}^{i,i+1}(\omega_1+\cdots+\omega_{\bar{N}}) H_{(i+1,\bar{N})}(j\omega_1,\ldots,j\omega_{\bar{N}}) \prod_{q=1}^{\bar{N}} U(j\omega_q) d\sigma_{\bar{N}\omega}}{\int_{\omega_1+,\ldots,+\omega_{\bar{N}}=\omega} \prod_{q=1}^{\bar{N}} U(j\omega_q) d\sigma_{\bar{N}\omega}} = \lambda_{\bar{N}}^{i,i+1}(\omega) G_{(i+1,\bar{N})}(j\omega) \quad (2 \le \bar{N} \le N, 1 \le i \le n-1) \tag{37}$$

Therefore, for two consecutive masses, the NOFRFs satisfy

$$\frac{G_{(i,\bar{N})}(j\omega)}{G_{(i+1,\bar{N})}(j\omega)} = \frac{Q_{i,L-1}(j\omega) - Q_{i,L}(j\omega)}{Q_{i+1,L-1}(j\omega) - Q_{i+1,L}(j\omega)} = \lambda_{\bar{N}}^{i,i+1}(\omega)(2 \le \bar{N} \le N, 1 \le i \le n-1) \quad (38)$$

Similarly, when $\bar{N}=1$, according to Eqs. (A3) and (32), the first order NOFRFs of the system satisfy

$$\Theta(j\omega)G_1(j\omega) = (\overbrace{0 \cdots 0}^{J-1} \quad 1 \quad \overbrace{0 \cdots 0}^{n-J})^T \quad (39)$$

It is known from Eq. (29) that

$$G_{(i,1)}(j\omega) = \lambda_1^{i,i+1}(\omega)G_{(i+1,1)}(j\omega) \quad (1 \le i \le n-1) \quad (40)$$

Therefore

$$\frac{G_{(i,1)}(j\omega)}{G_{(i+1,1)}(j\omega)} = \frac{Q_{(i,J)}(j\omega)}{Q_{(i+1,J)}(j\omega)} = \lambda_1^{i,i+1}(\omega) \quad (1 \le i \le n-1) \quad (41)$$

Equations (38) and (41) give a comprehensive description for the relationships between the NOFRFs of two consecutive masses of the nonlinear one-dimensional chain type system (26).

From Eqs. (38) and (40), it is known that the ratio of the $\bar{N}$th order NOFRFs of two consecutive mass, $\lambda_{\bar{N}}^{i,i+1}(\omega)$ $(1 \le \bar{N} \le N)$, is only dependent on the linear characteristic parameters of the one-dimensional chain type system. This implies that the propagation of the system *nonlinear effect* induced by the nonlinear component in the system is totally governed by the system linear characteristic parameters. This is an important property revealed in the present study. Based on this property, significant relationships between the NOFRFs of two consecutive masses can be obtained. The results are described in the following proposition.

PROPOSITION 1. *For two masses, which are located on the left of the nonlinear spring or on the right of the input force, there exists the following relationship between the NOFRFs of the two masses:*

$$\frac{G_{(i,1)}(j\omega)}{G_{(i+1,1)}(j\omega)} = \cdots = \frac{G_{(i,N)}(j\omega)}{G_{(i+1,N)}(j\omega)} \quad (1 \le i \le L-2, J \le i < n) \quad (42)$$

and for two masses located between the nonlinear spring and the input force, the following relationships hold:

$$\frac{G_{(i,1)}(j\omega)}{G_{(i+1,1)}(j\omega)} \ne \frac{G_{(i,2)}(j\omega)}{G_{(i+1,2)}(j\omega)} = \cdots = \frac{G_{(i,N)}(j\omega)}{G_{(i+1,N)}(j\omega)} \quad (L-1 \le i \le J-1) \quad (43)$$

The proof of the proposition is given in Appendix B.

From Proposition 1, a series of properties of the nonlinear one-dimensional chain type system (26) can be derived. These properties are summarized as follows.

(i) For two masses, which are on the left of the nonlinear spring or on the right of the input force, there exists the following relationship between the spectra of the displacements of the masses:

$$X_i(j\omega) = \lambda_1^{i,i+1}(j\omega)X_{i+1}(j\omega) \quad (1 \le i \le L-2, J \le i < n) \quad (44)$$

(ii) For any two masses, which are either on the left of the nonlinear spring or on the right of the input force, the following relationships hold:

$$\frac{G_{(i,1)}(j\omega)}{G_{(i+k,1)}(j\omega)} = \cdots = \frac{G_{(i,N)}(j\omega)}{G_{(i+k,N)}(j\omega)} = \lambda_1^{i,i+k}(\omega) \quad (1 \le i \le L-2 \quad \text{and} \quad i+k \le L-1 \quad \text{or} \quad J \le i < n \quad \text{and} \quad J < i+k \le n) \quad (45)$$

where

$$\lambda_1^{i,i+k}(\omega) = \prod_{d=0}^{k-1} \lambda_1^{i+d,i+d+1}(\omega) \quad (46)$$

(iii) For any two masses, which are either on the left of the nonlinear spring or on the right of the input force, the following relationships hold:

$$X_i(j\omega) = \lambda_1^{i,i+k}(\omega)X_{i+k}(j\omega) \quad (1 \le i \le L-2 \quad \text{and} \quad i+k \le L-1 \quad \text{or} \quad J \le i < n \quad \text{and} \quad J < i+k \le n) \quad (47)$$

(iv) For any two masses located between the nonlinear spring and the input force, the following relationship holds:

$$\frac{G_{(i,1)}(j\omega)}{G_{(i+k,1)}(j\omega)} \ne \frac{G_{(i,2)}(j\omega)}{G_{(i+k,2)}(j\omega)} = \cdots = \frac{G_{(i,N)}(j\omega)}{G_{(i+k,N)}(j\omega)} = \lambda_2^{i,i+k}(\omega) \quad (L-1 \le i \le J-1 \quad \text{and} \quad L \le i+k \le J) \quad (48)$$

and

$$\lambda_2^{i,i+k}(\omega) = \prod_{d=0}^{k-1} \lambda_2^{i+d,i+d+1}(\omega) \quad (49)$$

(v) For any two masses at the different sides of the nonlinear spring or at the different sides of the input force, the following relationships hold:

$$\frac{G_{(i,1)}(j\omega)}{G_{(k,1)}(j\omega)} \ne \frac{G_{(i,2)}(j\omega)}{G_{(k,2)}(j\omega)} = \cdots = \frac{G_{(i,N)}(j\omega)}{G_{(k,N)}(j\omega)} \quad (1 \le i \le L-1 \quad \text{and} \quad L \le k \le n \quad \text{or} \quad 1 \le i \le J-1 \quad \text{and} \quad J \le k \le n) \quad (50)$$

Property (i) is straightforward since, according to Eq. (6), the spectrum of the displacement of the ith mass can be expressed as

$$X_{i+1}(j\omega) = \sum_{k=1}^{N} G_{(i+1,k)}(j\omega)U_k(j\omega) \quad (51)$$

Using Proposition 1, Eq. (51) can be written as

$$X_{i+1}(j\omega) = \sum_{k=1}^{N} \lambda_k^{i,i+1}(j\omega)G_{(i,k)}(j\omega)U_k(j\omega) = \lambda_1^{i,i+1}(j\omega)\sum_{k=1}^{N} G_{(i,k)}(j\omega)U_k(j\omega) \quad (52)$$

Therefore, $X_{i+1}(j\omega) = \lambda_1^{i,i+1}(j\omega)X_i(j\omega)$.

The proof of properties (ii)–(v) also only needs some simple calculations. The details are therefore omitted here.

Proposition 1 and Properties (i)–(v) are an important development for the NOFRF based nonlinear system frequency domain analysis and are especially useful for the detection of nonlinearity in locally nonlinear one-dimensional chain type structures. Obviously, a direct application of these properties in the detection of nonlinearity in system (26) can be achieved by determining the NOFRFs associated with all the masses in the system, evaluating and comparing the ratios of the NOFRFs associated with two consecutive masses, and finally determining J in Eqs. (42) and

Table 1 The evaluated results of $G_1(j\omega_F)$, $G_3(j\omega_F)$, $G_2(j2\omega_F)$, and $G_4(j2\omega_F)$

	$G_1(j\omega_F)$ $(\times 10^{-6})$	$G_3(j\omega_F)$ $(\times 10^{-9})$	$G_2(j2\omega_F)$ $(\times 10^{-9})$	$G_4(j2\omega_F)$ $(\times 10^{-10})$
Mass 1	$-1.9442+2.8776i$	$5.4586-7.3663i$	$6.0215-12.9855i$	$-1.9521-3.4108i$
Mass 2	$-4.1766+4.8383i$	$11.5721-12.2812i$	$18.5089-19.1412i$	$-1.3474-7.1855i$
Mass 3	$-6.7369+5.0608i$	$18.3492-12.5736i$	$38.1986-9.3255i$	$3.9767-10.0350i$
Mass 4	$-9.2319+2.9520i$	$-12.7969+5.4557i$	$-38.0890+6.2165i$	$-4.6556+9.5167i$
Mass 5	$-10.7758-1.6643i$	$-5.4352+7.5923i$	$-16.5271+16.8545i$	$1.1500+6.3785i$
Mass 6	$-10.1014-8.3275i$	$1.2207+7.2432i$	$-1.2526+13.2872i$	$2.7770+2.3907i$
Mass 7	$-15.1122-0.8377i$	$6.0974+5.9104i$	$6.2132+5.7292i$	$2.2699-0.4817i$
Mass 8	$-17.3365+3.5237i$	$8.6436+4.8795i$	$8.6698+0.5735i$	$1.5053-1.8507i$

(43) from the evaluated NOFRFs' ratios so as to locate the position of the nonlinear component. Other more effective methods can also be developed based on the proposition and properties and will be discussed in details in other publications. In Sec. 4, simulation examples will be used to demonstrate the validity of these important properties with locally nonlinear one-dimensional chain type structures.

4 Numerical Study

To verify the analysis results in Sec. 3, a damped 8DOF oscillator was used to conduct numerical studies, in which the fourth spring was nonlinear. As widely used in modal analysis, the damping was assumed to be proportional to the stiffness, e.g., $C=\mu K$. The values of the system parameters were taken as

$$m_1=\cdots=m_8=1,\quad r_1=k_1=\cdots=k_8=3.5531\times 10^4,\quad \mu=0.01$$

$$r_2=0.8\times r_1^2,\quad r_3=0.4\times r_1^3,\quad w_1=\mu r_1,\quad w_2=0.1\mu^2 k_2$$

$$w_3=0$$

and the input was a harmonic force acting on the sixth mass, $u(t)=A\ \sin(2\pi\times 20t)$.

It is well-known that when a nonlinear system is subject to a harmonic input

$$u(t)=A\ \cos(\omega_F t+\beta) \tag{53}$$

superharmonics can appear in the system output response. These superharmonics can be expressed using the NOFRFs as follows [31]:

$$X(jk\omega_F)=\sum_{n=1}^{[(N-k+1)/2]} G_{k+2(n-1)}(jk\omega_F)A_{k+2(n-1)}(jk\omega_F)$$

$$(k=0,1,\ldots,N) \tag{54}$$

where $[\cdot]$ means to take the integer part, and

$$A_n(j(-n+2k)\omega_F)=\frac{1}{2^n}\frac{n!}{k!\,(n-k)!}|A|^n e^{j(-n+2k)\beta} \tag{55}$$

$$G_n(j(-n+2k)\omega_F)=H_n(\overbrace{j\omega_F,\cdots,j\omega_F}^{k},\overbrace{-j\omega_F,\cdots,-j\omega_F}^{n-k}) \tag{56}$$

If only the NOFRFs up to fourth order is considered, i.e., $N=4$, according to Eq. (54), the spectra of the displacements of the eight masses [32,33] can be written as

$$X_i(j\omega_F)=G_{(i,1)}(j\omega_F)A_1(j\omega_F)+G_{(i,3)}(j\omega_F)A_3(j\omega_F)$$

$$X_i(j2\omega_F)=G_{(i,2)}(j2\omega_F)A_2(j2\omega_F)+G_{(i,4)}(j2\omega_F)A_4(j2\omega_F)$$

$$X_i(j3\omega_F)=G_{(i,3)}(j3\omega_F)A_3(j3\omega_F)$$

$$X_i(j4\omega_F)=G_{(i,4)}(j4\omega_F)A_4(j4\omega_F)\quad (i=1,\ldots,8) \tag{57}$$

From Eq. (57), it is known that, using the method in Ref. [34], the system responses to two different inputs with the same waveform but different strengths are sufficient to be used to estimate the NOFRFs up to the fourth order. Therefore, in this numerical study, two sinusoidal input signals with amplitudes $A^{(1)}=0.8$ and $A^{(2)}=1.0$, respectively, were used. Simulation studies were conducted using the fourth-order Runge–Kutta method to obtain the responses of the system to the sinusoidal inputs. The responses under the two different inputs are denoted as $x_i^{(1)}$ and $x_i^{(2)}$ $(i=1,\ldots,8)$, whose corresponding FFT spectra are denoted as $X_i^{(1)}$ and $X_i^{(2)}$. $A_k(\cdot)$, $(k=1,2,3,4)$ in Eq. (57) corresponding the two different inputs will be denoted as $A_k^{(1)}(\cdot)$ and $A_k^{(2)}(\cdot)$, $(k=1,2,3,4)$, respectively. According to Eq. (57), the fundamental harmonic output components $X_i^{(1)}(j\omega_F)$ and $X_i^{(2)}(j\omega_F)$ $(i=1,\ldots,8)$ corresponding to the two different inputs can be expressed as

$$\begin{pmatrix} X_i^{(1)}(j\omega_F) \\ X_i^{(2)}(j\omega_F) \end{pmatrix}=\begin{pmatrix} A_1^{(1)}(j\omega_F) & A_3^{(1)}(j\omega_F) \\ A_1^{(2)}(j\omega_F) & A_3^{(2)}(j\omega_F) \end{pmatrix}\begin{pmatrix} G_{(i,1)}(j\omega_F) \\ G_{(i,3)}(j\omega_F) \end{pmatrix} \tag{58}$$

Therefore, $G_{(i,1)}(j\omega_F)$ and $G_{(i,3)}(j\omega_F)$ can be evaluated as

$$\begin{pmatrix} G_{(i,1)}(j\omega_F) \\ G_{(i,3)}(j\omega_F) \end{pmatrix}=\begin{pmatrix} A_1^{(1)}(j\omega_F) & A_3^{(1)}(j\omega_F) \\ A_1^{(2)}(j\omega_F) & A_3^{(2)}(j\omega_F) \end{pmatrix}^{-1}\begin{pmatrix} X_i^{(1)}(j\omega_F) \\ X_i^{(2)}(j\omega_F) \end{pmatrix} \tag{59}$$

Similarly $G_{(i,2)}(j2\omega_F)$ and $G_{(i,4)}(j2\omega_F)$ can also be obtained. The evaluated results of $G_1(j\omega_F)$, $G_3(j\omega_F)$, $G_2(j2\omega_F)$, and $G_4(j2\omega_F)$ for all masses are given in Table 1. According to the analysis results in Sec. 3, it is known that the following relationships should be tenable:

$$\lambda_1^{i,i+1}(j\omega_F)=\frac{G_{(i,1)}(j\omega_F)}{G_{(i+1,1)}(j\omega_F)}=\frac{G_{(i,3)}(j\omega_F)}{G_{(i+1,3)}(j\omega_F)}=\lambda_3^{i,i+1}(j\omega_F)$$

$$\text{for } i=1,2,6,7$$

$$\lambda_1^{i,i+1}(j\omega_F)=\frac{G_{(i,1)}(j\omega_F)}{G_{(i+1,1)}(j\omega_F)}\neq\frac{G_{(i,3)}(j\omega_F)}{G_{(i+1,3)}(j\omega_F)}=\lambda_3^{i,i+1}(j\omega_F)$$

$$\text{for } i=3,4,5 \tag{60}$$

$$\lambda_2^{i,i+1}(j2\omega_F)=\frac{G_{(i,2)}(j2\omega_F)}{G_{(i+1,2)}(j2\omega_F)}=\frac{G_{(i,4)}(j2\omega_F)}{G_{(i+1,4)}(j2\omega_F)}=\lambda_4^{i,i+1}(j2\omega_F)$$

$$\text{for } i=1,\ldots,7$$

From the NOFRFs in Table 1, $\lambda_1^{i,i+1}(j\omega_F)$, $\lambda_3^{i,i+1}(j\omega_F)$, $\lambda_2^{i,i+1}(j2\omega_F)$, and $\lambda_4^{i,i+1}(j2\omega_F)$ $(i=1,\ldots,7)$ can be evaluated. Moreover, from Eqs. (38) and (41), the theoretical values of $\lambda_1^{i,i+1}(j\omega_F)$, $\lambda_3^{i,i+1}(j\omega_F)$, $\lambda_2^{i,i+1}(j2\omega_F)$, and $\lambda_4^{i,i+1}(j2\omega_F)$ $(i=1,\ldots,7)$ can also be calculated. Both the evaluated and theoretical values of

Table 2 The evaluated and theoretical values of $\lambda_1^{i,i+1}(j\omega_F)$ and $\lambda_3^{i,i+1}(j\omega_F)$

	$\lambda_1^{i,i+1}(j\omega_F)$		$\lambda_3^{i,i+1}(j\omega_F)$	
	Evaluated	Theoretical	Evaluated	Theoretical
$i=1$	$0.5396-0.0639i$	$0.5396-0.0639i$	$0.5396-0.0639i$	$0.5396-0.0639i$
$i=2$	$0.7412-0.1614i$	$0.7412-0.1614i$	$0.7412-0.1614i$	$0.7412-0.1614i$
$i=3$	$0.8211-0.2856i$	$0.8211-0.2856i$	$-1.5678+0.3142i$	$-1.5678+0.3141i$
$i=4$	$0.7955-0.3968i$	$0.7955-0.3968i$	$1.2729+0.7743i$	$1.2730+0.7744i$
$i=5$	$0.7160-0.4255i$	$0.7160-0.4255i$	$0.8963+0.9014i$	$0.8963+0.9014i$
$i=6$	$0.6969+0.5124i$	$0.6969+0.5124i$	$0.6969+0.5124i$	$0.6969+0.5124i$
$i=7$	$0.8277+0.2166i$	$0.8277+0.2166i$	$0.8277+0.2166i$	$0.8277+0.2166i$

Table 3 The evaluated and theoretical values of $\lambda_2^{i,i+1}(j2\omega_F)$ and $\lambda_4^{i,i+1}(j2\omega_F)$

	$\lambda_2^{i,i+1}(j2\omega_F)$		$\lambda_4^{i,i+1}(j2\omega_F)$	
	Evaluated	Theoretical	Evaluated	Theoretical
$i=1$	$0.5078-0.1764i$	$0.5078-0.1765i$	$0.5078-0.1765i$	$0.5078-0.1765i$
$i=2$	$0.5727-0.3613i$	$0.5730-0.3611i$	$0.5729-0.3613i$	$0.5730-0.3611i$
$i=3$	$-1.0158+0.0791i$	$-1.0158+0.0791i$	$-1.0158+0.0791i$	$-1.0158+0.0791i$
$i=4$	$1.3178+0.9677i$	$1.3180+0.9670i$	$1.3176+0.9674i$	$1.3180+0.9670i$
$i=5$	$1.3735+1.1144i$	$1.3733+1.1145i$	$1.3735+1.1145i$	$1.3733+1.1145i$
$i=6$	$0.9568+1.2563i$	$0.9568+1.2562i$	$0.9568+1.2562i$	$0.9568+1.2562i$
$i=7$	$0.7570+0.6108i$	$0.7570+0.6107i$	$0.7570+0.6108i$	$0.7570+0.6107i$

$\lambda_1^{i,i+1}(j\omega_F)$, $\lambda_3^{i,i+1}(j\omega_F)$, $\lambda_2^{i,i+1}(j2\omega_F)$, and $\lambda_4^{i,i+1}(j2\omega_F)$ $(i=1,\ldots,7)$ are given in Tables 2 and 3.

It can be seen that the evaluated results match the theoretical results very well. Moreover, the results shown in Tables 2 and 3 have a strict accordance with the relationships in Eqs. (42) and (43). Therefore, the numerical study verifies the properties of the NOFRFs of locally nonlinear one-dimensional chain type system (26), as described in Sec. 3.

As indicated in the end of Sec. 3, the above procedure for validating the properties of the NOFRFs itself actually presents a method of detecting the position of nonlinearity in one-dimensional chain type structures. By imposing two excitation forces with the same waveform but different strengths at any point of the chain type structure respectively, as demonstrated above, the NOFRFs up to the fourth order associated with all masses can be estimated from the corresponding vibration responses of the system, and $|\lambda_1^{i,i+1}(j\omega_F)|$ and $|\lambda_3^{i,i+1}(j\omega_F)|$ can be calculated from the estimated NOFRFs. By determining the two consecutive masses for which $|\lambda_1^{i,i+1}(j\omega_F)| \neq |\lambda_3^{i,i+1}(j\omega_F)|$, it can be concluded that the component on the right side of the mass on the left is nonlinear. Although this standard detection procedure generally requires the vibration responses of all masses, Properties (iv) and (v) imply that the procedure can actually be implemented using only two measurements to determine whether the nonlinear element is located between the two measurement points. For example, if only the vibrations of the sixth and eighth masses are measured, then it can be known that $|\lambda_1^{6,8}(j\omega_F)|=|\lambda_3^{6,8}(j\omega_F)|$. Therefore one can conclude that there is no nonlinear component between mass 6 and mass 8.

5 Conclusions

In the present study, the relationships between the NOFRFs of nonlinear one-dimensional chain type structures have been investigated to reveal important properties of this class of nonlinear systems. The derivation have considered the more general case, where the input force can be added on any mass in the system and the system damping characteristics have also been taken into account. The results have considerable significance for the application of the NOFRF concept in engineering practices to locate the position of nonlinearity in locally nonlinear one-dimensional chain type systems so as to diagnose and locate faults in the systems, which make the system behave nonlinearly. Further research results on this application will be discussed in later publications.

Acknowledgment

The authors gratefully acknowledge the supports of the Engineering and Physical Science Research Council, U.K., and the Natural Science Foundation of China (Grant Nos. 10732060 and 50425516) for this work.

Nomenclature

$x(t)$, $u(t)$ = the output and input of the nonlinear system

$X(j\omega)$, $U(j\omega)$ = the spectrum of the system output and input

$h_n(\tau_1,\ldots,\tau_n)$ = the nth order Volterra kernel

$H_n(j\omega_1,\ldots,j\omega_n)$ = the nth order GFRF

$G_n(j\omega)$ = the nth order NOFRF

M, C, K = the system mass, damping, and stiffness matrices

m_i, c_i, k_i = the ith mass, damping, and stiffness parameter

$S_{LS}(\Delta)$ = the restoring force of the nonlinear spring

$S_{LC}(\Delta)$ = the restoring force of the nonlinear damper

r_i, w_i $(i=1,\ldots,P)$ = the nonlinear stiffness and damping characteristics parameters

F_{non} = the nonlinear force

$x_i(t)$, $X_i(j\omega)$ = the displacement and the output frequency response of the ith mass

$\boldsymbol{\Theta}(j\omega)$ = the transform function of the linear MDOF oscillator

$Q_{(i,l)}(j\omega)$ = the element of the ith row and the lth column of the inverse matrix of $\boldsymbol{\Theta}(j\omega)$

$h_{(i,j)}(\tau_1,\ldots,\tau_j)$ = the jth order Volterra kernel associated to the ith mass

$G_{(i,l)}(j\omega)$ = the lth order NOFRF associated to the ith mass

$\lambda_n^{i,i+1}(\omega_1+\cdots+\omega_n)$ = the ratio between the nth GFRFs of the ith and $(i+1)$th masses

$\lambda_n^{i,i+1}(j\omega)$ = the ratio between the nth NOFRFs of the ith and $(i+1)$th masses

$\mathbf{\Lambda}_n^{L-1,L}(j\omega_1,\ldots,j\omega_n)$ = the term introduced by the nonlinear force F_{non} for the nth order GFRF

$\mathbf{\Lambda}_n^{L-1,L}(j\omega)$ = the term introduced by the nonlinear force F_{non} for the nth order NOFRF

Appendix A: GFRFs of the Locally Nonlinear One-Dimensional Chain Type Structures

From Eq. (25), the GFRFs $H_{(i,j)}(j\omega_1,\ldots,j\omega_j)$, $(i=1,\ldots,n,\ j=1,\ldots,N)$ can be determined using the harmonic probing method [20,21].

First consider the input $u(t)$ is of a single harmonic

$$u(t)=e^{j\omega t} \tag{A1}$$

Substituting Eq. (A1) and

$$x_i(t)=H_{(i,1)}(j\omega)e^{j\omega t}\quad (i=1,\ldots,n) \tag{A2}$$

into Eq. (25) and extracting the coefficients of $e^{j\omega t}$ yields

$$(-M\omega^2+jC\omega+K)H_1(j\omega)=(\overbrace{0\cdots0}^{J-1}\quad 1\quad \overbrace{0\cdots0}^{n-J})^T \tag{A3}$$

where

$$H_1(j\omega)=(H_{(1,1)}(j\omega)\cdots H_{(n,1)}(j\omega))^T \tag{A4}$$

From Eq. (A4), it is known that

$$H_1(j\omega)=(-M\omega^2+jC\omega+K)^{-1}(\overbrace{0\cdots0}^{J-1}\quad 1\quad \overbrace{0\cdots0}^{n-J})^T \tag{A5}$$

Denote

$$\mathbf{\Theta}(j\omega)=-M\omega^2+jC\omega+K \tag{A6}$$

and

$$\mathbf{\Theta}^{-1}(j\omega)=\begin{bmatrix} Q_{(1,1)}(j\omega) & \cdots & Q_{(1,n)}(j\omega)\\ \vdots & \ddots & \vdots\\ Q_{(n,1)}(j\omega) & \cdots & Q_{(n,n)}(j\omega)\end{bmatrix} \tag{A7}$$

It can be obtained from Eqs. (A5)–(A7) that

$$H_{(i,1)}(j\omega)=Q_{(i,J)}(j\omega)\quad (i=1,\ldots,n) \tag{A8}$$

Thus, for any two consecutive masses, the relationship between the first order GFRFs can be expressed as

$$\frac{H_{(i,1)}(j\omega)}{H_{(i+1,1)}(j\omega)}=\frac{Q_{(i,J)}(j\omega)}{Q_{(i+1,J)}(j\omega)}=\lambda_1^{i,i+1}(\omega)\quad (i=1,\ldots,n-1) \tag{A9}$$

The above procedure used to analyze the relationships between the first order GFRFs can be extended to investigate the relationship between the $\bar{N}$th order GFRFs with $\bar{N}\geq 2$. To achieve this, consider the input

$$u(t)=\sum_{k=1}^{\bar{N}} e^{j\omega_k t} \tag{A10}$$

Substituting Eq. (A10) and

$$x_i(t)=H_{(i,1)}(j\omega_1)e^{j\omega_1 t}+\cdots+H_{(i,1)}(j\omega_{\bar{N}})e^{j\omega_N t}+\cdots+\bar{N}!\,H_{(i,\bar{N})}\times(j\omega_1,\ldots,j\omega_{\bar{N}})e^{j(\omega_1+\cdots+\omega_{\bar{N}})t}+\cdots(i=1,\ldots,n) \tag{A11}$$

into Eq. (25) and for the first and the last rows of Eq. (25), extracting the coefficients of $e^{j(\omega_1+\cdots+\omega_{\bar{N}})t}$ yields

$$(-m_1(\omega_1+\cdots+\omega_{\bar{N}})^2+j(c_1+c_2)(\omega_1+\cdots+\omega_{\bar{N}})+(k_1+k_2))H_{(1,\bar{N})}\times(j\omega_1,\ldots,j\omega_{\bar{N}})-(jc_2(\omega_1+\cdots+\omega_{\bar{N}})+k_2)H_{(2,\bar{N})}\times(j\omega_1,\ldots,j\omega_{\bar{N}})=0 \tag{A12}$$

$$(-m_n(\omega_1+\cdots+\omega_{\bar{N}})^2+jc_n(\omega_1+\cdots+\omega_{\bar{N}})+k_n)H_{(n,\bar{N})}\times(j\omega_1,\ldots,j\omega_{\bar{N}})-(jc_n(\omega_1+\cdots+\omega_{\bar{N}})+k_n)H_{(n-1,\bar{N})}\times(j\omega_1,\ldots,j\omega_{\bar{N}})=0 \tag{A13}$$

and similarly it can be deduced that, for the masses that are not connected to the Lth spring, the GFRFs satisfy the following relationships:

$$(-m_i(\omega_1+\cdots+\omega_{\bar{N}})^2+j(c_i+c_{i+1})(\omega_1+\cdots+\omega_{\bar{N}})+k_i+k_{i+1})H_{(i,\bar{N})}\times(j\omega_1,\ldots,j\omega_{\bar{N}})-(jc_i(\omega_1+\cdots+\omega_{\bar{N}})+k_i)H_{(i-1,\bar{N})}\times(j\omega_1,\cdots,j\omega_{\bar{N}})-(jc_{i+1}(\omega_1+\cdots+\omega_{\bar{N}})+k_{i+1})H_{(i+1,\bar{N})}\times(j\omega_1,\ldots,j\omega_{\bar{N}})=0\quad (i\neq 1,L-1,L,n) \tag{A14}$$

For the two masses that are connected to the Lth spring, the GFRFs satisfy the following relationships:

$$(-m_{L-1}(\omega_1+\cdots+\omega_{\bar{N}})^2+j(c_{L-1}+c_L)(\omega_1+\cdots+\omega_{\bar{N}})+k_{L-1}+k_L)H_{(L-1,\bar{N})}(j\omega_1,\ldots,j\omega_{\bar{N}})-(jc_{L-1}(\omega_1+\cdots+\omega_{\bar{N}})+k_{L-1})H_{(L-2,\bar{N})}(j\omega_1,\cdots,j\omega_{\bar{N}})-(jc_L(\omega_1+\cdots+\omega_{\bar{N}})+k_L)H_{(L,\bar{N})}(j\omega_1,\ldots,j\omega_{\bar{N}})+\mathbf{\Lambda}_{\bar{N}}^{L-1,L}(j\omega_1,\ldots,j\omega_{\bar{N}})=0 \tag{A15}$$

$$(-m_L(\omega_1+\cdots+\omega_{\bar{N}})^2+j(c_L+c_{L+1})(\omega_1+\cdots+\omega_{\bar{N}})+k_L+k_{L+1})H_{(L,\bar{N})}(j\omega_1,\ldots,j\omega_{\bar{N}})-(jc_L(\omega_1+\cdots+\omega_{\bar{N}})+k_L)H_{(L-1,\bar{N})}(j\omega_1,\cdots,j\omega_{\bar{N}})-(jc_{L+1}(\omega_1+\cdots+\omega_{\bar{N}})+k_{L+1})H_{(L+1,\bar{N})}(j\omega_1,\ldots,j\omega_{\bar{N}})-\mathbf{\Lambda}_{\bar{N}}^{L-1,L}(j\omega_1,\ldots,j\omega_{\bar{N}})=0 \tag{A16}$$

In Eqs. (A15) and (A16), $\mathbf{\Lambda}_{\bar{N}}^{L-1,L}(j\omega_1,\ldots,j\omega_{\bar{N}})$ represents the extra terms introduced by $F_{\text{non}}=\Sigma_{i=2}^{P}w_i(\dot{x}_{L-1}-\dot{x}_L)^i+\Sigma_{i=2}^{P}r_i(x_{L-1}-x_L)^i$ for the $\bar{N}$th order GFRFs, for example, for the second order GFRFs

$$\mathbf{\Lambda}_2^{L-1,L}(j\omega_1,j\omega_2)=(-w_2\omega_1\omega_2+r_2)(H_{(L-1,1)}(j\omega_1)H_{(L-1,1)}(j\omega_2)+H_{(L,1)}(j\omega_1)H_{(L,1)}(j\omega_2)-H_{(L-1,1)}(j\omega_1)H_{(L,1)}\times(j\omega_2)-H_{(L-1,1)}(j\omega_2)H_{(L,1)}(j\omega_1)) \tag{A17}$$

Denote

$$H_{\bar{N}}(j\omega_1,\ldots,j\omega_{\bar{N}})=(H_{(1,\bar{N})}(j\omega_1,\ldots,j\omega_{\bar{N}})\cdots H_{(n,\bar{N})}(j\omega_1,\ldots,j\omega_{\bar{N}}))^T \tag{A18}$$

and

$$\mathbf{\Lambda}_{\bar{N}}(j\omega_1,\ldots,j\omega_{\bar{N}})=(\overbrace{0\cdots0}^{L-2}\quad \mathbf{\Lambda}_{\bar{N}}^{L-1,L}(j\omega_1,\ldots,j\omega_{\bar{N}})\quad -\mathbf{\Lambda}_{\bar{N}}^{L-1,L}(j\omega_1,\ldots,j\omega_{\bar{N}})\quad \overbrace{0\cdots0}^{n-L})^T \tag{A19}$$

then Eqs. (A12)–(A16) can be written in a matrix form as

$$\mathbf{\Theta}(j(\omega_1+\cdots+\omega_{\bar{N}}))H_{\bar{N}}(j\omega_1,\ldots,j\omega_{\bar{N}})=\mathbf{\Lambda}_{\bar{N}}(j\omega_1,\ldots,j\omega_{\bar{N}}) \tag{A20}$$

so that

$$H_{\bar{N}}(j\omega_1, \ldots, j\omega_{\bar{N}}) = \boldsymbol{\Theta}^{-1}(j(\omega_1 + \cdots + \omega_{\bar{N}}))\boldsymbol{\Lambda}_{\bar{N}}(j\omega_1, \ldots, j\omega_{\bar{N}}) \tag{A21}$$

Therefore, for each mass, the $\bar{N}$th order GFRF can be calculated as

$$\begin{aligned} H_{(i,\bar{N})}(j\omega_1, \ldots, j\omega_{\bar{N}}) &= [Q_{i,L-1}(j(\omega_1 + \cdots + \omega_{\bar{N}})), Q_{i,L}(j(\omega_1 + \cdots + \omega_{\bar{N}}))] \\ &\times \begin{pmatrix} \boldsymbol{\Lambda}_{\bar{N}}^{L-1,L}(j\omega_1, \ldots, j\omega_{\bar{N}}) \\ -\boldsymbol{\Lambda}_{\bar{N}}^{L-1,L}(j\omega_1, \ldots, j\omega_{\bar{N}}) \end{pmatrix} (i = 1, \ldots, n) \end{aligned} \tag{A22}$$

Consequently, for two consecutive masses, the $\bar{N}$th order GFRFs have the following relationships:

$$\begin{aligned} \frac{H_{(i,\bar{N})}(j\omega_1, \ldots, j\omega_{\bar{N}})}{H_{(i+1,\bar{N})}(j\omega_1, \ldots, j\omega_{\bar{N}})} &= \frac{Q_{i,L-1}(j(\omega_1 + \cdots + \omega_{\bar{N}})) - Q_{i,L}(j(\omega_1 + \cdots + \omega_{\bar{N}}))}{Q_{i+1,L-1}(j(\omega_1 + \cdots + \omega_{\bar{N}})) - Q_{i+1,L}(j(\omega_1 + \cdots + \omega_{\bar{N}}))} \\ &= \lambda_{\bar{N}}^{i,i+1}(\omega_1 + \cdots + \omega_{\bar{N}}) \quad (i = 1, \ldots, n-1) \end{aligned} \tag{A23}$$

Appendix B: Proof of Proposition 1

For the first rows of Eqs. (33) and (38), it is known that

$$\begin{aligned} &[-m_1\omega^2 + j(c_1 + c_2)\omega + (k_1 + k_2)]G_{(1,\bar{N})}(j\omega) \\ &\quad - (jc_2\omega + k_2)G_{(2,\bar{N})}(j\omega) = 0 (1 \le \bar{N} \le N) \end{aligned} \tag{B1}$$

Therefore

$$\lambda_1^{1,2}(j\omega) = \cdots = \lambda_N^{1,2}(j\omega) = \frac{k_2 + jc_2\omega}{(-m_1\omega^2 + j\omega(c_1 + c_2) + k_1 + k_2)} \tag{B2}$$

Substituting Eq. (B2) into the second rows of Eqs. (33) and (38) yields

$$\begin{aligned} \lambda_1^{2,3}(\omega) &= \cdots = \lambda_N^{2,3}(\omega) \\ &= \frac{jc_3\omega + k_3}{[-m_2\omega^2 + (1 - \lambda_N^{1,2}(\omega))(j\omega c_2 + k_2) + j\omega c_3 + k_3]} \end{aligned} \tag{B3}$$

Iteratively using the above procedure until $i=(L-2)$, property (41) can be proved for $1 \le i \le L-2$.

Similarly, starting from the nth rows of Eqs. (33) and (38), and iteratively using the above procedure until $i=J$, property (41) can also be proved for $J \le i < N$.

From Eq. (37), it can be known that, for the masses located between the nonlinear spring and the input force, the following relationship is tenable:

$$\begin{aligned} \frac{G_{(i,2)}(j\omega)}{G_{(i+1,2)}(j\omega)} = \cdots = \frac{G_{(i,N)}(j\omega)}{G_{(i+1,N)}(j\omega)} &= \frac{Q_{i,L-1}(j\omega) - Q_{i,L}(j\omega)}{Q_{i+1,L-1}(j\omega) - Q_{i+1,L}(j\omega)} (L-1 \le i \le J-1) \end{aligned} \tag{B4}$$

So a part of property (42) is proved.

According to the having proved property (41), it can be known that

$$\lambda_1^{L-2,L-1}(\omega) = \frac{G_{(L-2,1)}(j\omega)}{G_{(L-1,1)}(j\omega)} = \cdots = \lambda_N^{L-2,L-1}(\omega) = \frac{G_{(L-2,N)}(j\omega)}{G_{(L-1,N)}(j\omega)} \tag{B5}$$

Substituting (B-5) into the following equations which are also the $(L-1)$th rows of Eqs. (33) and (38), i.e.,

$$\begin{aligned} &[-m_{L-1}\omega^2 + j(c_{L-1} + c_L)\omega + k_{L-1} + k_L]G_{(L-1,1)}(j\omega) \\ &\quad - (jc_{L-1}\omega + k_{L-1})G_{(L-2,1)}(j\omega) - (jc_L\omega + k_L)G_{(L,1)}(j\omega) = 0 \end{aligned} \tag{B6}$$

$$\begin{aligned} &[-m_{L-1}\omega^2 + j(c_{L-1} + c_L)\omega + k_{L-1} + k_L]G_{(L-1,\bar{N})}(j\omega) \\ &\quad - (jc_{L-1}\omega + k_{L-1})G_{(L-2,\bar{N})}(j\omega) - (jc_L\omega + k_L)G_{(L,\bar{N})}(j\omega) \\ &\quad + \boldsymbol{\Lambda}_{\bar{N}}^{L-1,L}(j\omega) = 0 \quad (2 \le \bar{N} \le N) \end{aligned} \tag{B7}$$

yields

$$\begin{aligned} \lambda_1^{L-1,L}(\omega) &= \frac{jc_L\omega + k_L}{[-m_{L-1}\omega^2 + (1 - \lambda_1^{L-2,L-1}(\omega))(j\omega c_{L-1} + k_{L-1}) + j\omega c_L + k_L]} \end{aligned} \tag{B8}$$

and

$$\begin{aligned} \lambda_{\bar{N}}^{L-1,L}(\omega) &= \frac{jc_L\omega + k_L}{[-m_{L-1}\omega^2 + (1 - \lambda_{\bar{N}}^{L-2,L-1}(\omega))(j\omega c_{L-1} + k_{L-1}) + j\omega c_L + k_L]} \\ &\times \left(1 + \frac{\boldsymbol{\Lambda}_{\bar{N}}^{L-1,L}(j\omega)}{jc_L\omega + k_L}\right) (2 \le \bar{N} \le N) \end{aligned} \tag{B9}$$

Therefore

$$\lambda_{\bar{N}}^{L-1,L}(\omega) = \lambda_1^{L-1,L}(\omega)\left(1 + \frac{\boldsymbol{\Lambda}_{\bar{N}}^{L-1,L}(j\omega)}{jc_L\omega + k_L}\right) \neq \lambda_1^{L-1,L}(\omega) \quad (2 \le \bar{N} \le N) \tag{B10}$$

Consequently, by substituting Eq. (B10) into the Lth rows of Eqs. (33) and (38), it can be proved that

$$\lambda_{\bar{N}}^{L,L+1}(\omega) \neq \lambda_1^{L,L+1}(\omega) \quad (2 \le \bar{N} \le N) \tag{B11}$$

Iteratively using the above procedure until $i=(J-1)$, property (42) can be proved for $L-1 \le i \le J-1$. Thus the proposition is proved. □

References

[1] Duhamel, D., Maceb, B. R., and Brennan, M. J., 2006, "Finite Element Analysis of the Vibrations of Waveguides and Periodic Structures," J. Sound Vib., **294**, pp. 205–220.

[2] Luongo, A., and Romeo, F., 2005, "Real Wave Vectors for Dynamic Analysis of Periodic Structures," J. Sound Vib., **279**, pp. 309–325.

[3] Romeo, F., and Luongo, A., 2003, "Vibration Reduction in Piecewise Bi-Coupled Periodic Structures," J. Sound Vib., **268**, pp. 601–615.

[4] Wei, J., and Petyt, M., 1997, "A Method of Analyzing Finite Periodic Structures, Part 1: Theory and Examples," J. Sound Vib., **202**, pp. 555–569.

[5] Mukherjee, S., and Parthan, S., 1996, "Normal Modes and Acoustic Response of Finite One- and Two-Dimensional Multi-Bay Periodic Panels," J. Sound Vib., **197**, pp. 527–545.

[6] Yuan, J., and Dickinson, S. M., 1995, "On the Determination of Phase Constants for the Study of the Free Vibration of Periodic Structures," J. Sound Vib., **179**, pp. 369–383.

[7] Sakellariou, J. S., and Fassois, S. D., 2006, "Stochastic Output Error Vibration-Based Damage Detection and Assessment in Structures Under Earthquake Excitation," J. Sound Vib., **297**, pp. 1048–1067.

[8] Mead, D. J., 1996, "Wave Propagation in Continuous Periodic Structures: Research Contributions From Southampton, 1964–1995," J. Sound Vib., **190**, pp. 495–524.

[9] Chi, C.-C., and Rosenberg, R. M., 1985, "On Damped Non-Linear Dynamic

Systems With Many Degrees of Freedom," Int. J. Non-Linear Mech., **20**, pp. 371–384.
[10] Vakakis, A. F., King, M. E., and Pearlstein, A. J., 1994, "Forced Localization in a Periodic Chain of Non-Linear Oscillators," Int. J. Non-Linear Mech., **29**, pp. 429–447.
[11] Royston, T. J., and Singh, R., 1996, "Periodic Response of Mechanical Systems With Local Non-Linearities Using an Enhanced Galerkin Technique," J. Sound Vib., **194**, pp. 243–263.
[12] Chakraborty, G., and Mallik, A. K., 2001, "Dynamics of a Weakly Non-Linear Periodic Chain," Int. J. Non-Linear Mech., **36**, pp. 375–389.
[13] Marathe, A., and Chatterjee, A., 2006, "Wave Attenuation in Nonlinear Periodic Structures Using Harmonic Balance and Multiple Scales," J. Sound Vib., **289**, pp. 871–888.
[14] Neild, S. A., Mcfadden, P. D., and Williams, M. S., 2001, "A Discrete Model of Vibrating Beam Using Time-Stepping Approach," J. Sound Vib., **239**, pp. 99–121.
[15] Zhu, H., and Wu, M., 2002, "The Characteristic Receptance Method for Damage Detection in Large Mono-Coupled Periodic Structures," J. Sound Vib., **251**, pp. 241–259.
[16] Fassois, S. D., and Sakellariou, J. S., 2007, "Time-Series Methods for Fault Detection and Identification in Vibrating Structures," Philos. Trans. R. Soc. London, Ser. A, **365**, pp. 411–448.
[17] Tsyfansky, S. L., and Beresnevich, V. I., 2000, "Non-Linear Vibration Method for Detection of Fatigue Cracks in Aircraft Wings," J. Sound Vib., **236**, pp. 49–60.
[18] Sundermeyer, J. N., and Weaver, R. L., 1995, "On Crack Identification and Characterization in a Beam by Nonlinear Vibration Analysis," J. Sound Vib., **183**, pp. 857–871.
[19] Hillis, A. J., Neild, S. A., Drinkwater, B. W., and Wilcox, P. D., 2006, "Global Crack Detection Using Bispectral Analysis," Proc. R. Soc. London, Ser. A, **462**, pp. 1515–1530.
[20] Rivola, A., and White, P. R., 1998, "Bispectral Analysis of the Bilinear Oscillator With Application to the Detection of Fatigue Cracks," J. Sound Vib., **216**, pp. 889–910.
[21] Peng, Z. K., Lang, Z. Q., and Billings, S. A., 2006, "Analysis of Multi-Degree-of-Freedom Nonlinear Systems Using Nonlinear Output Frequency Response Functions," the University of Sheffield, Research Report No. 927.
[22] Lang, Z. Q., and Billings, S. A., 2005, "Energy Transfer Properties of Nonlinear Systems in the Frequency Domain," Int. J. Control, **78**, pp. 345–362.
[23] Peng, Z. K., Lang, Z. Q., and Billings, S. A., 2007, "Nonlinear Output Frequency Response Functions for Multi-Input Nonlinear Volterra Systems," Int. J. Control, **80**, pp. 843–855.
[24] Sandberg, I. W., 1984, "A Perspective on System Theory," IEEE Trans. Circuits Syst., **31**, pp. 88–103.
[25] Boyd, S., and Chua, L., 1985, "Fading Memory and the Problem of Approximating Nonlinear Operators With Volterra Series," IEEE Trans. Circuits Syst., **32**, pp. 1150–1161.
[26] Lang, Z. Q., and Billings, S. A., 1996, "Output Frequency Characteristics of Nonlinear System," Int. J. Control, **64**, pp. 1049–1067.
[27] George, D. A., 1959, "Continuous Nonlinear Systems," M.I.T. Research Laboratory of Electronics, Cambridge, MA, Technical Report No. 335.
[28] Billings, S. A., and Peyton Jones, J. C., 1990, "Mapping Nonlinear Integro-Differential Equations Into the Frequency Domain," Int. J. Control, **52**, pp. 863–879.
[29] Peyton Jones, J. C., and Billings, S. A., 1989, "A Recursive Algorithm for the Computing the Frequency Response of a Class of Nonlinear Difference Equation Models," Int. J. Control, **50**, pp. 1925–1940.
[30] Billings, S. A., and Tsang, K. M., 1989, "Spectral Analysis for Nonlinear System, Part I: Parametric Non-Linear Spectral Analysis," Mech. Syst. Signal Process., **3**, pp. 319–339.
[31] Peng, Z. K., Lang, Z. Q., and Billings, S. A., 2007, "Resonances and Resonant Frequencies for a Class of Nonlinear Systems," J. Sound Vib., **300**, pp. 993–1014.
[32] Zhang, H., and Billings, S. A., 1993, "Analysing Non-Linear Systems in the Frequency Domain, I: The Transfer Function," Mech. Syst. Signal Process., **7**, pp. 531–550.
[33] Billings, S. A., and Zhang, H., 1994, "Analysing Nonlinear Systems in the Frequency Domain, II: The Phase Response," Mech. Syst. Signal Process., **8**, pp. 45–62.
[34] Worden, K., Manson, G., and Tomlinson, G. R., 1997, "A Harmonic Probing Algorithm for the Multi-Input Volterra Series," J. Sound Vib., **201**, pp. 67–84.

Strain Rate Effects and Rate-Dependent Constitutive Models of Lead-Based and Lead-Free Solders

Fei Qin
Mem. ASME
e-mail: qfei@bjut.edu.cn

Tong An

Na Chen

College of Mechanical Engineering and Applied Electronics Technology,
Beijing University of Technology,
Beijing 100124, P R China

As traditional lead-based solders are banned and replaced by lead-free solders, the drop impact reliability is becoming increasingly crucial because there is little understanding of mechanical behaviors of these lead-free solders at high strain rates. In this paper, mechanical properties of one lead-based solder, Sn37Pb, and two lead-free solders, Sn3.5Ag and Sn3.0Ag0.5Cu, were investigated at strain rates that ranged from 600 s^{-1} to 2200 s^{-1} by the split Hopkinson pressure and tensile bar technique. At high strain rates, tensile strengths of lead-free solders are about 1.5 times greater than that of the Sn37Pb solder, and also their ductility are significantly greater than that of the Sn37Pb. Based on the experimental data, strain rate dependent Johnson–Cook models for the three solders were derived and employed to predict behaviors of solder joints in a board level electronic package subjected to standard drop impact load. Results indicate that for the drop impact analysis of lead-free solder joints, the strain rate effect must be considered and rate-dependent material models of lead-free solders are indispensable.
[DOI: 10.1115/1.3168600]

Keywords: solder, lead-free, strain rate effect, constitutive model, drop impact

1 Introduction

For a long time the eutectic solder Sn37Pb (63% tin and 37% lead in weight) was widely used as an interconnecting alloy in microelectronic packaging technologies because of its advantages in manufacturing, mechanical properties, and costs. Nowadays, due to the harmfulness of the lead element to the environment, lead-based solders were banned in the European Union [1] and many other countries. As a result, a variety of lead-free solder alloys such as SnAg (tin and silver) and near-eutectic SnAgCu (tin, silver, and copper) alloy were used to replace lead-based solders. However, this replacement induces new challenges to manufacturers of electronic products. The major challenge is the drop impact reliability of mobile electronic devices such as mobile phones and personal digital assistants, etc. Researches [2–4] showed that lead-free solder joints, which are key parts functioned as electric signal channels, thermal conductors, and mechanical supports in microelectronic packages [5], exhibit much poorer performance than the eutectic Sn37Pb joint does in the drop impact tests specified by the Joint Electron Devices Engineering Council (JEDEC) [6]. Furthermore, under the drop impact load the main failure mode migrates from bulk fracture in Sn37Pb solder joints to interface cracking in lead-free solder joints [4,7]. Although this phenomenon has not been well understood, one explanation is that the high strain rate caused by the drop impact load enhances the bulk strengths of lead-free solder joints, and the interface between the solder joints and the printed circuit board (PCB) becomes relatively vulnerable. This explanation seems to suggest that strain rate affect the drop impact performance of lead-free solder joints critically.

The most commonly used drop impact testing condition is the condition H recommended by the JEDEC [6]. This condition is characterized by a half-sine acceleration pulse with a peak value of 2900 G (1 G=9.8 m/s^2) and a time duration of 0.3 ms. There are several different estimations on the strain rate level under this loading condition. Wang and Yi [8] and Siviour et al. [9] made estimations in a level of 10^3 s^{-1} based on general knowledge of impact problems. A strain rate of 10 s^{-1} was estimated by Suh et al. [4] without detailed explanation. More recently, Wong et al. [10] pointed out that the strain rate is in a range from 0.1 s^{-1} to 300 s^{-1} in mobile applications. Their estimation was based on that, during the drop impact testing of a board level package, the vibrations of the PCB and the component, which sandwich the solder joints, cause deformation of the solder joints. Hence, the strain rate is determined by the frequency of the PCB and the magnitude of strains in the solder joints. Considering the existence of higher frequency vibrating modes and plastic deformation in the solder joints, the strain rate was possibly underestimated by them. Although there are arguments on the magnitude of strain rate in the solder joints, the effect of strain rate on the behavior of solder joints, especially on the behaviors of lead-free solder joints, is drawing more and more attention.

Many experimental investigations on the strain rate effect were conducted at strain rates less than 1 s^{-1}. Earlier works [11–14] related to these low strain rates focused on the establishment of material models to describe creep behaviors of solder joints. Within the same range of strain rates, mechanical properties, especially the tensile properties of lead-free solders, were intensively investigated recently [15–23]. Most of these researches support that lead-free solders are more sensitive to strain rate than lead-based solders do, and the more solders contain Ag the more they are sensitive to strain rate.

As for the experimental works on strain rates greater than 1 s^{-1}, they mainly aimed to investigate the drop impact related behaviors of solders. At strain rates that ranged from 10^2 s^{-1} to 10^4 s^{-1}, the split Hopkinson pressure bar technique (SHPB) [24] was mainly used to characterize the mechanical properties of materials. Dynamic behaviors of lead-based solders were investigated by Lee and Dai [25] using the split Hopkinson torsional bar technique. Wang and Yi [8] obtained compressive stress-strain

Contributed by the Applied Mechanics Division of ASME for publication in the JOURNAL OF APPLIED MECHANICS. Manuscript received July 22, 2008; final manuscript received March 13, 2009; published online September 30, 2009. Review conducted by Horacio D. Espinosa.

curves of Sn37Pb solder at high strain rates that ranged from 340 s^{-1} to 1160 s^{-1} by the SHPB. Afterwards, tensile stress-strain curves of Sn37Pb solder were also investigated by Wang [26] using the split Hopkinson tensile bar technique (SHTB). Siviour et al. [9] investigated compressive stress-strain behaviors of Sn37Pb, Sn3.5Ag, and Sn3.0Ag0.5Cu solders at strain rates that ranged from 450 s^{-1} to 2720 s^{-1} and at various temperatures, and the strain rate sensitivities of the solders were discussed. Recently, Wong et al. [10] investigated compressive behaviors of Sn37Pb, Sn3.5Ag, Sn3.0Ag0.5Cu, and Sn1.0Ag0.1Cu solders at strain rates that ranged from 0.005 s^{-1} to 300 s^{-1} by using the drop-weight tester developed by them.

Although some experimental data are available currently, there is a diversity of those test data and a lack of tensile properties of lead-free solders at the strain rates matching the JEDEC standard drop impact conditions. Currently there are no applicable material models that can describe the high strain rate behaviors of solders. As a result, the linear elastic or rate-independent elastic-plastic material model was applied to solder joints in the drop impact simulations [27–30]. These models neglect strain rate effects completely and obviously lead to inaccurate predictions of stresses and strains in solder joints.

In order to take the strain rate effect into account, one preferable constitutive model is the Johnson–Cook model [31]. Although it is empirical in nature, the Johnson–Cook model has been widely used to simulate large strain and high strain rate deformation process of metals because of its simplicity and good agreement with experimental results [32–34]. Another advantage of the Johnson–Cook model is that it can be easily implanted into mainstream commercial finite element analysis tools so that engineers can conveniently use it to simulate the drop impact process of mobile electronic products.

In this paper, the mechanical behaviors of Sn37Pb, Sn3.5Ag, and Sn3.0Ag0.5Cu in quasistatic and at strain rates that ranged from 600 s^{-1} to 2200 s^{-1} were investigated by a conventional materials tester and by the SHPB and SHTB. The strain rate sensitivity, fracture strain, and tensile strength of the three solders were discussed and compared with the results from other researchers. Based on the experimental data we obtained, rate-independent trilinear elastic-plastic material models and rate-dependent Johnson–Cook models for the three solders were proposed and validated. Finally, the Johnson–Cook models were applied to predict behaviors of solder joints in a board level drop impact test specified by the JEDEC [6]. Strain rate, peeling stress, and equivalent plastic strain of the solder joints during the drop impact were predicted and compared with that by rate-independent material models.

2 Experimental Procedures

2.1 Specimen Preparation. Commercial ingots of Sn37Pb, Sn3.5Ag, and Sn3.0Ag0.5Cu were melted in a crucible and molded into rods. The process was intentionally slowed down to make sure that there were no voids formed in the rods. Then the rods were quickly immerged into water and aged for 15 days in the air to stable their microstructures. Finally, the rods were machined into cylindrical specimens in the specific dimension. Specimens used for quasistatic tensile and compressive tests have sizes of $\Phi 8 \times 56$ mm^2 and $\Phi 12 \times 12$ mm^2, respectively. Specimens for the SHPB tests have a size of $\Phi 12 \times 6$ mm^2. For the SHTB tests, specimens are of $\Phi 5 \times 8$ mm^2 in gauged part but have a total length of 40 mm with two end screws, which are used to install the specimen into the incident bar and output bar. More details of the specimen can be found in Fig. 1(*a*).

2.2 Quasistatic Compressive and Tensile Tests. The quasistatic compressive and tensile tests were conducted on an MTS-809 materials tester at the strain rate of 0.001 s^{-1}. Three specimens for each kind of solders were tested and the average of the three specimens' data was read as the final result of the solder.

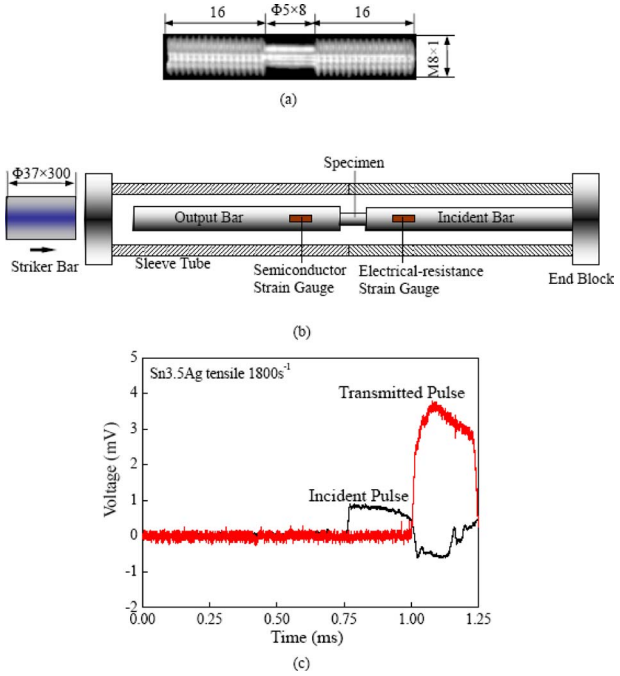

Fig. 1 (*a*) Specimen and its sizes for the split Hopkinson tensile bar (SHTB) tests, (*b*) schematic setup of the separated sleeve SHTB testing and (*c*) raw signals of the incident and transmitted pulses

2.3 SHPB and SHTB Tests. The SHPB is a well developed technique and has been widely used to test mechanical properties of materials at strain rates that ranged from 10^2 s^{-1} to 10^4 s^{-1}. An excellent review of the experimental technique was provided by Follansbee [35]. For the SHTB, there are various test setups. In this investigation, a separated sleeve SHTB device, which is based on the reflective SHTB device proposed by Nicholas [36], was used. Figure 1(*b*) shows a schematic setup of the device. It consists of a striker of $\Phi 37 \times 300$ mm^2, two separated steel circular tubes (the sleeve in Fig. 2(*b*)), and two identical AISI4340 steel bars of $\Phi 14.5 \times 1000$ mm^2 inside the sleeves. The cylindrical specimen was installed into the two bars by its screwed ends. During the test, the striker bar impacts the left end block and compresses the tubes to generate a stress pulse on the right end block. The right end block then produces tensile stress pulse in the incident bar and in the specimen. Two strain gauges were placed on the incident and output bars to measure the incident, reflected, and transmitted pulses. After about three reflections of the stress wave, a uniform stress state was achieved in the specimen. Then the strain rate $\dot{\varepsilon}(t)$, strain $\varepsilon(t)$, and $\sigma(t)$ stress in the specimen were calculated by the reflected strain pulses $\varepsilon_R(t)$ and the transmitted strain pulses $\varepsilon_T(t)$ [37]:

$$\dot{\varepsilon} = -\frac{2C_0}{l_0}\varepsilon_R, \quad \varepsilon = \int_0^t \dot{\varepsilon} dt = -\frac{2C_0}{l_0}\int_0^t \varepsilon_R dt, \quad \sigma = \frac{EA}{A_S}\varepsilon_T \quad (1)$$

where E and A are Young's modulus and the cross-section area of the specimen, and C_0 is the wave velocity in the bar. A_S and l_0 are the initial cross-section area and initial length of the specimen, respectively. In this investigation, Young's modulus and the mass density of the steel bar are 200 GPa and 7850 kg/m^3, respectively. The wave velocity in the bar is 5048 m/s.

In the reflective SHTB [36], there are noises caused by wave reflection at the specimen-bar connections. However, in the separated sleeve SHTB device used here the noise can be effectively suppressed since the specimen is subjected to a tensile stress pulse directly. For the test the strain rate that exceeds 1000 s^{-1}, a

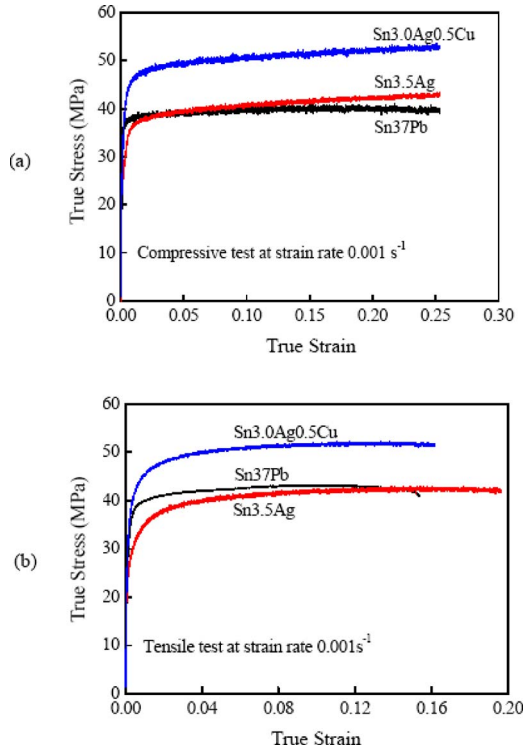

Fig. 2 True stress-strain curves at strain rate of 0.001 s^{-1}: (*a*) compressive and (*b*) tensile

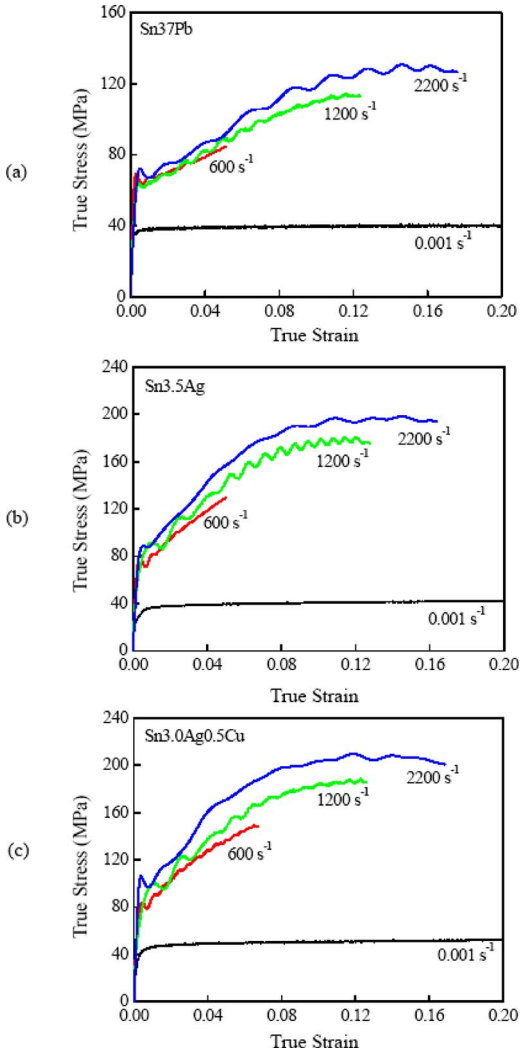

Fig. 3 Compressive true stress-strain curves at high strain rates: (*a*) Sn37Pb, (*b*) Sn3.5Ag, and (*c*) Sn3.0Ag0.5Cu

greater striking speed causes higher noise level; hence a more sensitive semiconductor strain gauge was used to acquire the transmitted signals. Typical recorded signals of a Sn3.5Ag specimen in a SHTB test at strain rate 1800 s^{-1} are presented in Fig. 1(*c*). A sampling frequency of 5 MHz was used.

All the SHPB and SHTB tests were carried out at room temperature. For each kind of solders, five specimens at one strain rate were tested. The final data were obtained by averaging the available data of the five specimens.

3 Results and Discussions

3.1 Quasistatic Behaviors. Young's modulus (E), yield stress (σ_y), ultimate tensile stress (UTS), and tensile fracture strain (ε_f) obtained from the quasistatic tests are listed in Table 1. The true stress-strain curves are shown in Fig. 2. Under quasistatic conditions, the Sn3.5Ag behaves similarly to the Sn37Pb, and its UTS is almost the same as that of the Sn37Pb. The Sn3.0Ag0.5Cu solder has the greatest UTS, but its fracture strain is the same as the Sn37Pb. There is no significant difference between the compressive and tensile behaviors for the three solders. Linear hardening and plastic flow at constant stress can be observed for the three solders. Based on the observation, trilinear elastic-plastic models were proposed for the three solders, and more detail about these models can be found in Sec. 4.

Table 1 Mechanical properties of the three solders from the quasistatic tensile tests at strain rate of 0.001 s^{-1}

Solders	E (GPa)	σ_y (MPa)	UTS (MPa)	ε_f
Sn37Pb	30	35	43	0.16
Sn3.5Ag	45	29	42	0.20
Sn3.5Ag0.5Cu	54	38	51	0.16

3.2 Compressive Behaviors at High Strain Rates. Figure 3 shows the true stress-strain relations acquired by the SHPB tests at three strain rates, 600 s^{-1}, 1200 s^{-1}, and 2200 s^{-1}. It shows that strain softening occurs as the true strain exceeds 0.1, and the softening becomes significant as the strain rate increases. The softening is possibly caused by the temperature rise induced by the heat transformed from plastic work during the high speed deformation, which is regarded as an adiabatic process. All the three solders are sensitive to strain rate, and their dynamic yield stresses are greatly higher than static ones. In order to compare strain rate sensitivities of the three solders, flow stresses at 2% true strain were plotted against strain rates in log-log scale, as shown in Fig. 4. The data were fitted by a straight line, and the gradient of the line can be interpreted as the strain rate sensitivity. As shown, sensitivities of the Sn37Pb, Sn3.5Ag, and Sn3.0Ag0.5Cu are 0.05, 0.15, and 0.11, respectively. The Sn3.5Ag is the most sensitive to the strain rate, while the Sn37Pb is the most insensitive. Similar conclusions were drawn by Wong et al. [10]. They presented sensitivities of 0.07, 0.10, and 0.11 for the Sn37Pb, Sn3.5Ag, and Sn3.0Ag0.5Cu solders at strain rates that ranged from 0.01 s^{-1} to 300 s^{-1} but by using flow stresses at 10% true strain.

3.3 Tensile Behaviors at High Strain Rates. Main tensile mechanical properties of the three solders, the UTS and its corresponding strain (ε^*), the percent reduction in area (PRA), and the

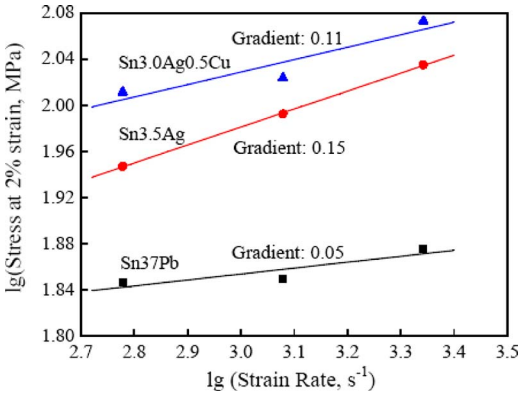

Fig. 4 Relations between the flow stresses at 2% strain and strain rates in log-log scale. The lead-free solders are more sensitive to strain rate than Sn37Pb.

percent elongation (PE) are summarized in Table 2. Figure 5 shows the true stress-strain relations obtained from the SHTB tests at three strain rates, 600 s^{-1}, 1200 s^{-1}, and 1800 s^{-1}. As discussed in Sec. 3.1, under quasistatic conditions the UTSs of the Sn3.5Ag and Sn3.0Ag0.5Cu are almost the same as that of the Sn37Pb. However, at high strain rates they are about 1.5 times greater than that of the Sn37Pb due to the strain rate effect. When the strain rate increases, their UTSs increase but the corresponding strains decrease slightly. As stress reaches the UTS, the necking process begins and it triggers an instable state in the specimen. This leads the stress drops down, as shown in Figs. 5(*b*) and 5(*c*). Figure 6 presents the photographs of specimens after the SHTB tests. For all the three solders, ruptures were observed under strain rates of 1200 s^{-1} and 1800 s^{-1} but not under a strain rate of 600 s^{-1}. A pronounced necking was observed in lead-free specimens but not in the Sn37Pb. From Table 2, the PRA and the PE of two lead-free solders are significantly greater than that of the Sn37Pb solder. It suggests that two lead-free solders experience greater plastic deformation before broken and they are more ductile than the Sn37Pb under high strain rates. This observation supports the notion that in a drop impact test lead-free solder joints prefer cracking along the solder joint-PCB interface to fracturing in solder bulk due to its increased bulk strength [7] and great ductility.

Since the tensile strength of solder is much more important in the reliability assessment of solder joints, there are a lot of experimental investigations on it. In order to present a clear and panoramic view of the sensitivity of the tensile strength to strain rate, UTSs acquired by different researchers at various strain rates for lead and lead-free solders were surveyed and presented in Fig. 7. It can be seen, for all the solders, that the UTS increases with the increasing of strain rate and it increases more sharply in a high strain rate range, especially for lead-free solders. At low strain rates, UTSs of lead-free solders are close to the Sn37Pb. However, at high strain rates, they are significantly greater than that of the Sn37Pb. Figure 7(*c*) shows that the SnAgCu solders have higher tensile strengths than the SnCu solders at the same strain rate.

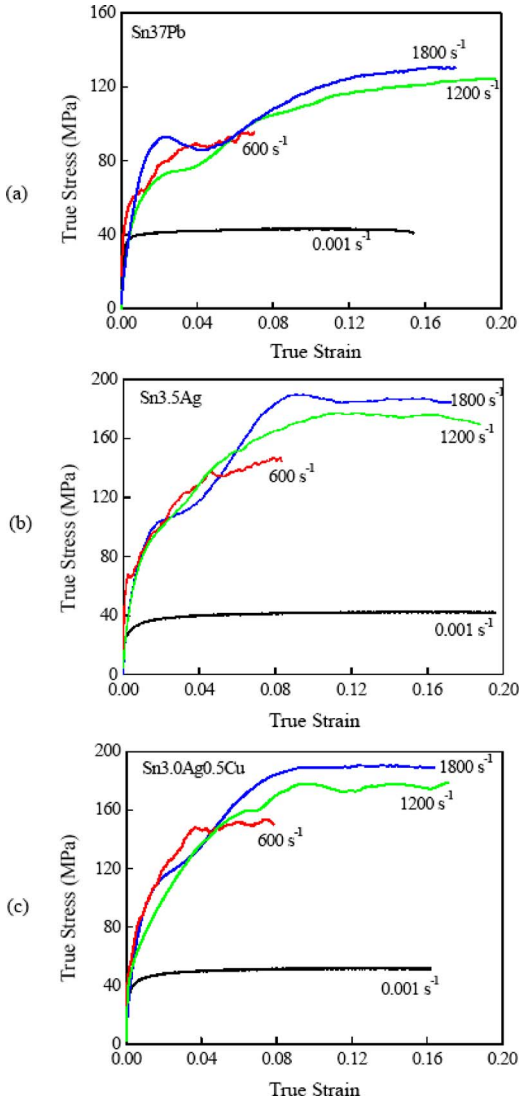

Fig. 5 Tensile true stress-strain curves at high strain rates: (*a*) Sn37Pb, (*b*) Sn3.5Ag, and (*c*) Sn3.0Ag0.5Cu

4 Rate-Independent Material Models

The rate-independent elastic-plastic model proposed by Wiese and Rzepka [30] was extensively used in numerical simulation of solder joints. Similar models in trilinear form were derived based on our quasistatic tensile test data in order to compare with rate-dependent models in Sec. 6. The model is characterized by three line segments and six parameters: $\varepsilon 1$, $\varepsilon 2$, $\varepsilon 3(=100\%)$, $\sigma 1$, $\sigma 2$, and $\sigma 3$. The first line segment defined by points (0, 0) and $(\varepsilon 1, \sigma 1)$ describes the elastic behavior of the materials. The second one defined by points $(\varepsilon 1, \sigma 1)$ and $(\varepsilon 2, \sigma 2)$ describes the

Table 2 Mechanical properties of the three solders at high strain rates. The yield stress (σ_y) was obtained from the compressive tests. The UTS and its corresponding strain (ε^*), the PRA, and PE were from the tensile tests.

	Sn37Pb				Sn3.5Ag				Sn3.0Ag0.5Cu			
$\dot{\varepsilon}$ (s^{-1})	σ_y (MPa)	UTS/ε^* (MPa/-)	PRA (%)	PE (%)	σ_y (MPa)	UTS/ε^* (MPa/-)	PRA (%)	PE (%)	σ_y (MPa)	UTS/ε^* (MPa/-)	PRA (%)	PE (%)
600	63	-	-	-	66	-	-	-	73	-	-	-
1200	58	103/0.158	50.7	42.9	72	158/0.116	83.2	64.6	83	162/0.100	81.6	65.5
1800	64	111/0.135	50.1	42.5	77	173/0.092	77.2	57.8	87	172/0.092	80.3	58.1

Fig. 6 Specimens after the SHTB tests. The two lead-free solders experienced greater plastic deformation before broken than Sn37Pb did.

initial plasticity. The third line defined by points $(\varepsilon 2, \sigma 2)$ and $(\varepsilon 3, \sigma 3)$ models the saturated plasticity. All the model parameters for the three solders derived by this research and by Wiese and Rzepka [30] are presented in Table 3. It is noted that Wiese's model may predict greater stress at large strain than ours.

5 Rate-Dependent Material Models

5.1 Johnson–Cook Constitutive Model. A general form of the Johnson–Cook model can be expressed as

$$\sigma = [A + B(\varepsilon^p)^n](1 + C \ln \dot{\varepsilon}^*)(1 - T^{*m}) \tag{2}$$

where σ, ε^p, and $\dot{\varepsilon}^*$ are the von Mises flow stress, the equivalent plastic strain, and the dimensionless strain rate, respectively. $\dot{\varepsilon}^*$ is defined as $\dot{\varepsilon}^* = \dot{\varepsilon}/\dot{\varepsilon}_0$, in which $\dot{\varepsilon}_0$ is a reference strain rate and a value of 0.001 s^{-1} was assigned to it in this research. T^* is the homologous temperature defined as $T^* = (T - T_r)/(T_m - T_r)$, in which T_r and T_m are the reference temperature and melting temperature of the materials, respectively. The reference temperature was assigned to be room temperature here. There are five material constants, A, B, C, m, and n in Eq. (2). Here A is the yield stress defined by the quasistatic compressive strain-stress data, B and n represent the effects of strain hardening, C is used to describe the strain rate effect, and m describes the effect of thermal softening.

5.2 Identification of Model Constants. The constants in the Johnson–Cook model can be identified by considering the three sets of brackets in Eq. (2) separately. The first step is to set out the constants in the first set of brackets. For the quasistatic test conducted at room temperature, $\dot{\varepsilon}^* = 1$ and $T = T_r$; thus Eq. (2) becomes

$$\sigma = A + B(\varepsilon^p)^n \tag{3}$$

The logarithm conversion of Eq. (3) is

$$\ln(\sigma - A) = \ln B + n \ln \varepsilon^p \tag{4}$$

where A is the initial yield stress, which can be derived from the stress-strain curve obtained from the quasistatic compressive tests directly. Here, for the Sn37Pb, Sn3.5Ag, and Sn3.0Ag0.5Cu, their A constants are 35 MPa, 29 MPa, and 38 MPa, respectively, as listed in Table 1. Picking up the points located between the yield point and the ultimate point on the stress-strain curves, let $x = \ln \varepsilon^p$ and $y = \ln(\sigma - A)$, then plot those points in x-y coordinate plane, and fit those points by a straight line $y = b_1 + k_1 x$. The slope of the line, k_1, is identified as the material constant n. The intercept, b_1, is identified as $\ln B$.

The next step is to identify the constant C. As for $\varepsilon^p = 0$ and $T = T_r$, Eq. (2) becomes

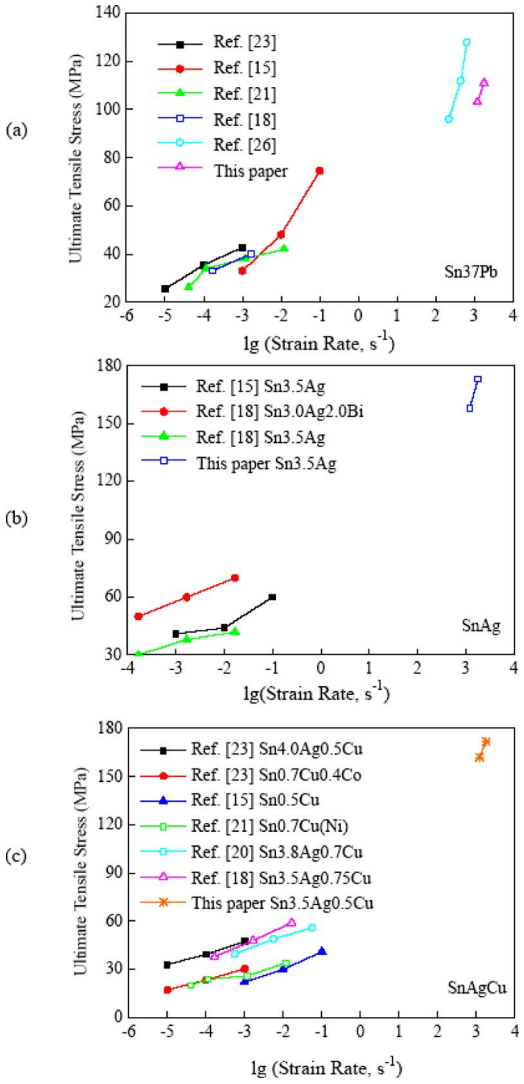

Fig. 7 Ultimate tensile stresses of solders at various strain rates: (*a*) Sn37Pb, (*b*) SnAg, and (*c*) SnAgCu and SnCu

$$\sigma/A = 1 + C \ln \dot{\varepsilon}^* \tag{5}$$

where σ is the dynamic yield stress at current strain rate, and its value for each solder is listed in Table 2. Let $x = \ln \dot{\varepsilon}^*$ and $y = \sigma/A$, for the three strain rates 600 s^{-1}, 1200 s^{-1}, and 2200 s^{-1}; the three points can be plotted in x-y coordinate plane. Fitting them by a straight line $y = b_2 + k_2 x$, then we can identify the constant C as k_2.

By the procedure described above and the compressive test data of the three solders, their Johnson–Cook models are derived and presented in Table 4. The m given in Table 4 is not strictly based on the experimental data and is picked up according to values used for most metal materials since the lack of experiments at a variety of temperatures.

5.3 Validation of Proposed Models and Discussions. In order to validate the Johnson–Cook constitutive models given in this paper, models defined by Table 4 were incorporated into the ABAQUS/EXPLICIT (a commercial finite element analysis software package) to simulate the SHPB and SHTB tests. Materials and geometries of the incident, output bars, and specimen were exactly the same as that in the experiments. Two steel bars and the specimen were modeled by element type CAX4R, which is a continuum axial symmetric two-dimensional four-node quadrilateral element in the ABAQUS [38]. In the SHPB simulation, element

Table 3 Elastic-plastic models based on the quasistatic tensile tests and from Ref. [30]

	Solders	ε_1 (%)	ε_2 (%)	σ_1 (MPa)	σ_2 (MPa)	σ_3 (MPa)
This paper	Sn37Pb	0.125	1.88	37.6	41.3	62.2
	Sn3.5Ag	0.078	3.35	35.0	40.2	56.9
	Sn3.0Ag0.5Cu	0.065	4.30	45.0	50.4	62.7
Wises et al. [30]	Sn37Pb	0.07	0.3	21	41	600
	Sn3.5Ag	0.1	0.4	41	64	700
	Sn3.0Ag0.5Cu	0.14	0.4	57.4	80	2500

Table 4 Material constants of the Johnson–Cook models for the three solders derived from the compressive tests

	A (MPa)	B (MPa)	C	n	m	T_m (K)
Sn37Pb	35	119	0.0369	0.57	0.8	456
Sn3.5Ag	29	243	0.0956	0.70	0.8	494
Sn3.0Ag0.5Cu	38	275	0.0713	0.71	0.7	490

sizes in the bars and specimen were 5 mm and 1.2 mm, respectively. Contact surfaces between the bar and the specimen were defined as hard contacts without friction, which implies that the contact is activated if and only if a pressure is built up between the two defined surfaces. In the SHTB simulation, element sizes in the bars and specimen were 5 mm and 0.3 mm, respectively. Thread connections between the specimen and two bars were neglected and treated as the tie constrains. The striker, sleeves, and end blocks were neglected in the model; instead, a stress pulse derived from experiments was exerted directly to the incident bar. Automatic time step option was chosen for all the simulations to ensure a stable solution.

The normal components of stress and strain in the axial direction of the specimen were picked up to plot the true stress-strain curves. To avoid boundary effects, stress and strain at the integral points of elements located in the middle of the specimen were used and averaged. The stress-strain curves from numerical simulations and Eq. (2) were compared with experimental data in Figs. 8–13. For all the cases, the simulation results agree quite well with that calculated by Eq. (2). This validates the numerical model we used.

When the strain rates are 600 s^{-1} and 1200 s^{-1}, there are good agreements between the simulation and the experimental results for all the three solders both under the compressive and tensile conditions. In the cases the strain rate is 2200 s^{-1} or 1800 s^{-1}, the agreement is acceptable but not so good, especially for the tensile cases. This is possibly due to the errors from both the experiment and the simulation. First, unlike in the SHPB tests, in the SHTB the specimen was connected into the incident and output bars by screw threads. Since the specimen material is softer than the steel bar, significant plastic deformation may occur in the screws under high strain rates such as 1800 s^{-1}, and this possibly leads to those disagreements, as shown in Figs. 9(*c*), 11(*c*), and 13(*c*). Second, softening or necking was observed in the experiments but the Johnson–Cook model is intrinsically not able to describe the behavior of work softening [39]. Besides, in the current simulation model, softening or necking was not taken into account. Fortunately, this does not affect the effectiveness of the Johnson–Cook models derived here because these model constants were determined by the compressive test data only.

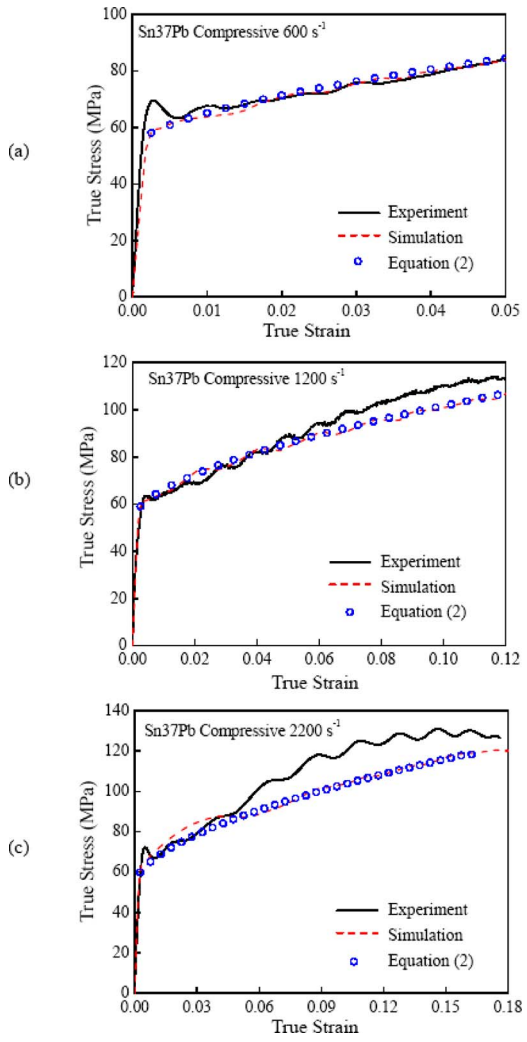

Fig. 8 Compressive true stress-strain curves of Sn37Pb at strain rates of (*a*) 600 s^{-1}, (*b*) 1200 s^{-1}, and (*c*) 2200 s^{-1}

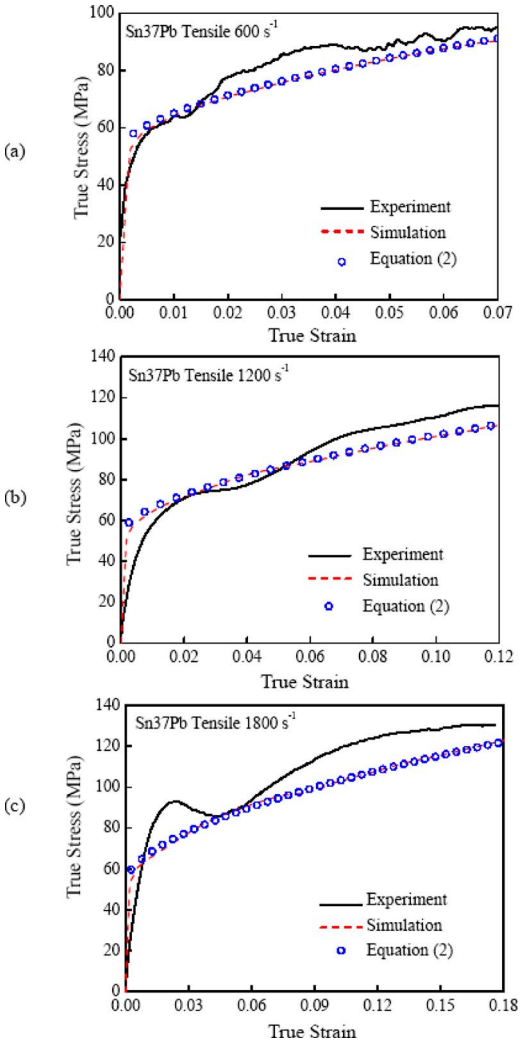

Fig. 9 Tensile true stress-strain curves of Sn37Pb at strain rates of (*a*) 600 s^{-1}, (*b*) 1200 s^{-1}, and (*c*) 1800 s^{-1}

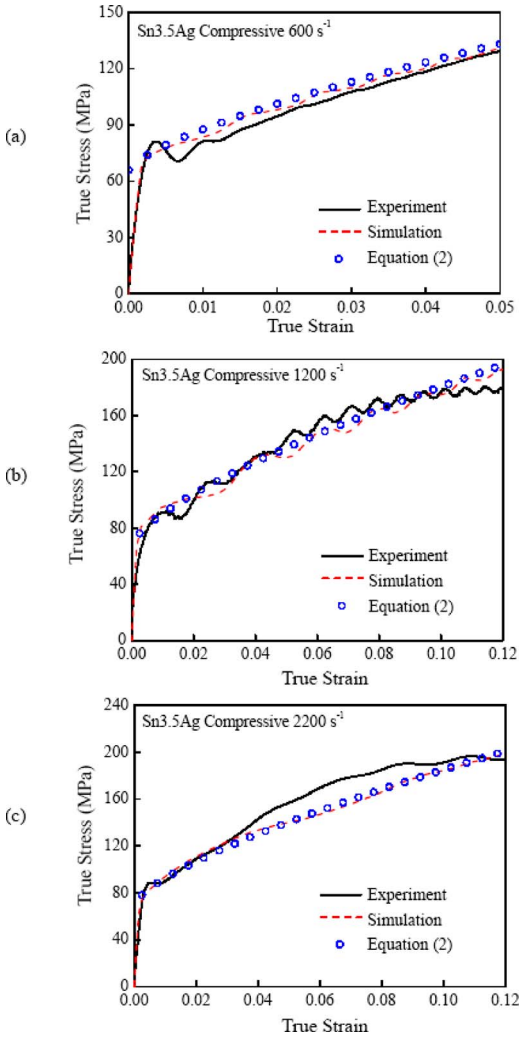

Fig. 10 Compressive true stress-strain curves of Sn3.5Ag at strain rates of (*a*) 600 s^{-1}, (*b*) 1200 s^{-1}, and (*c*) 2200 s^{-1}

6 Drop Impact Simulation of a Board Level Package

6.1 Models of Board Level Package Under the Drop Impact. Some fundamental models of a board level package under the JEDEC standard drop impact can be found in Refs. [40–42]. For clarity, a brief description of the drop impact test is presented here. A typical setup of the board level drop impact test recommended by the JEDEC [6] is shown in Fig. 14(*a*). During the test, an assembly consisting of a PCB and a component is mounted onto a metal base via screw bolts. Then the entire assembly is subjected to free fall along guide rods from a prescribed height, and the metal base impacts onto a rigid foundation and an impact loading is produced. A prescribed half-sine acceleration pulse can be achieved by manipulating the drop height and the dimension or materials of cushion pads. Since the stiffness of the metal base is exceedingly greater than that of the PCB, the half-sine acceleration pulse resulting from the impact predominantly transmits to the PCB via the metal base and the screw bolts with little distortion. Therefore, the board level drop impact test can be modeled as that the PCB is alone subjected to the half-sine acceleration pulse at points of mounting to the screw bolts, as shown in Fig. 14(*b*). Here $G(t)$ represents the acceleration pulse. This approach was called the input-G method proposed by Tee et al. [43]. Since the PCB has much larger warpage in its length direction than in the width direction, the PCB and the component can be modeled as two 3D beams with width neither more nor less than the diameter of the solder joint. Furthermore, the symmetry of the problem allows that only the right half of the structure in Fig. 14(*b*) is modeled. Thus the final model consists of solder joints and two cantilever beams, as shown in Fig. 14(*c*). Its finite element model is presented in Fig. 15.

6.2 Model Parameters. In current analysis, a component in a size of $6\times0.5\times1.02$ mm^3 was interconnected to a $50\times0.5\times1$ mm^3 PCB through Sn3.0Ag0.5Cu solder joints. The component contains a bare silicon die in a size of $3\times0.5\times0.26$ mm^3. A solder mask, substrate and Cu pads were taken into account. The diameter, standoff, and pitch of the solder joint were 0.35 mm, 0.28 mm, and 0.5 mm, respectively. Pad designs are solder mask define (SMD) on the component side and non solder mask define (NSMD) on the PCB side. Young's modulus E, Poisson's ratio ν, and density ρ of various materials used in the finite element model are listed in Table 5.

The element type was C3D8R in the ABAQUS [38], and there were 22,052 elements and 26,258 nodes totally. The drop impact test condition H defined by the JEDEC [6] was used, which is characterized by a half-sine impact acceleration pulse with a peak of 2900 G and a time duration of 0.3 ms.

6.3 Simulation Results and Discussions. In order to show the influence of material models on behaviors of solder joints, elastic, elastic-plastic, and strain rate-dependent Johnson–Cook

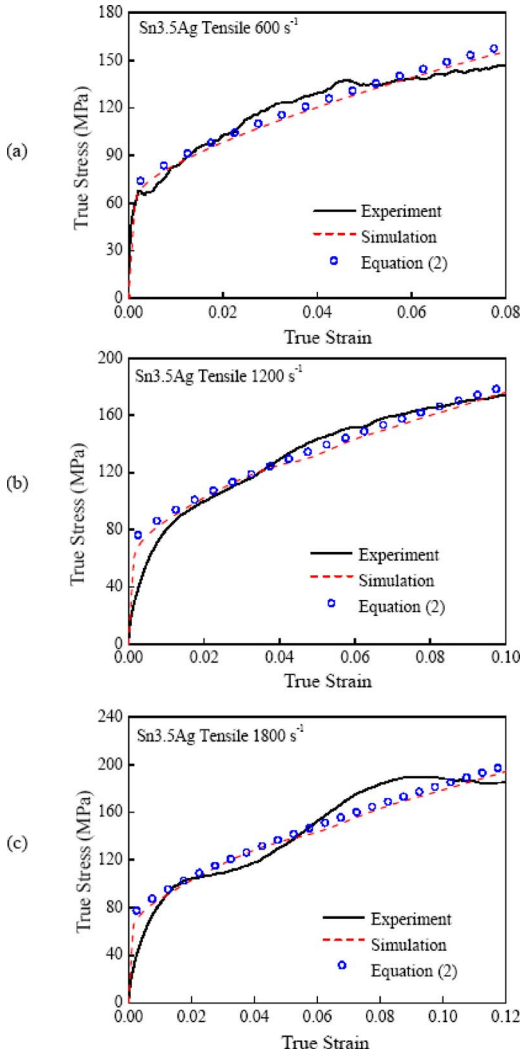

Fig. 11 Tensile true stress-strain curves of Sn3.5Ag at strain rates of (*a*) 600 s^{-1}, (*b*) 1200 s^{-1}, and (*c*) 1800 s^{-1}

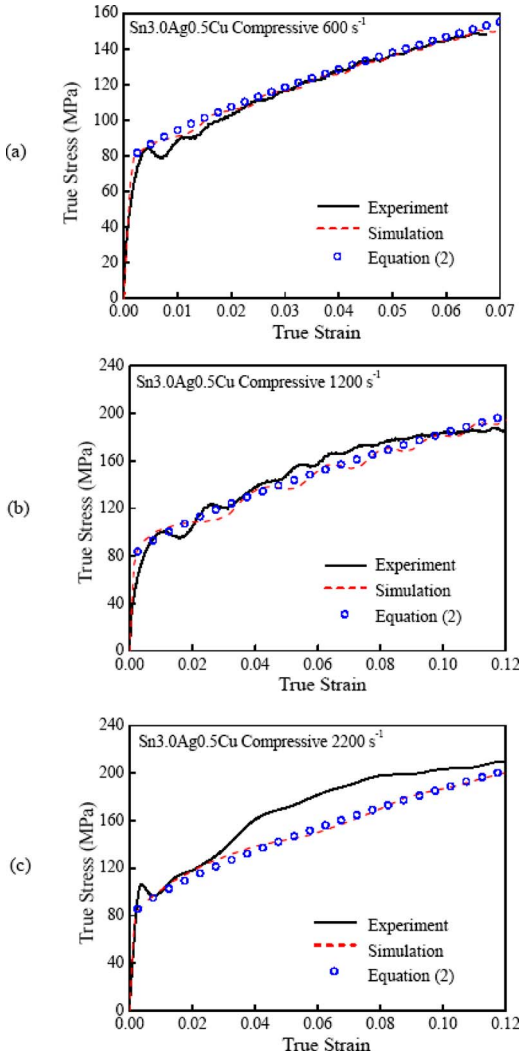

Fig. 12 Compressive true stress-strain curves of Sn3.0Ag0.5Cu at strain rates of (*a*) 600 s^{-1}, (*b*) 1200 s^{-1}, and (*c*) 2200 s^{-1}

models were used in the analysis, respectively. The elastic-plastic model and the Johnson–Cook constitutive model of the Sn3.0Ag0.5Cu solder defined by Tables 3 and 4 were used.

Numerical results indicate that the maximum strain rates in the solder joints computed by the elastic, the elastic-plastic, and the Johnson–Cook model are 136 s^{-1}, 1782 s^{-1}, and 922 s^{-1}, respectively. This result supports the estimations made by Wang and Yi [8] and Siviour et al. [9]. If plastic deformation is not considered, the strain rate is about 10^2 s^{-1}, which is close to the estimation made by Wong et al. [10]. Figure 16 shows the typical distributions of the maximum principal stress and strain rate in a solder joint at 0.42 ms, which were computed by the Johnson–Cook model.

The peeling stress, which is the normal stress component in a solder joint vertical to the PCB, is regarded as dominant stress component leading to the failure of solder joints [44]. The maximum peeling stress occurs at the interface between solder joints and the PCB in the most right solder joint (the critical solder joint). Histories of the peeling stresses, true strains, and equivalent plastic strains computed by the three material models at critical point in the critical solder joint are plotted in Fig. 17. It indicates that the elastic model predicts the greatest peeling stress and the least strain, while the elastic-plastic model predicts the least stress but the greatest strain. The Johnson–Cook model predicts the medial results. This is reasonable because the strain rate effect is included in the Johnson–Cook model. From Fig. 17(*c*), the elastic-plastic model predicts a four times greater equivalent plastic strain than the Johnson–Cook model does. This overestimation will lead to a wrong result when the equivalent plastic strain is used as a damage index in reliability assessments.

7 Conclusions

The mechanical properties of Sn37Pb, Sn3.5Ag, and Sn3.0Ag0.5Cu solders were investigated at high strain rates using the split Hopkinson pressure and tensile bar testing techniques. Based on the experimental data, constitutive models of the three solder alloys with and without the strain rate effect were derived, and the models were applied to predict behaviors of solder joints in a board level electronic package subjected to a standard drop impact load. Some conclusions can be drawn as follows:

(1) The two lead-free solders are more sensitive to strain rate than the lead-based solder does. At high strain rates, the tensile strengths of the lead-free solders are about 1.5 times greater than that of the Sn37Pb solder, and their ductility are significantly greater than that of the Sn37Pb.
(2) The great ductility and enhanced bulk strength of lead-free solders in high strain rate deformation make the solder joint-PCB interface vulnerable, and possibly lead to the mi-

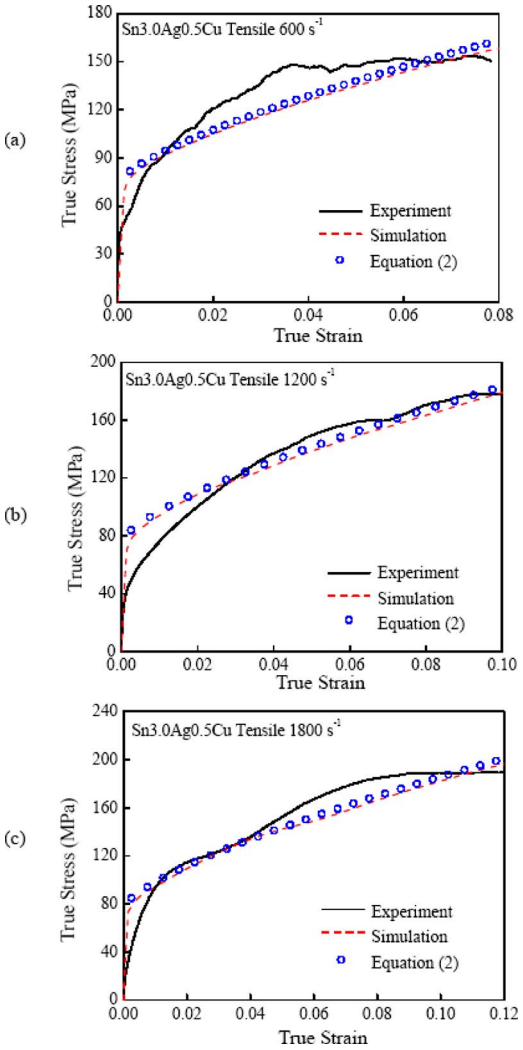

Fig. 13 Tensile true stress-strain curves of Sn3.0Ag0.5Cu at strain rates of (*a*) 600 s^{-1}, (*b*) 1200 s^{-1}, and (*c*) 1800 s^{-1}

gration of the main failure mode from bulk fracturing in lead-based solder joints to interface cracking in lead-free solder joints. In order to investigate the interfacial failure of lead-free solder joints under a drop impact load, the strain

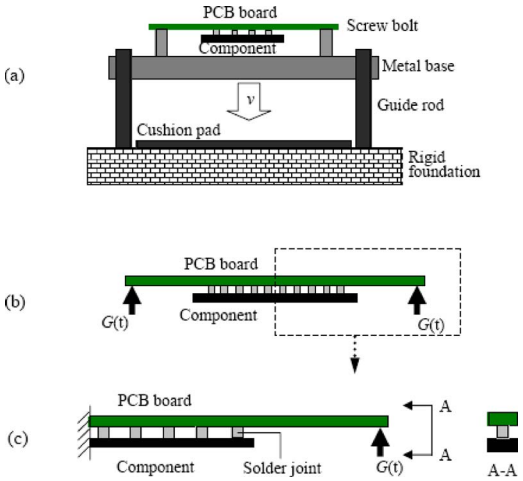

Fig. 14 (*a*) Schematic setup for the board level drop impact testing. (*b*) The input-G model. (*c*) The sliced double cantilever beam model.

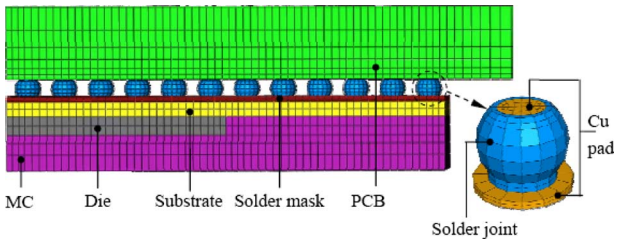

Fig. 15 Finite element model

rate effect and rate-dependent material models of lead-free solders are indispensable.

(3) Numerical results show that under the drop impact condition H defined by the JEDEC solder joints experience a strain rate in a level of 10^3 s^{-1}; therefore, it is imperative to take the strain rate effect into account in the drop impact analysis. The presented rate-dependent Johnson–Cook material models of lead-free solders can predict more realistic stresses and strains than rate-independent elastic-plastic models do, and they are applicable to simulate behaviors of lead-free solder joints in high strain rate deformation such as in the drop impact.

Acknowledgment

The authors appreciate helpful discussion with Dr. Bin Wang from University of Aberdeen, help provided by Professor Shisheng Hu from University of Science and Technology of China, and help by Professor Yongping Lei from Beijing University of Technology during the experimental work. The authors would like to thank the financial supports from the National Natural Science

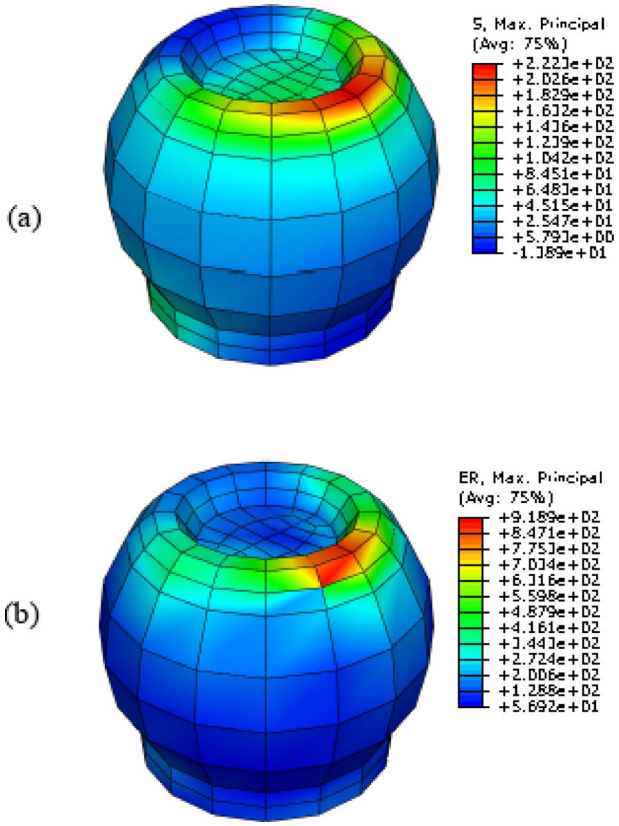

Fig. 16 Distributions of (*a*) maximum principal stress and (*b*) maximum principal strain rate in a solder joint at 0.42 ms, computed by the Johnson–Cook model. Strain rate of 10^3 s^{-1} was observed.

Table 5 Parameters used in the finite element model

Materials	E (GPa)	ν	ρ (kg/mm^3)
Die	131	0.23	2.33
Mold component (MC)	28	0.35	1.97
Cu pad	117	0.34	8.94
PCB	20	0.11	1.91
Solder mask	5	0.30	1.15
Substrate	26	0.11	2.00

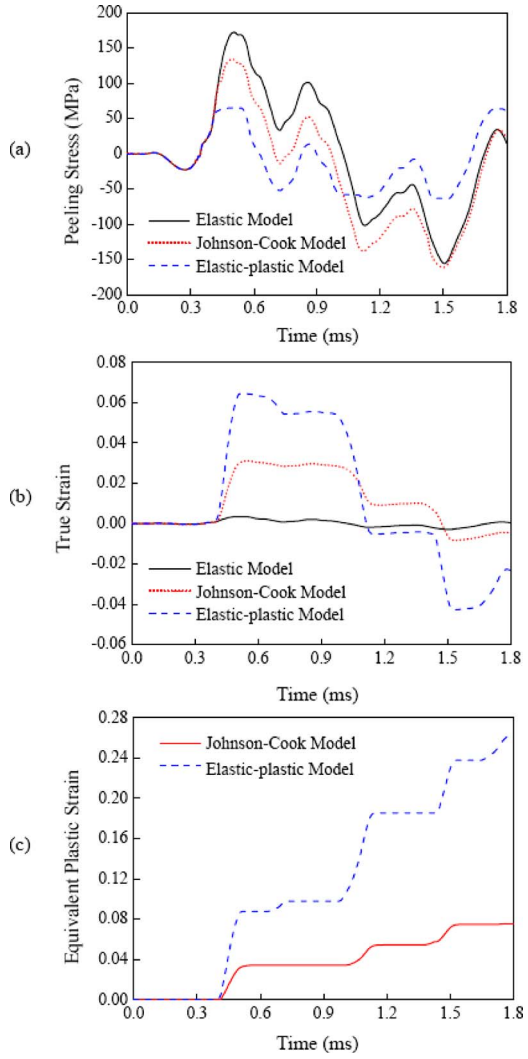

Fig. 17 (*a*) The peeling stress, (*b*) the true strain, and (*c*) the equivalent plastic strain predicted by different constitutive models

Foundation of China (NSFC) under Grant No.10572010 and from the Science & Technology Development Project of Beijing Education Committee under Contract No. KM200610005013.

References

[1] The European Parliament and The Council of the European Union, 2003, "Directive 2002/95/EC of the European Parliament and of the Council of 27 January 2003 on The Restriction of the Use of Certain Hazardous Substances in Electrical and Electronic Equipment (RoHS)," Official Journal of the European Union, **L37**, pp. 19–23.

[2] Zeng, K., and Tu, K. N., 2002, "Six Cases of Reliability Study of Pb-Free Solder Joints in Electronic Packaging Technology," Mater. Sci. Eng. R., **38**, pp. 55–105.

[3] Pang, J. H. L., and Che, F. X., 2006, "Drop Impact Analysis of Sn-Ag-Cu Solder Joints Using Dynamic High Strain Rate Plastic Strain as Impact Damage Driving Force," *IEEE Proceedings of the 56th Electronic Components an Technology Conference*, San Diego, CA, May 30–Jun. 2, pp. 49–54.

[4] Suh, D., Kim, D. W., Liu, P., Kim, H., J. A., Weninger, Kumar, C. M., Prasad, A., Grimsley, B. W., and Tejada, H. B., 2007, "Effects of Ag Content on Fracture Resistance of Sn-Ag-Cu Lead-Free Solders Under High-Strain Rate Conditions," Mater. Sci. Eng., A, **460–461**, pp. 595–603.

[5] Rao, R. T., Rymaszewski, E. J., and Klopfenstein, A. G., 1997, *Microelectronics Packaging Handbook*, 2nd ed., Chapman and Hall, New York.

[6] JEDEC Solid State Technology Association, 2003, "Board Level Drop Test Method of Components for Handheld Electronic Products," Arlington, Jul., JESD22-B111.

[7] Date, M., Shoji, T., Fujiyoshi, M., et al., 2004, "Impact Reliability of Solder Joints," *Proceedings of the 54th Electronic Components and Technology Conference*, IEEE, New York, pp. 668–674.

[8] Wang, B., and Yi, S., 2002, "Dynamic Plastic Behavior of 63wt%Sn37wt%Pb Eutectic Solder Under High Strain Rate," J. Mater. Sci. Lett., **21**, pp. 697–698.

[9] Siviour, C. R., Walley, S. M., Proud, W. G., and Field, J. E., 2005, "Mechanical Properties of SnPb and Lead-Free Solders at High Rates of Strain," J. Phys. D: Appl. Phys., **38**(22), pp. 4131–4139.

[10] Wong, E. H., Selvanayagam, C. S., Seah, S. K. W., van Driel, W. D., Caers, J. F. J. M., Zhao, X. J., Owens, N., Tan, L. C., Frear, D. R., Leoni, M., Lai, Y. S., and Yeah, C. L., 2008, "Stress-Strain Characteristics of Tin-Based Solder Alloys for Drop-Impact Modeling," J. Electron. Mater., **37**(6), pp. 829–836.

[11] Darveaux, R., and Banerji, K., 1992, "Constitutive Relations for Tin-Based Solder Joints," IEEE Trans. Compon., Hybrids, Manuf. Technol., **15**(6), pp. 1013–1024.

[12] Shi, X. Q., Zhou, W. H., Pang, L. J., and Wang, Z. P., 1999, "Effect of Temperature and Strain Rate on Mechanical Properties of 63Sn/37Pb Solder Alloy," ASME J. Electron. Packag., **121**(3), pp. 179–185.

[13] Wilde, J., Becker, K., Thoben, M., Blum, W., Jupitz, T., Wang, G. Z., and Cheng, Z. N., 2000, "Rate Dependent Constitutive Relations Based on Anand Model for 92.5Pb5Sn2.5Ag Solder," IEEE Trans. Adv. Packag., **23**(3), pp. 408–414.

[14] Amagai, M., Watanabe, M., Omiya, M., Kishimoto, K., and Shibuya, T., 2002, "Mechanical Characterization of Sn-Ag-Based Lead-Free Solders," Microelectron. Reliab., **42**(6), pp. 951–966.

[15] Plumbridge, W. J., and Gagg, C. R., 1999, "Effects of Strain Rate and Temperature on the Stress-Strain Response of Solder Alloys," J. Mater. Sci.: Mater. Electron., **10**, pp. 461–468.

[16] Kim, K. S., Huh, S. H., and Suganuma, K., 2002, "Effects of Cooling Speed on Microstructure and Tensile Properties of Sn-Ag-Cu Alloys," Mater. Sci. Eng., A, **333**(1–2), pp. 106–114.

[17] Nose, H., Sakane, M., and Tsukada, Y., 2003, "Temperature and Strain Rate Effects on Tensile Strength and Inelastic Constitutive Relationship of SnPb Solders," ASME J. Electron. Packag., **125**, pp. 59–66.

[18] Shohji, I., Yoshida, T., Takahashi, T., and Hioki, S., 2004, "Tensile Properties of Sn-Ag Based Lead-Free Solders and Strain Rate Sensitivity," Mater. Sci. Eng., A, **366**, pp. 50–55.

[19] Liang, J., Dariavach, N., and Shangguan, D., 2005, "Deformation Behavior of Solder Alloys Under Variable Strain Rate Shearing & Creep Conditions," *Proceedings of the Tenth International Symposium on Advanced Packaging Materials: Processes, Properties and Interfaces*, Mar. 16–18, IEEE, Irvine, CA, pp. 21–26.

[20] Pang, J. H. L., and Xiong, B. S., 2005, "Mechanical Properties for 95.5Sn-3.8Ag-0.7Cu Lead-Free Solder Alloy," IEEE Trans. Compon. Packag. Technol., **28**(4), pp. 830–840.

[21] Zhu, F., Zhang, H., Guan, R., and Liu, S., 2007, "The Effect of Temperature and Strain Rate on the Tensile Properties of a Sn99.3Cu0.7(Ni) Lead-Free Solder Alloy," Microelectron. Eng., **84**, pp. 144–150.

[22] Liang, J., Dariavach, N., Callahan, P., and Shangguan, D., 2007, "Inelastic Deformation and Fatigue of Solder Alloys Under Complicated Load Conditions," ASME J. Electron. Packag., **129**, pp. 195–204.

[23] Andersson, C., Sun, P., and Liu, J., 2008, "Tensile Properties and Microstructural Characterization of Sn-0.7Cu-0.4Co Bulk Solder Alloy for Electronics Applications," J. Alloys Compd., **457**, pp. 97–105.

[24] Hopkinson, B., 1914, "A Method of Measuring the Pressure Produced in the Impact of Bullets," Philos. Trans. R. Soc. London, Ser. A, **213**, pp. 437–456.

[25] Lee, S. W. R., and Dai, L. H., 2001, "Characterization of Strain Rate-Dependent Behavior of 63Sn-37Pb Solder Using Split Hopkinson Torsional Bars," *Proceedings of the 13th Symposium on Mechanics of SMT & Photonic Structures*, ASME International Mechanical Engineering Congress & Exposition, New York, pp. 1–6.

[26] Wang, B., 2006, "Dynamic Strength of Eutectic Solders," private communication.

[27] Tee, T. Y., Ng, H. S., Lim, C. T., Pek, E., and Zhong, Z. W., 2004, "Impact Life Prediction Modeling of TFBGA Packages Under Board Level Drop Test," Microelectron. Reliab., **44**(7), pp. 1131–1142.

[28] Chong, D. Y. R., Che, F. X., Pang, J. H. L., Ng, K., Tan, J. Y. N., and Low, P. T. H., 2006, "Drop Impact Reliability Testing for Lead-Free and Lead-Based Solder IC Packages," Microelectron. Reliab., **46**, pp. 1160–171.

[29] Tsai, T. Y., Yeh, C. L., Lai, Y. S., and Chen, R. S., 2007, "Transient Submodeling Analysis for Board-Level Drop Tests of Electronic Packages," IEEE Trans. Electron. Packag. Manuf., **30**(1), pp. 54–62.

[30] Wiese, S., and Rzepka, S., 2004, "Time-Independent Elastic–Plastic Behavior of Solder Materials," Microelectron. Reliab., **44**(12), pp. 1893–1900.

[31] Johnson, G. R., and Cook, W. H., 1983, "A Constitutive Model and Data for Metals Subjected to Large Strains, High Strain Rates and High Temperatures," *Proceedings of the Seventh International Symposium on Ballistics*, The Hague, The Netherlands, pp. 541–547.
[32] Yadav, S., and Ramesh, K. T., 1995, "The Mechanical Properties of Tungsten-Based Composites at Very High Strain Rates," Mater. Sci. Eng., **A203**, pp. 140–153.
[33] Umbrello, D., Saoubi, R. M., and Outeiro, J. C., 2007, "The Influence of Johnson–Cook Material Constants on Finite Element Simulation of Machining of AISI 316L Steel," Int. J. Mach. Tools Manuf., **47**, pp. 462–470.
[34] Dey, S., Borvik, T., Hopperstad, O. S., and Langseth, M., 2007, "On the Influence of Constitutive Relation in Projectile Impact of Steel Plate," Int. J. Impact Eng., **34**, pp. 464–486.
[35] Follansbee, P. S., 1985, "The Hopkinson Bar," *ASM Metals Handbook*, Vol. 8, ASM International, Materials Park, OH, pp. 198–203.
[36] Nicholas, T., 1981, "Tensile Testing of Materials at High Rates of Strain," Exp. Mech., **21**(5), pp. 177–185.
[37] Lindholm, U. S., 1964, "Some Experiments With the Split-Hopkinson Pressure Bar," J. Mech. Phys. Solids, **12**, pp. 317–335.
[38] ABAQUS 6.5 User's Manual, 2004, Hibbitt, Karlsson & Sorensen, Inc..
[39] Liang, R., and Khan, A. S., 1999, "A Critical Review of Experimental Results and Constitutive Models for BBC and FCC Metals Over a Wide Range of Strain Rates and Temperatures," Int. J. Plast., **15**(9), pp. 963–980.
[40] Suhir, E., 1988, "On a Paradoxical Phenomenon Related to Beams on Elastic Foundation: Could External Compliant Leads Reduce the Strength of a Surface-Mounted Device?," ASME J. Appl. Mech., **55**(4), pp. 818–821.
[41] Wong, E. H., 2005, "Dynamics of Board Level Drop Impact," ASME J. Electron. Packag., **127**, pp. 200–207.
[42] Yeh, C. L., Lai, Y. S., and Kao, C. L., 2006, "Evaluation of Board-Level Reliability of Electronic Packages Under Consecutive Drops," Microelectron. Reliab., **46**(7), pp. 1172–1182.
[43] Tee, T. Y., Luan, J., Pek, E., Lim, C. T., and Zhong, Z., 2004, "Novel Numerical and Experimental Analysis of Dynamic Responses Under Board Level Drop Test," *Proceedings of the Fifth International Conference on Thermal and Mechanical Simulation and Experiments in Microelectronics and Microsystems*, New York, pp. 133–140.
[44] Tee, T. Y., Luan, J., Pek, E., Lim, C. T., and Zhong, Z., 2004, "Advanced Experimental and Simulation Techniques for Analysis of Dynamic Responses During Drop Impact," *Proceedings of the 54th Electronic Components and Technology Conference*, Piscataway, NJ, pp. 1088–1094.

Inelastic Analysis of Fracture Propagation in Distal Radius

S. Pietruszczak
e-mail: pietrusz@mcmaster.ca

K. Gdela
e-mail: gdelakm@mcmaster.ca

Department of Civil Engineering,
McMaster University,
Hamilton, ON, L8S 4L7, Canada

The focus of this paper is on the description of progressive fracture in distal radius in the event of a fall onto an outstretched hand. The inception of fracture, which involves formation of a macrocrack in the cortical tissue, is defined by invoking a macroscopic failure criterion that accounts for inherent anisotropy of the material. The subsequent propagation of damage is described by employing a homogenization procedure in which the average properties of cortical tissue intercepted by a macrocrack are established. The framework is verified by performing a series of nonlinear finite element analyses. In particular, the experimental tests recently conducted by the authors and their colleagues on a number of cadaver radii under boundary conditions leading to Colles' fracture are simulated, and the results are compared with the experimental outcome.
[DOI: 10.1115/1.3168595]

1 Introduction

The fracture of the distal radius is typically the earliest clinical manifestation of osteoporosis [1,2] as the peak incidence occurs some 15 years before that of hip fracture. Consequently, the identification of individuals at risk for radial fracture would permit much earlier intervention to prevent irreversible bone loss, and perhaps avoid the future more devastating fractures of the hip and spine.

Currently, the most widely used technique for evaluation of the risk of fracture in clinical practice involves the measurement of bone mineral density (BMD), determined with dual energy X-ray absorptiometry (DXA). In this case, the assessment of fracture risk is based on the correlation between the baseline bone density and subsequent occurrence of fractures as observed in gender and race specified large groups of individuals followed over a number of years. Apparently, the BMD value alone does not provide a rigorous mechanical assessment; it only indicates the level of probability that an individual will suffer a fracture.

The first approach aimed at incorporating the actual geometry of a radius into fracture risk assessment was strictly experimental and involved mechanical testing simulating the condition of a fall onto an outstretched hand. This methodology was employed to establish a correlation between clinical measurements of bone mass with experimentally determined fracture load. It was noticed that clinical measurements such as BMD and BMC are not sufficient to explain variability of the data [3–5] and attention was turned to morphological measurements such as cortical cross-sectional area or moment of inertia [3,4,6,7]. Despite somewhat encouraging results, the experimental approach alone is quite restrictive as the clinical measures that are correlated with the mechanical competence vary from study to study.

An alternative methodology, which was developed and implemented more recently, involves numerical studies based on finite element (FE) analyses. The latter incorporates the actual geometry, material properties, and the specific boundary conditions corresponding to the considered event. In general, there are two alternative approaches to the problem, viz. micromechanical and continuum-level analysis. The simulations at the microlevel require generation of a micro-FE model from high resolution peripheral quantitative computed tomography (pQCT) images. In this case, the FE mesh includes details of the trabecular architecture [8,9] and, as a result, employs an excessive number of elements. In general, the procedures for creating the FE mesh are similar at both micro- and macrolevels. The primary difference is that, in the latter case, the in-plane spatial resolution of the images is coarser and the reconstructed volume is divided into much smaller number of elements. For both micro- and macrolevel approaches, the estimates of the fracture load can be considered reliable only if the description of mechanical properties of the bone tissue is adequate. In this context, most of the existing attempts are questionable as they do not incorporate the effects of inherent anisotropy of both strength and deformation characteristics, and/or do not properly address the notion of localized deformation.

In this study, the fracture process in a radius bone is investigated based on a nonlinear FE analysis, which incorporates an inelastic constitutive relation for the cortical bone tissue. The work is an extension of the previous research as reported earlier by Pietruszczak et al. [10]. The latter study involved a simplified approach in which the critical load causing fracture was estimated by examining the plastic admissibility of the predicted stress field. In the present work, a more rigorous approach is followed, which employs a homogenization technique for establishing the average properties of cortical tissue intercepted by a macrocrack. To the authors' knowledge, this is the first attempt to examine the propagation of fracture in the distal radius.

The primary objective of this work is to verify the predictive abilities of the proposed mathematical framework against a series of experimental tests recently conducted by the authors and their colleagues [11]. The experiments involved testing of a number of dry cadaver radii under the conditions leading to Colles' fracture. The structural tests were followed by a series of material tests on samples of cortical tissue that were extracted from the fractured radii. The mechanical testing was preceded with the clinical imaging of the bone specimens.

It has been recognized that for problems involving Colles' fracture, the best correlation between failure load and bone properties can be found in the cortical area [4,6,7,12]. Therefore, the focus in the mathematical formulation of the problem is on the description of cortical tissue properties. In subsequent sections, the formulation of the problem is first outlined, followed by a numerical study. The numerical part includes some parametric studies on idealized geometries that examine the influence of basic material parameters. Subsequently, the simulations of experimental tests are discussed, which address the issue of initiation and propagation of fracture in the distal radius.

Contributed by the Applied Mechanics Division of ASME for publication in the JOURNAL OF APPLIED MECHANICS. Manuscript received July 30, 2008; final manuscript received February 13, 2009; published online September 30, 2009. Review conducted by Professor Krishna Garikipati.

2 Methodology

As mentioned earlier, the mechanical competence of the radius is primarily due to the presence of the cortical shell. In mechanical terms, the cortical tissue may be considered as transversely isotropic, with the preferred material axis coinciding with that of the osteon system. The onset of Colles' fracture is associated with the *tensile* stress regime, and the bone material may be idealized as brittle elastic [11]. In this case, two basic notions need to be dealt with, namely the specification of conditions at failure and the description of localized deformation.

2.1 Tensile Fracture Criterion for Cortical Bone. The strength of the cortical tissue is significantly affected by the orientation of the osteons relative to the loading direction. The experimental evidence indicates that the tensile strength in the longitudinal direction is nearly three times larger than that in the transverse direction [13]. The variation in axial compressive strength shows a similar trend, with the respective values being significantly higher than those in the tension regime.

The fracture criterion employed in this work is analogous to that given in Ref. [10]. In what follows, the main assumptions embedded in the formulation are briefly reviewed. The considerations are restricted to the *tensile* regime which, as mentioned earlier, is of primary interest for problems involving the distal radius fracture.

The criterion invokes an assumption that the failure occurs when the normal component of the traction vector, acting on a plane with the unit normal n_i, reaches a critical value. Thus, the failure function is defined as

$$F = t^n(n_i) - c(n_i), \quad t^n = \sigma_{ij} n_i n_j, \quad c = c_o(1 + \Omega_{ij} n_i n_j) \tag{1}$$

where t^n is the normal stress, and c is the strength parameter. According to Eq. (1), the value of c is said to be orientation dependent and the bias in its distribution is defined by employing a symmetric traceless tensor Ω_{ij}, whose eigenvectors coincide with the principal material axes, while c_o represents the average value of c.

The orientation of the fracture/localization plane can be determined by maximizing F with respect to orientation n_i. Thus, the conditions at failure are defined as

$$\max_{n_i} F = \max_{n_i} [t^n(n_i) - c(n_i)] = 0 \tag{2}$$

The solution procedure involves constructing a supplementary function incorporating Lagrange multiplier λ, that is

$$G = \sigma_{kj} n_k n_j - c_o(1 + \Omega_{kj} n_k n_j) - \lambda(n_j n_j - 1) \tag{3}$$

The conditions for stationary value of this function lead to

$$\frac{\partial G}{\partial n_i} = 2(\sigma_{ij} n_j - c_o \Omega_{ij} n_j) - 2\lambda \delta_{ij} n_j = 0, \quad n_i n_i = 1 \tag{4}$$

from which

$$(B_{ij} - \lambda \delta_{ij}) n_j = 0, \quad B_{ij} = \sigma_{ij} - c_o \Omega_{ij} \tag{5}$$

Equation (5) defines an eigenvalue problem that can be solved to specify the direction cosines n_i. Clearly, if $\Omega_{ij}=0$ then the direction of the localization plane is coaxial with that of the maximum tensile stress, which is consistent with the standard criterion for an isotropic material. Note that the function $c(n_i)$ in Eq. (1) can be augmented by introducing higher-order dyadic products of $\Omega_{ij} n_i n_j$. This will allow incorporating more complex distributions of tensile strength, if the latter is indeed evidenced by the experimental data.

The fracture criterion (2) was verified experimentally in the work of Gdela et al. [11]. It has been demonstrated that the functional form (1) can adequately describe the directional dependence of both tensile strength and orientation of the localization plane.

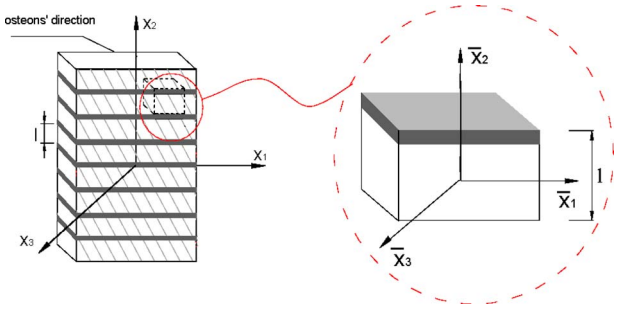

Fig. 1 Representative volume of cortical tissue intercepted by weakness planes

2.2 Description of Localized Deformation. The notion of an elastic-brittle material implies that when the fracture criterion (2) is met a localized deformation takes place associated with the formation of macrocracks. The localization commences on a plane for which max $F=0$ and the direction of macrocrack is identified with that of the critical plane.

In order to define the mechanical response, consider a representative volume of the material intercepted by a set of weakness planes (macrocracks) of spacing l. Refer the geometry of a typical unit cell to the frame of reference $\bar{x}_i$, such that $\bar{x}_2$-axis is normal to the interface, as shown in Fig. 1. The constitutive relations for the bone tissue and the weakness planes take the form

$$\dot{\bar{\sigma}}_{ij} = C_{ijkl} \dot{\bar{\varepsilon}}_{kl}; \quad \dot{\bar{t}}_i = k_{ij} [v_j] \tag{6}$$

In the equation above, $\bar{\sigma}_{ij}, \bar{\varepsilon}_{ij}$ are the local microstress/strain tensors, $\bar{t}_i$ is the traction at the interface, $[v_j]$ is the velocity discontinuity, and k_{ij} defines the mechanical properties along the weakness plane. Note that C_{ijkl} is an elastic transversely-isotropic operator, which may be formally defined as

$$\begin{aligned} C_{ijkl} = {} & a_1 \delta_{ij} \delta_{kl} + a_2(\nu_i \nu_j \delta_{kl} + \delta_{ij} \nu_k \nu_l) + a_3 \delta_{ki} \delta_{lj} + a_4 \nu_i \nu_j \nu_k \nu_l \\ & + a_5(\nu_i \nu_k \delta_{lj} + \nu_k \nu_j \delta_{li} + \nu_i \nu_l \delta_{kj} + \nu_l \nu_j \delta_{ik}) \end{aligned} \tag{7}$$

where a's are material constants and ν_i is a unit vector which specifies the preferred material direction. At the same time, k_{ij} is an elastoplastic operator, which is defined later in this section.

Following the framework of the homogenization approach [14,15] the velocity field within the unit cell can be expressed as

$$v_i = \dot{\varepsilon}_{ij} \bar{x}_j + \bar{v}_i(\bar{x}_2) \tag{8}$$

where ε_{ij} is the macrostrain tensor, and $\bar{v}_i$ is a discontinuous periodic field with the period of l. The microstrain rate $\dot{\bar{\varepsilon}}_{ij}$, corresponding to Eq. (8), is defined as

$$\dot{\bar{\varepsilon}}_{ij} = \dot{\varepsilon}_{ij} + 1/2 \left(\frac{\partial \bar{v}_i}{\partial \bar{x}_2} \delta_{2j} + \frac{\partial \bar{v}_j}{\partial \bar{x}_2} \delta_{2i} \right) \tag{9}$$

Substituting Eq. (9) in the first equation in Eq. (6) yields, after some transformations

$$\dot{\bar{\sigma}}_{ij} = C_{ijkl} \dot{\varepsilon}_{kl} + C_{ijk2} \frac{\partial \bar{v}_k}{\partial \bar{x}_2} \tag{10}$$

The stress field $\bar{\sigma}_{ij}$ is a self-equilibrated one, so that

$$\dot{\bar{\sigma}}_{ij,j} = 0 \Rightarrow C_{i2k2} \frac{\partial^2 \bar{v}_k}{\partial \bar{x}_2^2} = 0 \tag{11}$$

Since $\det C_{i2k2} \neq 0$, the latter equality implies

$$\frac{\partial^2 \bar{v}_i}{\partial \bar{x}_2^2} = 0 \Rightarrow \bar{v}_i = A_i \bar{x}_2; \quad [v_i] = -A_i l \tag{12}$$

where A_i=constant. Imposing now the traction continuity requirement $\dot{\bar{\sigma}}_{2j} = \dot{\bar{t}}_j$, and utilizing Eq. (10) together with Eqs. (6) and (12), yields

$$\dot{\bar{\sigma}}_{2j} = \dot{\bar{t}}_j \Rightarrow C_{2jkl}\dot{\bar{\varepsilon}}_{kl} + C_{2jk2}\frac{\partial \bar{v}_k}{\partial \bar{x}_2} = -k_{jk}A_k l \tag{13}$$

from which

$$A_k = -(C_{2kj2} + lk_{kj})^{-1} C_{2jmn}\dot{\bar{\varepsilon}}_{mn} \tag{14}$$

The representation (14) can be substituted in relation (10) to define the average macroscopic behavior. Noting that for the velocity field (12) the microstress remains constant within the considered unit cell, i.e., $\sigma_{ij} = \langle \bar{\sigma}_{ij} \rangle = \bar{\sigma}_{ij}$, one obtains

$$\dot{\sigma}_{ij} = \tilde{C}_{ijpq}\dot{\bar{\varepsilon}}_{pq}; \quad \tilde{C}_{ijpq} = C_{ijpq} - C_{ijk2}C_{2lpq}(C_{2kl2} + lk_{kl})^{-1} \tag{15}$$

Finally, the relation (15) can be referred to a global frame of reference by employing a standard transformation rule, that is,

$$\dot{\sigma}^*_{ij} = (\alpha_{im}\alpha_{jn}\alpha_{pr}\alpha_{qs}\tilde{C}_{mnrs})\dot{\varepsilon}^*_{pq} \tag{16}$$

where α_{ij} is the transformation tensor.

The above general solution, viz., Eq. (15), pertains to the case when the representative volume is intercepted by multiple discontinuity planes. The same methodology, leading to the same representation (Eq. (15)), may be implemented in the context of a domain intercepted by a single plane of weakness. In the latter case, $\bar{v}_i$ represents a discontinuous field whose components vanish on external boundaries. Consequently, the parameter l is then interpreted as a "characteristic dimension," associated with a given representative volume V; e.g., $l = \sqrt[3]{V}$, if the latter is perceived as a cuboidal cell.

The inverse relation to that of Eq. (15), i.e., the one defining the response in macrostress rates for an arbitrary macrostrain rate, may be obtained by writing the constitutive relations (6) in the form

$$\dot{\bar{\varepsilon}}_{ij} = D_{ijkl}\dot{\bar{\sigma}}_{kl}; \quad [v_i] = K_{ij}\dot{\bar{t}}_j \tag{17}$$

where $D_{ijkl} = C^{-1}_{ijkl}$ and $K_{ij} = k^{-1}_{ij}$. Incorporating now the continuity requirement $\dot{\bar{t}}_j = \dot{\bar{\sigma}}_{2j} = \dot{\bar{\sigma}}_{ij}\delta_{2i}$, one can write

$$[v_i] = K_{ij}\dot{\bar{t}}_j = K_{ij}\dot{\bar{\sigma}}_{pj}\delta_{2p} = -A_i l \Rightarrow A_i = -l^{-1}K_{iq}\dot{\bar{\sigma}}_{pq}\delta_{2p} \tag{18}$$

The macrostrain rate field, Eq. (9), can be expressed as

$$\dot{\varepsilon}_{ij} = D_{ijkl}\dot{\bar{\sigma}}_{kl} - 1/2(A_i\delta_{2j} + A_j\delta_{2i}) \tag{19}$$

which upon substitution of Eq. (18), together with the condition $\sigma_{ij} = \langle \bar{\sigma}_{ij} \rangle = \bar{\sigma}_{ij}$, yields

$$\dot{\varepsilon}_{ij} = \tilde{D}_{ijkl}\dot{\sigma}_{kl}, \quad \tilde{D}_{ijkl} = D_{ijkl} + 1/2l^{-1}(K_{il}\delta_{2k}\delta_{2j} + K_{jl}\delta_{2k}\delta_{2i}) \tag{20}$$

It is noted that if the deformation process results predominantly from sliding/separation along the interface, then the contribution from the intact bone may be perceived as negligible. Thus, considering the intact material as rigid, i.e., taking $D_{ijkl} \to 0$, yields

$$\tilde{D}_{ijkl} \approx 1/2l^{-1}(K_{il}\delta_{2k}\delta_{2j} + K_{jl}\delta_{2k}\delta_{2i}) \tag{21}$$

which provides a simple approximation, which may be sufficiently accurate in practical implementation.

The above outlined general methodology for the description of localized deformation is conceptually similar to that presented in earlier work (see Ref. [16]). The mathematical approach, however, is different. In order to complete the formulation, the functional form of the compliance (K_{ij}) and/or stiffness (k_{ij}) operators, viz., Eqs. (6) and (17), needs to be specified. Consider the interface behavior as elastoplastic strain softening, and define the yield function on the localization plane n_i as

$$f = t_i t_i - k^2 = 0, \quad k = k(\zeta), \quad \dot{\zeta} = [v^p_i]n_i \tag{22}$$

where $[v^p_i]$ is the irreversible part of velocity discontinuity. Following the standard plasticity procedure, i.e., satisfying the consistency condition

$$\dot{f} = 2t_i\dot{t}_i - 2kk'[v^p_i]n_i = 0, \quad [v^p_i] = \dot{\lambda}\frac{\partial f}{\partial t_i} \tag{23}$$

and employing the additivity postulate in the constitutive relation

$$\dot{t}_i = k^e_{ij}([v_j] - [v^p_j]) \tag{24}$$

one obtains

$$\dot{\lambda} = k^e_{ij}t_i[v_j]/2H; \quad H = k^e_{ij}t_i t_j + kk' t_i n_i \tag{25}$$

where k^e_{ij} is the elastic operator. Substituting now Eq. (25) in Eq. (24) yields

$$\dot{t}_i = k_{ij}[v_j], \quad k_{ij} = k^e_{ij} - k^e_{ip}k^e_{kj}t_k t_p/H \tag{26}$$

The softening function may be assumed in a simple exponential form

$$k = k_o e^{-\alpha\zeta} \Rightarrow k' = -\alpha k \tag{27}$$

where k_o defines the magnitude of the traction at the inception of localization, and α is a material parameter.

The inverse relation to Eq. (26) is obtained by evaluating the plastic multiplier directly from Eq. (23), that is

$$\dot{\lambda} = t_i\dot{t}_i/H_1, \quad H_1 = 2kk' t_i n_i \tag{28}$$

and substituting this representation in the additivity postulate

$$[v_i] = K^e_{ij}\dot{t}_j + [v^p_i] \Rightarrow [v_i] = K_{ij}\dot{t}_j, \quad K_{ij} = K^e_{ij} + t_i t_j/H_1 \tag{29}$$

where K^e_{ij} is the elastic compliance.

3 Numerical Analysis

The focal point of the work presented in this section is an inelastic finite element analysis aimed at the prediction of mechanical competence of the radius bone in a fall onto an outstretched hand. Contemporary commercial finite element packages include, in general, the basic elastic and inelastic material models. However, these models are based on classical continuum mechanics that assumes homogeneity and continuity of the material's microstructure and independence of the material response of the orientation of the coordinate system. The latter assumptions are restrictive as they exclude the effects of anisotropy, as well as those of localized deformation. Note that majority of available finite element packages offer the option to include user-defined material models in the analysis. This enables implementation of more complicated frameworks for describing the mechanical behavior.

With respect to the modeling of strain localization, the classical continuum formulations, such as plasticity or damage mechanics, are known to suffer from sensitivity to finite element discretization [17,18]. This drawback of local approaches has been addressed by introducing nonclassical frameworks. The best known in this category are: micropolar (Cosserat) continuum theory, nonlocal constitutive models, and gradient dependent material descriptions [18]. The mathematical framework presented in Sec. 2.2 belongs to the class of local approaches; it takes into account the effects of macrostructural heterogeneity via a homogenization procedure that is applied within the volume that is associated with each material point. The characteristic dimension l that is introduced in this model is defined in terms of geometry of the considered representative volume. It should be noted that the present

Table 1 Material parameters adopted in verification examples

Parameters of the model	Description
$E_x=17{,}400$ MPa	Young's modulus in preferred direction
$E_y=E_z=9600$ MPa	Young's moduli in transverse directions
$\upsilon_{yz}=0.2$	Poisson's ratio in plane of isotropy
$\upsilon_{xz}=\upsilon_{xz}=0.22$	Poisson's ratios in planes parallel to the preferred direction
$G_{xy}=G_{xz}=3500$ MPa	Shear moduli in planes parallel to preferred direction
$G_{yz}=E_y/2(1+\upsilon_{yz})$ (MPa)	Shear modulus in plane of isotropy
$c_0=140$ MPa	Tensile strength in preferred direction
$c_{90}=50$ MPa	Tensile strength in transverse direction
α (1/mm)—variable	Parameter that defines the rate of softening
$k_N=1\times10^9$ MPa/mm	Stiffness of the interface in normal direction per unit area
$k_T=5\times10^8$ MPa/mm	Stiffness of the interface in tangential direction per unit area

approach is, in fact, the only one that distinguishes between the properties of interface and those of intact material.

The presentation in this section is structured as follows. First, the issue of verification of the proposed framework is addressed. Some parametric studies are conducted that include idealized geometries and are focused on examining the influence of basic material parameters. Subsequently, inelastic analyses simulating the experimental tests conducted by Gdela et al. [11] are carried out. The focus is on modeling of the load-displacement characteristics as well as the fracture propagation pattern; the results are compared with the experimental data.

3.1 Verification of the Framework. The mathematical framework developed in Sec. 2 has been incorporated in the commercial FE package Cosmos/M through the user-defined Nstar.exe module. The key material parameters employed in the mathematical formulation are summarized in Table 1. The elastic response, which was assumed to be transversely isotropic, requires specification of five independent elastic constants. Verification of the fracture criterion involves an eigenvalue problem (5); the solution to which gives the maximum value of the fracture function (1) and the direction of the critical plane n_i. This part of analysis requires specification of strength parameters involved in representation (1), i.e., tensile strength in the preferred and the transverse directions c_0 and c_{90}, respectively.

After the onset of localization, the inelastic response involves determination of the stiffness operator k_{ij} for the interface. The latter is computed via Eq. (26). The analysis requires the specification of additional material parameters, viz., elastic properties of the interface (k_N, k_T, i.e., normal and tangential stiffness, respectively) and the softening parameter α. In general, the elastic constants for the interface should be large enough to ensure predominantly plastic behavior. The parameter α involved in Eq. (27) defines the rate of the strain softening and should assume a value that is representative of an elastic-brittle response. Here, no experimental information is available, so that the influence of this parameter is examined through some parametric studies. The key material parameters employed in all verification examples given here are based on average values provided in the literature and are listed in Table 1.

The first verification problem involved an inelastic FE analysis of a cantilever subjected to in-plane bending. In this part, the influence of the softening parameter on the ultimate load, the mesh objectivity, and the ability of the framework to model the fracture propagation process were examined. The finite element models of the analyzed structure are shown in Figs. 2(*a*) and 2(*b*). The cylindrical beam was 200 mm in length, with a hollow cross section of 20 mm in diameter and 2 mm wall thickness. The preferred material direction was assumed to be coaxial with the longitudinal axis.

In the primary simulation, the structure was discretized with 8-noded solid elements; 48 elements along the circumferential and 2 in the radial direction. A higher mesh density was assigned in the region adjacent to the support, where the fracture was expected to initiate. The model consisted of a total of 4992 elements. The cantilever was fixed in a circular embedment that was assigned isotropic elastic properties of steel. All nodes along the circumferential surface of the embedment were restrained against translational degrees of freedom. The loading consisted of vertical displacements applied uniformly over the cross-sectional area at the free end. Parametric studies were conducted for the softening parameter α in the range between 20 mm^{-1} and 100 mm^{-1}.

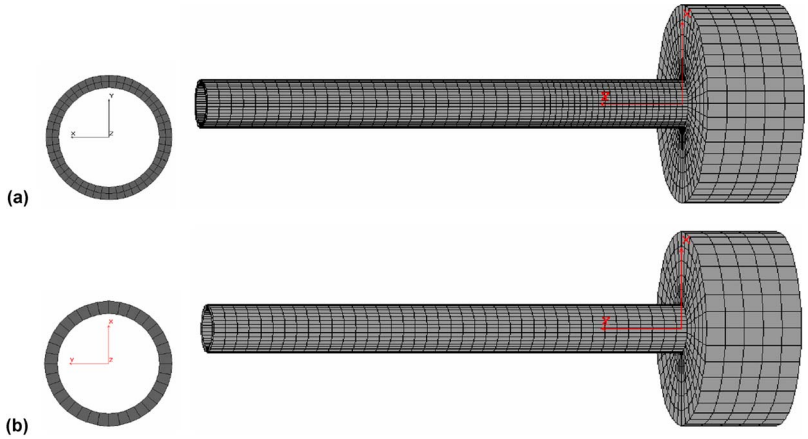

Fig. 2 FE model of cantilever; (*a*) primary mesh (4992 8-noded solid elements) and (*b*) resized mesh (1440 8-noded solid elements)

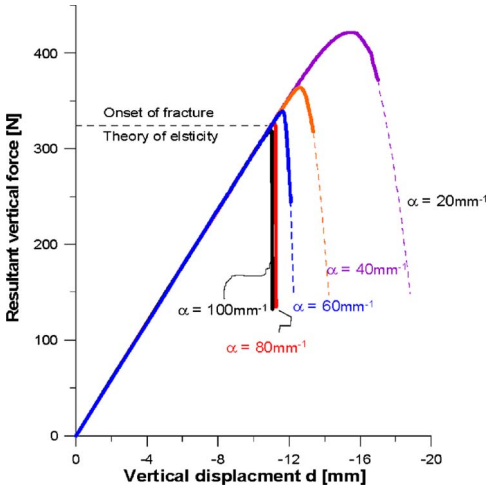

Fig. 3 Force-displacement characteristics for different values of α (Note: Solid lines correspond to results of FE analysis; dashed lines are approximations)

Figures 3–5 show the key results of this part of the parametric study. The force-displacement curves given in Fig. 3 indicate a strong dependency of the solution on the strain softening characteristics. In particular, the rate of softening, as governed by the parameter α, Eq. (27), significantly affects the prediction of the ultimate load. This is clearly evident for $\alpha < 60$ mm^{-1} when the material displays a more ductile behavior. However, an increase in the value of α beyond 60 mm^{-1}, which is indicative of brittle material, gives the solutions that are virtually invariant with respect to α; the differences are of the order of experimental scatter.

Figure 4 illustrates the second aspect of this analysis; i.e., verification of the fracture mode. It is evident that the onset of fracture occurs at the top fibers and the damaged zone progressively propagates downwards. At the ultimate load, nearly half of the cross section is fractured. The results are, in general, consistent with the standard mechanics of material approach.

Finally, Fig. 5 illustrates the influence of mesh size on the predicted mechanical response. The results presented here correspond to different values of the parameter α, and employ two different meshes (Fig. 2). The coarser mesh is uniform and incorporates 1440 elements; 36 along the circumference and 1 in the radial direction. It is evident from these results that the prediction of ultimate load is virtually unaffected by discretization. Some mesh

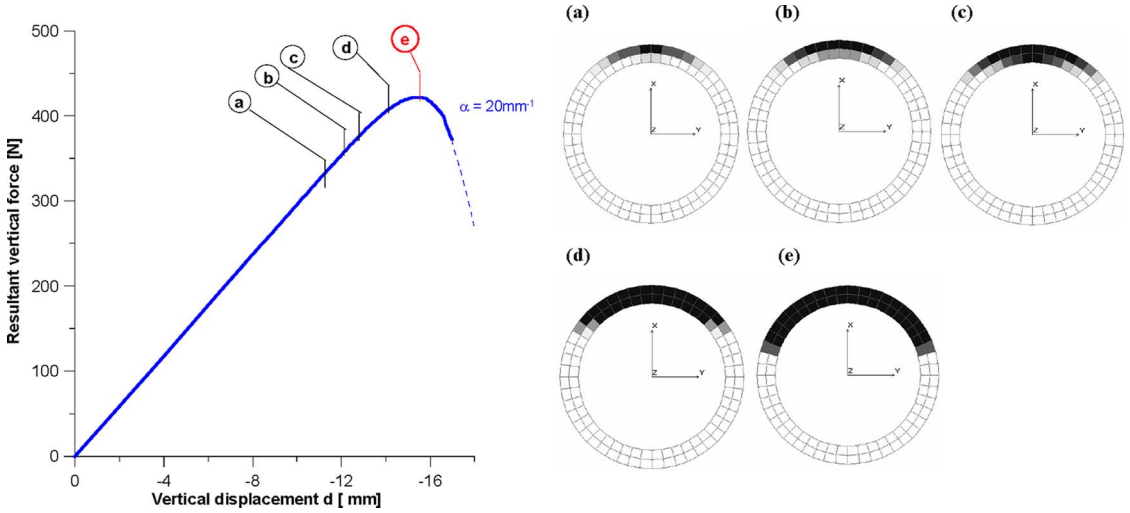

Fig. 4 Fracture propagation along the cross section adjacent to the support; α=20 mm^{-1}

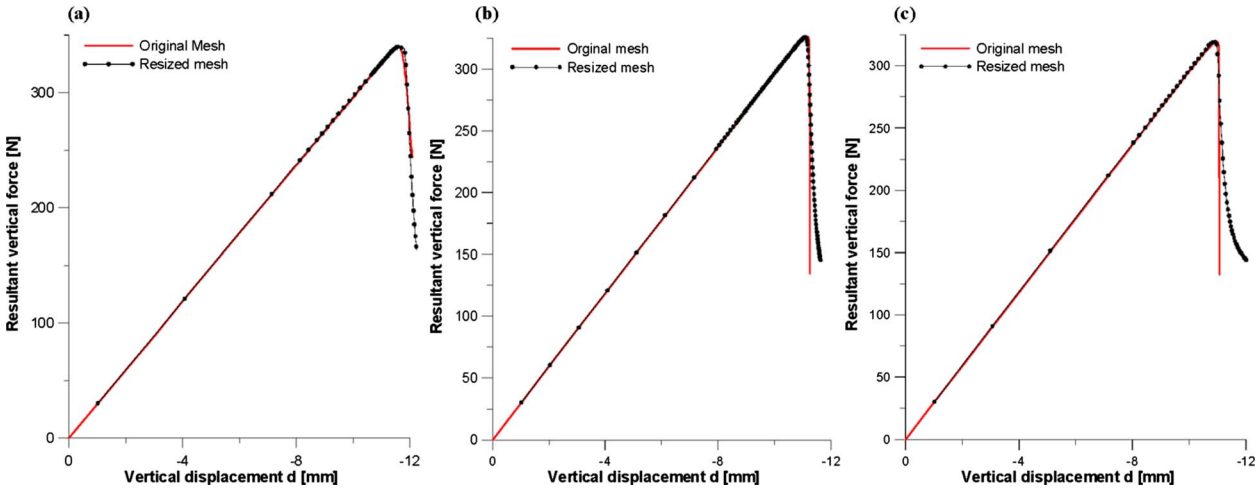

Fig. 5 Comparison of force-displacement characteristics for different mesh densities, i.e., original mesh (4992 elements) and resized mesh (1440 elements): (*a*) α=60 mm^{-1}, (*b*) α=80 mm^{-1}, and (*c*) α=100 mm^{-1}

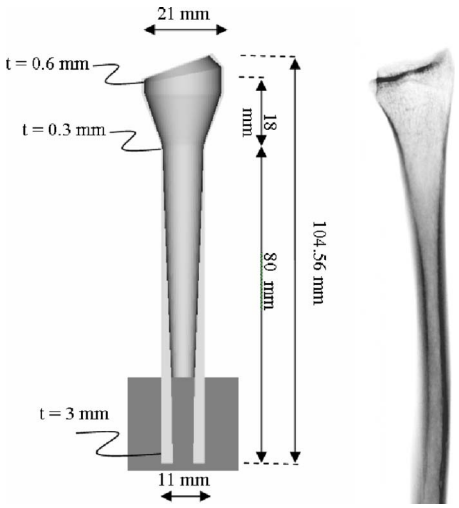

Fig. 6 The idealized FE geometry in comparison to X-ray image of a radius bone

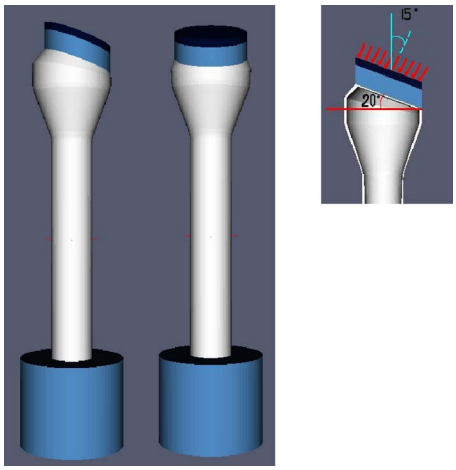

Fig. 7 3D visualization of the FE model of idealized bone geometry

sensitivity of the solution is observed only at advanced stages of deformation when the response becomes unstable on the macroscale (Figs. 5(*b*) and 5(*c*)). This, however, is of little practical significance as the fracture has already occurred.

The second verification problem examined here involved a radius bone, with idealized geometry (after Ref. [10]), subjected to eccentric load. The primary objective was to study the damage process and to asses if the predicted failure mechanism is representative of Colles' fracture.

The geometry is depicted in Fig. 6. The dimensions were chosen based on standard CT images published in the literature. The typical curvilinear features of the bone surface were modeled by a piecewise continuous linear approximation. The spatial characteristics were incorporated into Cosmos/M 2.95, and the volume of the cortical shell was generated. Each volume segment was meshed with eight-noded isoparametric elements; one along the circumferential and two in the radial directions. The material triad was assigned in such a way that for each element the preferred axis remained parallel to the longitudinal direction of the external surface of cortical shell at that location; the remaining two axes were confined to the plane perpendicular to it. The model incorporated approximately 31,200 solid elements. The thickness of the cortical shell was assumed to be within the range of 0.6 mm to 3 mm (Fig. 6). The bone was assumed to be embedded at the trimmed end and at the articular surface.

The loading consisted of applying uniform displacements distributed over the top of the steel plate (Fig. 7). In a palmar view, the displacements were applied toward the styloid and exhibited 15 deg deviation from the longitudinal direction of the shaft, while the radial tilt chosen for the model was 20 deg. In a lateral view, the displacements remained parallel to the longitudinal axis as the model displayed no palmar tilt.

The material properties for the bone tissue were the same as those listed in Table 1. The embedment was considered to be an isotropic elastic material ($E=3.4$ GPa, $\nu=0.34$). A parametric study was conducted for the softening parameter ranging from 60 mm^{-1} to 100 mm^{-1}.

The key results of the numerical simulations are presented in Figs. 8–11. Figure 8 shows the force-displacement characteristics obtained for the examined range of the softening parameter α. Similarly as in the case of the cantilever, the ultimate strength increases with a decrease in the value of α. For higher values though, which are representative of the elastic-brittle material, the changes are insignificant, i.e., of the order of experimental scatter. Note that the dashed lines in Fig. 8 show an extrapolation of the characteristics into post-failure regime. The purpose of this is to emphasize that the response remains unstable after the ultimate load is attained. Apparently, the approximation itself may not be accurate.

Figures 9 and 10 show the progressive evolution of fracture that corresponds to $\alpha=100$ mm^{-1}. In all these figures the damaged zone is depicted in black. It is clear that the onset of fracture and its propagation are both confined to the distal region of the radius

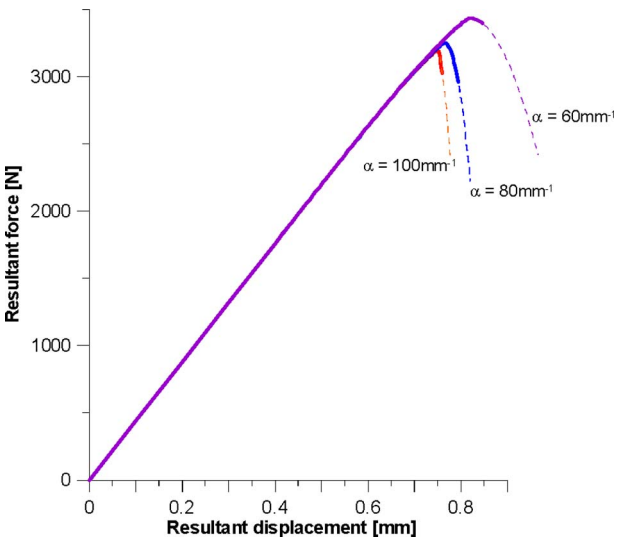

Fig. 8 Force-displacement characteristics

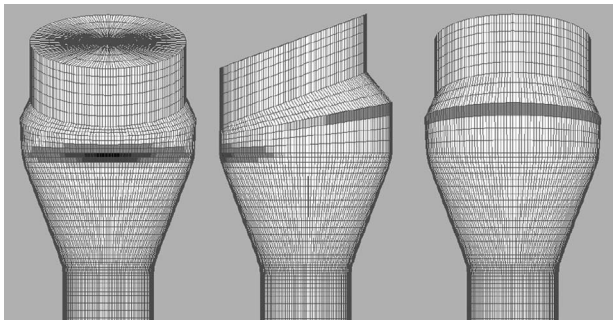

Fig. 9 Onset of fracture at 77% of ultimate load (Note: Black color indicates the fractured region)

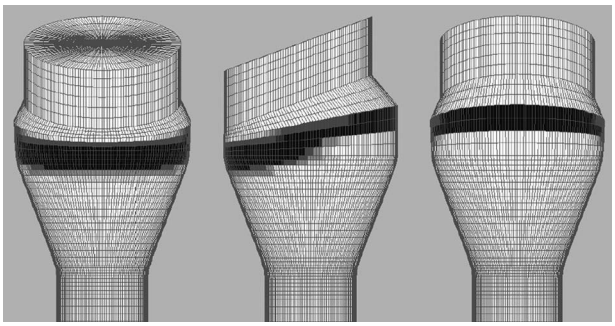

Fig. 10 Fractured region at 90% of ultimate load

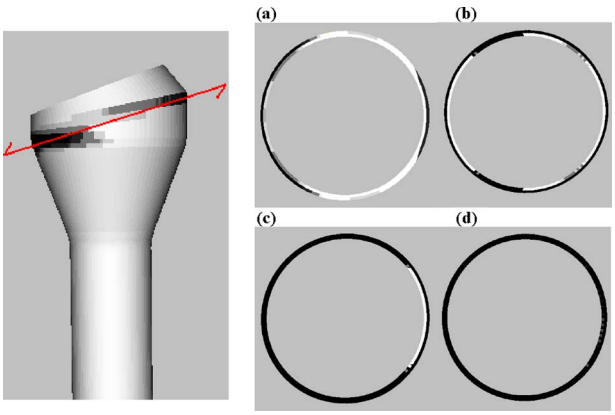

Fig. 11 Fracture propagation in critical cross section, as indicated on the left panel. Results correspond to (*a*) 82%, (*b*) 89%, and (*c*) 95% and 100% of ultimate load

bone, which is representative of Colles' fracture. Figure 11 shows the fracture propagation in the critical cross section of the bone, as indicated on the schematic picture attached to this figure. The fracture is initiated at the medial site of the idealized geometry and progresses along the circumference until the ultimate load is reached, at which stage the entire cross section is fractured.

3.2 Simulations of Experimental Tests. The primary focus here is on the inelastic analysis simulating the experimental tests on the entire radii as conducted by Gdela et al. [11]. The analysis was carried out for two specific bones labeled as No. 3 and No. 5 and the results of simulations have been compared with the experimental data in terms of both load-displacement characteristics and the fracture mode.

An important and a quite demanding aspect of numerical simulations of bone fracture is the generation of FE models of the actual bone geometry. The procedure employed here involved preliminary processing of the digital data obtained from CT scans for each bone in order to extract the external and internal contours of the cortical shell for consecutive cross sections. Subsequent processing was aimed at the conversion of the irregular sets of points for each cross section of the bone, obtained in preliminary processing, into a structured grid of points. This was done by developing an algorithm, which generated a set of sequentially numbered points, with specific spatial location, that allowed for the creation of hexahedral elements. In the next stage of the procedure, a separate code was developed to generate a proper input file enabling import of the structured grid into the Cosmos/M FE package. Note that in case of simulations involving highly irregular geometry, the assignment of material directions for every element becomes very complex. For the cortical bone tissue, it is known that the preferred direction is coaxial with that of the osteons (see Ref. [19]), and that the average direction of the osteons

Fig. 12 FE model of bone No. 3

is parallel to the bone's outer surface [20]. Thus, using the aforementioned procedures, the finite element mesh for the entire bone was generated in such a manner that the local coordinate system for each element was automatically aligned with the principal material triad, and the preferred axis was along the external bone surface parallel to the longitudinal direction of the cortical shell. The total number of isoparametric hexahedral elements for bones No. 3 and 5 was 60,000 and 31,680, respectively. Figure 12 shows the finite element discretization for bone No. 3, while Fig. 13 presents a 3D reconstruction of the FE geometry, together with the images of actual bones.

The key elastic and strength parameters incorporated in the simulations were consistent with those determined experimentally by Gdela et al. [11]. The respective values for bones No. 3 and 5 are summarized in Tables 2 and 3. Note that some of the *elastic* constants that were not explicitly determined were estimated based on the typical values for cortical tissue reported in the literature [13,20]. Furthermore, based on the results of verification problems discussed earlier, the value of the softening parameter was fixed as $\alpha=90$ mm^{-1}, which again is representative of an elastic-brittle material.

For each finite element model, the proximal and distal embedments were incorporated in order to emulate the actual test conditions. Figure 14 shows 3D visualizations of FE models for bones No. 3 and 5, together with images of the actual samples

Fig. 13 Actual bone image together with 3D visualization of FE model of bone No. 3; bone in: anterior–posterior, lateral, and posterior–anterior views, starting from the left

Table 2 Model parameters for bone No. 3

Parameters of the model	Value
E_x (MPa)	21,100
$E_y=E_z$ (MPa)	14,000
υ_{yz}	0.2
$\upsilon_{xy}=G_{xz}$	0.22
$G_{xy}=G_{xz}$ (MPa)	5000
G_{yz} (MPa)	5900
c_0 (MPa)	171.5
c_{90} (MPa)	14.4
α (1/mm)	90
k_N (MPa/mm)	1×10^9
k_T (MPa/mm)	5×10^8

Table 3 Model parameters for bone No. 5

Parameters of the model	Value
E_x (MPa)	27,500
$E_y=E_z$ (MPa)	19,000
υ_{yz}	0.2
$\upsilon_{xy}=\upsilon_{xz}$	0.22
$G_{xy}=G_{xz}$ (MPa)	5500
G_{yz} (MPa)	6000
c_0 (MPa)	174.9
c_{90} (MPa)	22.4
α (1/mm)	90
k_N (MPa/mm)	1×10^9
k_T (MPa/mm)	5×10^8

Fig. 14 3D visualization of FE model of (*a*) bone No. 3 and (*b*) bone No. 5, together with images of actual bone samples

used in the experiments. The embedment was considered to be an isotropic elastic material, and the elastic properties were those representative of polymethylmethacrylate (PMMA) used in the experiment ($E=3.4$ GPa, $\nu=0.34$). The loading plate was also modeled as an elastic material, with properties that were typical of a mild steel ($E=200$ GPa, $\nu=0.3$)

The loading consisted of vertical displacements applied to the steel plate at the same location as that in the experimental setup. All degrees of freedom were restrained at the bottom surface of the proximal cylindrical embedment.

The main results of numerical simulations are shown in Figs. 15–20. The focus here is on examining the propagation of fracture and the assessment of the fracture load magnitude. Figure 15 shows the load-displacement characteristics obtained for bones No. 3 and 5 together with the corresponding experimental curves. In both cases, the numerical prediction of the fracture load is in the range of 80–85% of the experimental value, which indicates a fairly reasonable agreement. It is apparent that inclusion of the trabecular bone would further improve the predictive abilities of the model; this, however, is beyond the scope of this study.

The evolution of the fracture zone is shown in Figs. 16 and 17 and Figs. 18 and 19, for bones No. 3 and 5, respectively. Again, it is evident that the location of the fracture and its extent are fairly consistent with the experimental data, as evidenced by the actual images of fractured samples.

Finally, some additional simulations were conducted for bone No. 5, which employed a coarser mesh. In particular, the number of elements in the radial direction was reduced from two to one, thus reducing the total number of elements to 16,560. The load-displacement characteristics for both mesh densities are shown at Fig. 20. It is evident that, once again, the solution is virtually the same as that employing a finer mesh.

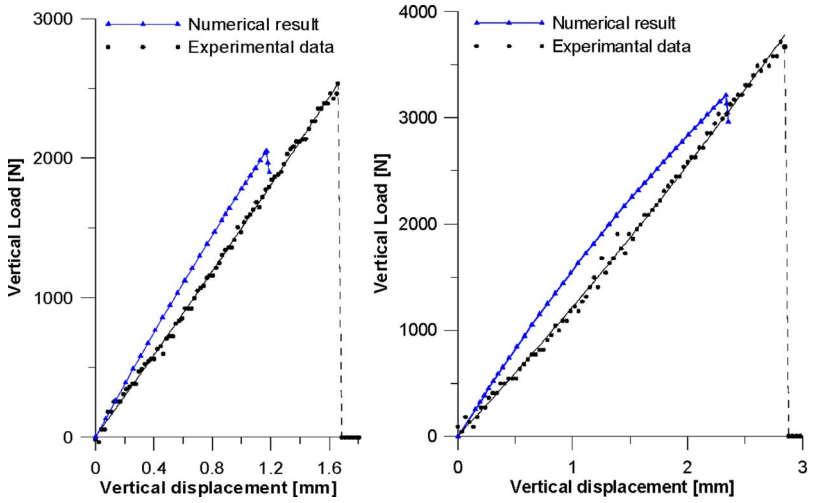

Fig. 15 Load-displacement characteristics for bones No. 3 and 5

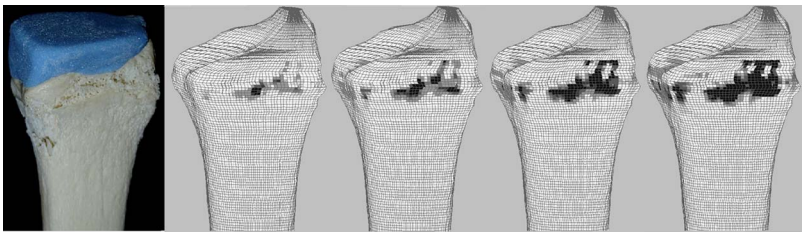

Fig. 16 Evolution of fracture zone for bone No. 3 (Note: Black color indicates the fractured region)

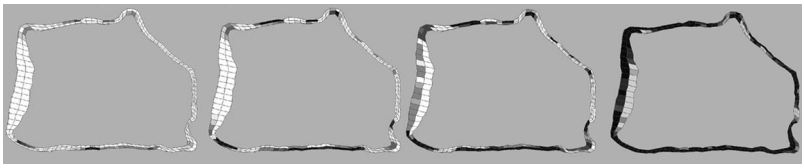

Fig. 17 Fracture propagation in critical cross section; bone No. 3

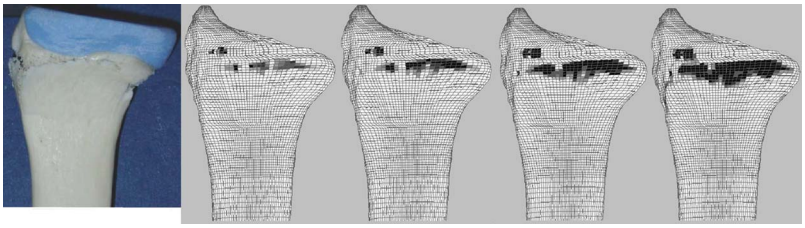

Fig. 18 Evolution of fracture zone for bone No. 5 (Note: Black color indicates the fractured region)

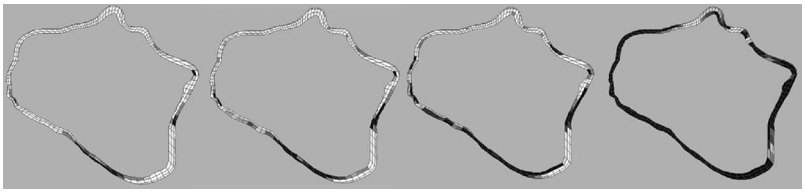

Fig. 19 Fracture propagation in critical cross section; bone No. 5

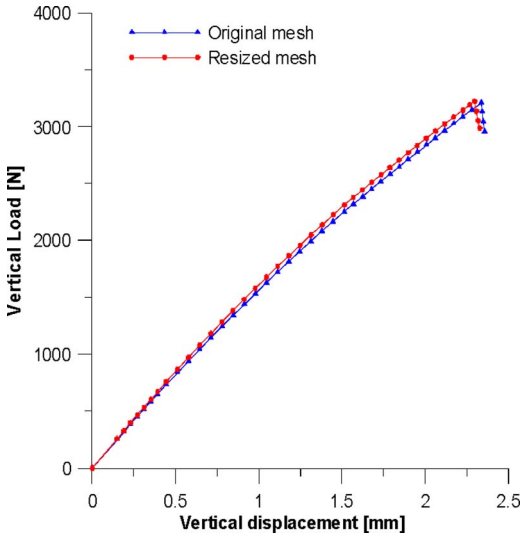

Fig. 20 Comparison of load-displacement characteristics of bone No. 5 for different mesh densities

4 Final Remarks

Osteoporosis affects tens of millions of people in the world and is recognized as the cause of 2.3 million fractures annually in Europe and the USA alone [21]. These fractures, rather than the disease itself, are responsible for the increase in morbidity and mortality among the elderly, together with a decline in the quality of their lives. In most cases, the actual fractures are the first clinical manifestation of osteoporosis, which otherwise is an asymptomatic disease. In this context, a reliable assessment of fracture risk in individuals proves to be of significant importance.

The work presented here was focused on the mechanical analysis of distal radius fracture known as Colles' fracture. The methodology employed for the assessment of mechanical competence was based on an inelastic continuum-level finite element analysis of the entire bone. Such an analysis takes into account the actual bone geometry as well as the inherent anisotropy of both the deformation and strength characteristics. In the first part of this article, the mathematical formulation of the problem was outlined. The primary focus was on the depiction of the onset of fracture within the cortical tissue and the subsequent description of localized deformation. Second part was focused on the finite element analysis of the fracture propagation process. The implementation of the mathematical formulation in the finite element software was

discussed and a number of verification problems were solved. Finally, inelastic finite element analyses were conducted simulating an actual experimental setup designed to produce a Colles' fracture and the results were compared with the experimental data.

The mathematical framework for the description of localized deformation in dried cortical tissue, as outlined in Sec. 2, addresses the key drawbacks of classical continuum formulations. In particular, it takes into account the anisotropic/heterogeneous nature of the fractured material. In addition, the basic material functions/parameters are identifiable from standard experimental tests, which is in contrast to other nonclassical frameworks. In the context of FE analysis, the framework ensures the mesh objectivity of the results (Figs. 5 and 20) and enables an adequate simulation of the process of fracture propagation. This again is in contrast to the standard numerical analyses of bone fracture, which often employ the existing commercial codes that have virtually no ability to properly account for material anisotropy and nonlinearity.

The proposed methodology, when applied to the actual bone geometry and boundary conditions, gave results that remained in a quite reasonable qualitative and quantitative agreement with the experimental data. The adopted approach was capable of capturing the actual fracture mode. In addition, the predicted fracture load was within 80–85% of the corresponding experimental value. Thus, the proposed framework has a high potential in fracture risk assessment; especially that it is individually oriented and computationally efficient. In order to further improve the predictive abilities of this approach, the influence of the trabecular bone needs to be examined. The latter requires an adequate mathematical formulation addressing the issue of heterogeneity and anisotropy of the trabecular network. This is a separate task that is quite complex (see Refs. [22] and [23]) as the description of microstructure of the trabecular bone still presents significant difficulties.

References

[1] Earnshaw, S. A., Cawte, S. A., Worley, A., and Hosking, D. J., 1998, "Colles' Fracture of the Wrist as an Indicator of Underlying Osteoporosis in Postmenopausal Women: A Prospective Study of Bone Mineral Density and Bone Turnover Rate," Osteoporosis Int., **8**(1), pp. 53–60.

[2] Mallmin, H., and Ljunghall, S., 1994, "Distal Radius Fracture is an Early Sign of General Osteoporosis: Bone Mass Measurements in a Population-Based Study," Osteoporosis Int., **4**(6), pp. 357–361.

[3] Eckstein, F., Kuhn, V., and Lochmuller, E. M., 2004, "Strength Prediction of the Distal Radius by Bone Densitometry-Evaluation Using Biomechanical Tests," Ann. Biomed. Eng., **32**(3), pp. 487–503.

[4] Muller, M. E., Webber, C. E., and Bouxsein, M. L., 2003, "Predicting the Failure Load of the Distal Radius," Osteoporosis Int., **14**(4), pp. 345–352.

[5] Myers, E. R., Hecker, A. T., Rooks, D. S., Hipp, J. A., and Hayes, W. C., 1993, "Geometric Variables From DXA of the Radius Predict Forearm Fracture Load In Vitro," Calcif. Tissue Int., **52**(3), pp. 199–204.

[6] Augat, P., Iida, H., Jiang, Y., Diao, E., and Genant, H. K., 1998, "Distal Radius Fractures: Mechanisms of Injury and Strength Prediction by Bone Mineral Assessment," J. Orthop. Res., **16**(5), pp. 629–635.

[7] Spadaro, J. A., Werner, F. W., Brenner, R. A., Fortino, M. D., Fay, L. A., and Edwards, W. T., 1994, "Cortical and Trabecular Bone Contribute Strength to the Osteopenic Distal Radius," J. Orthop. Res., **12**(2), pp. 211–218.

[8] Pistoia, W., van Rietbergen, B., Lochmuller, E. M., Lill, C. A., Eckstein, F., and Ruegsegger, P., 2002, "Estimation of Distal Radius Failure Load With Micro-Finite Element Analysis Models Based on Three-Dimensional Peripheral Quantitative Computed Tomography Images," Bone (N.Y.), **30**(6), pp. 842–848.

[9] Ulrich, D., van Rietbergen, B., Laib, A., and Ruegsegger, P., 1999, "Load Transfer Analysis of the Distal Radius From In-Vivo High-Resolution CT-Imaging," J. Biomech., **32**(8), pp. 821–828.

[10] Pietruszczak, S., Gdela, K., Inglis, D., and Webber, C. E., 2007, "On the Assessment of Brittle-Elastic Cortical Bone Failure in Distal Radius," Eng. Fract. Mech., **74**, pp. 1917–1927.

[11] Gdela, K., Pietruszczak, S., Lade, P. V., and Tsopelas, P., 2008, "On Colles' Fracture: An Experimental Study Involving Structural and Material Testing," ASME J. Appl. Mech., **75**(3), pp. 031002:1–031002:10.

[12] Lill, C. A., Goldhahn, J., Albrecht, A., Eckstein, F., Gatzka, C., and Schneider, E., 2003, "Impact of Bone Density on Distal Radius Fracture Patterns and Comparison Between Five Different Fracture Classifications," J. Orthop. Trauma, **17**(4), pp. 271–278.

[13] Reilly, D. T., and Burstein, A. H., 1975, "The Elastic and Ultimate Properties of Compact Bone Tissue," J. Biomech., **8**(6), pp. 393–405.

[14] Lydzba, D., 1998, "Homogenization Theories Applied to Porous Media Mechanics," Theor Appl. Mech., **36**(3), pp. 657–679.

[15] Suquet, P., 1987, "Elements of Homogenization for Inelastic Solid Mechanics," *Homogenization Techniques for Composite Media* (Lecture Notes in Physics, Vol. 272), Springer-Verlag, Berlin.

[16] Pietruszczak, S., 1999, "On Homogeneous and Localized Deformation in Water-Infiltrated Soils," Int. J. Damage Mech., **8**(3), pp. 233–253.

[17] Bazant, Z. P., and Pijaudier-Cabot, G., 1988, "Nonlocal Continuum Damage, Localization Instability and Convergence," ASME J. Appl. Mech., **55**, pp. 287–293.

[18] de Vree, J. H. P., Brekelmans, W. A. M., and van Gils, M. A. J., 1995, "Comparison of Nonlocal Approaches in Continuum Damage Mechanics," Comput. Struct., **55**, pp. 581–588.

[19] Ashman, R. B., Cowin, S. C., Van Buskirk, W. C., and Rice, J. C., 1984, "A Continuous Wave Technique for the Measurement of the Elastic Properties of Cortical Bone," J. Biomech., **17**(5), pp. 349–361.

[20] Martin, R. B., Burr, D. B., and Sharkey, N. A., 1998, *Skeletal Tissue Mechanics*, Springer-Verlag, New York.

[21] WHO, 2003, "Prevention and Management of Osteoporosis. Report of a WHO Scientific Group," W. H. O. Tech. Rep. Ser., **921**, pp. 1–192.

[22] Cowin, S. C., 1986, "Fabric Dependence of an Anisotropic Strength Criteria," Mech. Mater., **5**, pp. 251–260.

[23] Pietruszczak, S., Inglis, D., and Pande, G. N., 1999, "A Fabric-Dependent Fracture Criterion for Bone," J. Biomech., **32**(10), pp. 1071–1079.

Experimental Study of Electromagnetic Effects on Solid Copper Jets

Patrik Appelgren[1]
e-mail: patrik.appelgren@foi.se

Melker Skoglund

Patrik Lundberg

Lars Westerling

Anders Larsson[2]

Tomas Hurtig

Swedish Defence Research Agency (FOI),
Grindsjön Research Centre,
SE-147 25 Tumba, Sweden

In this paper we present a study of the interaction between an electric current pulse and a solid copper jet. Experiments were performed using a dedicated pulsed power supply delivering a current pulse of such amplitude, rise time, and duration that the jet is efficiently affected. The copper jet was created by using a shaped charge warhead. An electrode configuration consisting of two aluminum plates with a separation distance of 150 mm was used. The discharge current pulse and the voltages at the capacitors and at the electrodes were measured to obtain data on energy deposition in and the resistance of the jet and electrode contact region. X-ray diagnostics were used to radiograph the jet, and by analyzing the radiograph, the degree of disruption of the electrified jet could be obtained. It was found that a current pulse with an amplitude of 200–250 kA and a rise time of 16 μs could strongly enhance the natural fragmentation of the jet. In this case, the initial electric energy was 100 kJ and about 90% of the electric energy was deposited in the jet and electrodes. At the exit of the electrode region, the jet fragments formed rings with a radial velocity of up to 200 m/s, depending on the initial electric energy in the pulsed power supply. [DOI: 10.1115/1.3172251]

1 Introduction

When a high enough current is forced through a thin conductor, the conductor will be heated, melted, and eventually evaporated. If the deposition of electric energy is sufficiently fast, the conductor will explode electrically. The case is more complex if the conductor is moving so that new and unheated conductor material enters the active region where current is conducted. After the current interaction, the conductor may particulate and the fragments may transform into rings or thin disks. This is applied in an electric armor, where the current pulse is passed through a shaped charge jet to disrupt it and prevent it from penetrating the object to be protected. The principle of direct electrification of a solid copper jet created by a shaped charge is well known and was proposed by Walker [1] in the 1970s. In order to supply the current, Walker used a magnetic flux compression generator, which converts the chemical energy bond in explosives into electrical energy in terms of a current pulse. With a number of switches the current was diverted into the jet to affect it and demonstrate the principle. However, it was not until the late 1980s that the pulsed power technology had matured to a state where electric armor could become a realistic alternative to conventional protection. Experiments were reported by Pollock [2] in 1992 and an increasing number of papers related to electric armor have been reported since [3–14]. A major effort to boost the development of pulsed power technologies is the Army Technology Objective (ATO) program under U.S. Army. In parallel with research on the electric armor system concept itself [15,16], the program aims to improve pulsed power components such as capacitors, solid state switches, and diodes to meet the demands of a fieldable electric armor system. By increasing the energy density of capacitors and the current ratings of solid state components the more energy efficient and compact the system will be [17–19]. Demonstrations of this technology with live firings on vehicles fitted with electric armor were reported by Defence Science and Technology Laboratory (DSTL), UK [20] in 2002 and by BAE Systems in 2005 [21].

In this paper we present a study of the interaction between a current pulse and a solid copper jet created by a shaped charge warhead. Experiments were performed using a dedicated pulsed power supply (PPS) delivering a current pulse of sufficient amplitude, rise time, and duration to affect the jet efficiently. A medium caliber shaped charge and an electrode configuration consisting of two aluminum plates with a separation distance of 150 mm were used in the experiments. The discharge current pulse and the voltages across the capacitors and the electrodes were measured to obtain data on energy deposition in, and the resistance of, the jet and electrode contact region. X-ray diagnostics were used to radiograph the jet, and hence the disruption process could be studied and analyzed in relation to the energy deposition.

2 Current Interaction With Shaped Charge Jets

2.1 Electric Protection Concept. In its simplest design, the jet disruption system consists of a capacitor bank that stores a sufficient amount of energy, a transmission line to transfer the energy, and a pair of electrodes placed between the shaped charge and the protected objects. In addition a charge and dump circuit and control units are required. The shaped charge jet bridges the electrodes and the energy stored in the capacitors is released in the form of a strong current pulse. The jet is heated by the current until it is melted, vaporized, or disrupted by magnetic forces. The electrodes could be placed some distance away from the protected object, and hence allow for the disruption to develop until the jet fragment has lost its penetrative capability. In a simple system the electrodes are always charged, which may have implications in terms of personnel safety or ambient conditions. In more advanced systems the pulsed power system could use solid state diodes and switches [17,18]. Once a threat is detected the electrodes are connected to the capacitors via the closing of the switches. Diodes would prevent current and voltage reversals, and hence more of the capacitor's energy storage capability could be used.

[1]Also at the Division of Space and Plasma Physics, School of Electrical Engineering, Royal Institute of Technology, Stockholm, Sweden.

[2]Also at the Division for Electricity, Uppsala University, Uppsala, Sweden.

Contributed by the Applied Mechanics Division of ASME for publication in the JOURNAL OF APPLIED MECHANICS. Manuscript received October 29, 2008; final manuscript received February 2, 2009; published online September 30, 2009. Review conducted by Vikram Deshpande.

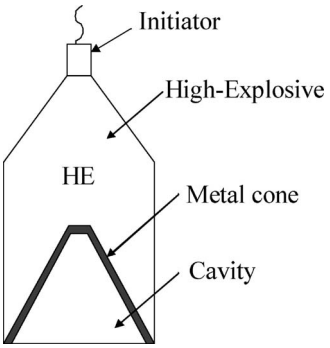

Fig. 1 Shaped charge with a conical metallic liner surrounded by high explosives (HE)

2.2 Shaped Charge Jet Characteristics. A shaped charge consists of a metallic liner, usually copper, in the shape of a cone surrounded by high explosives [22] (Fig. 1). When initiated the explosive deforms the metal cone into a metallic jet, having a velocity gradient (Fig. 2). The tip of the jet reaches a velocity of 7–8 km/s while the tail of the jet has a velocity of about 2 km/s. The mass of the jet depends on the diameter and wall thickness of the metal liner but is usually several tens of grams for a medium size warhead. A slug of lower velocity of about 0.5 km/s follows the rear part of the jet, and has a much higher mass but lacks penetrative capability. The shaped charge jet will stretch with time up to some point when instabilities will cause a fragmentation of the jet, which in turn, reduces the penetrative performance. The disruption of the jet by a current pulse serves to reduce the penetration of the jet to such an extent that the hull of an armored vehicle can absorb the remainder of the penetrator. A simple expression for the penetration P of a jet segment with constant velocity [22] is

$$P = l\sqrt{\frac{\rho_j}{\rho_T}} \tag{1}$$

where l is the length of the jet segment, and ρ_j and ρ_T are the mass densities of the jet and target, respectively. As a steel target and the copper jet have about the same mass density, the penetration will be approximately the length of the jet segment. The effect of the current interaction serves to increase the radial extension of a jet fragment on expense of its length, i.e., disk formation, and hence reduce the penetrative performance of the single fragment. An alternative description is that the fragment is vaporized and the effective density of the jet is decreased, reducing the penetration capability.

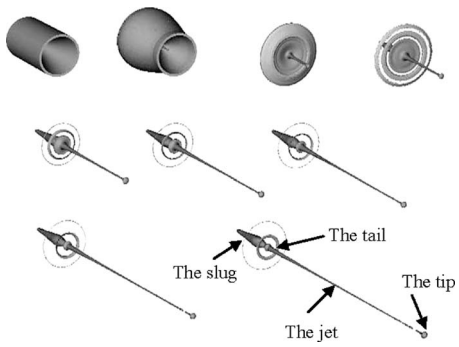

Fig. 2 Formation of a shaped charge jet. The two top left pictures show the shaped charge with its cylindrical casing visible, while the following pictures only show the metal liner and its formation to a jet. Due to its velocity gradient the jet stretches, accompanied by a decrease in diameter. The jet is followed by the slug of much higher mass but with lower velocity.

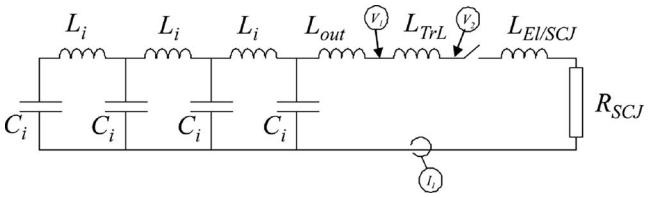

Fig. 3 The pulse forming network with four capacitor modules C_i connected via the pulse shaping inductors L_i. L_{out} is the inductance between the capacitor bank and the transmission line, L_{TrL} is the inductance of the transmission line, $L_{El/SCJ}$ is the inductance of the electrodes and the jet, R_{SCJ} is the resistance of the jet, and V_1, V_2, and I_1 are the voltage and current probes.

2.3 Jet Disruption Mechanisms. The general jet disruption mechanism is due to the current pulse, which enhances the development of the natural instability of a shaped charge jet and tears a fragment apart to something looking like a ring or a disk. There are several suggested mechanisms responsible for this [3–11].

2.3.1 Ohmic Heating. The jet will be heated by the current as the jet passes through the electrode region. Since it takes a finite time for the current to diffuse to the center of the jet and also to diffuse out of it, and because this time is of the order of the passage time, the jet surface will be heated more than the center. It also implies that the effective resistance of a jet will be higher than if the current had a homogeneous distribution. The mass of a jet is typically several tens of grams and the jet requires several kJ/g to melt and reach the vaporization temperature. As the heated jet looses mechanical strength and the magnetic force is strongest in the necks, the neck diameter is decreased, increasing the current density until it reaches a critical level where an explosion or vaporization of the necks can occur.

2.3.2 Magnetohydrodynamic Instabilities. Magnetohydrodynamic instabilities will develop due to the magnetic field associated with the axial current if the current amplitude is high enough during the time a jet segment is between the electrodes. Since the jet has a velocity gradient with the highest velocity at the tip, the required current amplitude will be lower for the slower parts of the jet. The natural breakup of a jet is accelerated by these instabilities.

2.3.3 Volume Disruption. During the passage of the electrodes, the jet experiences magnetic forces compressing the jet and preventing a radial expansion. As this compressing force disappears outside the electrode region, the jet is relaxed and free to expand radially, tearing the jet apart. The radial velocity is related to the current amplitude when a jet segment leaves the electrode region and the radius of the jet segment.

2.3.4 Disk Formation. The natural diameter variation along a jet prior to the fragmentation may be enhanced by the magnetic pressure, reducing the diameter of the neck and forcing the material away from the neck in the axial directions. Hence between two neighboring necks, the diameter of the jet will increase and eventually forms a thin disk.

3 Experimental Setup

3.1 Pulsed Power Supply and Transmission Lines. A 400 kJ PPS was used in the experiments [23]. The PPS consists of eight capacitors (22 kV, 50 kJ, 206 μF), arranged in a network with variable inductors between each pair of capacitors, according to Fig. 3. The design enables a wide range of output pulse shapes with minimal reassembly. The inductor values vary between 0.1 μH and 2 μH. For the system to deliver a square pulse, the

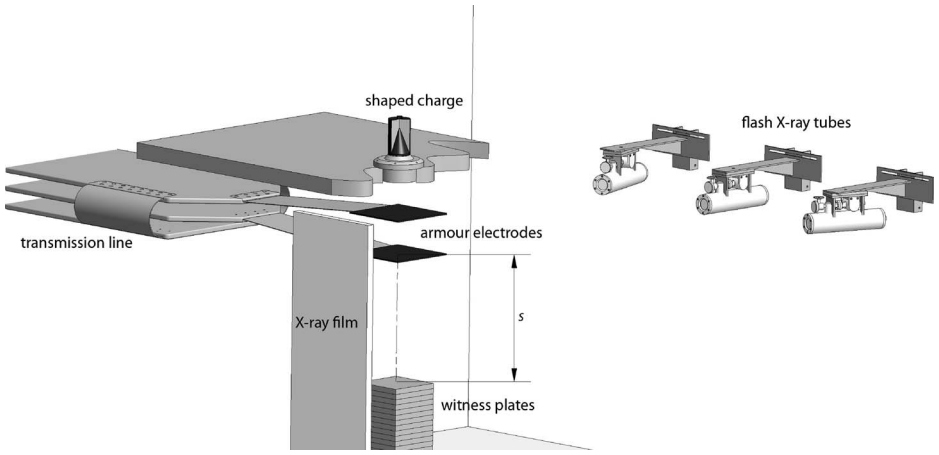

Fig. 4 The experimental setup with the shaped charge being fired vertically down through the electrodes into the target. Flash X-ray tubes project a shadow of the jet onto the X-ray film.

variable inductors and the load should have similar inductance values. The pulse discharge time T and system impedance Z in a pulse forming network with N modules is determined by the module capacitance C_i and inductance L_i according to

$$T = 2N\sqrt{L_i C_i} \tag{2}$$

$$Z = \sqrt{\frac{L_i}{C_i}} \tag{3}$$

In the experiments the inductors had a value of 380 nH, and hence the discharge time was 100 μs and the system impedance 30 mΩ. An increasing number of modules makes the pulse become more square shaped with shorter rise and fall times. The PPS is housed inside an ISO container and is remotely controlled via an optical fiber link. The output pulse is transferred to the load via a 4 m long and 0.6 m wide flat transmission line with low inductance. The transmission line consists of three layers of aluminum (20 mm thick) with the hot line in between the two outer return conductors (Fig. 4). Two thin (0.6 mm) and insulated copper sheets are used between the transmission line and the electrode pack (with a distance of around 2 m). The copper sheets are easily exchanged after an experiment if required.

3.2 Electrodes. The electric armor pack consisted of two 5 mm thick aluminum plate electrodes. The distance between the electrodes was 150 mm. The copper sheets used to connect the aluminum plates to the transmission line were clamped between the aluminum electrodes and thin glass fiber reinforced plastic plates placed behind the front electrode and in front of the back electrode. The glass fiber reinforced plastic plates served as a protection from debris. The electrodes are denoted as electrodes 1 and 2 in the order the jet hits them. Electrode 2 is connected to the high voltage terminal and electrode 1 to the grounded capacitor casing.

3.3 Test Stand. The shaped charge was placed on a typical test stand for shaped charge testing (Figs. 4 and 5). A thick steel plate prevents the shock wave and debris from hitting the electrodes. A steel target made of square tiles was used to absorb the residual jet. The target was positioned at a large distance behind the back electrode of the armor pack to allow the jet to expand to enable the X-ray radiographing.

3.4 Shaped Charge. The shaped charge warhead used had a straight conical liner made of copper. The jet tip has a velocity of 7.3 km/s. In the experiments the shaped charge has been positioned on a predefined distance relative to electrode 1. For the given electrode setting and experimental setup, the rear part of the jet will leave the electrode region 100 μs after the tip hits electrode 2 and closes the circuit.

3.5 Diagnostics. The PPS voltage and the voltage across the armor electrodes were measured with two high voltage probes (Tektronix P6015A). The current was measured using a CWT 4000XB (Power Electronics Measurement Ltd., Nottingham, UK), which is a flexible probe suitable for the flat transmission line used. All signals were transferred to the oscilloscopes via optical fiber links. Flash X-ray tubes (105 kV) were used to radiograph the jet (Fig. 6). All registration equipment (oscilloscopes and flash X-rays) was triggered by a signal from a pick-up probe inserted between the layers of the transmission line. The probe is sensitive to the time derivative of the magnetic field, which initially becomes large when the current starts to flow in the circuit. In the experiment with no current, a trigger foil was mounted on the second electrode and used for triggering.

4 Experimental Matrix

A series of experiments were performed to evaluate the effects of current and energy on the jet disruption. The setting of the pulsed power supply and of the electrode configuration was at an inductance of 380 nH in the pulse forming inductors and an electrode separation of 150 mm. The inductance of the transmission line and electrodes with shaped charge jet was approximately 500

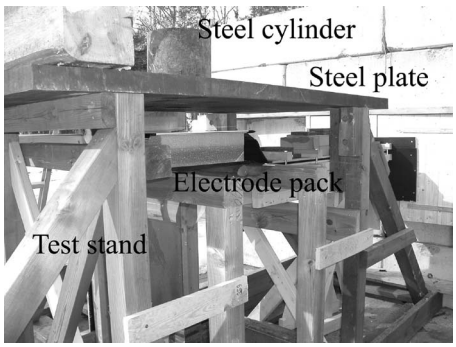

Fig. 5 Picture of the wooden test stand with a thick steel plate, protecting the electrodes and transmission line from pressure and shrapnel. The cylinder on top of the steel plate absorbs most of the fragments from the shaped charge.

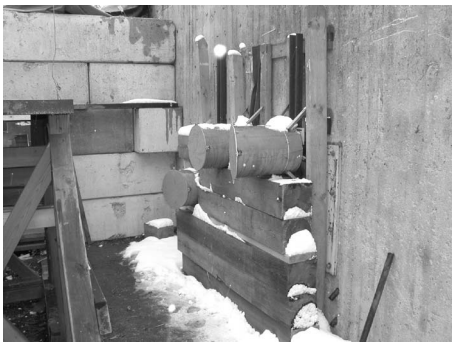

Fig. 6 The three flash X-ray tubes protected from shrapnel and pressure by their aluminum casings

nH. The effect of energy stored in the capacitors on the jet disruption was studied in a series of experiments, as given in Table 1.

5 Experimental Results and Analysis

5.1 Typical Recordings and Data Analysis. A typical current trace from an experiment is shown in Fig. 7. The capacitors were charged to 10.6 kV, corresponding to 96.3 kJ. The current rise time (10–90% of the peak current) was 16 μs, and the full width at half maximum (FWHM) value was 98 μs. The pulse width was 129 μs, measured from the onset of the current until it drops back down to 0 kA. Hence the current pulse is long enough to affect the jet tail part with a velocity of 2.7 km/s. The voltage traces measured at the capacitor bank terminal (probe V_1 in Fig. 3) and close to the load (probe V_2 in Fig. 3) are shown in Fig. 8. The capacitors are charged to 10.6 kV and at trigger, it drops instantaneously down to a level determined by the time derivative of the current and the total inductance of the circuit over which the probes measure. The (maximum) current time derivative is approximately 25 GA/s at the onset of discharge and is obtained from the current signal. The inductance L of the circuit determines current time derivative at the onset of discharge by the relation

Table 1 Experimental matrix

Energy in capacitors (kJ)	Electrode separation (mm)	X-ray times (μs)
0	150	31, 81, 81
39	150	36, 86, 86
58	150	36, 86, 86
96	150	36, 86, 86

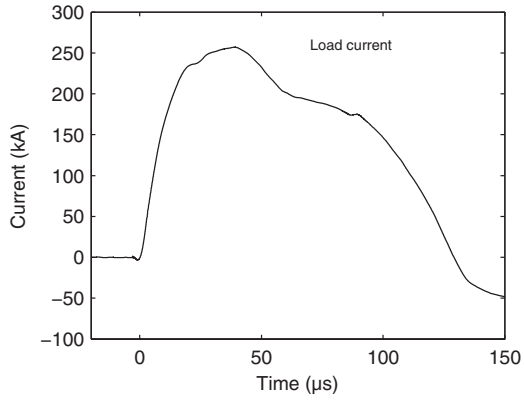

Fig. 7 Measured current pulse in the 96 kJ experiment

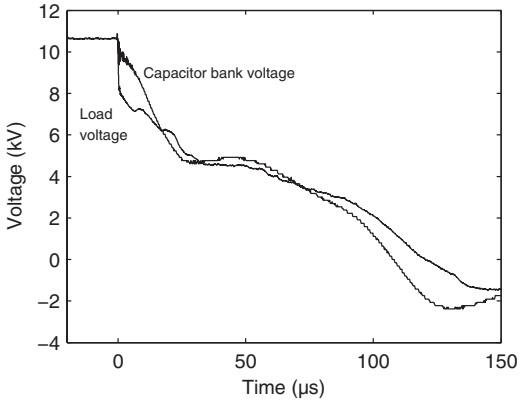

Fig. 8 Measured load voltage and capacitor bank output terminal voltages in the 96 kJ experiment. The drop in voltages at the time of trigger is due to the inductance distributed in the system.

$$\frac{di}{dt} = \frac{U}{L} \tag{4}$$

where U is the voltage at the time of the onset of discharge. The inductance of the load (jet and electrodes) is estimated by multiplying the current time derivative (derived from current measurement) with an inductance value such that the measured load voltage (by probe V_2) and the $L_{\mathrm{El/SCJ}} \cdot di/dt$ value agree at the time of discharge. In this way the load inductance is estimated to about 340 nH. Similarly the total inductance of load and transmission line can be obtained by fitting the $(L_{\mathrm{TrL}}+L_{\mathrm{El/SCJ}}) \cdot di/dt$ value to the capacitor bank voltage (by probe V_1) at the onset of discharge. This gives a total inductance of 420 nH, i.e., the transmission line can be attributed to 80 nH, which is a reasonable value. The measured voltage consists of two components: The inductive and the resistive voltage drop. The resistive component is obtained by subtracting the inductive component from the measured total voltage. The impedance of the load is obtained by simply dividing the measured voltage by the current. The load resistance is obtained by dividing the calculated resistive voltage component by the current. In this case the resistance varies between 20 mΩ and 25 mΩ during the current pulse, an average value of 22 mΩ in the time interval of 10–120 μs (Fig. 9). This resistance value includes that of the electrodes, the jet, and the contact between the electrodes and the jet. The total energy stored magnetically and deposited in the load is obtained by integrating the product of the measured voltage and the current. The resistively deposited energy is calculated by integrating the product of the resistive volt-

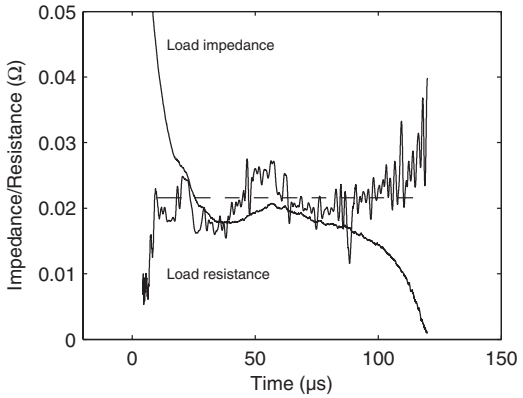

Fig. 9 Impedance and resistance of the electrodes and jet. The dashed line indicates the average resistance value of 21.6 mΩ.

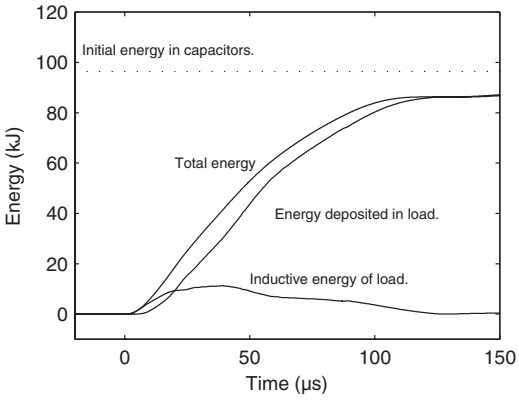

Fig. 10 The energy deposition in jet and electrodes during the interaction time

age component and the current. In Fig. 10 the total energy and the resistive losses are shown. The dotted line marks the energy stored (96.4 kJ) in the capacitors calculated from the measured capacitance of 1.71 mF and the capacitor bank voltage of 10.6 kV. This indicates that 90% of the energy is deposited in the jet and electrodes during the interaction time.

5.2 Effects of Energy and Current on Jet Disruption. The disruption of the jet was studied by using X-ray radiographs of the jet between and after the electrodes, where the effect of electrification begins to develop. For a given pulsed power supply setting, electrode configuration, and shaped charge setup, the charging voltage of the capacitor was varied, i.e., the stored energy. The general shape of the current pulses in the different experiments is the same, and the pulse lengths are identical. The amount of energy deposited in the jet and electrode region is 80–90% in all experiments. Figure 11 shows the jet 31 μs or 36 μs after it has made contact with electrode 2 for three different capacitor bank energies (0 kJ, 39 kJ, and 96 kJ). The jet disruption clearly increases with energy and the disruption begins earlier. Figure 12 shows the jet 50 μs later. The jet disruption is also in this picture evidently stronger for higher energies. The natural fragmentation of a jet is enhanced by the current and the number of fragments and rings agrees well with the number of fragments of a nonelectrified jet. Note that the rings are barely visible for the higher energy due to the lower density of the copper vapor.

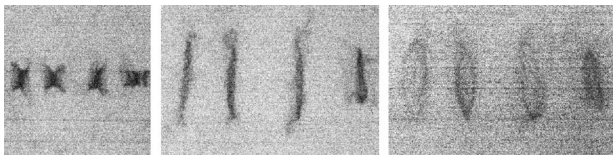

Fig. 13 X-ray pictures of four jet fragments at 36 μs (left) and 86 μs (center and right) after the jet made contact with electrode 2. The figure in the center depicts the same four fragments as in the figure in the right but from a different angle.

5.3 Radial Dispersion and Ring Formation. The radial dispersion and ring formation was observed in detail using flash X-ray tubes. Flash X-ray pictures of the jet were taken at different angles either simultaneously or at different times. Hence the disruption process could be recorded over time or the geometry of the jet particles be obtained by simultaneous depiction from different angles. Figure 13 shows the same four jet fragments identified in three X-ray pictures taken at different times. The left picture shows the jet fragments in the 58 kJ experiment at 36 μs. The center and right picture shows the same fragments taken at 86 μs from different angles. The jet fragments are transformed from cylinders into rings. The higher contrast along the circumference of the ring implies a ring shape rather than a disk, but that has to be investigated further. The ring formation process can be, at least qualitatively, observed in a single X-ray picture of the disturbed jet, where jet parts close to the electrodes are still cylinders and become more and more disturbed toward the tip. By measuring the diameter of jet fragments identified in the two

Fig. 11 X-ray pictures of jet disruption at different energies. From the top, 96 kJ, 39 kJ, and 0 kJ is stored in the capacitors. The pictures are taken 36 μs after contact is made by the tip with electrode 2 (the right of the two shadowed areas), except for the lower picture, which is taken 31 μs after contact. The jet tip has moved to a distance of 260 mm from electrode 2 after 36 μs.

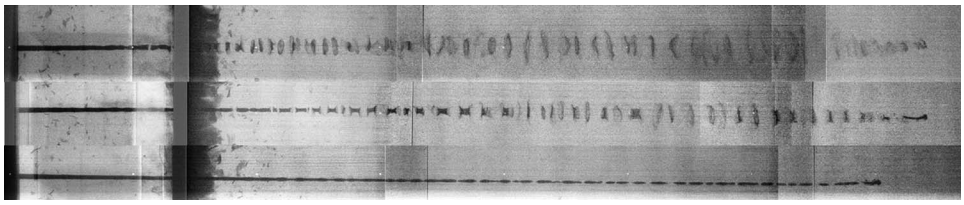

Fig. 12 X-ray pictures of jet disruption at different energies. From the top, 96 kJ, 39 kJ, and 0 kJ is stored in the capacitors. The pictures are taken 86 μs after contact is made by the tip with electrode 2, except for the lower picture, which is taken 81 μs after contact. The jet tip has moved to a distance of 620 mm from electrode 2 after 86 μs.

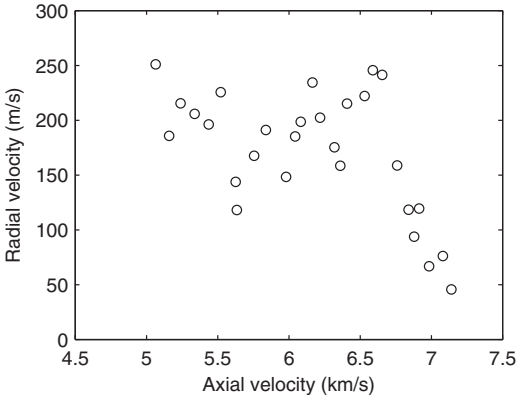

Fig. 14 Radial velocity for dispersed fragments in the 96 kJ experiments

X-ray pictures taken at different times, the radial velocity can be estimated. Since the rings are barely visible in the X-ray pictures, the true extension of them is probably larger than reported here. For such an analysis the X-ray pictures in the 96 kJ experiments are used. Both axial and radial velocities are obtained and plotted against each other in Fig. 14. There is a large spread in data but the fragments with axial velocities between velocities of 5 km/s and 6.6 km/s have radial velocities of approximately 200 m/s. In Fig. 15 the radial velocity is plotted versus the current (in the 96 kJ experiment) through a segment leaving the electrode region. There is a clear trend of increasing radial velocity with current. Note that the data are for segments with axial velocities higher than 5 km/s, interacting during the first 30 μs of the current pulse, i.e., the time of the rising flank of the current, as compared with Fig. 7. In the two X-ray pictures of the 96 kJ experiment (Figs. 11 and 12), the radial expansion is observed to start when a segment exits the electrode region. By assuming that all the jet segments in the 96 kJ experiment with axial velocities down to 3 km/s instantly receives a velocity of 200 m/s at exit of the electrode region, a simple estimation of the radial dispersion can be obtained and compared with the experiment. The radius of the jet before radial expansion is assumed to be 1 mm. Figure 16 shows the calculated radius of the jet segments versus the distance from the shaped charge cone base, 86 μs after the tip makes contact with the second electrode, i.e., the same time as in Fig. 12. The X-ray picture of the jet in the 96 kJ experiment is resized ten times in the radial direction and inserted into the graph. There is a good agreement in radius along the jet axis and implies that the radial velocity for the parts with axial velocities below 5 km/s is also around 200 m/s. A similar calculation is performed for the 39 kJ experiment and with an assumed radial velocity of 130 m/s at the exit of electrode 2 (Fig. 17). In the 39 kJ experiment the jet was slightly bent and a linear drift term was included in the envelope calculation. The agreement is good also for this calculation.

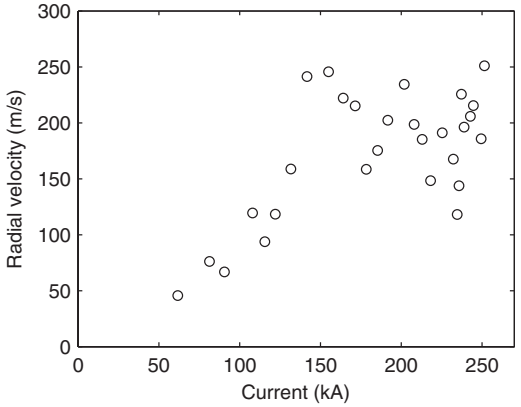

Fig. 15 Radial velocity of the dispersed fragments versus current level through them at their exit from the electrode region in the 96 kJ experiment

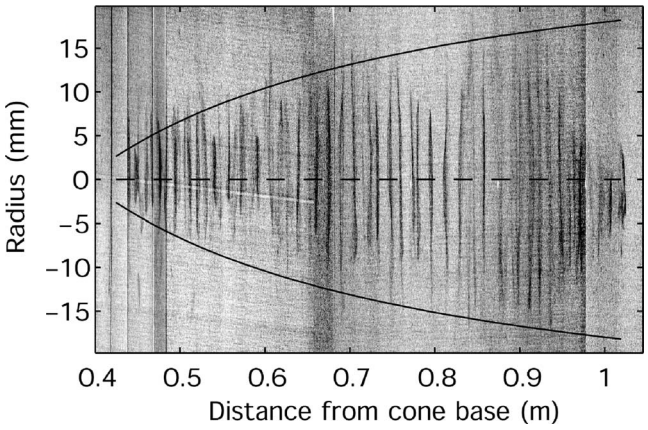

Fig. 16 The solid lines show an estimation of radius of the jet 86 μs after the tip made contact with the second electrode, assuming an instant radial velocity of 200 m/s of a segment at the exit of the electrode region (located at 0.4 m on the scale). The estimation is made for jet segments with velocities of 3–7.3 km/s. The X-ray picture of the 96 kJ experiment has been stretched in the radial direction.

6 Conclusions

An experimental arrangement has been established, where the interaction between a solid copper jet and a powerful electric current can be studied. A current pulse with an amplitude of 200–250 kA and a rise time of 16 μs could strongly enhance the natural fragmentation of the jet. In this case, the initial electric energy was 100 kJ and the electric power in the jet was above 1 GW. About 90% of the electric energy was deposited in the jet. This high energy efficiency was achieved because the current pulse length agreed well with the passage time of the jet and because the impedance of the pulsed power supply was well matched with the load (the electrodes and the jet). At the exit of the electrode region, the jet fragments formed rings with a radial velocity of up to 200 m/s, depending on the initial electric energy in the pulsed power supply. Due to the short interaction time between the current and the tip of the jet, the radial velocity of the jet tip ($v_{\text{axial}} > 6.6$ km/s) was as low as below 50 m/s.

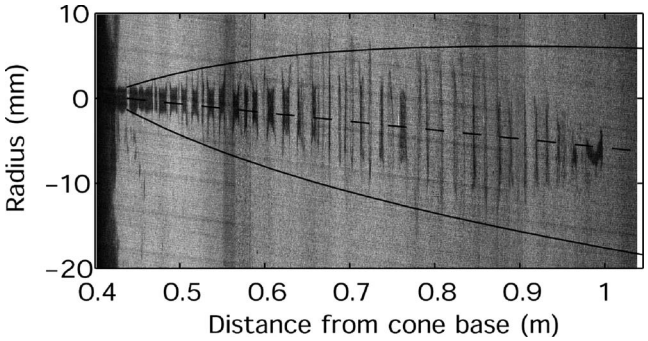

Fig. 17 The X-ray picture of the 39 kJ experiment with the estimation of the radius of the jet, assuming an instant radial velocity of 130 m/s of a segment at exit of the electrode region

References

[1] Walker, E. H., 1973, "Defeat of Shaped Charge Devices by Active Armour," U.S. Army Ballistic Research Laboratory, Paper No. BRL-MR-2309.

[2] Pollock, C. E., 1994, "Electromagnetic Effects on the Natural Hydrodynamic Instability of Stretching, High Velocity Metallic Jets," *Proceedings of the Fourth Megagauss Magnetic Field Generation and Pulsed Power Applications*, Nova Science Publishers, New York.

[3] Littlefield, D. L., and Powell, J. D., 1990, "The Effect of Electromagnetic Fields on the Stability of a Uniformly Elongating Plastic Jet," Phys. Fluids A, **2**(12), pp. 2240–2248.

[4] Littlefield, D. L., 1991, "Finite Conductivity Effects on the MHD Instabilities in Uniformly Elongating Plastic Jets," Phys. Fluids A, **3**(6), pp. 1666–1673.

[5] Shvetsov, G. A., and Matrosov, A. D., 1996, "Experimental Investigation of Shaped Charge Jets Disruption With Current Pulse," *Proceedings of the Seventh International Conference on Megagauss Magnetic Field Generation and Related Topics*, RFNC-VNIIEF, Sarov, Russia, Aug. 5–10.

[6] Babkin, A. V., Kruzkhov, V. A., Ladov, S. V., Marinin, V. M., and Fedorov, S. V., 1996, "The Behaviour of a Shaped Charge Jet Under the Effect of a Current Pulse," *Proceedings of the Seventh International Conference on Megagauss Magnetic Field Generation and Related Topics*, RFNC-VNIIEF, Sarov, Russia, Aug. 5–10, pp. 961–966.

[7] Shvetsov, G. A., Matrosov, A. D., Babkin, A. V., Ladov, S. V., and Fedorov, S. V., 1999, "Disruption of Shaped Charge Jets Due to Axial Current," *Proceedings of the 18th International Symposium on Ballistics*, San Antonio, TX, Nov. 15–19.

[8] Fedorov, S. V., Babkin, A. V., Ladov, S. V., Shvetsov, G. A., and Matrosov, A. D., 2000, "Possibilities of Controlling the Shaped-Charge Effect by Electromagnetic Actions," Combust., Explos. Shock Waves, **36**(6), pp. 792–808.

[9] Shvetsov, G. A., Matrosov, A. D., Fedorov, S. V., Babkin, A. V., and Ladov, S. V., 2001, "Quest of Possibility for Controlling the Shaped Charge Effect by Electromagnetic Actions," *Proceedings of the Fourth International All-Electric Combat Vehicle Conference*, Noordwijkerhout, The Netherlands.

[10] Shvetsov, G., Matrosov, D., Fedorov, S., Babkin, A., and Ladov, S., 2001, "Influence of Magnetic Fields on Shaped-Charge Performance," *Proceedings of IEEE Pulsed Power and Plasma Science Conference*, Las Vegas, NV.

[11] Shvetsov, G., and Matrosov, A., 2003, "Pulsed Power Against Terrorists," *Proceedings of IEEE Pulsed Power and Plasma Science Conference*, Dallas, TX, Jun. 15–18.

[12] Endersby, P., Middleton, N., and Stewart, K., 2005, "Practical Considerations in Electric Armour," All Electric Combat Vehicle Conference.

[13] Wickert, M., 2007, "Electric Armour Against Shaped Charges: Analysis of Jet Distortion With Respect to Jet Dynamics and Current Flow," IEEE Trans. Magn., **43**(1), pp. 426–429.

[14] Appelgren, P., Westerling, L., Skoglund, M., Lundberg, P., Hurtig, T., and Larsson, A., 2008, "Radial Jet Dispersion Due to Current Interaction in an Electric Armour Application," *Proceedings of the 24th International Symposium on Ballistics*, New Orleans, LA, Sept. 22–26.

[15] Barshaw, E., Chait, M., Danielson, G., Herrera, D., Khalil, G., Leathers, E., Argo, P., Bard, A., Frazier, G., and Marinos, B., 2004, "Integration and Test of a Dual Purpose Pulse Forming Network Into the P&E HWIL SIL," *Proceedings of the 24th Army Science Conference*, Nov. 29–Dec. 30.

[16] Barshaw, E. J., White, J., Danielson, G., Chait, M. J., Frazier, G., Dixon, B., Marinos, B., and Milner, D., 2007, "Integration and Test of a Second Generation Dual Purpose Pulse Forming Network Into the P&E HWIL SIL," IEEE Trans. Magn., **43**(1), pp. 226–229.

[17] Giorgi, D., Griffin, A., Navapanich, T., Tran, H., Fong, A., Celestin, G., and Spero, J., 2007, "Testing of a 130 kA 10 kV Light Activated Switch," *Proceedings of IEEE Pulsed Power and Plasma Science Conference*, Albuquerque, NM.

[18] O'Brien, H., Shaheen, W., Thomas, R. L., Crowley, T., Bayne, S. B., and Scozzie, C. J., 2007, "Evaluation of Advanced Si and SiC Switching Components for Army Pulsed Power Applications," IEEE Trans. Magn., **43**(1), pp. 259–264.

[19] Barshaw, E. J., White, J., Chait, M. J., Cornette, J. B., Bustamante, J., Folli, F., Biltchick, D., Borelli, G., Picci, G., and Rabuffi, M., 2007, "High Energy Density (HED) Biaxial-Oriented Poly-Propylene (BOPP) Capacitors For Pulse Power Applications," IEEE Trans. Magn., **43**(1), pp. 223–225.

[20] Defence Science and Technology Laboratory (DSTL), "New Age Electric Armour Tough Enough to Face Modern Threats," press release 2002-07-01.

[21] BAE Systems, 2007, presentation on the web site, http://www.baesystems.com/ProductsServices/l_and_a_gs_electromag_armor.html

[22] Walters, W. P., and Zukas, J. A., 1989, *Fundamentals of Shaped Charges*, Wiley, New York.

[23] Senior, P., Smith, I. R., Appelgren, P., Elfsberg, M., Lundberg, P., and Skoglund, M., 2006, "A 400kJ Mobile Pulsed Power System With Variable Pulse Forming," *Proceedings of the 11th Megagauss*, London, UK, pp. 257–261.

Qiang Yu
Post-Doctoral Researcher
Department of Civil and Environmental Engineering,
Northwestern University,
Evanston, IL 60208
e-mail: qiangyu@northwestern.edu

Zdeněk P. Bažant[1]
McCormick Institute Professor
W.P. Murphy Professor
Department of Civil and Materials Science,
Northwestern University,
Evanston, IL 60208
e-mail: z-bazant@northwestern.edu

John Bayldon
Post-Doctoral Researcher
e-mail: j-bayldon@northwestern.edu

Jia-Liang Le
Graduate Research Assistant
e-mail: jialiang-le@northwestern.edu

Department of Civil and Environmental Engineering,
Northwestern University,
Evanston, IL 60208

Ferhun C. Caner[2]
Associate Professor of the Institute of Energy Technologies,
Universitat Politècnica de Catalunya
e-mail: ferhun.caner@upc.edu

Wei Heok Ng
Post-Doctoral Researcher
e-mail: whn@umich.edu

Anthony M. Waas
Professor
e-mail: dcw@umich.edu

Department of Aerospace Engineering and Mechanical Engineering,
University of Michigan,
Ann Arbor, MI 48109-2122

Isaac M. Daniel
W.P. Murphy Professor
Department of Civil Engineering and Mechanical Engineering,
Northwestern University,
Evanston, IL 60208
e-mail: imdaniel@northwestern.edu

Scaling of Strength of Metal-Composite Joints—Part I: Experimental Investigation

Knowledge of the size effect on the strength of hybrid bimaterial joints of steel and fiber composites is important for new designs of large lightweight ships, large fuel-efficient aircrafts, and lightweight crashworthy automobiles. Three series of scaled geometrically similar specimens of symmetric double-lap joints with a rather broad size range (1:12) are manufactured. The specimens are tested to failure under tensile displacement-controlled loading, and at rates that ensure the peak load to be reached within approximately the same time. Two series, in which the laminate is fiberglass G-10/FR4, are tested at Northwestern University, and the third series, in which the laminate consists of NCT 301 carbon fibers, is tested at the University of Michigan. Except for the smallest specimens in test series I, all the specimens fail by propagation of interface fracture initiating at the bimaterial corner. All the specimens fail dynamically right after reaching the maximum load. This observation confirms high brittleness of the interface failure. Thus, it is not surprising that the experiments reveal a marked size effect, which leads to a 52% reduction in nominal interface shear strength. As far as the inevitable scatter permits it to see, the experimentally observed nominal strength values agree with the theoretical size effect derived in Part II of this study, where the size exponent of the theoretical large-size asymptotic power law is found to be −0.459 for series I and II, and −0.486 for series III. [DOI: 10.1115/1.3172254]

1 Introduction

Hybrid structures consisting of metals and fiber composites offer many advantages for the design of large lightweight ships [1] and fuel-efficient aircrafts. Metal-composite joints are a crucial element of such designs. Because of the cost of failure tests of large structures, laboratory tests must, in many situations, be conducted on a much reduced scale. Thus, it is essential to have a correct method to extrapolate the results obtained from small laboratory specimens to much larger structural parts.

For purely metallic structures, such extrapolation is relatively easy, since there is no deterministic size effect and the statistical size effect, which is relatively weak, is well understood. However, fiber composites are quasibrittle materials, which were shown [2–5] to exhibit, in general, a deterministic energetic size effect [6–10]. This size effect is much stronger than the statistical size effect observed in fatigue-embrittled metals.

[1]Corresponding author. Department of Civil and Environmental Engineering, Northwestern University, 2145 Sheridan Road, CEE/A135, Evanston, IL 60208.
[2]Visiting scholar at Northwestern University on leave from UPC.

Contributed by the Applied Mechanics Division of ASME for publication in the JOURNAL OF APPLIED MECHANICS. Manuscript received October 29, 2008; final manuscript received March 4, 2009; published online October 1, 2009. Review conducted by Robert M. McMeeking.

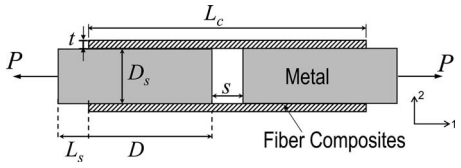

Fig. 1 Geometry of double-lap hybrid joint

In fracture mechanics of bimaterial joints, significant advances have already been made [11–16]. The same can be said of adhesive layers between two dissimilar materials [17–20]. However, the scaling of the strength of these joints does not seem to have been studied.

One complication in fracture mechanics of these joints is that the singularity exponent of the stress field at the tip of an interface crack is a complex number. In linear elastic fracture mechanics (LEFM), a nonzero imaginary part implies an oscillating crack opening profile with interpenetration of the opposite crack faces. After protracted debates, two conclusions eventually emerged [21,22]: First, the distance from crack tip over which LEFM predicts interpenetrations to occur is generally much smaller than the size of the fracture process zone (FPZ), which means that the interpenetrations are outside the range of validity of the LEFM solution. Second, in spite of the interpenetrations, the complex singularity field does give the correct energy release rate of a propagating interface crack [17,23,24], which is what really matters.

Another complication in hybrid joints is that the fracture initiates from the stress singularity at a reentrant corner. The same complication, of course, occurs for reentrant corners in homogeneous materials. For a finite corner angle, the real part of the exponent of the corner tip stress singularity in bimaterial, as well as homogeneous situations, is larger than $-\frac{1}{2}$. This implies the energy release rate at the corner to vanish, and so it is impossible to satisfy the energy balance for a sharp (LEFM) crack initiating from the corner. The way around this problem is to recognize that a finite FPZ must form at the corner first.

One way to approximate such an FPZ is to postulate an equivalent LEFM crack at the corner [25,26]. Together with the crack tip singularity, this introduces a pair of stress field singularities located very close to each other. But then a rigorous LEFM analysis becomes difficult and messy.

A better and more physical approach is to admit at the outset that both singularities actually lie within the domain of one FPZ, which envelops both the corner and crack tip. A realistic approximate way to deal with it is to consider that a cohesive crack with a given softening stress-separation relation emanates from the corner. Combining the exact corner and crack tip singular fields with the finite element analysis of cohesive fracture, Bažant and Yu [27] presented an accurate solution of this problem for symmetrically loaded corners of various angles in a homogeneous material, and derived by means of asymptotic matching the law of size effect in fracture at such corners [27]. However, for reentrant corners in bimaterial joints, the size effect appears to be unknown. To determine it is the goal of this two-part study.

The first part of this study presents experimental evidence of the size effect in hybrid joints. The second part, which follows, deals with the analytical formulation of the size effect, based on bimaterial interface fracture mechanics. Computational simulation of the size effect in hybrid joints is planned for a subsequent paper.

2 Choice of Test Specimens

Two types of specimen geometry and composition have been investigated—one at Northwestern University and another at the University of Michigan. The geometry of the double-lap metal-composite joints tested is shown in Fig. 1.

In each hybrid joint, there are eight bimaterial corners: four interior and four exterior. Based on the singularity exponent, the interface crack should start at the interior ones. The test results confirm it.

The nominal strength σ_N is a load parameter with the dimension of stress, and is here defined as $\sigma_N = P_{\max}/bD$. Here, $P_{\max}$ is the maximum load (which must be the failure load if load control is used), b is the width of the joint (in the third dimension), and D is the characteristic size (or dimension) of the joint (any in-plane dimension can be chosen as D since only the relative sizes matter). For this study, D is the length of the interface.

2.1 Specimen Dimensions. The greater the size effect ratio compared with the width of the scatter band, the lower is the ambiguity in identifying the size effect. For the typical random scatter in the testing of fiber composites, it is found that the size range must be at least 1:8 to produce a sufficient size effect range, and thus achieve unambiguous test results with a small enough error [8,28,10].

To avoid manufacturing specimens of variable sizes, which is normally more costly, some researchers tried to exploit the LEFM energy release rate function $g(\alpha)$ to deduce the size effect indirectly from specimens of one maximum cross section dimension, but different in shape or different in notch depth. Unfortunately, this method is fraught by large statistical error because the range of the so-called brittleness number [8,10] achievable by varying the geometry at constant maximum size is too limited [29].

Two series of geometrically similar specimens using the same type of laminate were manufactured and tested at Northwestern University (see Figs. 2(*a*) and 2(*b*)). A third series with a slightly different geometry was manufactured and tested at the University of Michigan to explore the size effect for a different type of laminate (see Fig. 2(*c*)).

In the first two test series, the steel blocks at each end are enlarged to accommodate the connectors of the steel chain through which the tensile load is applied. For the third test series, an additional 38.1 mm length is added to the steel bars at both ends so that wedge grips can be used for loading. Except for the aforementioned support parts, all the specimens within each test series are geometrically similar (which means the dimensions of D, D_s, L_c, L_s, t, and s have the same ratios for all the sizes). Such scaling makes detection and calibration of the size effect particularly easy because the material failure criteria expressed solely in terms of stresses and strains predict no size effect, i.e., the same with the nominal strength σ_N, regardless of the specimen size [6–9].

The specimens of series I and II were loaded in tension through chains at both ends to ensure that the tension resultant is centric. However, the specimens of series III were fixed at both ends against rotation and loaded at both ends by wedge grips. In general, such end fixtures could lead to tensile force eccentricity. However, thanks to careful attention to the alignment of end supports, the strain gauges on the opposite sides of the specimen gave nearly identical readings. This confirms that the resultant was centric.

The size ratios have been selected as 1:4:12 for series I and II, and 1:3:9:12 for test series III, both of which suffice to meet the aforementioned required breadth of the size range. There are three specimens in series I, and nine specimens in each of series II and III. In test series I there is thus only one specimen for each characteristic size D. In test series II there are three for each size, and in series III there are three for the two larger sizes, two for the smaller size, and one for the smallest size. The specimen dimensions in all the series are listed in Table 1. In series I, the smallest specimen was found to fail by tensile fracture of the laminate rather than by shear fracture along the interface, and to avoid it,

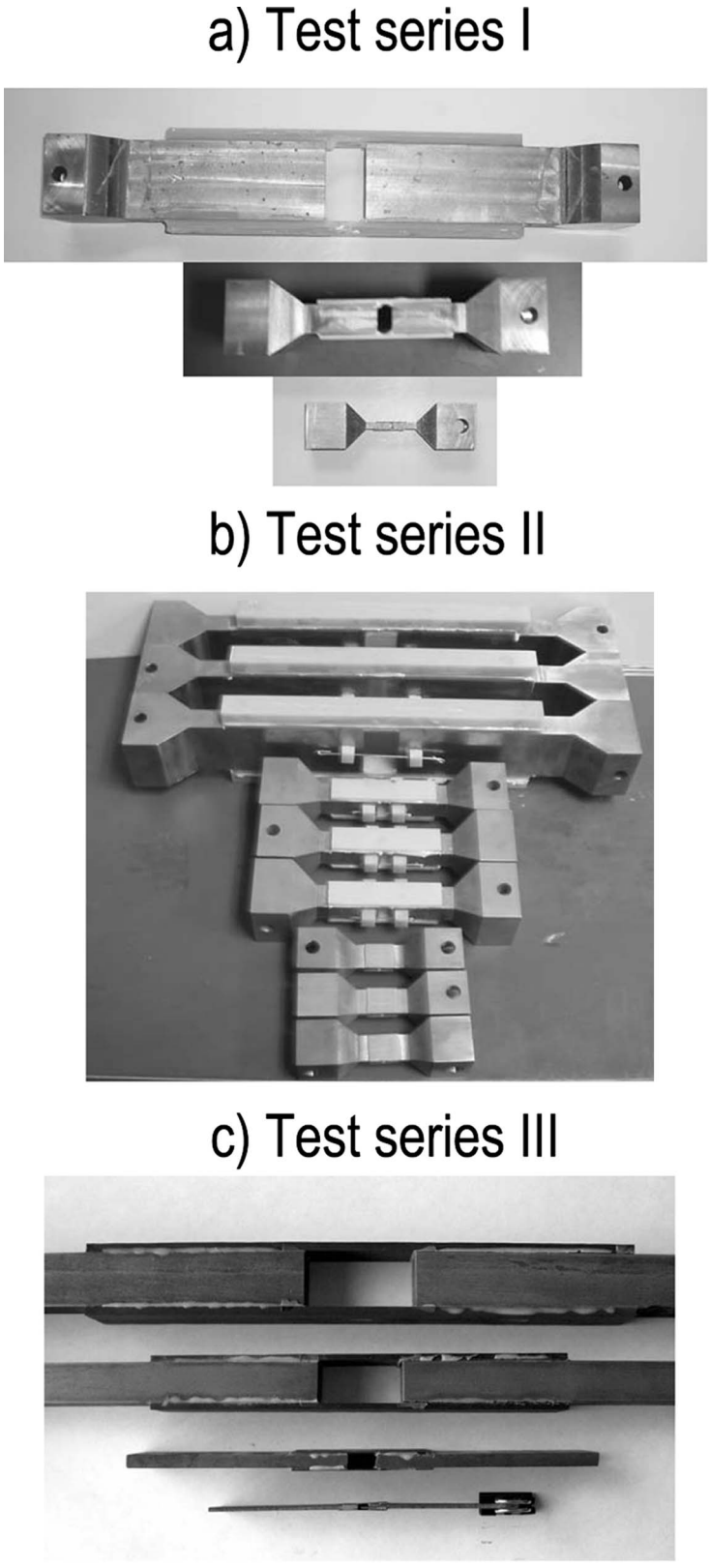

Fig. 2 Specimens of (*a*) test series I, (*b*) test series II, and (*c*) test series III

the relative laminate thickness in series II has been doubled. The other dimensions for series I and II are the same; the width $b = 20$ mm in series I and II, and $b = 25.4$ mm in series III. The optimal selection of D_s, s, L_c, and L_s was determined by finite element simulation [30] in order to ensure that: (1) the singular stress fields introduced by bimaterial corners would not appreciably interfere with each other, and that (2) the steel block would still be in the elastic range when the hybrid joint fails.

Table 1 Dimensions of specimens

Specimen	s (mm)	L_s (mm)	L_c (mm)	D_s (mm)	t (mm)	D (mm)
I-S-1	2.5	2.5	22.5	5	0.794	10
I-M-1	10	10	90	20	3.175	40
I-L-1	30	30	270	60	9.525	120
II-S-1,2,3	2.5	2.5	22.5	5	1.588	10
II-M-1,2,3	10	10	90	20	6.35	40
II-L-1,2,3	30	30	270	60	19.05	120
III-SS-1	3.175	6.35	15.875	1.5875	0.2413	6.35
III-S-1,2	9.525	19.05	47.625	4.7625	0.7366	19.05
III-M-1,2,3	28.575	57.15	142.875	14.2875	2.1844	57.15
III-L-1,2,3	38.1	76.2	190.5	19.05	2.9718	76.2

I: test series I; II: test series II; III: test series III.

2.2 Properties of Composites. The metal and the laminate are the same for series I and II. The metallic part is made of 1018 cold rolled steel having elastic modulus $E=200$ GPa and Poisson's ratio $\nu=0.3$. The composites of the hybrid joint are fiberglass-epoxy laminates (G-10/FR4 Epoxy Grade procured from McMaster-Carr, Inc.). The G-10/FR4 Garolite, manufactured by continuous weaving, is a glass-cloth laminate with epoxy resin binder. Although excellent tensile strength and high impact resistance is expected for the G-10/FR4 Garolite, the supplier does not provide precise information about its material properties, which are essential for theoretical analysis and numerical simulation. To determine these properties for series I and II, three types of test are carried out.

(1) The uniaxial tensile test is used to obtain the in-plane Young's modulus E_{11} and Poisson's ratio ν_{13}. Among different standard tensile test methods for composite materials, the Composites Research Advisory Group (GRAG) method 302, used to test axially orthotropic woven fiber-reinforced laminates [31], is selected. Accordingly, three specimens of length $L=260$ mm, width $W=20$ mm, thickness $t=1.588$ mm, and tab length $L_t=50$ mm are cut from one and the same G-10/FR4 Garolite sheet (see Fig. 3). To measure the longitudinal and transverse strains, a strain gauge is glued at the center to each specimen.
(2) The uniaxial compressive test is used to obtain the through-thickness Young's modulus E_{22} and Poisson's ratio ν_{21}. In contrast to the in-plane elastic properties and transverse shear modulus G_{12}, there exists no recognized national or international standard for measuring E_{22} and ν_{21}. The reason seems to be partly that strain and stress gradients are introduced by fabrication of thick sections [32], and partly that the through-thickness properties are dominated by the polymer matrix, which is isotropic. For the compressive test, three laminate prisms, with dimensions of $35\times15\times15$ mm^3, are cut from the same G-10/FR4 Garolite block and then bonded to a $50\times35\times35$ mm^3 steel block at each end (see Fig. 3). The strains of two gauges, glued at the opposite sides of each specimen, are averaged to eliminate a possible effect of compression eccentricity.
(3) The Iosipescu V-notched beam test is used to obtain the through-thickness shear modulus G_{21}. Three flat rectangular specimens with dimensions $76\times19.05\times4$ mm^3 are made, and two 90 deg angle notches, with faces oriented at ±45 deg to the longitudinal axis, are cut to the depth of 3.81 mm at the center of both edges (see Fig. 3). Biaxial strain gauges are bonded between the notches to measure the shear strains.

The following in-plane and through-thickness material properties of G-10/FR4 Garolite are obtained: $E_{11}=30.0$ GPa, $\upsilon_{13}=0.17$, $E_{22}=9.5$ GPa, $\upsilon_{21}=0.20$, and $G_{12}=3.0$ GPa.

The adhesive, which glues the steel and G-10/FR4 Garolite together, is the E-60HP metal-plastic bonder procured from McMaster-Carr, Inc. Although E-60HP provides high shear strength and peel resistance, its strength varies widely with the surface treatment. In test series I, the steel surface is sandblasted by extra coarse aggregate with glass beads (procured from Potters Industries, Inc.). In test series II, the steel surface is smooth.

In series III, the metallic part is the same as in series I and II. The composites are made using Newport NCT301 carbon laminates, which is a unidirectional tape laminate with an epoxy resin matrix, and the adhesive is NB1101 0.030 psf epoxy film adhe-

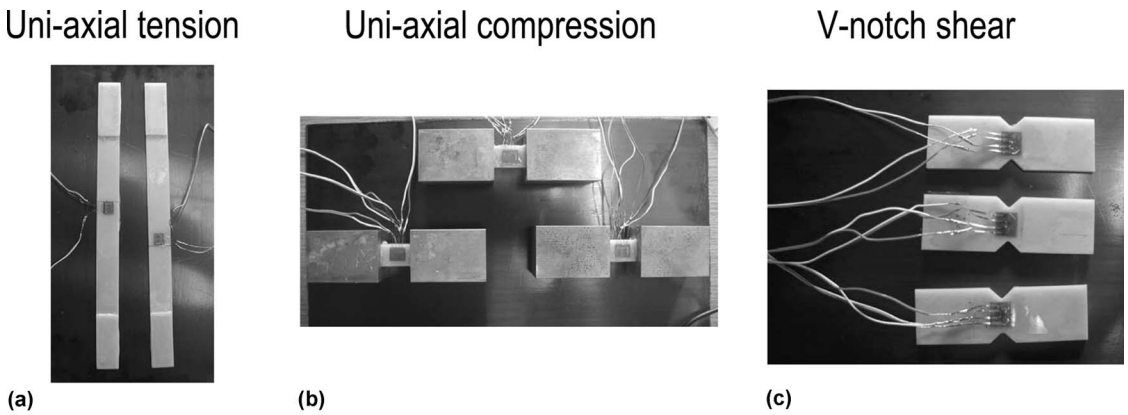

Fig. 3 Tests giving basic material properties of laminates: (*a*) tensile test, (*b*) through-thickness compressive test, and (*c*) V-notched beam test

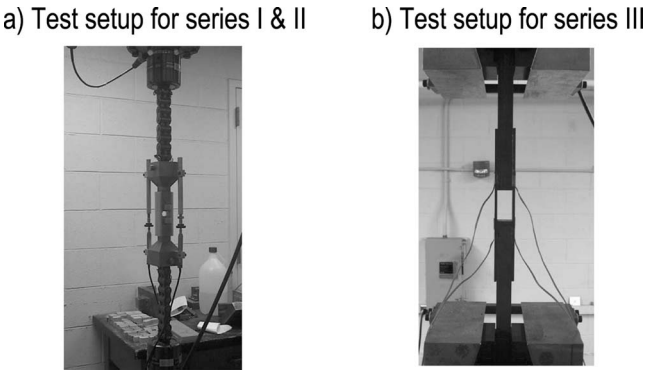

Fig. 4 (*a*) Test setup at Northwestern University; (*b*) test setup at the University of Michigan

sive. Both laminates and adhesives are produced by Newport Adhesives and Composites, Inc. According to the material data sheet, the properties for the uniaxial composites are: $E_{11}=125.5$ GPa, $\nu_{12}=\nu_{31}=0.304$, $E_{22}=9.0$ GPa, and $G_{12}=5.6$ GPa.

3 Size Effect Test

All the specimens are loaded under displacement control by a Material Testing Systems, Inc. (MTS) servohydraulic testing system. To ensure centric tensile load, a steel chain is connected to the specimen by a cylindrical pin for series I and II; see Fig. 4(*a*). In test series III, the specimens are fixed at both ends by wedge grips (Fig. 4(*b*)).

To isolate the rate dependence from the size effect, the fracture process zone in specimens of different sizes should get fully developed within about the same time [28]. To meet this requirement, the loading rates (rates of the stroke of loading piston) are chosen as 0.09 mm/min, 0.3 mm/min, and 0.9 mm/min for different sizes in test series I. At these rates, the peak loads are reached within 7–10 min. In test series II, the loading rates were 0.2 mm/min, 0.5 mm/min, and 0.8 mm/min, and the peak loads were reached within 5–6 min for all the sizes. In test series III, the loading rates were 0.152 mm/min, 0.456 mm/min, 0.760 mm/min, and 1.216 mm/min, and it took 3–6 min for all the specimens to reach their peak loads. Unlike test series I, in which only the load and stroke data were recorded, two linear variable displacement transducer (LVDT) devices in series II (Fig. 4(*a*)) and four strain gauges in series III (Fig. 4(*b*)) are installed at the opposite sides of each specimen to measure the relative displacement or strains and monitor a possible load eccentricity.

All the specimens failed in a brittle manner, which is documented by a sudden load drop after the specimens reached their peak loads in the load-displacement plots (see Figs. 5(*a*)–5(*c*)). The failure was dynamic and it occurred right after the peak load had been reached, and in the largest specimens there was a loud boom. All the specimens plotted in Figs. 5(*b*) and 5(*c*) exhibited interfacial failure.

Beside the interfacial failure in medium and large size specimens, another type of failure occurred in test series I. As shown in Fig. 5(*d*), the laminates of the smallest specimen failed by tensile fracture across the laminate, and a crack along the metal-

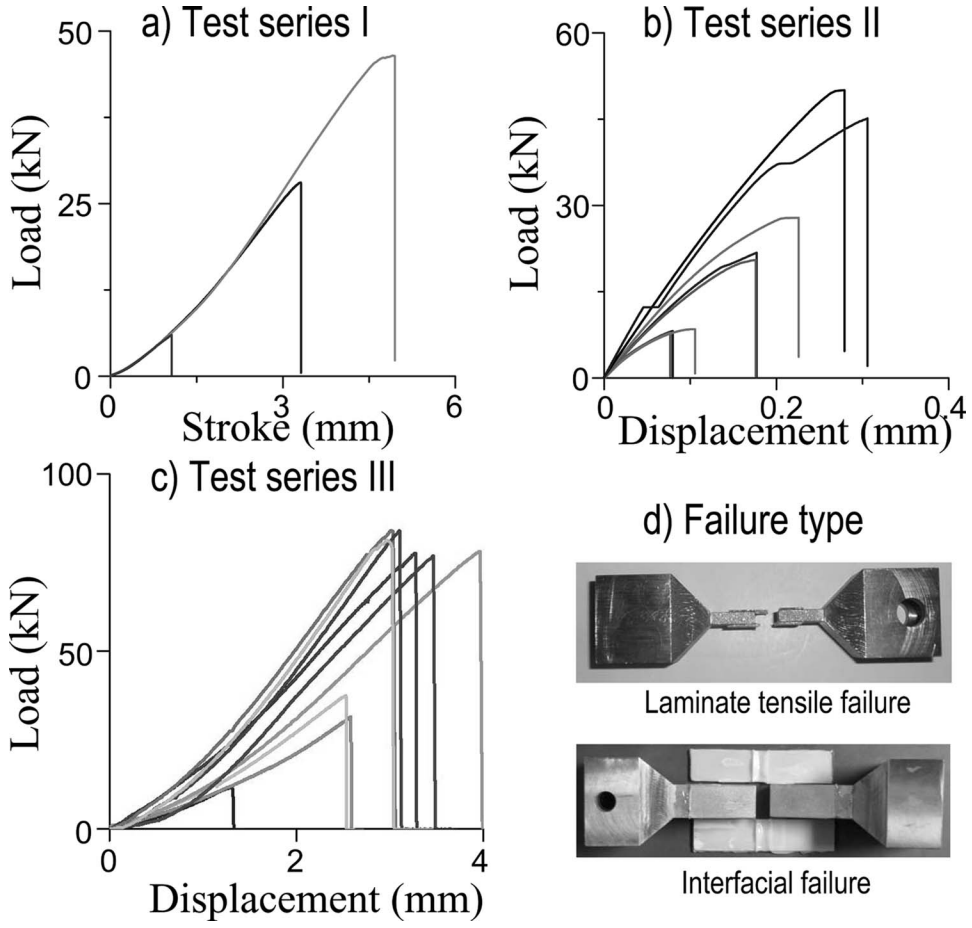

Fig. 5 Load-displacement deformation curves (*a*) of test series I, (*b*) of test series II, (*c*) of test series III, and (*d*) tensile fracture in laminates and shear fracture in bimaterial interface

Table 2 Recorded peak load

Specimen	P (kN)	Specimen	P (kN)	Specimen	P (kN)	Specimen	P (kN)
I-S-1	6.00[a]	I-M-1	28.09	I-L-1	46.49		
II-S-1	8.19	II-M-1	21.85	II-L-1	–		
II-S-2	7.89	II-M-2	27.90	II-L-2	50.01		
II-S-3	8.51	II-M-3	20.57	II-L-3	45.40		
III-SS-1	11.60	III-S-1	31.51	III-M-1	76.81	III-L-1	83.66
–	–	III-S-2	37.48	III-M-2	78.01	III-L-2	83.87
–	–	–	–	III-M-3	78.77	III-L-3	81.27

[a]Failed by tensile fracture of laminate.

composite interface could not develop fully. Therefore, the failure data for the smallest specimens are not comparable, and only the data for the medium and largest specimens of series I can be used. Obviously, the laminate thickness was too small in relation to the interface length, and it was for this reason that the laminate thickness was doubled for series II. Tensile fracture of the laminate also occurred in several of the smaller specimens in test series III. To identify the size effect exclusively on the interface shear strength, these tests had to be ignored.

4 Interpretation of Experimental Results

As known from the theory of crack interactions and stability [33], the fractures propagate from all the four inner corners simultaneously in a stable manner while the load is increasing (except for small differences due to inevitable random deviations from perfect symmetry). After the peak load, only one of the four interface cracks can grow, while the others must unload. The observations from the tests support this kind of fracture evolution.

The recorded peak loads for all the specimens of series I, II, and III are listed in Table 2 (only two peak loads are listed for the largest specimens of series II, because the electronic equipment malfunctioned in one test). The corresponding plots of $\log \sigma_N$ versus $\log D$, as shown in Figs. 6 and 7, for all test series, display a conspicuous size effect. For a fourfold size increase, the nominal strength reduction is significant (52% in series II and 40% in series III). In series I, the σ_N value for the smallest specimen, shown by a solid circle, cannot be used to calibrate the size effect law because the failure occurred in the laminate rather than the interface. Nevertheless, the σ_N value that would correspond to the interface failure must be higher than the solid circle point, and thus, series I, too, confirms a strong size effect.

The test data may be fitted by the size effect equation

$$\sigma_N = \sigma_0(1 + D/D_0)^{\lambda} \tag{1}$$

which is derived by asymptotic matching from fracture mechanics in Part II of this study; σ_0, D_0, and λ are constants. D_0 is called the transitional size, which generally equals the material characteristic length [8,10] times a geometry dependent factor obtainable from the equivalent LEFM. Since the size range is not broad enough and the scatter is not small enough to determine the exponent λ purely experimentally, the values $\lambda=-0.459$ for series I and II, and $\lambda=-0.486$ for series III, which give the asymptotic slopes in logarithmic size effect plots, are derived theoretically in Part II of this study [34]. They are seen to agree with the present test data.

Using nonlinear statistical regression of the test data, one finds $\sigma_0=47.8$ MPa and $D_0=20.77$ mm for test series II, with $\omega=8.7\%$, and $\sigma_0=98.0$ MPa and $D_0=18.75$ mm with $\omega=10.5\%$ for series III (where ω is the coefficient of variation of the regression errors, i.e., the standard error of regression divided by the data mean). When plotted in the double-logarithmic scales (Figs. 6 and 7), the negative curvature documenting the transition from quasiplastic behavior at small sizes to the LEFM for large sizes is clearly apparent. For test series I, the data exist for only two sizes, which is not statistically sufficient to fit a formula with two free parameters. However, the large-size asymptote of slope -0.459 agrees with series I data (see Fig. 6).

Figure 5(*b*) shows the load-displacement curves of series II specimens, all of which failed due to fracture propagation in the bimaterial interface. Note the sudden dynamic load drop after the peak for all the sizes. This means that the post-peak equilibrium path exhibits a snapback (i.e., runs to the left of the load drop). For all quasibrittle materials, the snapback takes place when the large-size asymptote is approached closely enough. In the fracture testing of concrete, the size above which the snapback occurs is quite large. The fact that here the snapback occurs even for the smallest specimen available means that, compared with other quasibrittle materials such as concrete, the stress-separation diagram of the cohesive interface crack must have a relatively steeper de-

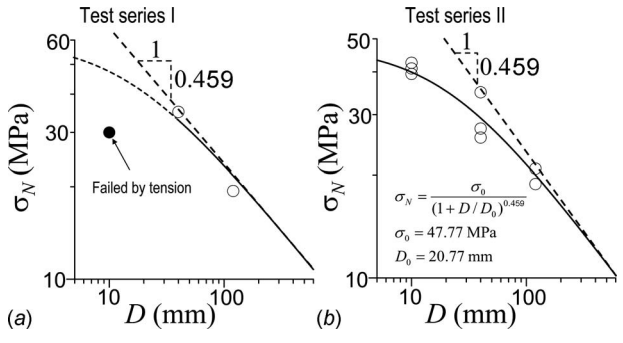

Fig. 6 Measured nominal strength values compared with optimum fit by size effect formula (solid curve): (*a*) test series I and (*b*) test series II

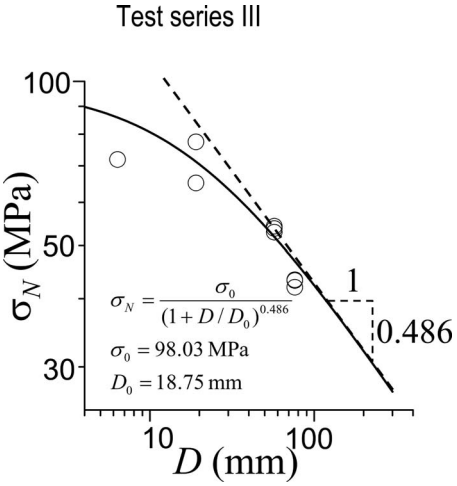

Fig. 7 Measured nominal strength of test series III compared with optimum fit by size effect formula

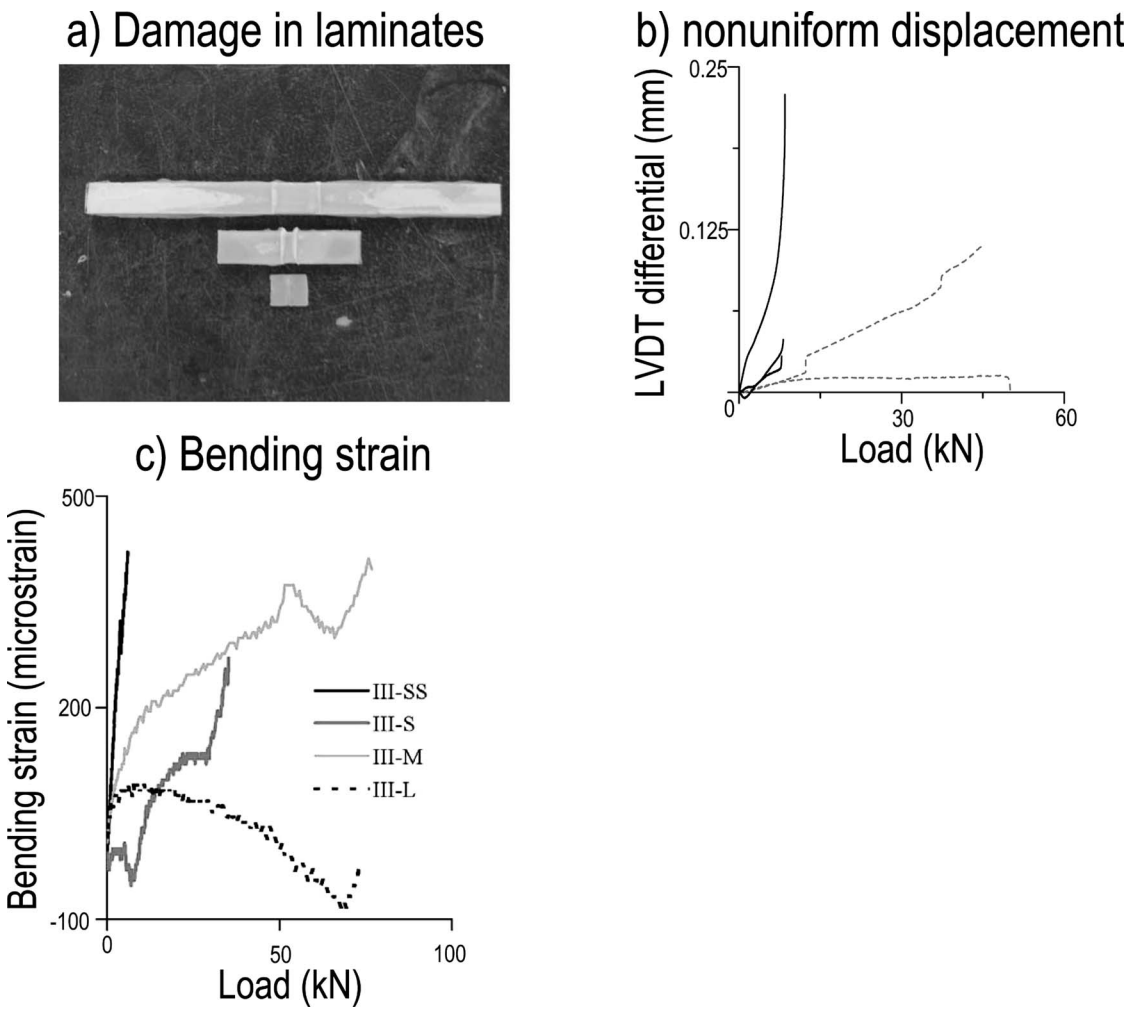

Fig. 8 (*a*) **Delamination pattern observed in test series II,** (*b*) **differences in readings of opposite LVDT gauges in test series II, and** (*c*) **strain differences at opposite specimen sides recorded in test series III**

scent, and the FPZ must be narrower [8,28] (a similar conclusion for fracture within laminates is also obtained in a previous study [35]).

Before the peak load, the FPZ must grow simultaneously at all the corners. But after the peak, the interface crack propagates from one corner only. From which one? This is decided by the corner singularity exponents. In the analytical study [34], which follows in Part II of this study, the stress singularity at the inner bimaterial corners (the corners closer to the center of test specimen) is much stronger than that at the outer corners. Thus, the crack should propagate from one of the four inner corners, or generally from a corner at which the stiffer bar (in this case the steel bar) terminates. This is confirmed by studying the damage pattern of the laminates after the failure test (see Fig. 8(*a*)). The formation of the cohesive interface fracture can be inferred from the delamination marks, which form because the crack advances in jumps. In the laminates of the small- and medium-size specimens of series II, the delamination marks are seen only in the region near the interior corners, while at the exterior corners, the laminates are almost intact. The crack development in the bimaterial interface is further documented by the laminate damage pattern in the large specimens of series II (see the photo in Fig. 8(*a*)), which shows the delamination to start from the inner corner and then gradually grows through the whole interface. A similar evolution of the delamination is also observed in series III.

For perfectly centric axial tensile loading, no bending moment will develop until the fracture localizes into one of the four interfaces in the hybrid joint. This means that the LVDT or strain gauges on opposite sides should give similar readings. The readings were not identical, but their difference was small enough to be attributed to inevitable errors in the alignment and material fabrication.

Figure 8(*b*) shows, by solid and dashed lines, the evolution of displacement differential with increasing load. Note that the small displacement nonuniformity in the small-size specimens has almost no effect on the peak load. For the two large-size specimens, one specimen displays a negligible displacement difference (a long horizontal portion of the dashed line), and the other shows substantial nonuniform displacement (ascending dashed line). Nonetheless, the peak load difference between these two specimens is insignificant compared with the coefficient of variation in the nonlinear size effect regression, which is $\omega=8.7\%$.

Unlike series I and II, the specimens of series III are loaded by wedge grips at both ends. This is a support condition which might introduce axial load eccentricity, with asymmetric stresses in the opposite laminates. Nevertheless, according to the readings of the four strain gauges bonded to the opposite sides of specimens, the difference between the strains at opposite sides was negligible,

with no appreciable effect on the nominal strength (see Fig. 8(*c*), which shows the typical strains due to bending moment for all the sizes).

5 Conclusions

The strength of metal-composite hybrid joints exhibits a strong size effect. A fourfold increase in size may cause the nominal strength to drop by more than 50%.

Experiments on geometrically similar specimens of different sizes agree with the theoretical size effect law [34], representing a smooth transition from quasiplastic behavior in the theoretical small-size limit to brittle (LEFM) behavior in the large-size limit.

Observation of the damage patterns in the failed specimens supports the theoretical prediction that the interface fracture should initiate at the corner, at which the stiffer of the two joined bars terminates.

The documented presence of size effect implies that the strength of metal-composite hybrid joints cannot be calculated from material models with failure criteria expressed solely in terms of stress and strain, which have been typical of elastic, plastic, and plastic-damage models. Rather, cohesive fracture mechanics or nonlocal damage mechanics, in which the failure criterion involves some type of energy or material length, must be used. Otherwise, the strength of large hybrid joints would be dangerously overestimated.

Acknowledgment

The experiments at Northwestern University were supported by the Office of Naval Research under Grant No. N00014-07-1-0313 from a program directed by Dr. Roshdy Barsoum.

References

[1] Barsoum, R. S., 2003, "The Best of Both Worlds: Hybrid Ship Hulls Use Composites & Steel," The AMPTIAC Quarterly, **7**(3), pp. 55–61.
[2] Bažant, Z. P., Daniel, I. M., and Li, Z., 1996, "Size Effect and Fracture Characteristics of Composite Laminates," ASME J. Eng. Mater. Technol., **118**(3), pp. 317–324.
[3] Bažant, Z. P., Kim, J.-J. H., Daniel, I. M., Becq-Giraudon, E., and Zi, G., 1999, "Size Effect on Compression Strength of Fiber Composites Failing by Kink Band Propagation," Int. J. Fract., **95**, pp. 103–141.
[4] Bažant, Z. P., Zhou, Y., Daniel, I. M., Caner, F. C., and Yu, Q., 2006, "Size Effect on Strength of Laminate-Foam Sandwich Plates," ASME J. Eng. Mater. Technol., **128**(3), pp. 366–374.
[5] Bažant, Z. P., Zhou, Y., Novák, D., and Daniel, I. M., 2004, "Size Effect on Flexural Strength of Fiber-Composite Laminate," ASME J. Eng. Mater. Technol., **126**, pp. 29–37.
[6] Bažant, Z. P., 1984, "Size Effect in Blunt Fracture: Concrete, Rock, Metal," J. Eng. Mech., **110**(4), pp. 518–535.
[7] Bažant, Z. P., 1997, "Scaling of Quasibrittle Fracture: Asymptotic Analysis," Int. J. Fract., **83**(1), pp. 19–40.
[8] Bažant, Z. P., 2002, *Scaling of Structural Strength*, 2nd ed., Elsevier, London, UK.
[9] Bažant, Z. P., 2004, "Scaling Theory for Quasibrittle Structural Failure," Proc. Natl. Acad. Sci. U.S.A., **101**(37), pp. 13400–13407.
[10] RILEM Committee TC QFS, 2004, "Quasibrittle Fracture Scaling and Size Effect—Final Report," Mater. Struct., **37**(272), pp. 547–586.
[11] Melograna, J. D., and Grenested, J. L., 2002, "Adhesion of Stainless Steel to Fiber Reinforced Vinyl-Ester Composite," J. Compos. Technol. Res., **24**(4), pp. 254–260.
[12] Bahei-El-Din, Y. A., and Dvorak, G. J., 2001, "New Designs of Adhesive Joints for Thick Composite Laminates," Compos. Sci. Technol., **61**, pp. 19–40.
[13] Dvorak, G. J., Zhang, J., and Canyurt, O., 2001, "Adhesive Tongue-and-Groove Joints for Thick Composite Laminates," Compos. Sci. Technol., **61**, pp. 1123–1142.
[14] Liu, D., and Fleck, N. A., 1999, "Scale Effect in the Initiation of Cracking of a Scarf Joint," Int. J. Fract., **95**, pp. 67–88.
[15] Grenestedt, J. L., and Hallstrom, S., 1997, "Crack Initiation From Homogeneous and Bi-Material Corners," ASME J. Appl. Mech., **64**(4), pp. 811–818.
[16] Groth, H. L., 1988, "Stress Singularities and Fracture at Interface Corners in Bonded Joints," Int. J. Adhes. Adhes., **8**(2), pp. 107–113.
[17] Malyshev, B. M., and Salganik, R. L., 1965, "The Strength of Adhesive Joints Using the Theory of Cracks," Int. J. Fract. Mech., **1**, pp. 114–128.
[18] Achenbach, J. D., Keer, L. M., Khetan, R. P., and Chen, S. H., 1979, "Loss of Adhesion at the Tip of an Interfacial Crack," J. Elast., **9**(4), pp. 397–424.
[19] Comninou, M., 1978, "The Interfacial Crack in a Shear Field," ASME J. Appl. Mech., **45**, pp. 287–290.
[20] Comninou, M., 1977, "The Interfacial Crack," ASME J. Appl. Mech., **44**, pp. 631–636.
[21] Rice, J. R., 1988, "Elastic Fracture Mechanics Concepts for Interface Cracks," ASME J. Appl. Mech., **55**, pp. 98–103.
[22] Hutchinson, J. W., Mear, M. E., and Rice, J. R., 1987, "Crack Paralleling an Interface Between Dissimilar Materials," ASME J. Appl. Mech., **55**, pp. 828–832.
[23] Suo, Z., 1990, "Singularities, Interfaces and Cracks in Dissimilar Anisotropic Media," Proc. R. Soc. London, Ser. A, **427**, pp. 331–358.
[24] Agrawal, A., and Karlsson, A. M., 2006, "Obtaining Model Mixity for a Bimaterial Interface Cracks Using the Virtual Crack Closure Technique," Int. J. Fract., **141**, pp. 75–98.
[25] Ritchie, R. O., Knott, J. F., and Rice, J. R., 1973, "On the Relation Between Critical Tensile Stress and Fracture Toughness in Mild Steel," J. Mech. Phys. Solids, **21**, pp. 395–410.
[26] Kosai, M., Kobayashi, A. S., and Ramulu, M., 1993, "Tear Straps in Airplane Fuselage," *Durability of Metal Aircraft Structures*, Atlanta Technology, Atlanta, GA, pp. 443–457.
[27] Bažant, Z. P., and Yu, Q., 2006, "Size Effect on Strength of Quasibrittle Structures With Reentrant Corners Symmetrically Loaded in Tension," J. Eng. Mech., **132**(11), pp. 1168–1176.
[28] Bažant, Z. P., and Planas, J., 1998, *Fracture and Size Effect in Concrete and Other Quasibrittle Materials*, CRC, Boca Raton, FL.
[29] Tang, T., Bažant, Z. P., Yang, S., and Zollinger, D., 1996, "Variable-Notch One-Size Test Method for Fracture Energy and Process Zone Length," Eng. Fract. Mech., **55**(3), pp. 383–404.
[30] Bažant, Z. P., Caner, F. C., Le, J.-L., and Yu, Q., 2008, "Scaling of Strength of Metal-Composite Joints," *Proceedings of the 49th AIAA/ASME/ASCE/AHS/ASC Structures, Structural Dynamics and Materials Conference*, Schaumburg, IL, Apr. 7–10, Paper No. 2093.
[31] Godwin, E. W., 2000, "Tension," *Mechanical Testing of Advanced Fiber Composites*, J. M. Hodgkinson, ed., CRC, Boca Raton, FL, pp. 43–74.
[32] Broughton, W. R., 2000, "Through-Thickness Testing," *Mechanical Testing of Advanced Fiber Composites*, J. M. Hodgkinson, ed., CRC, Boca Raton, FL, pp. 143–169.
[33] Bažant, Z. P., and Cedolin, L., 1991, *Stability of Structures: Elastic, Inelastic, Fracture and Damage Theories*, Oxford University, New York.
[34] Le, J.-L., Bažant, Z. P., and Yu, Q., 2010, "Scaling of Strength of Metal-Composite Joints—Part II: Interface Fracture Analysis," ASME J. Appl. Mech., **77**, p. 011012.
[35] Beghini, A., Cusatis, G., and Bažant, Z. P., 2008, "Spectral Stiffness Microplane Model for Quasibrittle Composite Laminates—Part II: Calibration and Validation," ASME J. Appl. Mech., **75**(2), p. 021010.

Jia-Liang Le
Graduate Research Assistant
Department of Civil and Environmental Engineering,
Northwestern University,
2145 Sheridan Road,
Evanston, IL 60208
e-mail: jialiang-le@northwestern.edu

Zdeněk P. Bažant[1]
McCormick Institute Professor and W. P. Murphy Professor
Departments of Civil Engineering and Materials Science,
Northwestern University,
2145 Sheridan Road, CEE/A135,
Evanston, IL 60208
e-mail: z-bazant@northwestern.edu

Qiang Yu
Postdoctoral Researcher
Department of Civil and Environmental Engineering,
Northwestern University,
2145 Sheridan Road,
Evanston, IL 60208
e-mail: qiangyu@northwestern.edu

Scaling of Strength of Metal-Composite Joints—Part II: Interface Fracture Analysis

The effect of the size of hybrid metal-composite joint on its nominal strength, experimentally demonstrated in the preceding paper (part I), is modeled mathematically. Fracture initiation from a reentrant corner at the interface of a metallic bar and a fiber composite laminate sheet is analyzed. The fracture process zone (or cohesive zone) at the corner is approximated as an equivalent sharp crack according to the linear elastic fracture mechanics (LEFM). The asymptotic singular stress and displacement fields surrounding the corner tip and the tip of an interface crack emanating from the corner tip are calculated by means of complex potentials. The singularity exponents of both fields are generally complex. Since the real part of the stress singularity exponent for the corner tip is not $-\frac{1}{2}$*, as required for finiteness of the energy flux into the tip, the interface crack propagation criterion is based on the singular field of the interface crack considered to be embedded in a more remote singular near-tip field of the corner from which, in turn, the boundaries are remote. The large-size asymptotic size effect on the nominal strength of the hybrid joint is derived from the LEFM considering the interface crack length to be much smaller than the structure size. The deviation from LEFM due to finiteness of the interface crack length, along with the small-size asymptotic condition of quasiplastic strength, allows an approximate general size effect law for hybrid joints to be derived via asymptotic matching. This law fits closely the experimental results reported in the preceding paper. Numerical validation according to the cohesive crack model is relegated to a forthcoming paper.* [DOI: 10.1115/1.3172152]

1 Introduction

The preceding first part of this study [1] presented experimental evidence of a strong size effect on the strength of hybrid joints of metal to polymer-fiber composite. The objective of the second part is a mathematical analysis of the observed size effect.

In the past four decades, extensive analytical studies have been devoted to the effect of structure size on the strength of structures made of quasibrittle materials. These are brittle heterogeneous materials, which include concrete, as the archetypical case, fiber composites, sea ice, rocks, tough ceramics, stiff cohesive soils, rigid foams, wood, paper, bone, etc., and all brittle materials on a sufficiently small scale. In quasibrittle structures, the maximum load is reached after a stable development of either a large crack, or a large fracture process zone (FPZ) with distributed cracking. The latter case leads to Type 1 energetic size effect, which transits in the large-size limit to the Weibull statistical size effect. In the former case, the pre-existing crack is approximately equivalent to a notch, which leads to Type 2 energetic size effect [2,3].

Williams' solution [4] showed the dependence of the stress singularity exponent on the angle of a corner in a homogeneous body. A general approximate size effect law was recently derived for fracture emanating from a reentrant corner of arbitrary angle, provided that the loading is symmetric and the body is homogeneous and isotropic [5]. This size effect formulation now needs to be extended to a corner at the interface between two different materials, one of which is orthotropic. Compared with a reentrant corner in a homogeneous material, the analysis of a reentrant bimaterial corner is complicated by the fact that the stress singularity exponent can be a complex number if the material mismatch is severe enough.

The size effect is defined for geometrically similar structures and represents the effect of structure size D (or characteristic dimension) on a load parameter of the dimension of stress. This parameter is normally chosen as the nominal strength, which is defined as $\sigma_N = P_{\max}/bD$, where $P_{\max}$ = maximum load, b = width of the structure (in the third dimension), and D = characteristic dimension, which may be chosen arbitrarily since only the ratio of σ_N values matters. Here we chose D = interface length (Fig. 1(*a*)). To avoid small secondary effects of the length of crack front edge in the third dimension (stemming from a transition from plane strain to plane stress along the edge), it is better to consider two-dimensional similarity, i.e., b = constant.

According to elasticity with strength limit, nonsoftening plasticity or any theory in which the material failure criterion is characterized solely in terms of stresses and strains, σ_N is independent of structure size D [6,7,2] when geometrically similar structures are compared. Any deviation from this classical situation is called the size effect. The Weibull statistical size effect is negligible when the FPZ or the crack length at failure is large, and also when the crack can initiate at one point only (the corner). Therefore, the size effect in the joints is energetic (i.e., nonstatistical), being caused by the presence of material fracture energy G_f or material characteristic length l_0 in the material failure criterion.

Similar to the previous size effect analysis for many other quasibrittle structures [5,2,3,8,9], the size effect law will be asymptotically anchored at the large-size limit in linear elastic fracture mechanics (LEFM). The transition to small-size behavior and extension to various corner angles in the joint will be approximated by asymptotic matching. For reentrant corners (or V-notches) in a homogeneous body, this kind of approach has already been shown to lead to good agreement with experiments [5].

[1]Corresponding author.

Contributed by the Applied Mechanics Division of ASME for publication in the JOURNAL OF APPLIED MECHANICS. Manuscript received October 29, 2008; final manuscript received April 13, 2009; published online October 1, 2009. Review conducted by Robert M. McMeeking.

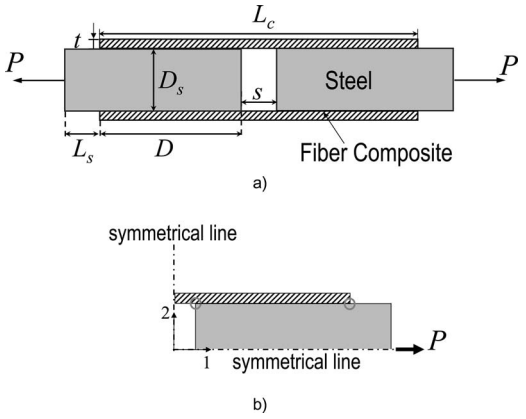

Fig. 1 Geometry of double-lap hybrid joint

2 Stress Singularity Exponent

In the double-lap joint considered here, both the structure and the loading are symmetric. Before the peak load is attained, the elastic field must be symmetric as well. Therefore, we analyze only one quarter of the specimen (Fig. 1(*b*)). In this quarter, there are two critical bimaterial corners where the corner geometry and material mismatch cause singularity and stress concentration. To identify the critical corner from which the crack propagates, the stress singularity exponents must be calculated.

The stress singularity exponents for bimaterial wedges have been extensively studied for isotropic materials [10,11]. For general orthotropic-orthotropic interfaces or orthotropic-isotropic interfaces, various numerical approaches, such as the finite difference method with eigenvalue analysis, and the finite element iterative method, have been used to determine the singularity exponent and the surrounding asymptotic elastic field [12–14].

In this study, an analytical approach using the complex field method is adopted to calculate the singularity for bimaterial wedges (shown in Fig. 2) [15]. Under plane loading condition, the elastic field in each layer of material (including the displacements, boundary tractions, and stress fields) may be represented by two holomorphic functions $f_1(z_1)$ and $f_2(z_2)$, where $z_j=x+\mu_j y (j=1,2)$; μ_j is the root with positive imaginary part of the fourth order equation

$$\lambda\mu^4 + 2\rho\lambda^{1/2}\mu^2 + 1 = 0 \tag{1}$$

Here $\lambda=s_{11}/s_{22}$ and $\rho=0.5(2s_{12}+s_{66})(s_{11}s_{22})^{-1/2}$; s_{ij} refers to the elements of the general material compliance matrix, and subscripts i and j refer to Cartesian coordinates $x_i (i=1,2)$. When the conditions of equilibrium and compatibility are imposed and the singularity lies on the left side as the observer travels in the positive, or counterclockwise, direction of the arc, the corresponding displacement, stress, and resultant forces on the arc can be represented by these two functions as follows [16]:

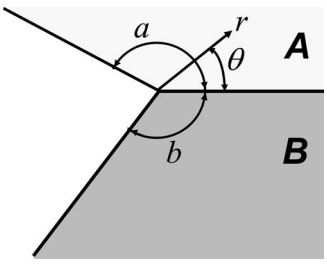

Fig. 2 Geometry of bimaterial wedge

$$u_i = 2\ \mathrm{Re}\sum_{j=1}^{2} A_{ij} f_j(z_j) \tag{2}$$

$$\sigma_{2i} = 2\ \mathrm{Re}\sum_{j=1}^{2} L_{ij} f_j'(z_j) \tag{3}$$

$$\sigma_{1i} = -2\ \mathrm{Re}\sum_{j=1}^{2} L_{ij}\mu_j f_j'(z_j) \tag{4}$$

$$T_i = -2\ \mathrm{Re}\sum_{j=1}^{2} L_{ij} f_j(z_j) \tag{5}$$

where matrices $\mathbf{A}$ and $\mathbf{L}$ are defined as

$$\mathbf{A} = \begin{Bmatrix} s_{11}\mu_1^2 + s_{12} & s_{11}\mu_2^2 + s_{12} \\ s_{21}\mu_1 + s_{22}/\mu_1 & s_{22}\mu_2 + s_{22}/\mu_2 \end{Bmatrix} \tag{6}$$

$$\mathbf{L} = \begin{Bmatrix} -\mu_1 & -\mu_2 \\ 1 & 1 \end{Bmatrix} \tag{7}$$

Near the corner tip, the displacement field as a function of polar coordinates (r,θ) (Fig. 2) may be assumed to be separable, and the dependence on radial coordinate r to be a power law of some exponent δ, which can be either real or complex. The corresponding stress field has a singular term proportional to $r^{\delta-1}$. Hence, the complex potentials near the bimaterial corner tip may be expressed, for both materials, as follows [15]:

$$f_k(z_k) = \phi_k z_k^{\delta} = \phi_k r^{\delta}(\cos\theta + \mu_k \sin\theta)^{\delta} \quad (k=1,2) \tag{8}$$

To write these potentials in a more compact form, we define for each material the vectors: $\mathbf{\Phi}=[\phi_1,\phi_2]^T$, $\mathbf{Z}=[z_1,0;0,z_2]$, and $\mathbf{F}=[f_1,f_2]^T$ (where T denotes a transpose). For each material, the corresponding displacements and resultant forces can be written in the matrix form as

$$\mathbf{u} = [u_1,u_2]^T = \mathbf{A}\cdot\mathbf{F} + \overline{\mathbf{A}}\cdot\overline{\mathbf{F}} = \mathbf{A}\cdot\mathbf{Z}^{\delta}\cdot\mathbf{\Phi} + \overline{\mathbf{A}}\cdot\overline{\mathbf{Z}}^{\delta}\cdot\overline{\mathbf{\Phi}} \tag{9}$$

$$-\mathbf{T} = [-T_1,-T_2]^T = \mathbf{L}\cdot\mathbf{F} + \overline{\mathbf{L}}\cdot\overline{\mathbf{F}} = \mathbf{L}\cdot\mathbf{Z}^{\delta}\cdot\mathbf{\Phi} + \overline{\mathbf{L}}\cdot\overline{\mathbf{Z}}^{\delta}\cdot\overline{\mathbf{\Phi}} \tag{10}$$

where the overbar denotes the conjugate of a complex matrix.

Finally, one needs to impose the boundary conditions: a traction-free exterior boundary ($\theta=a,-b:\mathbf{T}=0$); and the continuity of displacements and tractions at the interface between two materials; $\theta=0$: $\mathbf{T}_A=\mathbf{T}_B$ and $\mathbf{u}_A=\mathbf{u}_B$. This results in a system of linear equations, with the matrix form

$$\mathbf{K}(\delta)\nu = \begin{bmatrix} \mathbf{Y_A} & \mathbf{1} & \mathbf{0} & \mathbf{0} \\ \mathbf{0} & \mathbf{0} & \mathbf{Y_B} & \mathbf{1} \\ \mathbf{1} & \mathbf{1} & -\mathbf{1} & -\mathbf{1} \\ \mathbf{B_A} & -\overline{\mathbf{B}}_\mathbf{A} & -\mathbf{B_B} & -\overline{\mathbf{B}}_\mathbf{B} \end{bmatrix} \begin{Bmatrix} (\mathbf{L\Phi})_A \\ (\overline{\mathbf{L\Phi}})_A \\ (\mathbf{L\Phi})_B \\ (\overline{\mathbf{L\Phi}})_B \end{Bmatrix} = 0 \tag{11}$$

where $\mathbf{1}=[1,0;0,1]$ and $\mathbf{0}=[0,0;0,0]$. Submatrices $\mathbf{Y}_k$ and $\mathbf{B}_k$ (where k=A, B=labels of materials A and B) are defined as

$$\mathbf{Y}_k = \overline{\mathbf{L}}_k[\overline{\mathbf{Z}}_k(\theta_k)]^{-\delta}\overline{\mathbf{L}}_k^{-1}\mathbf{L}_k[\mathbf{Z}_k(\theta_k)]^{\delta}\mathbf{L}_k^{-1} \tag{12}$$

$$\mathbf{B}_k = i\mathbf{A}_k\mathbf{L}_k^{-1} \tag{13}$$

where $i^2=-1$. It may be noted that the submatrix $\mathbf{Y}_k$ defined above cannot be directly applied to isotropic materials ($\mu_k=i$) because $\mathbf{L}_k$ is not invertible. However, one can calculate $\mathbf{Y}_k$ by taking the limit of $\mu_k\to i$ ($\mathbf{B}_k$ is well defined for isotropic materials) [15,17]. The displacement singularity δ must be solved from the condition $\det(\mathbf{K})=0$. To solve it numerically, it is the easiest to seek the value of δ for which the condition number of matrix $\mathbf{K}$ becomes very large.

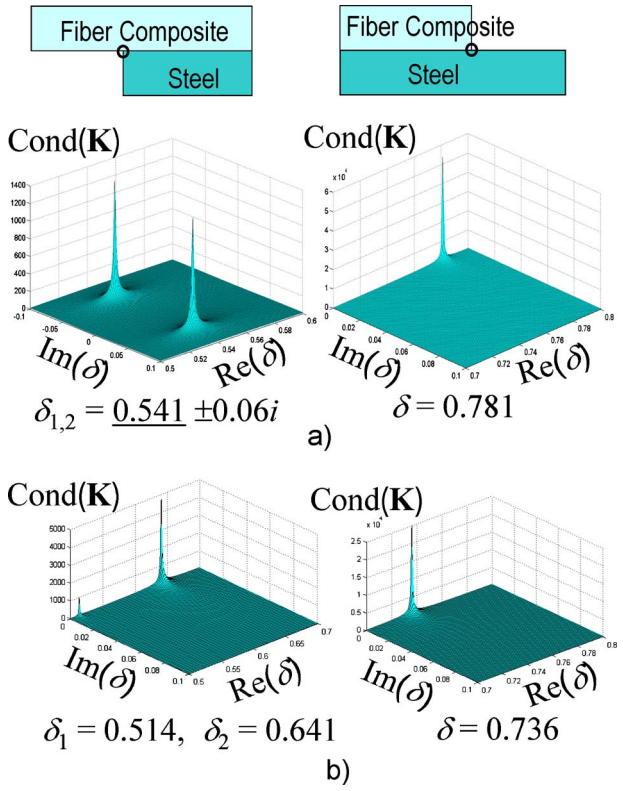

Fig. 3 Exponent of displacement singularity of hybrid joint: (*a*) test series I and II and (*b*) test series III

Three test series have been reported in the preceding paper [1]. The orthotropic elastic constants of the fiber composite used in test series I and II are E_1=30 GPa, E_2=9.5 GPa, ν_{12}=0.2, and G_{12}=3.0 GPa. The elastic constants of composite used in test series III are E_1=125.5 GPa, E_2=9.0 GPa, ν_{12}=0.3, and G_{12}=5.6 GPa. For steel, which is isotropic, E=200 GPa and ν=0.3. Figure 3 shows in the complex plane the plot of det(**K**) for the displacement singularity. For the joint used in test series I and II, the displacement field at the left corner (at which the stiffer material terminates) is found to exhibit singularities with exponents being a pair of complex conjugates $\delta=0.541\pm0.06i$ and, at the right corner (at which the softer material terminates), a real displacement singularity δ=0.781. For the joint used in test series III, the displacement at the left corner exhibits two real displacement singularities: δ_1=0.514 and δ_2=0.641, while at the right corner there is a real displacement singularity with δ=0.736. So, for all the joints tested, the singularity at the left corner is much stronger than it is at the right corner. Hence, the crack is expected to start propagating from the left corner, which agrees with the experimental observations [1]. The left corner is that which governs the strength of the hybrid joint, and so the fracture needs to be investigated only for that corner.

3 Fracture of Bimaterial Corner and Size Effect Law Asymptote

Various fracture criteria have been proposed to characterize the crack initiation for general bimaterial corners [18–20]. Due to the nature of mix-mode fracture at bimaterial corner, the use of stress intensity factors as a fracture criterion generally necessitates an empirical equation involving the stress intensity factors for different modes [21]. As an empirical approach to certain situations, such as bimaterial butt joints, one may simply use a critical value of the stress intensity factor as a fracture criterion [22–24]. A more general and effective approach is to consider the energy release rate or the corresponding fracture energy as the failure criterion [25].

Consider a bimaterial corner with the strongest stress singularity $\lambda=\kappa\pm i\eta$. The corresponding near-tip stress field can be written as

$$\sigma_{ij}=\mathrm{Re}[Hr^{i\eta}\alpha_{ij}(\theta)]r^{\kappa} \tag{14}$$

where H is the stress intensity factor, and α_{ij} is the distribution of stress. Both of them are complex, in general. Dimensional analysis shows that H must have the form

$$H=\frac{P}{bD}D^{-\kappa}|h(\eta,\varphi)|e^{i(\omega-\eta\ln D)} \tag{15}$$

where P is the applied load, b is the width of the joint, D is the characteristic size of the joint (chosen as the interface length), $h(\eta,\varphi)$ is the dimensionless complex stress intensity factor, φ is the effective loading angle (which combines the effects of loading angle and boundary conditions), and ω is the phase angle of $h(\eta,\varphi)$.

For a general bimaterial wedge, the exponents of displacement singularities can be either a pair of complex conjugates, a single real number or two unequal real numbers depending on the degree of material mismatch and the geometry. For the former two cases, Eq. (14) represents the entire singular stress field [19,26], while for the latter case, Eq. (14) represents only the singular stress field corresponding to the strongest stress singularity. The entire singular stress zone may be written as $\sigma_{ij}=H_1r^{\kappa_1}\alpha_{ij}(\theta)+H_2r^{\kappa_2}\beta_{ij}(\theta)$. For symmetric structures made of homogenous materials, κ_1 and κ_2 correspond to the symmetric and antisymmetric modes of fracture (Modes I and II) (the simplest example is the homogenous reentrant corner analyzed in Ref. [5]). Depending on the loading, it is possible that only one of them governs the entire stress field.

Because of the lack of symmetry of bimaterial joints, the symmetric and antisymmetric modes do not exist, and κ_1 and κ_2 always coexist. Many studies showed the importance of considering both singularities to properly obtain the entire singular stress field for a bimaterial joint [21,27,28]. Nevertheless, for the large-size asymptotic size effect, only the singular stress field corresponding to the strongest singularity is relevant. So, in what follows, only the corner tip singular field corresponding to the strongest stress singularity is considered.

Once the crack initiates from the corner tip, it will propagate along the path that corresponds to the highest energy release rate or the lowest fracture energy dissipation. The adhesive layer connecting the fiber composite and the steel is as thin as possible and is generally much weaker than both materials in normal hybrid joint designs. So, the crack is expected to propagate along the interface.

The initiation of a crack, or macrocrack, requires formation of a microcracking zone of a certain finite characteristic length l_{FPZ} within (and possibly near) the adhesive layer. This zone, called the fracture process zone (FPZ), develops stably and transmits cohesive stresses. As soon as the full FPZ develops, the maximum load is attained. After that, the equilibrium load is expected to decrease, which requires the geometry to be positive [9], i.e., the stress intensity factor to increase with the crack length when the load is constant. A positive geometry is normally satisfied but, of course, needs to be verified.

In analogy to the derivation of the size effect law for cracks in homogenous solids [2], we may assume that, not too close to the FPZ, the effect of a finite-size FPZ on the elastic field is approximately equivalent to the effect of an interface crack, whose length c_f is proportional to length l_{FPZ} of the FPZ, and is roughly $l_{\mathrm{FPZ}}/2$) [2,9,29]. Therefore, what matters at maximum load is the asymptotic field close (but not too close) to an interfacial crack, rather than to a corner. It has been shown [17] that the stress singularity exponent of an interfacial crack must have the form

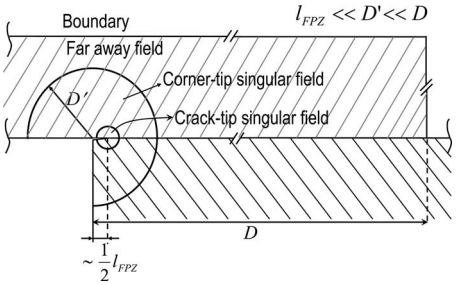

Fig. 4 Interfacial crack embedded in the singular near-tip field of corner

$$\lambda_{\text{crack}} = -\tfrac{1}{2} + i\eta' \tag{16}$$

In the foregoing, a distinction is made among (1) the near-tip asymptotic field of the imagined effective crack assumed to have a similar global effect as the actual FPZ; (2) the near-tip field of the corner prevailing not too close to the tip of the crack so that it can envelop the near-tip field of the crack; and (3) the far-away field affected by the boundary conditions (Fig. 4). These three fields are here matched energetically, through the strength of the singularities. Note that the second field corresponds to what has been conceived as the intermediate asymptotic—an important concept conceived and rigorously developed by Barenblatt [30,31], which has apparently not yet been used in fracture mechanics.

The intermediate asymptotic is attained if $D \gg D' \gg l_{\text{FPZ}}$ (where D' is the size of the corner tip singular field), and the near-tip field of a crack is applicable only if the radial distance from the crack tip $r \ll l_{\text{FPZ}}$ (Fig. 4), i.e., in the large-size asymptotic limit. In this limit, the asymptotic near-tip field of the hypothetical interfacial crack of length c_f, substituted for the FPZ, must be surrounded by the singular stress field of a bimaterial corner tip corresponding to the strongest stress singularity (except if the laminate thickness were too small, which has been checked not to occur in practical situations). Therefore, the stress intensity factor K at the interfacial crack tip will depend on the stress field, whose magnitude is characterized by the stress intensity factor H of the corner tip. By dimensional analysis, the two stress intensity factors may be related as follows [19,22]:

$$Kc_f^{i\eta'} = Hc_f^{\kappa+0.5} c_f^{i\eta} \zeta \tag{17}$$

where ζ is the dimensionless complex number. Such a relation has been analytically derived for the case of a crack emanating from a homogeneous notch tip [32,33]. For the interfacial crack, the near-tip stresses on the crack line ahead of the tip and the opening displacements (or crack face separations) behind the tip can be expressed as [17,34]

$$\alpha\sigma_{yy} + i\sigma_{xy} = K(2\pi r)^{-1/2} r^{i\eta'} \tag{18}$$

$$\alpha^{-1}\delta_y + i\delta_x = \frac{K}{E}(r/2\pi)^{1/2} r^{i\eta'} m \tag{19}$$

where $\delta_i = u_i(-r, 0^+) - u_i(-r, 0^-) =$ displacement jump behind the crack tip, m is the dimensionless complex number characterizing the geometry of the structure, E is any one of the elastic moduli of either material, and α is the constant reflecting the material orthotropy.

The energy release rate $\mathcal{G}$ represents the energy flux into the crack tip. The flux can be obtained as the work required for the crack to advance by an infinitesimal distance, Δ, divided by Δ. Therefore,

$$\mathcal{G} = \lim_{\Delta\to 0} \frac{1}{2\Delta} \int_0^{\Delta} [\sigma_{yy}(x)\delta_y(\Delta - x) + \sigma_{xy}(x)\delta_x(\Delta - x)]\mathrm{d}x \tag{20}$$

Noting Eqs. (18) and (19) and introducing the dimensionless variable $\xi = x/\Delta$, one obtains

$$\mathcal{G} = \frac{|K|^2|m|}{2E} \int_0^1 \sqrt{\frac{1-\xi}{\xi}} \cos\left[\eta' \ln\left(\frac{1-\xi}{\xi}\right) + \psi\right] \mathrm{d}\xi \tag{21}$$

The foregoing integral can be shown to be a constant [35,36]. Therefore, the energy release rate function for an interfacial crack can be always written as

$$\mathcal{G} = \frac{CK\bar{K}}{E} \tag{22}$$

Upon substituting Eqs. (17) and (15) into the foregoing equation, one obtains

$$\mathcal{G} = \frac{\sigma^2 D^{-2\kappa}}{Ec_f^{-1-2\kappa}} |g|^2 \tag{23}$$

where $\sigma =$ nominal stress $= P/bD$ and $|g| = C|\xi||h|$. Within the LEFM framework, a crack can propagate once $\mathcal{G}$ reaches a certain critical value G_f, called the fracture energy, and this also represents the condition of maximum load P. From Eq. (23), one obtains the LEFM expression of nominal strength $\sigma_N (= P_{\max}/bD)$ of the bimaterial joint

$$\sigma_N = |g|^{-1} \sqrt{EG_f} c_f^{-\kappa-0.5} D^{\kappa} \tag{24}$$

This equation represents the large-size asymptote of the size effect law. Clearly, this asymptote is a power scaling law, with an exponent directly related to the real part of the exponent of the strongest stress singularity at the bimaterial corner.

Evidently, Eq. (24) applies to fracture of a certain single mode. Let us now rewrite this equation for the case of a reentrant corner made of a homogenous material under symmetric tensile loadings, which is mode I fracture. In this case, only one real stress singularity governs the entire singular stress field (for a homogeneous reentrant corner under general loading conditions, there are two unequal real stress singularities, which correspond to symmetric and asymmetric fracture modes). The effective size of FPZ can be expressed as $c_f = \gamma l_0$, in which $l_0 = EG_f/f_t'^2 =$ Irwin's characteristic length. Equation (24) may then be written in an alternative form

$$\sigma_N = f_t' k (D/c_f)^{\kappa} \tag{25}$$

where $k = (|g|\sqrt{\gamma})^{-1}$, and f_t' is the tensile strength of the material. This equation has the same form as the large-size asymptote of the general size effect law for a reentrant corner under symmetric tensile loading (Eq. (16) in Ref. [5]), which has recently been derived on the basis of the strength criterion; i.e., the peak load is attained when the tensile stress at the center of FPZ reaches the material tensile strength. The equivalence between Eqs. (25) and (16) in Ref. [5] is to be expected, since the strength criterion for single-mode fracture must be a special case of the present energy criterion.

4 General Size Effect Law Via Asymptotic Matching

A general approximate formula for the size effect on the nominal strength σ_N, spanning all the sizes and a range of corner angles, can be obtained through asymptotic matching [2]. The geometry of a hybrid joint with various corner angles is shown in Fig. 5.

A general approximate size effect equation has recently been developed for symmetrically loaded reentrant corners in homogenous materials of various corner angles. In that case, the entire singular stress field is governed solely by one real stress singularity [5]. For the general case of bimaterial joints in which the singularities are either a pair of complex conjugates or two un-

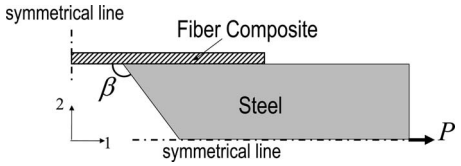

Fig. 5 General geometry of hybrid joint with varying joint angle

equal real numbers, the aforementioned analysis shows that only the real part of the strongest singularity exponent matters for the energy release rate at the large size limit. Therefore, an equation of similar type can be used to approximate the general size effect law for the hybrid joint

$$\sigma_N = \sigma_0 \left(1 + \frac{D}{D_{0\beta}}\right)^{\kappa(\beta)} \tag{26}$$

where σ_0 and $D_{0\beta}$ are parameters yet to be determined, κ is the real part of the exponent of the strongest stress singularity at the bimaterial corner, which is a function of corner angle β. The foregoing equation has been set up to match the following three essential asymptotic conditions.

(1) For $D/l_0 \to 0$, there must be no size effect since the FPZ occupies the whole structure (what matters in that case is solely the material strength, and not the energy release because the failure is quasiplastic).
(2) For $D/l_0 \to \infty$, Eq. (26) must match Eq. (24) as the large-size asymptote of the size effect law.
(3) For $\beta \to \pi$ (smooth surface, no corner), the size effect of this type must vanish (in that case, a cohesive crack initiates from a smooth surface, which leads to another type of size effect, Type 1 [2,3,37], which does not represent the limit case of the present size effect).

Note that the foregoing equation does not apply for the limiting case $\beta \to 0$. It is found that, in this limit, the structure may have a negative geometry (i.e., the derivative of the energy release rate function with respect to the crack length at constant load is negative). In that case, the maximum load does not occur at crack initiation, since the crack grows stably at increasing load, and the size effect is different (known as Type 3 size effect law [2,3]).

On the other hand, Eq. (26) for $\beta \to \pi$ does not continuously approach the Type 1 size effect law either. A generalization would be needed to describe the transition to Type 3 size effect law [3] (for $\beta \to 0$) and to Type 1 size effect (for $\beta \to \pi$).

By matching asymptotic condition 2 for arbitrary corner angles, one further obtains

$$\frac{\sigma_0(\beta)}{D_{0\beta}^{\kappa}} = \frac{\sqrt{EG_f(\beta)}}{|g(\beta)| c_f^{\kappa+0.5}} \tag{27}$$

Parameters $\sigma_0(\beta)$ and $D_{0\beta}$ can be easily obtained by calibrating the model on the basis of available size effect data. Nevertheless, it is impossible to obtain the fracture toughness, $G_f(\beta)$, and the effective size of FPZ, c_f, since, for a certain joint angle, there is only one matching condition involving these two fracture parameters. Note that, in general, the fracture toughness $G_f(\beta)$ can vary with the joint angle β due to mode mixity. The dependence of G_f on the mode mixity can be expressed as [17,34]

$$G_f = F(G_{\mathrm{I}}, G_{\mathrm{II}}, \phi) \tag{28}$$

where G_{I} and G_{II} denote the mode I and mode II fracture toughness. Phase angle ϕ, characterizing the degree of mode mixity, is defined for interfacial crack problems as [17,34,38]

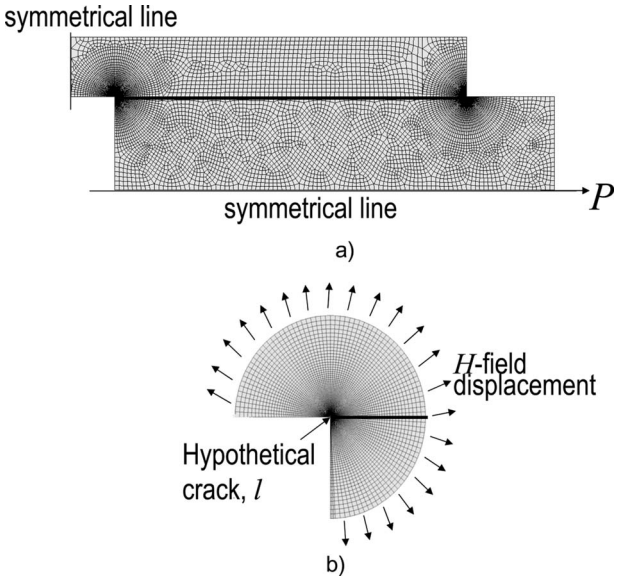

Fig. 6 (*a*) Finite element model of hybrid joint and (*b*) finite element model of ancillary boundary layer problem

$$\phi = \tan^{-1}\left[\frac{\mathrm{Im}(Kl^{i\eta'})}{\mathrm{Re}(Kl^{i\eta'})}\right] \tag{29}$$

where l is an arbitrary length scale, which might be chosen as the fracture process zone size (or multiple of atomic dimensions [38]). The stress intensity factor for the interfacial crack K is given by Eq. (17). The dimensionless complex number ζ in Eq. (17) depends on the geometry [21,22]. Hence, the phase angle ϕ varies with the geometry (joint angle). Therefore, these two fracture parameters, G_f and c_f, cannot be determined merely by fitting of the experimental size effect data, even if two sets of size effect data for two different joint angles are considered.

To overcome this obstacle, G_f needs to be estimated by numerical simulation with the cohesive crack model [39], where the cohesive law may be calibrated by the available experimental size effect data reported in the preceding paper [1]. Then the effective fracture process zone size c_f can be obtained from Eq. (27).

5 Numerical Evaluation of Model Parameters

In the foregoing calibration by Eq. (27), the model parameter $|g|$ needs to be determined by finite element analysis. To illustrate the numerical procedure, let us consider the joint used in test series II. In the numerical model, all the elastic moduli of the composite are normalized relative to the elastic modulus of steel, taken as $E = E(\text{steel}) = 1$, and the applied force P and the characteristic dimension D are chosen as 1.

Parameter $|g|$ can be obtained by calculating the energy release rate at the tip of the interfacial crack, which lies well within the singular stress field characterized by H. This parameter can be calculated in two steps, as follows.

First, the singular stress zone is obtained by finite element analysis of the joint. In the linear elastic finite element model, eight-node quadrilateral elements are used for both materials, as shown in Fig. 6(*a*). To obtain the singular field, normally expressed in polar coordinates, the regions near the bimaterial corners are meshed by numerous rings of elements, which are progressively refined on approach to the tip so that the ratio between the smallest and largest element sizes is about 1: 100.

Figure 7 shows, in the logarithmic scale, the profiles of magnitude of normal and shear stress ($\sigma_{\theta\theta}$ and $\sigma_{r\theta}$) along the interface, for both corners. For the left corner of the joint (Fig. 7(*a*)), the slopes of the asymptotes of $|\sigma_{\theta\theta}|$ and $|\sigma_{r\theta}|$ in the logarithmic scale

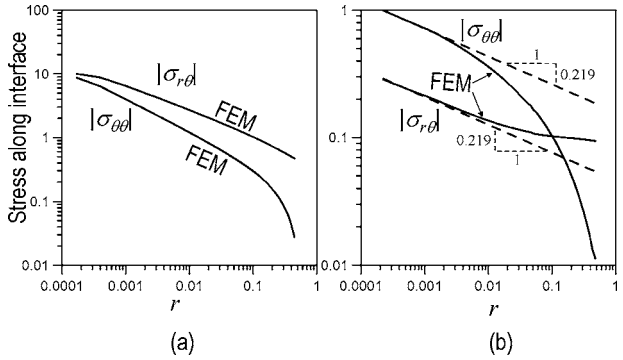

Fig. 7 Normal and shear stress along the interface: (*a*) left corner and (*b*) right corner

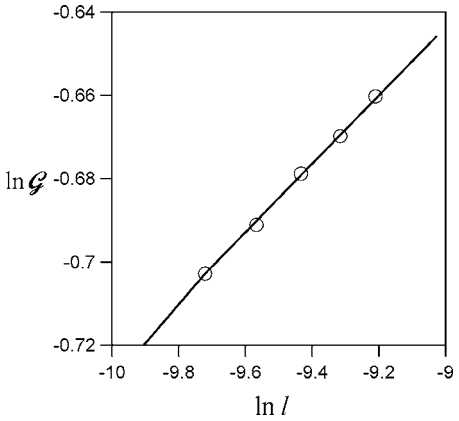

Fig. 8 Energy release rate at the hypothetical interfacial crack tip

plot are not the same. This difference is due to the fact that the exponent of stress singularity at this corner is complex. The asymptotic stress field is given by Eq. (14), which can further be expressed as

$$\sigma_{ij} = |H||\alpha_{ij}(\theta)|r^{\kappa}\cos(\vartheta_{ij} + \eta \ln r) \tag{30}$$

It is obvious that the dependence of σ_{ij} on r is not a simple power law. Due to the unknown variable ϑ_{ij}, which characterizes the mode mixity, it is impossible to determine the complex exponent of stress singularity simply by matching the stress profile along the interface only, and so the reach of the singular stress zone is not known. As for the stress profile oscillation, which must occur sufficiently close to the corner tip, its region is normally very small due to the very small value of the imaginary part η. It is for this reason that this oscillation is not generally reflected in finite element results.

At the right corner of the joint, the asymptotes of $|\sigma_{\theta\theta}|$ and $|\sigma_{r\theta}|$ are seen to have the same slope (Fig. 7(*b*)). This indicates that the stress singularity at that corner must be real and the near-tip stress field is given by $\sigma_{ij}=Hr^{\kappa}\alpha_{ij}(\theta)$ [26]. By matching the asymptotic stress field, the stress singularity exponent is found to be -0.219, and so the corresponding displacement singularity exponent is 0.781. This validates the previous calculations made by the complex potential method.

Second, one needs to solve an ancillary boundary layer problem which couples the inner stress field caused by the interfacial crack to the outer singular H-field. The boundary layer problem consisting of a semicircular region (fiber composite) and a quartercircular region (steel) (Fig. 6(*b*)) is subjected to displacements of the asymptotic H-field, which can be directly obtained from the FEM analysis in the step 1. Since the exact reach of the H-field is not determined, the H-field displacement is extracted at a reasonably small radius ($r/D \approx 0.01$). The interfacial crack length l is chosen to be very small compared with the dimension of the boundary layer. This ensures the crack to lie well within the H-field. The energy release rate $\mathcal{G}$ at the interfacial crack tip is directly calculated via the J-integral using the commercial FEM software ABAQUS [40]. When the loading, dimension, and elastic constants are normalized, one may rewrite Eq. (23) as follows:

$$\log \mathcal{G} = (1 + 2\kappa)\log(l) + 2\log|g| \tag{31}$$

Upon considering various small crack lengths l, one obtains the relationship between $\log \mathcal{G}$ and $\log l$ (Fig. 8). It is seen to follow a straight line, whose slope is 0.082. This agrees well with the value of $(1+2\kappa)$. One can then easily obtain the value $|g|=1.042$.

6 Conclusions

With the help of asymptotic matching, a general approximate size effect law for the strength of hybrid metal-composite joints can be derived from the near-tip asymptotic stress fields of a bimaterial corner and of an interface crack emanating from this corner.

The size effect law derived is validated by comparison with size effect experiments on metal-composite joints with two kinds of fiber-polymer composites.

The size effect in hybrid joints is quite strong. Thus it is unsafe to design large hybrid joints on the basis of classical material failure criteria expressed in terms of stresses or strains, or both.

Neither it is safe to extrapolate from small-scale laboratory tests of hybrid joints to large structure sizes without considering the size effect.

Acknowledgment

The present analysis was supported under ONR Grant No. N00014-07-1-0313 to Northwestern University, from a program directed by Dr. Roshdy Barsoum.

References

[1] Yu, Q., Bažant, Z. P., Bayldon, J., Le, J.-L., Caner, F. C., Ng, W. H., Waas, A. M., and Daniel, I. M., (2010), "Scaling of Strength of Metal-Composite Joints—Part I: Experimental Investigation," ASME J. Appl. Mech., **77**, p. 011011.
[2] Bažant, Z. P., 2005, *Scaling of Structural Strength*, 2nd ed., Elsevier, London.
[3] Bažant, Z. P., 2004, "Scaling Theory for Quasibrittle Structural Failure," Proc. Natl. Acad. Sci. U.S.A., **101**(37), pp. 13400–13407.
[4] Williams, M. L., 1952, "Stress Singularities Resulting From Various Boundary Conditions in Angular Corners of Plates in Extension," ASME J. Appl. Mech., **74**, pp. 526–528.
[5] Bažant, Z. P., and Yu, Q., 2006, "Size Effect on Strength of Quasibrittle Structures With Reentrant Corners Symmetrically Loaded in Tension," J. Eng. Mech., **132**(11), pp. 1168–1176.
[6] Bažant, Z. P., 1984, "Size Effect in Blunt Fracture: Concrete, Rock, Metal," J. Eng. Mech., **110**(4), pp. 518–535.
[7] Bažant, Z. P., 1993, "Scaling Laws in Mechanics of Failure," J. Eng. Mech., **119**(9), pp. 1828–1844.
[8] Bažant, Z. P., 1997, "Scaling of Quasibrittle Fracture: Asymptotic Analysis," Int. J. Fract., **83**(1), pp. 19–40.
[9] Bažant, Z. P., and Planas, J., 1997, *Fracture and Size Effect in Concrete and Other Quasibrittle Materials*, CRC, Boca Raton, FL.
[10] Bogy, D. B., 1971, "Two Edge-Bonded Elastic Wedges of Different Materials and Wedge Angles Under Surface Tractions," ASME J. Appl. Mech., **38**, pp. 377–385.
[11] Hein, V. L., and Erdogan, F., 1971, "Stress Singularities in a Two-Material Wedge," Int. J. Fract. Mech., **7**, pp. 317–330.
[12] Achenbach, J. D., Bažant, Z. P., and Khetan, R. P., 1976, "Elastodynamic Near-Tip Fields for a Crack Propagating Along the Interface of Two Orthotropic Solids," Int. J. Eng. Sci., **14**, pp. 811–818.
[13] Barsoum, R. S., 1988, "Application of the Finite Element Iterative Method to the Eigenvalue Problem and a Crack Between Dissimilar Media," Int. J. Numer. Methods Eng., **26**, pp. 541–554.
[14] Barsoum, R. S., and Freese, C. E., 1984, "An Interative Approach for the Evaluation of Delamination Stresses in Laminated Composite," Int. J. Numer. Methods Eng., **20**, pp. 1415–1431.
[15] Desmorat, R., and Leckie, F. A., 1998, "Singularities in Bimaterials: Parametric Study of an Isotropic/Anisotropic Joint," Eur. J. Mech. A/Solids, **17**, pp.

33–52.
[16] Lekhnitskii, S. G., 1968, *Anisotropic Plates*, Gorden & Beach Science, London.
[17] Suo, Z., 1990, "Singularities, Interfaces and Cracks in Dissimilar Anisotropic Media," Proc. R. Soc. London, Ser. A, **427**, pp. 331–358.
[18] Gomez, F. J., and Elices, M., 2003, "A Fracture Criterion for Sharp V-Notched Samples," Int. J. Fract., **123**, pp. 163–175.
[19] Grenestedt, J. L., and Hallstrom, S., 1997, "Crack Initiation From Homogeneous and Bimaterial Corners," ASME J. Appl. Mech., **64**, pp. 811–818.
[20] Leguillon, D., 2002, "Strength or Toughness? A Criterion for Crack Onset at a Notch," Eur. J. Mech. A/Solids, **21**, pp. 61–72.
[21] Labossiere, P. E. W., Duun, M. L., and Cunningham, S. J., 2002, "Application of Bimaterial Interface Corner Failure Mechanics to Silicon/Glass Anodic Bonds," J. Mech. Phys. Solids, **50**, pp. 405–433.
[22] Liu, D., and Fleck, N. A., 1999, "Scale Effect in the Initiation of Cracking of a Scarf Joint," Int. J. Fract., **95**, pp. 67–88.
[23] Reedy, E. D., Jr., 1993, "Asymptotic Interface-Corner Solutions for Butt Tensile Joints," Int. J. Solids Struct., **30**(6), pp. 767–777.
[24] Reedy, E. D., Jr., 2000, "Comparison Between Interface Corner and Interfacial Fracture Analysis of an Adhesively-Bonded Butt Joint," Int. J. Solids Struct., **37**, pp. 2429–2442.
[25] Zhang, Z., and Suo, Z., 2007, "Split Singularities and the Competition Between Crack Penetration and Debond at a Bimaterial Interface," Int. J. Solids Struct., **44**, pp. 4559–4573.
[26] Banks-Sills, L., and Sherer, A., 2002, "A Conservative Integral for Determining Stress Intensity Factors of a Bimaterial Notch," Int. J. Fract., **115**, pp. 1–26.
[27] Liu, X. H., Suo, Z., and Ma, Q., 1998, "Split Singularities: Stress Field Near the Edge of a Silicon Die on a Polymer Substrate," Acta Mater., **47**(1), pp. 67–76.
[28] Munz, D., and Yang, Y. Y., 1993, "Stress Near the Edge of Bonded Dissimilar Materials Described by Two Stress Intensity Factors," Int. J. Fract., **60**, pp. 169–177.
[29] Bažant, Z. P., Zhou, Y., Daniel, I. M., Caner, F. C., and Yu, Q., 2006, "Size Effect on Strength of Laminate-Foam Sandwich Plates," ASME J. Eng. Mater. Technol., **128**(3), pp. 366–374.
[30] Barenblatt, G. I., 1978, *Similarity, Self-Similarity and Intermediate Asymptotics*, Girometeoizdat, Moscow.
[31] Barenblatt, G. I., 1996, *Scaling, Self-Similarity and Intermediate Asymptotics*, Cambridge University Press, Cambridge, UK.
[32] Muki, R., and Westmann, R. A., 1974, "Crack Emanating From an Open Notch," J. Elast., **4**(3), pp. 173–186.
[33] Westmann, R. A., 1975, "Geometrical Effects in Adhesive Joints," Int. J. Eng. Sci., **13**, pp. 369–391.
[34] Hutchinson, J. W., and Suo, Z., 1992, "Mixed Mode Cracking in Layered Materials," Adv. Appl. Mech., **29**, pp. 64–191.
[35] Agrawal, A., and Karlsson, A. M., 2006, "Obtaining Model Mixity for a Bimaterial Interface Crack Using the Virtual Crack Closure Technique," Int. J. Fract., **141**, pp. 75–98.
[36] Toya, M., 1992, "On the Mode I and Mode II Energy Release Rates of an Interface Crack," Int. J. Fract., **56**, pp. 345–352.
[37] Bažant, Z. P., and Xi, Y., 1991, "Statistical Size Effect in Quasi-Brittle Structures: II. Nonlocal Theory," J. Eng. Mech., **117**(11), pp. 2623–2640.
[38] Rice, J. R., 1988, "Elastic Fracture Mechanics Concepts for Interface Cracks," ASME J. Appl. Mech., **55**, pp. 98–103.
[39] Caner, F. C., and Bažant, Z. P., 2009, "Size Effect on Strength of laminate-Foam Sandwich Plates: Finite Element Analysis With Interface Fracture," Composites, Part B, **40**(5), pp. 337–348.
[40] 2006, ABAQUS/Standard Users Manual, *Version 6.6*, Hibbitt, Karlsson & Sorensen Inc., Pawtucket, RI.

Importance of Higher Order Modes and Refined Theories in Free Vibration Analysis of Composite Plates

S. Brischetto[1]
Department of Aeronautics and Space Engineering,
Politecnico di Torino,
Turin 10129, Italy
e-mail: salvatore.brischetto@polito.it

E. Carrera
Professor of Aerospace Structures and Aeroelasticity
Department of Aeronautics and Space Engineering,
Politecnico di Torino,
Turin 10129, Italy

This paper evaluates frequencies of higher-order modes in the free vibration response of simply-supported multilayered orthotropic composite plates. Closed-form solutions in harmonic forms are given for the governing equations related to classical and refined plate theories. Typical cross-ply (0 deg/90 deg) laminated panels (10 and 20 layers) are considered in the numerical investigation (these were suggested by European Aeronautic Defence and Space Company (EADS) in the framework of the "Composites and Adaptive Structures: Simulation, Experimentation and Modeling" (CASSEM) European Union (EU) project. The Carrera unified formulation has been employed to implement the considered theories: the classical lamination theory, the first-order shear deformation theory, the equivalent single layer model with fourth-order of expansion in the thickness direction z, and the layerwise model with linear order of expansion in z for each layer. Higher-order frequencies and the related harmonic modes are computed by varying the number of wavelengths (m,n) in the two-plate directions and the degrees of freedom in the plate theories. It can be concluded above all that—refined plate models lead to higher-order frequencies, which cannot be computed by simplified plate theories—frequencies related to high values of wavelengths, even the fundamental ones, can be wrongly predicted when using classical plate theories, even though thin plate geometries are analyzed. [DOI: 10.1115/1.3173605]

1 Introduction

The application of composite materials in aircraft and space vehicles has increased rapidly over the past 3 decades due to their high strength and low weight. Composite materials offer many advantages, with respect to traditional metallic ones. However, a number of complicating effects arises in their design, analysis, modeling, and manufacturing [1]. In this work, attention is directed to the evaluation of frequencies for higher modes in the free vibration response. The behavior and design of vibrating shells and plates have been extensively discussed in the reports by Leissa [2,3], and more recently in the book by Werner [4], among others.

In the most general case of three-dimensional (3D) analyses, the number of frequencies for a free vibration problem is infinite: three displacement components (three degrees of freedom (DOF)) in each point (which are ∞ in the three directions x,y,z) leads to $3\times\infty^3$ vibration modes. Assumptions are made in the thickness direction z in the case of a two-dimensional plate/shell problem, that is, the three displacements in each point are expressed in terms of a given number of degrees of freedom (NDOF), which varies from theory to theory. As a result, the number of vibration modes is $\text{NDOF}\times\infty^2$. For beams it would be $\text{NDOF}\times\infty^1$. In the case of the application of computational models, such as the finite element method (FEM), the number of modes is a finite number; it coincides with the number of employed degrees of freedom: $\Sigma_1^{\text{Node}}\text{NDOF}_i$, where "Node" denotes the number of nodes used in the FE mathematical model, and NDOF_i is the NDOF in the i-node. Limitations of FE method are overcome by using the statistical energy analysis (SEA) method, which is usually preferred in case of higher modes such as acoustics problems [5]. It appears clear that some modes are tragically lost in simplified models (such as two-dimensional models) as well as in computational ones.

The case in which closed-form solutions are available for a given set of differential governing equations is of particular interest. Interest is herein focused on simply-supported multilayered plates made of orthotropic layers for which Navier type solutions exist. Harmonic forms are assumed for the unknown variables in the in-plane directions (x,y) for each couple of wave numbers (m,n). The number of vibration modes is in this case simply given by the NDOF of the adopted plate theory for each couple of integer (m,n) values. Since (m,n) can assume infinity values, the number of modes is $\text{NDOF}\times\infty^2$, as in the continuous case. In the above described scenario, the two following points are of interest as far as the evaluation of higher modes is concerned.

1. Different plate theories lead to different numbers of vibration modes, and higher modes related to higher NDOF can only be obtained by implementing refined plate theories.
2. Other higher vibration modes can be obtained by considering high values of m,n.

In conclusion, a complete investigation of higher vibration modes requires the use of refined theories and higher numbers of the couple (m,n). This investigation is the subject of the present paper. An overview on available works on this topic is made in the following.

The main features of free vibration analysis for composite plates have been discussed in the paper by Noor [6]; this paper summarizes results based on two-dimensional plate theories for a low-frequency free vibration analysis of simply-supported cross-ply laminated plates consisting of a large number of layers. These results show that the error in the predictions of the classical plate

[1]Corresponding author.

Contributed by the Applied Mechanics Division of ASME for publication in the JOURNAL OF APPLIED MECHANICS. Manuscript received March 12, 2008; final manuscript received April 14, 2009; published online October 5, 2009. Review conducted by Anthony Waas.

theories is highly dependent on the number and stacking of the layers, the degree of orthotropy of the individual layers, and the thickness ratio of the plate. Liew et al. [7] wrote a review of existing literature on the vibration analysis of thick plates (132 publications were cited) up to 1995.

The main aim of this paper is to understand the importance of advanced and refined two-dimensional models in the case of higher modes for the free vibration response of multilayered composite plates. Shuyu [8] wrote that shear deformation and the rotary inertia could be ignored for thin plates, but for higher frequencies, even if the plate is very thin, the shear deformation cannot be ignored, so classical theories are suitable only for thin plates and vibrational orders of low natural frequency. These conclusions refer to isotropic plates, and the situation drops away for composite plates. Thick isotropic plates are considered in Refs. [9,10] for low frequencies and the finite element method. Different boundary conditions, shapes of the considered plate, and thickness ratios are considered in Refs. [11–18], but they are restricted to isotropic shells and plates and to low and medium frequencies. Interesting conclusions were obtained for homogeneous plates, in the case of high-frequency investigations, by Zhao et al. [19] who introduced a discrete singular convolution (DSC) algorithm to investigate square isotropic plates with six distinct boundary conditions. The method was applied for high-frequency vibration analysis by providing extremely accurate frequency parameters for plates vibrating in the first 5000 modes, and an increase in mesh size is clearly shown for high mode numbers. Via new hierarchical functions, Beslin and Nicolas [20] investigated very high modes (up to 2048) for rectangular steel plates with different boundary conditions. Other interesting investigations for high frequencies, in the case of analytical or numerical solutions, are reported in Refs. [21–25]. In particular, Wei et al. [25] investigated high-frequency vibrations of structures for isotropic plates, by means of the DSC algorithm. The investigation considered the first 7100 modes of the beam and the first 4500 modes of the two-span plates.

The above cited works all concern homogeneous structures, however, the situation becomes more critical in the case of laminated structures. A substantial number of papers have been dedicated to the free vibrational response of multilayered plates, in particular, for low and medium frequencies ranges. Among these papers, Ref. [26] is of particular interest, where Kim and Hwang applied a modal parameter estimation technique to investigate natural frequencies and damping ratios of cross-ply and angle-ply composite laminates. Gorman and Ding [27] used the superposition method to obtain the first six modes for orthotropic plates and the first four modes for cross-ply plates. Comparisons, for low modes, between the traditional superposition method and the superposition-Galerkin method are reported in Ref. [28]. Cross-ply and angle-ply laminated plates with different boundary conditions are considered in Refs. [29,30]; the first paper is about a recursive solution based on a Lagrange multiplier method, and the second is about a finite element method (based on a third-order shear deformation theory), which, in the case of linear analysis, underlines the effects of wide-to-thickness ratio, material anisotropy, fiber orientation, aspect ratio, boundary conditions, and number of layers. In Refs. [31–35], for the case of analytical, semi-analytical, and finite element solutions, advanced theories such as mixed approaches, higher-order zig-zag theories, and higher-order discrete layer methods have been proposed for composite sandwiches and laminated plates, shells, beams and blades; all these investigations are restricted to low and natural frequencies. Other investigations about the free vibrations of composite structures, in the range of low and medium frequencies, are presented in Refs. [36–39].

Papers that consider higher mode investigations are not so numerous, and these are even less in the cases of thick plates and/or composite structures. Reference [40], which applies a displacement finite element based on C^0-continuous displacements to simply-supported homogeneous and laminated plates in the case of thick structures and high frequencies modes, is of interest. A comparison with the exact solution of higher-order theories (HOTs), the first-order shear deformation theory (FSDT), and the classical lamination theory (CLT) is proposed for the first five antisymmetric modes and the first three symmetric modes. In Refs. [41,42], by means of the hierarchical finite element method (HFEM) and the Galerkin element method (GEM), respectively, the vibration analysis of laminated rectangular plates and damped sandwich plates is led over a wide frequency range.

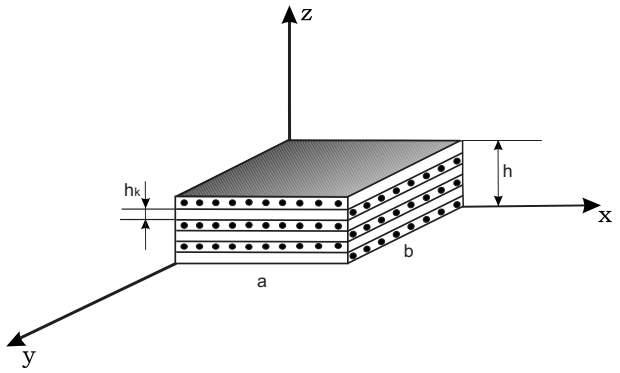

Fig. 1 Geometry and notations for the considered multilayered plates

In the recent past, the free vibration response of multilayered plates and shells has been investigated in various articles by employing the Carrera unified formulation (CUF): The transverse normal stress effects have been evaluated in Ref. [43], the benefits of mixed models based on the Reissner's mixed variational theorem have been considered in Ref. [44], and the advantages of layer-wise mixed models have been outlined in Ref. [45]. The present paper uses CUF to explore frequencies of higher-order free vibration modes, according to points 1 and 2. The aim is duplicate—to show the limitations of classical theories, such as the CLT and the FSDT—to predict the frequencies of the higher modes. Two refined plate theories are employed for this purpose: the first is based on an equivalent single layer (ESL) approach with fourth-order expansion of displacements in the thickness direction z; the second one is a layerwise (LW) model with linear expansion in the z direction in each layer. Numerical solutions are given in closed form in the case of two cross-ply laminated plates whose data have been provided by EADS in the framework of the EU FP7 project known as CASSEM.

The paper has been organized as follows: Sec. 2 illustrates the kinematics of plate theories; Sec. 3 outlines the governing equations; and the numerical analysis and conclusions are given in Secs. 4 and 5, respectively.

2 Kinematic Description of the Considered Plate Theories

Classical theories (such as the CLT and the FSDT), refined models (such as the ESL with fourth-order of expansion ($N=4$) and the LW with linear order of expansion in the z direction ($N=1$)) are employed for the dynamic analysis of laminated plates. These theories are developed in the framework of the CUF [46,47].

2.1 Classical Theories: CLT and FSDT. Multilayered plates are structures in which one dimension, the thickness, is one or two orders of magnitude less than the in-plane ones. This peculiarity leads to the possibility of modeling these structures as a two-dimensional continuum (see Fig. 1).

Classical two-dimensional theories such as CLT and FSDT are models in which the number of variables does not depend on the

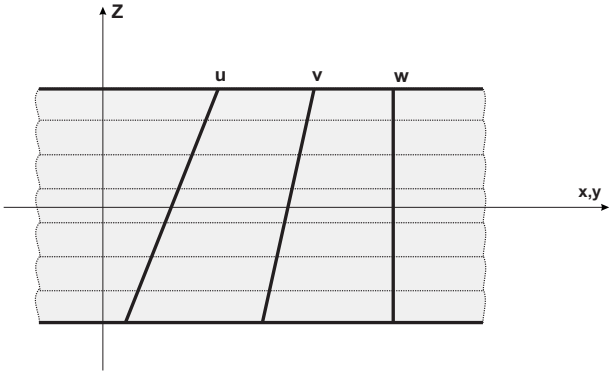

Fig. 2 Displacements distribution in thickness direction in case of CLT and FSDT

number of layers (for a detailed overview see Ref. [48]). Kirchhoff hypotheses are considered in the CLT case as follows:

(1) Straight lines perpendicular to the midsurface before deformation remain straight after deformation.
(2) The transverse normals do not experience elongation.
(3) The transverse normals rotate in order to remain perpendicular to the midsurface after deformation.

The first two assumptions imply that the transverse displacement is independent of the transverse (or thickness) coordinate, and that the transverse normal strain ϵ_{zz} is neglected. The third assumption results in zero transverse shear strains ($\epsilon_{xz}=\epsilon_{yz}=0$). The displacement field (u,v,w) can then be described by using the following relations:

$$u(x,y,z) = u_0(x,y) - z\frac{\partial w_0}{\partial x}$$
$$v(x,y,z) = v_0(x,y) - z\frac{\partial w_0}{\partial y} \quad (1)$$
$$w(x,y,z) = w_0(x,y)$$

where the index 0 indicates midsurface displacement values.

The third of the above hypothesis is removed in the FSDT case, and the transverse normals do not remain perpendicular to the midsurface after deformation. The displacement field of FSDT is as follows:

$$u(x,y,z) = u_0(x,y) + z\Phi_x(x,y)$$
$$v(x,y,z) = v_0(x,y) + z\Phi_y(x,y) \quad (2)$$
$$w(x,y,z) = w_0(x,y)$$

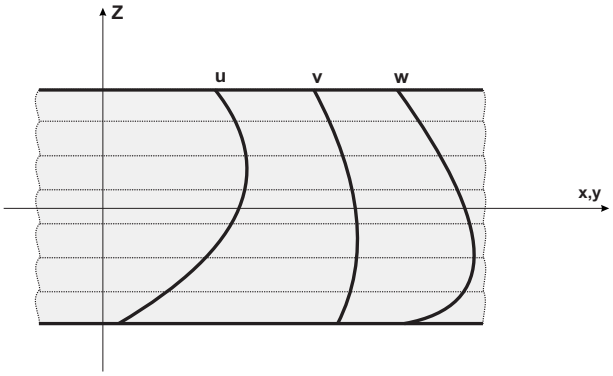

Fig. 3 Displacements distribution in thickness direction in case of ESL(N=4)

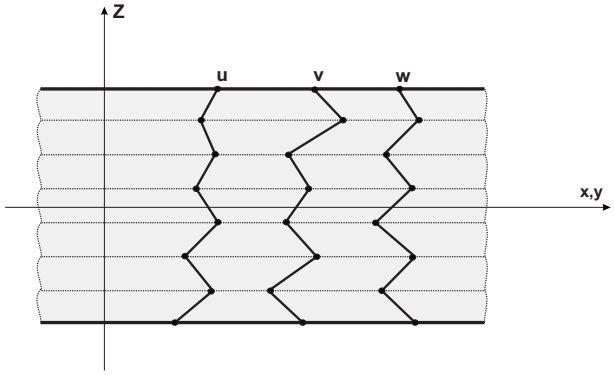

Fig. 4 Displacements distribution in thickness direction in case of LW(N=1)

where

$$\frac{\partial u}{\partial z} = \Phi_x, \quad \frac{\partial v}{\partial z} = \Phi_y \quad (3)$$

denote the rotations of the $z-y$ and $z-x$ planes, respectively. Figure 2 shows the displacements field in z direction of a typical laminate, in the case of CLT and FSDT. For these two classical kinematics, plane-stress conditions are applied as in Ref. [49] to avoid the so called Poisson locking phenomena.

2.2 Carrera Unified Formulation and Refined Models. The key point of the CUF is the use of generalized assumptions for the primary variables of the problem; the generic variable $\boldsymbol{a}$ is expanded using a set of thickness functions that depend only on the thickness coordinate z (a detailed description of the CUF can be found in Refs. [46,47]):

$$\boldsymbol{a}(x,y,z) = F_\tau(z)\boldsymbol{a}_\tau(x,y) \quad (4)$$

where $\tau=0,1,\ldots,N$, and N is the desired order of the expansion. F_τ are the employed thickness functions. ESL and LW approaches can be both developed by appropriate choice of thickness functions.

Equivalent single layer models are based on the assumption of a global description of the displacement field along the whole plate thickness; a Taylor expansion is used as follows:

$$\boldsymbol{u}(x,y,z) = F_\tau(z)\boldsymbol{u}_\tau(x,y) = z^r\boldsymbol{u}_r, \quad r=0,1,2,\ldots,N \quad (5)$$

N is a free parameter that can assume values from 1 (linear) to 4 (fourth order). The case $N=4$ is used in this work as follows:

$$u(x,y,z) = u_0(x,y) + zu_1(x,y) + z^2u_2(x,y) + z^3u_3(x,y) + z^4u_4(x,y)$$
$$v(x,y,z) = v_0(x,y) + zv_1(x,y) + z^2v_2(x,y) + z^3v_3(x,y) + z^4v_4(x,y)$$
$$w(x,y,z) = w_0(x,y) + zw_1(x,y) + z^2w_2(x,y) + z^3w_3(x,y) + z^4w_4(x,y) \quad (6)$$

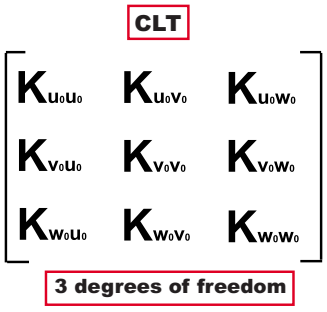

Fig. 5 Multilayer stiffness matrix for CLT

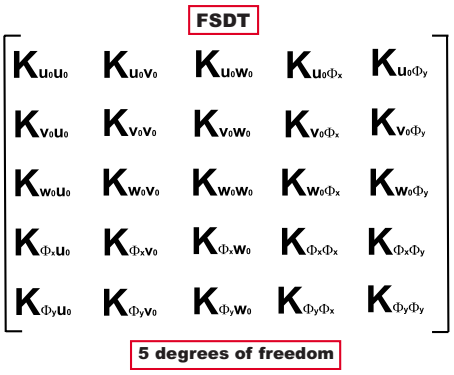

Fig. 6 Multilayer stiffness matrix for FSDT

Related displacement fields in the z direction are drawn in Fig. 3.

A layerwise description includes an independent expansion for each layer k as follows:

$$\boldsymbol{u}^k(x,y,z) = F_t(z)\boldsymbol{u}_t^k(x,y) + F_b(z)\boldsymbol{u}_b^k(x,y) + F_r(z)\boldsymbol{u}_r^k(x,y) = F_\tau \boldsymbol{u}_\tau^k \tag{7}$$

with

$$\tau = t,b,r, \quad r = 2, \ldots, N, \quad k = 1,2, \ldots, N_L$$

where t and b mean top and bottom of the considered layer, and r represents the higher-order terms of expansion up to the fourth ($N=4$); N_L is the number of layers. F_τ are appropriate combinations of Legendre polynomials (see Refs. [46,47]). In the present investigation a LW model with $N=1$ will be used as follows:

$$\begin{aligned} u^k(x,y,z) &= F_t(z)u_t^k(x,y) + F_b(z)u_b^k(x,y) \\ v^k(x,y,z) &= F_t(z)v_t^k(x,y) + F_b(z)v_b^k(x,y) \\ w^k(x,y,z) &= F_t(z)w_t^k(x,y) + F_b(z)w_b^k(x,y) \end{aligned} \tag{8}$$

The displacement forms in the z direction are considered in Fig. 4.

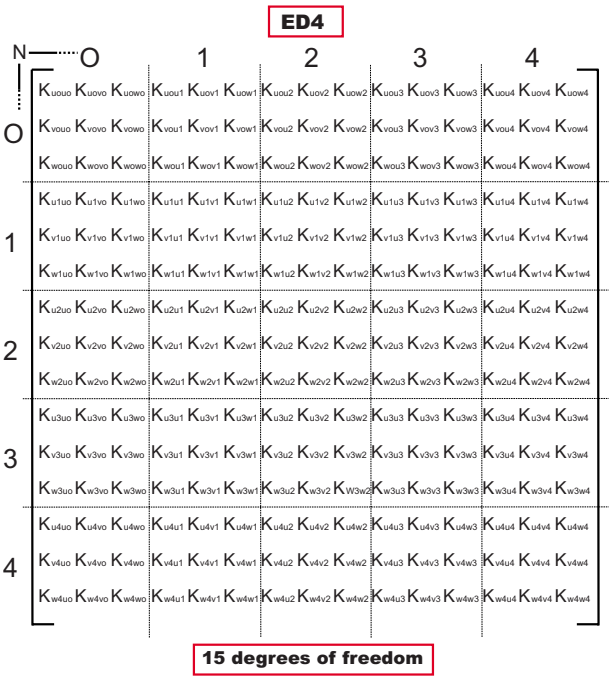

Fig. 7 Multilayer stiffness matrix for ESL(N=4)

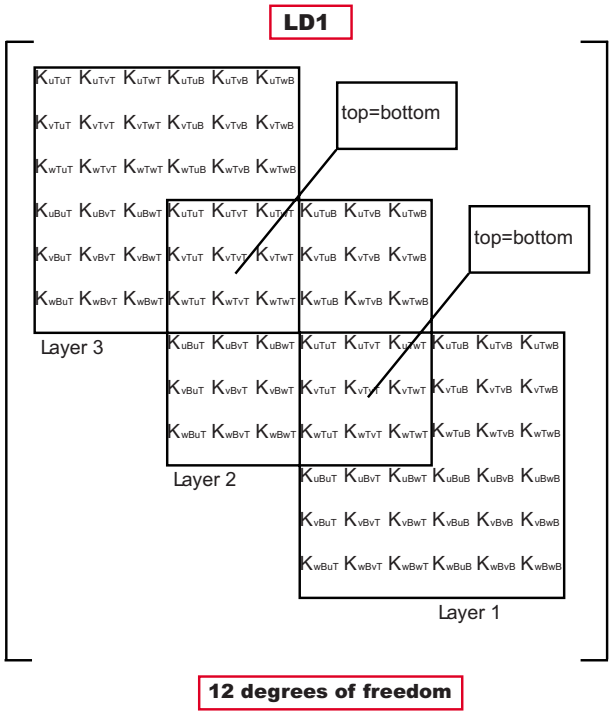

Fig. 8 Multilayer stiffness matrix for LW(N=1) in case of a three-layered plate

CLT and FSDT can be obtained as particular cases of ESL models ($N=1$), by using a penalty technique on. CLT is obtained by forcing constant w and infinite transverse shear correction factor; FSDT has constant w and the transverse shear correction factor is equal to 1 (see Refs. [46,47]).

3 Governing Equations and Fundamental Nuclei

For a dynamic problem related to multilayered plates, the principle of virtual displacements (PVDs) states [47],

$$\int_V (\delta\boldsymbol{\epsilon}_{pG}^T\boldsymbol{\sigma}_{pC} + \delta\boldsymbol{\epsilon}_{nG}^T\boldsymbol{\sigma}_{nC})dV = \delta L^{\text{in}} + \delta L^e \tag{9}$$

where subscripts p and n indicate in-plane and out-plane components, respectively; $\boldsymbol{\sigma}$ and $\boldsymbol{\epsilon}$ are the stress and strain vectors, δL^{in} is the virtual variation of inertial work, δL^e is the virtual variation of external work, and V is the considered volume.

The governing equations of the proposed models can be obtained upon substitution of geometrical relations, constitutive equations, and by applying the unified formulation by Carrera [46,47].

Geometrical relations link strain components to displacement vector, they are introduced in Eq. (9) where the subscript G is considered. The following relations hold in case of a plate:

$$\boldsymbol{\epsilon}_{pG}^k = [\epsilon_{xx}, \epsilon_{yy}, \gamma_{xy}]^{kT} = \boldsymbol{D}_p\boldsymbol{u}^k, \quad \boldsymbol{\epsilon}_{nG}^k = [\gamma_{xz}, \gamma_{yz}, \epsilon_{zz}]^{kT} = (\boldsymbol{D}_{np} + \boldsymbol{D}_{nz})\boldsymbol{u}^k \tag{10}$$

where $\boldsymbol{\epsilon}_{pG}^k$ and $\boldsymbol{\epsilon}_{nG}^k$ are the in-plane and out-plane strain components, respectively. $\boldsymbol{u}^k = [u^k, v^k, w^k]$ is the displacement vector, and k indicates the considered layer. The explicit form of the introduced arrays are as follows:

Table 1 Number of frequencies for the two considered plates

	$m=n=500$	
	$N_L=10$ (10-layered plate)	$N_L=20$ (20-layered plate)
CLT ($m\times n\times$NDOF)	$500\times500\times3=750{,}000$	$500\times500\times3=750{,}000$
FSDT ($m\times n\times$NDOF)	$500\times500\times5=1{,}250{,}000$	$500\times500\times5=1{,}250{,}000$
ESL($N=4$) ($m\times n\times$NDOF)	$500\times500\times15=3{,}750{,}000$	$500\times500\times15=3{,}750{,}000$
LW($N=1$) ($m\times n\times((N_L+1)\times3)$)	$500\times500\times33=8{,}250{,}000$	$500\times500\times63=15{,}750{,}000$

Table 2 Geometry and materials of multilayered plates in Refs. [50,51]

	Assessment [50]
$\frac{G_{12}}{E_T}=\frac{G_{13}}{E_T}$	0.50
$\frac{G_{23}}{E_T}$	0.35
$\nu_{12}=\nu_{13}$	0.30
ν_{23}	0.49
N_L(No. of layers)	10
θ(orientation)	0 deg/90 deg/…
$a=b$ (m)	-
$\frac{a}{h}$	5

	Assessment [51]
$\frac{E_L}{E_T}$	40
$\frac{G_{12}}{E_T}=\frac{G_{13}}{E_T}$	0.50
$\frac{G_{23}}{E_T}$	0.60
$\nu_{12}=\nu_{13}=\nu_{23}$	0.25
N_L(No. of layers)	4
θ(orientation)	0 deg/90 deg/90 deg /0 deg
$a=b$ (m)	-

Table 3 Free vibration response of a simply-supported square plate. Fundamental circular frequency $\bar{\omega}=\omega h\sqrt{\rho/E_T}$. Wavelengths $m=n=1$.

E_L/E_T	3	30
3D [50]	0.2530	0.4027
CLT	0.2858	0.6322
FSDT	0.2576	0.4306
ESL($N=1$)	0.2576	0.4306
LW($N=1$)	0.2534	0.4042
ESL($N=4$)	0.2539	0.4078
LW($N=4$)	0.2530	0.4027

$$\boldsymbol{D}_p=\begin{bmatrix}\partial_x & 0 & 0\\ 0 & \partial_y & 0\\ \partial_y & \partial_x & 0\end{bmatrix},\quad \boldsymbol{D}_{np}=\begin{bmatrix}0 & 0 & \partial_x\\ 0 & 0 & \partial_y\\ 0 & 0 & 0\end{bmatrix},\quad \boldsymbol{D}_{nz}=\begin{bmatrix}\partial_z & 0 & 0\\ 0 & \partial_z & 0\\ 0 & 0 & \partial_z\end{bmatrix} \tag{11}$$

the symbol ∂ indicates the partial derivatives.

Constitutive equations link stress components to strain components. They are introduced in Eq. (9) where the subscript C is considered. The following relations hold:

$$\boldsymbol{\sigma}_{pC}^k=[\sigma_{xx},\sigma_{yy},\sigma_{xy}]^{kT}=\boldsymbol{C}_{pp}^k\boldsymbol{\epsilon}_{pG}^k+\boldsymbol{C}_{pn}^k\boldsymbol{\epsilon}_{nG}^k,$$
$$\boldsymbol{\sigma}_{nC}^k=[\sigma_{xz},\sigma_{yz},\sigma_{zz}]^{kT}=\boldsymbol{C}_{np}^k\boldsymbol{\epsilon}_{pG}^k+\boldsymbol{C}_{nn}^k\boldsymbol{\epsilon}_{nG}^k \tag{12}$$

The explicit form of the introduced arrays are as follows:

$$\boldsymbol{C}_{pp}^k=\begin{bmatrix}C_{11} & C_{12} & C_{16}\\ C_{12} & C_{22} & C_{26}\\ C_{16} & C_{26} & C_{66}\end{bmatrix}^k,\quad \boldsymbol{C}_{pn}^k=\begin{bmatrix}0 & 0 & C_{13}\\ 0 & 0 & C_{23}\\ 0 & 0 & C_{36}\end{bmatrix}^k$$
$$\boldsymbol{C}_{np}^k=\begin{bmatrix}0 & 0 & 0\\ 0 & 0 & 0\\ C_{13} & C_{23} & C_{36}\end{bmatrix}^k,\quad \boldsymbol{C}_{nn}^k=\begin{bmatrix}C_{55} & C_{45} & 0\\ C_{45} & C_{44} & 0\\ 0 & 0 & C_{33}\end{bmatrix}^k \tag{13}$$

Closed form solutions are obtained for particular cases such as simply-supported plates, and particular conditions for the material properties. In this case the governing equations can be exactly solved. The following harmonic assumptions can be made for the field variables (see Refs. [43,47]):

$$u_\tau^k=\sum_{m,n}U_\tau^k\cos\frac{m\pi x_k}{a_k}\sin\frac{n\pi y_k}{b_k}e^{i\omega_{mn}t}\quad k=1,N_L$$
$$v_\tau^k=\sum_{m,n}V_\tau^k\sin\frac{m\pi x_k}{a_k}\cos\frac{n\pi y_k}{b_k}e^{i\omega_{mn}t}\quad \tau=t,b,r \tag{14}$$
$$w_\tau^k=\sum_{m,n}W_\tau^k\sin\frac{m\pi x_k}{a_k}\sin\frac{n\pi y_k}{b_k}e^{i\omega_{mn}t}\quad r=2,\ldots,N$$

in which a_k and b_k are the plate lengths in the x_k and y_k directions, respectively; U_τ^k, V_τ^k, and W_τ^k are the displacement amplitudes, while m and n are the correspondent wave numbers; $i=\sqrt{-1}$, t is the time, and ω_{mn} is the circular frequency. These assumptions correspond to the simply-supported boundary conditions. The sys-

Table 4 Free vibration response of a simply-supported square plate. Fundamental circular frequency $\bar{\omega}=\omega\sqrt{\frac{a^4\rho}{E_Th^2}}$. Wavelengths $m=n=1$.

a/h	2	4	10	20	100
CLT [51]	15.830	17.907	18.652	18.767	18.804
FSDT [51]	5.492	9.369	15.083	17.583	18.751
ESL($N=1$)	5.919	9.936	15.524	17.763	18.759
LW($N=1$)	5.414	9.473	15.334	17.703	18.761
ESL($N=4$)	5.380	9.384	15.232	17.655	18.754
LW($N=4$)	5.260	9.224	15.148	17.626	18.753

Table 5 Geometry and materials of multilayered plates for the two proposed benchmarks

	Material
E_{11} (GPa)	310
E_{22} (GPa)	6.50
E_{33} (GPa)	6.50
ν_{12}	0.365
ν_{13}	0.365
ν_{23}	0.365
G_{12} (GPa)	4.30
G_{13} (GPa)	4.30
G_{23} (GPa)	4.30
ρ (kg/m^3)	1500
	Benchmark 1
h_k(kth layer) (m)	0.0001
N_L(No. of layers)	10
θ(orientation)	0 deg/90 deg/…
a (m)	1.5
b (m)	1.5
	Benchmark 2
h_k(kth layer) (m)	0.0001
N_L(No. of layers)	20
θ(orientation)	0 deg/90 deg/…
a (m)	0.75
b (m)	0.75

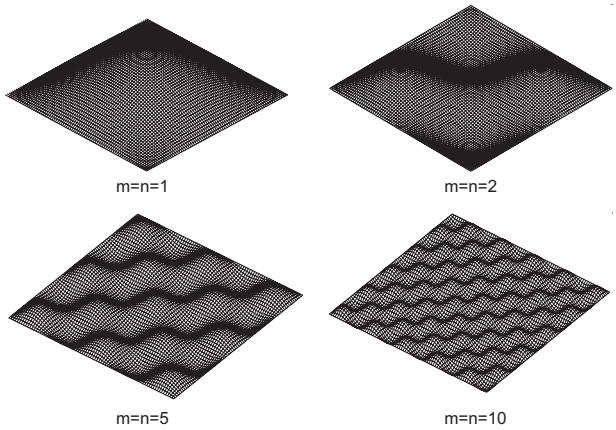

Fig. 9 Examples of in-plane modes

tem of governing equations, at multilayered plate level could be formally written as in the following:

$$\boldsymbol{Ku} = \boldsymbol{M\ddot{u}} \tag{15}$$

The stiffness matrix $\boldsymbol{K}$ and the inertial matrix $\boldsymbol{M}$ are assembled via indices τ and s for the order of expansion in the thickness direction z, and via the index k for the multilayer assembling (ESL or

Table 6 Benchmark 1, 10-layered plate, and $a/h=1500$. Comparison between classical, HOT, and LW theories. Circular frequencies parameter $\bar{\omega}=\omega\sqrt{a^4\rho/10^6E_Th^2}$.

					$m=1,\ n=1$					
CLT	0.0203	23.108	24.076							
FSDT	0.0203	23.108	24.076	6339.3	6339.3					
ESL(N=4)	0.0203	23.113	24.076	7617.3	5750.7	5750.7	15,285	47,267	11,540	31,616
	11,540	35,684	23,869	23,869	35,684					
LW(N=1)	0.0203	23.108	24.076	5772.8	5772.8	7646.5	11,688	11,688	15,482	17,890
	17,890	23,698	24,521	24,521	32,480	31,696	31,696	39,439	39,439	41,987
	47,530	47,530	83,970	80,981	52,244	73,175	55,246	55,245	62,947	61,134
	63,392	61,134	63,392							
					$m=5,\ n=5$					
CLT	0.5078	115.54	120.38							
FSDT	0.5078	115.54	120.38	6340.4	6340.3					
ESL(N=4)	0.5077	115.56	120.38	5752.0	5751.8	7617.2	……	……	……	……
LW(N=1)	0.5078	115.54	120.38	5773.9	5774.0	7646.5	……	……	……	……
					$m=10,\ n=10$					
CLT	2.0313	231.08	240.76							
FSDT	2.0299	231.08	240.75	6343.5	6344.0					
ESL(N=4)	2.0295	231.12	240.75	5755.8	5755.3	7617.1	……	……	……	……
LW(N=1)	2.0298	231.08	240.75	5777.4	5777.9	7646.3	……	……	……	……
					$m=50,\ n=50$					
CLT	50.737	1155.4	1203.8							
FSDT	49.873	1154.9	1203.3	6443.8	6458.1					
ESL(N=4)	49.684	1155.1	1203.0	5878.5	5865.6	7613.4	……	……	……	……
LW(N=1)	49.696	1154.9	1203.0	5887.2	5900.2	7642.8	……	……	……	……
					$m=100,\ n=100$					
CLT	202.38	2311.1	2407.6							
FSDT	189.67	2306.8	2403.3	6801.4	6748.8					
ESL(N=4)	187.13	2307.2	2401.5	6244.1	6197.7	7604.1	……	……	……	……
LW(N=1)	187.25	2306.8	2401.5	6218.0	6264.8	7634.1	……	……	……	……
					$m=500,\ n=500$					
CLT	4657.4	11,584	12,038							
FSDT	2379.6	11,196	11,514	13,639	13,961					
ESL(N=4)	2216.2	7576.2	11,116	11,433	12,981	13,145	……	……	……	……
LW(N=1)	2220.2	7609.8	11,111	11,431	13,011	13,146	……	……	……	……

Table 7 Benchmark 2, 20-layered plate, and $a/h=375$. Comparison between classical, HOT, and LW theories. Circular frequencies parameter $\bar{\omega}=\omega\sqrt{a^4\rho/10^6 E_T h^2}$.

					$m=1,\ n=1$					
CLT	0.0205	5.7765	6.0183							
FSDT	0.0205	5.7765	6.0182	396.21	396.20					
ESL($N=4$)	0.0205	5.7776	6.0182	359.43	359.42	476.03	955.24	2953.8	721.18	721.18
	1975.8	2230.0	1491.7	1491.6	2230.0					
LW($N=1$)	0.0205	5.7765	6.0182	359.69	359.70	476.38	721.54	721.54	955.71	1087.8
	1087.8	1440.9	1460.9	1460.9	1842.8	1842.8	1935.0	2236.1	2236.1	2441.0
	2642.7	2642.7	2961.9	3064.8	3064.8	3504.1	3504.1	3500.5	3961.6	3961.6
	4059.6	4437.3	4437.3	4641.5	4929.3	4929.3	5247.5	5433.3	5433.3	10495
	10,399	5877.6	10,121	5940.6	5940.6	9690.6	9146.1	6529.4	6437.8	6437.8
	8527.4	6904.9	6904.9	7196.8	7315.9	7315.9	7640.9	7640.9	7868.9	7923.2
	7923.2	7850.6	7850.6							
					$m=5,\ n=5$					
CLT	0.5128	28.882	30.091							
FSDT	0.5113	28.882	30.091	397.21	397.36					
ESL($N=4$)	0.5111	28.888	30.090	360.67	360.54	475.99	.....	.....	.....	.....
LW($N=1$)	0.5111	28.882	30.090	360.80	360.94	476.34	.....	.....	.....	.....
					$m=10,\ n=10$					
CLT	2.0504	57.765	60.183							
FSDT	2.0273	57.761	60.178	400.35	400.93					
ESL($N=4$)	2.0228	57.772	60.172	364.51	363.99	475.87	.....	.....	.....	.....
LW($N=1$)	2.0229	57.761	60.172	364.26	364.78	476.23	.....	.....	.....	.....
					$m=50,\ n=50$					
CLT	50.550	288.85	300.91							
FSDT	40.649	288.33	300.36	500.71	490.60					
ESL($N=4$)	39.321	288.39	299.03	475.24	460.75	469.45	.....	.....	.....	.....
LW($N=1$)	39.336	288.33	299.03	460.93	469.66	475.60	.....	.....	.....	.....
					$m=100,\ n=100$					
CLT	194.03	601.83	577.89							
FSDT	112.44	574.19	596.91	727.21	704.64					
ESL($N=4$)	106.26	466.69	574.18	605.33	682.55	694.41	.....	.....	.....	.....
LW($N=1$)	106.27	467.08	574.06	605.33	682.58	694.54	.....	.....	.....	.....
					$m=500,\ n=500$					
CLT	2557.8	2923.5	3009.1							
FSDT	671.32	2820.0	3087.6	3100.0	2832.1					
ESL($N=4$)	654.92	771.34	1107.4	2015.5	2495.8	2508.4	.....	.....	.....	.....
LW($N=1$)	640.60	759.49	1101.4	1507.8	1943.4	2394.3	.....	.....	.....	.....

LW). Upon substitution of Eq. (14) in Eq. (15), the free vibration response leads to an eigenvalue problem as follows:

$$\|\boldsymbol{K}-\omega_{mn}^2\boldsymbol{M}\|=0 \tag{16}$$

3.1 Numbers of Higher Modes for the Considered Problems. By giving the in-plane wave numbers m and n, the number of vibration modes is equal to the number of degrees of freedom of the considered two-dimensional model. In other words, the number of eigenvalues (circular frequencies) depends on the dimension of the multilayer level matrix $\boldsymbol{K}$. CLT, FSDT, and ESL models have a number of degrees of freedom that does not depend on the number of layers. CLT has three total degrees of freedom and the matrix $\boldsymbol{K}$ has dimension 3×3, see Fig. 5. FSDT has five degrees of freedom and $\boldsymbol{K}$ is 5×5 (Fig. 6). The ESL model with $N=4$ has 15 DOFs for the whole plate and the stiffness matrix has dimension 15×15, as illustrated in Fig. 7. The above dimensions do not change when the number of layers is changed. This is not true for the case of layer-wise analyses, which have a number of degrees of freedom that depends on the number of the considered layers. The LW theory with $N=1$ has 6 DOFs for each layer k; this leads, for the two considered laminates, 10 and 20 layers, to 33 DOFs and 63 DOFs, respectively. The corresponding stiffness matrices $\boldsymbol{K}$ have dimension 33×33 in the 10-layer case and 63×63 in the 20-layer case. Figure 8 shows the case of the LW model ($N=1$) for a three layer plate as an example. In this case, the matrix dimension is 12×12.

In conclusion, for each couple (m,n), we obtain 3 eigenvalues for the CLT, 5 for the FSDT, 15 for the ESL($N=4$), and 33 and 63 eigenvalues for the LW($N=1$). These eigenvalues represent the number of modes related to the same in-plane harmonic mode. It is clear that only refined theories permit higher-order modes to be investigated. Table 1 shows the number of frequencies for the four considered theories for the two cases of 10- and 20-layered plates. The case in which the couple of positive integers (m,n) varies from 1 to 500 is considered. It is evident that some modes are tragically lost when using simplified plate model analyses.

4 Results and Discussion

Two assessments are first made to demonstrate the effectiveness of the considered refined models. A higher vibration modes analysis is then made by referring to two benchmarks.

4.1 Assessments. The problem proposed by Noor and Burton in Ref. [50] is reconsidered. A 3D solution was given in Ref. [50] for a simply-supported 10-layered plate with a thickness ratio $a/h=5$; the geometry and material are reported in Table 2, and the

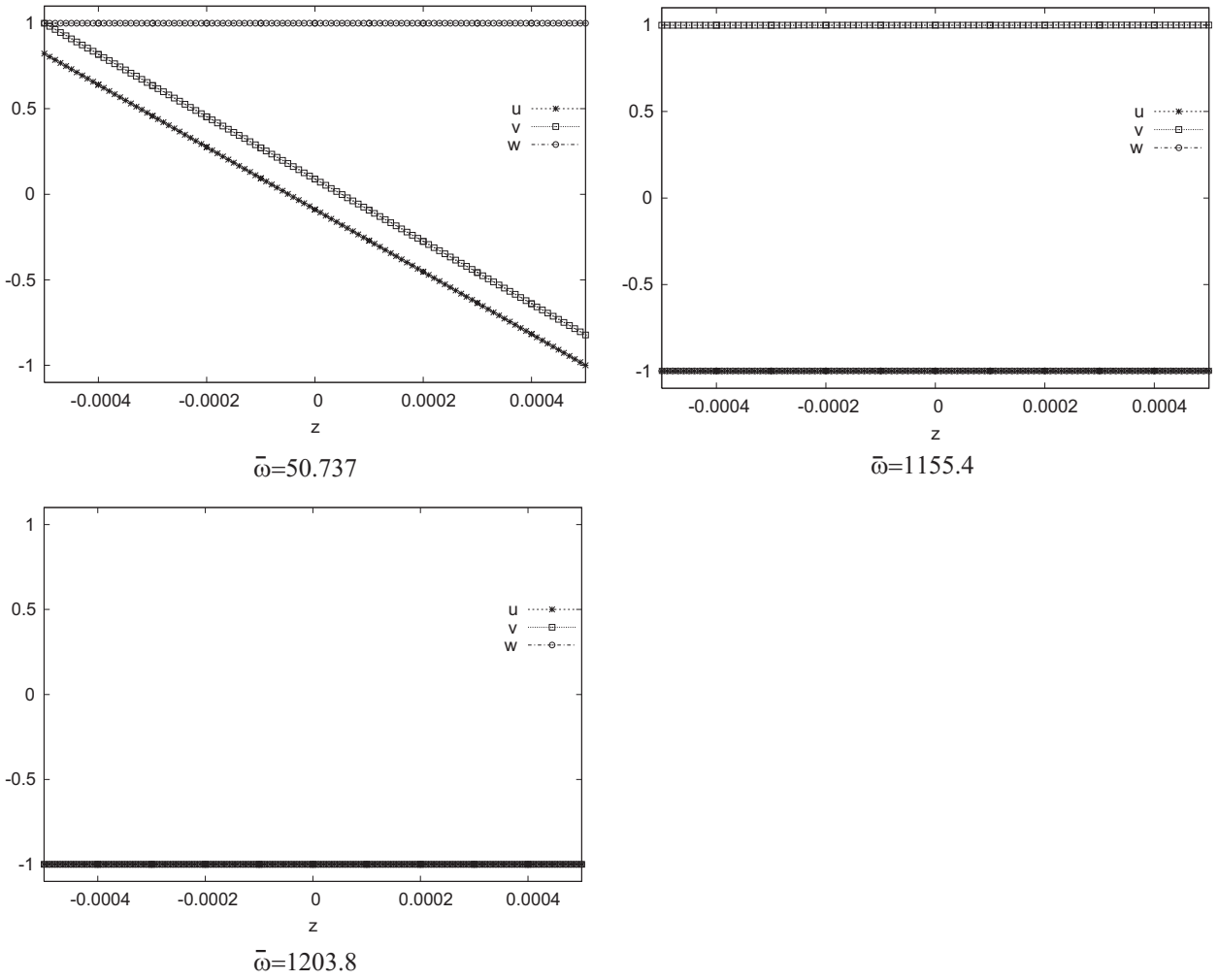

Fig. 10 Benchmark 1, ten-layered plate, $m=n=50$. Through the thickness z distribution of CLT modes.

results are given in Table 3. Two orthotropic ratio values (E_L/E_T) are investigated for a very thick plate. These results demonstrate the effectiveness of the implemented plate models; in particular, the LW analysis coincides with the 3D results. The CLT and FSDT results by Reddy and Phan [51] are compared with the present analyses in Table 4. Very thick and thin geometries have been considered, and the material data and geometry are indicated in Table 2. Table 4 shows that, for a thin plate ($a/h=100$), the differences between ESL and LW models decrease, and a lower order of expansion can be applied. CLT and FSDT are inadequate because they do not consider typical effects connected to multilayered composite plates such as in-plane and transverse anisotropy. In these two assessments, attention has been restricted to the fundamental frequency parameter.

4.2 Benchmarks Discussion. Frequencies related to higher vibration modes have been discussed for two-plate problems. These consist of two cross-ply laminated plates with the material data and geometry indicated in Table 5. These plates were suggested by EADS in the framework of the CASSEM EU project. Benchmark 1 considers a 10-layered plate with a thickness ratio $a/h=1500$, while benchmark 2 coincides with a 20-layered plate with a thickness ratio $a/h=375$. Fiber orientation 0 deg/90 deg are only considered for the sake of brevity. Further orientations are not investigated because they do not introduce more remarks.

By assigning the number of waves (m,n) in the two in-plane directions (Fig. 9), a number of modes, equal to the number of degrees of freedom of the considered two-dimensional models, are obtained. Tables 6 and 7 show the obtained results for the following wave number values (m,n): (1,1), (5,5), (10,10), (50,50), (100,100), and (500,500). These cases cover a large range of frequencies, from low to higher modes. For the sake of brevity, the complete set of frequencies is only given once, in correspondence to the $m=n=1$ case. Since the number of frequencies differs from theory to theory, a check is required to recognize the mode. This can be done by plotting the three displacement components in the thickness direction z. Figures 10–13 plot some modes for the four considered theories in the case of a 10-layered plate with $m=n=50$. For refined models, such as the ESL($N=4$) and LW($N=1$), there are other modes that have not been indicated in Figs. 12 and 13, which are typical of these refined theories. These modes are not considered in CLT and FSDT analyses. Frequencies can be compared if and only if these refer to the same mode. Comparing Fig. 12 (ESL($N=4$)) and Fig. 13 (LW($N=1$)), it is clear that the corresponding modes are: $\bar{\omega}=49.684$ (ESL($N=4$)) and $\bar{\omega}=49.696$ (LW($N=1$)), $\bar{\omega}=1155.1$ (ESL($N=4$)) and $\bar{\omega}=1154.9$ (LW($N=1$)), $\bar{\omega}=1203.0$ (ESL($N=4$)) and $\bar{\omega}=1203.0$ (LW($N=1$)), $\bar{\omega}=5878.5$ (ESL($N=4$)) and $\bar{\omega}=5900.2$ (LW($N=1$)), $\bar{\omega}=5865.6$ (ESL($N=4$)) and $\bar{\omega}=5887.2$ (LW($N=1$)), and $\bar{\omega}=7613.4$ (ESL($N=4$)) and $\bar{\omega}=7642.8$ (LW($N=1$)). The fundamental frequencies for each pair of wave numbers are underlined in Tables 6 and 7. For low values of (m,n), there are no differences between CLT, FSDT, ESL($N=4$), and LW($N=1$) for either benchmark. If the in-plane waves number is increased, the differ-

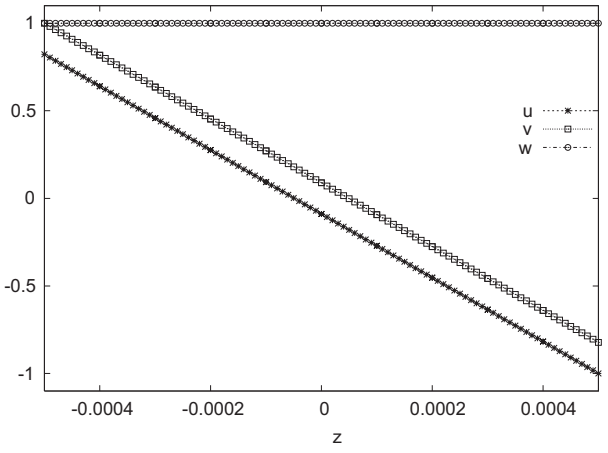

$\bar{\omega}$=49.873

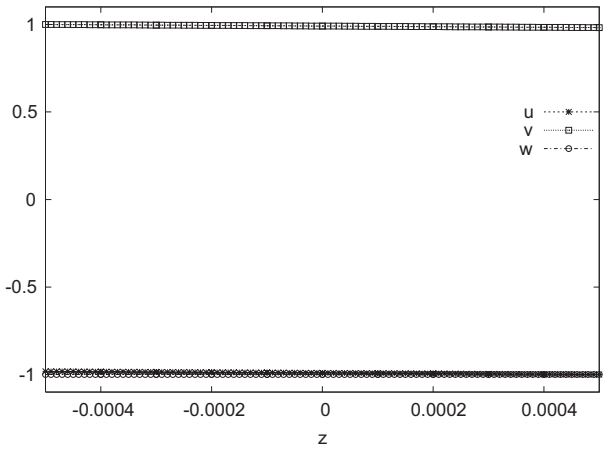

$\bar{\omega}$=1154.9

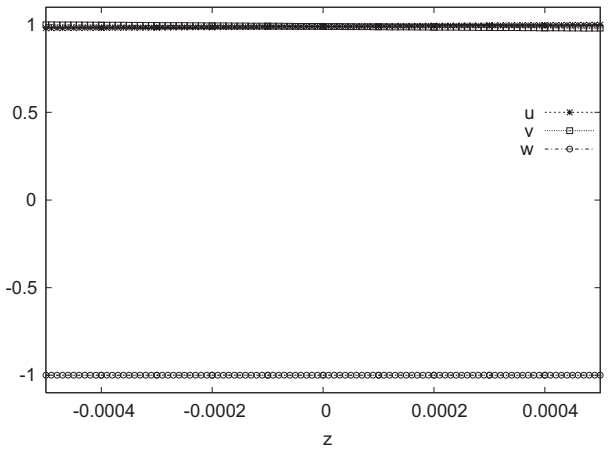

$\bar{\omega}$=1203.3

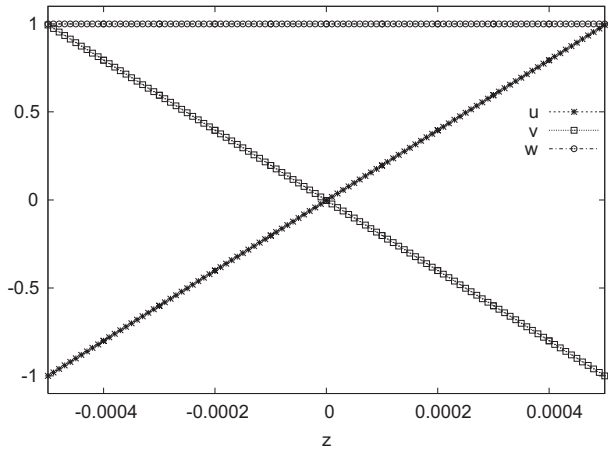

$\bar{\omega}$=6443.8

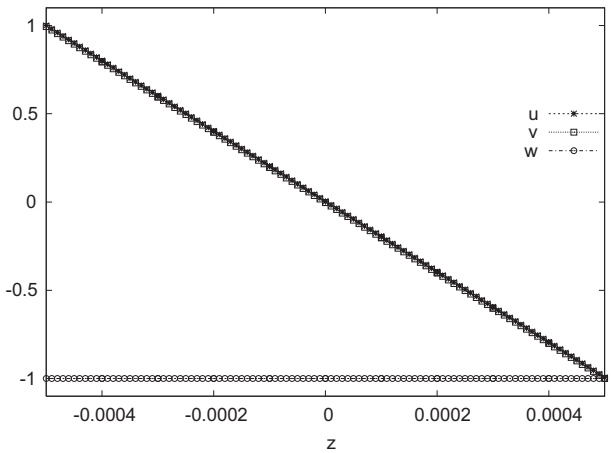

$\bar{\omega}$=6458.1

Fig. 11 Benchmark 1, ten-layered plate, $m=n=50$. Through the thickness z distribution of FSDT modes.

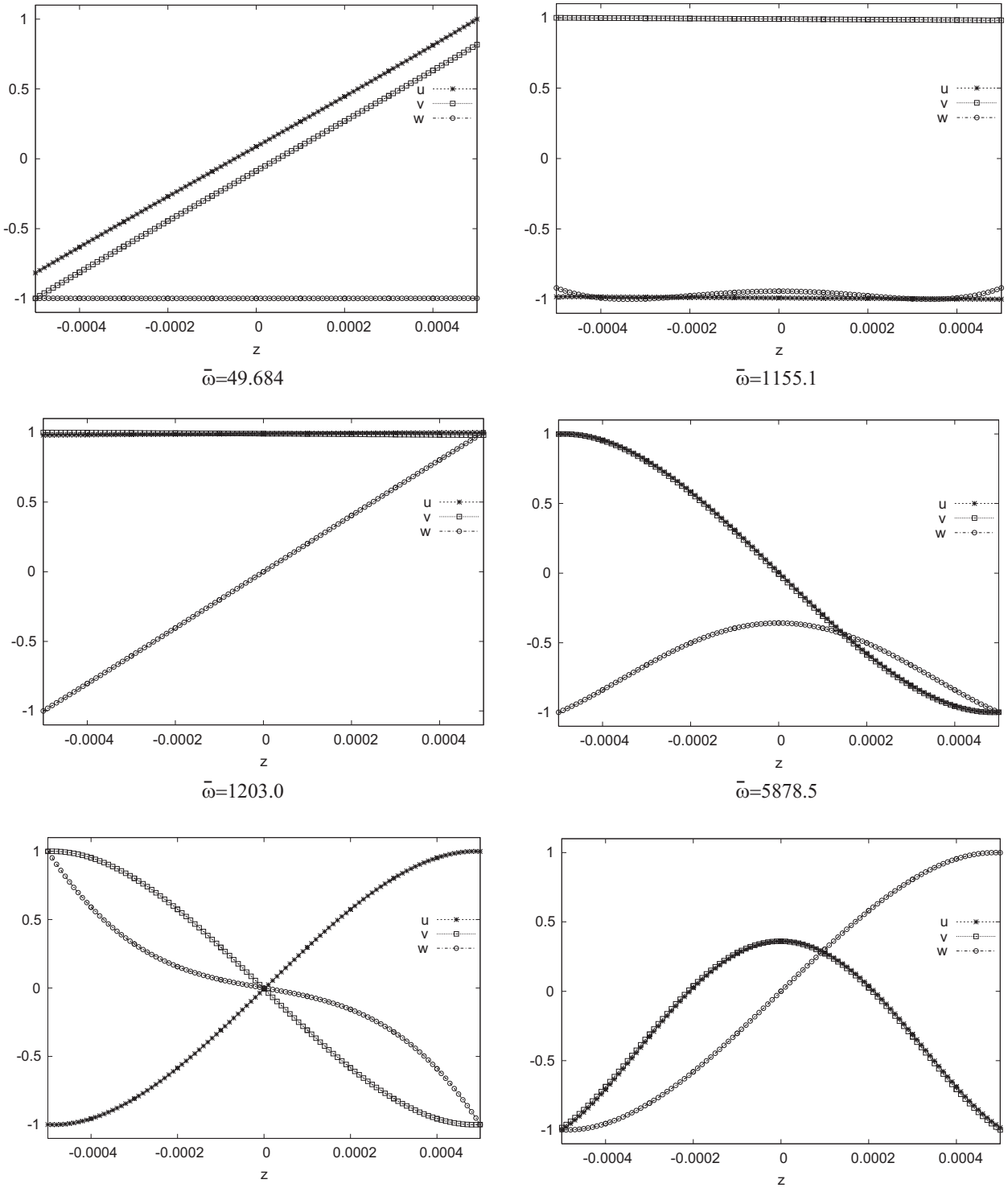

Fig. 12 Benchmark 1, ten-layered plate, $m=n=50$. Through the thickness z distribution of first six ESL($N=4$) modes (the total number of modes is 15).

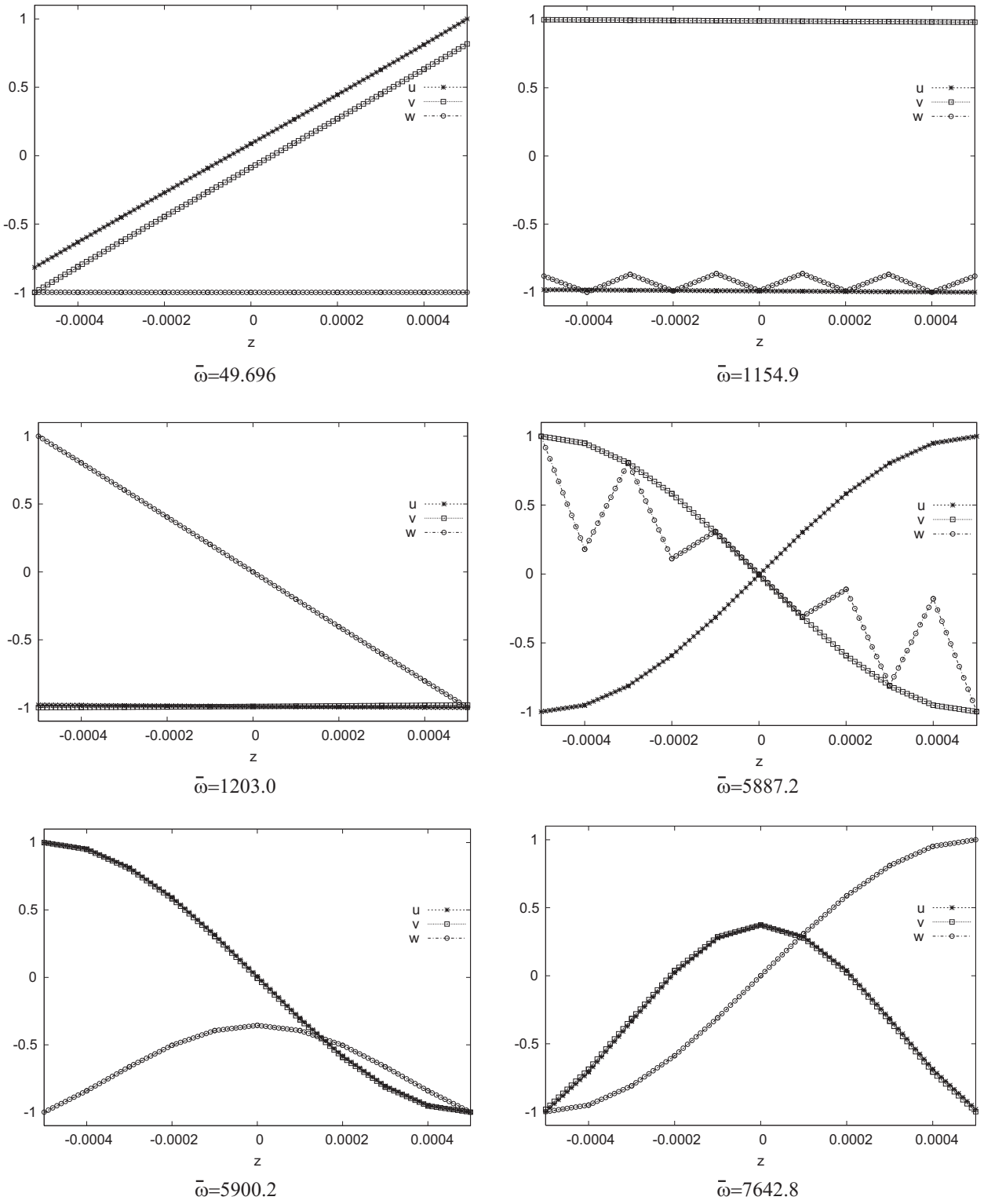

Fig. 13 Benchmark 1, ten-layered plate, $m=n=50$. Through the thickness z distribution of first six LW($N=1$) modes (the total number of modes is 33).

Table 8 Benchmark 1, 10-layered plate, and $a/h=1500$. Fundamental frequency f in Hz for different waves number. $\Delta\%=|f_{CLT}-f_i/f_{CLT}\cdot 100|$ is the difference between CLT and other theories.

m,n	CLT	FSDT	$\Delta\%$	ESL($N=4$)	$\Delta\%$	LW($N=1$)	$\Delta\%$
1,1	2.98913	2.98913	(0.00)	2.98913	(0.00)	2.98913	(0.00)
1,2	8.56982	8.56982	(0.00)	8.56982	(0.00)	8.56982	(0.00)
2,1	8.56982	8.56982	(0.00)	8.56982	(0.00)	8.56982	(0.00)
2,2	11.9565	11.9565	(0.00)	11.9565	(0.00)	11.9712	(0.12)
5,5	74.7724	74.7724	(0.00)	74.7724	(0.00)	74.7724	(0.00)
5,10	214.172	214.039	(0.06)	214.010	(0.08)	214.010	(0.08)
10,5	214.172	214.039	(0.06)	214.010	(0.08)	214.010	(0.08)
10,10	299.104	298.898	(0.07)	298.839	(0.09)	298.883	(0.07)
10,50	5126.14	5044.27	(1.60)	5026.30	(1.95)	5026.89	(1.94)
50,10	5126.14	5044.27	(1.60)	5026.30	(1.95)	5026.89	(1.94)
50,50	7470.91	7343.69	(1.70)	7315.86	(2.07)	7317.62	(2.05)
100,100	29,800.0	27,928.5	(6.28)	27,554.5	(7.53)	27,572.1	(7.48)
500,500	685,792	350,391	(48.9)	326,330	(52.4)	326,890	(52.3)

ences between classical theories (CLT and FSDT) and refined models become more evident; these differences are larger for the 20-layered plate than the 10-layered one. These results are summarized in Tables 8 and 9 and in Figs. 14 and 15, where these differences are clearly shown. Table 8 shows that the differences become critical ($>1\%$) for a value of waves number ($m=10$, $n=50$) that is larger than the case of Table 9 ($m=5$, $n=10$); this means that both the thickness ratio of the plate, and the number and stacking of the layers are fundamental parameters of the considered problems. These considerations are confirmed by Figs. 14 and 15. It should be noticed that the error can be larger than 50% for the higher modes related to high values of m and n.

5 Conclusions

A comparison between classical theories (classical lamination theory and first-order shear deformation theory) and refined ones (equivalent single layer with fourth-order of expansion and layer

Table 9 Benchmark 2, 20 layered plate, $a/h=375$. Fundamental frequency f in Hz for different waves number. $\Delta\%=|f_{CLT}-f_i/f_{CLT}\cdot 100|$ is the difference between CLT and other theories.

m,n	CLT	FSDT	$\Delta\%$	ESL($N=4$)	$\Delta\%$	LW($N=1$)	$\Delta\%$
1,1	24.1486	24.1486	(0.00)	24.1486	(0.00)	24.1486	(0.00)
1,2	69.2606	69.1500	(0.16)	69.1500	(0.16)	69.1500	(0.16)
2,1	69.2606	69.1500	(0.16)	69.1500	(0.16)	69.1500	(0.16)
2,2	96.7100	96.5900	(0.12)	96.5900	(0.12)	96.5900	(0.12)
5,5	604.069	602.302	(0.29)	602.067	(0.33)	602.067	(0.33)
5,10	1730.22	1712.67	(1.01)	1709.25	(1.21)	1709.14	(1.22)
10,5	1730.22	1712.67	(1.01)	1709.25	(1.21)	1709.14	(1.22)
10,10	2415.33	2388.12	(1.13)	2382.82	(1.35)	2382.94	(1.34)
10,50	41,143.4	33,351.0	(18.9)	32,276.7	(21.6)	32,287.3	(21.5)
50,10	41,143.4	33,351.0	(18.9)	32,276.7	(21.6)	32,287.3	(21.5)
50,50	59,547.0	47,883.8	(19.6)	46,319.5	(22.2)	46,337.1	(22.2)
100,100	228,564	132,452	(42.1)	125,172	(45.2)	125,184	(45.2)
500,500	3,013,045	790,803	(73.7)	771,485	(74.4)	754,616	(74.9)

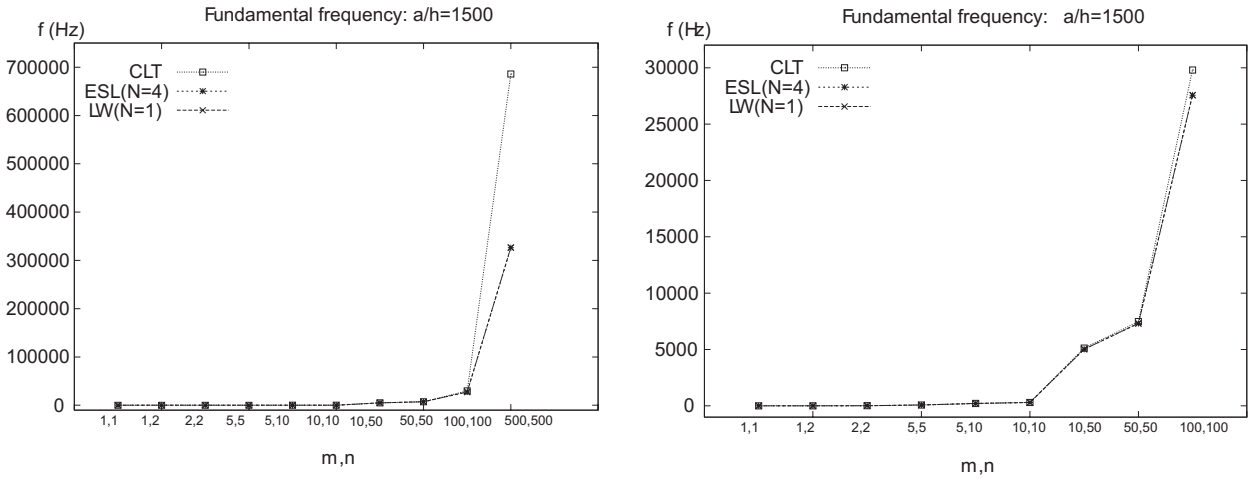

Fig. 14 Benchmark 1, fundamental frequencies in Hz for the ten-layered plate. Comparison between CLT, ESL($N=4$), and LW($N=1$) results. The figure on the right is a zoom of the figure on the left side.

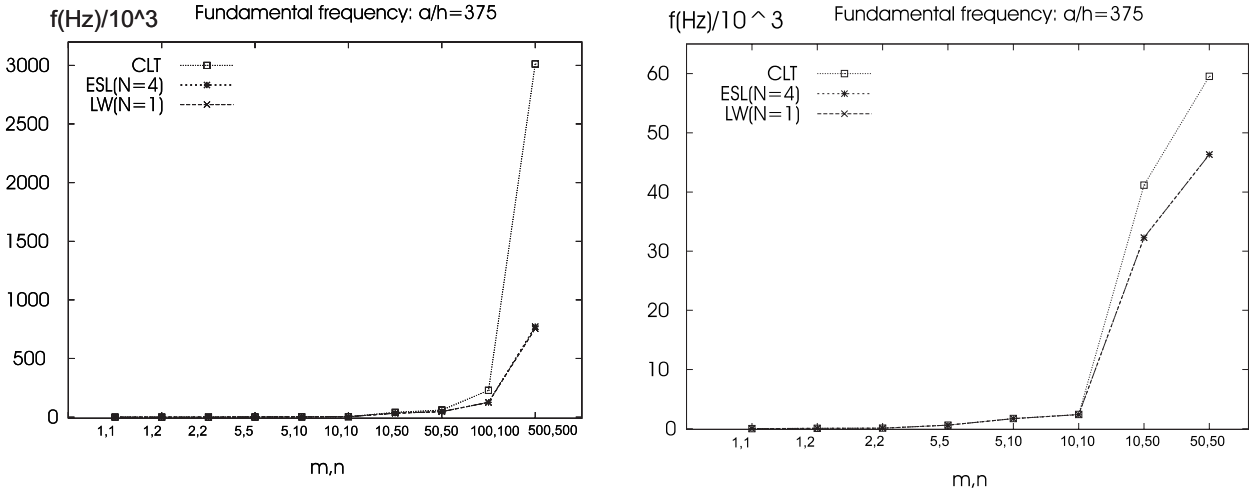

Fig. 15 Benchmark 2, fundamental frequencies in Hz for the 20-layered plate. Comparison between CLT, ESL(N=4), and LW(N=1) results. The figure on the right is a zoom of the figure on the left side.

wise with linear evaluation in z) has been addressed in this paper for the free vibration response of simply-supported multilayered composite plates. A closed-form solution has been discussed for a 10-layer and a 20-layered plate. A large range of frequencies (from low to high values of in-plane wave numbers) has been considered to show the importance of refined models in the numerical evaluation of higher modes. It has been concluded that the use of refined models is mandatory for higher mode evaluation even though thin plate geometries are considered. The presented results could be of some help to assess computational models, such as the finite element method and SEA, for the analysis of higher vibration modes in laminated plates.

Acknowledgment

This work has been carried out in the framework of STREP EU project CASSEM under Contract No. NMP-CT-2005-013517, and two regional projects Piemonte 2004: E40 and E59.

References

[1] Bogdanovich, A. E., and Sierakowski, R. L., 1999, "Composite Materials and Structures: Science, Technology and Applications—A Compendium of Books, Review Papers and Other Sources of Informations," Appl. Mech. Rev., **52**(12), pp. 351–366.
[2] Leissa, A. W., 1969, "Vibration of Plates," NASA Report No. SP-160.
[3] Leissa, A. W., 1973, "Vibration of Shells," NASA Report No. SP-288.
[4] Werner, S., 2004, *Vibrations of Shells and Plates*, 3rd ed., CRC, New York/Dekker, New York.
[5] De Rosa, S., Franco, F., and Ricci, F., 1999, *Introduzione alla Tecnica Statistico-Energetica (S.E.A.) per la Dinamica Strutturale e l'Acustica Interna*, Liguori Editore, Napoli.
[6] Noor, A. K., 1973, "Free Vibrations of Multilayered Composite Plates," AIAA J., **11**(7), pp. 1038–1039.
[7] Liew, K. M., Xiang, Y., and Kitipornchai, S., 1995, "Research on Thick Plate Vibration: A Literature Survey," J. Sound Vib., **180**(1), pp. 163–176.
[8] Shuyu, L., 2001, "Study on the Flexural Vibration of Rectangular Thin Plates With Free Boundary Conditions," J. Sound Vib., **239**(5), pp. 1063–1071.
[9] Leung, A. Y. T., and Zhu, B., 2004, "Transverse Vibration of Thick Polygonal Plates Using Analytically Integrated Trapezoidal Fourier p-Element," Comput. Struct., **82**(2–3), pp. 109–119.
[10] Batra, R. C., and Aimmanee, S., 2005, "Vibration of Thick Isotropic Plates With Higher Order Shear and Normal Deformable Plate Theories," Comput. Struct., **83**(12–13), pp. 934–955.
[11] Gorman, D. J., 2006, "Exact Solutions for the Free In-Plane Vibration of Rectangular Plates With Two Opposite Edges Simply Supported," J. Sound Vib., **294**(1–2), pp. 131–161.
[12] Gorman, D. J., 2004, "Accurate Analytical Type Solutions for the Free In-Plane Vibration of Clamped and Simply Supported Rectangular Plates," J. Sound Vib., **276**(1–2), pp. 311–333.
[13] Taher, H. R. D., Omidi, M., Zadpoor, A. A., and Nikooyan, A. A., 2006, "Free Vibration of Circular and Annular Plates With Variable Thickness and Different Combinations of Boundary Conditions," J. Sound Vib., **296**(4–5), pp. 1084–1092.
[14] Aimmanee, S., and Batra, R. C., 2007, "Analytical Solution for Vibration of an Incompressibile Isotropic Linear Elastic Rectangular Plate, and Frequencies Missed in Previous Solutions," J. Sound Vib., **302**(3), pp. 613–620.
[15] Batra, R. C., and Aimmanee, S., 2003, "Missing Frequencies in Previous Exact Solutions of Free Vibrations of Simply Supported Rectangular Plates," J. Sound Vib., **265**(4), pp. 887–896.
[16] Batra, R. C., Vidoli, S., and Vestroni, F., 2002, "Plane Wave Solutions and Modal Analysis in Higher Order Shear and Normal Deformable Plate Theories," J. Sound Vib., **257**(1), pp. 63–88.
[17] Bardell, N. S., Langley, R. S., and Dunsdon, J. M., 1996, "On the Free In-Plane Vibration of Isotropic Rectangular Plates," J. Sound Vib., **191**(3), pp. 459–467.
[18] Liew, K. M., and Yang, B., 1999, "Three-Dimensional Elasticity Solutions for Free Vibrations of Circular Plates: A Polynomial-Ritz Analysis," Comput. Methods Appl. Mech. Eng., **175**(1–2), pp. 189–201.
[19] Zhao, Y. B., Wei, G. W., and Xiang, Y., 2002, "Discrete Singular Convolution for the Prediction of High Frequency Vibration of Plates," Int. J. Solids Struct., **39**(1), pp. 65–88.
[20] Beslin, O., and Nicolas, J., 1997, "A Hierarchical Functions Set for Predicting Very High Order Plate Bending Modes With Any Boundary Conditions," J. Sound Vib., **202**(5), pp. 633–655.
[21] Oosterhout, G. M., van der Hoogt, P. J. M., and Spiering, R. M. E. J., 1995, "Accurate Calculation Methods for Natural Frequencies of Plates With Special Attention to the Higher Modes," J. Sound Vib., **183**(1), pp. 33–47.
[22] Sakiyama, T., and Huang, M., 1998, "Free Vibration Analysis of Rectangular Plates With Variable Thickness," J. Sound Vib., **216**(3), pp. 379–397.
[23] Mindlin, R. D., 2006, *An Introduction to the Mathematical Theory of Vibrations of Elastic Plates*, J. Yang, ed., World Scientific, Singapore/University of Nebraska-Lincoln.
[24] Bouthier, O. M., and Bernhard, R. J., 1995, "Simple Models of the Energetics of Transversely Vibrating Plates," J. Sound Vib., **182**(1), pp. 149–166.
[25] Wei, G. W., Zhao, Y. B., and Xiang, Y., 2002, "A Novel Approach for the Analysis of High-Frequency Vibrations," J. Sound Vib., **257**(2), pp. 207–246.
[26] Kim, H.-Y., and Hwang, W., 2001, "Estimation of Normal Mode and Other System Parameters of Composite Laminated Plates," Compos. Struct., **53**(3), pp. 345–354.
[27] Gorman D. J. and Ding, W., 2003, "Accurate Free Vibration Analysis of Completely Free Symmetric Cross-Ply Rectangular Laminated Plates," Compos. Struct., **60**(3), pp. 359–365.
[28] Gorman, D. J., 2000, "Free Vibration Analysis of Completely Free Rectangular Plates by the Superposition-Galerkin Method," J. Sound Vib., **237**(5), pp. 901–914.
[29] Ye, J. Q., 1997, "A Three-Dimensional Free Vibration Analysis of Cross-Ply Laminated Rectangular Plate With Clamped Edges," Comput. Methods Appl. Mech. Eng., **140**(3–4), pp. 383–392.
[30] Topal, U., Uzman, U. V., 2007, "Free Vibration Analysis of Laminated Plates Using Higher-Order Shear Deformation Theory," *Proceedings in Physics*, Vol. 111, Springer, Netherlands, pp. 493–498.
[31] Jung, S. N., Nagaraj, V. T., and Chopra, I., 2001, "Refined Structural Dynamics Model for Composite Rotor Blades," AIAA J., **39**(2), pp. 339–348.
[32] Cho, M., and Kim, J.-S., 2001, "Higher-Order Zig-Zag Theory for Laminated Composites With Multiple Delaminations," ASME J. Appl. Mech., **68**(6), pp. 869–877.
[33] Plagianakos, T. S., and Saravanos, D. A., 2004, "High-Order Layer Wise Mechanics and Finite Element for the Damped Dynamic of Sandwich Composite Beams," Int. J. Solids Struct., **41**(24–25), pp. 6853–6871.
[34] Rao, M. K., and Desai, Y. M., 2004, "Analytical Solutions for Vibrations of Laminated and Sandwich Plates Using Mixed Theory," Compos. Struct.,

63(3–4), pp. 361–373.
[35] Plagianakos, T. S., and Saravanos, D. A., 2003, "Mechanics and Finite Elements for the Damped Dynamic Characteristics of Curvilinear Laminates and Composite Shell Structures," J. Sound Vib., **263**(2), pp. 399–414.
[36] Sun, C. T., and Whitney, J. M., 1972, "On Theories for the Dynamic Response of Laminated Plates," 13th ASME and SAE Structures, Structural Dynamics and Materials Conference, San Antonio, TX, April 10–12.
[37] Wang, C. M., 1996, "Vibration Frequencies of Simply Supported Polygonal Sandwich Plates Via Kirchhoff Solutions," J. Sound Vib., **190**(2), pp. 255–260.
[38] Nayak, A. K., Moy, S. S. J., and Shenoi, R. A., 2002, "Free Vibration Analysis of Composite Sandwich Plates Based on Reddy's Higher-Order Theory," Composites, Part B, **33**(7), pp. 505–519.
[39] Messina, A., and Soldatos, K. P., 1999, "Vibration of Completely Free Composite Plates and Cylindrical Shell Panels by a Higher-Order Theory," Int. J. Mech. Sci., **41**(8), pp. 891–918.
[40] Tessler, A., Saether, E., and Tsui, T., 1995, "Vibration of Thick Laminated Plates," J. Sound Vib., **179**(3), pp. 475–498.
[41] Han, W., and Petyt, M., 1997, "Geometrically Nonlinear Vibration Analysis of Thin, Rectangular Plates Using the Hierarchical Finite Element Method—II: 1st Mode of Laminated Plates and Higher Modes of Isotropic and Laminated Plates," Comput. Struct., **63**(2), pp. 309–318.
[42] Zhang, Q. J., and Sainsbury, M. G., 2000, "The Galerkin Element Method Applied to the Vibration of Rectangular Damped Sandwich Plates," Comput. Struct., **74**(6), pp. 717–730.
[43] Carrera, E., 1999, "A Study of Transverse Normal Stress Effect on Vibration of Multilayered Plates and Shells," J. Sound Vib., **225**(5), pp. 803–829.
[44] Carrera, E., 1999, "A Reissner's Mixed Variational Theorem Applied to Vibrational Analysis of Multilayered Shells," ASME J. Appl. Mech., **66**(1), pp. 69–78.
[45] Carrera, E., 1998, "Layer-Wise Mixed Models for Accurate Vibration Analysis of Multilayered Plates," ASME J. Appl. Mech., **65**(4), pp. 820–828.
[46] Carrera, E., 1995, "A Class of Two Dimensional Theories for Multilayered Plates Analysis," Atti Accad. Sci. Torino, Cl. Sci. Fis., Mat. Nat., **19–20**, pp. 49–87.
[47] Carrera, E., 2002, "Theories and Finite Elements for Multilayered, Anisotropic, Composite Plates and Shells," Arch. Comput. Methods Eng., **9**(2), pp. 87–140.
[48] Reddy, J. N., 2004, *Mechanics of Laminated Composite Plates and Shells, Theory and Analysis*, 2nd ed., CRC, New York.
[49] Carrera, E., and Brischetto, S., 2008, "Analysis of Thickness Locking in Classical, Refined and Mixed Multilayered Plate Theories," Compos. Struct., **82**(4), pp. 549–562.
[50] Noor, A. K., and Burton, W. S., 1989, "Stress and Free Vibration Analysis of Multilayered Composite Plates," Compos. Struct., **11**(3), pp. 183–204.
[51] Reddy, J. N., and Phan, N. D., 1985, "Stability and Vibration of Isotropic, Orthotropic and Laminated Plates According to a Higher Order Shear Deformation Theory," J. Sound Vib., **98**(2), pp. 157–170.

The Magnetic Viscous Damping Effect on the Natural Frequency of a Beam Plate Subject to an In-Plane Magnetic Field

Jui-Lin Lee
Department of Automation Engineering,
Nan Kai University of Technology,
Nantou, Taiwan 542, R.O.C.

Chun-Bo Lin
Department of Industrial Engineering and Management,
Overseas Chinese University,
Taichung, Taiwan 407, R.O.C.

Several magnetic force models were developed to interpret various phenomena of a soft ferromagnetic beam plate subjected to a uniform external magnetic field with different incident angles. In this paper, a new transverse magnetic force model for the interface between a ferromagnetic material and the air is derived with the continuation of magnetoelastic stress across the material boundary. It is noted that both the normal and the tangential components of magnetic field on the material boundary are considered in this model. By applying such a transverse magnetic force and the effect of magnetic viscous damping, a new theoretical model is constructed in this study to predict the natural frequency of a soft ferromagnetic beam plate placed in an in-plane magnetic field. The numerical results of the present study are displayed graphically and compared with the experimental data, which appeared in literature to assure the exactness of the present work. [DOI: 10.1115/1.3168602]

Keywords: magnetic viscous damping, magnetic force model, magnetoelasticity

1 Introduction

Due to the low rate of irradiation swelling, the ferromagnetic structure made of ferrite steel was adopted as the first wall in a fusion reactor. The interaction between the magnetic field and the deformation of the structure is a relevant concern in such an environment of strong magnetic field. Several models of the magnetic force were developed by earlier investigators in studying the magnetoelastic problem of a ferromagnetic plate. Moon and Pao [1] applied the body couple model to explain the experimental result for the magnetoelastic buckling of a cantilevered thin plate in a transverse magnetic field. Using the formulation of magnetic body force provided by Brown [2], Pao and Yeh [3] derived a linear theory and a magnetic force model to study the magnetoelastic buckling problem of an infinite plate. Eringen [4] and Eringen and Maugin [5] applied a different type of magnetic body force to develop another magnetic force model, which was compatible with that addressed by Pao and Yeh [3] while the magnetic field was perpendicular to a ferromagnetic plate. Sabir and Maugin [6] adopted such a force model to study the fracture problem of paramagnets and soft ferromagnets. Based on variational principle, Zhou et al. [7] established a magnetic force model to explain the result of the magnetic buckling experiment conducted by Moon and Pao [1].

Takagi et al. [8] arranged an experiment to measure the change in natural frequency for a thin plate subjected to an in-plane magnetic field. Based on variational principle, a new model of magnetic force to investigate the problem of in-plane magnetic field was derived [9,10]. Such a model is different from those aforementioned in dealing the problem of transverse magnetic field. Zhou and Miya [10] used this model to obtain theoretical curves for the natural frequency of beam plate under an in-plane magnetic field and compared the results with the experimental data given by Takagi et al. [8]. Without considering the effect of magnetic viscous damping, their theoretical predictions of the natural frequency concavely increase with the in-plane magnetic field but the experimental data are convex curves. The magnetic viscous damping was evoked by the coupling between transverse motion of plate and in-plane magnetic fields. This effect was taken into account by Takagi and Tani [11] when they studied the dynamic behavior of a thin plate under a magnetic field composed of a uniform in-plane component and a time-varying transverse part. They applied a modal magnetic damping (MMD) method and used a finite element method (FEM) to find the natural frequency and the corresponding vibration mode. Lin [12] employed the Galerkin method to consider the destabilizing effect of the magnetic viscous damping on the panel flutter. Notice that the aforementioned investigators used FEM to determine the distribution of magnetic field around a ferromagnetic beam plate because it is difficult to obtain an analytic solution.

In this paper, a new magnetic force model is developed by employing the continuation of magnetoelastic traction across the boundary between the air and a ferromagnetic material. This model contains the contribution of the tangential and normal components of magnetic field on the boundary and has the resultant form similar to that given by Zhou and Zheng [9]. Based on the complex variable method in plane magnetoelasticity, the magnetic field around an elliptic inclusion can be found in an analytic form [13]. Such a distribution of magnetic field and the magnetic force model derived from the present work are applied to study the magnetoelastic problem of a beam plate with large slenderness ratio. By applying Galerkin method and considering the magnetic viscous damping effect on a beam plate, a theoretical formulation for the variation in natural frequency on the in-plane magnetic field is found. Since the difference in shape exists between an elliptic inclusion and a plate of uniform thickness, it is necessary to check the validity of magnetic field distribution assumed in this study. By the comparison between the results of theoretical model with an elliptic inclusion and that found from the FEM with a beam plate of uniform thickness, the present approach is guaranteed to be a proper method. Furthermore, a pertinent parameter is introduced to modify the distribution of magnetic force. In order to illustrate the availability of the present approach, the theoretical

Contributed by the Applied Mechanics Division of ASME for publication in the JOURNAL OF APPLIED MECHANICS. Manuscript received July 25, 2008; final manuscript received June 2, 2009; published online October 5, 2009. Review conducted by Zhigang Suo.

predictions of the natural frequency will be presented in a graphical form and compared with the experimental data.

2 Natural Frequency of a Beam Plate Subjected to an In-Plane Magnetic Field

The governing equation of static magnetic field can be expressed as

$$B_{i,i} = 0, \quad e_{ijk} H_{k,j} = 0 \tag{1}$$

where B_i and H_k are the magnetic induction (or magnetic flux density) and the magnetic intensity; e_{ijk} and (,) denote the permutation symbol and the partial differential with respect to the space variable, respectively.

The corresponding constitutive law takes the form

$$B_j = \mu_0 (H_j + M_j) = \mu_0 \mu_r H_j \tag{2}$$

with

$$M_j = \chi H_j, \quad \mu_r = 1 + \chi \tag{3}$$

where M_j denotes the magnetization, $\mu_0 = 4\pi \times 10^{-7} N/A^2$ is a universal constant, χ and μ_r are the magnetic susceptibility and the relative magnetic permeability, respectively. For linear soft ferromagnetic materials, $\chi(\sim 10^2 - 10^5) \gg 1$ [14].

From the expression of magnetic body force proposed by Brown [2], Pao and Yeh [3] discarded the effect of magnetostriction and obtained

$$t_{ij,i} + f_j^M = 0 \tag{4}$$

where

$$t_{ij} = \tau_{ij} + \frac{\mu_0}{\chi} M_i M_j, \quad \tau_{ij} = \lambda \delta_{ij} u_{k,k} + G(u_{i,j} + u_{j,i}), \quad f_j^M = \mu_0 M_i H_{j,i} \tag{5}$$

The symbol t_{ij} and τ_{ij} denote the magnetoelastic stresses and the elastic stresses, λ and G are Lamé's constants, and δ_{ij} is the Kronecker delta. It is noted that f_j^M indicates the magnetic body force. For an interface between the air (or vacuum) and a ferromagnetic material, the magnetic field quantities in the air and the material are remarked by superscripts (1) and (2), respectively. Since there are no displacement and magnetization in the air, $t_{ij}^{(1)} = 0$ can be found. Furthermore, the replacement of $M_i^{(1)}$ with $(B_i^{(1)} - \mu_0 H_i^{(1)})/\mu_0$ can be concluded from Eq. (2). Therefore, the magnetic body force in the air becomes

$$\begin{aligned} f_j^{M(1)} &= (B_i^{(1)} - \mu_0 H_i^{(1)}) H_{j,i}^{(1)} = B_i^{(1)} H_{j,i}^{(1)} - \mu_0 H_i^{(1)} H_{j,i}^{(1)} = (B_i^{(1)} H_j^{(1)})_{,i} \\ &\quad - B_{i,i}^{(1)} H_j^{(1)} - \mu_0 H_i^{(1)} H_{i,j}^{(1)} = \left(B_i^{(1)} H_j^{(1)} - \frac{1}{2} \mu_0 H_k^{(1)} H_k^{(1)} \delta_{ij} \right)_{,i} \\ &= t_{ij,i}^{M(1)} \end{aligned} \tag{6}$$

where

$$t_{ij}^{M(1)} = B_i^{(1)} H_j^{(1)} - \tfrac{1}{2} \mu_0 H_k^{(1)} H_k^{(1)} \delta_{ij} \tag{7}$$

denotes the Maxwell stress [3]. Notice that the total stress t_{ij}^T is defined as the sum of the magnetoelastic stress and the Maxwell stress, i.e., $t_{ij}^T = t_{ij} + t_{ij}^M$. In the derivation of Eq. (6), the relations $B_{i,i}^{(1)} = 0$ and $H_{j,i}^{(1)} = H_{i,j}^{(1)}$, which can be deduced from Eq. (1), are adopted. Alternatively, the magnetic body force in the ferromagnetic material can be written as

$$\begin{aligned} f_j^{M(2)} &= \mu_0 M_i^{(2)} H_{j,i}^{(2)} = \mu_0 \chi_2 H_i^{(2)} H_{j,i}^{(2)} = \mu_0 \chi_2 H_i^{(2)} H_{i,j}^{(2)} \\ &= \left(\frac{\mu_0 \chi_2}{2} H_k^{(2)} H_k^{(2)} \delta_{ij} \right)_{,i} \end{aligned} \tag{8}$$

In earlier studies, several investigators criticized the adoption of Maxwell stress. McMeeking and Landis [15] and Suo et al. [16] obtained the total stress from the derivative of free energy for the electrostatic problem. This means that the total stress can be obtained from the equation like the constitutive law instead of applying the Maxwell stress derived from the electromagnetic body force. Although the necessity of the Maxell stress is questioned in the above papers, nevertheless, the results of total stress remain the same as the summation of the Cauchy stress and the Maxwell stress. Furthermore, Rinaldi and Brenner [17] denoted that replacing the effect of magnetic body force f^M, as shown in Eq. (5), with the Maxwell stress may cause disconformity in torque, the rate of working and rate of mechanical energy exchange for the case of ferrofluid flows with asymmetric Maxwell stress tensor. Since the present work is a static problem with linear isotropic magnetic materials, the Maxwell stress tensor is symmetric and the four quantities (force, torque, rate of working, and rate of mechanical energy exchange) in Eqs. (2.4a-d) given by Rinaldi and Brenner [17] equal zero. Thus the error caused by using the Maxwell stress tensor to replace the effect of magnetic body force vanishes in this study. Despite the criticism on the essentiality of introducing the Maxwell stress, the total stress, which is the sum of the magnetoelastic stress t_{ij} in Eq. (5) and the Maxwell stress t_{ij}^M in magnetoelastic problem, is still valid just like the case of electrostatic problem with dielectric solid. Therefore, the usage of Maxwell stress is just an intermediate mathematic procedure in obtaining the total stress rather than try to separate the effect between the elastic and magnetic loading. Thus the expression of total stress and the following derivation in this work can be applied.

By employing Eqs. (4) and (6)–(8), the continuation of the surface tractions $t_{ij}^T n_i$ across the interface between air and material gives rise to

$$\left(t_{ij}^{(2)} + \frac{\mu_0 \chi_2}{2} H_k^{(2)} H_k^{(2)} \delta_{ij} \right) n_i = \left(B_i^{(1)} H_j^{(1)} - \frac{1}{2} \mu_0 H_k^{(1)} H_k^{(1)} \delta_{ij} \right) n_i \tag{9}$$

where n_i is the unit normal vector on the material surface. Hence the equation

$$t_{nn}^{(2)} + \frac{\mu_0 \chi_2}{2} [(H_n^{(2)})^2 + (H_t^{(2)})^2] = B_n^{(1)} H_n^{(1)} - \frac{\mu_0}{2} [(H_n^{(1)})^2 + (H_t^{(1)})^2] \tag{10}$$

can be found. In which the subscripts n and t indicate the normal and tangential components on the boundary. Via the use of Eq. (2) and the continuation of magnetic field across the interface, one can obtain

$$B_n^{(1)} = B_n^{(2)}, \quad H_t^{(1)} = H_t^{(2)}, \quad B_n^{(1)} = \mu_0 H_n^{(1)}, \quad B_n^{(2)} = \mu_0 \mu_{r2} H_n^{(2)} \tag{11}$$

By substituting Eq. (11) into Eq. (10), the normal stress on the material surface can be found as

$$\begin{aligned} t_{nn}^{(2)} &= B_n^{(1)} H_n^{(1)} - \frac{\mu_0}{2} [(H_n^{(1)})^2 + (H_t^{(1)})^2] - \frac{\mu_0 \chi_2}{2} [(H_n^{(2)})^2 + (H_t^{(2)})^2] \\ &= \frac{1}{\mu_0} (B_n^{(1)})^2 - \frac{\mu_0}{2} \left[\left(\frac{B_n^{(1)}}{\mu_0} \right)^2 + (H_t^{(2)})^2 \right] - \frac{\mu_0 \chi_2}{2} [(H_n^{(2)})^2 + (H_t^{(2)})^2] \\ &= \frac{\mu_0}{2} \left[\left(\frac{B_n^{(2)}}{\mu_0} \right)^2 - (H_t^{(2)})^2 \right] - \frac{\mu_0 \chi_2}{2} [(H_n^{(2)})^2 + (H_t^{(2)})^2] \\ &= \frac{\mu_0 (\mu_{r2}^2 - \chi_2)}{2} (H_n^{(2)})^2 - \frac{\mu_0 \mu_{r2}}{2} (H_t^{(2)})^2 = \frac{\mu_0 (\mu_{r2} \chi_2 + 1)}{2} (H_n^{(2)})^2 \\ &\quad - \frac{\mu_0 \mu_{r2}}{2} (H_t^{(2)})^2 \end{aligned} \tag{12}$$

Such a magnetoelastic stress component, which is evoked by the discontinuity of material properties across the boundary, can be viewed as the normal stress acting on the material surface. Thus the transverse magnetic force $q_n(x)$ equals the magnetoelastic stress component $t_{nn}^{(2)}$. Therefore, Eq. (12) can be approximated by

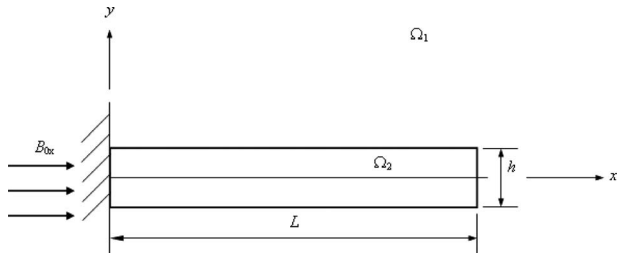

Fig. 1 A ferromagnetic cantilevered beam plate in an in-plane magnetic induction

$$q_n(x) = \mathbf{n}\cdot\mathbf{t} = t_{nn}^{(2)} \approx \frac{\mu_0\mu_{r2}\chi_2}{2}(H_n^{(2)})^2 - \frac{\mu_0\mu_{r2}}{2}(H_t^{(2)})^2 \quad (13)$$

for a soft ferromagnetic material with high relative magnetic permeability ($\mu_r \sim \chi \gg 1$). The symbols $\mathbf{n}$ and $\mathbf{t}$ denote unit normal vector and stress tensor, respectively, on the material surface. This formulation is close to the result

$$q_n(x) \approx \frac{\mu_0\mu_{r2}\chi_2}{2}(H_n^{(2)})^2 - \frac{\mu_0\chi_2}{2}(H_t^{(2)})^2 \quad (14)$$

derived by Zhou and Zheng [9] and Zhou and Miya [10] with the variational principle.

Consider a ferromagnetic cantilevered beam plate subjected to an in-plane magnetic induction, as shown in Fig. 1. Since the beam plate is placed horizontally, only the x component B_{0x} of magnetic induction exists. In this figure, both domains of the air matrix and the beam plate are denoted by Ω_1 and Ω_2, respectively. The equation of motion for the beam plate with length L, thickness h, and density ρ can be expressed as

$$D\frac{\partial^4 w}{\partial x^4} - N_x\frac{\partial^2 w}{\partial x^2} - \frac{\partial N_x}{\partial x}\frac{\partial w}{\partial x} = -\rho h\frac{\partial^2 w}{\partial t^2} + q_y^m(x) + q_y^L(x) \quad 0 < x < L \quad (15)$$

where w is the transverse deflection and

$$D = Eh^3/12(1-\nu^2) \quad (16)$$

is the flexural rigidity of the plate with Young's modulus E and Poisson's ratio ν. Furthermore, the symbol N_x indicates the in-plane force on the beam plate, $q_y^m(x)$ and $q_y^L(x)$ are the transverse magnetic force and Lorentz force. The corresponding boundary conditions of Eq. (15) are

$$w = \frac{\partial w}{\partial x} = 0 \quad \text{for} \quad x = 0 \quad (17)$$

and

$$\frac{\partial^2 w}{\partial x^2} = \frac{\partial^3 w}{\partial x^3} = 0 \quad \text{for} \quad x = L \quad (18)$$

Now the resultant magnetic force acting on the boundary of material can be obtained from Eq. (12) as

$$q_y^m(x) = (t_{yy}^{(2)}|_{y=h/2} - t_{yy}^{(2)}|_{y=-h/2}) = \frac{\mu_0(\mu_{r2}\chi_2+1)}{2}\{[H_y^{(2)}(x,h/2)]^2 - [H_y^{(2)}(x,-h/2)]^2\} - \frac{\mu_0\mu_{r2}}{2}\{[H_x^{(2)}(x,h/2)]^2 - [H_x^{(2)}(x,-h/2)]^2\} \quad (19)$$

Here the superscript (2) in $H_j^{(2)}(j=x,y)$ and the subscript 2 in χ_2 and μ_{r2} indicate that those quantities are on the domain Ω_2 of beam plate.

It is known that the coupling between the transverse motion of beam plate and the applied in-plane magnetic induction will generate conducting current density [12]

$$\mathbf{J} = \sigma(\mathbf{v}\times\mathbf{B}) \quad (20)$$

on the plate, where σ and $\mathbf{v}$ are the electric conductivity and the velocity of the plate and $\mathbf{B}$ denotes the applied in-plane magnetic induction. For the present study, it is convenient to assume

$$\mathbf{v} = \frac{\partial w}{\partial t}\mathbf{e}_y, \quad \mathbf{B} = B_x\mathbf{e}_x + B_u\mathbf{e}_u \quad (21)$$

The symbols $\mathbf{e}_x$, $\mathbf{e}_y$, and $\mathbf{e}_u$ are unit bases of the coordinate system. Then the Lorentz force $\mathbf{f}^L(=f_x^L\mathbf{e}_x+f_y^L\mathbf{e}_y)$ per unit volume can be found as

$$\mathbf{f}^L = \mathbf{J}\times\mathbf{B} = \sigma(\mathbf{v}\times\mathbf{B})\times\mathbf{B} = \sigma[(\mathbf{v}\cdot\mathbf{B})\mathbf{B} - \mathbf{v}(\mathbf{B}\cdot\mathbf{B})] \quad (22)$$

Substituting Eq. (21) into Eq. (22) and integrating over the plate yield

$$q_x^L(x) = \int_x^L f_x^L dx = \sigma\left[\int_x^L B_{0x}B_y^{(2)}(s,0)ds\right]\frac{\partial w}{\partial t}$$

$$q_y^L(x) = \int_{-h/2}^{h/2} f_y^L dy = -\sigma\left\{\int_{-h/2}^{h/2} B_{0x}^2 dy\right\}\frac{\partial w}{\partial t} = -\sigma h B_{0x}^2\frac{\partial w}{\partial t} \quad (23)$$

Here B_{0x} is the applied magnetic induction, as shown in Fig. 1. The magnetic body force $f_j^{M(2)}$ in Eq. (8) will cause an in-plane magnetic force on the beam plate as

$$q_x^m(x) = \int_x^L\int_{-h/2}^{h/2} f_x^{M(2)}(\hat{x},y)dyd\hat{x} \quad (24)$$

where

$$f_x^{M(2)} = \frac{\mu_0\chi_2}{2}\frac{\partial}{\partial x}\{[H_x^{(2)}(x,y)]^2 + [H_y^{(2)}(x,y)]^2\} \quad (25)$$

is the magnetic body force directed along the x-direction. Combining the magnetic force in Eq. (24) and the Lorentz force in Eq. (23), one can find the in-plane magnetic force N_x as

$$N_x(x) = q_x^m(x) + q_x^L(x) \quad (26)$$

In employing the Galerkin method, the transverse deflection can be expressed as

$$w(x,t) = \alpha\hat{w}(x)e^{i\omega t} \quad (27)$$

In which α is a small positive constant and $\hat{w}(x)$ is the normalized eigenfunction corresponding to the natural frequency ω [10]. The deformation in Eq. (27) leads to the transformation between coordinate $\hat{y}$ in the deformed state and the coordinate y in the undeformed state as follows:

$$\hat{y} = y + a\hat{w}(x)e^{i\omega t} \quad (28)$$

Therefore, the magnetic field on the deformed state and that on the undeformed state can be related by

$$H_k^{(2)}(x,\hat{y}) = H_k^{(2)}(x,y) + \alpha\frac{\partial H_k^{(2)}(x,y)}{\partial y}\hat{w}(x)e^{i\omega t} + O(\alpha^2) \quad k = x,y \quad (29)$$

Those terms with order 2 and higher order of α can be neglected in the following derivations.

With the boundary conditions of magnetic field as

$$\mu_0\mu_{r2}H_y^{(2)}(x,\hat{y}_\pm) = B_y^{(2)}(x,\hat{y}_\pm) = B_y^{(1)}(x,\hat{y}_\pm) = \mu_0 H_y^{(1)}(x,\hat{y}_\pm),$$

$$H_x^{(2)}(x,\hat{y}_\pm) = H_x^{(1)}(x,\hat{y}_\pm) \quad (30)$$

on the surface of the deformed beam plate, the magnetic force in Eq. (19) can be found by the use of Eq. (29). It renders

$$q_y^m(x) \approx -\frac{\mu_0\mu_{r2}}{2}\{[H_x^{(2)}(x,\hat{y}_+)]^2 - [H_x^{(2)}(x,\hat{y}_-)]^2\}$$
$$\approx -\frac{\mu_0\mu_{r2}}{2}\left\{\left[H_x^{(2)}(x,h/2) + \alpha\hat{w}(x)e^{i\omega t}\ \left.\frac{\partial H_x^{(2)}}{\partial y}\right|_{y=h/2}\right]^2 - \left[H_x^{(2)}(x,-h/2) + \alpha\hat{w}(x)e^{i\omega t}\ \left.\frac{\partial H_x^{(2)}}{\partial y}\right|_{y=-h/2}\right]^2\right\}$$
$$= -\frac{\mu_0\mu_{r2}}{2}\left\{\left[H_x^{(1)}(x,h/2) + \alpha\hat{w}(x)e^{i\omega t}\ \left.\frac{\partial H_x^{(1)}}{\partial y}\right|_{y=h/2}\right]^2 - \left[H_x^{(1)}(x,-h/2) + \alpha\hat{w}(x)e^{i\omega t}\ \left.\frac{\partial H_x^{(1)}}{\partial y}\right|_{y=-h/2}\right]^2\right\} \quad (31)$$

in which $h=2b$ is used and those terms with order 2 and higher order of α are neglected. The symbols $\hat{y}_\pm = \pm h/2 + \alpha\hat{w}(x)e^{i\omega t}$ represent y coordinate of the upper and the lower surfaces of the beam plate on the deformed state. Without loss of generality, the magnetic field $H_x^{(1)}$ can assumed to be presented in a form as

$$H_x^{(1)}(x,y) = U + Vy + O(y^2) \approx U + Vy \quad (32)$$

with

$$V = \frac{\partial H_x^{(1)}(x,y)}{\partial y} = H_{x,y}^{(1)}(x,y) \quad (33)$$

and the higher order of y can be neglected due to $y \sim h/2$ in the present consideration. Putting Eq. (32) into Eq. (31) and dropping the terms with order 2 of α yield

$$q_y^m(x) \approx \alpha\hat{q}_y^m(x)e^{i\omega t} \quad (34)$$

where

$$\hat{q}_y^m(x) = -\mu_0\mu_{r2}h\hat{w}(x)V^2 \approx -\mu_0\mu_{r2}h\hat{w}(x)[H_{x,y}^{(1)}(x,y)]^2$$
$$= -\mu_0\mu_{r2}h\hat{w}(x)[H_{x,y}^{(2)}(x,y)]^2 \quad (35)$$

The Lorentz force in Eq. (23) can be manipulated by the use of Eq. (27). It gives

$$q_y^L(x) \approx \alpha\hat{q}_y^L(x)e^{i\omega t} \quad (36)$$

with

$$\hat{q}_y^L(x) = -i\omega\sigma hB_{0x}^2\hat{w}(x) \quad (37)$$

In order to illustrate the application of this approach, let us apply the above formulation to a ferromagnetic cantilevered beam plate subjected to an in-plane magnetic field. Substituting Eqs. (27), (34), and (36) into Eq. (15), one can obtain the eigenvalue equation of $\hat{w}(x)$ as

$$D\frac{\partial^4\hat{w}(x)}{\partial x^4} - N_x(x)\frac{\partial^2\hat{w}(x)}{\partial x^2} - \frac{\partial N_x(x)}{\partial x}\frac{\partial\hat{w}(x)}{\partial x} = \rho h\omega^2\hat{w}(x) + \hat{q}_y^m(x) + \hat{q}_y^L(x), \quad 0 < x < L \quad (38)$$

where the quantities $\hat{q}_y^m(x)$ and $\hat{q}_y^L(x)$ can be found from Eqs. (35) and (37), respectively. As denoted in Eq. (26), the in-plane force $N_x(x)$ is the summation of $q_x^m(x)$ and $q_x^L(x)$. The corresponding boundary conditions of Eq. (38) can be written as

$$\hat{w}(x) = \frac{\partial\hat{w}(x)}{\partial x} = 0 \quad \text{for} \quad x = 0 \quad (39)$$

and

$$\frac{\partial^2\hat{w}(x)}{\partial x^2} = \frac{\partial^3\hat{w}(x)}{\partial x^3} \quad \text{for} \quad x = L \quad (40)$$

By applying the Galerkin method, the corresponding natural frequency of Eq. (38) for a beam plate under an in-plane magnetic field can be expressed as

$$\omega^2 = \omega_1^2 + \frac{1}{\Delta}\int_0^L N_x(x)\left[\frac{d\hat{w}(x)}{dx}\right]^2 dx - \frac{1}{\Delta}\int_0^L \hat{q}_y^m(x)\hat{w}(x)dx - \frac{1}{\Delta}\int_0^L \hat{q}_y^L(x)\hat{w}(x)dx \approx \omega_1^2 - Q^M + iQ^L\omega \quad (41)$$

where

$$Q^M = \frac{1}{\Delta}\int_0^L \left\{\hat{q}_y^m(x)\hat{w}(x) - N_x(x)\left[\frac{d\hat{w}(x)}{dx}\right]^2\right\}dx, \quad Q^L = \frac{\sigma}{\rho}B_{0x}^2,$$
$$\Delta = \rho h\int_0^L [\hat{w}(x)]^2 dx \quad (42)$$

and

$$\omega_1^2 = \frac{1}{\Delta}\int_0^L D\frac{d^4\hat{w}(x)}{dx^4}\hat{w}(x)dx$$
$$\hat{w}(x) = (\sin\ \gamma x - \sinh\ \gamma x) + \frac{(\cos\ \gamma L + \cosh\ \gamma L)}{(\sin\ \gamma L - \sinh\ \gamma L)}(\cos\ \gamma x - \cosh\ \gamma x) \quad (43)$$

The symbols $\hat{w}(x)$ in Eq. (39) and ω_1 in Eq. (41) represent the natural frequency and the corresponding eigenfunction (or mode shape) of the transverse deflection for a beam plate free from any magnetic loading. For the vibration of a cantilevered plate, the eigenfunction $\hat{w}(x)$ in Eq. (43) was derived by Meirovitch [18]. The natural frequency of a beam plate subjected to an in-plane magnetic field can be solved from Eq. (41) as

$$\omega = \omega_R + i\omega_I = \frac{iQ^L \pm \sqrt{4(\omega_1^2 - Q^M) - (Q^L)^2}}{2} \quad (44)$$

in which the real part ω_R indicates the frequency of the beam plate and the imaginary part ω_I is related to the amplitude of beam plate vibration. Therefore, only ω_R is relevant in the following numerical examples about the natural frequency. It is convenient to introduce the following quantities:

$$d_1 = \frac{1}{\Delta}\int_0^L \hat{q}_y^m(x)\hat{w}(x)dx, \quad d_2 = \frac{1}{\Delta}\int_0^L N_x(x)\left[\frac{d\hat{w}(x)}{dx}\right]^2 dx \quad (45)$$

which are the two terms in Q^M that appeared in Eq. (42). The estimation $d_2 \ll d_1$ was concluded by Zhou and Miya [10] with finite element method and can also be found with the estimation in the Appendix. It is remarked that the contribution of the in-plane force $N_x(x)$ on the change in natural frequency is insignificant and then can be discarded in the following numerical illustrations. Thus

$$Q^M \approx \frac{1}{\Delta}\int_0^L \hat{q}_y^m(x)\hat{w}(x)dx \quad (46)$$

Referring to Eq. (35), one can find that such a term is related to the differentiation $H_{x,y}^{(1)}(x)$ of magnetic field.

For a typical spring-damper-mass system, the characteristic parameter s on the displacement $u=\hat{u}e^{st}$ satisfies

$$s = \frac{-c \pm \sqrt{c^2 - 4mk}}{2m} = \frac{-c}{2m} \pm \sqrt{\left(\frac{c}{2m}\right)^2 - \frac{k}{m}}$$
$$= \frac{-c}{2m} \pm i\sqrt{\frac{k}{m} - \left(\frac{c}{2m}\right)^2} \quad (47)$$

The damping ratio can be defined as

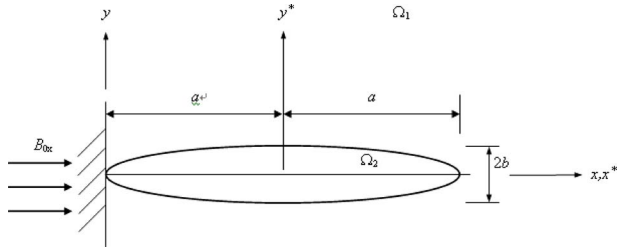

Fig. 2 A ferromagnetic cantilevered elliptic beam plate in an in-plane magnetic induction

$$\xi = \frac{c}{2m\omega} = \frac{c}{2m\sqrt{k/m}} \tag{48}$$

By comparing Eq. (44) with Eq. (47) and using $s=i\omega$, the corresponding damping ratio for the present problem takes the form

$$\xi = \frac{Q^L/2}{\sqrt{\omega_1^2 - Q^M}} \tag{49}$$

3 Approximation of Magnetic Field Distribution

Since it is difficult to obtain the distribution of magnetic field on the beam plate subjected to an in-plane magnetic induction by an analytic method, the magnetic field in an approximated case is introduced in the following paragraph. By applying the complex variable method in-plane magnetoelasticity [19], Lin [13] solved the magnetoelastic problem with an elastic elliptic inclusion. The magnetic fields at the point $z^*(=x^*+iy^*)$ are provided in that study as

$$H_x^{(1)} + iH_y^{(1)} = \frac{B_x^{(1)} + iB_y^{(1)}}{\mu_0\mu_{r1}} = \overline{h_1'(z^*)} = \left(\frac{\bar{g}}{2} + \frac{\bar{\beta}}{a-b}\right) + \left(\frac{\bar{g}}{2} - \frac{\bar{\beta}}{a-b}\right)\frac{\overline{z^*}}{\sqrt{\overline{z^{*2}} - (a^2-b^2)}} \tag{50}$$

on the matrix and

$$H_x^{(2)} + iH_y^{(2)} = \frac{B_x^{(2)} + iB_y^{(2)}}{\mu_0\mu_{r2}} = \overline{h_2'(z^*)} = \frac{2\bar{m}_1}{a+b} \tag{51}$$

on the soft ferromagnetic elliptic inclusion with the major semi-axis a and minor semi-axis b, as shown in Fig. 2. Here the origin of the coordinate (x^*, y^*) is located at the center of the inclusion and the quantities on the matrix and the inclusion are indicated by the superscripts (1) and (2) as denoted in the previous section. In Eqs. (50) and (51), the overhead bar (—) means the complex conjugate and the symbols g, β, and m_1 are given as

$$g = \frac{B_0 e^{-i\theta}}{\mu_0\mu_{r1}}, \quad \beta = \frac{\mu_{r1}-\mu_{r2}}{\mu_{r1}+\mu_{r2}}\frac{a+b}{2}\bar{g} + \frac{2\mu_{r2}}{\mu_{r1}+\mu_{r2}}pm_1$$

$$m_1 = \frac{\mu_{r1}[(\mu_{r2}+\mu_{r1})g(a+b) + (\mu_{r2}-\mu_{r1})\bar{g}(a-b)]}{(\mu_{r2}+\mu_{r1})^2 - (\mu_{r2}-\mu_{r1})^2 p^2} \tag{52}$$

where

$$p = \frac{a-b}{a+b} \tag{53}$$

and the symbol θ is the angle between the incident direction of magnetic induction and the x-axis. In the case of in-plane magnetic induction, we can assign $\theta=0$ in this paper. Now the matrix is composed of air, and $\mu_{r1}=1$ can be taken. Since the magnetic force on the plate is applied via the upper and the lower surfaces in the present study, it is pertinent to consider the magnetic field on the matrix (Ω_1) in the following derivation. Taking $z^*=x^*+iy^*=(x-a)+iy$ and $a \gg b, y$ for a slender inclusion, we have

$$\frac{1}{\sqrt{\overline{z^{*2}} - (a^2-b^2)}} = \{-[x(2a-x)^2 + y^2 - b^2 + 2i(x-a)y]\}^{-1/2} \approx \frac{-(x-a)y}{[x(2a-x)]^{3/2}} - i\frac{1}{[x(2a-x)]^{1/2}} \tag{54}$$

Substituting Eqs. (52)–(54) into Eq. (50) and taking $B_0 e^{-i\theta} = B_{0x}$, $\mu_{r1}=1$ for a thin beam plate under an in-plane magnetic field give rise to

$$H_x^{(1)} + iH_y^{(1)} \approx \left\{A - \frac{Ca^2 y}{[x(2a-x)]^{3/2}} - i\frac{C(x-a)}{[x(2a-x)]^{1/2}}\right\}\frac{B_{0x}}{\mu_0} \tag{55}$$

with

$$A = \frac{1}{(a-b)}\left\{\frac{a-b\mu_{r2}}{1+\mu_{r2}} + \frac{4p\mu_{r2}(\mu_{r2}a+b)}{(\mu_{r2}+1)[(\mu_{r2}^2+1)(1-p^2)+2\mu_{r2}(1+p^2)]}\right\}$$

$$C = \frac{1}{(a-b)}\left\{\frac{a\mu_{r2}-b}{1+\mu_{r2}} - \frac{4p\mu_{r2}(\mu_{r2}a+b)}{(\mu_{r2}+1)[(\mu_{r2}^2+1)(1-p^2)+2\mu_{r2}(1+p^2)]}\right\} \tag{56}$$

Putting Eq. (55) into Eq. (35) with $L=2a$ and dropping the terms with order 2 of α and those terms, which is not related to the dynamic property of the beam plate, yield

$$\hat{q}_y^m(x) \approx -\mu_0\mu_{r2}h\hat{w}(x)[H_{x,y}^{(1)}(x)]^2 \approx -\frac{L^4C^2h}{16[x(L-x)]^3}\hat{w}(x)\frac{\mu_{r2}B_{0x}^2}{\mu_0} \tag{57}$$

with

$$H_{x,y}^{(1)}(x) \approx -\frac{Ca^2}{[x(2a-x)]^{3/2}}\frac{B_{0x}}{\mu_0} = -\frac{CL^2}{4[x(L-x)]^{3/2}}\frac{B_{0x}}{\mu_0} \tag{58}$$

It is observed that only the coefficient C remains in $\hat{q}_y^m(x)$ and the last approximation in Eq. (57) can be concluded by the use of Eq. (55).

The distribution of magnetic field in Eq. (55) is derived from the case of elliptic inclusion. Notice that the thickness at a point near both edges of a thin elliptic inclusion (i.e., $b \ll a$) is much smaller than that on the central region. This feature is different from a beam plate of a uniform thickness. In order to verify the introduction of elliptic beam plate as an approximate case is adequate for the present problem, a finite element analysis of magnetic field with package software ANSYS is provided. The diagram of material number for the finite element model is shown in Fig. 3. In this model, the element type "PLAN13" is adopted and the elements with material numbers 1 and 2, which denote the air and the beam plate, respectively. It is noted that the fixed end is assumed to be made of a diamagnetic material (i.e., $\mu_r \approx 1$). Therefore, both the fixed end and the air have similar magnetic properties and can apply the same material number in the FEM model of magnetic analysis. Following the experiment data conducted by Takagi et al. [8], the geometry size of the beam plate is taken as $L=100$ mm and $h=0.29$ mm or 0.5 mm. It is assigned that the thickness of air layer above (or below) the beam plate is 20 times as much as the thickness of beam plate. For the sake of clear presentation, the vertical size of the element in Fig. 3 is amplified by a factor of 5. A magnetic loading with vector potential +1 on the upper edge and −1 on the lower edge of the present model is applied. From the finite element analysis with the above description, the distribution of magnetic field on the air matrix and beam

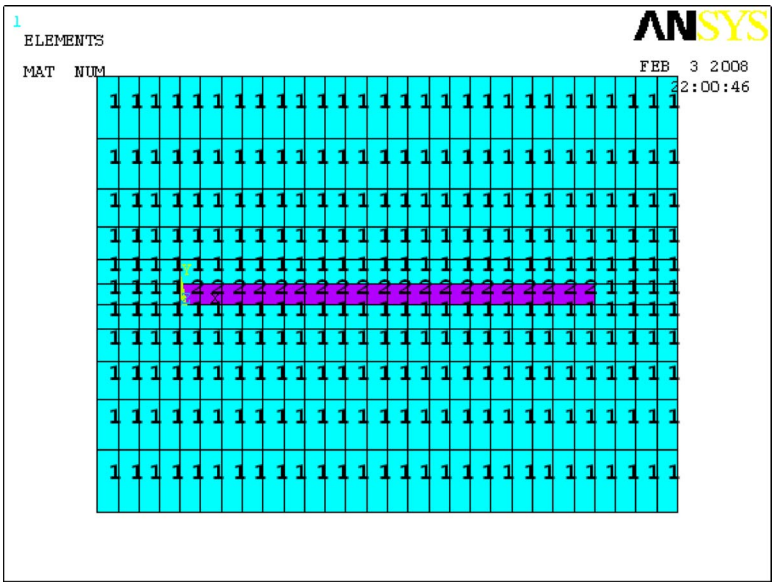

Fig. 3 The material number for a FEM model of a beam plate on the in-plane magnetic induction

plate is displayed with vectors, as shown in Fig. 4. In Fig. 4(*a*), $\mu_{r1}=\mu_{r2}=1$ is taken and the magnetic field is uniform with arrowhead directed to the right. Alternatively, $\mu_{r1}=1$ and $\mu_{r2}=12$ (i.e., $\chi_2=11$) is adopted in Fig. 4(*b*) and then the lines of the applied magnetic field (or induction) are observed to be attracted by the beam plate with higher relative magnetic permeability. The value of magnetic field obtained from Fig. 4(*b*) can be divided by the uniform value from Fig. 4(*a*) and then the normalized magnetic field $H_x^{(1)}(x)/(B_{0x}/\mu_0)$ can be found. It is noted that B_{0x}/μ_0 has a constant value.

As presented in Eq. (35), the term $H_{x,y}^{(1)}(x)$ is dominant in obtaining the magnetic force $\hat{q}_y^m(x)$, which is relevant in this study. The normalized differentiations $H_{x,y}^{(1)}(x)/(B_{0x}/\mu_0)$ of magnetic field obtained from both the finite element analysis and Eq. (58) of this study with $L/h=100/0.29$ and $L/h=100/0.5$ are depicted in Figs. 5(*a*) and 5(*b*), respectively. In these figures, the notation $H_{x,y}^{(1)}(x)/(B_{0x}/\mu_0)$ denotes the differentiation of magnetic field on the air near the surface of the beam plate. It is viewed that the results of present theoretical analysis are close to that of the finite element analysis with ANSYS.

From Figs. 5(*a*) and 5(*b*), the derivative of magnetic field in Eq. (58) for a beam plate with elliptic shape possesses singularity on both edges of beam plate but that from finite element analysis keeps finite on both edges of a beam plate with uniform thickness. Such a feature is evoked by the difference in shape between an elliptic beam and a beam of uniform thickness. Therefore, a parameter x_r is recommended to conduct the available area of Eq. (58), as shown in Fig. 5(*b*). In other words, Eqs. (35) and (58) are workable for the range $(1-x_r)/2\leq X/L\leq(1+x_r)/2$. For example, $x_r=0.95$ indicates the range $0.025\leq X/L\leq 0.975$. If the value of X/L lies outside this range, the differentiation $H_{x,y}^{(1)}(x)$ of magnetic field and the magnetic force $\hat{q}_y^m(x)$ are assumed to be uniform as the dotted lines in Fig. 5(*b*) on both ends of the beam plate, and then the curves of $\hat{q}_y^m(x)$ (also $H_{x,y}^{(1)}(x)$) keep continuous. Obviously, such a modification is also valid in Fig. 5(*a*) for the beam plate with different thicknesses. Thus the expression of $\hat{q}_y^m(x)$ in Eq. (35) can be modified as follows:

$$\hat{q}_y^m(x)=\begin{cases}\left[-\dfrac{4C^2h}{(1-x_r^2)^3L^2}\hat{w}(x)\big|_{x=(1-x_r)L/2}\right]\dfrac{\mu_{r2}B_{0x}^2}{\mu_0} & \text{for} \quad x<\dfrac{(1-x_r)L}{2}\\ -\dfrac{L^4C^2h}{16[x(L-x)]^3}\hat{w}(x)\dfrac{\mu_{r2}B_{0x}^2}{\mu_0} & \text{for} \quad \dfrac{(1-x_r)L}{2}\leq x\leq\dfrac{(1+x_r)L}{2}\\ \left[-\dfrac{4C^2h}{(1-x_r^2)^3L^2}\hat{w}(x)\big|_{x=(1+x_r)L/2}\right]\dfrac{\mu_{r2}B_{0x}^2}{\mu_0} & \text{for} \quad x>\dfrac{(1+x_r)L}{2}\end{cases} \tag{59}$$

Here the magnetic force is continuous at the points $x=(1\pm x_r)L/2$ and becomes uniform when $x<(1-x_r)L/2$ and $x>(1+x_r)L/2$. The parameter x_r, which governs the applicable range of Eqs. (35), (58), (A1), and (A4), can be found via the use of experiment results provided by Takagi et al. [8] in Sec. 4.

4 Numerical Results

In order to guarantee that the present approach is meaningful, the numerical results of this work will be provided and compared with the data provided in the previous study. The corresponding eigenvalue $\gamma L=1.875$ for the eigenfunction presented in Eq. (43)

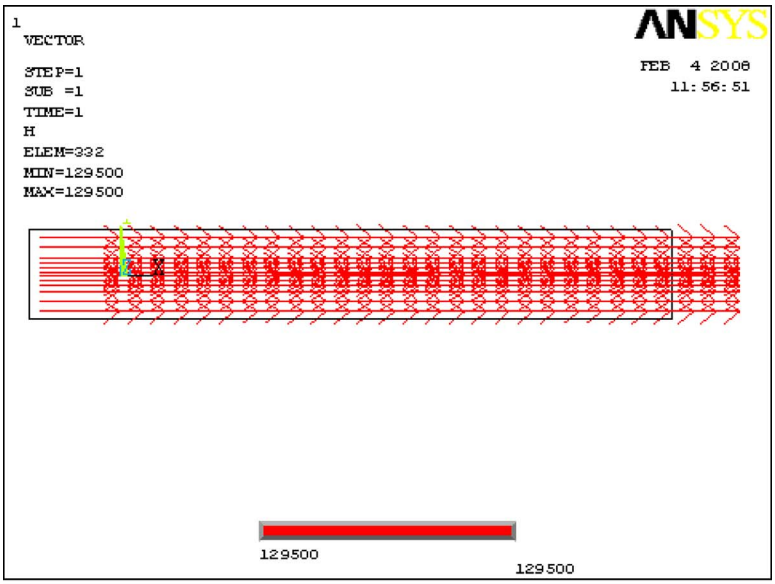

(a)

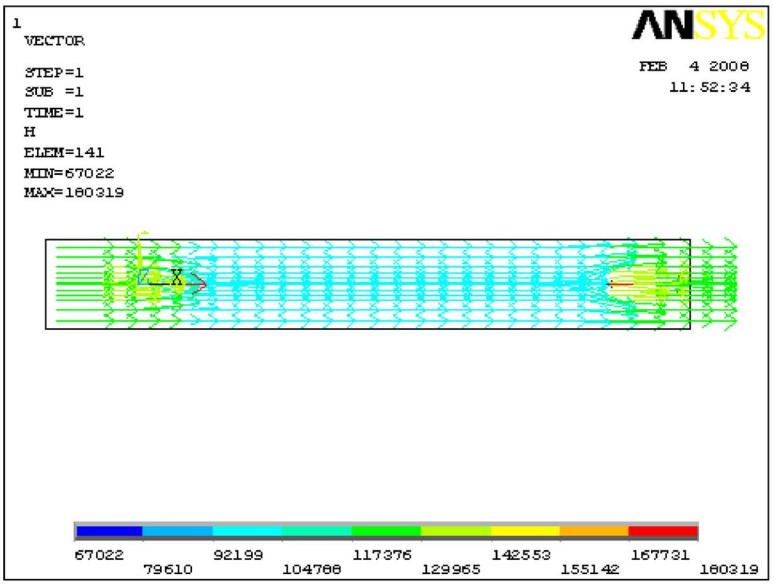

(b)

Fig. 4 The FEM output for the distribution of magnetic field on a cantilevered beam plate subjected to an in-plane magnetic induction: (*a*) $\mu_{r1}=\mu_{r2}=1$ and (*b*) $\mu_{r1}=1$, $\mu_{r2}=12$

is given by Meirovitch (pp. 161–166 of Ref. [18].). With the material properties given as $\rho=7800$ kg/m^3, $\sigma=2,300,000$ S/m, $\chi_2=7-15$, and $L=100$ mm, the relevant experimental data provided in Ref. [8] are presented in Fig. 6(*a*) for $h=0.29$ mm and $h=0.5$ mm for Fig. 6(*b*). By taking $\chi_2=11$, the material data (ρ and σ) and the geometry data (L and h), which are presented above, the theoretical predictions of this study for the variation in natural frequency on the magnetic induction and the results given by Zhou and Miya [10] with theoretical method are also depicted in these figures. The range of x_r is 0.95–0.965 with $L/h=100/0.29$ in Fig. 6(*a*) and $x_r=0.92-0.935$ for $L/h=100/0.5$ in Fig. 6(*b*). For a fixed value of the applied magnetic induction B_{0x}, the increase in natural frequency with x_r can be observed from Fig. 6. Since x_r conducts the available range for the distribution of magnetic field derivative in Eq. (58) with singularity on both edges of the thin elliptic inclusion, the higher value of x_r may cause higher transverse magnetic force $\hat{q}_y^m(x)$ and higher value of natural frequency ω_R.

The variation in natural frequency on the applied magnetic induction under different values of χ_2 is presented in Fig. 7. In this figure, the parameter x_r is chosen as 0.955 with $L/h=100/0.29$ in Fig. 7(*a*) and $x_r=0.925$ with $L/h=100/0.5$ in Fig. 7(*b*). It is observed that the natural frequency increases with χ_2 under a fixed value of the applied magnetic induction.

In order to understand the damping character of the present problem, the variation in damping ratio presented in Eq. (49) on the applied magnetic induction is provided in Fig. 8 with the same L/h ratio and x_r as that given in Fig. 6. The corresponding experimental results in Ref. [8] and the theoretical predictions in Ref.

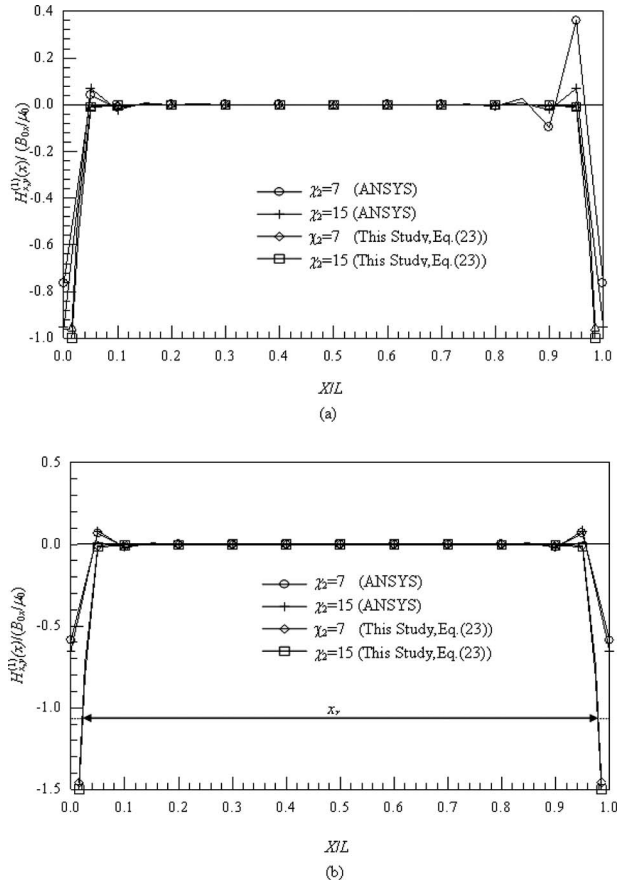

Fig. 5 The normalized differentiation $H^{(1)}_{x,y}(x)/(B_{0x}/\mu_0)$ of magnetic field for a cantilevered beam plate on an in-plane magnetic induction: (*a*) L/h=100/0.29 and (*b*) L/h=100/0.5

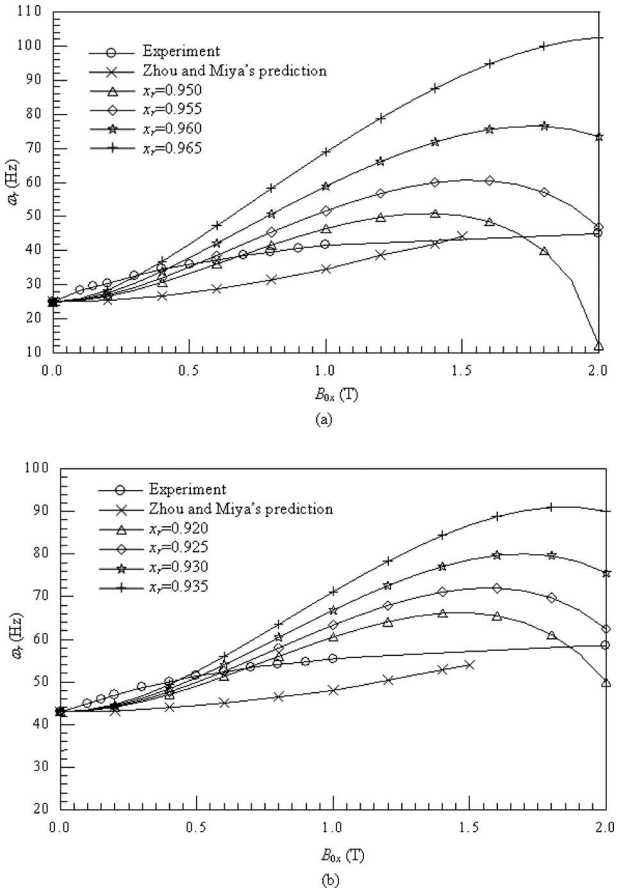

Fig. 6 The variation in natural frequency of a cantilevered beam plate on the in-plane magnetic induction with χ_2=11: (*a*) L/h=100/0.29 and (*b*) L/h=100/0.5

[10] are also shown in this figure. One can find that the damping ratio will decrease with the increase in the value of parameter x_r and the deviation between the damping ratio obtained from this study and the experiment increases with the increase in the applied magnetic induction B_{0x}.

5 Discussion

Without including the effect of magnetic viscous damping, Zhou and Miya [10] obtained concave curves for the variation in natural frequency on the strength of applied magnetic induction by theoretical method rather than the convex curves in the experimental data, as shown in Fig. 6. Furthermore, larger slenderness ratio of beam plate may make the derivative of magnetic field in Eq. (58) and the result of finite element analysis closer to each other, as shown in Fig. 5, and will result in higher x_r, as presented in Fig. 6. Alternatively, the theoretical curves in Fig. 6 are concave when the applied magnetic induction B_{0x} increases from 0 T up to 0.6 T and becomes convex for further increase in B_{0x}. The convex feature of the theoretical curves on higher strength of the applied magnetic induction is evoked by the magnetic viscous damping effect of Lorentz force. Therefore, the deviation between the experimental data and the present theoretical results is small when the value of applied magnetic induction is below 2 T. If the viscous damping effect of Lorentz force is discounted, the theoretical curves become pure concave and can be used to compare with experimental ones up to B_{0x}=1 T. Such a feature is similar to that derived from Ref. [10].

Referring to Eqs. (35) and (42) and Fig. 5, it is found that higher x_r may cause higher value of $\omega_1^2 - Q^M$ and the value of damping ratio is reduced, as shown in Fig. 8. Without considering the damping effect of Lorentz force or taking higher value of x_r will make the theoretical curve of damping ratio and that of experiment data more close, as shown in Fig. 8, but the convex feature for the theoretical curves of frequency becomes unobvious, as presented in Fig. 6. Thus the difference in frequency between the theoretical and the experimental results is magnified for higher value of B_{0x}. The deviation between the theoretical predictions and the experimental results, as shown in Fig. 8, may be caused by approximating a beam of uniform thickness with an elliptic beam. Nevertheless, the damping feature of the present problem can be characterized in this study. Furthermore, it is remarked that taking x_r=0.955 for the case of h=0.29 mm and x_r =0.925 for h=0.5 mm with χ_2=11 in the present approach can yield proper predictions for the frequency of a beam plate subjected to an in-plane magnetic field up to 2 T.

6 Concluding Remarks

In this paper, a compact theoretical approach is developed to investigate the natural frequency of a beam plate subjected to an in-plane magnetic field. By applying the new magnetic force model developed in this paper and the distribution of magnetic field deduced from the complex variable method for the elliptic inclusion problem and considering the magnetic viscous damping effect of Lorentz force, the natural frequency of beam plate can be predicted. The Galerkin method is adopted to determine the numerical value of natural frequency. A parameter governing the available range for the distribution of magnetic field and magnetic force on an elliptic inclusion is introduced in the theoretical calculation to modify the deviation of magnetic field and magnetic force caused by the shape difference between an elliptic inclusion

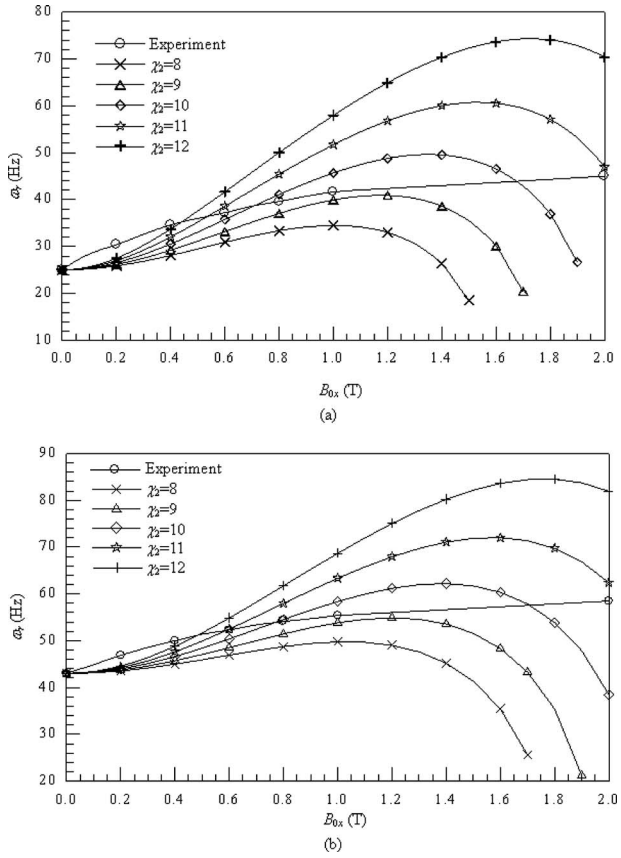

Fig. 7 The variation in natural frequency of a cantilevered beam plate on the in-plane magnetic induction: (*a*) $L/h=100/0.29$ with $x_r=0.955$ and (*b*) $L/h=100/0.5$ with $x_r=0.925$

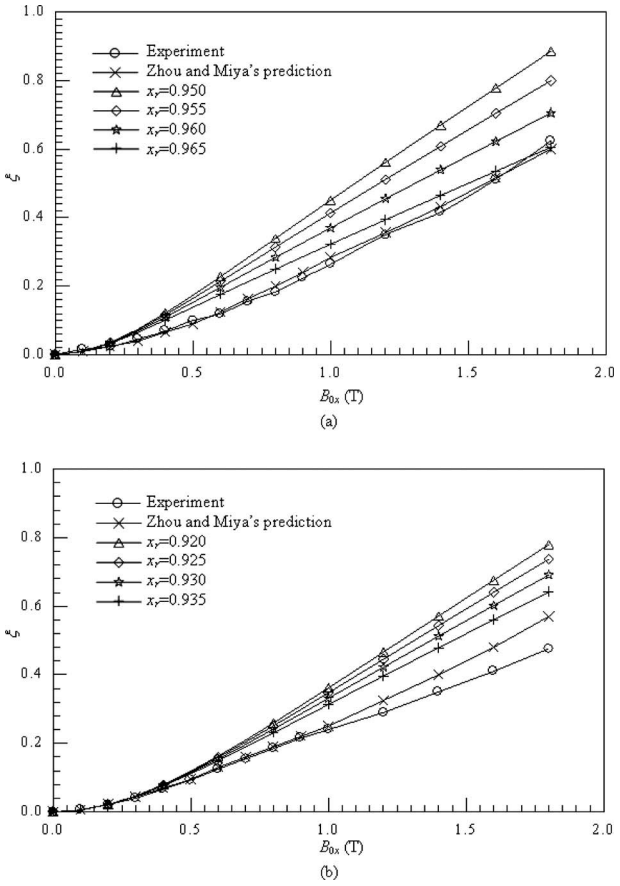

Fig. 8 The variation in damping ratio of a cantilevered beam plate on the in-plane magnetic induction with $\chi_2=11$: (*a*) $L/h=100/0.29$ and (*b*) $L/h=100/0.5$

and a beam plate of uniform thickness. It is noted that the theoretical results obtained in the present study are close to the experimental data when the magnetic induction increases from 0 T up to 2 T. Furthermore, the convex character of the theoretical curve can be also found. Such a result is compatible with the experimental measurement.

Acknowledgment

The authors would like to thank the financial support by the National Science Council, R.O.C. through Grant No. NSC-93-2212-E-252-003.

Appendix

Applying Eqs. (24), (25), (30), and (55) with the aforementioned notations $\hat{y}_\pm=\pm h/2+\alpha\hat{w}(x)e^{i\omega t}$ on the deformed plate surfaces, we can obtain

$$q_x^m(x)=\frac{\mu_0\mu_{r2}}{2}\int_x^L\int_{\hat{y}_-}^{\hat{y}_+}\frac{\partial}{\partial\hat{x}}\{[H_x^{(2)}(\hat{x},\hat{y})]^2+[H_y^{(2)}(\hat{x},\hat{y})]^2\}d\hat{y}d\hat{x}$$

$$=\frac{\mu_0\mu_{r2}}{2}\int_x^L\frac{\partial}{\partial\hat{x}}\int_{\hat{y}_-}^{\hat{y}_+}\{[H_x^{(2)}(\hat{x},\hat{y})]^2+[H_y^{(2)}(\hat{x},\hat{y})]^2\}d\hat{y}d\hat{x}$$

$$=\frac{\mu_0\mu_{r2}}{2}\int_x^L\frac{\partial}{\partial\hat{x}}[G_x^{(2)}(\hat{x},\hat{y}_+)-G_x^{(2)}(\hat{x},\hat{y}_-)+G_y^{(2)}(\hat{x},\hat{y}_+)$$

$$-G_y^{(2)}(\hat{x},\hat{y}_-)]d\hat{x}=\frac{\mu_0\mu_{r2}}{2}\int_x^L\frac{\partial}{\partial\hat{x}}\Bigg\{G_x^{(1)}(\hat{x},\hat{y}_+)-G_x^{(1)}(\hat{x},\hat{y}_-)$$

$$+\frac{1}{\mu_{r2}^2}[G_y^{(1)}(\hat{x},\hat{y}_+)-G_y^{(1)}(\hat{x},\hat{y}_-)]\Bigg\}d\hat{x}$$

$$\approx-\left\{\frac{\hat{w}(\hat{x})}{[\hat{x}(L-\hat{x})]^{3/2}}\Bigg|_{\hat{x}=x}^{L}\right\}\frac{\alpha ACL^2h}{4}\frac{\mu_{r2}B_{0x}^2}{\mu_0}e^{i\omega t}\tag{A1}$$

Here, those terms that do not relate to the plate motion are discarded. The function $G_k^{(2)}(x,y)$ satisfies

$$\frac{\partial G_k^{(2)}(x,y)}{\partial y}=[H_k^{(2)}(x,y)]^2\quad k=x,y\tag{A2}$$

and hence the expansion

$$G_k^{(2)}(x,\hat{y})=G_k^{(2)}(x,y)+\alpha\frac{\partial G_k^{(2)}(x,y)}{\partial y}\hat{w}(x)e^{i\omega t}+O(\alpha^2)\approx G_k^{(2)}(x,y)$$

$$+\alpha[H_k^{(2)}(x,y)]^2\hat{w}(x)e^{i\omega t}\quad k=x,y\tag{A3}$$

can be derived by employing Eq. (28). Notice that Eq. (A3) is applied in the derivation of Eq. (A1). Since $H_x(x,y)$ is continuous across the upper and the lower surfaces of the plate as denoted in Eq. (30), it is reasonable to assume $G_x^{(2)}(x,\hat{y}_\pm)=G_x^{(1)}(x,\hat{y}_\pm)$. The function $G_x^{(1)}(x,\hat{y}_\pm)$ can be obtained by replacing the superscript (2) in Eq. (A2) with the superscript (1).

By the use of Eqs. (2), (23), (27), (55), and (56), the component $q_x^L(x)$ of Lorentz force is found as

$$q_x^L(x) = \sigma B_{0x}\left[\int_x^L B_y^{(2)}(s,0)ds\right]\frac{\partial w}{\partial t} \approx \sigma B_{0x}\left[\int_x^L B_y^{(2)}(s,h/2)ds\right]$$
$$\times[i\alpha\omega\hat{w}(x)e^{i\omega t}] = \sigma B_{0x}\left[\int_x^L B_y^{(1)}(s,h/2)ds\right][i\alpha\omega\hat{w}(x)e^{i\omega t}]$$
$$= i\alpha\omega\sigma B_{0x}^2\left[\int_x^L -\frac{C(s-L/2)}{[s(L-s)]^{1/2}}ds\right][\hat{w}(x)e^{i\omega t}] =$$
$$-i\alpha\omega\sigma\mu_{r2}C[x(L-x)]^{1/2}B_{0x}^2(\hat{w}e^{i\omega t}) \quad \text{(A4)}$$

in which the approximation $B_y^{(2)}(s,0) \approx B_y^{(2)}(s,h/2)$ is deduced from that the variation in the magnetic field along the transverse direction of a very thin plate is not abrupt.

By the use of Eqs. (24), (25), (36), (37), (43), (58), (A1), (A2), and (A4), the estimation $d_2 \ll d_1$ can be concluded.

References

[1] Moon, F. C., and Pao, Y. H., 1968, "Magnetoelastic Buckling of a Thin Plate," ASME J. Appl. Mech., **35**, pp. 53–58.

[2] Brown, W. F., Jr., 1966, *Magnetoelastic Interactions*, Springer-Verlag, New York.

[3] Pao, Y. H., and Yeh, C. S., 1973, "A Linear Theory for Soft Ferromagnetic Elastic Solids," Int. J. Eng. Sci., **11**, pp. 415–436.

[4] Eringen, A. C., 1989, "Theory of Electromagnetic Elastic Plates," Int. J. Eng. Sci., **27**, pp. 363–375.

[5] Eringen, A. C., and Maugin, G. A., 1990, *Electrodynamics of Continua*, Vol. I, Springer-Verlag, New York.

[6] Sabir, M., and Maugin, G. A., 1996, "On the Fracture of Paramagnets and Soft Ferromagnets," Int. J. Non-Linear Mech., **31**, pp. 425–440.

[7] Zhou, Y. H., Zheng, X. J., and Miya, K., 1995, "Magnetoelastic Bending and Snapping of Ferromagnetic Plates in Oblique Magnetic Fields," Fusion Eng. Des., **30**, pp. 325–337.

[8] Takagi, T., Tani, J., Matsubara, Y., and Mogi, I., 1995, "Dynamic Behavior of Fusion Structural Components Under Strong Magnetic Fields," Fusion Eng. Des., **27**, pp. 481–489.

[9] Zhou, Y. H., and Zheng, X. J., 1997, "A General Expression of Magnetic Force for Soft Ferromagnetic Plates in Complex Magnetic Fields," Int. J. Eng. Sci., **35**, pp. 1405–1417.

[10] Zhou, Y. H., and Miya, K., 1998, "A Theoretical Prediction of Natural Frequency of a Ferromagnetic Beam Plate With Low Susceptibility in an In-Plane Magnetic Field," ASME J. Appl. Mech., **65**, pp. 121–126.

[11] Takagi, T., and Tani, J., 1993, "A New Numerical Analysis Method of Dynamic Behavior of a Thin Plate Under Magnetic Field Considering Magnetic Viscous Damping Effect," Int. J. Appl. Electromagn. Mater., **4**, pp. 35–42.

[12] Lin, C. B., 1999, "Destabilizing Effect of In-Plane Magnetic Field on Panel Flutter," J. Mech., **15**, pp. 79–88.

[13] Lin, C. B., 2003, "On a Bounded Elliptic Elastic Inclusion in Plane Magnetoelasticity," Int. J. Solids Struct., **40**, pp. 1547–1565.

[14] Moon, F. C., 1984, *Magneto-Solid Mechanics*, Wiley, New York.

[15] McMeeking, R. M., and Landis, C. M., 2005, "Electrostatic Forces and Stored Energy for Deformable Dielectric Materials," ASME J. Appl. Mech., **72**, pp. 581–590.

[16] Suo, Z., Zhao, X., and Greene, W. H., 2008, "A Nonlinear Field Theory of Deformable Dielectrics," J. Mech. Phys. Solids, **56**, pp. 467–486.

[17] Rinaldi, C., and Brenner, H., 2002, "Body Versus Surface Forces in Continuum Mechanics: Is the Maxwell Stress Tensor a Physically Objective Cauchy Stress?" Phys. Rev. E, **65**, p. 036615.

[18] Meirovitch, L., 1967, *Analytical Methods in Vibrations*, Macmillan, New York.

[19] Lin, C. B., and Yeh, C. S., 2002, "The Magnetoelastic Problem of a Crack in a Soft Ferromagnetic Solid," Int. J. Solids Struct., **39**, pp. 1–17.

Diagnostic-Photographic Determination of Drag/Lift/Torque Coefficients of a High Speed Rigid Body in a Water Column

Peter C. Chu

Chenwu Fan

Naval Ocean Analysis and Prediction Laboratory,
Naval Postgraduate School,
Monterey, CA 94025

Paul R. Gefken
Polter Laboratory,
SRI International,
Menlo Park, CA 94025

Prediction of a rigid body falling through water column with a high speed (such as Mk-84 bomb) needs formulas for drag/lift and torque coefficients, which depend on various physical processes such as free surface penetration and bubbles. A semi-empirical method is developed in this study to determine the drag/lift and torque coefficients for a fast-moving rigid body in a water column. The theoretical part is to derive the relationships (called diagnostic relationships) between (drag, lift, and torque) coefficients and (position and orientation) of the rigid body from the three momentum equations and the three moment of momentum equations. The empirical part is to collect data of trajectory and orientation of a fast-moving rigid body using multiple high-speed video cameras (10,000 Hz). Substitution of the digital photographic data into the theoretical relationships leads to semi-empirical formulas of drag/lift and torque coefficients, which are functions of the Reynolds number, attack angle, and rotation rate. This method was verified by 1/12th Mk-84 bomb strike experiment with various tail configurations (tail section with four fins, two fins, and no fin and no-tail section) conducted at the SRI test site. The cost of this method is much lower than the traditional method using the wind tunnel. Various trajectory patterns are found for different tail configurations.
[DOI: 10.1115/1.3173767]

Keywords: body-flow interaction, drag coefficient, lift coefficient, torque coefficient, fast rigid body in water column, diagnostic-photographic method

1 Introduction

Prediction of a fast-moving rigid body in a water column has wide scientific significance and technical application. The dynamics of a rigid body allows one to set up six nonlinear equations for the most general motion: three momentum equations and three moment of momentum equations. The scientific studies of the hydrodynamic characteristics of a rigid body in a water column involve nonlinear dynamics, body and multiphase fluid interaction, free surface penetration, and stability theory.

The technical application of the hydrodynamics of a rigid body with high speed into fluid includes aeronautics, navigation, and civil engineering. Recently, the scientific problem about the movement of a rigid body in water column drew attention to the naval research. This is due to the threat of mine and maritime improvised explosive device (IED). Prediction of a fast falling rigid body in the water column contributes to the bomb breaching for mine and maritime IED clearance in surf and very shallow water zones with depth shallower than 12.2 m (i.e., 40 ft), according to U.S. Navy's standards.

To predict rigid body maneuvering in water column, accurate calculation of hydrodynamic forces and torques is difficult due to unknown drag, lift, and torque coefficients. Determination of these coefficients is crucial for the prediction [1–3]. Different from traditional methods used in aerodynamics, such as using the wind tunnel, we present a new efficient and low cost method to determine the drag, lift, and torque coefficients. This method consists of theoretical and empirical parts. The theoretical part is to establish dynamical relationships between hydrodynamic coefficients (e.g., drag, lift, and torque coefficients) and kinematics of the rigid body (e.g., position and orientation). The empirical part is to conduct experiments through shooting the rigid body into the water tank with high-speed video (HSV) cameras at 10,000 frames per second (fps) to record its underwater position and orientation. Semi-empirical formulas can be established for the drag, lift, and torque coefficients by substituting the digital data of rigid body's location and orientation from the HSV cameras into the dynamical relationships.

The rest of the paper is outlined as follows. Sections 2 and 3 describe the hydrodynamic forces, torques, and basic dynamics. Section 4 presents the diagnostic relationships for the drag/lift and torque coefficients, which were derived from the momentum and moment of momentum equations. Section 5 depicts the empirical method. Sections 6 and 7 show the semi-empirical formulas for the drag/lift and torque coefficients and the verification. Section 8 describes the tail section damage effects. Section 9 presents the conclusions.

2 Hydrodynamic Forces and Torques

2.1 Drag/Lift Forces. The earth-fixed coordinate system is used with the unit vectors $(\mathbf{i}, \mathbf{j})$ in the horizontal plane and the unit vector $\mathbf{k}$ in the vertical direction. Consider an axially symmetric rigid body such as a bomb falling through a water column. The two end-points of the body (i.e., head and tail points) are represented by $\mathbf{r}_h(t)$ and $\mathbf{r}_t(t)$. The difference between the two vectors in the nondimensional form

$$\mathbf{e} = \frac{\mathbf{r}_h - \mathbf{r}_t}{|\mathbf{r}_h - \mathbf{r}_t|} \tag{1}$$

is the unit vector representing the body's main axis direction (Fig. 1). The centers of mass (o_m) and volume (o_v) are located on the

Contributed by the Applied Mechanics Division of ASME for publication in the JOURNAL OF APPLIED MECHANICS. Manuscript received August 25, 2008; final manuscript received May 12, 2009; published online October 5, 2009. Review conducted by Nadine Aubry.

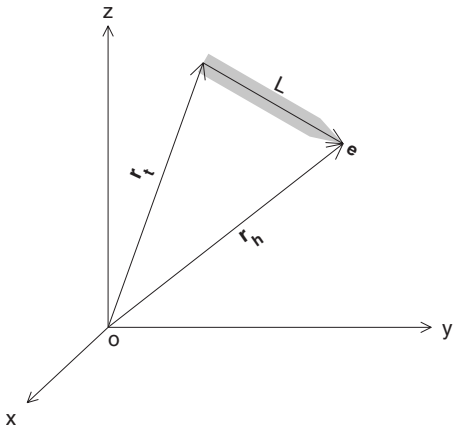

Fig. 1 Position vectors $\mathbf{r}_h$, $\mathbf{r}_t$, and the unit vector e

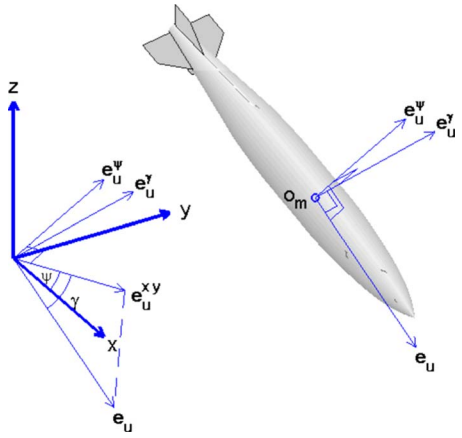

Fig. 3 Illustration of unit vectors ($\mathbf{e}_u, \mathbf{e}_u^{\psi}, \mathbf{e}_u^{\gamma}$, and $\mathbf{e}_u^{xy}$) with $\mathbf{e}_v^{xy}$ the projection of $\mathbf{e}_u$ on the *xy* plane

main axis with σ the distance between o_v and o_m, which has a positive (negative) value when the direction from o_v to o_m is the same (opposite) as the unit vector $\mathbf{e}$ (Fig. 2). The location (or called translation) of the body is represented by the position of o_m

$$\mathbf{r}(t) = x\mathbf{i} + y\mathbf{j} + z\mathbf{k} \tag{2}$$

The translation velocity is given by

$$\frac{d\mathbf{r}_o}{dt} = \mathbf{u}, \quad \mathbf{u} = U\mathbf{e}_u \tag{3}$$

where U and $\mathbf{e}_u$ are the speed and unit vector of the rigid-body velocity. Let β be the angle of the body's main axis with the horizontal plane, γ be the angle of the body's velocity $\mathbf{u}$ with the horizontal plane, and α be the attack angle between the direction of the main body axis ($\mathbf{e}$) and the direction of the body velocity ($\mathbf{e}_u$) [4] (Fig. 2)

$$\alpha = \cos^{-1}(\mathbf{e}_u \bullet \mathbf{e}), \quad \beta = \sin^{-1}(\mathbf{e} \bullet \mathbf{k}), \quad \gamma = \sin^{-1}(\mathbf{e}_u \bullet \mathbf{k}) \tag{4}$$

Usually, the unit vector $\mathbf{e}_u$ is represented by (Fig. 3)

$$\mathbf{e}_u = \cos\ \gamma \cos\ \psi\mathbf{i} + \cos\ \gamma \sin\ \psi\mathbf{j} + \sin\ \gamma\mathbf{k} \tag{5}$$

where ψ is the azimuth angle. Differentiation of Eq. (5) with respect to t gives

$$\frac{d\mathbf{e}_u}{dt} = \frac{d\gamma}{dt}\mathbf{e}_u^{\gamma} + \frac{d\psi}{dt}\cos\ \gamma\mathbf{e}_u^{\psi} \tag{6}$$

where

$$\mathbf{e}_u^{\psi} = -\sin\ \psi\mathbf{i} + \cos\ \psi\mathbf{j}, \quad \mathbf{e}_u^{\gamma} = -\sin\ \gamma\cos\ \psi\mathbf{i} - \sin\ \gamma\sin\ \psi\mathbf{j} + \cos\ \gamma\mathbf{k} \tag{7}$$

are unit vectors. It is clear that

$$\mathbf{e}_u^{\psi} \perp \mathbf{e}_u, \quad \mathbf{e}_u^{\gamma} \perp \mathbf{e}_u, \quad \mathbf{e}_u^{\gamma} \perp \mathbf{e}_u^{\psi} \tag{8}$$

Let $\mathbf{V}_w$ be the water velocity. Water-to-body relative velocity $\mathbf{V}$ (called the relative velocity) is represented by

$$\mathbf{V} \equiv \mathbf{V}_w - \mathbf{u} \approx -\mathbf{u} = -U\mathbf{e}_u \tag{9}$$

Here, the water velocity is assumed much smaller than the rigid-body velocity. A third basic unit vector ($\mathbf{e}_m^h$) can be defined perpendicular to both $\mathbf{e}$ and $\mathbf{e}_u$

$$\mathbf{e}_m^h = \frac{\mathbf{e}_u \times \mathbf{e}}{|\mathbf{e}_u \times \mathbf{e}|} \tag{10}$$

The drag force ($\mathbf{F}_d$) is in the opposite direction of the rigid-body velocity. The lift force ($\mathbf{F}_l$) is in the plane constructed by the two vectors ($\mathbf{e}$ and $\mathbf{e}_u$) (i.e., perpendicular to $\mathbf{e}_m^h$) and perpendicular to $\mathbf{e}_u$, and therefore the lift force is in the same direction as $\mathbf{e}_m^h \times \mathbf{e}_u$. Both drag and lift forces, exerting on the center of volume, are represented by

$$\mathbf{F}_d = -f_d\mathbf{e}_u, \quad \mathbf{F}_l = f_l\mathbf{e}_l, \quad \mathbf{e}_l = \mathbf{e}_m^h \times \mathbf{e}_u \tag{11}$$

where f_d and f_1 are the magnitudes of the forces. The magnitudes (f_d, f_l) are represented by the drag law [5]

$$f_d = \tfrac{1}{2}C_d\rho A_w U^2, \quad f_l = \tfrac{1}{2}C_l\rho A_w U^2 \tag{12}$$

where ρ is water density; A_w is the under water projection area; C_d and C_l are the drag and lift coefficients, which are determined by the experiments.

Bomb is a fast-moving rigid body usually with four fins. Two fins in the same plane are called the pair of fins. For simplicity, these fins are treated approximately as the NACA0015 airfoils (Fig. 4) with known drag and lift coefficients [6]. Using these

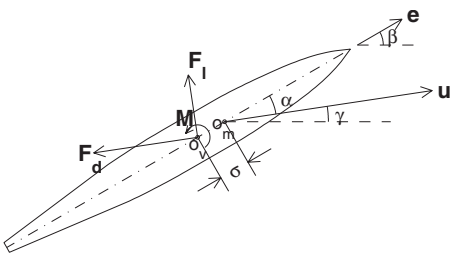

Fig. 2 Attack angle (α), angles (β, γ), center of volume (o_v), center of mass (o_m), and drag and lift forces (exerted on o_v). Note that σ is distance between o_v and o_m with positive (negative) value when the direction from o_v to o_m is the same (opposite) as the unit vector e.

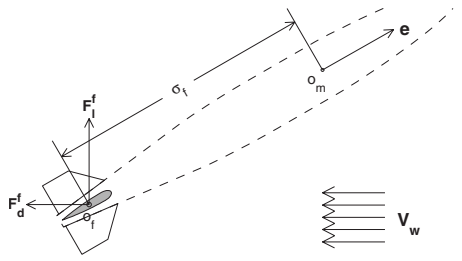

Fig. 4 Axial and cross-axial velocity ($\mathbf{u}_a^f, \mathbf{u}_c^f$), associated hydrodynamic forces on a pair of fins ($\mathbf{F}_a^f, \mathbf{F}_c^f$) and the distance between o_f and o_m (i.e., σ_f) with positive (negative) value when the direction from o_f to o_m is the same (opposite) as the unit vector e

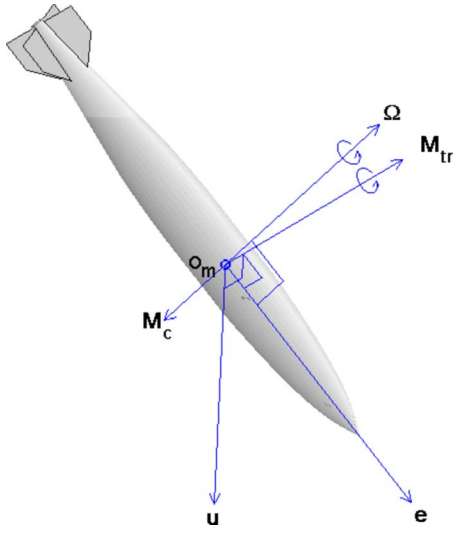

Fig. 5 Illustration of Ω, M_{tr}, and M_c

coefficients, the combined drag and lift forces on a pair of fins ($\mathbf{F}_c^f$) can be calculated. If the bomb has n pairs of fins, the total drag and lift forces on the fins are represented by $n\mathbf{F}_c^f$.

2.2 Hydrodynamic Torque. Since the drag/lift forces are exerted on the center of volume (o_v), the hydrodynamic torque (relative to center of mass, o_m) $\mathbf{M}_h$ is computed by

$$\mathbf{M}_h = -\sigma\mathbf{e} \times (\mathbf{F}_d + \mathbf{F}_l) - n\sigma_f\mathbf{e} \times \mathbf{F}_c^f + \mathbf{M}_{\text{tr}} + \mathbf{M}_{\text{rot}} \tag{13}$$

where the first two terms in the righthand side of Eq. (13) represent the torque by the drag and lift forces; $\mathbf{M}_{\text{tr}}$ is the antitranslation torque by the moment of drag/lift forces; and $\mathbf{M}_{\text{rot}}$ is the antirotation torque. $\mathbf{M}_{\text{tr}}$ is perpendicular to both $\mathbf{e}_u$ (the direction of $\mathbf{V}$) and $\mathbf{e}$ (the body orientation), and therefore it is in the same direction of the unit vector $\mathbf{e}_m^h$

$$\mathbf{M}_{\text{tr}} = M_{\text{tr}}\mathbf{e}_m^h \tag{14}$$

with M_{tr} being its magnitude calculated by the drag law [4]

$$M_{\text{tr}} = \tfrac{1}{2}C_m\rho A_w L_w U^2 \tag{15}$$

Here, C_m is the antitranslation torque coefficient.

2.3 Antirotation Torque. The antirotation torque acts as the rigid body rotates. Let $\mathbf{\Omega}^*$ be the rigid body's angular velocity vector, which is decomposed into two parts, with one along the unit vector $\mathbf{e}$ (bank angle) and the other $\mathbf{\Omega}$ (azimuthal and elevation angles) perpendicular to $\mathbf{e}$ (Fig. 5)

$$\Omega^* = \Omega_s\mathbf{e} + \mathbf{\Omega} \tag{16}$$

Let $\mathbf{e}_\omega$ be the unit vector in the direction of $\mathbf{\Omega}$

$$\Omega = \Omega\mathbf{e}_\omega, \quad \Omega = |\mathbf{\Omega}| \tag{17}$$

The unit vector $\mathbf{e}_\omega$ is perpendicular to $\mathbf{e}$

$$\mathbf{e}_\omega \cdot \mathbf{e} = 0 \tag{18}$$

Time rate of change of the unit vector $\mathbf{e}$ (main axis direction) is given by

$$\frac{d\mathbf{e}}{dt} = \mathbf{\Omega}^* \times \mathbf{e} = \mathbf{\Omega} \times \mathbf{e}. \tag{19}$$

Vector product between Eq. (19) and the unit vector $\mathbf{e}$ gives

$$\mathbf{e} \times \frac{d\mathbf{e}}{dt} = \mathbf{\Omega} = \Omega\mathbf{e}_\omega \tag{20}$$

Differentiation of Eq. (16) with respect to time t and use of Eq. (20) lead to [7]

$$\frac{d\mathbf{\Omega}^*}{dt} = \frac{d\Omega_s}{dt}\mathbf{e} + \Omega_s(\mathbf{\Omega} \times \mathbf{e}) + \frac{d\mathbf{\Omega}}{dt} \tag{21}$$

The antirotation torque ($\mathbf{M}_{\text{rot}}$) is against the rotation of the rigid body $\mathbf{\Omega}^*$. It can be decomposed into two parts

$$\mathbf{M}_{\text{rot}} = \mathbf{M}_s + \mathbf{M}_c \tag{22}$$

where the torque $\mathbf{M}_s$ (resistant to self-spinning, $\Omega_s\mathbf{e}$) parallels the main axis of the body (i.e., the unit vector $\mathbf{e}$)

$$\mathbf{M}_s = -M_s\mathbf{e}, \tag{23}$$

and the torque $\mathbf{M}_c$ is perpendicular to the unit vector $\mathbf{e}$

$$\mathbf{M}_c = -M_c\mathbf{e}_\omega, \quad \mathbf{e}_\omega \perp \mathbf{e}, \tag{24}$$

where M_s and M_c are the corresponding scalar parts. The drag law shows that [8]

$$M_s = \tfrac{1}{2}C_s\rho A_w L_w^3|\Omega_s|\Omega_s \tag{25}$$

$$M_c = \tfrac{1}{2}CF(\mu)\rho A_w L_w V_r^2, \quad \mu \equiv \Omega L_w/V \tag{26}$$

where the function $F(\mu)$ is obtained from the surface integration of torque due to cross-body hydrodynamic force (perpendicular to the body) [9]

$$F(\mu) \equiv \begin{cases} \dfrac{1}{6\mu} & \text{for } \mu \geq 1/2 \\ \left[\left(\dfrac{1}{4} - \mu^2\right) + \dfrac{4}{3}\mu^2 + \dfrac{1}{2\mu^2}\left(\dfrac{1}{16} - \mu^4\right)\right] & \text{for } \mu < 1/2 \end{cases} \tag{27}$$

Here, V_r is the projection of the water-to-body relative velocity on the vector $\mathbf{e}_r = \mathbf{e}_\omega \times \mathbf{e}$. Using Eq. (9) we have

$$V_r = \mathbf{V} \cdot \mathbf{e}_r = -U\mathbf{e}_u \cdot (\mathbf{e}_\omega \times \mathbf{e}) \tag{28}$$

In Eqs. (25) and (26), C_s is the torque coefficient for self-spinning; C is the drag coefficient due to cross-body flow. For a cylindrical body, the coefficient C is given by [10]

$$C = \begin{cases} 1.9276 + 8/\text{Re} & \text{if Re} \leq 12 \\ 1.261 + 16/\text{Re} & \text{if } 12 < \text{Re} \leq 180 \\ 0.855 + 89/\text{Re} & \text{if } 180 < \text{Re} \leq 2000 \\ 0.84 + 0.00003\,\text{Re} & \text{if } 2000 < \text{Re} \leq 12{,}000 \\ 1.2 - 4/\delta & \text{if } 12{,}000 < \text{Re} \leq 150000,\ \delta \geq 10 \\ 0.835 - 0.35/\delta & \text{if } 12{,}000 < \text{Re} \leq 150000,\ 2 \leq \delta < 10 \\ 0.7 - 0.08/\delta & \text{if } 12{,}000 < \text{Re} \leq 150{,}000,\ \delta < 2 \\ 1.875 - 0.0000045\,\text{Re} & \text{if } 150000 < \text{Re} \leq 350{,}000 \\ 1/(641550/\text{Re} + 1.5) & \text{if Re} > 350{,}000. \end{cases} \tag{29}$$

Here, δ is the aspect ratio of the rigid body; $\text{Re} = UD/\nu$, is the Reynolds number with D the effective diameter of rigid body.

3 Dynamics

3.1 Momentum Equation. Differentiation of Eq. (3) with respect to time t gives the acceleration of the rigid body

Table 1 Hopkinson scaling laws

Physical parameter	Symbol	Units	Required scaling for dimensionless quantities to have same value at all scales	Naturally scaled value with replica scaling in Earth's gravitational field
Length	L	L	L/S	L/S
Time	t	t	t/S	t/S
Mass	m	m	m/S^3	m/S^3
Displacement	x	L	x/S	x/S
Velocity	V	L/t	V	V
Acceleration	a	L/t^2	aS	aS
Density	ρ	m/L^3	ρ	ρ
Stress	σ	m/Lt^2	σ	σ
Strain	ε	1	ε	ε
Modulus	E	m/Lt^2	E	E
Strength	Y	m/Lt^2	Y	Y
Strain Rate	ε'	$1/t$	$\varepsilon' S$	$\varepsilon' S$
Gravity	g	L/t^2	gS	g
Viscosity	υ	$\sigma/\varepsilon' = m/Lt$	υ/S	υ
Fracture toughness	K	$\sigma L^{1/2} = m/L^{1/2}t^2$	$K/S^{1/2}$	K/S

$$\frac{d\mathbf{u}}{dt} = \frac{dU}{dt}\mathbf{e}_u + U\frac{d\mathbf{e}_u}{dt} \tag{30}$$

The momentum equation in the earth-fixed coordinate system is given by (Fig. 3)

$$m\left(\frac{dU}{dt}\mathbf{e}_u + U\frac{d\mathbf{e}_u}{dt}\right) = \mathbf{F} \tag{31}$$

where $\mathbf{F}$ is the resultant force consisting of

$$\mathbf{F} = \mathbf{F}_g + \mathbf{F}_b + \mathbf{F}_d + \mathbf{F}_l + n\mathbf{F}_c^f \tag{32}$$

Here,

$$\mathbf{F}_g = -mg\mathbf{k}, \quad \mathbf{F}_b = \rho\Pi g\mathbf{k} \tag{33}$$

are the gravity and buoyancy force and Π is the volume of the rigid body. For bomb without fin ($n=0$), the resultant force is represented by

$$\mathbf{F} = \mathbf{F}_g + \mathbf{F}_b + \mathbf{F}_d + \mathbf{F}_l \tag{34}$$

Inner products between Eq. (31) and the unit vectors ($\mathbf{e}_u, \mathbf{e}_u^{\psi}$, and $\mathbf{e}_u^{y}$ for $n=0$ lead to

$$m\frac{dU}{dt} = (\rho\Pi - m)g\mathbf{k} \bullet \mathbf{e}_u - f_d \tag{35}$$

$$mU\frac{d\gamma}{dt} = [(\rho\Pi - m)g\mathbf{k} + f_l\mathbf{e}_l] \bullet \mathbf{e}_u^{\gamma} \tag{36}$$

$$mU\cos\gamma\frac{d\psi}{dt} = [(\rho\Pi - m)g\mathbf{k} + f_l\mathbf{e}_l] \bullet \mathbf{e}_u^{\psi} \tag{37}$$

Here, we use Eq. (8) and the condition $\mathbf{e}_l \perp \mathbf{e}_v$ (i.e., the lift force perpendicular to the drag force). The vector $[(\rho\Pi - m)g\mathbf{k} + f_l\mathbf{e}_l]$ in Eqs. (36) and (37) can be represented by

$$[(\rho\Pi - m)\mathbf{k} + f_l\mathbf{e}_l] = \left(m\frac{dU}{dt} + f_d\right)\mathbf{e}_u + mU\frac{d\gamma}{dt}\mathbf{e}_u^{\gamma} + mU\cos\gamma\frac{d\psi}{dt}\mathbf{e}_u^{\psi} \tag{38}$$

with the magnitude of $(mdU/dt + f_d)$ in the direction of $\mathbf{e}_u$, $mUd\gamma/dt$ in the direction of $\mathbf{e}_u^{\gamma}$, and $mU\cos\gamma d\psi/dt$ in the direction of $\mathbf{e}_u^{\psi}$. Inner product of Eq. (38) by the unit vector $\mathbf{e}_l$ leads to

$$[(-m + \rho\Pi)g\mathbf{k} + f_l\mathbf{e}_l] \bullet \mathbf{e}_l = \left[mU\frac{d\gamma}{dt}\mathbf{e}_u^{\gamma} + mU\cos\gamma\frac{d\psi}{dt}\mathbf{e}_u^{\psi}\right] \bullet \mathbf{e}_l \tag{39}$$

where the condition ($\mathbf{e}_u \perp \mathbf{e}_l$) is used (see Eq. (11)).

3.2 Moment of Momentum Equation. The moment of momentum equation (relative to center of mass) is given by

$$\mathbf{J} \bullet \frac{d\mathbf{\Omega}^*}{dt} = \mathbf{M}_b + \mathbf{M}_h \tag{40}$$

where

$$\mathbf{M}_b = -\sigma\mathbf{e} \times (\rho\Pi g\mathbf{k}) \tag{41}$$

is the torque by buoyancy force (called the buoyancy torque). $\mathbf{J}$ is gyration tensor. In the body-fixed coordinate system $\mathbf{J}$ is a diagonal matrix [8]

$$\mathbf{J} = \begin{bmatrix} J_1 & 0 & 0 \\ 0 & J_2 & 0 \\ 0 & 0 & J_3 \end{bmatrix} \tag{42}$$

with J_1, J_2, and J_3 as the moments of inertia. For axially symmetric rigid body such as bomb, $J_2 = J_3$. Substitution of Eq. (13) into Eq. (40) and use of Eqs. (11) and (22) lead to

$$\mathbf{J} \bullet \frac{d\mathbf{\Omega}^*}{dt} = \mathbf{M}_s + \hat{\mathbf{M}} \tag{43}$$

where

$$\hat{\mathbf{M}} \equiv -\sigma\rho\Pi g\mathbf{e} \times \mathbf{k} - \sigma(f_d\mathbf{e} \times \mathbf{e}_u + f_l\mathbf{e} \times \mathbf{e}_l) - n\sigma_f f_c^f \mathbf{e} \times \mathbf{e}_c^f + \mathbf{M}_{\text{tr}} + \mathbf{M}_c \tag{44}$$

Since $\mathbf{M}_s$ is the antiself-spinning torque, which parallels the unit vector $\mathbf{e}$, and $\hat{\mathbf{M}}$ is the torque perpendicular to the unit vector $\mathbf{e}$, the moment of momentum Eq. (43) can be decomposed into two components with one parallel to $\mathbf{e}$ [11]

$$J_1\frac{d\Omega_s}{dt} = -M_s \tag{45}$$

and the other perpendicular to $\mathbf{e}$

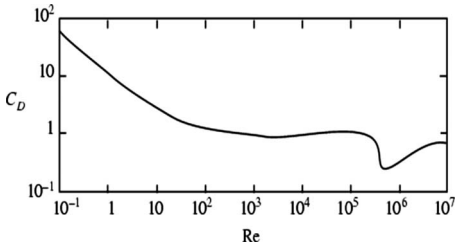

Fig. 6 Drag coefficient versus Reynolds number for a circular cross section (after Ref. [10])

$$\frac{d\boldsymbol{\Omega}}{dt} = \frac{\hat{\mathbf{M}}}{J_2} - \Omega_s(\boldsymbol{\Omega} \times \mathbf{e}) \tag{46}$$

where Eq. (24) is used. For a rigid body with very slow or no self-spinning (such as bomb), $\Omega_s \simeq 0$, Eq. (46) becomes

$$J_2 \frac{d\boldsymbol{\Omega}}{dt} = \hat{\mathbf{M}} \tag{47}$$

4 Determination of the Hydrodynamic Coefficients

The momentum Eqs. (35) and (39) can be rewritten by

$$C_d = \frac{2[(\rho\Pi - m)g\mathbf{k} \bullet \mathbf{e}_u - mdU/dt]}{\rho A_w U^2} \tag{48}$$

$$C_l = \frac{2[mU(\mathbf{e}_u^{\gamma} d\gamma/dt + \mathbf{e}_u^{\psi} \cos\ \gamma d\psi/dt) \bullet \mathbf{e}_l - (\rho\Pi - m)g\mathbf{k} \bullet \mathbf{e}_l]}{\rho A_w U^2} \tag{49}$$

Inner products of Eq. (47) by the unit vectors $\mathbf{e}_m^h$ (direction of $\mathbf{M}_{\text{tr}}$) for without fin ($n=0$) and $\mathbf{e}_\omega$ (direction of $\mathbf{M}_{\text{ae}}$) lead to

$$C_m = \frac{J_2 \dfrac{d\boldsymbol{\Omega}}{dt} \bullet \mathbf{e}_m^h + \sigma\rho\Pi g(\mathbf{e} \times \mathbf{k}) \bullet \mathbf{e}_m^h}{\dfrac{1}{2}\rho A_w L_w U^2} + CF(\Omega L_w / V_r)\frac{V_r^2}{U^2}\mathbf{e}_\omega \bullet \mathbf{e}_m^h$$

$$+ \frac{\sigma}{L_w}[C_d(\mathbf{e} \times \mathbf{e}_u) \bullet \mathbf{e}_m^h + C_l(\mathbf{e} \times \mathbf{e}_l) \bullet \mathbf{e}_m^h] \tag{50}$$

Equations (48)–(50) are used to determine the coefficients (C_d, C_l, and C_m). In the righthand sides of Eqs. (48)–(50), the unit vectors ($\mathbf{e}$, $\mathbf{e}_v$, and $\mathbf{e}_\omega$) are essential, and the other unit vectors ($\mathbf{e}_l$, $\mathbf{e}_m^h$, $\mathbf{e}_u^{\psi}$, and $\mathbf{e}_u^{\gamma}$) are derived.

Accurate prediction of a high-speed rigid body's location and orientation in the water column needs realistic values of the drag/lift and torque coefficients (C_d, C_l, and C_m). Among these coefficients, C_d, C_l, and C_m depend on the attack angle (α). Effects of special phenomena, such as surface impact, bubbles, and free surface penetration on the movement of rigid body, are represented in the change of these coefficients. Thus, if the time evolutions of unit vectors ($\mathbf{e}$, $\mathbf{e}_u$, and $\mathbf{e}_\omega$) and variables (x, y, z, U, ψ, and χ) are measured, time evolutions of the drag/lift and torque coefficients (C_d, C_l, and C_m) can be obtained using the diagnostic relationships (48)–(50). The rotation rate Ω is calculated from the time series of (ψ, χ).

Table 2 Drag coefficients between full-scale and 1/12-scale models

Flow type	Reynolds number	Drag coefficient	Full scale bomb velocity (m/s)	1/12 scale bomb velocity (m/s)
Laminar	$<10^3$	400–0.6	<0.002	<0.027
Laminar	10^3–3×10^5	0.6–0.5	0.002–0.67	0.027–7.8
Turbulent	$>3\times10^5$	<0.2	>0.67	>7.8

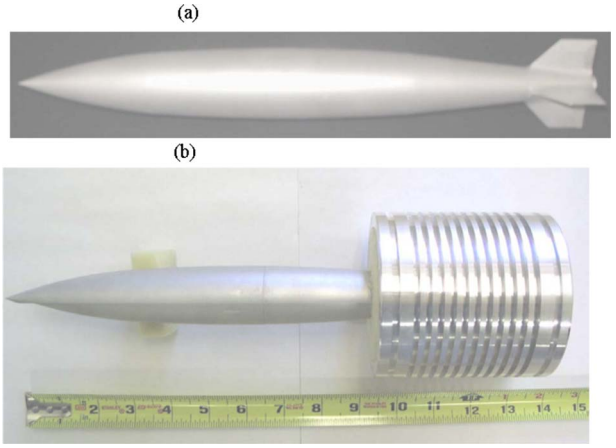

Fig. 7 Photography of 1/12th scale model Mk-84 bomb: (*a*) warhead with tail section and four fins and (*b*) sabot

With large-amount of derived (C_d, C_l, and C_m) data, instantaneous relationships (semi-empirical formulas) can be established statistically between C_d, C_l, and C_m and basic parameters such as the attack angle α, Reynolds number (Re), and the rotation rate Ω. A traditional method for this purpose is to conduct experiments in the wind tunnel. Use of wind tunnel may be feasible for determining the drag/lift and torque coefficients of a rigid body in the air, but not realistic in the water especially the rigid body with high speed such as bomb.

5 Empirical Method

5.1 General Description. As alternative to the wind tunnel method, an empirical method is used to measure time evolutions of rigid body's head and tail points $\mathbf{r}_h(t)$ and $\mathbf{r}_t(t)$ using HSV cameras [12]. From the $\mathbf{r}_h(t)$, and $\mathbf{r}_t(t)$ data, the time series of the unit vectors ($\mathbf{e}$, $\mathbf{e}_u$, and $\mathbf{e}_\omega$), variables (x, y, z, U, ψ, χ), and attack angle (α) can be calculated using Eqs. (3)–(5) and (23). With the diagnostic relationships (48)–(50), time evolutions of the drag/lift and torque coefficients (C_d, C_l, and C_m) can be obtained.

5.2 Hopkinson Scaling Laws. The Hopkinson scaling laws are derived by normalizing the governing equations so that all terms are dimensionless, as shown in Table 1. The first three columns in the table below list the relevant physical parameters for dynamic structural and material response, their standard symbols, and their dimensional units. The first three (length, time, and mass) are basic parameters. The dimensions of all the other quantities can be expressed as powers of the basic parameters. The

Fig. 8 Overview experimental arrangement

Table 3 Summary of Mk-84 underwater trajectory experimental matrix

Launch No.	Model type	Water-entry velocity (m/s)	Water-entry impact angle (deg)
1	I (tail with four fins)	132	89.2
2	I (tail with four fins)	297	90.0
3	I (tail with four fins)	295	88.8
4	I (tail with four fins)	302	88.5
5	I (tail with four fins)	227	88.0
6	I (tail with four fins)	219	89.0
7	I (tail with four fins)	119	88.2
8	II (tail with two fins)	Impacted sabot	Stripper plate
9	II (tail with two fins)	Impacted sabot	Stripper plate
10	II (tail with two fins)	295	90.0
11	II (tail with two fins)	290	90.0
12	II (tail with two fins)	Impacted sabot	Stripper plate
13	IV (no tail)	297	85.7
14	IV (no tail)	301	90.0
15	IV (no tail)	301	88.7
16	III (tail with no fin)	304	90.0
17	III (tail with no fin)	297	87.0
18	III (tail with no fin)	291	88.1
19	II (tail with 2 fins)	297	90.0

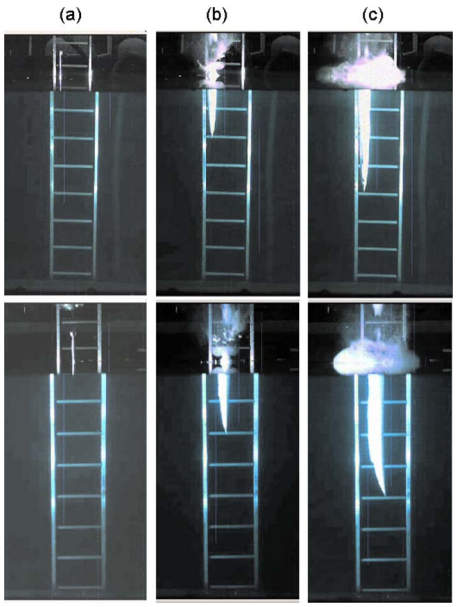

Fig. 9 Two HSV images for Launch-3 (Type-I) at water-entry velocity of 295 ms^{-1}: (*a*) initial water entry, (*b*) $t=22.8$ ms, and (*c*) $t=44.4$ ms

fourth column lists the required scaling for each of the parameters in dimensionless form to have the same value at all scales. That is, these entries define how each parameter should be scaled in order for the governing equations to give the same solution at all scales. For example, all of the length dimensions scale by the factor $1/S$. Just like length, time scales as $1/S$, but mass scales as $1/S^3$. The required scaling for the other quantities is then simply a matter of their actual dimensions in terms of L, t, and m. For example, velocity has dimensions L/t. Both L and t scale as $1/S$, so the ratio L/t is unchanged. Thus, velocities are the same at all scales. However, acceleration has dimensions L/t^2, and since both L and t scale as $1/S$, L/t^2 scales as S. Thus, accelerations at small scale are larger than at full scale by the inverse of the scale factor. A tremendous advantage of Hopkinson scaling is that density, stress, and strain are independent of scale.

The last column in the table lists the naturally scaled values of the parameters if the same materials are used and if the experiment is performed in a $1-g$ gravitational field. These can be compared with the previous column, which lists the scaling we desire for each parameter. Thus, all the parameters for which the last two columns are identical conveniently and naturally scale properly. However, the last three parameters—g, υ, and K—do not naturally scale properly. For example, if gravitational effects are important, gravity should be increased by the factor S. For the scale model Mk84 experiments described in this report, gravity mainly plays a role during the water surface waves that are generated during the initial impact. For the most part, these effects are second order and can be neglected. The effect of nonscaling viscosity or kinematic viscosity is related to the Reynolds number and drag coefficient value. The kinematic viscosity is typically a second-order effect at high velocities and may be a first-order effect at lower velocities, depending on the shape of the curve of drag coefficient versus Reynolds number. Lastly, the nonscaling of fracture toughness will not play a role, since there are no bombs casing failure mechanisms. When conducting experiments at a reduced scale, it is critical that all physical parameters of the problem are well understood. In water the Mk84 bomb will generate and travel in a cavitated column. The dynamics of motion are dominated by the pressure drag on the body produced by turbulent low-drag conditions, which will persist down to velocities of about 7.8 m/s for the scale models. For velocities less than 7.8 m/s, the dynamics of motion are dominated by laminar flow with frictional drag on the skin of the bomb casing in the form of viscous forces. The curve in Fig. 6 shows an empirical relationship between the drag coefficient and Reynolds number (ratio of inertial-to-viscous forces) for a given set of flow parameters around a circular cross section. This curve implies that the dominant forces acting on the submerged bomb may be determined as a function of the Reynolds number and, thus, of its velocity, throughout the trajectory. For exact similarity between the 1/12- and full-scale models, their respective Reynolds numbers must be equal. However, to achieve this exact similitude would require performing the scale-model experiments in a medium for which the kinematic viscosity has been reduced by the scale factor. The curve in Fig. 6 shows three distinct domains: for Reynolds numbers up to 10^3, the drag coefficient decreases monotonically to around 0.6, and for Reynolds numbers between 10^3 and 3×10^5 the drag coefficient is nearly constant at 0.5 to 0.6. Turbulent flow separation occurs for Reynolds numbers greater than 4×10^3, and the drag coefficient tends to be below 0.2.

Table 2 shows a comparison of the velocities at full scale and 1/12 scale for each of the three different domains. The first domain, in which the drag coefficient changes significantly with a change in Reynolds number, represents the primary region in which the scale models will not simulate the full-scale drag coefficient. However, this domain on the curve represents velocities of less than 0.002 m/s and is, therefore, insignificant for the practical purpose of our study. Instead, the majority of the bomb motion occurs in a turbulent flow region. The drag coefficient tends to be very small in this region, and it is likely that the small-scale models provide a good simulation of the full-scale models for velocities down to 7.8 m/s for 1/12 scale. The scale models overpredict the drag coefficient by a factor of about two or three for velocities between 7.8 m/s and 0.027 m/s for 1/12 scale. For these velocities, flow past the scale models is laminar with a constant drag coefficient of 0.5 to 0.6, whereas the full-scale model is experiencing turbulent flow with a drag coefficient of less than 0.2. In summary, Hopkinson scaling provides a good representation of the full-scale motion over about 95% of the velocity range between 450 m/s and 0 m/s.

5.3 Model Design and Construction. Details of the full-scale Mk84 with a guidance tail section were obtained from Boeing Corporation with the mass inertia properties for the complete

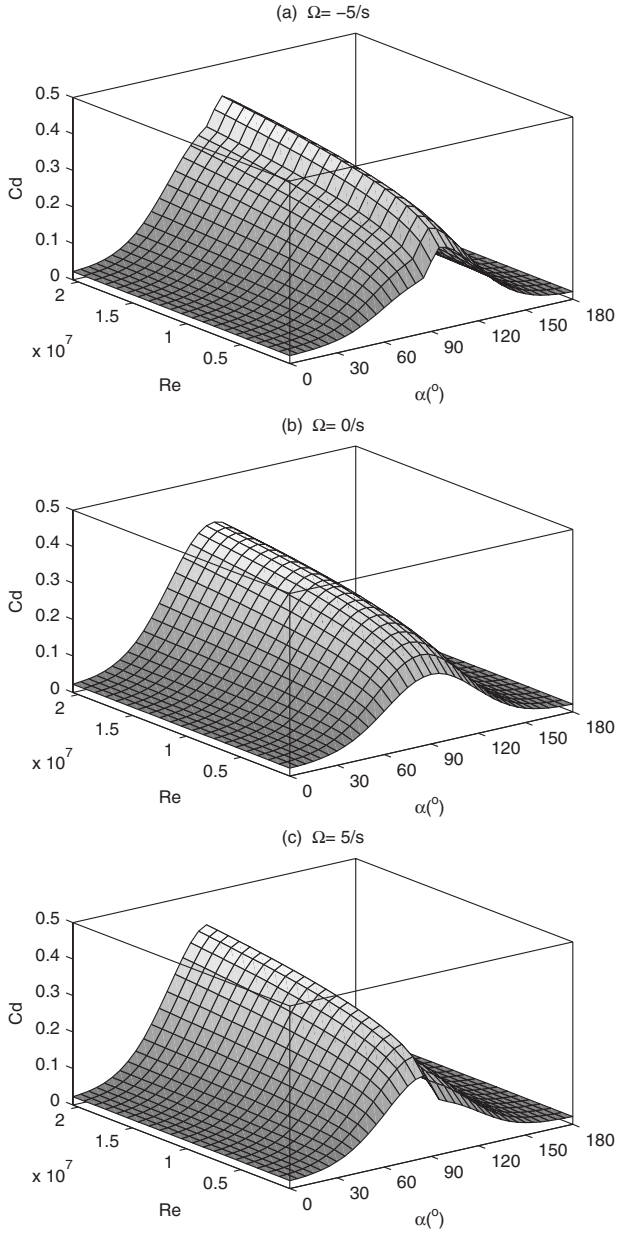

Fig. 10 Dependence of C_d on the Reynolds number (Re) and attack angle (α) for three different values of Ω: (*a*) −5 s^{-1}, (*b*) 0 s^{-1}, and (*c*) 5 s^{-1}

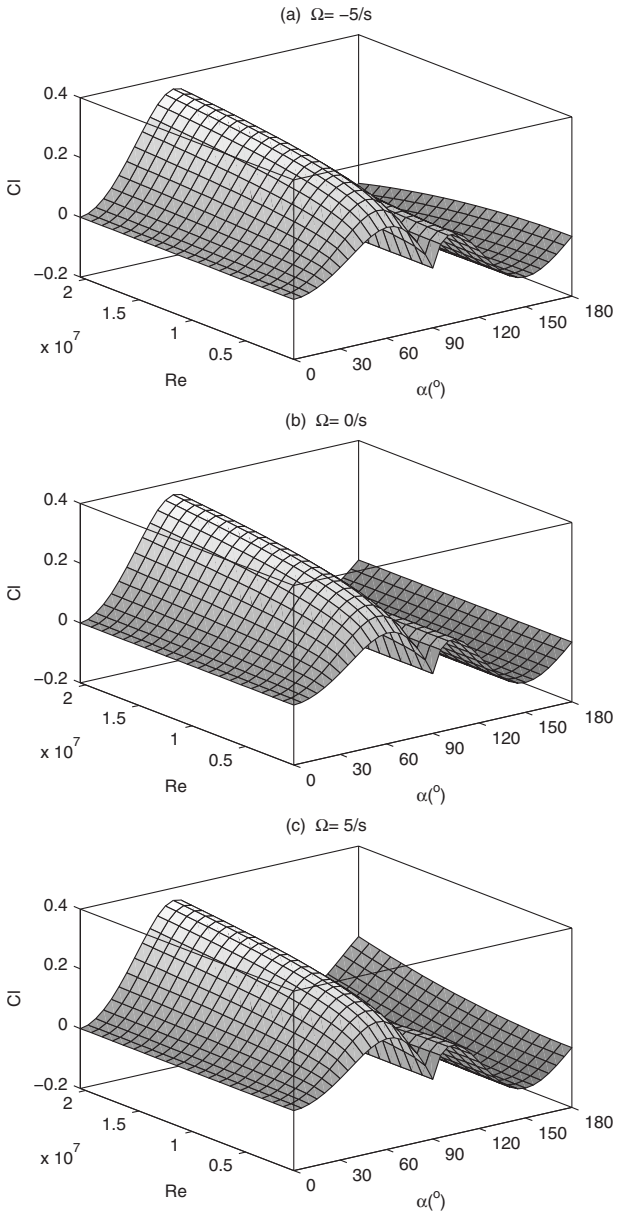

Fig. 11 Dependence of C_l on the Reynolds number (Re) and attack angle (α) for three different values of Ω: (*a*) −5 s^{-1}, (*b*) 0 s^{-1}, and (*c*) 5 s^{-1}

Mk84 warhead and tail section, as well as for the modifications to the tail section, including removal of two fins, four fins, and the complete tail section. We developed a closed form analytical model to determine the outer casing material and thickness and type of internal components and their location for the 1/12-scale model to match the scaled total mass, center of gravity and radius of gyration values for the Mk84 bomb with the different tail configurations. Here, the overall outer shape of the scaled Mk84 bomb represented an exact dimensional replica of the full-scale system. Figure 7 shows the overall design details of each model configuration. The outer casing was made from 7075-T6 aluminum. For the models with a tail section, the casing was fabricated in two pieces that were screwed together near the center point. To obtain the correct mass properties, a copper plug was inserted inside the model and then the remaining internal cavity was filled with a low density Epoxy. For all of the models with a tail section, only small differences in the copper plug size was required to match the mass properties. For these models the Epoxy had a density of 0.546 kg/m^3. For the model with no-tail section, two copper plugs were required and the Epoxy density had to be increased to 1.168 kg/m^3 by adding Tungsten powder. Four types of model Mk-84 bombs were constructed: Type-I (tail with 4 fins), Type-II (tail with two fins), Type-III (tail with no fins), and Type-IV (no tail).

5.4 Experiment Procedure. Two experiments were conducted to demonstrate the feasibility of this method with 1/12th scale model of the general purpose bomb (Mk-84) as the fast-moving rigid body. The first experiment was conducted at the Monterey Bay Aquarium Research Institute (MBARI) unmanned underwater vehicle test tank ($9.14 \times 13.72 \times 9.14$ m^3) filled with standard sea water [13,14]. The second experiment was conducted at a 6 m deep by 9 m diameter pool, located at the SRI's Corral Hollow Experiment Site [15]. A pneumatic launcher (gas gun) was used to shoot the 1/12th model Mk-84 bomb into the water tank in the first (second) experiment with velocities up to 100 m/s (454

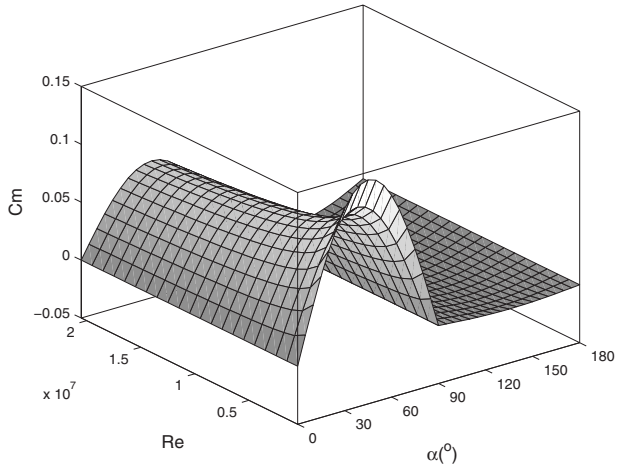

Fig. 12 Dependence of C_m on the Reynolds number (Re) and attack angle (α)

m/s) (Fig. 8). Since the implementation is very similar between the two experiments and the second experiment has much larger speed, the second experiment is presented here to illustrate this method.

Models of Mk-84 bombs with and without tail section are taken as examples to illustrate the methodology for determination of the drag/lift and torque coefficients (C_d, C_l, and C_m), and, in turn, the prediction of location and orientation of a fast-moving rigid body through the water column. The primary objective is to determine the Mk-84 trajectory through the very shallow water zone to provide an estimate of the maximum bomb-to-target standoff and required fuse delay time for optimum target lethality. Because it is possible that a portion, or all, of the guidance tail section may become separated from the warhead during water entry, it is necessary to determine the Mk-84 trajectory for a variety of different tail configurations, ranging from a warhead with a completely intact tail section and four fins to a warhead with the tail section completely.

Using the Hopkinson scaling laws, 1/12-scale Mk-84 bomb models were designed and constructed in SRI that matched the overall casing shape and mass inertial properties of the full-scale Mk-84 prototype. To model the different possible damaged tail configurations, we fabricated models that consisted of the warhead section with a complete tail section and four fins, a complete tail section and two fins, a complete tail section and no fins, and with the tail section removed. For the complete Mk-84 bomb system, including the warhead with tail section and four fins (Type-I), tail section and two fins (Type-II), tail section and no fin (Type-III), and no-tail section (Type-IV), were launched at different nominal water-entry velocity regimes from 120.0 m/s to 308.8 m/s. Table 3 summarizes the overall experimental matrix and water-entry conditions. Typically, the water-impact angle of entry was between 88 deg and 90 deg. In Launches 10, 11, and 12 the sabot failed to fully support the scale model within the gun during the launch phase, resulting in the scale model impacting the sabot stripper plate before impacting the water. Sequences of images from the two orthogonal HSV cameras were generated for each launch (Fig. 9).

The gas gun (0.10 m diameter and 1.52 m long) barrel was evacuated before launching the scale model to prevent an air blast from disturbing the water surface prior to the model impacting the water surface. At the end of the gas gun there was a steel ring to strip the sabot from the scale model. At high velocities there is some deviation from the theoretical calibration curve, which may be attributed to gas blow by around the sabot or friction. For the maximum gun operating pressure of 2,500 psi, we were able to

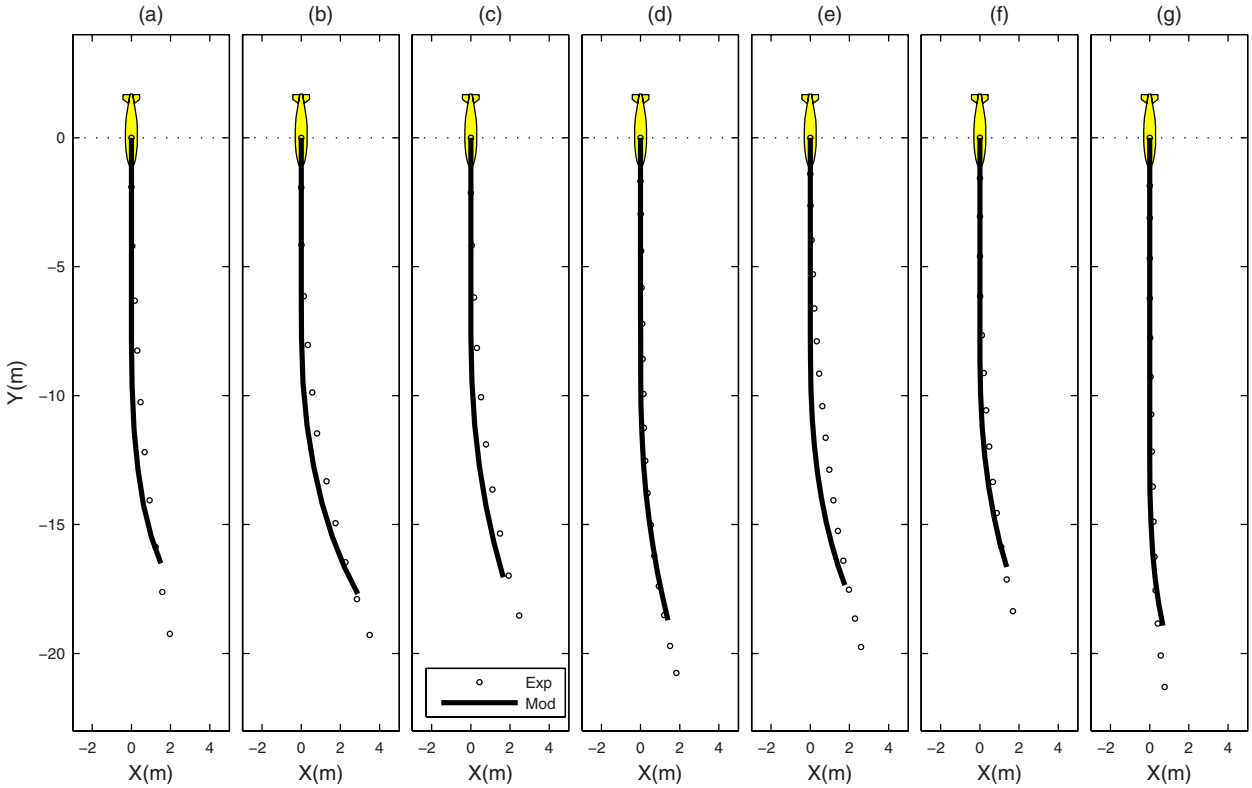

Fig. 13 Comparison between predicted and observed trajectories for Mk-84 warhead with tail section and four fins (Type-1) with initial water-entry speed: (*a*) 132 ms^{-1}, (*b*) 297 ms^{-1}, (*c*) 295 ms^{-1}, (*d*) 302 ms^{-1}, (*e*) 227 ms^{-1}, (*f*) 219 ms^{-1}, and (*g*) 119 ms^{-1}

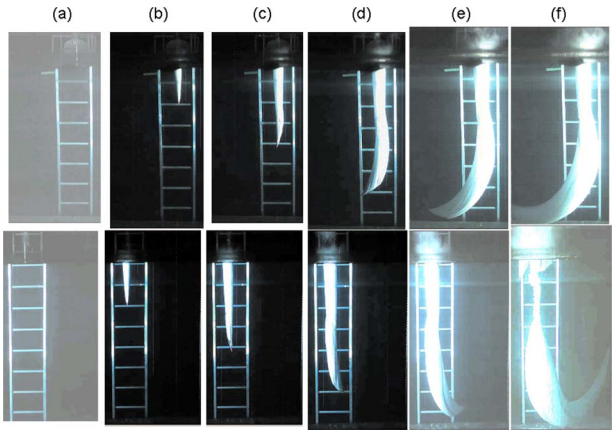

Fig. 14 Two HSV images for Launch-11 (Type-II) at water-entry velocity of 290 ms^{-1}: (a) initial water entry, (*b*) *t*=21.6 ms, (*c*) *t*=48.0 ms, (*d*) *t*=75.6 ms, (*e*) *t*=116.4 ms, and (*f*) *t* =344.4 ms

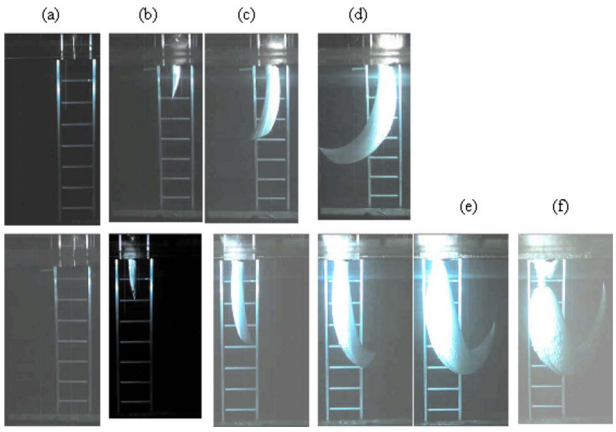

Fig. 16 Two HSV images for Launch-17 (Type-III) at water-entry velocity of 298 ms^{-1}: (*a*) initial water entry, (*b*) *t* =22.8 ms, (*c*) *t*=55.2 ms, (*d*) *t*=99.0 ms, (*e*) *t*=211.2 ms, and (*f*) *t*=376.2 ms. Note that for time longer than 99.0 ms, only one HSV camera got the pictures.

achieve a nominal water-entry velocity of about 305 m/s.

Two orthogonal periscope housings were positioned in the water tank to allow simultaneous above-water and below-water visualization of the model trajectory. The housings supported Phantom-7 HSV cameras, which were run at 10,000 fps. Five high-intensity short duration (30 ms) flash bulbs were used to front-light the scale model as it entered the water and traveled under water. The HSV cameras and flash bulbs were triggered at the time the sabot was released within the gun.

5.5 Data Retrieval. Upon completion of the launch phase, the video from each camera was converted to digital format. The digital video for each view was then analyzed frame by frame (10,000 Hz) in order to determine the bomb's position. The bomb's two-end (top and bottom) positions were input into a MATLAB generated grid, similar to the ones within the water tank. The first point to impact the water surface was always plotted first. This facilitated tracking of the initial entry point throughout the water column. Since only one ladder (Fig. 9) is used as the reference, 2D data in the $(y,\ z)$ plane were retrieved. This means that the x position of the projectile stays at zero.

After the data analysis, 16 time series of the unit vectors ($\mathbf{e}$, $\mathbf{e}_u$, and $\mathbf{e}_\omega$) variables (x, y, z, U, ψ, χ, and Ω), and attack angle (α) were obtained for the four types of the model Mk-84 bombs. All the experimental data have been converted to full-scale values using the Hopkinson scaling laws (see Table 1). For example, the length and time are multiplied by S(=12), and the mass is multiplied by S^3(=1728).

We divided the 16 time series into two groups: (a) Launches 13, 14, 15 (called the working data) for determining semi-empirical formulas for the drag/lift and torque coefficients (C_d, C_l, and C_m), and (b) rest of the data for evaluating the semi-empirical formulas (called evaluation data).

5.6 Source of Errors. There were several sources of error that hindered the determination of the bomb's exact position within the water column. Locations above or below the camera's focal point were subjected to parallax distortion. Placing the cameras as far back as possible, while still being able to resolve the individual grid squares, minimized this error. Second, the background grid (ladder in Fig. 9) was located behind the bomb's trajectory plane. This resulted in the bomb appearing larger than normal. This error was minimized by not allowing the plotted points to exceed the particular bomb's length. Third, an object injected into the water will generate an air cavity. This air cavity

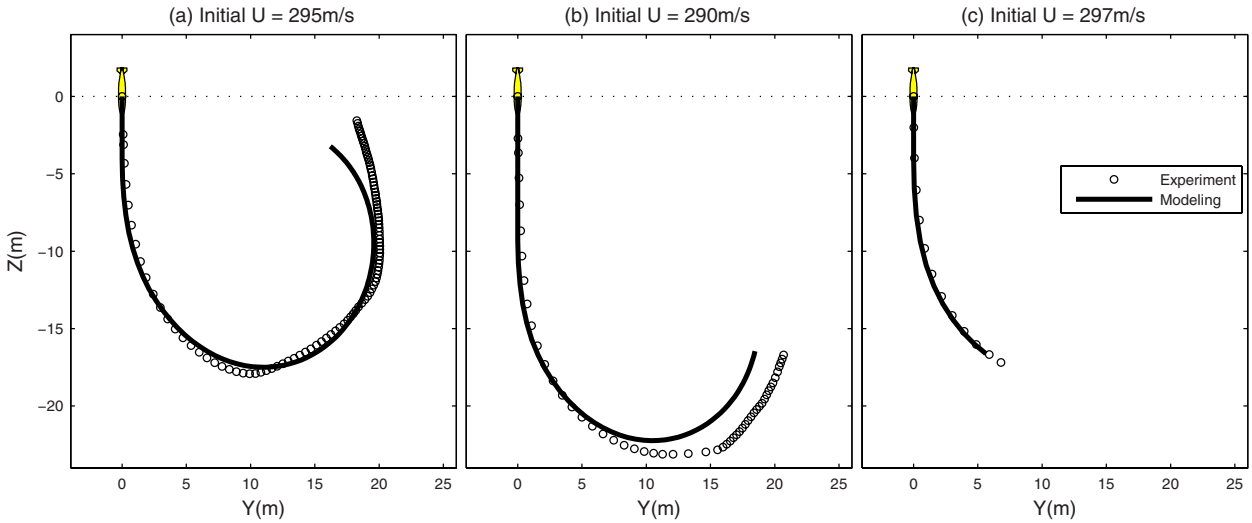

Fig. 15 Comparison between predicted and observed trajectories for Mk-84 warhead with tail section and two fins (Type-II) with initial water-entry speed: (*a*) 295 ms^{-1}, (*b*) 290 ms^{-1}, and (*c*) 297 ms^{-1}

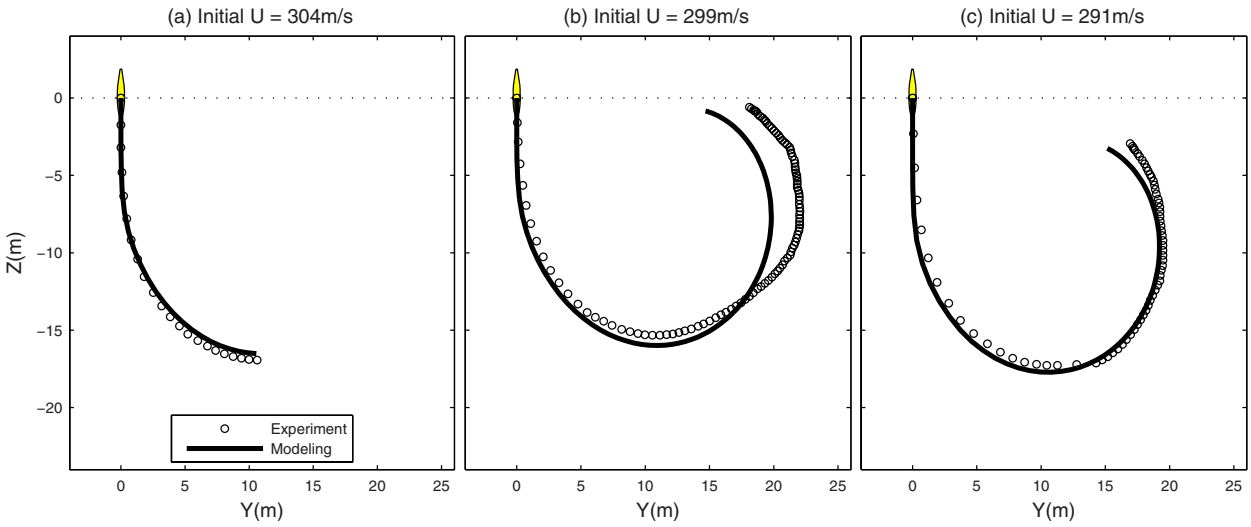

Fig. 17 Comparison between predicted and observed trajectories for Mk-84 warhead with tail section and no fin (Type-II) with initial water-entry speed: (*a*) 304 ms^{-1}, (*b*) 298 ms^{-1}, and (*c*) 291 ms^{-1}

can greatly affect the initial motion, particularly at very high speeds. The air cavity effect was deemed to be minimal when two 10,000 Hz HSV cameras were used.

6 Semi-Empirical Formulas

Statistical analysis was conducted on the working data set (Type-IV: Launch-13, -14, and -15) at each time step (data rate is 10,000 Hz) between (C_d, C_l, and C_m) and (Re, α, and Ω). The following semi-empirical formulas have been established

$$C_d = 0.02 + 0.35e^{-2(\alpha - \pi/2)^2}\left(\frac{\mathrm{Re}}{\mathrm{Re}^*}\right)^{0.2} + 0.008\Omega \sin\theta \quad (51)$$

$$C_l = \begin{cases} 0.35 \sin(\theta_1)\left(\dfrac{\mathrm{Re}}{\mathrm{Re}^*}\right)^{0.2} & \text{if } \alpha \le \dfrac{\pi}{2} \\ 0.1 \sin(\theta_2) - 0.015\Omega\left(\dfrac{\mathrm{Re}}{\mathrm{Re}^*}\right)^2 \sin(\theta_2^{0.85}) & \text{if } \alpha > \dfrac{\pi}{2} \end{cases} \quad (52)$$

$$C_m = \begin{cases} 0.07 \sin(2\alpha)\left(\dfrac{\mathrm{Re}^*}{\mathrm{Re}}\right)^{0.2} & \text{if } \alpha \le \dfrac{\pi}{2} \\ 0.02 \sin(2\alpha)\sqrt{\left(\dfrac{\mathrm{Re}}{\mathrm{Re}^*}\right)} & \text{if } \alpha > \dfrac{\pi}{2} \end{cases} \quad (53)$$

Here, $\mathrm{Re}^* = 1.810^7$, is the critical Reynolds number, and

$$\theta \equiv (\pi^{2.2} - (\pi - |\pi - 2\alpha|)^{2.2})^{1/2.2}\mathrm{sign}(\pi - 2\alpha) \quad (54)$$

$$\theta_1 = \pi\left(\frac{2\alpha}{\pi}\right)^{1.8}, \quad \theta_2 = 2\pi\left(\frac{2\alpha}{\pi} - 1\right)^{0.7} \quad (55)$$

The semi-empirical formulas (51)–(53) show that the drag/lift coefficients (C_d and C_l) depend more on Re and α and less on the rotation rate Ω. For the same attack angle (α), C_d increases with Re. For the same Re, C_d increases with α monotonically from 0 deg to 90 deg and reduces monotonically with α from 90 deg to 180 deg with a maximum value for α=90 deg (Fig. 10). The dependence of lift coefficient C_l on Re and α is a little complicated than C_d, especially for the attack angle larger than 90 deg (Fig. 11). The torque coefficient C_m depends only on Re and α (Fig. 12).

7 Verification of the Semi-Empirical Formulas

7.1 Experimental Results

7.1.1 Type-I. This type is for the complete Mk-84 bomb system, including the warhead with tail section and four fins. Seven launches (Launch-1–Launch-7) were conducted at different nominal water-entry velocity regimes (119–302 m/s). Figure 9 shows a sequence of images from the two orthogonal HSV cameras for a nominal velocity of 295 m/s (Launch-3). The cavitated column generated by the Mk-84 bomb motion consists of a tapered cone that has a maximum full-scale diameter at the end of the tail section of about 0.9 m. This is about a factor of two larger than the maximum bomb diameter of 0.45 m. This cavity shape was about the same for all of the initial water-entry velocities between 119 m/s and 302 m/s.

Figure 13 shows the comparison of bomb's translation and orientation for Type-I (Launch-1 to Launch-7) between the calculated and observed data. Both calculated and observed trajectories show similar patterns. For the low velocity regime of about 125

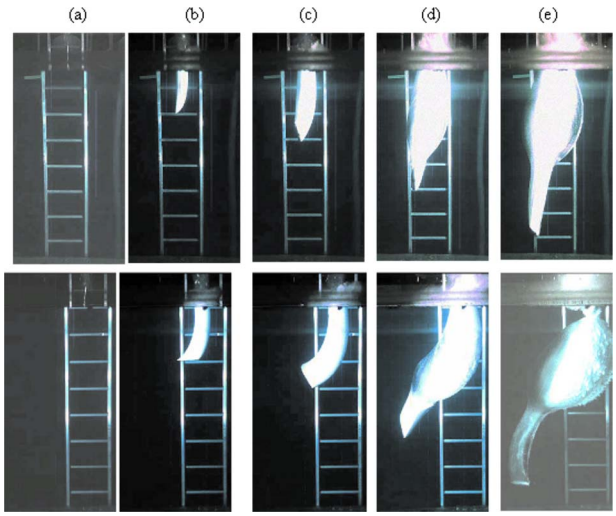

Fig. 18 Two HSV images for Launch-13 (Type-IV) at water-entry velocity of 296 ms^{-1}: (*a*) initial water entry, (*b*) *t* =30.0 ms, (*c*) *t*=51.6 ms, (*d*) *t*=155.4 ms, and (*e*) *t*=418.2 ms

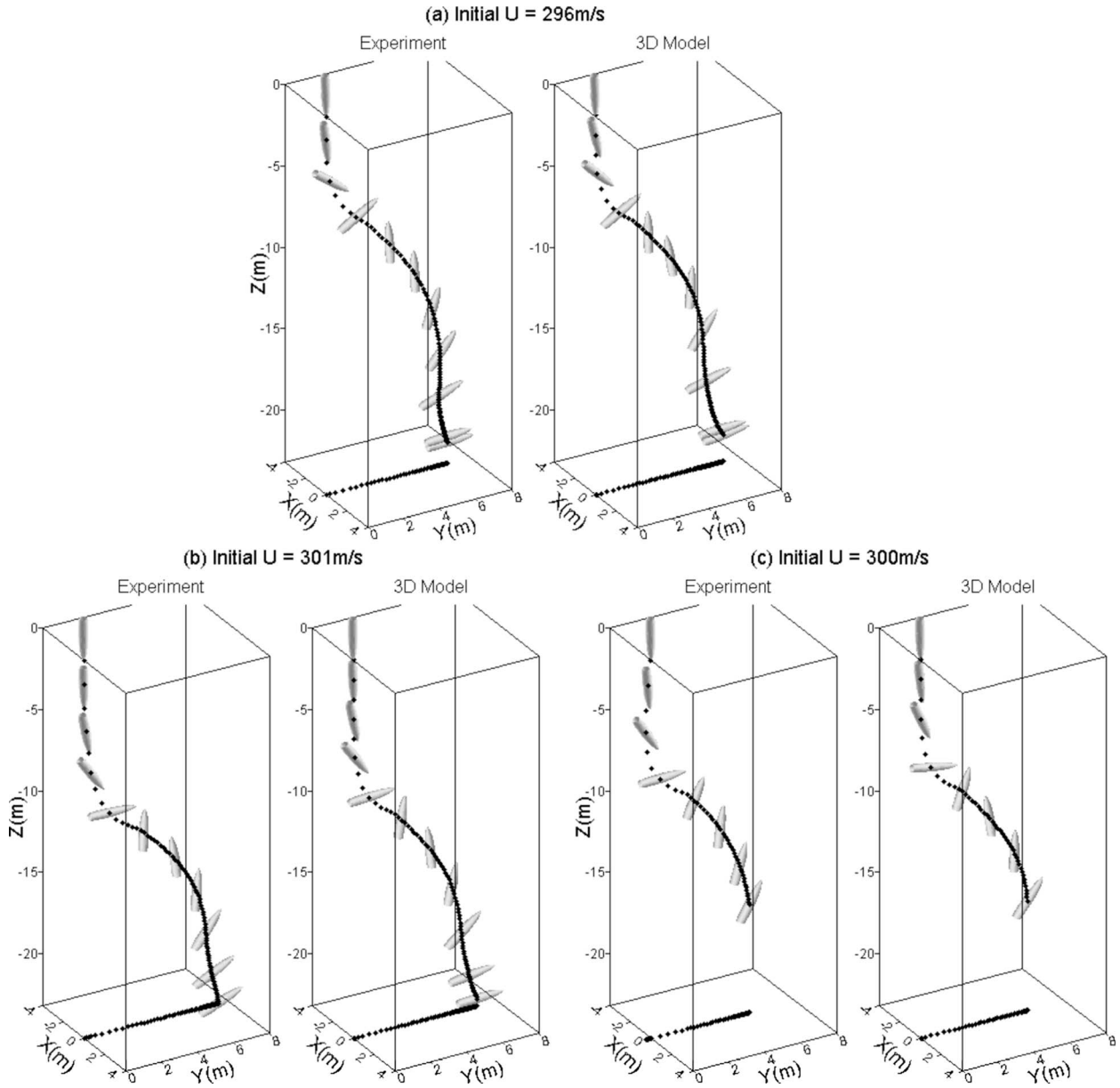

Fig. 19 Comparison between predicted and observed trajectories for Mk-84 warhead with no-tail section (Type-1V) with initial water-entry speed: (*a*) 296 ms^{-1}, (*b*) 301 ms^{-1}, and (*c*) 301 ms^{-1}

m/s (Launach-1 and Launch-7), at a full-scale depth of 12 m, the horizontal position ranged between 0.1 m (Launch-7, Fig. 13(*g*)) and 0.67 m (Launch-1, Fig. 13(*a*)). The bomb trajectories are quite stable without oscillation and tumbling no matter the water-entry velocity is high or low.

7.1.2 Type-II. This type is for the modified Mk84 bomb system including the warhead with a tail section and two fins. Three launches (Launch-10, -11, and -19) were conducted at an average water-entry velocity of about 294 m/s. Figure 14 shows a sequence of images (Launch-11) from the two orthogonal HSV cameras with a water-entry velocity of 290 m/s. The cavitated column generated by the bomb motion consists of a tapered cone that has a maximum full-scale diameter at the end of the tail section of about 0.9 m. This is about a factor of two larger than the maximum bomb diameter of 0.45 m. Thus, the initial cavity shape was about the same as for the model with a tail section and four fins, as described above.

Figure 15 shows the comparison of bomb's translation and orientation for Type-II (Launch-10, -11, and -19) between the calculated and observed data. Both calculated and observed trajectories show similar patterns. At full-scale depth of 12.2 m (i.e., 40 ft), the horizontal position ranged between 0.53 m (Launch-11) and 2.1 m (Launch-10). These values are about a factor of two larger than the values measured for Mk-84 bomb configuration with a tail section and four fins. Also, there seems to be no correlation between trajectory path and initial impact angle. The removal of two fins causes the bomb to eventually make a 180 deg turn and travel toward the surface. The 12.2 m depth is reached at about 45 ms after water entry.

7.1.3 Type-III. This type is for the modified Mk-84 bomb system, including the warhead with a tail section and no fin. Three launches (Launch-16, -17, and -18) were conducted at an average water-entry velocity of about 298 m/s. Figure 16 shows a sequence of images (Launch-17) from the two orthogonal HSV

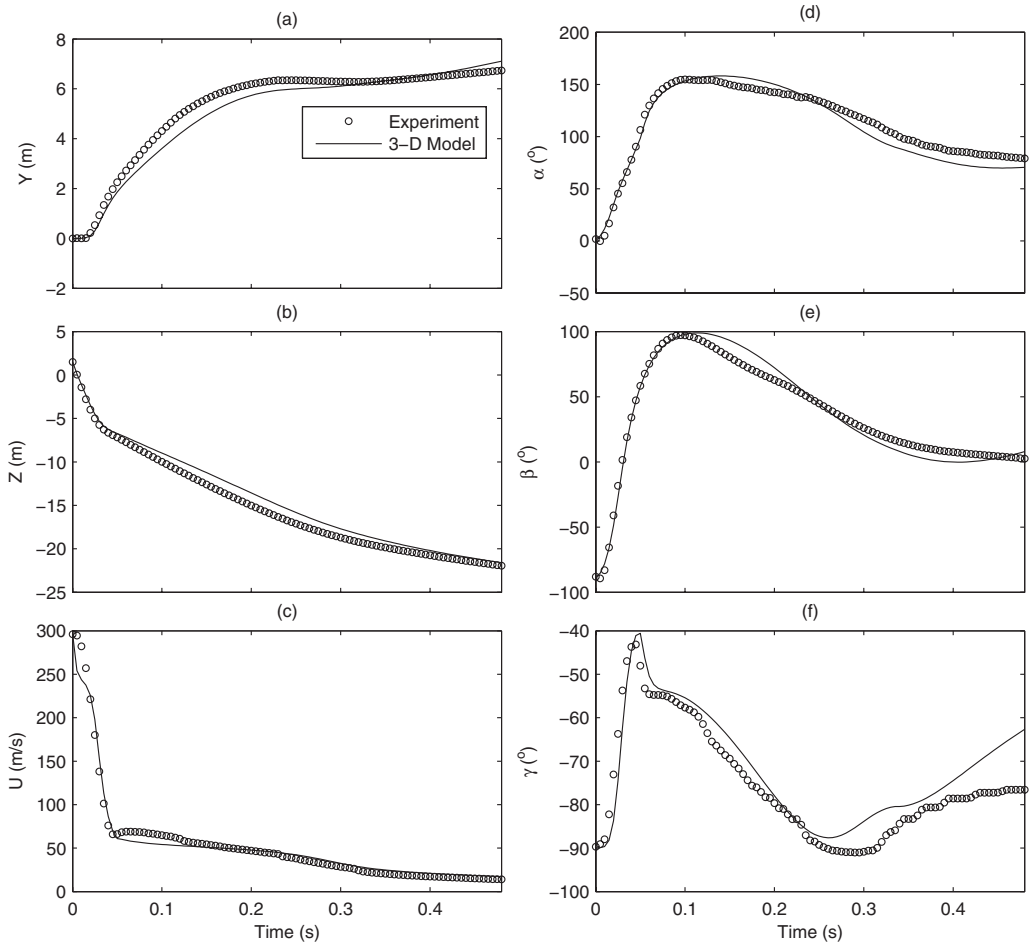

Fig. 20 Time-evolutions between predicted (solid) and observed (dotted) for Launch-13: (*a*) horizontal position (*y*) of o_m, (*b*) depth position (*z*) of o_m, (*c*) bomb speed (*U*), (*d*) angle γ, (*e*) angle β, and (*f*) attack angle α

cameras with a water-entry velocity of 297 m/s. The cavitated column generated by the bomb motion consists of a tapered cone that has a maximum full-scale diameter at the end of the tail section of about 0.9 m. This is about a factor of two larger than the maximum bomb diameter of 0.45 m. Thus, the initial cavity shape was about the same as for the model with a tail section and four fins and for the model with two fins, as described above.

Figure 17 shows the comparison of bomb's translation and orientation for Type-III (Launch-16, -17, and -18) between the calculated and observed data. Both calculated and observed trajectories show similar patterns. At full-scale depth of 12.2 m (i.e., 40 ft), the horizontal position ranges between 2.1 m (Launch-18) and 3.5 m (Launch-17). These values are about a factor of 9.5 and 3.5, respectively, larger than the values measured for an Mk-84 warhead with a tail section and four fins. Also, there seems to be no correlation between trajectory path and angle of impact. As shown in Figs. 15 and 16, the removal of four fins causes the bomb eventually to make a 180 deg turn and travel toward the surface in a manner similar to the trajectory for a bomb with a tail section and two fins. The 12.2 m depth is reached at about 47 ms after water entry. In general, the model with a tail section and no fins shows a decrease in overall trajectory stability compared with a model with a tail section and two fins. This is evident primarily through larger horizontal positions.

7.1.4 Type-IV. This type is for the modified Mk-84 bomb system, including the warhead and no-tail section. Three launches (Launch-13, -14, and -15) were conducted at an average water-entry velocity of about 299 m/s. Figure 18 shows a sequence of images (Launch-13) from the two orthogonal HSV cameras with a water-entry velocity of 297 m/s. The cavitated column generated by the bomb motion consists of a tapered cone that has a maximum full-scale diameter at the end of the tail section of about 0.9 m. This is about a factor of two larger than the maximum bomb diameter of 0.45 m. Thus, the initial cavity shape was about the same as for the model with a tail section (four, two, and no fins), as described above.

7.2 Model-Data Intercomparison. The momentum equations (35)–(37) and the moment of momentum equations (45) and (46) were integrated numerically integrated using Eqs. (51)–(53) for C_d, C_l, and C_m and the same parameters (such as the density ratio, length, radius, the center of volume, and the center of mass) and the drop initial conditions (speed and orientation) as in Type-III (tail without fin) and Type-IV (no tail) (see Table 3). The validity of the semi-empirical formulas (51)–(53) are verified through a comparison between calculated and observed bomb trajectories, orientations, and velocities.

Figure 19 shows the comparison of bomb's translation and orientation for Type-IV (Launch-13, -14, and -15) between the calculated and observed data. Both calculated and observed trajectories show similar patterns. At full-scale depth of 12.2 m (i.e., 40 ft), the bomb has rotated 180 deg such that the bomb is moving tail first. When the nose reaches a depth of 12.2 m, the nose horizontal position is between 5.5 m and 7.2 m. Launch-13 had a deviation of 4.3 deg from the vertical water-entry angle, which was the largest deviation in all of the launches. However, com-

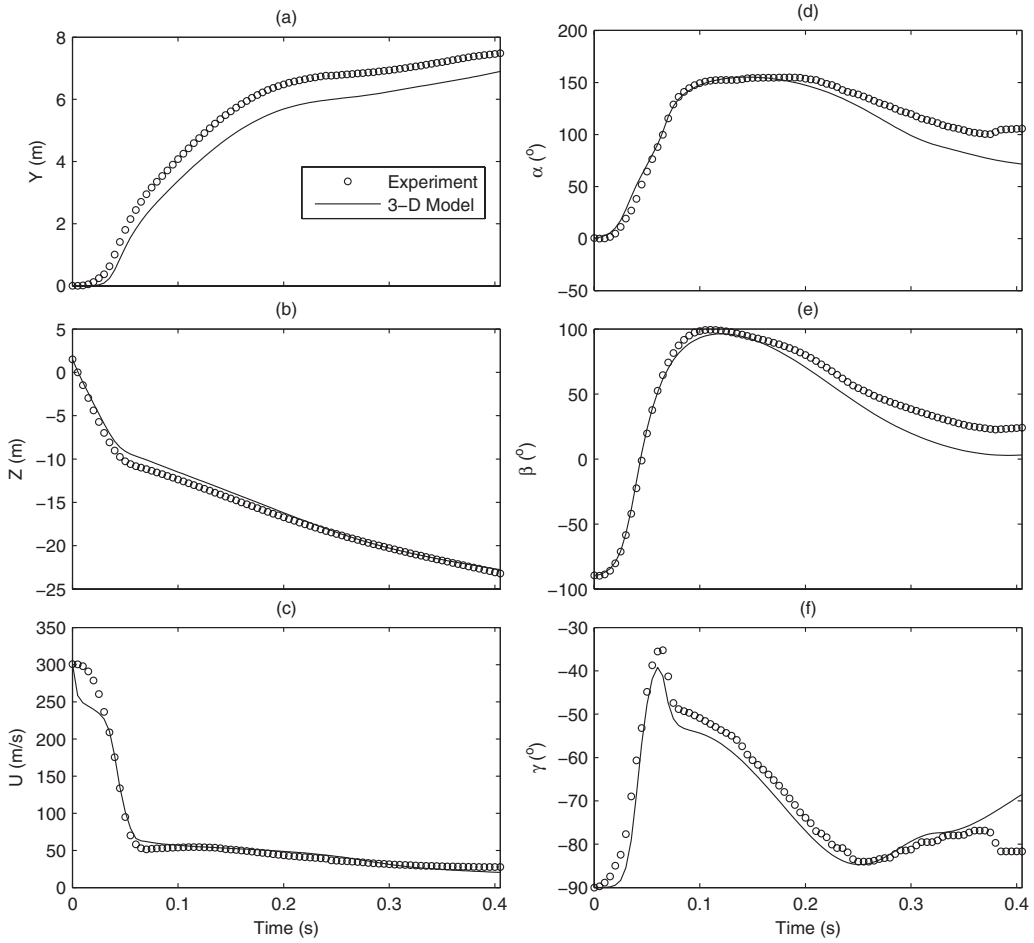

Fig. 21 Time-evolutions between predicted (solid) and observed (dotted) for Launch-14: (*a*) horizontal position (*y*) of o_m, (*b*) depth position (*z*) of o_m, (*c*) bomb speed (*U*), (*d*) angle γ, (*e*) angle β, and (*f*) attack angle α

parison of the trajectories in Launch-13 and Launch-14, in which a 90 deg water-entry angle was obtained, indicates that there is no correlation between impact angle and trajectory path. Thus, the trajectory motion is dominated by instability of the bomb within the cavitated region. Different from the Mk-84 bomb with a tail section and no fin (or two fins), the Type-IV bombs never move up toward the surface (Fig. 19). Although the model is fully 3D, in order to compare it with the 2D data set (see Sec. 5.5), only the 2D components in the (y, z) plan were computed. That is why the x position of the projectile stays zero in Fig. 19.

Figures 20–22 show the comparison between predicted and observed time evolutions of the horizontal shift (y) and depth position (z) of the center of mass (o_m), bomb speed (U), and angles (α, β, γ). At the water entry, the horizontal shift (y) is set to zero. The predicted values of these variables are consistent to the corresponding observed values. This confirms the validity of the semi-empirical formulas (53)–(55) for drag/lift and torque coefficients (C_d, C_l, and C_m). The three launches show the same interesting results. The bomb nose reaches the 12.2 m depth at about 110 ms after water entry. At this depth the bomb nose velocity decreased by about 82%. The horizontal deviation (y) of o_m increases rapidly at first and then slowly with time, and about 6 m from the entry point as the bomb reached the depth of 12.2 m.

8 Tail Section Damage Effects

The experiments conducted with different tail configurations were performed to determine the effects on bomb trajectory for different possible postulated damage levels to the tail section. Because the tail section is comprised mostly of internal stiffeners with an external skin, it may be weaker than the warhead section and, therefore, may be damaged during initial water entry or during tail slap within the cavitated region. Figure 23 shows the maximum measured trajectories for each tail configuration for a nominal water-entry velocity of about 297 ms^{-1}, i.e., Launch-2 (Type-I), Launch-19 (Type-II), Launch-17 (Type-III), and Launch-13 (Type-IV).

Table 4 summarizes data comparison of the overall trajectory behavior for the different tail configurations. For each trajectory parameter we show the value associated with a particular tail configuration and the percentage difference compared with a complete bomb having a tail section and four fins. The horizontal position shift y (noting that $y=0$ at the water entry) significantly increases with increased levels of damage to the tail section. For a model with a tail section and two fins, no fins, and no-tail section, the horizontal position values increase by 120%, 259%, and 575% (i.e., from 0.9 m to 2.12 m, 3.46 m, and 6.50 m), respectively. With regard to travel time at 12.2 m depth, only the no-tail configuration shows a significant increase of 179% (from 46.2 ms to 129. 5 ms).

9 Conclusions

A new dynamic-photographic method has been developed to determine the drag/lift and torque coefficients (C_d, C_l, and C_m) of a fast-moving rigid body in the water column. This method contains two parts: (1) establishment of the diagnostic relationship between C_d, C_l, and C_m and the rigid body's trajectory and orien-

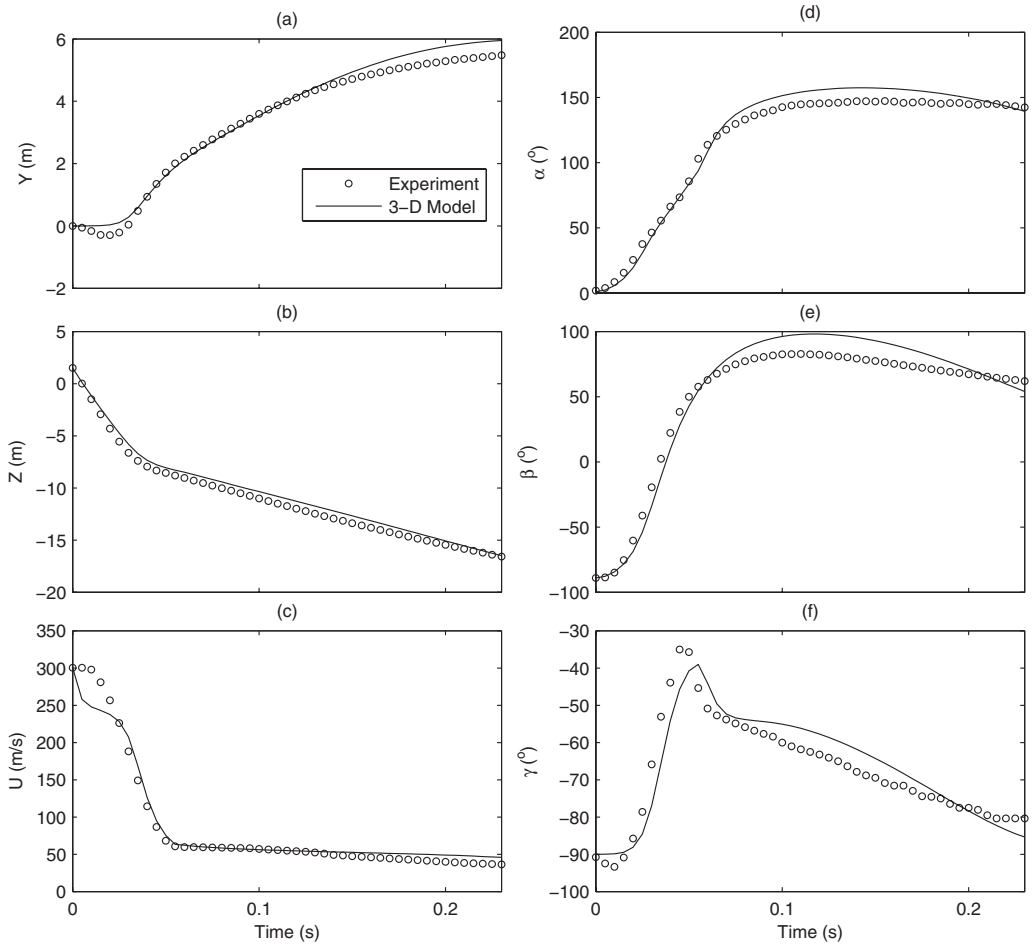

Fig. 22 Time-evolutions between predicted (solid) and observed (dotted) for Launch-15: (*a*) horizontal position (*y*) of o_m, (*b*) depth position (*z*) of o_m, (*c*) bomb speed (*U*), (*d*) angle γ, (*e*) angle β, and (*f*) attack angle α

tation, and (2) data collection of trajectory and orientation of a fast-moving rigid body using multiple high-speed video cameras (10,000 Hz). Using the digital photographic data, semi-empirical formulas of C_d, C_l, and C_m versus Reynolds number, attack angle, and rotation rate can be established. The cost of this method is much lower than the traditional method using the wind tunnel to determine C_d, C_l, and C_m.

To demonstrate the feasibility and powerfulness of this method, an experiment was conducted with 1/12th scale model of the general purpose bomb (Mk-84) as the fast-moving rigid body at a 6 m deep by 9 m diameter pool, located at the SRI's Corral Hollow Experiment Site. A gas gun was used to shoot the 1/12th model Mk-84 bomb into the water tank with velocities up to 304 ms^{-1}. Four types of Mk-84 model bombs were used for a total of 16 launches for the experiment: warhead with tail section and four fins (Type-1), with tail section and two fins (Type-1I), with tail section and no fin (Type-1II), and with no-tail section (Type-IV). Among them, data from three launches in Type-IV were used to get the semi-empirical formulas for C_d, C_l, and C_m. The rest of data were used for verification.

The momentum equations and moment of momentum equations were integrated with the same parameters (such as the density ratio, length, radius, the center of volume, and the center of mass) and the drop initial conditions (speed and orientation) as in the observations after using the semi-empirical formulas for C_d, C_l, and C_m. Consistency between calculated and observed bomb trajectories, orientations, and velocities show the powerfulness of this method.

Both calculated (solving dynamic equations with the semi-empirical formulas) and experimental data show similar results. The cavitated column generated by the Mk-84 bomb motion consists of a tapered cone that has a maximum full-scale diameter at the end of the tail section of about 0.9 m. This is about a factor of 2 larger than the maximum bomb diameter of 0.45 m. This cavity shape was about the same for all of the initial water-entry velocities and four types of model bombs.

The horizontal nose position significantly increases with increased levels of damage to the tail section. For a model with a tail section and two fins, no fins, and no-tail section, the horizontal position values increase by 120%, 259%, and 575%, respectively. With regard to travel time at 12.2 m (i.e., 40 ft) depth, only the no-tail configuration shows a significant increase of 179%.

For bomb with a tail section and four fins, its trajectories are quite stable without oscillation and tumbling whether the water-entry velocity is high or low. Removal of two fins causes the bomb to eventually make a 180 deg turn and to travel toward the surface. Although having a similar trajectory pattern (i.e., making a 180 deg turn and traveling toward the surface), the removal of four fins shows a decrease in overall trajectory stability compared with a model with a tail section and two fins. This is evident primarily through larger horizontal positions. For Mk-84 bomb without a tail section, the bomb has rotated for 180 deg at full-scale depth of 12.2 m, such that the bomb moves tail first. Different from the Mk-84 bomb with a tail section and no fin (or two fins), the Mk-84 bombs without a tail section never move up toward the surface.

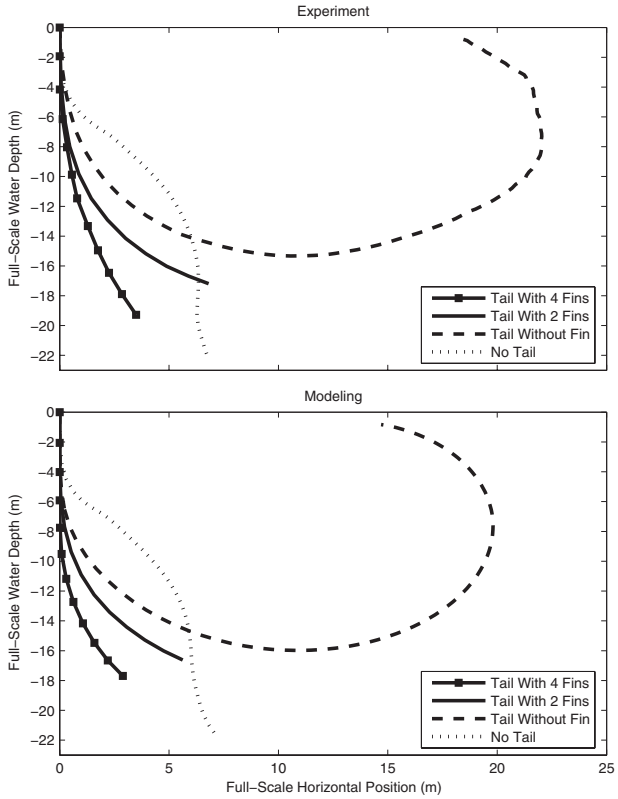

Fig. 23 Trajectories for Mk-84 warhead with different tail configurations

Acknowledgment

The Office of Naval Research Breaching Technology Program (Grant No. N0001405WR20209) and Naval Oceanographic Office supported this study. The program manager is Brian Almquist.

Table 4 Horizontal position shift and travel time at depth of 12.2 m (i.e., 40 ft) for Mk-84 warhead with different tail configurations

Model type	Horizontal position shift y (m)	Travel time (ms)
Tail with four fins	0.96	46.2
Tail with two fins	2.12	46.2
Tail with nonfins	3.46	49.8
No tail	6.50	129.5

References

[1] Chu, P. C., and Fan, C. W., 2006, "Prediction of Falling Cylinder Through Air-Water-Sediment Columns," ASME J. Appl. Mech., **73**, pp. 300–314.
[2] Chu, P. C., and Fan, C. W., 2005, "Pseudocylinder Parameterization for Mine Impact Burial Prediction," ASME J. Fluids Eng., **127**, pp. 1215–1220.
[3] Chu, P. C., (2009), "Mine Impact Burial Prediction From One to Three Dimensions," Appl. Mech. Rev., **62**(1), p. 010802.
[4] Munson, B. R., and Cronin, D. J., 1998, "Airfoils and Wings," *The Handbook of Fluid Dynamics*, R. W. Johnson, ed., CRC Press, New York.
[5] Von Mises, R., 1959, *Theory of Flight*, Dover, New York, pp. 564–585.
[6] Klimas, P. C., 1992, "Tailored Airfoils for Vertical Axis Wind Turbines," Sandia Report No. SAND84–1062.
[7] Chu, P. C., and Fan, C. W., 2007, "Mine Impact Burial Model (IMPACT35) Verification and Improvement Using Sediment Bearing Factor Method," IEEE J. Ocean. Eng., **32**(1), pp. 34–48.
[8] Chu, P. C., Fan, C. W., Evans, A. D., and Gilles, A., 2004, "Triple Coordinate Transforms for Prediction of Falling Cylinder Through the Water Column," ASME J. Appl. Mech., **71**, pp. 292–298.
[9] Rouse, H., 1938, *Fluid Mechanics for Hydraulic Engineers*, McGraw-Hill, New York.
[10] Crowe, C. T., Roberson, J. A., and Elger, D. F., 2001, *Engineering Fluid Mechanics*, Wiley, New York.
[11] White, F. M., 1974, *Viscous Fluid Flow*, McGraw-Hill, New York.
[12] Chu, P. C., Gilles, A., and Fan, C. W., 2005, "Experiment of Falling Cylinder Through the Water Column," Exp. Therm. Fluid Sci., **29**, pp. 555–568.
[13] Chu, P. C., Ray, G., Fleischer, P., and Gefken, P., 2006, "Development of Three Dimensional Bomb Maneuvering Model," Seventh Monterey International Symposium on Technology and Mine Problems, NPS, Monterey, CA, May 1–4, p. 10, DVD-ROM.
[14] Ray, G., 2006, "Bomb Strike Experiments for Mine Countermeasure," MS thesis, Naval Postgraduate School, Monterey, CA
[15] Gefken, P. R., 2006, "Evaluation of Precision-Guided Bomb Trajectory Through Water Using Scale-Model Experiments," SRI Final Technical Report No. PYU-16600.

Internal Resonance of a Floating Roof Subjected to Nonlinear Sloshing

M. Utsumi
Department of Machine Element,
Technical Research Laboratory,
IHI Corporation,
1 Shinnakaharacho, Isogo-ku, Yokohama,
Kanagawa Prefecture 235-8501, Japan

K. Ishida
Energy and Plant,
IHI Corporation,
1-1, Toyosu 3-chome, Koto-ku,
Tokyo 135-8710, Japan

M. Hizume
IHI Plant Construction,
1-1, Toyosu 3-chome, Koto-ku,
Tokyo 135-8710, Japan

Internal resonance in the vibration of a floating roof coupled with nonlinear sloshing in a circular cylindrical oil storage tank is investigated. The nonlinear system exhibits internal resonance when nonlinear terms of the governing equation have a dominant frequency close to a certain modal frequency of the system. Numerical results show that when internal resonance occurs, the responses of stresses in a floating roof exhibit a long-duration period of large amplitude despite a short duration of the earthquake excitation applied to the tank. Due to the presence of internal resonance, the underestimation of the stresses associated with the use of the linear theory becomes more marked, and thus the importance of nonlinearity of sloshing in the stress estimation is accentuated. It is illustrated that the magnitudes of the stresses increase with the increase in the liquid-filling level, and that the effect of internal resonance on the stresses noted in the case of sinusoidal excitation appears under real earthquake excitation. A method for reducing the stresses is proposed. [DOI: 10.1115/1.3173768]

1 Introduction

The vibration analysis of a floating roof subjected to liquid sloshing in a circular cylindrical tank has received substantial attention in estimating the safety of oil storage tanks. The oscillatory motion of a floating roof is near resonance with low-frequency components of earthquake ground motions. In the case of resonance, finite amplitude oscillations occur and thus the nonlinearity of sloshing should be considered in the vibration analysis. However, the vibration of a floating roof has been analyzed using the linearized theory under the assumption of small amplitude sloshing [1–4], though extensive studies have been carried out on the nonlinear sloshing problem with a free liquid surface [5–13]. Thus, the effect of the nonlinearity of sloshing on the magnitudes of stresses occurring in a floating roof has not been investigated. In a previous paper [14], the vibration of a floating roof due to nonlinear sloshing was analyzed and it was shown that the consideration of nonlinearity is obligatory to avoid underestimation of the stresses. Furthermore, an experimental validation was presented, which illustrated that the nonlinear solution of the liquid surface displacement is in good agreement with the experimental result [15], and that the linear analysis results in underestimation of the sloshing wave height. However, the previous work did not address internal resonance, which is an important phenomenon of this nonlinear system and accentuates the importance of the consideration of the nonlinearity of sloshing in the stress estimation. In the present paper, the effect of internal resonance on the stresses is investigated and it is shown that the internal resonance effect noted in the case of sinusoidal excitation may appear when a broad-band real earthquake excitation is applied. A 30,000 m^3 floating roof tank (FRT), which was damaged by the 2003 Tokachi-oki earthquake [16] is employed as a typical example. A method for reducing the stresses in the floating roof pontoon is proposed.

2 Analysis

2.1 Computational Model. We consider a circular cylindrical tank with a floating roof, as shown in Fig. 1, where $O-r\varphi z$ is the moving coordinate system fixed to the tank, a is the radius of the tank, and h is the liquid-filling level. The floating roof consisting of deck, pontoon, and stiffeners is modeled as an axisymmetric elastic shell. The detailed parameters for the floating roof geometry are given in the section that is dedicated to the description of the numerical example. The analysis is performed under the assumption that the liquid motion is inviscid, incompressible, and irrotational, and that the wall and bottom of the tank are rigid. The nonlinearity of the boundary conditions at the interface between the liquid and the floating roof is considered. The static position of the interface is considered a plane expressed by $z=h$ and $0 \leq r \leq a$ in formulating the nonlinear boundary conditions, because the variation in the z coordinate of the static position is very small compared with the liquid-filling level and the difference between the radii of the tank wall and the floating roof is much smaller than the tank radius.

2.2 Variational Form of Governing Equations. In this paper, governing equations are expressed in a weighted-residual form based on a variational principle. This expression is helpful for applying the computationally-efficient Galerkin method to this nonlinear problem. The Lagrangian density of the liquid is equal to the pressure [17]. Therefore, the time integral of the Lagrangian of the liquid can be expressed as follows:

$$\int_{t_1}^{t_2} L_f dt = \int_{t_1}^{t_2} \int \int \int_V p_l dV dt \tag{1}$$

where L_f is the Lagrangian of the liquid, V is the liquid domain, and p_1 is the liquid pressure given by

$$p_l = -\rho_f \left[\frac{\partial \phi}{\partial t} + g(z-h) + r\cos\varphi \ddot{f}_x(t) + r\sin\varphi \ddot{f}_y(t) + \frac{1}{2}(\nabla\phi)^2 + \dot{G}(t) \right] \tag{2}$$

where ρ_f is the liquid density; ϕ is the velocity potential, which describes the liquid motion relative to the moving tank; g is the gravitational acceleration; $\ddot{f}_x(t)$ and $\ddot{f}_y(t)$ are the earthquake acceleration inputs in the x and y directions, respectively; and $G(t)$ is an arbitrary time-dependent function. By adding the time integral of the Lagrangian of the floating roof determined by the finite

Contributed by the Applied Mechanics Division of ASME for publication in the JOURNAL OF APPLIED MECHANICS. Manuscript received August 27, 2008; final manuscript received April 22, 2009; published online October 5, 2009. Review conducted by Wei-Chau Xie.

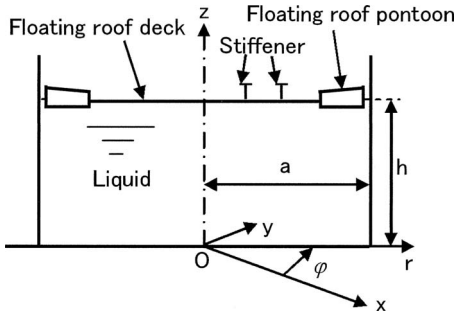

Fig. 1 Computational model

element method and applying the mathematical procedures explained in Appendix A to the calculus of variations for the total Lagrangian, the required variational form of the governing equations can be obtained as follows:

$$\rho_f \int\int\int_V \nabla^2\phi\delta\phi dV - \rho_f \int_0^{2\pi}\int_0^h \left.\frac{\partial\phi}{\partial r}\right|_{r=a} \delta\phi|_{r=a} a dz d\varphi + \rho_f \int_0^{2\pi}\int_0^a \left.\frac{\partial\phi}{\partial z}\right|_{z=0} \delta\phi|_{z=0} r dr d\varphi - \rho_f \int_0^{2\pi}\int_0^a \left(\frac{\partial\bar{u}}{\partial t} + \left.\frac{\partial\phi}{\partial z}\right|_{z=h-\bar{u}} + \left.\frac{\partial\phi}{\partial r}\right|_{z=h-\bar{u}} \frac{\partial\bar{u}}{\partial r} + \frac{1}{r^2}\left.\frac{\partial\phi}{\partial\varphi}\right|_{z=h-\bar{u}} \frac{\partial\bar{u}}{\partial\varphi}\right) \delta\phi|_{z=h-\bar{u}} r dr d\varphi + \sum_{m=0}^{\infty} [-\delta\mathbf{X}'^t_{mx}(\mathbf{M}'_m\ddot{\mathbf{X}}'_{mx} + \mathbf{K}'_m\mathbf{X}'_{mx}) - \delta\mathbf{X}'^t_{my}(\mathbf{M}'_m\ddot{\mathbf{X}}'_{my} + \mathbf{K}'_m\mathbf{X}'_{my})] + \rho_f \int_0^{2\pi}\int_0^a \left\{ \left.\frac{\partial\phi}{\partial t}\right|_{z=h-\bar{u}} - g\bar{u} + r\cos\varphi\ddot{f}_x(t) + r\sin\varphi\ddot{f}_y(t) + \frac{1}{2}\left[\left(\frac{\partial\phi}{\partial r}\right)^2 + \left(\frac{1}{r}\frac{\partial\phi}{\partial\varphi}\right)^2 + \left(\frac{\partial\phi}{\partial z}\right)^2\right]_{z=h-\bar{u}} \right\} \delta\bar{u} r dr d\varphi + \sum_{\text{elem}} \int_0^{2\pi}\int_0^{l_e} \rho_r h_r \{[-\ddot{f}_x(t)\cos\varphi - \ddot{f}_y(t)\sin\varphi]\delta\bar{w} + [\ddot{f}_x(t)\sin\varphi - \ddot{f}_y(t)\cos\varphi]\delta\bar{v}\} r ds d\varphi - \rho_f \delta G \int_0^{2\pi}\int_0^a \frac{\partial\bar{u}}{\partial t} r dr d\varphi = 0 \tag{3}$$

where $\bar{u}$, $\bar{v}$, and $\bar{w}$ are the displacement components of the floating roof in the $-z$, φ, and r directions, respectively; m is the circumferential wave number of the displacement; $\mathbf{X}'_{mx}$ and $\mathbf{X}'_{my}$ are displacement components resulting from the x and y components of the excitation, respectively; $\mathbf{M}'_m$ and $\mathbf{K}'_m$ are the mass and stiffness matrices that are common to both $\mathbf{X}'_{mx}$ and $\mathbf{X}'_{my}$; l_e is the length of the generatrix of each shell element; s is the local coordinate defined along the generatrix of each shell element; and ρ_r and h_r are the density and thickness of the element. Because the variations in the velocity potential, the floating roof displacement, and the arbitrary time-dependent function are arbitrary and independent of one another, we obtain the system of governing equations. The first term of Eq. (3) yields the Laplace equation corresponding to the condition of continuity in the liquid domain as follows:

$$\nabla^2\phi = 0 \tag{4}$$

The second and third terms of Eq. (3) give the boundary conditions on the liquid-tank interface as follows:

$$\left.\frac{\partial\phi}{\partial r}\right|_{r=a} = 0, \qquad \left.\frac{\partial\phi}{\partial z}\right|_{z=0} = 0 \tag{5}$$

In a similar manner, the fourth term of Eq. (3) represents the condition that on the moving interface S, the normal velocity components of the fluid particle and the floating roof are equal to each other; the fifth to seventh terms of Eq. (3) lead to the equation of motion for the floating roof subjected to the liquid pressure and the inertial force due to the excitation; and the last term of Eq. (3) yields the volume constant condition.

2.3 Nonlinear Differential Equations. From Eqs. (4) and (5), we express the velocity potential as follows:

$$\phi(r,\varphi,z,t) = \sum_{m=0}^{\infty}\sum_{n=1}^{\infty} [\dot{A}_{mnx}(t)\cos m\varphi + \dot{A}_{mny}(t)\sin m\varphi] J_m(\lambda_{mn} r)\frac{\cosh(\lambda_{mn} z)}{\cosh(\lambda_{mn} h)} \tag{6}$$

where A_{mnx} and A_{mny} are the generalized coordinates, J_m is the mth order Bessel function of the first kind, and λ_{mn} is the nth positive root of $J'_m(\lambda a)=0$.

The kth components of $\mathbf{X}'_{mx}$ and $\mathbf{X}'_{my}$ can be expressed as

$$X'_{mxk}(t) = \sum_{p=1}^{\infty} T'_{mkp} E_{mpx}(t), \quad X'_{myk}(t) = \sum_{p=1}^{\infty} T'_{mkp} E_{mpy}(t) \tag{7}$$

where T'_{mkp} is the kth component of the pth eigenvector obtained by solving the eigenvalue problem $|-\Omega^2\mathbf{M}'_m + \mathbf{K}'_m| = 0$, while $E_{mpx}(t)$ and $E_{mpy}(t)$ are the modal coordinates. In terms of these modal coordinates, the floating roof displacement at an arbitrary position can be expressed, e.g., as

$$\bar{u}(r,\varphi,t) = \sum_{m=0}^{\infty}\sum_{p=1}^{\infty} [E_{mpx}(t)\cos m\varphi + E_{mpy}(t)\sin m\varphi] S_{mp}(r) \tag{8}$$

where $S_{mp}(r)$ is the modal function.

By substituting Eqs. (6)–(8) into the variational principle (3) and cancelling the coefficients of the variations δA_{mqx}, δA_{mqy}, δE_{mqx}, and δE_{mqy}, we can lead to nonlinear ordinary differential equations for the generalized coordinates. These equations can be expressed in the following matrix form:

$$\overline{\mathbf{M}}_1\ddot{\mathbf{x}}_1 + \overline{\mathbf{K}}_1\mathbf{x}_1 = \mathbf{F}\ddot{\mathbf{f}}(t) + \mathbf{G}_1 \tag{9}$$

$$\overline{\mathbf{M}}_m\ddot{\mathbf{x}}_m + \overline{\mathbf{K}}_m\mathbf{x}_m = \mathbf{G}_m \quad (m = 0,2) \tag{10}$$

where $\mathbf{x}_m$ is defined as $\mathbf{x}_m^t = \{\mathbf{x}_{m1}^t, \mathbf{x}_{m2}^t, \ldots, \mathbf{x}_{mn_{\max}}^t\}$ with $\mathbf{x}_{mn}^t = \{A_{mnx}, A_{mny}, E_{mnx}, E_{mny}\}$ for each value of m; $\ddot{\mathbf{f}}(t)$ is the tank excitation vector given by $\{\ddot{f}_x(t), \ddot{f}_y(t)\}^t$; and $\mathbf{G}_m$ $(m=0-2)$ represents the nonlinear terms. The coefficients $\overline{\mathbf{M}}_m$, $\overline{\mathbf{K}}_m$, and $\mathbf{F}$ of the linear terms and some examples of the lengthy nonlinear terms are presented in the previous paper [14]. The nonlinear term $\mathbf{G}_1$ in Eq. (9) contains cubic functions for the components of $\mathbf{x}_1$ and products of the components of $\mathbf{x}_1$ and $\mathbf{x}_m$ $(m=0,2)$. The nonlinear terms $\mathbf{G}_0$ and $\mathbf{G}_2$ in Eq. (10) are expressed in terms of quadratic functions for the components of $\mathbf{x}_1$. By solving Eqs. (9) and (10), the response of the system can be determined.

For each circumferential wave number m, the nth eigenfrequency ω_{mn} of the linearized system can be determined by solving the eigenvalue problem $|-\omega^2\overline{\mathbf{M}}_m + \overline{\mathbf{K}}_m| = 0$, as can be seen from Eqs. (9) and (10). The corresponding mode is called ω_{mn}-mode in the subsequent discussion. In ω_{mn}-mode, $\mathbf{x}_{mn}$ is predominant to the other components $\mathbf{x}_{mn'}$ $(n' \neq n)$ and ω_{mn} is close to the sloshing frequency $[g\lambda_{mn}\tanh(\lambda_{mn}h)]^{1/2}$. These trends can be confirmed numerically.

When the excitation frequency is close to ω_{11}, the components of $\mathbf{x}_{11}$ are predominantly of the form $\sin\omega_{11}t$. As can be seen from

Table 1 Parameters of numerical example (30,000 m^3 oil storage tank)

Radius of tank, a	21.35 m
Liquid-filling level, h	21.75 m
Liquid density, ρ_f	845 kg/m^3
Radius of floating roof, b	21.2 m
Radius of deck, b_1	18.9 m
Compartment in pontoon is not present	
Distance between deck and upper end of inner rim, H_1	0.335 m
Distance between deck and lower end of inner rim, H_2	0.075 m
Height of outer rim, H	0.71 m
Slope $\tan^{-1}(dz/dr)$ of deck	0.002 deg
Slope $\tan^{-1}(dz/dr)$ of top of pontoon	3 deg
Slope $\tan^{-1}(dz/dr)$ of bottom of pontoon	−4.4 deg
Thickness (deck)	0.0045 m
Thickness (top and bottom of pontoon)	0.0045 m
Thickness (outer rim of pontoon)	0.006 m
Thickness (inner rim of pontoon)	0.015 m
Radial coordinates of stiffeners	$2.75+3i$ $(i=0-4)$
Height and breadth of stiffeners	0.1 m, 0.2 m
Thickness of stiffeners	0.0045 m
Density of floating roof	7850 kg/m^3
Young's modulus of floating roof	2.1×10^{11} (N/m^2)
Poisson's ratio of floating roof	0.3

Eq. (10), ω_{0n}- and ω_{2n}-modes are excited by the nonlinear terms $\mathbf{G}_0$ and $\mathbf{G}_2$, respectively. These nonlinear terms are expressed in terms of quadratic functions for the components of $\mathbf{x}_1$ and are consequently of the form $\sin^2 \omega_{11}t=\frac{1}{2}(1-\cos 2\omega_{11}t)$, whose dominant frequency is $2\omega_{11}$. Hence, a resonance occurs when ω_{0n} or ω_{2n} is equal to $2\omega_{11}$ for a certain value of n. This type of resonance is referred to as internal resonance and is distinguished from normal linear resonance of a directly excited mode.

When $\omega_{0n}=2\omega_{11}$, ω_{0n}- and ω_{11}-modes interact with each other, while in the case of $\omega_{2n}=2\omega_{11}$, the interaction between ω_{2n}- and ω_{11}-modes occurs. These interactions may be considered as those between the modal components represented by the generalized coordinates $\mathbf{x}_{mn}$ $(m=0,2)$ and $\mathbf{x}_{1n}$ of the admissible functions (Eqs. (6)–(8)), because in ω_{mn}-mode, $\mathbf{x}_{mn}$ is predominant to the other components $\mathbf{x}_{mn'}$ $(n'\neq n)$ as mentioned above.

3 Numerical Examples

Numerical calculation was conducted for a 30,000 m^3 tank. Parameters of this tank are presented in Table 1. The detailed geometry of the floating roof used for the numerical example is shown in Fig. 2. The damping effect is considered by adding the damping term $\mu\phi|_{z=h}$ to the quantity in the brace of Eq. (3) and determining the constant μ as $\mu=2\zeta_{mn}\omega_{mn}$ $[\zeta_{mn}=0.01, \omega_{mn}^2=g\lambda_{mn}\tanh(\lambda_{mn}h)]$ for each modal component of ϕ given by Eq. (6). Confirmation of this type of damping is presented in Appendix B. For the radial displacement of the outer rim of the pontoon relative to the tank wall, spring-support and damping constants

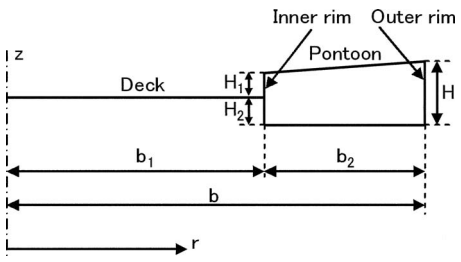

Fig. 2 Geometry of floating roof used for numerical example

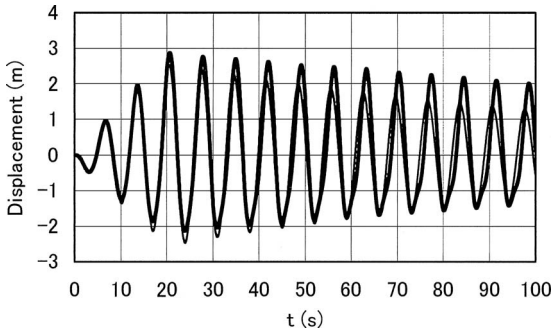

Fig. 3 Response of vertical displacement of floating roof at outer rim of pontoon (thin line, linear; thick line, nonlinear)

per unit area 86,000 N/m^3 and 5000 Ns/m^3 were taken into account. The excitations were given as $\ddot{f}_x(t)=0.16\sin(\omega t)$ $(0\leq t\leq 6\pi/\omega)$, $\ddot{f}_x(t)=0$ $(6\pi/\omega<t)$, and $\ddot{f}_y(t)=0$ $(0\leq t)$, where $\omega=1.05\omega_{11}$. The period of the fundamental sloshing mode is $2\pi/\omega_{11}=7.02$ s. The sinusoidal excitation of the duration of three periods is often employed to model earthquake excitations [15], because the sinusoidal excitation is useful in conducting a simulation study for the resonant and critical case while incorporating the finiteness of the duration of earthquake strong motion. In the numerical analysis of Eqs. (9) and (10), the modes of up to $n=7$ are retained.

Figure 3 shows the response of the vertical displacement at the outer rim of the pontoon. For the sake of comparison, the solution obtained by the linear analysis is shown using a thin line. It can be seen from Fig. 3 that the positive maximal values of the nonlinear response are larger than those of the linear solution.

The responses of stresses are illustrated in Fig. 4, showing the radial bending stress σ_s at the outer end of the bottom of pontoon

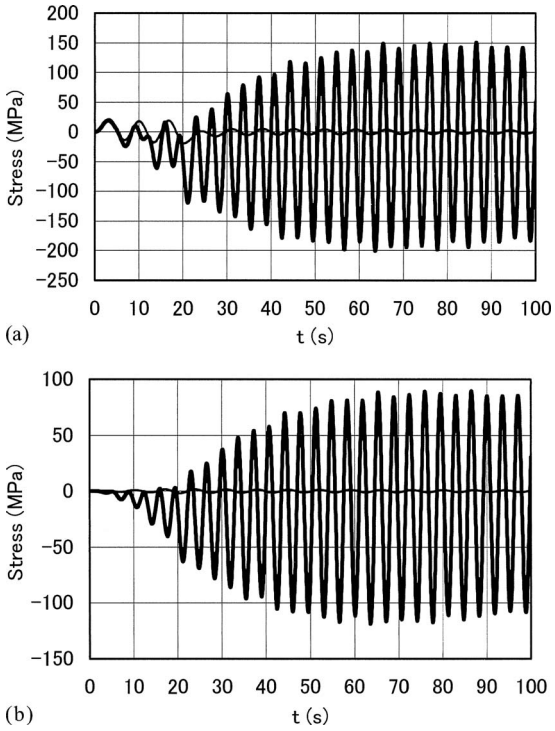

Fig. 4 Responses of stresses (thin lines, linear; thick lines, nonlinear). (*a*) Radial bending stress σ_s at outer end $(r,\varphi)=(b,0)$ of bottom of pontoon. (*b*) Hoop membrane stress σ_φ at the same position.

Table 2 Eigenfrequencies $\omega_{mn}/2\pi$ (Hz) of floating roof coupled with sloshing

	$m=0$	$m=1$	$m=2$
$n=1$	0.2106	0.1425	0.1930
$n=2$	0.2874	0.2486	0.2863
$n=3$	0.3544	0.3190	0.3565
$n=4$	0.4260	0.3871	0.4322

(Fig. 4(*a*)) and the hoop membrane stress σ_φ at the same position (Fig. 4(*b*)). The bending stress is calculated by subtracting the stress value at $\zeta=-0.5h_r$ from that at $\zeta=0.5h_r$ and dividing the difference by 2, where h_r is the thickness at the position of interest and ζ is the coordinate measured along the normal of the midplane of the shell. The positive direction of ζ is $+z$ on the bottom of the pontoon. The membrane stress is the mean of the stress values at $\zeta=-0.5h_r$ and $\zeta=0.5h_r$. The stresses shown in Fig. 4 were found to reach high levels by searching the maximum absolute values of the membrane and bending stresses for each stress component at all places over the floating roof.

It can be seen from Fig. 4 that the stress responses in the nonlinear sloshing reach much higher levels than those in the linear liquid motion. To examine the physical reason for these results, the eigenfrequencies ω_{mn} are presented in Table 2. We see that the system possesses internal resonances $\omega_{02}=2\omega_{11}$ and $\omega_{22}=2\omega_{11}$ noted in Sec. 2.3. Therefore, ω_{02}-mode and ω_{22}-mode vibrations are caused by internal resonances. Because both ω_{02} and ω_{22} are equal to $2\omega_{11}$, it is not clear which of these modes results in the large nonlinear responses of the stresses. In order to answer this question, an example of the circumferential variations in the nonlinear responses is shown in Fig. 5. It can be seen from Fig. 5 that the mode with circumferential wave number 2 is predominant. This means that the cause of the large stresses is ω_{22}-mode.

Mode shapes of ω_{02}- and ω_{22}-modes near the pontoon are shown in Figs. 6(*a*) and 6(*b*), respectively. We see that ω_{02}-mode exhibits almost a rigid-body displacement of the pontoon, while ω_{22}-mode shows a large elastic deformation of the pontoon. Thus, to examine the physical reason for the large stresses, it is necessary not only to confirm the existence of internal resonances but also to predict the contributions of the modes associated with internal resonances to the stresses. The large deformation of ω_{22}-mode is due to the fact that rigidity of the inner and outer rims of the pontoon (cylindrical shells) is low for the mode with circumferential wave number 2. Because of this low rigidity, the torsional rigidity of the pontoon-ring is low for circumferential wave number 2. The nonlinear analysis tool developed in this study is based on the mode decomposition, thereby providing the physical insight into the effects of internal resonances on the stresses. Furthermore, the tool is computationally-efficient and requires a small amount of computation time and cost to predict the magnitudes of the stresses.

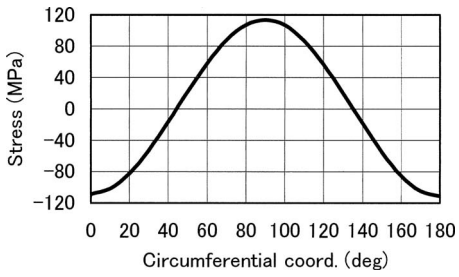

Fig. 5 Circumferential variation of hoop membrane stress σ_φ shown in Fig. 4(*b*) (nonlinear, $t=60$ s)

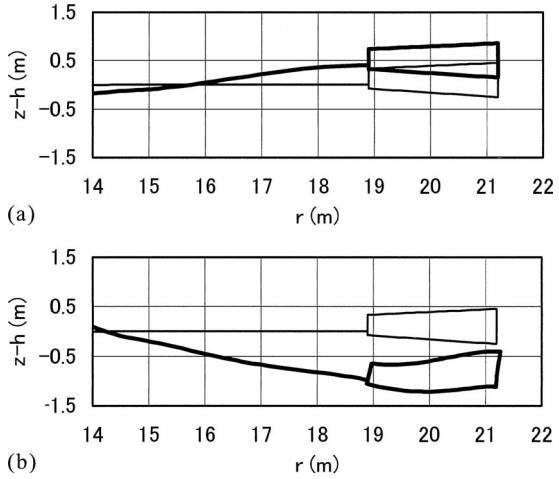

Fig. 6 Mode shapes of floating roof (thin lines, undisturbed position): (*a*) ω_{02}-mode and (*b*) ω_{22}-mode

As shown in Fig. 4, the nonlinear responses of the stresses exhibit a long-duration period of large amplitude after the excitation ends at $t=21$ s. The reason for this can be explained as follows. The ω_{22}-mode is excited by the nonlinear term expressed in terms of the mode with circumferential wave number 1. This nonlinear term decays very gradually and behaves almost as an stationary excitation against ω_{22}-mode because the damping of sloshing is light. Consequently, ω_{22}-mode vibration grows and the stresses become large after the excitation ends at $t=21$ s. Thus, the stresses not only reach high levels but also show long duration even for the short duration of the earthquake excitation, when internal resonance occurs.

Due to the presence of internal resonance, the floating roof displacement response in the nonlinear sloshing decays significantly slower than that in the linear liquid motion, as can be seen from Fig. 3. By comparing Figs. 3 and 4, we see that the internal resonance effect is more marked for the stresses than for the vertical displacement of the floating roof. We attribute this to the following reasons: (1) For the vertical displacement, the rigid-body pitching oscillation mode contributes a predominant portion to the response and thus the effect of ω_{22}-mode vibration caused by internal resonance is relatively small; and (2) for the stresses, on the other hand, the rigid-body mode does not have any contribution and therefore the effect of ω_{22}-mode is significantly accentuated. Consequently, consideration of the internal resonance effect in the estimation of the response magnitude is more important for the stresses than for the vertical displacement of the floating roof.

Table 3 shows dependence of the eigenfrequencies and the stresses on the liquid-filling level h. The symbols $\sigma_{s\,\max}$ and $\sigma_{\varphi\,\max}$ denote the values of σ_s and σ_φ when their absolute values reach maximum in the time response analysis. When the liquid-filling level h decreases from the original value $h=21.75$ m (Table 1), the ratio ω_{22}/ω_{11} increases from 2. Therefore, the internal resonance effect disappears and the absolute values of $\sigma_{s\,\max}$ and $\sigma_{\varphi\,\max}$ reduce. The reason for $\omega_{22}>2\omega_{11}$ for low liquid-filling levels can be explained as follows. The eigenfrequencies ω_{mn} are approximated by $[g\lambda_{mn}\tanh(\lambda_{mn}h)]^{1/2}$, where $\lambda_{22}=6.706/a$ is larger than $\lambda_{11}=1.8412/a$. As h increases, $\tanh(\lambda_{22}h)$ converges to unity more rapidly than $\tanh(\lambda_{11}h)$. Therefore, ω_{22} remains almost constant over the wide range of the liquid-filling level h, while ω_{11} reduces with decreasing h, as can be seen from Table 3. Thus, ω_{22} becomes larger than $2\omega_{11}$ for low liquid-filling levels.

One significant observation made from Table 3 is that the increase in the liquid-filling level h from the original value h

Table 3 Dependence of eigenfrequencies and stresses on liquid-filling level

$\frac{h}{h_1}$ (h_1=21.75 m)	$\frac{\omega_{11}}{2\pi}$ (Hz)	$\frac{\omega_{22}}{2\pi}$ (Hz)	$\frac{\omega_{22}}{\omega_{11}}$	$\sigma_{s.\max}$ (MPa)	$\sigma_{\varphi.\max}$ (MPa)
1.25	0.1446	0.2863	1.9799	−216.3	−128.4
1.10	0.1436	0.2863	1.9937	−211.5	−125.4
1.00	0.1425	0.2863	2.0091	−200.8	−118.7
0.90	0.1410	0.2863	2.0305	−184.8	−109.1
0.75	0.1374	0.2863	2.0837	−156.2	−91.7
0.50	0.1251	0.2860	2.2862	−144.7	−83.5

=21.75 m results in a further increase in the absolute values of the stresses although ω_{22}/ω_{11} becomes slightly smaller than 2. This is because the frequency of the first sloshing mode with circumferential wave number 1 is slightly lower than ω_{11} due to the nonlinearity of sloshing, as can be seen from Fig. 3. One is therefore led to the conclusion that the substantial internal resonance condition instead of the nominal internal resonance condition should be considered to explain the result for the case in which ω_{22}/ω_{11} is slightly smaller than 2.

The presence of internal resonance is confirmed not only by the magnitudes of the responses but also by the times at which the responses reach maximum. Table 4 shows these times $t_{\max}$. It can be seen that $t_{\max}$ increases as the internal resonance effect becomes strong due to the increase in the liquid-filling level h. Examples of the responses at internal detuning shifted from the exact internal resonance condition are shown in Fig. 7. The times taken for the stresses to reach their maximum values are short in contrast to the case of Fig. 4.

The influences of internal resonance and simultaneous internal resonance conditions on the dynamic behavior of systems with liquid containers are well documented in Ref. [9]. The influences were treated under both deterministic and random excitations. We have treated the sinusoidal case over limited period of time in an effort to simulate the effect of earthquakes, and found that the internal resonance effect on the stress in a floating roof is much larger than that on the sloshing wave height. However, the earthquake signals are known to be random and nonstationary. To take into account the broad-band spectrum characteristic and nonstationarity of the excitation, the responses to a real earthquake excitation are calculated. The acceleration record of this earthquake is shown in Fig. 8(*a*), while the Fourier transform of the acceleration record divided by the squared angular frequency is presented in Fig. 8(*b*). We see that the earthquake excitation is considerably broad-band, and that the dominant frequency 0.13 Hz of this earthquake excitation is close to the eigenfrequency $\omega_{11}/2\pi$ =0.1425 Hz of the system. The responses to this earthquake excitation are presented in Fig. 9. The results show that the nonlinear response of the vertical displacement of the roof decays significantly slower than the linear solution (Fig. 9(*a*)), and that the nonlinear responses of the stresses show a long-duration period of large amplitude after the excitation decays (Figs. 9(*b*) and 9(*c*)).

Table 4 Times at which absolute values of stresses reach maximum

h/h_1 (h_1=21.75 m)	$t_{\max}$(s) for σ_s	$t_{\max}$(s) for σ_φ
1.25	84.1	84.1
1.10	84.4	84.4
1.00	63.6	63.6
0.90	57.0	57.0
0.75	36.3	36.3
0.50	23.5	27.5

These results illustrate that the internal resonance effects noted in the case of sinusoidal excitation appear when a broad-band real earthquake excitation is applied.

One feature of this example is that the slope angles of the top and bottom of the pontoon are large. Figure 10 shows results for the case in which these slope angles are reduced to 0.8 deg. By comparing the results shown in Figs. 4 and 10, it can be seen that the reduction in the slope angles is helpful for reducing the stresses.

4 Conclusions

Internal resonance in the vibration of a floating roof subjected to nonlinear sloshing in a circular cylindrical tank has been investigated. It was shown that vibration of a mode in which high stresses occur can be induced by internal resonance. In this case, the underestimation of the stresses associated with the use of the linearized theory becomes more significant than in the case of internal detuning, because the nonlinear responses of the stresses exhibit a long-duration period of large amplitude after the excitation ends. Consequently, consideration of the nonlinearity of sloshing is of particular importance in order to obtain reasonable safety estimations for floating roofs. Numerical results for a 30,000 m^3 oil storage tank illustrate that (1) the magnitudes of the stresses increase with the increase in the liquid-filling level, (2)

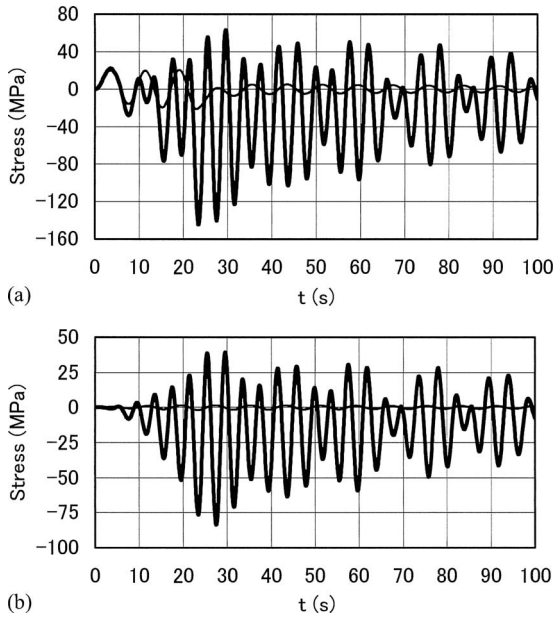

Fig. 7 Responses of stresses (the case in which internal resonance is not present, h=10.875 m; thin lines, linear; thick lines, nonlinear). (*a*) Radial bending stress σ_s at outer end $(r,\varphi)=(b,0)$ of bottom of pontoon. (*b*) Hoop membrane stress σ_φ at the same position.

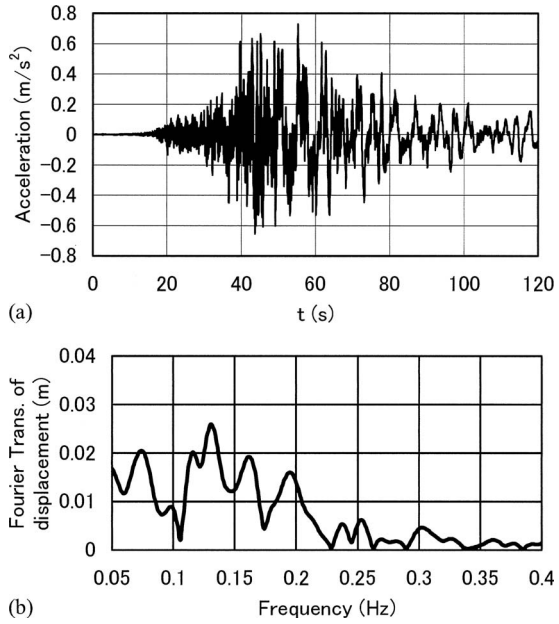

Fig. 8 Earthquake ground motion record (2003 Tokachi-oki, HKD129EW): (*a*) acceleration record; (*b*) Fourier transform of the acceleration record divided by squared angular frequency

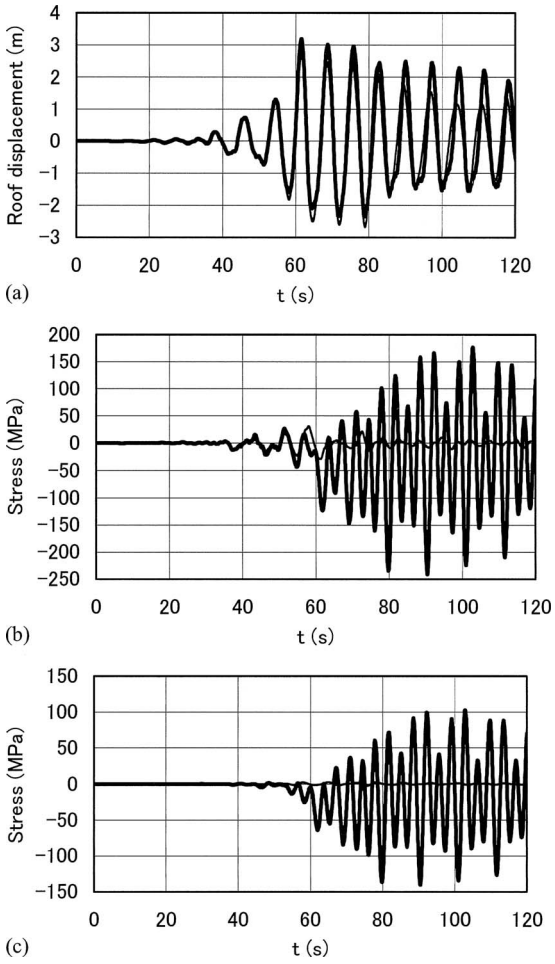

Fig. 9 Responses to an actual earthquake ground motion record 2003 Tokachi-oki (thin lines, linear; thick lines, nonlinear). (*a*) Vertical displacement of floating roof at outer rim of pontoon; (*b*) radial bending stress σ_s at outer end $(r,\varphi)=(b,0)$ of bottom of pontoon. (*c*) Hoop membrane stress σ_φ at the same position.

the internal resonance effects on the stresses and sloshing wave height noted in the case of sinusoidal excitation appear when a broad-band real earthquake excitation is applied; and (3) the stresses can be reduced by decreasing the slope angles of the top and bottom of the pontoon.

The influence of internal resonance on the stresses in a floating roof was not studied in the past. The nonlinear analysis tool developed in this study based on the mode decomposition is helpful for predicting the internal resonance effect on the stresses. Furthermore, the tool is computationally-efficient and requires a small amount of computation time and cost to predict the magnitudes of the stresses and to conduct the parametric studies for reducing the stresses.

Appendix A: Derivation of Eq. (3)

A detailed derivation of Eq. (3) is presented because Eq. (3) forms the cornerstone of this paper. We first substitute Eq. (2) into Eq. (1) and calculate the variation of the functional. We must consider the variation for the liquid domain as well as for the liquid pressure because the liquid domain is variable [18]. The variation $d(\delta V)$ is related to the displacement $\bar{u}$ of the floating roof in the $-z$ direction as follows:

$$d(\delta V) = -\delta\bar{u}\cos(\mathbf{N}_S,z)dS \tag{A1}$$

where $\mathbf{N}_S$ is the outward unit normal vector of the interface S between the liquid and the floating roof, and $\cos(\mathbf{N}_S,z)$ is the cosine of the angle between $\mathbf{N}_S$ and the z direction. By using Eq. (A1), the variation of the functional given by Eq. (1) can be expressed as

$$\delta\int_{t_1}^{t_2} L_f dt = \int_{t_1}^{t_2}\left[\int\int\int_V \delta p_l dV - \int\int_S p_l\delta\bar{u}\cos(\mathbf{N}_S,z)dS\right]dt \tag{A2}$$

Using Eq. (2), the term with δp_l can be expressed as

$$\int_{t_1}^{t_2}\int\int\int_V \delta p_l dV dt = \int_{t_1}^{t_2}\int\int\int_V (-\rho_f)\left[\frac{\partial(\delta\phi)}{\partial t} + \nabla\phi\cdot\nabla(\delta\phi) + \delta\dot{G}\right]dVdt \tag{A3}$$

For further transformation of Eq. (A3), the following relations hold:

$$\int\int\int_V \frac{\partial(\delta\phi)}{\partial t}dV = \frac{\partial}{\partial t}\int\int\int_V \delta\phi dV + \int\int_S \delta\phi\frac{\partial\bar{u}}{\partial t}\cos(\mathbf{N}_S,z)dS \tag{A4}$$

$$\int\int\int_V \frac{\partial(\delta G)}{\partial t}dV = \frac{\partial}{\partial t}\int\int\int_V \delta G dV + \int\int_S \delta G\frac{\partial\bar{u}}{\partial t}\cos(\mathbf{N}_S,z)dS \tag{A5}$$

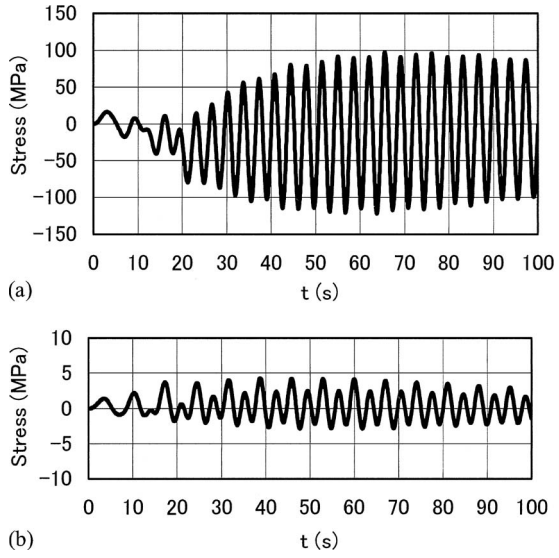

Fig. 10 Nonlinear responses of stresses (the case in which slope angles of pontoon are reduced). (*a*) Radial bending stress σ_s at outer end $(r,\varphi)=(b,0)$ of bottom of pontoon. (*b*) Hoop membrane stress σ_φ at the same position.

$$\int\int\int_V \nabla\phi\cdot\nabla(\delta\phi)dV=\int\int_S \nabla\phi\cdot\mathbf{N}_S\delta\phi dS+\int\int_W \nabla\phi\cdot\mathbf{N}_W\delta\phi dW-\int\int\int_V \nabla^2\phi\delta\phi dV \tag{A6}$$

Equations (A4) and (A5) arise from the fact that the time derivative of an integral over a time-varying domain (the first term on the right-hand side of each equation) is equal to the sum of an integral of the time derivative of the integrand over the instantaneous domain (the left-hand side of each equation) and an integral of the outward flux of the integrand over the moving boundary surface. Equation (A6) can be derived by using Green's theorem. In Eq. (A6), W is the wall and bottom of the tank and $\mathbf{N}_W$ is the outward unit normal vector of W.

Substituting Eqs. (A4)–(A6) into Eq. (A3) and noting that $\delta\phi=\delta G=0$ at the time integration limits $t=t_1$ and $t=t_2$, we transform Eq. (A2) into

$$\delta\int_{t_1}^{t_2} L_f dt=\int_{t_1}^{t_2}\left[\rho_f\int\int\int_V \nabla^2\phi\delta\phi dV-\rho_f\int\int_W \nabla\phi\cdot\mathbf{N}_W\delta\phi dW+\rho_f\int\int_S\left\{-\frac{\partial\bar{u}}{\partial t}\cos(\mathbf{N}_S,z)-\nabla\phi\cdot\mathbf{N}_S\right\}\delta\phi dS-\int\int_S p_l\delta\bar{u}\cos(\mathbf{N}_S,z)dS-\rho_f\delta G\int\int_S\frac{\partial\bar{u}}{\partial t}\cos(\mathbf{N}_S,z)dS\right]dt \tag{A7}$$

Because the interface S is expressed by $f(r,\varphi,z,t)\equiv z+\bar{u}(r,\varphi,t)-h=0$ and the position vector of S is given by $\mathbf{X}=\mathbf{e}_x r\cos\varphi+\mathbf{e}_y r\sin\varphi+\mathbf{e}_z[h-\bar{u}(r,\varphi,t)]$, the nonlinear expressions of the normal vector $\mathbf{N}_S$ and the surface element dS can be obtained as follows:

$$\mathbf{N}_S=\frac{\text{grad}\,f}{|\text{grad}\,f|}=\left[\mathbf{e}_r\frac{\partial\bar{u}}{\partial r}+\mathbf{e}_\varphi\frac{1}{r}\frac{\partial\bar{u}}{\partial\varphi}+\mathbf{e}_z\right]\left[\left(\frac{\partial\bar{u}}{\partial r}\right)^2+\left(\frac{1}{r}\frac{\partial\bar{u}}{\partial\varphi}\right)^2+1\right]^{-1/2} \tag{A8}$$

$$dS=\left|\frac{\partial\mathbf{X}}{\partial r}\times\frac{\partial\mathbf{X}}{\partial\varphi}\right|drd\varphi=\left[\left(\frac{\partial\bar{u}}{\partial r}\right)^2+\left(\frac{1}{r}\frac{\partial\bar{u}}{\partial\varphi}\right)^2+1\right]^{1/2}rdrd\varphi \tag{A9}$$

Substituting Eqs. (A8) and (A9) into Eq. (A7), we obtain the first through fourth, sixth, and eighth terms of Eq. (3).

Next, the motion of the floating roof is formulated based on the finite element approach using the ring shell elements. A nodal displacement vector is defined for a node i and is decomposed into two components with different circumferential variations as follows:

$$\begin{Bmatrix}\bar{u}_i\\ \bar{v}_i\\ \bar{w}_i\\ \left(\frac{\partial\bar{w}}{\partial s}\right)_i\end{Bmatrix}=\sum_{m=0}^{\infty}\begin{Bmatrix}\bar{u}_{mx,i}\cos m\varphi+\bar{u}_{my,i}\sin m\varphi\\ \bar{v}_{mx,i}\sin m\varphi-\bar{v}_{my,i}\cos m\varphi\\ \bar{w}_{mx,i}\cos m\varphi+\bar{w}_{my,i}\sin m\varphi\\ \left(\frac{\partial\bar{w}}{\partial s}\right)_{mx,i}\cos m\varphi+\left(\frac{\partial\bar{w}}{\partial s}\right)_{my,i}\sin m\varphi\end{Bmatrix} \tag{A10}$$

By calculating the kinetic and potential energies following the procedure of the finite element method, the variation in the action for the floating roof can be expressed as

$$\delta\int_{t_1}^{t_2}L_r dt=\delta\int_{t_1}^{t_2}\frac{1}{2}\sum_{m=0}^{\infty}[(\dot{\mathbf{X}}_{mx}^t\mathbf{M}_m\dot{\mathbf{X}}_{mx}-\mathbf{X}_{mx}^t\mathbf{K}_m\mathbf{X}_{mx})+(\dot{\mathbf{X}}_{my}^t\mathbf{M}_m\dot{\mathbf{X}}_{my}-\mathbf{X}_{my}^t\mathbf{K}_m\mathbf{X}_{my})]dt=\int_{t_1}^{t_2}\sum_{m=0}^{\infty}[-\delta\mathbf{X}_{mx}^t(\mathbf{M}_m\ddot{\mathbf{X}}_{mx}+\mathbf{K}_m\mathbf{X}_{mx})-\delta\mathbf{X}_{my}^t(\mathbf{M}_m\ddot{\mathbf{X}}_{my}+\mathbf{K}_m\mathbf{X}_{my})]dt \tag{A11}$$

where $\mathbf{M}_m$ and $\mathbf{K}_m$ are the mass and stiffness matrices, and $\mathbf{X}_{mx}$ and $\mathbf{X}_{my}$ are the collections of $\{\bar{u}_{mx,i},\bar{v}_{mx,i},\bar{w}_{mx,i},(\partial\bar{w}/\partial s)_{mx,i}\}^t$ and $\{\bar{u}_{my,i},\bar{v}_{my,i},\bar{w}_{my,i},(\partial\bar{w}/\partial s)_{my,i}\}^t$, respectively. The mass and stiffness matrices are common to both $\mathbf{X}_{mx}$ and $\mathbf{X}_{my}$. Because the dimension of these matrices is very large, much computation time and cost are required to transform the equations of motion expressed in terms of the nodal displacements into modal equations. To solve this problem, the floating roof is decomposed into several components $c(c=1,2,3,\ldots)$, and their equations of motion are as follows:

$$\mathbf{M}_{mc}\ddot{\mathbf{X}}_{mxc}+\mathbf{K}_{mc}\mathbf{X}_{mxc}=\mathbf{0} \tag{A12}$$

Equation (A12) is expressed in the following form:

$$\begin{bmatrix}\mathbf{M}_{mc11} & \mathbf{M}_{mc12}\\ \mathbf{M}_{mc21} & \mathbf{M}_{mc22}\end{bmatrix}\begin{Bmatrix}\ddot{\mathbf{X}}_{mxc1}\\ \ddot{\mathbf{X}}_{mxc2}\end{Bmatrix}+\begin{bmatrix}\mathbf{K}_{mc11} & \mathbf{K}_{mc12}\\ \mathbf{K}_{mc21} & \mathbf{K}_{mc22}\end{bmatrix}\begin{Bmatrix}\mathbf{X}_{mxc1}\\ \mathbf{X}_{mxc2}\end{Bmatrix}=\begin{Bmatrix}\mathbf{0}\\ \mathbf{0}\end{Bmatrix} \tag{A13}$$

where $\mathbf{X}_{mxc1}$ is the collection of the displacements of the nodes that are not at the joints with the adjacent components while $\mathbf{X}_{mxc2}$ is the collection of the other nodal displacements. The eigenmodes of $\mathbf{X}_{mxc1}$ under the condition that $\mathbf{X}_{mxc2}$ is fixed to zero can be determined by solving the eigenvalue problem (A14), while the static solution of $\mathbf{X}_{mxc1}$ for the case in which $\mathbf{X}_{mxc2}$ is arbitrarily given can be obtained as Eq. (A15) by neglecting the inertia term of Eq. (A13).

$$(-\omega^2\mathbf{M}_{mc11}+\mathbf{K}_{mc11})\mathbf{X}_{mxc1}=\mathbf{0} \tag{A14}$$

$$\mathbf{X}_{mxc1} = -\mathbf{K}_{mc11}^{-1}\mathbf{K}_{mc12}\mathbf{X}_{mxc2} \tag{A15}$$

Expressing $\mathbf{X}_{mxc1}$ by the sum of the linear combination of the eigenmodes and the static solution yields,

$$\begin{Bmatrix} \mathbf{X}_{mxc1} \\ \mathbf{X}_{mxc2} \end{Bmatrix} = \begin{bmatrix} \mathbf{T}_{mc11} & -\mathbf{K}_{mc11}^{-1}\mathbf{K}_{mc12} \\ \mathbf{O} & \mathbf{I} \end{bmatrix} \begin{Bmatrix} \mathbf{q}_{mxc1} \\ \mathbf{X}_{mxc2} \end{Bmatrix} \tag{A16}$$

where $\mathbf{T}_{mc11}$ is the modal transformation matrix whose columns are the eigenvectors of the eigenvalue problem (A14) and $\mathbf{q}_{mxc1}$ is the modal coordinates. The dimension of $\mathbf{q}_{mxc1}$ and $\mathbf{X}_{mxc2}$ can be made much smaller than the dimension of $\mathbf{X}_{mxc1}$. Therefore, the dimension of the numerical problem to be solved can be markedly reduced by the transformation (A16). By defining

$$\mathbf{C}_{mc} = \begin{bmatrix} \mathbf{T}_{mc11} & -\mathbf{K}_{mc11}^{-1}\mathbf{K}_{mc12} \\ \mathbf{O} & \mathbf{I} \end{bmatrix}, \quad \mathbf{X}'_{mxc} = \begin{Bmatrix} \mathbf{q}_{mxc1} \\ \mathbf{X}_{mxc2} \end{Bmatrix} \tag{A17}$$

Equation (A16) can be expressed as

$$\mathbf{X}_{mxc} = \mathbf{C}_{mc}\mathbf{X}'_{mxc} \tag{A18}$$

Repeating the foregoing procedures for each component $c(c=1,2,3,\ldots)$, the global form of Eq. (A18) for the whole floating roof structure can be obtained as

$$\mathbf{X}_{mx} = \mathbf{C}_m\mathbf{X}'_{mx} \tag{A19}$$

Similarly, the corresponding equation $\mathbf{X}_{my}=\mathbf{C}_m\mathbf{X}'_{my}$ can be obtained for the displacement components with subscript y. By substituting these equations into Eq. (A11) and defining the following matrices:

$$\mathbf{M}'_m = \mathbf{C}_m^t\mathbf{M}_m\mathbf{C}_m, \quad \mathbf{K}'_m = \mathbf{C}_m^t\mathbf{K}_m\mathbf{C}_m \tag{A20}$$

we can derive the fifth term of Eq. (3). The seventh term of Eq. (3) can be derived by considering the virtual work done by the inertial force for each element of the floating roof.

Appendix B: Validity of Damping Term $\mu\phi|_{z=h}$ Used in Numerical Calculation

Letting $\mathbf{E}_{m\beta}$ and $\mathbf{A}_{m\beta}$ be the collections of $\mathbf{E}_{mp\beta}$ $(p=1,2,\ldots)$ and $A_{mn\beta}$ $(n=1,2,\ldots)$, respectively, for $\beta=x$ and y, linear homogeneous terms of Eqs. (9) and (10) can be expressed in the following form:

$$-\tilde{\mathbf{M}}_m\ddot{\mathbf{E}}_{m\beta} - \tilde{\mathbf{K}}_m\mathbf{E}_{m\beta} + \mathbf{C}_m^{(1)}\ddot{\mathbf{A}}_{m\beta} - \mathbf{C}_m^{(2)}\mathbf{E}_{m\beta} = \mathbf{0} \tag{B1}$$

$$-\mathbf{C}_m^{(4)}\ddot{\mathbf{E}}_{m\beta} - \mathbf{C}_m^{(5)}\ddot{\mathbf{A}}_{m\beta} = \mathbf{0} \tag{B2}$$

where $\tilde{\mathbf{M}}_m$ and $\tilde{\mathbf{K}}_m$ are the modal mass and stiffness matrices of the floating roof uncoupled with the liquid motion and $\mathbf{C}_m^{(1)}$ etc. are constant matrices. By adding the damping term $\mu\phi|_{z=h}$ to the quantity in the brace of Eq. (3), Eq. (B1) is modified to

$$-\tilde{\mathbf{M}}_m\ddot{\mathbf{E}}_{m\beta} - \tilde{\mathbf{K}}_m\mathbf{E}_{m\beta} + \mathbf{C}_m^{(1)}\ddot{\mathbf{A}}_{m\beta} + \boldsymbol{\mu}_m\mathbf{C}_m^{(1)}\dot{\mathbf{A}}_{m\beta} - \mathbf{C}_m^{(2)}\mathbf{E}_{m\beta} = \mathbf{0} \tag{B3}$$

where $\boldsymbol{\mu}_m$ is the diagonal matrix whose nth diagonal element is equal to $2\zeta_{mn}\omega_{mn}$. Solving Eq. (B2) with respect to $\mathbf{A}_{m\beta}$ and substituting the resulting equation into Eq. (B3), we obtain

$$\hat{\mathbf{m}}_m\ddot{\mathbf{A}}_{m\beta} + \hat{\mathbf{c}}_m\dot{\mathbf{A}}_{m\beta} + \hat{\mathbf{k}}_m\mathbf{A}_{m\beta} = \mathbf{0} \tag{B4}$$

where

$$\hat{\mathbf{m}}_m = \tilde{\mathbf{M}}_m(\mathbf{C}_m^{(4)})^{-1}\mathbf{C}_m^{(5)} + \mathbf{C}_m^{(1)} \tag{B5}$$

$$\hat{\mathbf{c}}_m = \boldsymbol{\mu}_m\mathbf{C}_m^{(1)} \tag{B6}$$

$$\hat{\mathbf{k}}_m = \tilde{\mathbf{K}}_m(\mathbf{C}_m^{(4)})^{-1}\mathbf{C}_m^{(5)} + \mathbf{C}_m^{(2)}(\mathbf{C}_m^{(4)})^{-1}\mathbf{C}_m^{(5)} \tag{B7}$$

By using the eigenvectors of $\hat{\mathbf{m}}_m^{-1}\hat{\mathbf{k}}_m$, the following transformation can be made:

$$\mathbf{A}_{m\beta} = \mathbf{S}_m\mathbf{p}_{m\beta} \tag{B8}$$

where $\mathbf{S}_m$ is the collection of the eigenvectors and $\mathbf{p}_{m\beta}$ is the collection of the modal coordinates for these eigenvectors. Substituting Eq. (B8) into Eq. (B4) and premultiplying by $\mathbf{S}_m^{-1}\hat{\mathbf{m}}_m^{-1}$, we obtain

$$\ddot{\mathbf{p}}_{m\beta} + \mathbf{S}_m^{-1}(\hat{\mathbf{m}}_m^{-1}\hat{\mathbf{c}}_m)\mathbf{S}_m\dot{\mathbf{p}}_{m\beta} + \mathbf{S}_m^{-1}(\hat{\mathbf{m}}_m^{-1}\hat{\mathbf{k}}_m)\mathbf{S}_m\mathbf{p}_{m\beta} = \mathbf{0} \tag{B9}$$

Because the mass of the floating roof is much smaller than the liquid mass, the first term of Eq. (B5) can be neglected. Hence, the coefficient of the damping term of Eq. (B9) can be approximated as

$$\mathbf{S}_m^{-1}(\hat{\mathbf{m}}_m^{-1}\hat{\mathbf{c}}_m)\mathbf{S}_m \cong \mathbf{S}_m^{-1}\boldsymbol{\mu}_m\mathbf{S}_m \tag{B10}$$

The matrix $\mathbf{S}_m$ is diagonally dominant because for the nth eigenvector, the nth component $\dot{A}_{mn\beta}$ is predominant to the other components $\dot{A}_{mn'\beta}$ $(n'\neq n)$ as mentioned in Sec. 2.3. Therefore, $\mathbf{S}_m^{-1}\boldsymbol{\mu}_m\mathbf{S}_m$ is diagonally dominant and its nth diagonal components is close to $2\zeta_{mn}\omega_{mn}$. The coefficient $\mathbf{S}_m^{-1}(\hat{\mathbf{m}}_m^{-1}\hat{\mathbf{k}}_m)\mathbf{S}_m$ of $\mathbf{p}_{m\beta}$ in Eq. (B9) is a diagonal matrix whose nth diagonal element is close to $\omega_{mn}^2 = g\lambda_{mn}\tanh(\lambda_{mn}h)$ as mentioned in Sec. 2.3. Hence, Eq. (B9) indicates that the damping ratio ζ_{mn} is introduced into the sloshing mode with eigenfrequency ω_{mn}.

References

[1] Nakagawa, K., 1955, "On the Vibration of an Elevated Water Tank-II," Technol. Rep. Osaka Univ., **5**, pp. 317–336.

[2] Kondo, H., 1978, "Free Vibration Analysis for Vertical Motion of a Floating Roof," Trans. Jpn. Soc. Mech. Eng., **44**, pp. 1214–1223.

[3] Sakai, F., Nishimura, M., and Ogawa, H., 1984, "Sloshing Behavior of Floating Roof Oil Storage Tanks," Comput. Struc., **19**, pp. 183–192.

[4] Shimizu, S., Naito, K., and Koyama, Y., 1984, "A Study on Sloshing Behaviors of Floating Roof Oil Storage Tanks During Earthquake Excited by Three-Dimensional Dynamic Simulator," Ishikawajima-Harima Eng. Rev., **24**, pp. 379–384.

[5] 1966, "The Dynamic Behavior of Liquids in Moving Containers," NASA Report No. SP-106.

[6] Ibrahim, R. A., Pilipchuk, V. N., and Ikeda, T., 2001, "Recent Advances in Liquid Sloshing Dynamics," Appl. Mech. Rev., **54**, pp. 133–199.

[7] Bauer, H. F., Chang, S. S., and Wang, J. T. S., 1971, "Nonlinear Liquid Motion in a Longitudinally Excited Container With Elastic Bottom," AIAA J., **9**, pp. 2333–2339.

[8] Ibrahim, R. I., and El-Sayad, M. A., 1999, "Simultaneous Parametric and Internal Resonances in Systems Involving Strong Nonlinearities," J. Sound Vib., **225**, pp. 857–885.

[9] Ibrahim, R. A., 2005, *Liquid Sloshing Dynamics: Theory and Applications*, Cambridge University Press, Cambridge, England.

[10] Ikeda, T., and Nakagawa, N., 1997, "Nonlinear Vibrations of a Structure Caused by Water Sloshing in a Rectangular Tank," J. Sound Vib., **201**, pp. 23–41.

[11] Ikeda, T., and Nakagawa, N., 1995, "Nonlinear Vibrations of a Structure Caused by Water Sloshing in a Cylindrical Tank," Pressure Vessels and Piping Divison Conference, ASME PVP-Vol. 310, pp. 63–76.

[12] Peterson, L. D., Crawley, E. F., and Hansman, R. J., 1989, "Nonlinear Slosh Coupled to the Dynamics of a Spacecraft," AIAA J., **27**, pp. 1230–1240.

[13] Utsumi, M., Kimura, K., and Sakata, M., 1987, "The Non-Stationary Random Vibration of an Elastic Circular Cylindrical Liquid Storage Tank in Simulated Earthquake Excitation (Straightforward Analysis of Tank Wall Deformation)," JSME Int. J., Ser. III, **30**, pp. 467–475.

[14] Utsumi, M., and Ishida, K., 2008, "Vibration Analysis of a Floating Roof Taking Into Account the Nonlinearity of Sloshing," ASME J. Appl. Mech., **75**, p. 041008.

[15] Yamauchi, Y., Kamei, A., Zama, S., and Uchida, Y., 2006, "Seismic Design of Floating Roof of Oil Storage Tanks Under Liquid Sloshing," Sloshing and Fluid Structure Vibration, ASME Pressure Vessels and Piping Division Conference, Paper No. PVP2006-ICPVT-11-93280.

[16] Nishi, H., 2008, "Sloshing Behavior and Safety of the Floating Roof of Oil Storage Tanks Under Long-Period Strong Ground Motion," Ph.D. thesis, Yokohama National University, Yokohama, Japan.

[17] Seliger, R. L., and Whitham, G. B., 1968, "Variational Principles in Continuum Mechanics," Proc. R. Soc. London, Ser. A, **305**, pp. 1–25.

[18] Utsumi, M., 1998, "Low-Gravity Propellant Slosh Analysis Using Spherical Coordinates," J. Fluids Struct., **12**, pp. 57–83.

Shape of a Soft Container Under Hydrostatic Load

Gil Iosilevskii
Faculty of Aerospace Engineering,
Technion,
Haifa 32000, Israel
e-mail: igil@aerodyne.technion.ac.il

This paper concerns an open container, formed by bending lengthwise a long strip of weightless nonstretchable impermeable fabric and holding its long edges parallel and horizontal. Given that the container is filled to the rim with fluid, closed form analytical solution is obtained for the capacity of the container and the shape of its envelope. [DOI: 10.1115/1.3173765]

Keywords: soft vessel, underwater lifting device, nonlinear shell theory, inextensible beamshell

1 Introduction

Vessels made of soft impermeable fabric come in multitude of shapes and have multitude of uses. In particular, they can be used as containers for fluid [1,2], or as underwater lifting devices. This short exposition addresses a long (actually, infinitely long) canal-like tub, formed by bending lengthwise a strip of weightless nonstretchable fabric and sealing its open ends. The long edges are fixed straight, horizontal, and parallel to each other. The tub is either filled to the rim with fluid (Fig. 1) to be used as a container, or submerged in fluid and filled full with air to be used as an underwater lifting device. We seek the shape of the tub's cross section and its capacity.

2 Formulation

For the sake of definiteness, select an auxiliary rectilinear coordinate system C with the x-axis connecting the two long edges across the opening, the z-axis midway between the long edges and parallel to them, and the y-axis pointing to the same side to which the envelope extends (i.e., along the direction of gravity if the fluid within the envelope is denser than the fluid outside it).

Let l, x_0, ρ, and g be the width of the fabric forming the tub, half the distance between its long edges (it is implicitly understood that $2x_0 < l$), the (absolute) difference between the density of the fluid within the tub and the fluid outside it, and the acceleration of gravity, respectively.

With respect to C, the cross section shape of the tub can be defined by the pair of (yet unknown) functions on $[0,l]$, x_s and y_s, such that for any t in $[0,l]$

$$x = x_s(t), \quad y = y_s(t) \tag{1}$$

Without a loss of generality it will be assumed henceforth that t represents the distance from one of the edges measured along the envelope (the arc-length). In this case these two functions satisfy

$$x_s'^2 + y_s'^2 = 1 \tag{2}$$

on $(0,l)$, where the prime stands for the respective derivative. Moreover, by the choice of the coordinate system

$$x_s(0) = -x_s(l) = -x_0, \quad y_s(0) = y_s(l) = 0 \tag{3a}$$

$$x_s(l/2) = 0, \quad y_s'(l/2) = 0 \tag{3b}$$

Because of the difference in the densities of the fluid in the interior and in the exterior of the tub, hydrostatic pressure

$$p_s = \rho g y_s \tag{4}$$

acts on its envelope. We seek the functions x_s and y_s.

3 Solution

Pertinent equations governing these two functions can be found in Ref. [3]; for completeness of this presentation, they are recapitulated below.

Let T_s be a scalar-valued function on $(0,l)$, representing the tension in the envelope. Referring to Fig. 1, equilibrium conditions (the y- and x-components of the force balance) for an infinitesimally small element of the envelope are

$$p_s x_s' + (T_s y_s')' = 0 \tag{5a}$$

$$p_s y_s' - (T_s x_s')' = 0 \tag{5b}$$

These two equations can be straightforwardly solved for T_s and T_s' to obtain

$$T_s = -p_s \frac{x_s'^2 + y_s'^2}{y_s'' x_s' - x_s'' y_s'} \tag{6a}$$

$$T_s' = -p_s \frac{x_s'' x_s' + y_s'' y_s'}{y_s'' x_s' - x_s'' y_s'} \tag{6b}$$

But

$$2(x_s'' x_s' + y_s'' y_s') = (x_s'^2 + y_s'^2)' = 0 \tag{7}$$

by Eq. (2), and therefore T_s' is identically zero on $(0,l)$ by Eq. (6*b*). Consequently,

$$T_s(t) = T_0 \tag{8}$$

for each t in $(0,l)$; T_0 is yet unknown. Since only normal forces act on the envelope, Eq. (8) could have been anticipated. At the same time, using Eqs. (8), (4), and (2), Eq. (6*a*) can be recast as

$$y_s'' x_s' - x_s'' y_s' + \frac{\rho g y_s}{T_0} = 0 \tag{9}$$

Adjusting the notation, Eqs. (8) and (9) can be identified with the respective equations (O.24) in Ref. [3].

In order to proceed we suggest multiplying Eq. (9) by y_s'. Noting that

$$(y_s'' x_s' - x_s'' y_s') y_s' = -x_s''(x_s'^2 + y_s'^2) = -x_s'' \tag{10}$$

by Eqs. (2) and (7), and, of course, that $2y_s y_s' = (y_s^2)'$, the resulting equation

$$-x_s'' + \frac{\rho g}{2T_0}(y_s^2)' = 0 \tag{11}$$

can be readily integrated to obtain

$$x_s' = \frac{\rho g y_s^2}{2T_0} + C_1 \tag{12}$$

where C_1 is an unknown constant (in addition to T_0).

Substituting this equation back in Eq. (2) yields a simple first-order equation for y_s

$$y_s'^2 = 1 - \left(\frac{\rho g y_s^2}{2T_0} + C_1\right)^2 \tag{13}$$

Before actually solving it, we would like to use it in order to interpret C_1 in terms of meaningful quantities. In fact, at the middle of the envelope (where $t = l/2$), the left hand side of Eq. (13) vanishes by symmetry considerations (see Eq. (3*b*)), whereas $y_s(l/2) = y_0$, which is the maximal draft of the tub. Hence

Contributed by the Applied Mechanics Division of ASME for publication in the JOURNAL OF APPLIED MECHANICS. Manuscript received August 29, 2008; final manuscript received April 11, 2009; published online September 30, 2009. Review conducted by Matthew R. Begley.

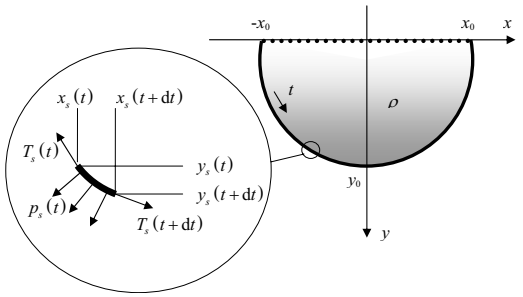

Fig. 1 The tub (right) and the element of its envelope

$$C_1 = \pm 1 - \frac{\rho g y_0^2}{2T_0} \tag{14}$$

But $y_s(t) \leq y_0$ for any t in $[0,l]$, and therefore the choice of the minus sign in Eq. (14) yields negative values on the right hand side of Eq. (13), which are inadmissible.

With the plus sign in Eq. (14), Eq. (13) can be recast as

$$y_s' = \pm 2k\sqrt{\left(1 - k^2\left(1 - \frac{y_s^2}{y_0^2}\right)\right)\left(1 - \frac{y_s^2}{y_0^2}\right)} \tag{15}$$

where the sign switches between the right and left sides of the envelope, and

$$k^2 = \rho g y_0^2/(4T_0) \tag{16}$$

is a convenient dimensionless (but yet unknown) parameter. Concurrently

$$x_s' = 1 - 2k^2\left(1 - \frac{y_s^2}{y_0^2}\right) \tag{17}$$

by Eqs. (12), (14), and (16). We emphasize that at this stage both y_0 and k, which replace T_0 and C_1 as integration constants, are unknown.

Let θ_s be an auxiliary function on $[0,l]$ into $[-\pi/2,\pi/2]$, such that for each t in $[0,l]$

$$y_s(t) = y_0 \cos(\theta_s(t)) \tag{18}$$

With this, Eqs. (15) and (17) take on the respective forms

$$\theta_s' = -\frac{2k}{y_0}\sqrt{1 - k^2 \sin^2 \theta_s} \tag{19}$$

$$x_s' = 1 - 2k^2 \sin^2 \theta_s \tag{20}$$

Integrating Eq. (19) between $t=l/2$ (where $\theta_s=x_s=0$) and any t yields

$$\frac{t}{l} = \frac{1}{2}\left(1 + \frac{y_0}{l}\frac{F(\theta_s(t),k)}{k}\right) \tag{21}$$

where $F(\theta,k)=\int_0^\theta(\sqrt{1-k^2\sin^2\tau})^{-1}d\tau$ is an incomplete elliptic integral of the first kind [4, Art. 8.111]. Similarly, integrating the ratio of Eqs. (19) and (20)

$$\frac{d\theta_s}{dx_s} = -\frac{2k}{y_0}\frac{\sqrt{1 - k^2 \sin^2 \theta_s}}{1 - 2k^2 \sin^2 \theta_s} \tag{22}$$

in the same limits yields

$$\frac{x_s}{y_0} = \frac{E(\theta_s,k)}{k} - \frac{F(\theta_s,k)}{2k} \tag{23}$$

where $E(\theta,k)=\int_0^\theta(\sqrt{1-k^2\sin^2\tau})d\tau$ is an incomplete elliptic integral of the second kind [4].

At the edge $t=l$ of the envelope, $x_s(l)=x_0$, $t-l/2=l/2$, and $\theta_s(l)=\pi/2$, and hence Eqs. (21) and (23) reduce to

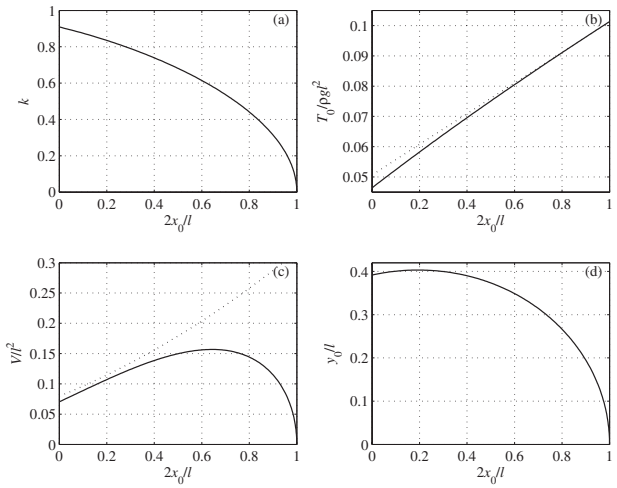

Fig. 2 Following clockwise from the upper left corner, displayed in the figure are the solution (Eq. (27)) of Eq. (26), the tension in the envelope (Eq. (28)), the draft (Eq. (24)), and the area (Eq. (30)). The dashed lines are approximations.

$$\frac{y_0}{l} = \frac{k}{\mathrm{K}(k)} \tag{24}$$

$$\frac{x_0}{y_0} = \frac{\mathrm{E}(k)}{k} - \frac{\mathrm{K}(k)}{2k} \tag{25}$$

where $\mathrm{E}(k)=E(\pi/2,k)$ and $\mathrm{K}(k)=F(\pi/2,k)$ are the respective complete integrals. Since both x_0 and l are known, the product of Eqs. (25) and (24) provides the equation

$$\frac{\mathrm{E}(k)}{\mathrm{K}(k)} = \frac{1}{2} + \frac{x_0}{l} \tag{26}$$

for k. Its (numerical) solution

$$k = \kappa(x_0/l) \tag{27}$$

can be found in Fig. 2(*a*).

Once k is related with the ratio x_0/l, the rest is simple. In particular

$$T_0 = \frac{\rho g l^2}{4\mathrm{K}^2(k)} \tag{28}$$

by Eqs. (16) and (24), whereas the shape of the envelope can be reconstructed with

$$\frac{x_s}{l} = \frac{E(\theta_s,k)}{\mathrm{K}(k)} - \frac{1}{2}\frac{F(\theta_s,k)}{\mathrm{K}(k)} \tag{29a}$$

$$\frac{y_s}{l} = \frac{k}{\mathrm{K}(k)}\cos\theta_s \tag{29b}$$

$$\frac{t}{l} = \frac{1}{2}\left(1 + \frac{F(\theta_s,k)}{\mathrm{K}(k)}\right) \tag{29c}$$

The first of these is the conjunction of Eqs. (23) and (24); the second is the conjunction of Eqs. (18) and (24); and the last is the conjunction of Eqs. (21) and (24). Practically, the one-to-one correspondence (Eq. (29*c*)) between t and $\theta_s(t)$ can be discarded, and θ_s be treated in Eqs. (29*a*) and (29*b*) as an independent variable spanning the interval $[-\pi/2,\pi/2]$.

Knowledge of the tension allows quick computation of the area V contained within the envelope. In fact, the "weight" (per unit length) of the fluid contained within the envelope $\rho V g$ should be

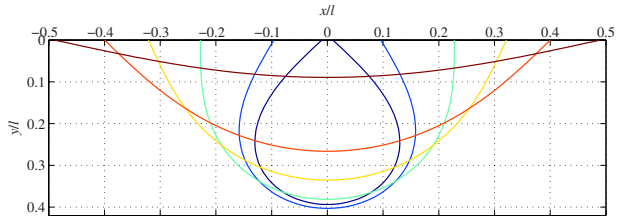

Fig. 3 Few sample shapes. The third, fourth, and fifth shapes (counting from the outside) correspond to the maximum area ($2x_0/l \approx 0.643$), vertical edges ($2x_0/l \approx 0.457$), and maximum draft ($2x_0/l \approx 0.195$), respectively.

equal to the y-component of the force applied to the envelope at its edges $2T_0 y_s'(0)$. But $y_s'(0) = 2k\sqrt{1-k^2}$ by Eqs. (15) and (3*a*), whereas T_0 is given by Eq. (28). Hence

$$V = l^2 \frac{k\sqrt{1-k^2}}{\mathrm{K}^2(k)} \tag{30}$$

It is shown in Fig. 2(*b*). For future reference we also note that

$$x_s'(0) = 1 - 2k^2 \tag{31}$$

by Eq. (21).

4 Analysis

Sample shapes of the tub's section can be found in Fig. 3 for few values of $2x_0/l$, which is the ratio of the distance between the edges to the length of the envelope. Several observations are noteworthy:

The edges of the tub become vertical when $k = 1/\sqrt{2}$, i.e., when $2x_0/l = 2\mathrm{E}(1/\sqrt{2})\mathrm{K}^{-1}(1/\sqrt{2}) - 1 \approx 0.457$. The first of these relations immediately follows Eq. (31); the second immediately follows the first by Eq. (26). For smaller values of $2x_0/l$, the tub is wider than the distance between its edges (i.e., it looks like a balloon), while for larger values, the tub is contained between its edges.

The maximum area of the tub for a given length l of the envelope, approximately $0.157l^2$, is obtained when $k = k_* \approx 0.582$, which is the root of

$$\frac{\mathrm{E}(k)}{\mathrm{K}(k)} = \frac{3}{2} - 2k^2 \tag{32}$$

It corresponds to $2x_0/l = 2 - 4k_*^2 \approx 0.643$. Equation (32) follows the differentiation of Eq. (30) with respect to k; the last relation follows Eq. (32) by Eq. (26); the volume itself is obtained by substituting k_* in Eq. (30) This optimal (volumewise) distance between the edges is rather surprising since it corresponds to a relatively shallow-draft tub, fully contained between its edges.

When the edges are brought toward each other, the area of the tub becomes comparable with (albeit somewhat smaller than) the area $l^2/4\pi(1+2(x/l))^2$ of a circle having the same circumference. This reference is shown by the dashed line in Fig. 2(*b*).

Remarkably simple, almost linear, behavior of the envelope tension with the distance between the edges suggests that it can probably be approximated analytically. Thus, with $2x_0/l = 1 - k^2 + \cdots$, by Eq. (26), and $T_0 = (\rho g l^2/\pi^2)(1 - k^2/2 + \cdots)$, by Eq. (28), one readily finds that $T_0 = (\rho g l^2/\pi^2)((1/2) + (x_0/l) + \cdots)$. This approximation is shown by the dashed line in Fig. 2(*c*). Note that the maximal tension in the envelope $\rho g l^2/\pi^2$ is obtained in the limit when it is opened flat ($2x_0 \to l$), whereas the minimal tension is obtained when the edges touch.

The maximum draft of the tub for a given length l of the envelope, approximately $0.403l$, is obtained when $k = k_+ \approx 0.837$, which is the root of

$$\frac{\mathrm{E}(k)}{\mathrm{K}(k)} = 2 - 2k^2 \tag{33}$$

It corresponds to $2x_0/l = 3 - 4k_+^2 \approx 0.195$. Equation (33) follows the differentiation of Eq. (24) with respect to k; the last relation follows Eq. (33) by Eq. (26); the draft itself is obtained by substituting k_+ in Eq. (24).

Acknowledgment

The author would like to thank Dr. N. Drimer from the Coastal and Marine Research Institute for bringing the problem to his attention and Professor D. Givoli from the Faculty of Aerospace Engineering for his helpful comments.

References

[1] Parker, D. A., 1988, "The Equilibrium of a Flexible Membrane Under Hydrostatic Pressure," Int. J. Math. Educ. Sci. Technol., **19**(1), pp. 169–174.
[2] Wang, C. Y., and Watson, L. T., 1981, "The Fluid-Filled Cylindrical Membrane Container," J. Eng. Math., **15**(2), pp. 81–88.
[3] Libai, A., and Simmonds, J. G., 1988, *The Nonlinear Theory of Elastic Shells. One Spatial Dimension*, Academic, San Diego, CA, pp. 101–103.
[4] Gradshteyn, I. S., and Ryzhik, I. M., 1980, *Table of Integrals, Series, and Products*, Academic, Orlando, FL, pp. 904–905.

Constitutive Modeling of Electrostrictive Polymers Using a Hyperelasticity-Based Approach

A. W. Richards

G. M. Odegard[1]

Department of Mechanical Engineering-Engineering Mechanics,
Michigan Technological University,
Houghton, MI 49931

The use of constitutive equations to describe the electromechanical behavior of electrostrictive materials began over 100 years ago. While these equations have been used to model a host of ceramic-based and polymer-based electroactive materials, a fully characterized model has not yet been developed to predict the response of transversely isotropic polymer electrostrictives. A constitutive model is developed within a thermodynamic and hyperelastic framework that incorporates the transversely isotropic material symmetry that is present in many polymer-based electrostrictives. The resulting constitutive model is characterized for three electrostrictive polymer systems using empirical data that are available in the literature. The model has a relatively simple functional form that is easily adaptable to other polymer electrostrictive material systems. [DOI: 10.1115/1.3173766]

Keywords: electroactive materials, electrostriction, MEMS, polyurethane elastomers

1 Introduction

Polymer-based electrostrictive materials became a focal point of research for applications that require large magnitudes of actuation and significant weight-savings [1–23]. These applications range from microelectromechanical systems (MEMS) to artificial muscles. The use of these materials in engineering applications requires accurate and flexible constitutive relations to relate loads, deformation, electric displacement, and applied electrical field.

In the late 19th century and the early part of the 20th century, several studies reported a relationship between the applied electric field, stress field, and strain field for cylindrical condensers [24–33]. In the middle portion of the 20th century, many scholars studied the broader applications of electrostrictive materials and established more specific definitions of electrostrictive behavior. In 1941, Stratton [34] defined electrostriction as simply the elastic deformation of a dielectric under the forces exerted by an electrostatic field. However, numerous authors [35–42] generally agreed that electrostrictive materials exhibit a constitutive behavior that can be described in a thermodynamic framework. More recently, many studies employed this thermodynamic framework for electrostrictive materials [43–56].

The objective of this study is to establish a hyperelastic framework for modeling polymer-based electrostrictive materials with transverse-isotropic material symmetry. The resulting constitutive model is characterized for three electrostrictive polymer systems using empirical data that are available in the literature. The thermodynamic framework of the modeling approach is established first followed by the characterization of material parameters.

2 Kinematics and Balance Laws

Consider a region of a material manifold $\mathfrak{R}$ embedded in a three-dimensional Euclidean space with its volume enclosed by the surface $\partial\mathfrak{R}$. A material point of the region in its reference state is located by its rectangular coordinate vector $\mathbf{X}$ at time $t=0$, whose components are taken with respect to the mutually perpendicular basis set $e=\{\mathbf{e}_1,\mathbf{e}_2,\mathbf{e}_3\}$. For any time $t>0$, the region deforms to the spatial configuration $\mathfrak{R}_t$ with surface $\partial\mathfrak{R}_t$. The coordinate of the material point in the spatial configuration is given by the vector $\mathbf{x}$. The coordinates in the reference and spatial configurations are related by

$$\mathbf{x} = \chi(\mathbf{X},t) \tag{1}$$

The deformation gradient tensor is given by

$$F_{iK} = \frac{\partial x_i}{\partial X_K} \tag{2}$$

The right Cauchy–Green deformation tensor is defined as $\mathbf{C}=\mathbf{F}^T\mathbf{F}$, whose eigenvalues are the squares of the principal stretches associated with the deformation of Eq. (1). The region is subjected to an electric field vector denoted in $\mathfrak{R}$ as the Lagrangian electric field $\mathbf{E}$.

Over $\mathfrak{R}$, the mass balance is

$$\dot{\rho} = 0 \tag{3}$$

where the superposed dot indicates a material derivative and ρ is the mass density of the material. The balance of linear momentum, assuming static conditions and no body forces, is

$$\text{div}\ \mathbf{FS} = \mathbf{o} \tag{4}$$

where div is the divergence operator with respect to the reference configuration, $\mathbf{S}$ is the second Piola–Kirchhoff stress tensor, and $\mathbf{o}$ is the null vector. The angular momentum balance of the system is simply the proof of the symmetry of the second Piola–Kirchhoff stress tensor.

$$\mathbf{S} = \mathbf{S}^T \tag{5}$$

These three balance principles can be easily established using standard techniques [57,58]. The energy balance in the reference configuration, which includes the energy of the electric field, is [39,59–61]

$$-\rho\dot{U} + (1/2)\mathbf{S}:\dot{\mathbf{C}} + \mathbf{E}\cdot\dot{\mathbf{D}} + \text{div}\ \mathbf{Q} + \rho h = 0 \tag{6}$$

where U is the specific internal energy, $\mathbf{D}$ is the Lagrangian electric displacement vector, $\mathbf{Q}$ is the heat flux vector, and h is the volumetric thermal heat source. It has been shown that $\mathbf{E}$ and $\mathbf{D}$ are work conjugates for a deformable dielectric [62]. The second law of thermodynamics for the reference configuration is [59]

$$\rho\dot{\eta} - \frac{1}{\theta}\text{div}\ \mathbf{Q} + \left(\frac{1}{\theta^2}\right)\mathbf{Q}\cdot\text{grad}\ \theta - \frac{\rho h}{\theta} \geq 0 \tag{7}$$

where θ is the temperature and grad is the gradient function with respect to the reference configuration. The free energy of the systems is defined as [59]

$$\psi = U - \theta\eta - \left(\frac{1}{\rho}\right)\mathbf{E}\cdot\mathbf{D} \tag{8}$$

The Clausius–Duhem inequality is established by substitution of Eqs. (6) and (8) into Eq. (7)

$$-\rho(\dot{\theta}\eta + \dot{\psi}) + (1/2)\mathbf{S}:\dot{\mathbf{C}} - \dot{\mathbf{E}}\cdot\mathbf{D} + \left(\frac{1}{\theta}\right)\mathbf{Q}\cdot\text{grad}\ \theta \geq 0 \tag{9}$$

Therefore, Eqs. (3)–(6) constitute 8 scalar field equations for 22 scalar quantities (ρ, $\mathbf{S}$, $\mathbf{x}$, $\mathbf{D}$, ψ, θ, $\mathbf{E}$, and η with h prescribed).

[1]Corresponding author.

Contributed by the Applied Mechanics Division of ASME for publication in the JOURNAL OF APPLIED MECHANICS. Manuscript received August 11, 2008; final manuscript received April 13, 2009; published online October 5, 2009. Review conducted by Zhigang Suo.

Therefore, 14 constitutive equations are required to completely describe the electromechanical behavior of the material.

The appropriate boundary conditions of the electric field and the electric displacement vector are important in the solution of boundary value problems. It has been shown [63] that in the absence of surface charges the normal component of the electric displacement and the tangent component of the electric field with respect to $\partial\mathfrak{R}$ must be continuous across $\partial\mathfrak{R}$.

3 Constitutive Modeling

Similar to Eringen [59], it is assumed that the thermodynamic forces for $\mathfrak{R}$ are $\mathbf{C}$, $\mathbf{E}$, and θ. Therefore, the remaining parameters are thermodynamic fluxes, and these are used to establish the following constitutive relations:

$$\mathbf{S} = \hat{\mathbf{S}}(\mathbf{C},\mathbf{E},\theta) \tag{10a}$$

$$\mathbf{D} = \hat{\mathbf{D}}(\mathbf{C},\mathbf{E},\theta) \tag{10b}$$

$$\eta = \hat{\eta}(\mathbf{C},\mathbf{E},\theta) \tag{10c}$$

$$\Psi = \hat{\Psi}(\mathbf{C},\mathbf{E},\theta) \tag{10d}$$

where $\Psi=\rho\psi$, and use has been made of the principle of equipresence [57,58] in which a variable present as an independent variable in one constitutive equation is present in all other constitutive equations. Expanding Eq. (10*d*),

$$\dot{\Psi} = \frac{\partial\hat{\Psi}(\mathbf{C},\mathbf{E},\theta)}{\partial\mathbf{C}}:\dot{\mathbf{C}} + \frac{\partial\hat{\Psi}(\mathbf{C},\mathbf{E},\theta)}{\partial\mathbf{E}}\cdot\dot{\mathbf{E}} + \frac{\partial\hat{\Psi}(\mathbf{C},\mathbf{E},\theta)}{\partial\theta}\dot{\theta} \tag{11}$$

Substitution of Eq. (11) into Eq. (9) yields

$$\left[\frac{1}{2}\mathbf{S} - \frac{\partial\hat{\Psi}(\mathbf{C},\mathbf{E},\theta)}{\partial\mathbf{C}}\right]:\dot{\mathbf{C}} - \left[\mathbf{D} + \frac{\partial\hat{\Psi}(\mathbf{C},\mathbf{E},\theta)}{\partial\mathbf{E}}\right]\cdot\dot{\mathbf{E}} - \left[\frac{\partial\hat{\Psi}(\mathbf{C},\mathbf{E},\theta)}{\partial\theta} + \rho\eta\right]\dot{\theta} + \left(\frac{1}{\theta}\right)\mathbf{Q}\cdot\text{grad }\theta \geq 0 \tag{12}$$

In general, this modified form of the Clausius–Duhem inequality must hold for arbitrary values of the thermodynamic forces $\dot{\mathbf{C}}$, $\dot{\mathbf{E}}$, and $\dot{\theta}$. Therefore,

$$\mathbf{S} = 2\frac{\partial\hat{\Psi}(\mathbf{C},\mathbf{E},\theta)}{\partial\mathbf{C}} \tag{13a}$$

$$\mathbf{D} = -\frac{\partial\hat{\Psi}(\mathbf{C},\mathbf{E},\theta)}{\partial\mathbf{E}} \tag{13b}$$

$$\rho\eta = -\frac{\partial\hat{\Psi}(\mathbf{C},\mathbf{E},\theta)}{\partial\theta} \tag{13c}$$

$$\left(\frac{1}{\theta}\right)\mathbf{Q}\cdot\text{grad }\theta \geq 0 \tag{13d}$$

These equations represent general forms of the constitutive equations. The specific form of $\hat{\Psi}$ depends on the assumptions of material symmetry and behavior.

Whereas many electroactive materials are crystalline (e.g., piezoelectrics), most electrostrictive polymers are composed of amorphous regions that contain small electroactive crystallites attached to polymer chains [19–23]. A schematic of the molecular structure of a typical electrostrictive polymer is shown in Fig. 1. Although the crystallites themselves are electroactive, the overall material cannot exhibit a bulk electrostrictive effect unless the crystallites are aligned using a biasing field during processing so that their electroactively induced strains all act in the same direction with respect to an applied electric field. A schematic of the molecular structure of a polarized electrostrictive polymer is shown in Fig. 2. As shown in Fig. 2, the direction of polarization of the electrostrictive polymer creates an axis of symmetry. Along this axis, the crystallites are oriented normal to the axis of symmetry. Each crystallite is oriented at a statistically random angle about the axis of symmetry. For a bulk sample of the electrostrictive polymer, the statistical orientation of the crystallites results in reflectional and rotational symmetries with respect to the axis of symmetry (Fig. 2). With these material symmetries, the bulk electrostrictive polymer is classified as a transversely isotropic material [64]. It will be henceforth assumed that the axis of symmetry of $\mathfrak{R}$ is aligned with the $\mathbf{e}_1$ basis vector.

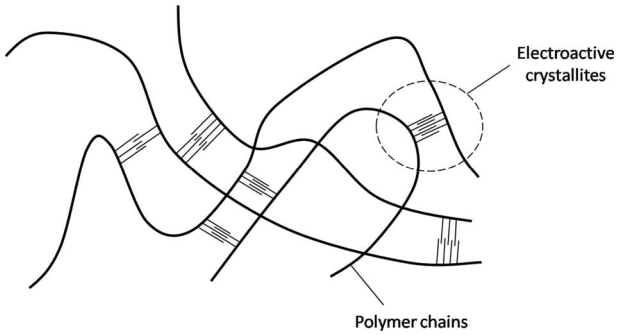

Fig. 1 Schematic of the molecular chains in an unpolarized electrostrictive polymer

For the given material symmetry and symmetry axis vector, a set of scalar invariants for $\mathbf{C}$ include $I_1=\text{tr}(\mathbf{C})$, $I_2=1/2[(\text{tr }\mathbf{C})^2-\text{tr}(\mathbf{C}^2)]$, $I_3=\det\mathbf{C}$, $I_4=C_{11}$, and $I_5={C_{12}}^2+{C_{13}}^2$, where $tr(\bullet)$ denotes the trace operator [64]. The scalar invariants for the vector $\mathbf{E}$ are E_1 and $E_2^2+E_3^2$. Scalar invariants for the coupling of $\mathbf{C}$ and $\mathbf{E}$ are $E_\alpha C_{1\alpha}$, $E_\alpha C_{\alpha\beta}C_{1\beta}$, and $E_\alpha C_{\alpha\beta}E_\beta$, where subscripts α and β have values of 2 and 3 and obey the summation convention. Together with the scalar invariant θ for temperature, a total of 11 invariants can be used to formulate the functional form of the constitutive equation (10*d*).

To simplify this process of establishing a functional form of the constitutive equation (10*d*), some additional assumptions need to be made regarding the material behavior. First, it has been shown [23] that while electroactive responses tend to be linear with θ, dielectric responses appear to be nonlinear with θ. Second, it has been observed that electrostrictive materials do not exhibit a reverse electroactive effect [36]. That is, an electric displacement is not generated when a mechanical load is applied to the material in the absence of an electric field, as is observed in piezoelectric materials. Third, residual electric displacements are observed for electroactive polymers that have been polarized [23]. The polarization of the material results in a nonzero $\mathbf{D}$ vector when the electric field vanishes. Fourth, electrostrictive materials exhibit a response that depends on E_1^2, while piezoelectric materials exhibit

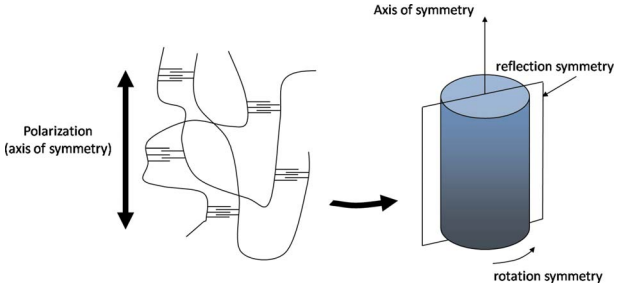

Fig. 2 Molecular structure of a polarized electrostrictive polymer (left) and the resulting bulk-level material symmetry (right)

a dependence on E_1. Fifth, electrostrictive polymers tend to be elastomeric and thus incompressible. Finally, no electroactive response is expected for the case in which $E_1=0$. With these assumptions and the invariants given above, the free-energy density is postulated to be

$$\Psi = A_1 + A_2 + A_3 + A_4 \tag{14}$$

where A_1, A_2, A_3, and A_4 are the elastic, electrostrictive, dielectric, and residual electric displacement responses, respectively. The elastic response is given by

$$A_1 = \tfrac{1}{2}(\alpha_1 + \alpha_2 T)(I_1 - 3) + \tfrac{1}{2}(\alpha_3 + \alpha_4 T)(I_2 - 3) + \tfrac{1}{2}\alpha_5 T I_1 - \tfrac{1}{2}p(I_3 - 1) \tag{15}$$

The electrostrictive response is

$$A_2 = -\tfrac{1}{2}(\alpha_6 + \alpha_7 T)E_1^2(I_4 - 1) \tag{16}$$

The dielectric response is

$$A_3 = -\tfrac{1}{2}(\alpha_8 + \alpha_9 T + \alpha_{10}T^2)E_1^2 - \tfrac{1}{2}(\alpha_{11} + \alpha_{12}T + \alpha_{13}T^2)(E_2^2 + E_3^2) \tag{17}$$

The residual electric displacement is established with

$$A_4 = -D_0 E_1 \tag{18}$$

In Eqs. (15)–(17), $\alpha_1, \alpha_2, \ldots, \alpha_{13}$ are material parameters, D_0 is the residual electric displacement, and T is the change in the ambient temperature T_0 resulting in the current absolute temperature θ ($\theta = T_0 + T$). The first two terms on the right-hand side of Eq. (15) are the Mooney–Rivlin response of the material (with temperature-dependent material properties), the third term introduces the thermal expansion coefficient α_5 and the last term enforces incompressibility with the Lagrange multiplier p. Substitution of Eqs. (14)–(18) into Eqs. (13*a*) and (13*b*) yields the constitutive equations for the stress tensor

$$\mathbf{S} = [(\alpha_1 + \alpha_2 T) + I_1(\alpha_3 + \alpha_4 T) + \alpha_5 T]\mathbf{I} - (\alpha_3 + \alpha_4 T)\mathbf{C} - pI_3\mathbf{C}^{-1} - (\alpha_6 + \alpha_7 T)E_1^2(\mathbf{e}_1 \otimes \mathbf{e}_1) \tag{19}$$

and the electric displacement vector components

$$D_1 = (\alpha_6 + \alpha_7 T)E_1(I_4 - 1) + (\alpha_8 + \alpha_9 T + \alpha_{10}T^2)E_1 + D_0 \tag{20a}$$

$$D_2 = (\alpha_{11} + \alpha_{12}T + \alpha_{13}T^2)E_2 \tag{20b}$$

$$D_3 = (\alpha_{11} + \alpha_{12}T + \alpha_{13}T^2)E_3 \tag{20c}$$

where $\mathbf{I}$ is the identity tensor. Note the nonlinear dependence of E_1 and I_4 on D_1 in Eq. (20*a*). The stress components S_{11}, S_{22}, S_{33}, S_{23}, S_{13}, and S_{12} are expected to vanish in the undeformed state with no applied electrical field and temperature change ($\mathbf{C}=\mathbf{I}$, $I_1=3$, $I_4=1$, $\mathbf{E}=\mathbf{o}$, $T=0$). Under this condition, Eq. (19) reveals

$$p = \alpha_1 + 2\alpha_3 \tag{21}$$

To simplify these expressions, the following quantities are defined as follows:

$$\beta_1(T) = \alpha_1 + \alpha_2 T \tag{22a}$$

$$\beta_2(T) = \alpha_3 + \alpha_4 T \tag{22b}$$

$$\beta_3(T) = \alpha_5 T \tag{22c}$$

$$\beta_4(T) = \alpha_6 + \alpha_7 T \tag{22d}$$

$$\beta_5(T) = \alpha_8 + \alpha_9 T + \alpha_{10}T^2 \tag{22e}$$

$$\beta_6(T) = \alpha_{11} + \alpha_{12}T + \alpha_{13}T^2 \tag{22f}$$

which are clearly temperature-dependent material properties, which are necessary to model with polymer materials below the glass transition temperature. Substitution of Eqs. (22*a*)–(22*f*) into Eqs. (19) and (20*a*)–(20*c*) results in a modified form of the constitutive equations for stress

$$\mathbf{S} = [\beta_1 + I_1\beta_2 + \beta_3]\mathbf{I} - \beta_2\mathbf{C} - pI_3\mathbf{C}^{-1} - \beta_4 E_1^2(\mathbf{e}_1 \otimes \mathbf{e}_1) \tag{23}$$

and electrical displacement

$$D_1 = \beta_4 E_1(I_4 - 1) + \beta_5 E_1 + D_0 \tag{24a}$$

$$D_2 = \beta_6 E_2 \tag{24b}$$

$$D_3 = \beta_6 E_3 \tag{24c}$$

where the temperature arguments associated with the temperature-dependent material parameters have been removed for brevity. Equations (23) and (24*a*)–(24*c*) describe the general three-dimensional electromechanical behavior of an incompressible electrostrictive polymer material. Equation (14) can be expressed in terms of the temperature-dependent parameters of Eqs. (22*a*)–(22*f*).

$$\Psi = \tfrac{1}{2}\beta_1(I_1 - 3) + \tfrac{1}{2}\beta_2(I_2 - 3) + \tfrac{1}{2}\beta_3 I_1 - \tfrac{1}{2}p(I_3 - 1) - \tfrac{1}{2}\beta_4 E_1^2(I_4 - 1) - \tfrac{1}{2}\beta_5 E_1^2 - \tfrac{1}{2}\beta_6(E_2^2 + E_3^2) - P_0 E_1 \tag{25}$$

Equation (25) is in a form that can be conveniently used to determine the response for specific electrostrictive polymer materials, which is demonstrated in Sec. 4.

4 Material Parameters

To demonstrate the functionality of the proposed constitutive model, the material parameters need to be quantitatively established for a sampling of electrostrictive polymer materials. Using data from the literature [20], the values of some of the material constants in Eqs. (23) and (24*a*)–(24*c*) have been determined at room temperature for three electrostrictive polyurethane material systems: PS 2000, PS 1000, and PM 2000. Details on these material systems may be found elsewhere [20]. The electromechanical properties of the materials were established by equating the mechanical components of the free-energy density given by Eq. (25) with an equivalent expression found elsewhere [65], with which the material parameters from the literature [20] have been characterized. The equating of the free energies was performed for four different boundary conditions: shear deformation with no applied electric field, axial elongation with no applied electric field, transversely applied electric field, and axial elongation with an applied electric field. It is important to note that the energy expression from the literature [65] was not established in a large-deformation hyperelastic framework, so the applied deformations in the current analysis were relatively small.

For each prescribed deformation and electric field, material parameters were determined by minimizing the sum of the squares of the errors between the free energies from the proposed model and those found in the literature. The material parameters were iteratively updated to minimize the differences in the free energies. As a result, the proposed model was characterized for the three material systems. The applied isochoric deformations and electric fields were specifically chosen to efficiently determine the material parameters in the constitutive equations given by Eqs. (23) and (24*a*)–(24*c*). The details of each deformation are given below.

4.1 Shear Deformation With No Applied Electric Field. For the case of simple shear deformation at the ambient temperature and no applied electric field ($\mathbf{E}=\mathbf{o}$), Eq. (1) is

$$x_1 = X_1 + \gamma X_2 \tag{26a}$$

$$x_2 = X_2 \tag{26b}$$

Table 1 Isotheral electromechanical material parameters for electrostrictive polymers at room temperature

	β_1 (MPa)	β_2 (MPa)	β_3 (MPa)	β_4 (MPa)m^2/V^2	β_5 (MPa)m^2/V^2	β_6 (MPa)m^2/V^2
PS 2000	11.2	1.6	0.0	$-2.1(10^{-16})$	$5.4(10^{-17})$	$5.4(10^{-17})$
PS 1000	6.3	0.9	0.0	$1.6(10^{-15})$	$6.4(10^{-17})$	$6.4(10^{-17})$
PM 2000	2.2	0.3	0.0	$8.4(10^{-16})$	$6.9(10^{-17})$	$6.9(10^{-17})$

$$x_3 = X_3 \tag{26c}$$

where γ is the shear strain. The components of $\mathbf{C}$ with respect to the basis set are $C_{11}=C_{33}=1$, $C_{22}=1+\gamma^2$, $C_{12}=\gamma$, and $C_{23}=C_{13}=0$. Based on these assumptions, Eq. (25) simplifies to

$$\Psi = \tfrac{1}{2}(\beta_1 + \beta_2)\gamma^2 \tag{27}$$

Together with the proceeding applied deformation, comparison of the strain energy function from the literature [65] with the corresponding material properties [20] for deformations in the range of $\gamma=0\rightarrow 0.02$ established the values of β_1 and β_2 shown in Table 1.

4.2 Axial Elongation With No Applied Electric Field. For the case of a uniaxial tension along the $\mathbf{e}_1$ axis at the ambient temperature with no applied electric field, Eq. (1) is

$$x_1 = \lambda X_1 \tag{28a}$$

$$x_2 = \frac{1}{\sqrt{\lambda}} X_2 \tag{28b}$$

$$x_3 = \frac{1}{\sqrt{\lambda}} X_3 \tag{28c}$$

where λ is the principal stretch along the $\mathbf{e}_1$ axis. The components of $\mathbf{C}$ with respect to the basis set are $C_{11}=\lambda^2$, $C_{22}=C_{33}=1/\lambda$, and $C_{23}=C_{13}=C_{12}=0$. Based on these assumptions, Eq. (25) simplifies to

$$\Psi = \frac{1}{2}\beta_1\left(\lambda^2 + \frac{2}{\lambda} - 3\right) + \frac{1}{2}\beta_2\left(2\lambda + \frac{1}{\lambda^2} - 3\right) \tag{29}$$

With the assumption that $\beta_1/\beta_2=7$ [66], the sum of the squares of the error were minimized between Eqs. (27) and (29) and the free energy found from the literature [65] for the range of $1\leq\lambda<1.02$. The resulting values of β_1 and β_2 are listed in Table 1 for all three polymer systems. These two material parameters represent the hyperelastic response of the electrostrictive polymers in the absence of an electric field.

4.3 Transversely Applied Electric Field. For the case of no deformation at the ambient temperature and an applied electric field of $\mathbf{E}=E\mathbf{e}_2+E\mathbf{e}_3$, Eq. (25) simplifies to

$$\Psi = -\beta_6 E^2 \tag{30}$$

Comparison of Eq. (30) with the small-deformation free-energy equation [65] reveals that β_6 is the permittivity in the $\mathbf{e}_2$ and $\mathbf{e}_3$ directions, which are perpendicular to the axis of symmetry. If it is assumed that permittivity in the $\mathbf{e}_1$ direction is the same, then it is apparent from Eq. (25) that $\beta_5=\beta_6$. From the data on the three polymer systems [20], the resulting values of β_5 and β_6 are shown in Table 1.

4.4 Axial Elongation With Applied Electric Field. For the case of uniaxial tension along the $\mathbf{e}_1$ axis at the ambient temperature and an applied electric field of $\mathbf{E}=E\mathbf{e}_1$ with no initial electric displacement, Eq. (1) is

$$x_1 = \lambda X_1 \tag{31a}$$

$$x_2 = \frac{1}{\sqrt{\lambda}} X_2 \tag{31b}$$

$$x_3 = \frac{1}{\sqrt{\lambda}} X_3 \tag{31c}$$

where λ is the principal stretch along the $\mathbf{e}_1$ axis. The components of $\mathbf{C}$ with respect to the basis set are $C_{11}=\lambda^2$, $C_{22}=C_{33}=1/\lambda$, and $C_{23}=C_{13}=C_{12}=0$. For this condition, Eq. (25) simplifies to

$$\Psi = \frac{1}{2}\beta_1\left(\lambda^2 + \frac{2}{\lambda} - 3\right) + \frac{1}{2}\beta_2\left(2\lambda + \frac{1}{\lambda^2} - 3\right) - \frac{1}{2}\beta_4 E^2(\lambda^2 - 1) - \frac{1}{2}\beta_5 E^2 \tag{32}$$

Although the assumption of no initial electric displacement is not realistic, it is necessary here for illustrative purposes because the formulation from the literature [20] did not include it. Therefore, for an accurate characterization of the current model using data from the model of Ref. [20], the initial electric displacement must be set to zero. Because the material parameters β_1, β_2, β_5, and β_6 have been determined with the preceding loading conditions, the only unknown parameter in Eq. (32) is the material parameter β_4 (β_3 is zero-valued at room temperature), which serves as an electromechanical coupling parameter, which is analogous to the piezoelectric constant in piezoelectric materials. For each material, the value of β_4 was determined by comparing the free energies from Eq. (32) and from the literature [20] and minimizing the sum of the squares of the errors between the two energies by iteratively adjusting the β_4 parameter. The energies were compared for a deformation range of $1\leq\lambda<1.02$ and an applied electric field of $E=1$ GV. The resulting values of β_4 for the three electrostrictive polymers are listed in Table 1.

5 Conclusions

The characterization of the model in this paper demonstrates its functional simplicity. The scalar free-energy density expression of Eq. (25) and the resulting constitutive relationships of Eqs. (23) and (24*a*)–(24*c*) have a relatively simple form and are very powerful in that they can describe the large-deformation behavior of the material as a function of temperature, applied deformations, and applied electric fields. Although a limited number of material parameters were established for the three electrostrictive elastomers, a full set of electrothermal-mechanical data on these materials could be used to fully characterize the model.

References

[1] Bauer, F., Fousson, E., and Zhang, Q. M., 2006, "Recent Advances in Highly Electrostrictive P(VDF-TrFE-CFE) Terpolymers," IEEE Trans. Dielectr. Electr. Insul., **13**(5), pp. 1149–1154.

[2] Bauer-Gogonea, S., Camacho-Gonzalez, F., Schwodiauer, R., Ploss, B., and Bauer, S., 2007, "Nonlinear Capacitance Dilatometry for Investigating Elastic and Electromechanical Properties of Ferroelectrets," Appl. Phys. Lett., **91**(12), p. 122901.

[3] Beom, H. G., Kim, Y. H., Kim, C. B., and Cho, C., 2008, "Modified Boundary Layer Analysis of an Electrode in an Electrostrictive Material," Arch. Appl. Mech., **78**(3), pp. 191–209.

[4] Butkewitsch, S., and Scheinbeim, J., 2006, "Dielectric Properties of a Hydrated Sulfonated Poly(Styrene-Ethylene/Butylenes-Styrene) Triblock Copolymer," Appl. Surf. Sci., **252**(23), pp. 8277–8286.
[5] Diaconu, I., Dorohoi, D. O., and Topoliceanu, F., 2006, "Electrostriction of a Polyurethane Elastomer-Based Polyester," IEEE Sens. J., **6**(4), pp. 876–880.
[6] Dubois, P., Rosset, S., Koster, S., Stauffer, J., Mikhailov, S., Dadras, M., de Rooij, N. F., and Shea, H., 2006, "Microactuators Based on Ion Implanted Dielectric Electroactive Polymer (EAP) Membranes," Sens. Actuators, A, **130–131**, pp. 147–154.
[7] Galler, N., Ditlbacher, H., Steinberger, B., Hohenau, A., Dansachmuller, M., Camacho-Gonzales, F., Bauer, S., Krenn, J. R., Leitner, A., and Aussenegg, F. R., 2006, "Electrically Actuated Elastomers for Electro-Optical Modulators," Appl. Phys. B: Lasers Opt., **85**(1), pp. 7–10.
[8] Ha, J. Y., Jeong, D. Y., Kim, J. S., and Yoon, S. J., 2007, "Fabrication of an Optical Grating Using High Electrostrictive Strain Polymer as a Template," J. Opt. A, Pure Appl. Opt., **9**(2), pp. 170–173.
[9] Xu, H., Shen, D., and Zhang, Q., 2007, "Structural and Ferroelectric Response in Vinylidene Fluoride/Trifluoroethylene/Hexafluoropropylene Terpolymers," Polymer, **48**(7), pp. 2124–2129.
[10] Kim, B. H., Choi, H. J., Park, H. S., Jeong, Y. D., Do Jeong, H., Lee, J. O., and Jo, N. J., 2006, "Preparation and Properties of Polyurethane/MMT Nanocomposite Actuators," Compos. Interfaces, **13**(2–3), pp. 285–297.
[11] Lam, T. Y., Lau, S. T., Chao, C., Chan, H. L. W., Choy, C. L., Cheung, W. Y., and Wong, S. P., 2007, "Characterization of Proton Irradiated Copolymer Thin Films for Microelectromechanical System Applications," Appl. Phys. Lett., **90**(4), p. 043511.
[12] Li, Z. M., Wang, Y. H., and Cheng, Z. Y., 2006, "Electromechanical Properties of Poly(Vinylidene-Fluoride-Chlorotrifluoroethylene) Copolymer," Appl. Phys. Lett., **88**(6), p. 062904.
[13] Pimpin, A., Suzuki, Y., and Kasagi, N., 2007, "Microelectrostrictive Actuator With Large Out-of-Plane Deformation for Flow-Control Application," J. Microelectromech. Syst., **16**(3), pp. 753–764.
[14] Ren, K., Liu, Y. M., Hofmann, H., Zhang, Q. M., and Blottman, J., 2007, "An Active Energy Harvesting Scheme With an Electroactive Polymer," Appl. Phys. Lett., **91**(13), p. 132910.
[15] Zhang, S., Huang, C., Klein, R. J., Xia, F., Zhang, Q. M., and Cheng, Z. Y., and 2007, "High Performance Electroactive Polymers and Nano-Composites for Artificial Muscles," J. Intell. Mater. Syst. Struct., **18**(2), pp. 133–145.
[16] Spillmann, C. M., Ratna, B. R., and Naciri, J., 2007, "Anisotropic Actuation in Electroclinic Liquid Crystal Elastomers," Appl. Phys. Lett., **90**(2), p. 021911.
[17] Xia, F., Tadigadapa, S., and Zhang, Q. M., 2006, "Electroactive Polymer Based Microfluidic Pump," Sens. Actuators, A, **125**(2), pp. 346–352.
[18] Zhang, S. H., Neese, B., Ren, K. L., Chu, B. J., Xia, F., Xu, T., Tadigadapa, S., Wang, Q., Zhang, Q. M., and Bauer, F., 2006, "Relaxor Ferroelectric Polymers, Thin Film Devices, and Ink-Jet Microprinting for Thin Film Device Fabrication," Ferroelectrics, **342**, pp. 43–56.
[19] Zhang, Q. M., Li, H. F., Poh, M., Xia, F., Cheng, Z. Y., Xu, H. S., and Huang, C., 2002, "An All-Organic Composite Actuator Material With a High Dielectric Constant," Nature (London), **419**(6904), pp. 284–287.
[20] Guillot, F. M., and Balizer, E., 2003, "Electrostrictive Effect in Polyurethanes," J. Appl. Polym. Sci., **89**(2), pp. 399–404.
[21] Shkel, Y. M., and Klingenberg, D. J., 1998, "Electrostriction of Polarizable Materials: Comparison of Models With Experimental Data," J. Appl. Phys., **83**(12), pp. 7834–7843.
[22] Shankar, R., Ghosh, T. K., and Spontak, R. J., 2007, "Electroactive Nanostructured Polymers as Tunable Actuators," Adv. Mater., **19**(17), pp. 2218–2223.
[23] Su, J., Ounaies, Z., and Harrison, J. S., 1999, "Ferroelectric and Piezoelectric Properties of Blends of Poly(Vinylidene Fluoride-Trifluorethylene) and a Graft Elastomer," *Proceedings of the Materials Research Society Symposium*, Q. M. Zhang, T. Furukawa, Y. Bar-Cohen, and J. Scheinbeim, eds., Materials Research Society, Boston, MA, pp. 95–100.
[24] Lorberg, H., 1884, "Ueber Electrostriction," Ann. Phys. Chem., **21**, pp. 300–329.
[25] Sacerdote, M. P., 1899, "Deformations Electriques Des Dielectriques Solides Isotropes," J. Phys. Theor. Appl., **8**(1), pp. 457–471.
[26] Sacerdote, M. P., 1901, "Sur un Cas Particulier de Deformation Electrique D'un Dielectrique Solide Isotrope," J. Phys. Theor. Appl., **10**, pp. 196–200.
[27] Adams, E. P., 1911, "On Electrostriction," Philos. Mag., **6**(22), pp. 889–900.
[28] Kemble, E. C., 1916, "Note on the End Effect in the Electrostriction of Cylindrical Condensers," Phys. Rev., **7**(6), pp. 614–624.
[29] Pauthenier, M., 1926, "Mesure Photgraphique de l'electrostriction dans le cas du Tetrachlorure de Carbone," C. R. Hebd. Seances Acad. Sci., **182**, pp. 121–123.
[30] Cady, W. G., 1929, "Electroelastic and Pyroelectric Phenomena," *International Critical Tables of Numerical Data, Physics, Chemistry and Technology*, E. W. Washburn, ed., McGraw-Hill, New York, pp. 207–212.
[31] Pauthenier, M., 1924, "L''Electrostriction Dans Les Liquides Tres Peu Birefringents," J. Phys. Radium, **5**, pp. 312–320.
[32] Bruhat, M. M. G., and Pauthenier, M., 1925, "Sur la Theorie de l'Electrostriction dans les Liquides Isolants," J. Phys. Radium, **6**(1), pp. 1–9.
[33] Ze, N. T., 1928, "Etude Experimentale des Deformations et des Changements de proprietes Optiques du Quartz Sous L'Influence du Champ Electrique," J. Phys. Radium, **9**(1), pp. 13–37.
[34] Stratton, J. A., 1941, *Electromagnetic Theory*, McGraw-Hill, New York.
[35] Mason, W. P., 1950, *Piezoelectric Crystals and Their Application to Ultrasonics*, Van Nostrand, New York.
[36] von Hippel, A. R., 1954, *Dielectrics and Waves*, Chapman and Hall, New York.
[37] Devonshire, A. F., 1954, "Theory of Ferroelectrics," Adv. Phys., **3**(10), pp. 85–130.
[38] Nye, J. F., 1957, *Physical Properties of Crystals: Their Representation by Tensors and Matrices*, Clarendon, Oxford.
[39] Landau, L. D., and Lifshitz, E. M., 1960, *Electrodynamics of Continuous Media*, Pergamon, New York.
[40] Eringen, A. C., 1962, *Nonlinear Theory of Continuous Media*, McGraw-Hill, New York.
[41] Toupin, R. A., 1956, "The Elastic Dielectric," Journal of Rational Mechanics and Analysis, **5**, pp. 850–915.
[42] Baumhauer, J. C., and Tiersten, H. F., 1973, "Nonlinear Electroelastic Equations for Small Fields Superposed on a Bias," J. Acoust. Soc. Am., **54**(4), pp. 1017–1034.
[43] Van Sterkenburg, S. W. P., 1991, "Measurement of the Electrostrictive Tensor of 8 Alkali-Halides," J. Phys. D, **24**(10), pp. 1853–1857.
[44] Meng, Z. Y., and Cross, L. E., 1985, "Determination of the Electrostriction Tensor Components in Single-Crystal CaF_2 From the Uniaxial-Stress Dependence of the Dielectric Permittivity," J. Appl. Phys., **57**(2), pp. 488–491.
[45] Damjanovic, D., 1998, "Ferroelectric, Dielectric and Piezoelectric Properties of Ferroelectric Thin Films and Ceramics," Rep. Prog. Phys., **61**(9), pp. 1267–1324.
[46] Sundar, V., and Newnham, R. E., 1992, "Electrostriction and Polarization," Ferroelectrics, **135**(1–4), pp. 431–446.
[47] Tiersten, H. F., 1971, "On the Nonlinear Equations of Thermo-Electroelasticity," Int. J. Eng. Sci., **9**, pp. 587–604.
[48] McMeeking, R. M., Landis, C. M., and Jimenez, S. M. A., 2007, "A Principle of Virtual Work for Combined Electrostatic and Mechanical Loading of Materials," Int. J. Non-Linear Mech., **42**(6), pp. 831–838.
[49] McMeeking, R. M., and Landis, C. M., 2005, "Electrostatic Forces and Stored Energy for Deformable Dielectric Materials," Trans. ASME, J. Appl. Mech., **72**(4), pp. 581–590.
[50] Dorfmann, A., and Ogden, R. W., 2005, "Nonlinear Electroelasticity," Acta Mech., **174**(3–4), pp. 167–183.
[51] Pao, Y. H., 1978, "Electromagnetic Forces in Deformable Continua," *Mechanics Today*, Vol. 4, S. Nemat-Nasser, ed., Pergamon, New York, pp. 209–305.
[52] Maugin, G. A., 1988, *Continuum Mechanics of Electromagnetic Solids*, North-Holland, Amsterdam.
[53] Eringen, A. C., and Maugin, G. A., 1990, *Electrodynamics of Continua: I Foundations and Solid Media*, Springer, New York.
[54] Eringen, A. C., and Maugin, G. A., 1990, *Electrodynamics of Continua: II Fluids and Complex Media*, Springer, New York.
[55] Hutter, K., van de Ven, A. A. F., and Ursescu, A., 2006, *Electromagnetic Field Matter Interactions in Thermoelastic Solids and Viscous Fluids*, Springer, New York.
[56] Zhao, X. H., and Suo, Z. G., 2008, "Electrostriction in Elastic Dielectrics Undergoing Large Deformation," J. Appl. Phys., **104**(12), p. 123530.
[57] Truesdell, C. A., and Toupin, R. A., 1960, "The Classical Field Theories," *Encyclopedia of Physics*, Vol. III/1, S. Flugge, ed., Springer-Verlag, Berlin, Germany.
[58] Truesdell, C., and Noll, W., 2004, *The Non-Linear Field Theories of Mechanics*, Springer-Verlag, New York.
[59] Eringen, A. C., 1999, *Microcontinuum Field Theories*, Springer-Verlag, New York.
[60] de Groot, S. R., and Suttorp, L. G., 1972, *Foundations of Electrodynamics*, American Elsevier, New York.
[61] Eringen, A. C., 1967, *Mechanics of Continua*, Wiley, New York.
[62] Suo, Z. G., Zhao, X. H., and Greene, W. H., 2008, "A Nonlinear Field Theory of Deformable Dielectrics," J. Mech. Phys. Solids, **56**(2), pp. 467–486.
[63] Bustamante, R., Dorfmann, A., and Ogden, R. W., 2008, "Nonlinear Electroelastostatics: A Variational Framework," ZAMP, **60**(1), pp. 154–177.
[64] Spencer, A. J. M., 1971, "Theory of Invariants," *Continuum Physics*, Vol. 1, A. C. Eringen, ed., Academic, New York, pp. 239–353.
[65] Guillot, F. M., Jarzynski, J., and Balizer, E., 2001, "Measurement of Electrostrictive Coefficients of Polymer Films," J. Acoust. Soc. Am., **110**(6), pp. 2980–2990.
[66] Anand, L., 1986, "Moderate Deformations in Extension Torsion of Incompressible Isotropic Elastic-Materials," J. Mech. Phys. Solids, **34**(3), pp. 293–304.